NASA/CR—2000-210244 R99AEB169

Aeroacoustic Prediction Codes

P. Gliebe
GE Aircraft Engines, Cincinnati, Ohio

R. Mani
GE-Corporate Research Development, Schenectady, New York

H. Shin
GE Aircraft Engines, Cincinnati, Ohio

B. Mitchell, G. Ashford, S. Salamah, and S. Connell
GE-Corporate Research Development, Schenectady, New York

August 2000

The NASA STI Program Office . . . in Profile

Since its founding, NASA has been dedicated to the advancement of aeronautics and space science. The NASA Scientific and Technical Information (STI) Program Office plays a key part in helping NASA maintain this important role.

The NASA STI Program Office is operated by Langley Research Center, the Lead Center for NASA's scientific and technical information. The NASA STI Program Office provides access to the NASA STI Database, the largest collection of aeronautical and space science STI in the world. The Program Office is also NASA's institutional mechanism for disseminating the results of its research and development activities. These results are published by NASA in the NASA STI Report Series, which includes the following report types:

- TECHNICAL PUBLICATION. Reports of completed research or a major significant phase of research that present the results of NASA programs and include extensive data or theoretical analysis. Includes compilations of significant scientific and technical data and information deemed to be of continuing reference value. NASA's counterpart of peer-reviewed formal professional papers but has less stringent limitations on manuscript length and extent of graphic presentations.

- TECHNICAL MEMORANDUM. Scientific and technical findings that are preliminary or of specialized interest, e.g., quick release reports, working papers, and bibliographies that contain minimal annotation. Does not contain extensive analysis.

- CONTRACTOR REPORT. Scientific and technical findings by NASA-sponsored contractors and grantees.

- CONFERENCE PUBLICATION. Collecte papers from scientific and technical conferences, symposia, seminars, or othe meetings sponsored or cosponsored by NASA.

- SPECIAL PUBLICATION. Scientific, technical, or historical information from NASA programs, projects, and missions, often concerned with subjects having substantial public interest.

- TECHNICAL TRANSLATION. English-language translations of foreign scientifi and technical material pertinent to NAS/ mission.

Specialized services that complement the ST Program Office's diverse offerings include creating custom thesauri, building customize data bases, organizing and publishing resea results . . . even providing videos.

For more information about the NASA STI Program Office, see the following:

- Access the NASA STI Program Home Pa at ***http://www.sti.nasa.gov***

- E-mail your question via the Internet to help@sti.nasa.gov

- Fax your question to the NASA Access Help Desk at (301) 621-0134

- Telephone the NASA Access Help Desk a (301) 621-0390

- Write to:
  NASA Access Help Desk
  NASA Center for AeroSpace Informatio
  7121 Standard Drive
  Hanover, MD 21076

NASA/CR—2000-210244

R99AEB169

Aeroacoustic Prediction Codes

P. Gliebe
GE Aircraft Engines, Cincinnati, Ohio

R. Mani
GE-Corporate Research Development, Schenectady, New York

H. Shin
GE Aircraft Engines, Cincinnati, Ohio

B. Mitchell, G. Ashford, S. Salamah, and S. Connell
GE-Corporate Research Development, Schenectady, New York

Prepared under Contract NAS3–27720

National Aeronautics and
Space Administration

Glenn Research Center

August 2000

Available from

NASA Center for Aerospace Information
7121 Standard Drive
Hanover, MD 21076
Price Code: A14

National Technical Information Serv
5285 Port Royal R
Springfield, VA 22
Price Code: A

Available electronically at http://gltrs.grc.nasa.gov/GLTRS

Table of Contents

Table of Contents (Continued)

Table of Contents (Continued)

Table of Contents (Concluded)

List of Illustrations

List of Illustrations (Continued)

List of Illustrations (Continued)

List of Illustrations (Continued)

List of Illustrations (Continued)

List of Illustrations (Continued)

List of Illustrations (Continued)

List of Illustrations (Continued)

List of Illustrations (Concluded)

List of Tables

1.0 Introduction

1.1 Background

The NASA Advanced Subsonic Transport Technology (AST) Noise Reduction Program has a goal of demonstrating a 10-decibel (dB) reduction in effective perceived noise level (EPNL) for several classes of civil aircraft, relative to 1992 technology aircraft community noise levels. Of this 10-dB reduction in EPNL, a 6-dB reduction in engine or propulsion system noise level is targeted. The remaining reduction is targeted to be demonstrated from reductions in airframe noise, from improvements in aircraft performance, and from defining improved operational (takeoff and landing) procedures. A key ingredient to achieving the 6-dB propulsion system noise reduction goal is having accurate design and analysis tools and codes available that capture the important physics of engine noise generation, propagation, and radiation for each of the significant component noise sources in an aircraft engine. These tools should enable designers to carry out design studies, investigate new concepts for noise reduction, explain observed results from tests and experiments, and guide the design of features that will provide the required noise reduction.

GE Aircraft Engines (GEAE) has been actively developing component noise prediction models and codes for many years under Independent Research and Development (IR&D) funding and NASA contract. Model and code developments include jet noise modeling for complex nozzle configurations (the MGB code), fan broadband and tone noise generation and suppression models and codes, and engine system noise modeling and prediction methods.

The program described herein was built on the above GEAE noise model development foundations and expertise and was carefully planned to focus on the technical areas deemed most important to system noise reduction. It was observed that significant progress was being made in other NASA-sponsored programs with other contractors on fan harmonic tone noise modeling and on jet noise modeling. The emphasis in this program was therefore on new and improved models for the various sources of fan "broadband" noise and combustor-related core noise. Improved models and codes in these technology areas would then compliment, rather than duplicate, other NASA-sponsored work, allowing the NASA AST program to be more productive. A philosophy of the NASA AST Noise Reduction Program is that participating contractors could divide the work to be done and share the results with others (to as great an extent as possible) without compromising proprietary information. This philosophy was adopted to avoid wasting funding by having each contractor develop the same technologies. It was in the spirit of this philosophy that the program reported herein was designed.

It was also expected that much of the modeling and code development for fan noise could be transferable (with some additional development) to low pressure turbine (LPT) noise — another significant noise source for some engine applications. GEAE plans to exploit this in future programs. In addition, needed improvements were identified in the analytic descriptions of three-dimensional (3D) turbulence velocity correlation functions that make up the noise source descriptions for turbulence-generated broadband noise for fans and jets. Because of this, a task was included to quantify these turbulence correlations for fan broadband noise source model application.

1.2 Objectives

The objective of this program was to establish validated prediction and design analysis tools — methods and codes — applicable to high-bypass commercial turbofans for: (1) fan broadband noise, (2) fan multiple pure tone (MPT) noise, and (3) low-emissions combustor (LEC) noise.

The program consisted of four major subtasks, as follows:

- Subtask 1 – Improved Aeroacoustic Turbulence Model
- Subtask 2 – Fan Broadband Noise Model
- Subtask 3 – Fan MPT Noise Model
- Subtask 4 – Core Noise Model

Subtask 1 provides improvements in turbulence descriptions and guidance for modeling that feed into the fan broadband noise model development effort of subtask 2. Subtasks 1 and 2 combined focus on the eventual objective of reducing broadband noise from high-bypass engines. The third subtask addresses MPT fan noise generated due to rotor-bound shock wave formations produced when fan rotors operate at supersonic tip speeds. Subtask 4 addresses possible sources of core noise from newer, low-emissions combustors.

1.3 Technical Approach

1.3.1 Subtask 1 – Improved Aeroacoustic Turbulence Model

The objective of this subtask was to glean as much information from existing data and prediction models as possible and to guide formulation and calibration of the fan broadband noise modeling effort of subtask 2. A data-mining effort was carried out using past GE experimental program results where turbulence measurements were made.

Existing data from GEAE Low Speed Research Compressor (LSRC) test programs were reviewed for relevant turbulence information that could help quantify the turbulence characteristics identified in past and current modeling efforts as playing a role in fan stage broadband noise generation. The LSRC is a four-stage compressor with inlet guide vanes. Samples of such turbulence measurements are reported by Camp and Shin (Reference 1). Under an IR&D project during 1996, a special build of the LSRC was configured to simulate a fan stage with large axial spacing, and extensive rotor wake hot-wire surveys were made. Extensive use was made of these data in developing empirical models for rotor wake mean flow and turbulence characteristics. In a complimentary program, Professor William Davenport of Virginia Tech modeled the tip section of the rotor of this LSRC fan simulation in a linear cascade facility and carried out extensive unsteady flow survey measurements under a NASA grant.

Additional data analyses were carried out on the hot-wire rotor wake measurements made on the GEAE Universal Propulsion Simulator (UPS) fan at NASA Lewis in 1994 (Reference 2) to extract turbulence spectral and length-scale parameters relevant to fan broadband noise produced by rotor wakes.

Existing data from GEAE UPS acoustic test programs were reviewed and analyzed in detail to quantify the behavior of fan broadband noise as a function of fan tip speed and geometry changes. Fan broadband noise spectral shape changes, forward versus aft radiation differences, and directivity patterns were identified for the fan tested in the 1994 UPS test at NASA (Reference 3).

1.4 Subtask 2 – Fan Broadband Noise Model

This subtask aims at producing a quantitatively accurate prediction procedure for broadband noise from high-bypass fans. Under NASA contract NAS3-26617 (Task Order 33) detailed analyses and

code development were initiated for fan broadband noise due to inlet turbulence interacting with a blade row. The sources of turbulence considered in that effort were boundary layer turbulence and turbulence in the wake of an upstream blade row. Many development needs for improving the broadband noise prediction were identified, based on this study (and prior internal GEAE work), reported in Reference 4. The improvements and extensions recommended in Reference 4 form the basis of this subtask.

With the current GEAE model for quadrupole noise (Reference 4), the relatively weak attenuation of the rotor locked flowfield gives divergent "quadrupole" noise contributions for transonic and supersonic relative inlet Mach numbers, when interactions with inflow turbulence are considered. The current GEAE procedure of including quadrupole noise does, to some extent, account for "shock" turbulence interaction as a source of broadband noise, but it is probably only valid for weak shocks; therefore, extensions to handle strong shocks are required. Finally, source noncompactness effects on "potential" flow field-gust interaction (quadrupole noise) have been found to be crucial to avoid overestimation of broadband noise, particularly at high frequencies. GEAE therefore extended the current quadrupole source model described above to include strong shocks and source noncompactness effects.

The quadrupole component is predicted to be the dominant contribution to turbulence/blade-row-interaction noise; therefore, the focus is on improving this aspect of the model. The dipole contribution is currently predicted to be very small except at low tip speeds and low frequencies. Because of this, to expend resources to improve the dipole model currently used is not considered worthwhile. The extension, for example, to a cascade response formulation (the current model, Reference 4, uses an isolated airfoil response formulation) would probably not appreciably change the relative importance of the dipole source and therefore not improve the absolute noise level prediction.

An extension to three-dimensional blade rows, and consequently to treated ducts, was addressed initially by consideration of blades of infinite span and the introduction of correlation lengths in the spanwise direction in the model formulation. This modeling approach was extended to rectangular ducts, followed by annular ducts. The current model (Reference 4) uses a two-dimensional strip theory assumption and therefore has no radial mode content. The extension to an infinite-span 3D model recognizes the spanwise correlation length separately from the axial and transverse correlation lengths. This has the effect of dividing the annulus into incoherent strips, each with a spanwise correlation length (the current 2D model assumes perfect coherence along the span). The 3D rectangular duct model extension incorporates a modal expansion of each of the strips, assuming as a first approximation a "top hat" energy distribution, into the duct acoustic modes. The annular duct extension replaces the rectangular duct sine/cosine duct mode amplitude functions with appropriate annular duct Bessel Functions.

Broadband noise entails consideration of a wide range of frequencies and a large number of propagating modes for each frequency; hence, a relatively simple formulation is needed initially to consider treatment effects and predict farfield directivity. A duct suppression model and a directivity prediction model, along the lines of the cut-off ratio dependency ideas developed by Dr. Ed Rice while at NASA Lewis, were developed under subcontract to Dr. Rice through Hersh Acoustical Engineering. The Rice cut-off ratio model assumes equal energy participation for all cut-on modes for a given frequency. The model development extensions to 3D annular ducts provide both circumferential and radial mode energy distributions at each computed frequency. The Rice directivity

model was extended to couple with the in-duct source modal power prediction to estimate the farfield radiation on a mode-by-mode basis and sum the modal contributions in the farfield.

Measurements presented at the NASA-sponsored Boeing workshop on fan broadband noise (April 11–12, 1995) suggest that the turbulence incident on both rotors and stators is strongly nonisotropic and distinctly (spatially) inhomogeneous. Although the current model incorporates a 2D axisymmetric turbulence model, it is not based on length scales normally measured by single-point probe or hot-wire systems and does not distinguish between circumferential and spanwise length scales and intensities. Narrowband analysis of broadband noise indicates (at least based on the Boeing workshop results) that "haystacking" of broadband noise around the blade-passing frequency (BPF) harmonics occurs at subsonic speeds for inlet-radiated noise. In the data presented by Boeing, haystacking is not evident at supersonic tip speeds and is often less evident in the exhaust direction. All these spectral effects and changes with tip speed should be modeled in the prediction. The current turbulence model was therefore reformulated and extended to include separate spanwise and circumferential length scales and to have the option of basing the streamwise and cross-stream component turbulence spectra on single-point measurements and corresponding single-point, time-delayed correlation length scales.

The phrase "self-noise" can be defined as the noise emitted by a blade row with no turbulence explicitly incident on it. At the Boeing workshop, removal of boundary layer turbulence by suction yielded considerably smaller changes in noise (especially for the so-called 100% suction case) than would be indicated by the changes in boundary layer thickness and turbulence intensity induced by suction. This implies that self-noise is a significant noise source. A less empirical accounting of self-noise from a blade row is therefore a key requirement for accurate broadband noise prediction. An improved self-noise model was therefore developed, based on extending past semiempirical models for self-noise, using concepts employed in the turbulence/blade-row-interaction models.

1.5 Subtask 3 – Fan MPT Noise Model

The objective of this task was to establish an simple MPT noise prediction procedure based on uniform-rotor Computational Fluid Dynamics (CFD) analysis of BPF tonal content in conjunction with information on an engineering (statistical) correlation of blade-to-blade nonuniformities effects. This enables rapid estimation of the MPT content of real fans based on anticipated blade-to-blade variations.

It has been assessed that the trend to wide-chord fans with fewer blades will result in lower frequency MPT noise, which is harder to attenuate with current inlet treatment depth and length restrictions. MPT noise is not just a community noise contribution issue (advanced cycles with higher bypass ratios have lower jet noise, so the MPT noise at takeoff sets a noise floor), but it is also a cabin noise issue. According to current thinking, MPT noise arises from the rotation or spinning of the steady, circumferentially nonuniform, flowfield locked to the rotor. Apparently, small variations of rotor blade geometry from blade to blade generate shaft-order harmonic frequency tones in the farfield.

A prediction model and associated computer code were developed for predicting the spectral characteristics of fan MPT or "buzz saw" noise. To model the physics properly, the prediction of MPT noise requires transonic steady CFD capability with special ability to capture small blade-to-blade variations. An adaptive mesh CFD code developed at GE was therefore applied (in both 2D and 3D versions) to the problem of predicting the MPT content of a transonic rotor with blade-to-blade variations. A unique aspect of this subtask is that, since full annulus blade-to-blade CFD calculation

with detailed specification of blade-to-blade variations is impractical as a routine exercise, an "approximation procedure" amenable for use at the design stage was developed. This approximation procedure establishes redistribution of blade-passing tone harmonic energy into the subharmonic frequencies based on a statistically based correlation between subharmonic spectrum shape, the statistically derived blade-to-blade geometry variations, and superposition of elemental blade geometry variation CFD solutions.

As a first step, the likely variations in blade geometry were established in terms of design variables that are of significance — such as stagger angle, pitch, camber angle, thickness, etc. A statistical analysis of existing fan blade inspection and tolerance data was carried out to generate mean and standard deviation levels for these parameters.

Calculations based on these 2D and 3D CFD methods were accomplished for representative rotor designs, with no blade-to-blade variations, to predict BPF harmonic noise for perfectly uniform rotors. Following this, a systematic study of individual parametric variations (for example, variations of stagger angle corresponding to fixed mean and fixed standard deviation) using full-annulus CFD were carried out. In these full-annulus predictions, the MPT spectra were assessed relative to the BPF harmonic levels associated with the uniform rotor cases.

Since a full-annulus, blade-to-blade CFD calculation with detailed specification of blade-to-blade variations is impractical as a routine exercise, an "engineering procedure" amenable for use at the design stage was developed, based on the concept of superposition of elementary or "baseline" blade geometry variation solutions.

The resulting MPT noise prediction model and procedure were validated against GEAE proprietary engine fan data for three cases for which blade-to-blade variation geometry inspection data were available. Cases were run for two additional scale-model fan rotors (one radial and one swept design) that will be tested as part of Area of Interest 14 of the CPN contract, at NASA Lewis. Further validation of the model can be carried out in the future.

1.6 Subtask 4 – Core Noise Model

Although many current production engine designs do not produce a significant level of core noise, experimental evidence shows that newer low-emissions combustors produce noise levels as much as 5–8 dB higher than their predecessors. As other engine component noise sources (fan and jet) are reduced, core noise can set a floor to real reduction in total engine noise. A good core noise prediction model is needed that reflects modern, low-emissions combustor technology so that the core noise floor can be identified and the means for lowering that floor can be explored if required.

It is well known that combustion processes can generate farfield noise. Hot spots (circumferential and radial variations of total temperature) at the combustor exit induce pressure waves as they convect through a multistage turbine. This makes a multistage turbine both beneficial (in terms of attenuating pressure waves at combustor exit) and detrimental, by providing a means for conversion of hot spots to noise.

Two core noise prediction models were developed in Subtask 4 to predict the directivity and spectral content of the farfield noise generated by low-emission combustors for high-bypass engines. First, existing GEAE acoustic data were analyzed to extract combustor acoustic power output and correlate it as a function of the combustor operating parameters. Multiple regression techniques were used to develop empirical expressions for the dependency of combustor-related core noise on various

cycle parameters and combustor geometric parameters. A multilobe spectral model was used. The model used GEAE proprietary engine data for both advanced low-emissions (dual-annular combustor or DAC) and conventional low-emissions (single-annular combustor or SAC) designs. The new correlation was compared with the existing GEAE empirical model, and the effects of combustor-related core noise on total engine system flyover noise were assessed for the old and modern combustors (for selected 1992 technology aircraft missions).

Second, an analytical/computational model for the transmission and propagation of combustor unsteady temperature fluctuations or hot spots through downstream turbine stages, which can generate farfield noise, was developed. The spectrum of these hot spots was quantified using a GEAE 3D combustor flow analysis code, and then multiple-blade-row actuator disk theory was used to determine the transmitted farfield noise. A simple radiation model (one which determines farfield radiation as a function of cut-off ratio) was employed, similar to that developed for fan broadband noise, to predict the farfield sound directivity from in-duct power levels.

The radial profile and spectrum of temperature fluctuations emitted by combustors was estimated using the well-known GE CONCERT3D CFD combustor code. Since these fluctuations arise from turbulent mixing, the values of turbulent kinetic energy and dissipation rate were used to derive an approximate length scale associated with the fluctuations. Multiblade-row actuator disk theory applied to the multistage turbines was used to evaluate the contribution of combustor-hot-spot/turbine interactions to farfield noise. The actuator disk approach appears to be a valid approximation because turbine chord and pitch are small compared to typical wavelengths of combustor noise. The actuator disk theory analysis determines both the transmission loss of noise (pressure waves) generated in the combustor and the generation of noise by convection of hot spots (entropy waves) through the turbine stages. A simple radiation model based on cut-off ratio was used to determine directivity.

The described CFD analysis, coupled with the actuator disk theory model, will help in diagnosing the significant mechanisms (such as combustor-generated pressure waves versus turbine-generated pressure waves resulting from the combustor-generated entropy wave transmission) and will help in identifying why low-emission combustors are observed to be noisier than older generation combustors. The model will also provide guidance in improving and fine-tuning the combustor-related core noise empirical correlation.

2.0 Summary

As part of the NASA Advanced Subsonic Transport (AST) Noise Reduction Technology effort, computer codes are being developed to provide quantitative prediction, design, and analysis capability for aircraft engine noise sources. Several prediction methods and codes were developed, in the program reported herein, for the purpose of providing accurate design and analysis tools that can identify and define lower-noise aircraft engines. These methods and codes focus on fan broadband and "buzz saw" noise and on low-emissions-combustor noise. They compliment the work done by other contractors under the NASA AST program to develop methods and codes for fan harmonic tone noise and jet noise. The methods and codes developed and reported herein employ a wide range of approaches, from the strictly empirical to the completely computational, with some being semi-empirical, analytical, and/or analytical/computational. Emphasis was placed on capturing the essential physics while still considering the method or code utility as a practical design and analysis tool for everyday engineering use.

The following paragraphs summarize the methods and codes developed, the interesting results and observations noted in the course of exercising the methods and codes, and the validation carried out to quantify the accuracy of the codes in terms of predicting absolute levels and parametric trends.

2.1 Fan Aeroacoustic Turbulence Model Development

A primary contributor to engine source noise is the high-bypass fan component. Hugh-bypass fans generate both tones and broadband noise. This effort focused on providing an improved model for the fan rotor exit flow mean and turbulence properties for use in predicting the broadband noise generated by rotor exit flow turbulence interaction with the downstream stator vanes. An empirical correlation was developed using the results of hot-wire surveys from a low-speed fan stage test, and the correlation was validated with a set of scale-model, high-speed fan test hot-wire survey data.

A low-speed fan stage (LSFS) simulation test was previously carried out under a GEAE IR&D project, and three-axis hot-wire probe measurements were made, so that all three components of the mean and turbulent velocity field could be assessed. The measurements were made at five axial locations behind the rotor, corresponding to a range of spacing-to-chord ratios from 0.13 to 2.0. Data were taken at three fan throttle settings, corresponding to three fan loading conditions, all at the same fan tip speed of 210 ft/s.

The LSFS data obtained from the IR&D project were believed to be the most complete set of rotor exit survey data available for development of an empirical model, so they was used as the basis for empirical correlations subsequently developed under this NASA program. Empirical correlations explored were taken from past published wake data methods found in the literature. The approach finally adopted was that of Wygnanski, Champagne, and Marasli (Reference 5). This approach based the evolution of both mean and turbulence properties on scaling with the airfoil trailing-edge momentum thickness. Reasonable correlations were obtained for fan/rotor spanwise locations outside the end-wall secondary flow regions, and the correlations were found to agree well with similar (but much more limited) data taken on a high-speed fan stage under a previous NASA test program. These data are reported in Reference 2.

A cooperative effort with Dr. Chunille Hah of NASA Lewis also used CFD to predict the measured flowfield results — and hopefully to provide guidance on developing the correlation. Reasonable

agreement was obtained between the CFD code results and the hot-wire results, substantiating the results of this program. These results also suggest that it may be possible to use CFD to produce the needed turbulence information for prediction of fan broadband noise in the near future.

The final outcome of this study was a set of empirical, algebraic formulas that can be used to predict mean velocity and turbulence properties in the rotor exit wake region. Guidance is also given for how to estimate the rotor end-wall turbulence properties, based on the rotor wake properties just outside the end-wall regions. The results of these rotor wake correlations were used to generate rotor exit and stator inlet wake mean velocity and turbulence distributions for the fan stage tested in References 2 and 3 at several fan tip speeds. Acoustic predictions were made using the fan broadband rotor/stator-interaction noise model described in Reference 4 and using a preliminary version of the model reported herein in a later section. Results showed that, compared with the old wake model employed in Reference 4, the new wake correlation model significantly increases predicted high-frequency noise, over the range of fan speeds investigated. For supersonic tip speeds, the increase is less and is significant only for the forward radiation; aft-radiation effects are relatively small.

2.2 Fan Broadband Noise Model Development

Five areas of activity were pursued that constituted the principal efforts to improve the GEAE fan broadband noise model:

1. A fundamental CFD-based study was carried out aimed at clarifying the role of quadrupole and dipole noise in fan noise. A case of a single shear wave interacting with a blade row with loading was studied. Two-dimensional CFD was used. The conclusion of this study was that even for pressure ratios exceeding 1.2 in these studies and for frequencies exceeding three times blade passing frequency, quadrupole noise is a significant contributor to upstream-radiated noise.
2. The extension of the basic GEAE fan noise model to include 3D effects was carried out. Noise generation in an annulus was considered. The decomposition of the 3D model using Fourier Bessel analysis into a sequence of 2D problems was carried out. Complexities were introduced by the need to use spanwise eigenfunctions based on Bessel function.
3. Directivity effects were discussed, and a simplified procedure for predicting directivity based on a frequency parameter and cut-off ratio of the duct modes of interest was developed.
4. The ability to construct an adequate anisotropic turbulence model based only on single-point, two-component measurements was demonstrated.
5. An improved model for predicting self-noise from a blade row (for example, the noise as would be emitted with no incoming turbulence) was developed.

The revised GEAE fan broadband noise model, incorporating the results of all the new developments under the present contract, was applied to 10 cases of experimental data from scale-model fans. A key aspect of the predictions for the last four cases is the use of 3D Reynolds-averaged Navier–Stokes (RANS) CFD. It should be noted that 3D RANS CFD is not merely a useful tool in broadband noise prediction, it is an essential element if true pretest predictions are to be made. Length scales needed to predict noise are currently not available in any obvious sense from the RANS results, and this area needs further evaluation. The theory-data comparisons for the 10 cases evaluated provide reasonable agreement given the many possible sources of error. Variations of noise with tip speed and pressure ratio (at fixed speed) are well predicted. The bulk of the theory/data comparisons are

for the power watt level (PWL) spectrum, and more exploration is needed for directivity effects and effects of treated walls. The theory developed in this contract does incorporate an approximate method for predicting the effects of treated walls.

2.3 Fan Multiple Pure Tone Model Development

MPT or "buzz saw" noise is generated in fans with supersonic tip speeds and occurs at the part-speed cutback condition associated with takeoff. It is a significant component of both cabin and environmental noise associated with the fan. At part-speed conditions, a bow shock forms and propagates a significant distance upstream. The strength an position of the upstream running normal shock is very sensitive to blade geometry variations. The resulting azimuthal pressure field upstream of the fan contains discrete tones below the blade-passing frequency that are multiples of shaft orders. The geometry variations typically arise from manufacturing tolerances. Stagger angle differences of as small as 0.1° can give rise to significant MPT noise.

The objective of the work presented here is to develop and validate a CFD based model for predicting the MPT's from specified blade geometry variations. For a variety of reasons, 3D CFD methods were required. It was found that amplitudes of the various MPT components were linear with blade shape changes. Using this result, a prediction method based on a superposition technique was developed. The model requires a multiple-passage CFD simulation where one blade (two passages) has been modified. Using this simulation, the dependency of the upstream pressure field on a blade change can be derived. The MPT spectra for a fan where the geometry of all blades has been changed can be estimated by superposing the solutions for the individual changes. The method was validated using two sets of engine acoustic data.

2.4 Low-Emissions Combustor Noise Model Development

The motivation for this study is the observation that, under conditions of low-power operation, core noise from an aircraft engine (which tends to be in the range of 400 Hz to 1 kHz for modern high-bypass turbofans) equipped with a low-emission combustor (LEC) appears to be much more pronounced than from an engine equipped with a standard combustor (SC). The difference in peak sound pressure level (SPL) between the two combustor types associated with core noise can be as high as 10 to 15 dB. The difference is virtually nonexistent at full power. A key difference between a LEC and a SC at low power is that staged combustion (such as radially staged) employed with a LEC results in much more spatially inhomogeneous heat release in the LEC case. The associated inhomogeneous temperature field can be a source of a large temperature fluctuation, often called a "hot spot" or entropy wave. Hot spots, when convected through multistage turbomachinery, can generate noise in the farfield. The possibility of this difference in temperature fluctuations at the combustor exit being the cause of the farfield noise difference was examined in the present effort.

A 3D CFD calculation was first carried out for a LEC and an SC operating at low power. Using the fast-chemistry, "mixed is burned" model, the level of temperature fluctuations at combustor exit for the two cases were calculated. The mean temperature as well as temperature fluctuations were circumferentially averaged to obtain radially averaged information.

An actuator disk based multistage turbomachinery analysis was used to compute noise generated aft of the turbomachinery due to the entropy waves incident on the turbomachinery. In the case of turbomachinery with all blade rows being unchoked, the method of solution is essentially as has

appeared in earlier literature. The case where a blade row may be choked (and it is not the most downstream blade row) turns out to need special treatment. A spectral representation of the incident fluctuations (Fourier transform of the spatial correlation) is employed to predict the power spectra.

The 3D CFD cannot yield the length scales needed to fully characterize the temperature fluctuations. Some preliminary ideas on how to estimate the needed length scales and also present comparisons between theory and data for farfield SPL for a LEC and an SC at low power were examined. The directivity model used to go from a power spectrum to a farfield SPL spectrum is similar to that used for the broadband noise model, based on a partitioning of the acoustic power according to frequency and cut-off ratio. To minimize the amount of steady flow turbine aerodynamic information needed to implement the calculation, the turbine aerodynamics was assumed to be in accord with a free-vortex design.

The results of this modeling indicate the high plausibility of differences in temperature fluctuations (at combustor exit) being the cause of increased core noise observed from a LEC, relative to an SC, at low-power operation.

2.5 System Noise Impact Relative To NASA Goals

A system noise assessment model was put together to evaluate potential noise reduction concept effects on total aircraft system noise. This model is based on the 1992 Technology Noise Level study carried out by Boeing under the NASA AST Noise Reduction Program, documented in Reference 5. In this study, Boeing defines four referee or baseline aircraft:

1. Business Jet
2. Small Twin
3. Medium Twin
4. Large Quad (four engines)

Using the component noise levels and aircraft operating conditions defined in Reference 5, spreadsheet models for the small twin, the medium twin, and the large quad aircraft were created. These models estimate the approximate benefit to total aircraft system noise of adding a noise reduction feature to one (or more) of the engine components. Thus, based on any noise-reduction potential identified during the course of developing the codes and methods described above, a system noise benefit can be calculated and compared with the NASA AST goals (Section 1.1, page 1).

Candidate noise-reduction features identified during the course of developing the prediction codes and models summarized earlier include the following:

- Fan broadband noise reduction by wake control, such as rotor wake blowing.
- Fan MPT noise reduction by fan blade forward sweep.
- Combustor-related core noise reduction by fuel nozzle pattern optimization.

Estimates were made of the component noise reductions attainable with these features, and these were then input to the system assessment models. From the results of these computations, a total of 2.5-dB reduction in engine EPNL was estimated on the average, depending on the aircraft (small twin versus medium twin versus large quad) and the operating condition (sideline, takeoff, or approach). Although the total estimated reduction falls short of the NASA goal of 6-dB engine noise

reduction, the results are a significant fraction of the goal when considering that many other concepts and features, being developed by NASA in-house researchers and other contractors, can contribute to the total goal.

Although the above goal assessments have only scratched the surface of what can be done once validated prediction tools are available, it has been demonstrated that producing and using such tools for discovering and optimizing noise reduction concepts, through a solid understanding and modeling of the fundamental noise generation physics, holds great promise.

2.6 System Community Noise Impact of Multiple-Pure-Tone (MPT) Noise Elimination

A study was carried out to assess the potential impact on aircraft community noise of substantially reducing, if not eliminating, multiple-pure-tone (MPT) or "buzz saw" noise from the engine noise spectrum. The objective of this study was to establish the potential system noise benefits of developing noise reduction concepts for reducing or eliminating "buzz saw" noise. There are other benefits to reducing or eliminating MPT noise, including reductions in aircraft cabin interior noise during climb-out and cruise portions of the mission or flight. Reduction of the MPT signature to "acceptable" levels inside the aircraft cabin provides a further benefit in that less aircraft fuselage cabin sound insulation is needed to achieve "acceptable" levels, thus decreasing aircraft weight and hence reducing mission fuel burn for a given passenger payload.

2.6.1 Approach

The approach to carrying out this study was to first generate a "strawman" aircraft engine fan inlet MPT component EPNL model. A set of scale-model fan data, where only fan inlet-radiated noise was measured, was selected for analysis. The "strawman" MPT noise EPNL model was developed using database decomposition and regression and scaling methods. Then this model was used to evaluate the effect of reducing or eliminating the MPT component to EPNL, using the Boeing 1992 baseline aircraft as the reference, as described in Reference 6. Results were generated for three aircraft types described in Reference 6; a large four-engine (quad) aircraft, a medium two-engine (twin) aircraft, and a small two-engine (twin) aircraft.

2.6.2 MPT Component EPNL Model Methodology

The "strawman" MPT component EPNL model was developed by carrying out a component decomposition of a set of scale-model fan data representative of typical aircraft engine fans, where only the fan inlet component was isolated. The data set chosen for this decomposition analysis is given in Reference 7. The fan design, designated "Rotor 11," has 44 blades and 86 stator vanes. The test data configurations given in Reference 7 cover a range of rotor-to-stator axial spacings from 0.5 to 2.3 rotor chords and vane counts of 44 and 86. Data were taken in an anechoic chamber wherein the fan exhaust was ducted outside of the chamber, so the microphone array inside the chamber only measured fan inlet-radiated noise. A turbulence-control structure (TCS) was employed to eliminate inflow distortion and turbulence noise sources.

The sound pressure level 1/3-octave spectra reported in Reference 7 were decomposed by first locating and editing the fan blade-passing-frequency tones and the next three harmonics. A generic fan broadband noise spectrum shape was then fitted to the edited data in the frequency bands higher

than blade-passing frequency, based on the spectral shape function given in Reference 8. The resulting "anchored" spectrum shape was then subtracted from the edited 1/3-octave spectra to arrive at an "excess noise" spectrum. This excess noise spectrum is dominated by MPT noise when the rotor tip speed is supersonic. At subsonic tip speeds, there was still observed to be some "excess noise" remaining, speculated to be the result of sources other than pure rotor/stator interaction or rotor-alone noise. Examples include support strut noise, flow noise from downstream duct struts, throttling valve, etc.

The total fan noise spectra were scaled to full size and "flown," using a typical aircraft mission, to generate effective perceived noise levels. The edited spectra (total spectra minus fan BPF tones and higher harmonics) were also "flown." Finally, the anchored broadband noise generic spectra were also scaled and "flown." From these three sets of EPNL data, the contributions of fan tones and "excess noise" were evaluated.

The "excess noise" EPNL trends were correlated using multiple linear regression techniques. Dependent variables identified as being statistically significant were: (1) acoustic range (ft), (2) fan vane/blade ratio, (3) fan rotor/stator spacing and chord ratio, (4) fan pressure ratio, and (5) fan tip speed Mach number. The resulting fan inlet "excess noise" EPNL correlation is as follows:

$$Y = C_0 + C_1 X_1 + C_3 X_3 + C_4 X_4 + C_{44} X_4^2 + C_{51} X_5 X_1 + C_{52} X_5 X_3 + C_{54} X_5 X_4 + C_{63} X_6 X_3 + C_{64} X_6 X_4 + C_{65} X_6 X_5 + C_{66} X_6^2$$

where the variables X_1 through X_6 are defined as follows:

X_1 = Altitude (acoustic range)/1000 ft
X_2 = Fan vane/blade ratio
X_3 = Fan rotor-to-stator spacing/chord ratio
X_4 = Fan pressure ratio
X_5 = Fan tip mach number regime indicator: $X_5 = 1$ for $M_t < 1.0$, $X_5 = 0$ for $M_t \geq 1.0$
X_6 = Fan tip speed mach number, $M_t = U_t/C_s$.

And where Y = ΔEPNL due to "excess noise" — noise over and above that from the fan BPF harmonics and fan broadband noise. Note that the variable X_5 is essentially a "switch" to denote a change or "jump" in level of excess noise when the rotor tip speed goes supersonic. Because there are crossproduct or interaction terms involving X_5, the resulting change or jump amplitude is a function of the other parameters as well.

The above equation was determined from a least squares, multiple-regression analysis with interaction terms included, that is, crossproducts of the above variables. The final equation was derived by successive, stepwise elimination of those terms and crossproducts that were found to have a high probability of being statistically insignificant. GEAE practice is to discard terms when the coefficients have a p-value greater than 5%. The above equation was alternatively derived using a "stepwise regression" routine in a statistical analysis software package called "Minitab," which begins with only first-order terms and successively adds and drops terms in order to reduce standard deviation and increase R^2. The "stepwise regression" method failed to find X_4 main effects terms, so they were added manually, which then gave the same equation as was obtained by the successive,

stepwise elimination approach. The equation presented above has an R^2 value of 84.6% and a standard deviation σ of 0.31 dB. The values of the constants are tabulated in Table 1.

Table 1. Excess Noise Correlation Equation Coefficients

Coefficient	Value
C_0	+249.80
C_1	+0.35945
C_3	+2.4011
C_4	−352.46
C_5	−92.762
C_{44}	+214.54
C_{51}	−0.2686
C_{52}	+0.73022
C_{53}	−0.5409
C_{54}	+33.632
C_{63}	−2.0673
C_{64}	−209.78
C_{65}	+49.520
C_{66}	+121.60

2.6.3 MPT Noise Reduction Community Noise Benefits Methodology

For each of the aircraft types selected from Reference 6, the above MPT noise component EPNL model was used to evaluate the EPNL contribution to the fan inlet components given in Reference 6. The potential noise reduction was then assumed to be equal to (optimistically) the MPT contribution itself, and the improved fan inlet component EPNL was assumed to be equal to the baseline 1992 trechnology level, reduced by the MPT contribution. The system noise was then recomputed using simple logarithmic summing of components.

The results of this analysis are given in Table 2. The analysis was carried out for the three community noise certification conditions: sideline, takeoff, and approach. For the cases where the fan rotor tip speed is subsonic, the "excess noise" is not MPT related but reflects other extraneous noise sources not completely identified or understood.

An example of the noise component contributions for the medium twin is shown in Figure 1 for the three certification conditions. From Table 2, it is seen that the impact of MPT noise on the total fan inlet noise component is about 2 dB at cutback, but total system noise benefit is only about 0.5 dB.

Table 2. MPT Impact Study Results

Aircraft	Condition	M_t	MPT ΔEPNL	System ΔEPNL
Medium Twin	Sideline	1.3	1.5	0.1
	Takeoff	1.1	2.3	0.5
	Approach	0.79	2.3	1.2
Large Quad	Sideline	1.23	1.8	0.2
	Takeoff	1.05	2.2	0.6
	Approach	0.82	2.4	1.3
Small Twin	Sideline	1.35	1.3	0.1
	Takeoff	1.2	2.1	0.1
	Approach	0.87	2.1	1.1

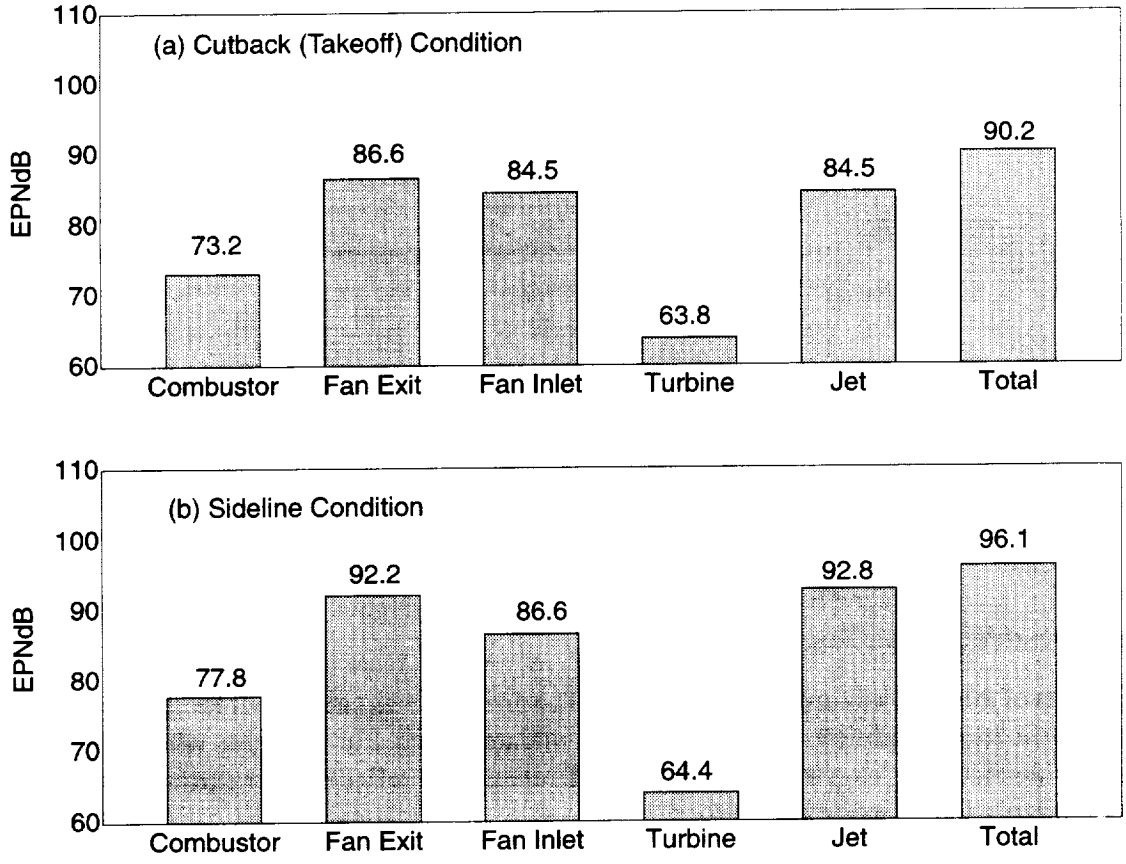

Figure 1. Baseline Noise Levels: Components for 1992 Technology Medium Twin Aircraft

This is because the fan inlet is typically not a dominant contributor to aircraft noise except at approach, so reducing it does not have a significant effect. Similar trends were obtained for the large quad aircraft and the small twin aircraft, although the system benefit for the small twin was significantly smaller, at cutback, because the relative contribution of fan inlet noise was smaller. Figure 2 shows the component contributions at cutback for the large quad and the small twin, and it can be seen from this figure and Figure 1a that the small twin has a lower fan inlet contribution relative to the total engine noise.

2.6.4 Conclusions

The results of this study indicate that a substantial reduction of MPT noise produces only a small amount of system community noise reduction in effective perceived noise level. The approximate benefits are estimated to be about 01 to 0.2 EPNdB at sideline and 0.5 to 0.6 dB at takeoff (with cutback procedure). Although "excess noise" reduction benefits were calculated for approach, they are not attributable to MPT noise, because the fan tip speed at this condition is subsonic; therefore, rotor bow shock formations cannot be present. Nonetheless, there is a possibility that additional noise reduction may be possible if the "excess noise" observed at subsonic tip speeds were understood.

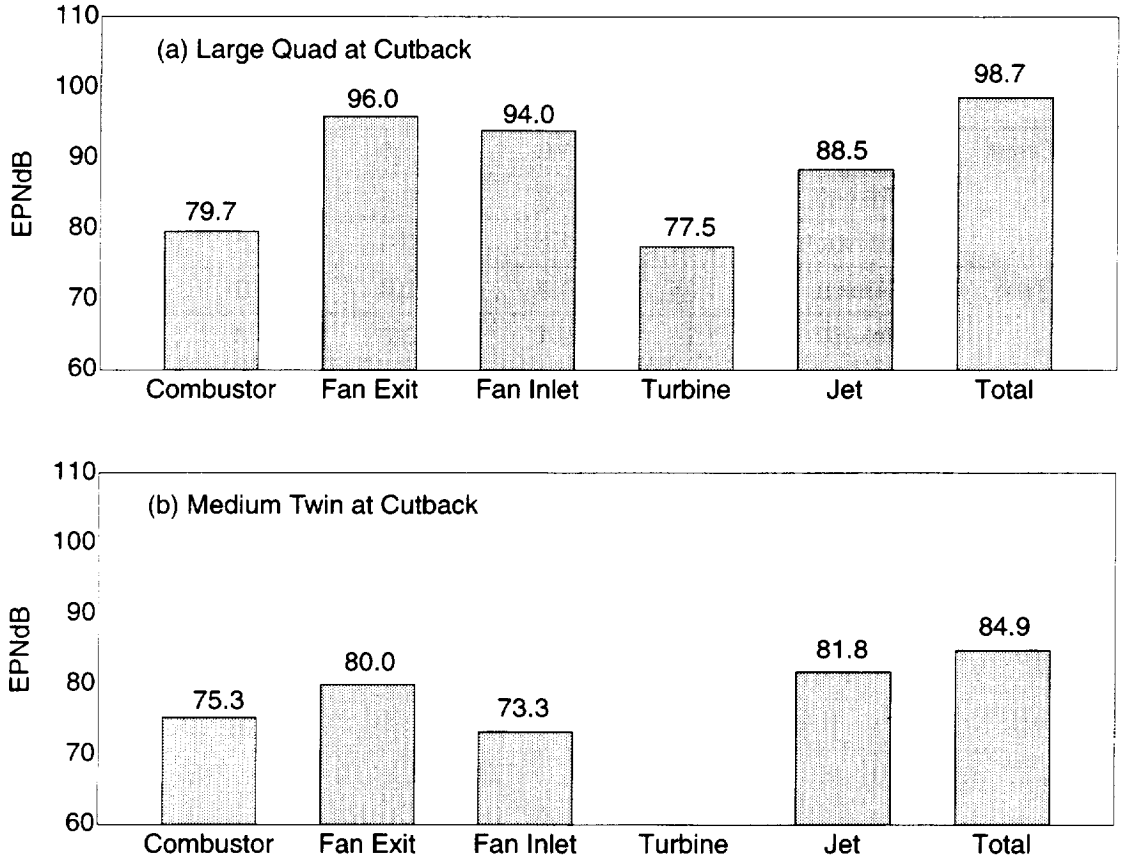

Figure 2. Cutback Component Breakdown for Large Quad and Small Twin Aircraft from 1992 Technology Study (Reference 6)

2.6.5 Effect of Other Noise-Reduction Features

In addition to the effects of MPT noise reduction as described above, the effects of fan broadband noise reduction and core noise reduction were also estimated, using the above-described 1992 Technology baseline aircraft definitions. It was concluded that fan broadband noise could be reduced by either decreasing rotor wake turbulence or by using fewer fan stator vanes. It is reasonable to assume that either of these methods, or a combination, could conceivably yield a 3-dB reduction in fan noise. It was also observed that there can be as much as a 5-dB difference in combustor-related core noise if the fuel nozzle staging is "nonoptimum" from a noise point of view.

By using the 1992 Technology Aircraft models described above, taken from Reference 6, these reduction estimates were incorporated into the system noise models, including the MPT noise reductions estimated above, and the resulting system benefits are listed in Table 3.

Table 3. System Noise Reduction Estimates for Combined Reductions In Fan MPT Noise, Fan Broadband Noise, and Core Noise

Aircraft	Condition	M_t	ΔEPNL			
			MPT	Fan BB	Core	System
Medium Twin	Sideline	1.3	1.5	3.0	5.0	1.5
	Takeoff	1.1	2.3	3.0	5.0	2.4
	Approach	0.79	2.3	3.0	5.0	4.1
Large Quad	Sideline	1.23	1.8	3.0	5.0	1.6
	Takeoff	1.05	2.2	3.0	5.0	3.2
	Approach	0.82	2.4	3.0	5.0	4.1
Small Twin	Sideline	1.35	1.3	3.0	5.0	0.6
	Takeoff	1.2	2.1	3.0	5.0	1.5
	Approach	0.87	2.1	3.0	5.0	3.8

From Table 3, it can be seen that the estimated total system noise reduction varies from about 1.5 to 4.1 dB, depending on the aircraft type and the community noise certification condition.

3.0 Improved Aeroacoustic Turbulence Model for Fan Broadband Noise

Studies such as Reference 9 have shown that fan noise will be a significant contributor to total system noise, even at high power settings, for future engines with bypass ratios significantly higher than current practice. In particular, it was shown in Reference 10 that fan broadband noise will be a limiting noise source as methods for reducing fan tone noise are developed to the point where tones no longer control the total fan noise levels. It then becomes even more important to have accurate prediction models, for fan broadband noise, that reflect the significant physical mechanisms for broadband noise generation, so that these models can be used to develop an understanding of the controlling parameters and explore ways to reduce the noise generation.

GE has been actively developing fan component noise prediction models and codes for many years, under IR&D and under NASA sponsorship. Past fan broadband noise modeling efforts include rotor noise (References 11 through 13) and stator noise (References 4 and 11). Although the relative role of rotor and stator noise is still a controversial issue, and perhaps a function of the fan design and the test environment, it is still accepted that stator noise can be a significant contributor. A primary ingredient to stator-generated noise is the unsteady, turbulent, flowfield at the fan rotor exit. No general procedure or model is currently accepted for predicting this rotor exit turbulent flowfield. Therefore, a major objective of the work reported herein was to establish such a method, if possible.

As part of the NASA Advanced Subsonic Transport Noise Reduction Technology effort, computer codes are being developed to provide quantitative prediction, design, and analysis capability for aircraft engine noise sources. A main ingredient to engine source noise is the contribution of the high-bypass fan, which generates both tones and broadband noise. The effort reported in this section focused on providing an improved model for the fan rotor exit flow mean and turbulence properties, for use in predicting the broadband noise generated by rotor exit flow turbulence interaction with the downstream stator vanes. An empirical correlation was developed, using the results of hot-wire surveys from a low-speed fan stage test, and the correlation was validated with a set of scale-model, high-speed fan test hot-wire survey data.

3.1 Objectives and Approach

The primary objective of this project was to establish a validated prediction and design analysis tool for the mean and turbulent unsteady flow behind a fan rotor, to be used for defining the input gust description for prediction of stator-generated broadband noise. A secondary objective was to evaluate the improvements in fan broadband noise prediction capability that arise from incorporating these improvements in modeling of the rotor exit turbulence flowfield.

The basic approach was to develop, to as great an extent possible, a generalized fan rotor exit flow wake mean profile and turbulence definition by empirical correlation of existing experimental rotor exit flowfield data. A literature survey and in-house data review were carried out to establish the most relevant sources of data for carrying out this correlation. Based on results of the survey and data review, it was decided to use an existing set of rotor exit hot-wire data taken on a GEAE LSRC fan stage simulation test. These data were chosen because they were the most extensive available at the time, covered a wide range of radial and downstream distances, and included fan loading excursions. The approach taken was to use the LSRC fan stage test results, even though they were

for a high radius-ratio (0.85) configuration and for a low tip speed (210 ft/s), to develop the correlation and then to substantiate the correlation with high tip speed results taken on a GEAE UPS (Reference 2).

Data from available hot-wire flowfield measurements were examined for the purpose of developing an improved aeroacoustic turbulence model for use in predicting the rotor/stator interaction broadband noise of an axial flow fan. The main data source for this study came from three-dimensional wake and turbulence measurements, on a modified LSRC configuration, carried out at the GEAE Aerodynamics Research Laboratory (ARL). The original LSRC was designed to be typical of modern compressor stage designs and had a high hub/tip ratio of 0.85. It contained four stages of low-aspect-ratio, high-solidity blading with shrouded stators and inlet guide vanes (IGV). For the rotor wake measurements test, which was done under an IR&D project in early 1996, the IGV were removed to eliminate rotor wake contamination by IGV wakes. The first stator and second rotor blading were removed and replaced with smooth hub and casing spools to give more axial spacing for detailed wake properties measurements behind the first-stage rotor.

The low-speed fan stage (LSFS) simulation survey employed three-axis, hot-wire probe measurements so that all three components of the mean and turbulent velocity field could be obtained. The measurements were made at four axial locations behind the rotor, corresponding to a range of spacing-to-chord ratios of 0.13 to 2.0. Data were taken at three fan throttle settings, corresponding to three fan loading conditions, all at the same fan tip speed of 210 ft/s.

This data were correlated using various methods proposed in the literature, and an empirical rotor exit turbulence model was developed from these correlations. The empirical model was then validated using existing hot-wire data from a scale-model, high-speed fan typical of high-bypass fan stages. The resulting validated turbulence model was then incorporated into an existing fan broadband noise prediction model computer code.

The LSFS data obtained from the IR&D project were deemed the most complete set of rotor exit survey data available for development of an empirical model, so they were used as the basis for the empirical correlations subsequently developed under this NASA program. The empirical correlation approaches were taken from wake data methods found in the literature. The approach finally adopted was that of Wygnanski, Champagne, and Marasli (Reference 5) and based the evolution of both mean and turbulence properties on scaling with the airfoil trailing-edge momentum thickness. Reasonable correlations were obtained for fan rotor spanwise locations outside the end-wall secondary flow regions, and the correlations were found to agree well with similar (but much more limited) data taken on a high-speed fan stage under a previous NASA test program.

A cooperative effort with Dr. Chunill Hah of NASA Lewis was also carried out to use CFD to predict the measured flowfield results — and hopefully provide guidance on developing the correlation. Agreement between the CFD code results and the hot-wire results was reasonable and provided substantiation for the results obtained in this program, although the CFD results were not used directly in the subsequent modeling and correlation development. These results also suggest that it may be possible to use CFD to produce the needed turbulence information for prediction of fan broadband noise in the not-to-distant future.

A set of empirical, algebraic formulas that can be used to predict the mean velocity and turbulence properties in the rotor exit wake region provide the final outcome of this study. Guidance is also

given for how to estimate the rotor end-wall turbulence properties, based on the rotor wake properties just outside the end-wall regions.

A critical assumption made in selecting this approach was that Mach number effects on the rotor wake evolution and behavior are of second order, compared to the viscous effects and rotor loading effects that determine the wake behavior to first order. It is worth noting that the LSRC blades and vanes are designed to simulate the corresponding high-speed compressible surface pressure distributions, so the Mach number effects are implicitly modeled, as long as there are no significant shock-boundary layer interaction effects. This is probably a reasonable assumption as long as the rotor inlet relative Mach number is below approximately 1.1.

The correlation approach selected is based on methodology suggested by Wygnanski et al. (Reference 5), which employs airfoil trailing-edge momentum thickness as a key scaling parameter. Although Wygnanski et al. developed this method for isolated body shapes (cylinders, flat plates, bluff bodies, etc.) it was found to work well for the rotor blade data selected. The approach does assume "similarity" in the sense that the wake should be fully developed, and therefore the regions for which the normalization and correlation are valid should be sufficiently far downstream to be in the fully developed, similarity region. As will be discussed in later sections, the majority of the data do in fact exhibit similarity behavior, and the data which do not are clearly identifiable.

3.2 Data Base Description

Rotor wake profile data from the GEAE UPS tested at NASA Lewis Research Center (Reference 2) and the LSRC tested at the GEAE Aerodynamics Research Lab (ARL) were identified for wake characteristics analysis. Data from several LSRC configurations tested in the past several years were reviewed, including data where one blade in the rotor row was replaced by a cylindrical rod. All data were obtained using a two-sensor, hot-wire probe (x-probe) except for the data obtained from modified LSRC fan stage simulation. The LSFS data were obtained using a three-sensor probe, for obtaining three-dimensional wake turbulence information.

3.2.1 Wake Data from the UPS Fan

Two-sensor x-probe hot-wire flowfield measurements were made behind the fan rotor, in front of the outlet guide vanes (OGV), and at two circumferential locations behind the OGV at three fan speeds on the UPS fan stage (Figure 3). The test was conducted at the NASA 9×15-ft Low Speed Wind Tunnel (LSWT) at NASA Lewis Research Center in Cleveland, Ohio, in 1994. The fan design is shown in Figure 4. The fan rotor is a 22-in diameter, wide-chord design having 22 blades. The design tip speed is 1215 ft/s. The design pressure ratio is 1.5, and the bypass ratio is 9.0.

The UPS fan rotor exit hot-wire surveys were conducted as part of a comprehensive aerodynamic performance and acoustic evaluation of a series of fan rotor designs carried out in the NASA Lewis 9×15-ft LSWT in 1994. Reference 3 provides a detailed description of the NASA LSWT, which is located in the return leg of the NASA Lewis 8×6-ft supersonic wind tunnel. The area contraction ration is 8:1, and the test section is 28.67-ft long. The test section wall diverges slightly to account for longitudinal boundary layer buildup. The cross-sectional dimensions are 9-ft high by 15-ft wide at the test section entry, and 9-ft high by 15.25-ft wide at the test section exit. The ceiling and floor are completely closed, but the side walls are 11% open, a result of four 4-in slots that run the entire length of the test section. The test section velocity can be varied from a minimum of 50 ft/s to a maximum of 250 ft/s, which corresponds to a range of Mach numbers from 0.05 to 0.23.

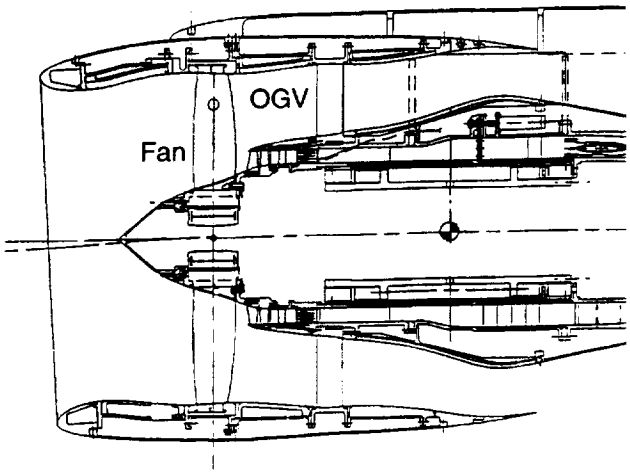

Figure 3. UPS Design Configuration

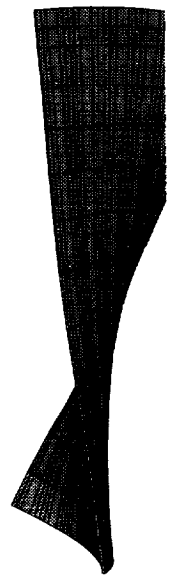

Figure 4. Unswept Composite Fan Blade

Flowfield measurements were made behind the fan rotor, at several axial stations downstream of the rotor trailing edge, using an x-probe hot-wire anemometer. The objectives of these measurements were (1) to quantify the rotor wake mean velocity profile characteristics so they could be correlated with the corresponding noise measurements and (2) to establish a database of acoustic data and corresponding wake data that could be used as a set for the NASA-funded fan rotor/stator tone noise prediction model (V072). The measurements were also used to assess currently used semiempirical models for predicting rotor wake mean velocity profile harmonic amplitude characteristics. These results were reported in References 2 and 3.

A Compaq Prolinea 486 PC was reconfigured and modified as a data-acquisition system. The system consists of a TSI IFA100-4 hot-wire anemometer for two x-probe sensors, a KinaticSystem analog/digital (A/D) convertor that has four channels with 250-kHz A/D speed, two Rotadata actuators, a Wavetek pulse generator for a clean external trigger, and the PC for the whole system control (Figure 5). The probes were modified by TSI to withstand the high flow velocity and preclude sensor prong vibration. The actuators were mounted to the UPS model at two circumferential locations so that data could be obtained from two sensors at the same time.

The probe calibration was conducted before and after the test at the GEAE ARL free-jet facility. The calibration requires the x-probe to be yawed in the free-stream at several velocities. From the corresponding output voltages, a calibration look-up table can be generated. The technique requires fewer assumptions than traditional methods based on King's law (Reference 14). The phase-locked, averaged data (3000 data points for one complete revolution) were obtained from seven immersions at each axial location. In addition, instantaneous data for estimating turbulence properties were obtained at three immersions at each axial location. Data were taken at three fan speeds, corresponding to approximate approach, cutback and sideline acoustic certification conditions. The corrected fan speeds were 7497, 10,080 and 12,000 RPM respectively.

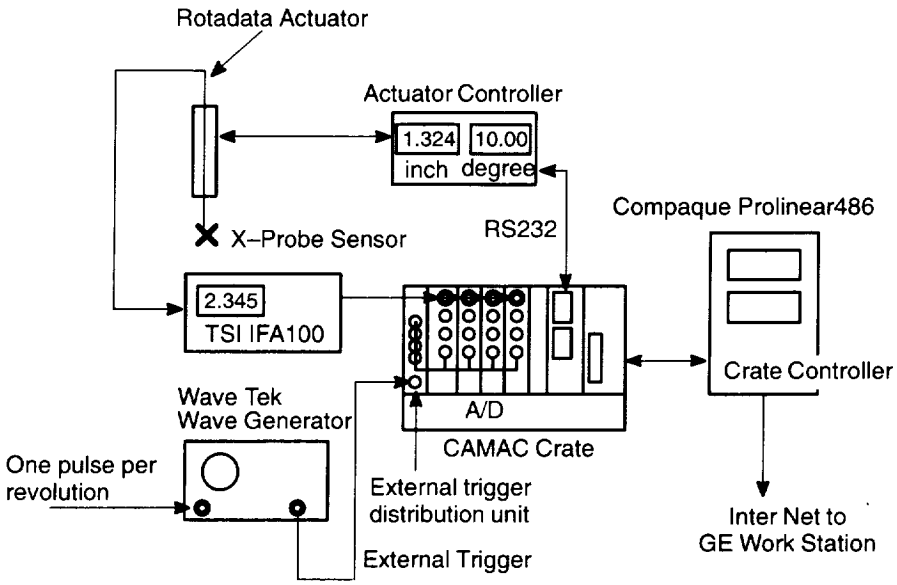

Figure 5. Hot-Wire Data Acquisition System

The hot-wire measurements were processed to calculate relative velocity behind the rotor. Figure 6 shows relative velocity plotted against blade passage period over five blade passages, at the low fan speed condition (7,497 rpm), at 56.0% radial immersion from casing. The amplitude of the velocity profile excursions are reduced significantly at the downstream axial station near the OGV leading edge, relative to the fan rotor exit plane, due to viscous decay with downstream distance. It is also noted that the wake profiles look more nearly sinusoidal at the OGV leading edge, compared to the irregular shape measured at the rotor trailing edge. The data at the seven radial immersions were analyzed at each axial location and rpm condition, and contour plots of the total absolute velocity measured by the hot wire were generated as shown in Figure 7, a contour plot at the low-speed condition of 7,497 rpm for the axial station 0.5 inches downstream from fan trailing edge. The absolute velocity data obtained from this test program provided useful information on the gust velocity distribution seen by the OGV. More detailed data analysis of these data are reported in the NASA Contractor Final Informal Report, Reference 2. This data set will be discussed further in later sections of this report.

3.2.2 Data from Low-Speed Research Compressor Fan Simulator

The LSRC is an experimental facility/rig that duplicates the essential features of a small, high-speed-compressor flowfield in a large, low-speed machine where very detailed investigations of the flow can be made. The LSRC has a constant casing diameter of 1.54-m (60.0-in). The axis of rotation of the compressor is vertical, and flow enters from the top through a calibrated bellmouth/inlet system that filters and measures the flow. The LSRC has four compressor stages and IGV but was modified for these measurements by removing the IGV row, the first stator, and the second rotor as shown in Figure 8. This modification allowed wake properties at various downstream locations to be measured without interference from downstream blade rows and without the upstream effects of an IGV row. The additional stages downstream of the LSFS simulation provide additional pressure rise so that the front (fan) stage can be throttled over a wide range to assess loading effects.

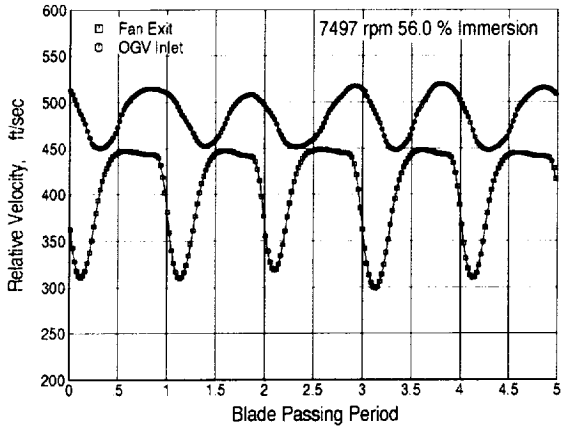

Figure 6. Typical Wake Profile at Fan Exit and OGV Inlet

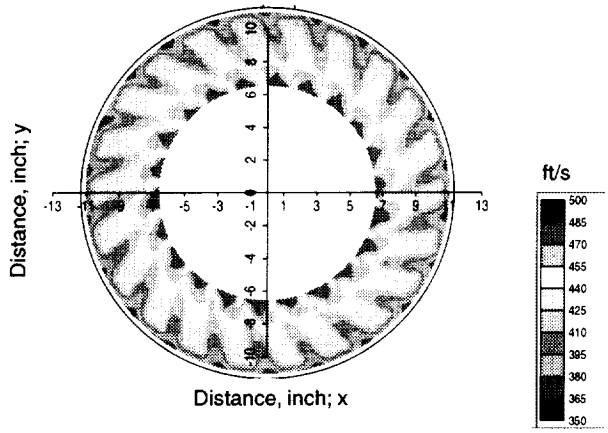

Figure 7. Absolute Velocity Contour Plot 0.5-in Downstream From the Fan Trailing Edge

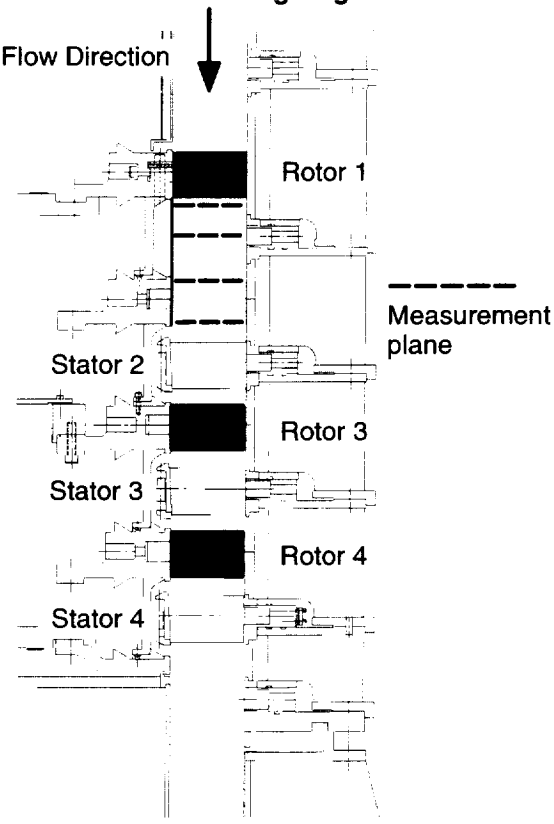

Figure 8. Low-Speed Research Compressor Configuration for Acoustic Prediction Code Development

Measurements were made at 14 immersions for each of the five selected axial locations. Surveys were taken at three different throttle settings to provide information on the effects of rotor loading. After passing through the blading, air is exhausted through a large circular throttle plate that can be raised or lowered to change the compressor back pressure by varying the exit area.

Typical of modern designs, the compressor first-stage rotor had high-hub/tip-ratio, low-aspect-ratio, high-solidity blading, with shrouded stators and IGV. The blading was a low-speed, aerodynamic

model of the imbedded stages of a highly loaded, high-reaction, nine-stage high-pressure compressor. The rotor airfoil designs showed sufficient performance improvement over the previous designs that its design features were transformed to high speed and incorporated into the core compressor of the NASA/GEAE Energy Efficient Engine (E^3). The rotor airfoil is shown in Figure 9. A list of rotor blading geometric parameters is given in Table 4.

Table 4. LSRC Fan Simulation Rotor Geometry

Parameter	Hub	Pitch	Tip
Radius, inch	25.5	27.75	30
Chord, inch	3.76	3.76	3.76
Solidity	1.265	1.163	1.076
Stagger Angle (°)	42.90	50.36	56.93
Camber Angle (°)	40.10	31.80	30.70

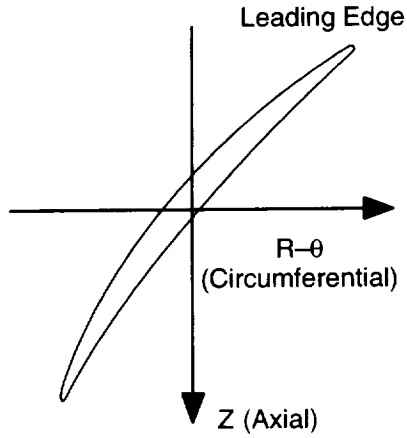

Figure 9. Rotor Airfoil Section

A triple hot-wire sensor, as shown in Figure 10, custom made by DANTEC, was used with a DANTEC anemometer to measure the three-dimensional, unsteady and steady velocities. A new probe calibration method and data reduction procedure were developed for this test. The probe calibration was conducted at the Aerodynamics Research Laboratory (ARL) free jet facility at GEAE. The hot-wire probe was calibrated in the potential core of a precision calibration jet over a velocity range from 50 ft/s to 200 ft/s, and over the expected yaw (–30° to +30°) and pitch (–20° to +20°) angles of the LSRC fan simulation flowfield. From the corresponding output voltages of three sensors, a three-dimensional calibration look-up table was generated.

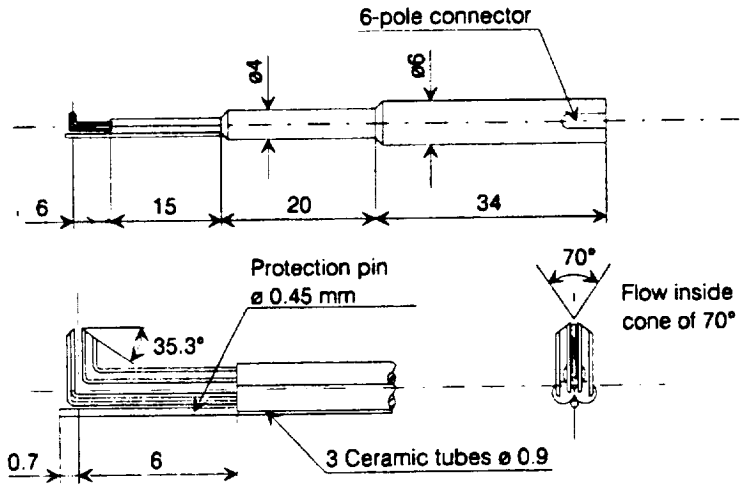

Figure 10. Three-Sensor Hot-Wire Probe

The look-up table is used to invert the three hot-wire voltages from the three sensors into 3D velocity vectors, without any assumptions regarding the cooling law of the the wires or their angular sensitivity response. This was done in the following steps.

- The data reduction program searches to find the node that is closest to the point corresponding to the instantaneous data read from three sensors, and then finds all of the elements that touch this node.
- The program then finds which of the elements contains the point.
- The instantaneous 3D velocity vector is obtained by interpolating using the element that is known to contain the point.

The 3D measurements of velocities downstream of the first rotor were made using the three-sensor hot-wire probe as just described. Data were taken at three throttle settings on the constant speed line, as shown in Figure 11, corresponding to rotor lift coefficients of 0.596, 0.786, and 0.852, having approximate incidence angles of –12.35°, –8.4°, and –6.72°, respectively. Measurements were made at 14 immersions for each of the five selected axial locations upstream and downstream of the first rotor. The upstream survey was also done at 0.5 inch upstream of the rotor leading edge. The four downstream axial stations correspond to axial distances of 0.5, 2.2, 5.0 and 7.5 inches downstream of the first rotor trailing edge. These distances correspond to normalized distances relative to projected axial chord of 0.17, 0.76, 1.74, and 2.6 respectively. Table 5 is a summary of the LSFS operating parameters.

Pressure Coefficient

$$\psi' = \frac{c_p T_1}{\frac{1}{2} U_t^2}\left[\left(\frac{\Delta P}{P_1} + 1\right)^{\frac{\gamma-1}{\gamma}} - 1\right]$$

where T_1, P_1 are total conditions.

Flow Coefficient

$$\phi = \frac{\dot{m}}{\bar{\rho} A U_t}$$

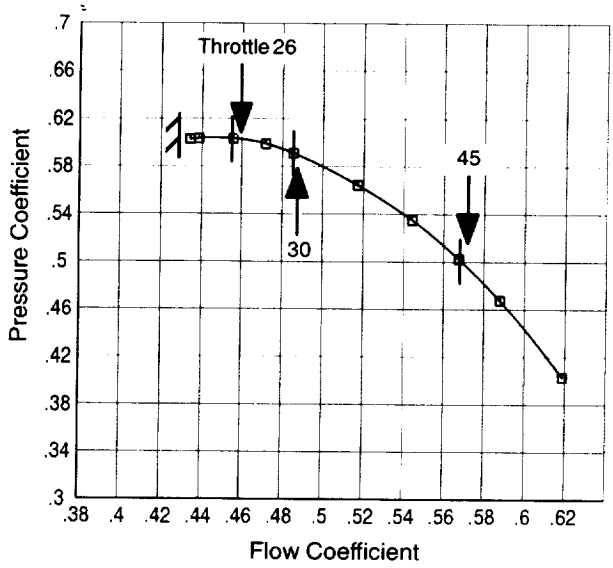

Figure 11. Stage Characteristics for a First Rotor and Test Points

Table 5. LSRC Fan Simulation Operating Parameters

Parameter	Throttle 45	Throttle 30	Throttle 26
Flow Coefficient	0.568	0.486	0.456
Pressure Rise Coefficient	0.499	0.589	0.602
Rotor Pitch-Line Lift Coefficient	0.569	0.7862	0.8529
Rotor Pitch-Line Drag Coefficient	0.1169	0.0675	0.08014
Rotor Pitch-Line Incidence Angle (°)	–12.35	–8.4	–6.72

The data-acquisition process for sampling the hot-wire output voltages is very similar to the one shown in Figure 5. The raw bridge output signal contains random as well as phase-related information. With the probe sensor positioned at 90° (normal to the LSRC axis), the probe could be rotated through the expected flow yaw angle range using a Rotadata actuator system. A rotor one-per-rev. signal was fed into the external trigger input of WaveTech Model 145 wave generator to generate a sharp –5-volts pulse that was fed into the stop trigger of the A/D converter module. The A/D converter speed was set to 50-kHz and 2000 sample memory was allocated in the 2-megabyte sample memory module with posttrigger mode.

The data-acquisition program initialized the A/D converter and located the probe for the first measurement position. The hot-wire probe signal digitization was initiated but was not stored in memory until the A/D converter received the trigger signal from the wave generator (which was triggered by the one-per-rev signal from an optical sensor). Data were taken for four seconds at each probe immersion and transported to the computer. The instantaneous voltage data were converted to the velocity vector components using the 3D look-up table. Two hundred and fifty sets of data were taken and averaged at each of 250 phase-locked positions for averaged velocity vectors.

3.3 NASA CFD Study Results

Computational calculations were carried out of the 3D, viscous flow behind the LSRC rotor, using a CFD code developed by Dr. Chunille Hah of NASA Lewis Research Center. The code used was HAH3D, which solves the full 3D, nonlinear, incompressible Navier–Stokes equations for turbomachinery flows. The purpose of this calculation was to provide confirmation of the basic rotor exit wake/end-wall structure being measured and to help guide the subsequent normalization and correlation of the measurements. NASA was also interested in validating their CFD code with this data set. The sample relative velocity color contour plots in Figure 12 compare the CFD results with the experimental data. The overall flow characteristics, including the wake structure and tip vortex formation, were well predicted by the CFD analysis. Figure 13 compares the measured and predicted rotor wake velocity profiles at 50% immersion at several axial stations downstream of the rotor trailing edge, and these results also indicate that the CFD model captures the measured wake spreading and decay.

3.4 Low-Speed Fan Stage Data Analysis

This section describes the analysis carried out using the data obtained from the LSRC fan stage simulation, with an objective of establishing a generalized correlation for both the mean wake behavior and the turbulence properties as required for input to fan broadband noise prediction codes.

3.4.1 Data Analysis Approach

As stated in Section 3.1, the primary objective of this effort was to develop an improved version of the wake mean flow and turbulence model currently employed in the GEAE fan broadband noise prediction codes. The current wake model is documented in Reference 10. This model draws upon a simplified approximation for the wake based on semitheoretical similarity models and empirical correlations for simple isolated body wakes in low-speed flows. The approach taken was to first evaluate the validity/generality of the wake model in Reference 10 and then explore alternative hypotheses and formulations. The purpose was not to verify the currently available formulations,

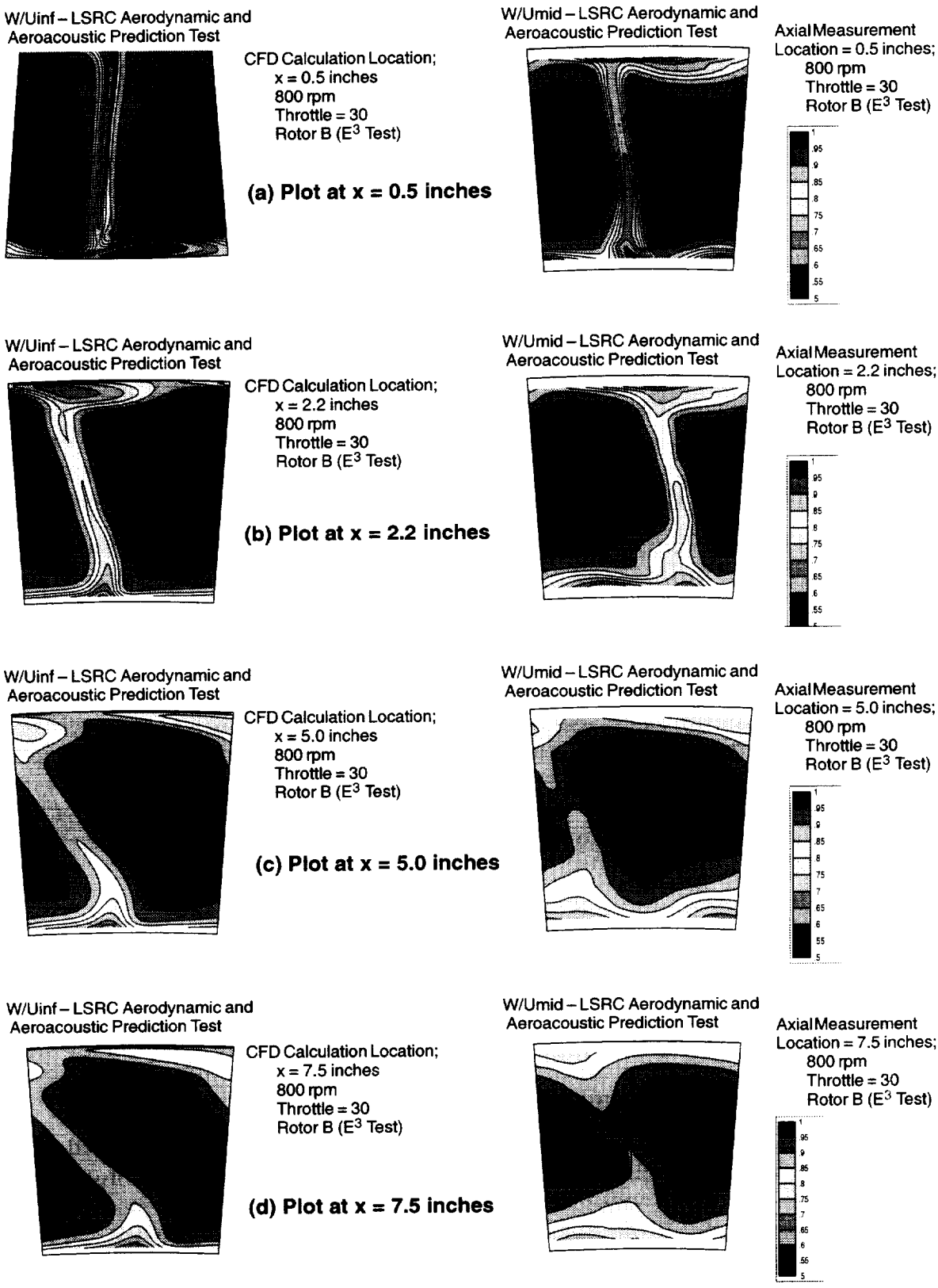

Figure 12. Nondimensionalized Relative Velocity Contours Downstream from Rotor Trailing Edge

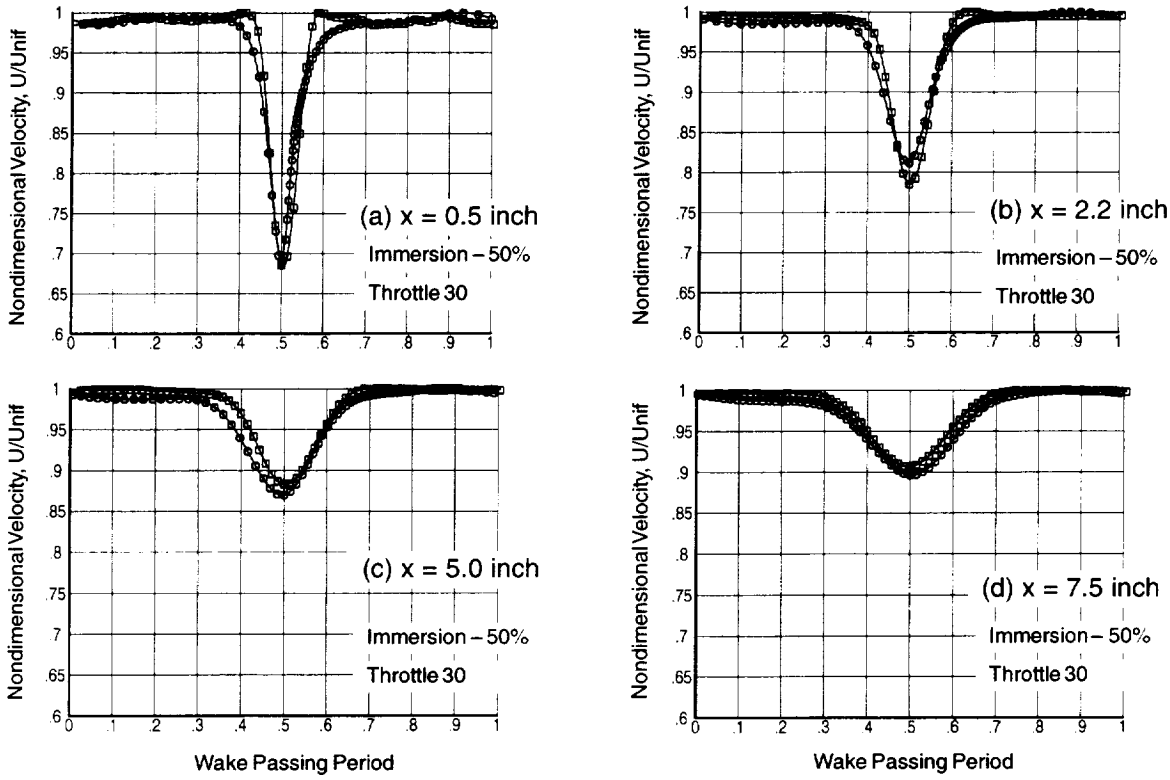

Figure 13. Nondimensionalized Relative Velocity Comparison Between Experimental Data and the Result of CFD at 50% Immersion

but to see which models (or modifications of them) suggest the best way to normalize and correlate the data. In reviewing literature and data on wake flows, the correlation and normalization methods suggested by Wygnanski et al., Reference 5, were identified as prime alternative candidates.

The first step in the data analysis was to normalize and correlate the wake mean velocity profile information, in terms of wake centerline velocity deficit and wake "half width." The model in Reference 10, hereafter referred to as the "old wake model," used the mean velocity deficit and wake width as scaling parameters for the wake turbulence velocities and length scales, and so the approach was also pursued in this study.

During the course of analyzing the data, it became apparent that there were "wake" zones and "end wall" zones displaying distinctly different behavior along the rotor span. The end-wall zones occupied an untypically large portion of the rotor span for this test fan stage, due to the high radius ratio (0.85) of the rotor annulus. For a typical high-bypass fan, the end-wall zones are only a small fraction of the annulus area, so it became apparent that correlation of these data had to be separated into two zones, with the "wake zone" data taken from the 30, 50, and 65% immersion surveys only.

3.4.2 Periodic Unsteady Transverse Velocities

The data in Figures 12 and 13 show the rotor synchronized flowfield, as perceived by an observer fixed to the rotor, and compare the CFD predictions with the hot-wire measurement results. For the purpose of quantifying the noise generation process associated with the rotor wake flow interacting with a downstream stator vane row, it is the flowfield perceived by the stator that is of concern. Of

particular interest is the unsteady, fluctuating, turbulent component normal to the total velocity vector at the vane leading edge. Rotor noise prediction methods, such as described in References 12 and 13, compute fluctuating loads on the blades, and hence noise, from a knowledge (measured or predicted) of this component of the fluctuating velocities normal to the rotor inlet total relative velocity vector. Similarly, stator noise prediction methods (References 4 and 11) require knowledge of the fluctuating velocity component normal to the total absolute velocity vector.

The periodic unsteady transverse velocities, denoted by v^+, were computed by constructing instantaneous vector diagrams with the ensemble-averaged velocities and the instantaneous velocities. The time-mean velocity was determined by arithmetically averaging the ensemble-averaged velocities for all of the equally spaced time increments across the blade spacing. From this, a single time-mean vector diagram was constructed. Then, for each of the time increments, an instantaneous vector diagram was computed. From the one steady (circumferentially averaged) vector diagram and the many instantaneous vector diagrams, the periodic unsteady velocities v^+ were computed, as described in Reference 2. For the throttle 30 case, Figure 14 shows this v^+ component of velocity,

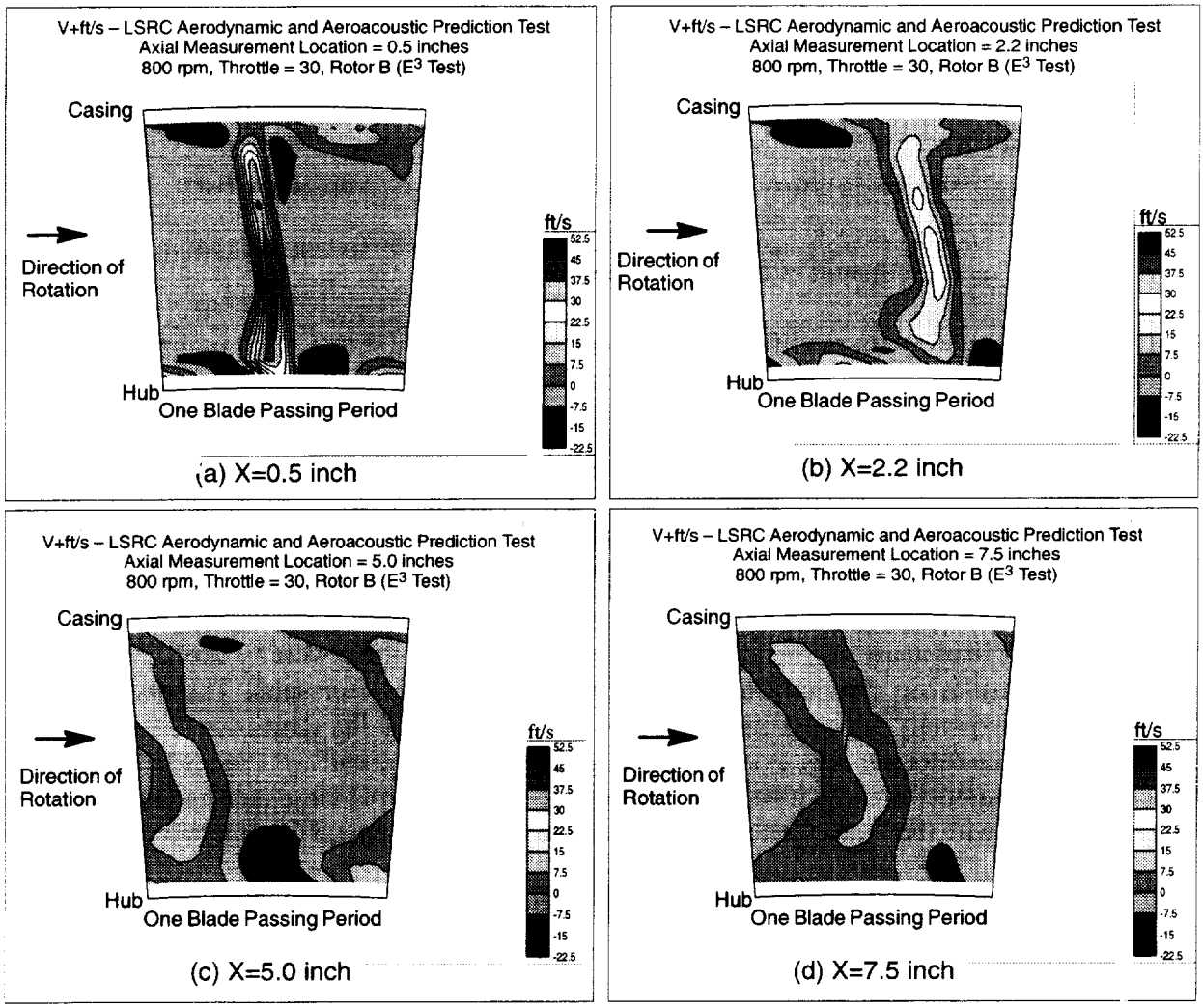

Figure 14. Contour Variation of V+ Along Axial Locations

in terms of color contour plots at each axial measurement station downstream of the rotor. The strong effect of the tip vortex can clearly be seen in the tip region at the closest axial station (0.5 inches downstream), but it decays rapidly with increasing axial distance downstream. The unsteady transverse velocities are also large in the wake region. Acoustically, it is usually thought that the tip and wake regions are of the most concern, in terms of defining the gust amplitude impinging on the downstream stator.

3.4.3 Mean Velocity and Turbulence Properties

Figure 15 (details a-d) shows the hot-wire survey average relative velocity distributions over one pitch at 50% immersion, in terms of relative velocity contour plots, at throttle setting 45 for four axial positions. Also included in this figure are the mean relative velocity profiles and the turbulence intensity profiles at 50% immersion. Detail a, at an axial distance 0.5 inches downstream of the rotor trailing edge (TE), shows wider wake widths on the pressure side than on the suction side, indicating a high negative incidence angle for the throttle setting 45 case. This corresponds to the unloaded point on the pressure coefficient (PC) versus the flow coefficient (FC) characteristic shown in Figure 11, corresponding to a rotor lift coefficient of approximately 0.596. A well-defined wake profile is observed at 50% immersion, but the contour plot shows that tip and hub secondary flows occupy a large portion of the span. Because of this, the wake core flow region (region where secondary flows do not interact with the wake) downstream of the rotor was observed to be a limited fraction of the span, and the shapes of wake profile varied significantly outside of the region of 35% to 65% immersion.

Figures 16 and 17 display the relative velocity contour plots and 50% immersion wake profiles for throttle settings 30 and 26, respectively. These figures show very symmetric wake profiles for immersions between 35% and 65% at all four axial positions. The contour plots show the wake profile width spreading as one goes downstream, while velocity profile plots illustrate the velocity deficit decay very well. The turbulence velocity profiles at 50% immersion are also seen to be symmetric for throttle settings 30 and 26. The horizontal length of the solid and dashed lines between filled symbols indicate the wake widths from wake mean velocity profiles (solid lines) and turbulence velocity profiles (dashed lines). By definition, the semi-wake width is defined as the width of the wake where the velocity deficit is equal to one-half the wake centerline defect. The different wake widths measured from these velocity and turbulence wake profiles are needed for correlation of the wake turbulence properties.

The approach taken was to develop the correlation using the LSFS data and then validate the resulting correlation using the UPS fan wake data described is Section 6, page 187. The correlation approach was to normalize the wake properties data with more-or-less traditional descriptors of wake characteristics such as wake half-width and wake maximum velocity defect, as well as some indicator of blade loading, such as wake momentum thickness.

Experience has shown that these wake-characterization descriptors may not capture all the features; therein lies a potential expectation for prediction model uncertainty and inaccuracy. One example that dramatically illustrates this effect was reported in Reference 15. In this article, the authors describe an experiment where one blade of a rotor stage was replaced by a cylindrical rod whose size was selected to produce exactly (within experimental measurement accuracy) the same wake mean velocity defect and wake half-width. A downstream stator vane was instrumented with surface hot-film gages that recorded the time-unsteady surface fluid shear stresses over the vane surface. An

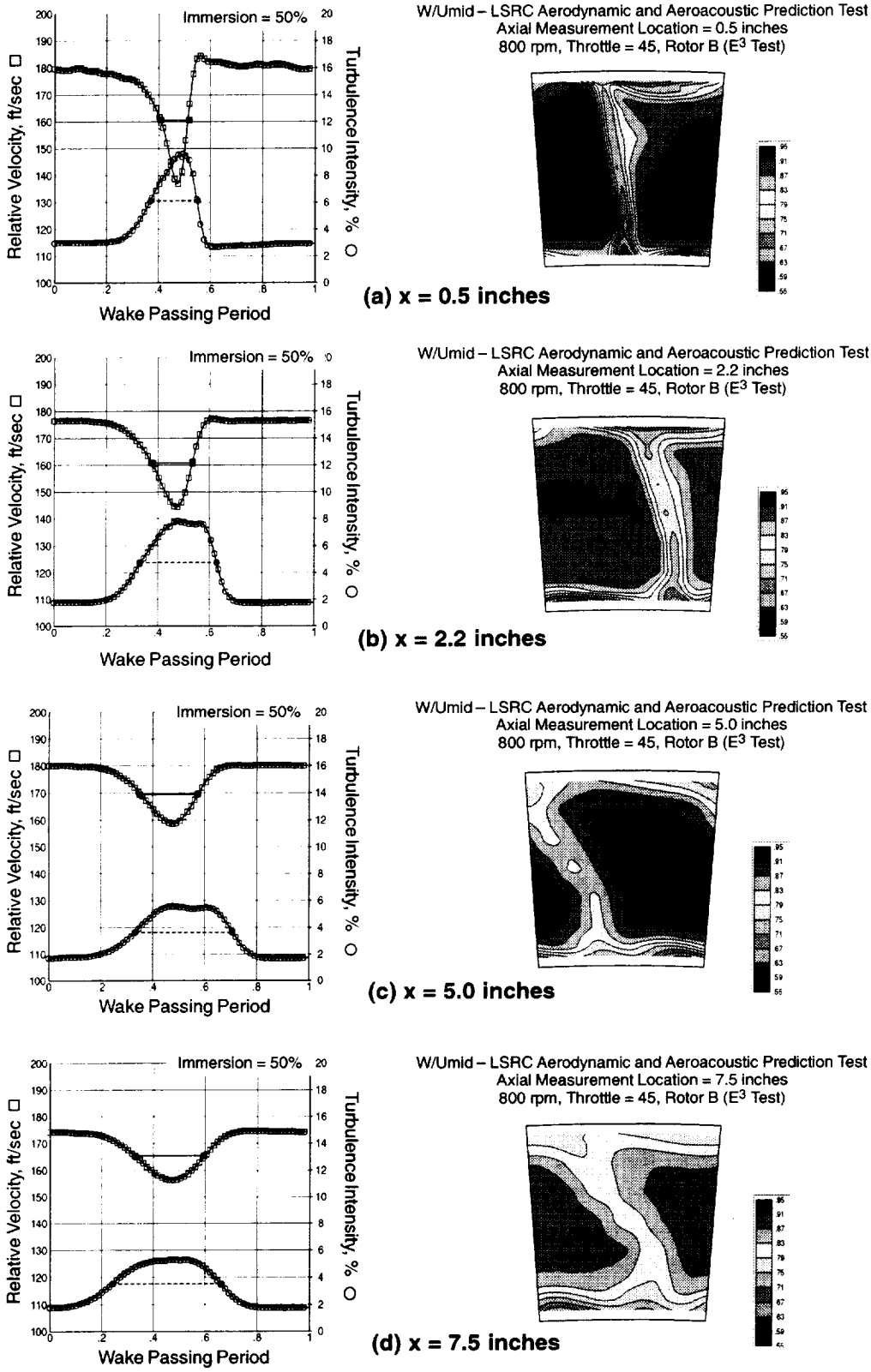

Figure 15. Average Relative Velocity Profiles at 50% Immersion and Relative Velocity Contour Plots for 0.5, 2.2, 5.0, and 7.5 Inches Downstream of the TE of Rotor 1 – Throttle Position 45

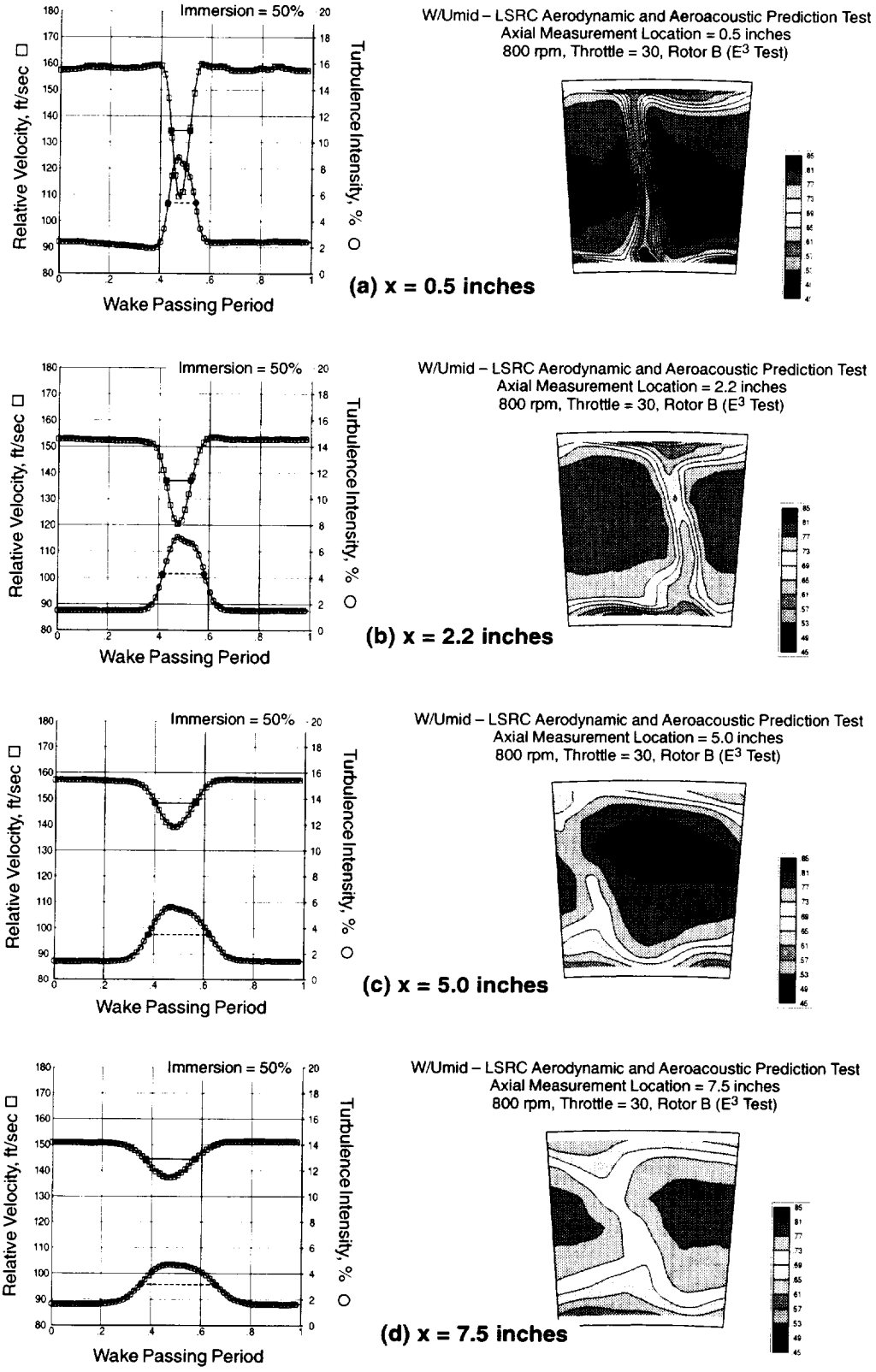

Figure 16. Average Relative Velocity Profile at 50% Immersion and Relative Velocity Contour Plots for 0.5, 2.2, 5.0, and 7.5 Inches Downstream of the TE of Rotor 1 – Throttle Position 30

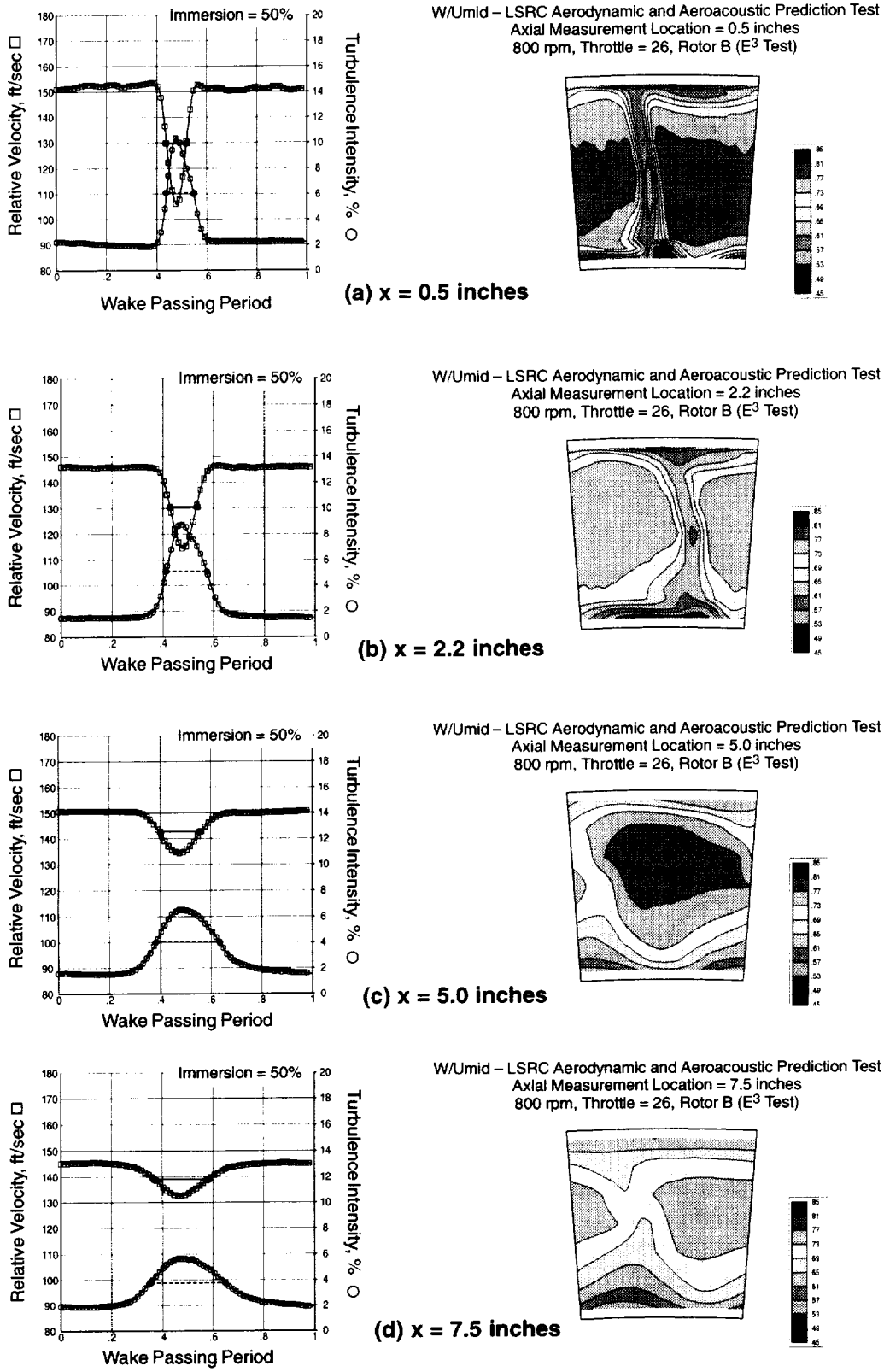

Figure 17. Average Relative Velocity Profile at 50% Immersion and Relative Velocity Contour Plots for 0.5, 2.2, 5.0, and 7.5 Inches Downstream of the TE of Rotor 1 – Throttle Position 26

ensemble-average of this spatially distributed signal was computed to give a space-time diagram for the wake unsteadiness along the chord of the vane at 50% immersion. This result, taken from Reference 15, is shown in Figure 18.

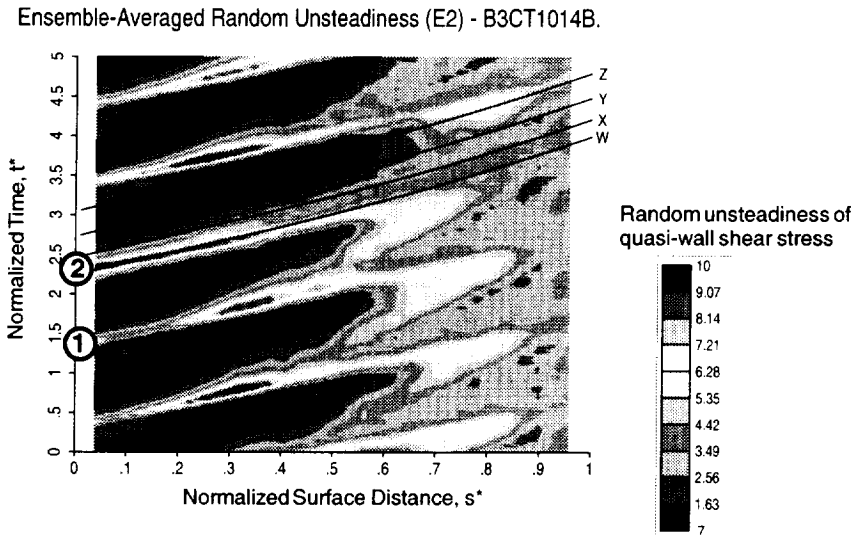

Figure 18. Random Unsteadiness Showing the Effect of Wake Turbulence Intensity on Boundary Layer Development, Suction Surface, Compressor Third Stage

The space-time diagram in Figure 18 shows results for both the rod and the rotor airfoil wakes, where stator chordwise surface distance is plotted along the abscissa and time, in units of wake passing period, is plotted along the ordinate, at midspan. The indicated space-time picture for Event 2 is for the rod wake, which has a peak turbulence intensity of 16%, compared with the indicated space-time picture for Event 1, a rotor blade wake, which has a peak turbulence intensity of 5.5%. Clearly there is a fundamental difference in turbulence intensity of the wakes, even though the wake mean velocity profiles were very nearly the same. Thus we cannot expect the correlation approach to yield total collapse or correlation of all wake data, especially if rotor airfoil shapes are significantly different.

3.4.4 Comparison with Existing Correlation Functions

Three different correlation models were investigated, and this section discusses the results of analyzing the collected data using these three methods.

Wake Mean Velocity Profile Shape: Wake profile data from the previously described LSFS at 35%, 50%, and 65% immersion were selected for the first step of the wake characteristics analysis. One of the characteristics in defining a rotor wake is the mean velocity profile. The shape of the profile is directly related to the harmonic content of the rotor wake/stator generated tone noise. The measured wake velocity was normalized as described in the following formulas, employing the methodology of Reference 2, and tangential distance from the rotor wake centerline is normalized as follows:

$$\eta = y/(\delta/2) \qquad (1)$$

where: y = tangential distance from wake centerline
δ = semiwake width (wake width at half-depth)

Wakes of downstream locations possessing self-similar properties should collapse to a single curve when appropriately normalized. In the past, a similarity profile of wake data has commonly been represented by the *Gaussian function:*

$$W_d/W_{dc} = e^{-0.693\eta^2} \tag{2}$$

where W_d is the local deficit in relative velocity in the wake at a distance x downstream from the rotor trailing edge and at tangential distance y from the wake centerline, referred to the free-stream velocity outside of the wake. W_{dc} is the deficit in wake centerline relative velocity at distance x from the rotor trailing edge.

Another function that has been shown to model wake profiles is the *hyperbolic secant function*, proposed in Reference 2, which has the form:

$$W_d/W_{dc} = \text{sech}\,(1.317\eta) \tag{3}$$

In addition to the above traditional formulae, an expression for this similarity profile was developed using a *Fourier Series expansion* of the form:

$$W_d/W_{dc} = A_0 + \sum_{n=1}^{N} [A_n \cos(n\pi x/L) + B_n \sin(n\pi x/L)] \tag{4}$$

where: A_n, B_n = Fourier coefficients
$A_0/2$ = Average value of function
$2L$ = Period of function
n = Harmonic number
N = Total number of harmonics in curve fit.

Consistent with the Gaussian and hyperbolic secant profile functions, which require establishing a correlation of W_{dc} as a function of downstream distance from the rotor blade trailing edge, and as a function of loading, the coefficients A_n and B_n and the parameter L can be a function of these same parameters. It is therefore appropriate to attempt to correlate these wake harmonic coefficients directly, as opposed to the classical approach of carrying out a Fourier Analysis of the expressions given by Equations (2) and (3).

The wake similarity profiles resulting from the Gaussian, hyperbolic secant, and Fourier Series formulas above are compared in Figures 19 through 21 for the UPS fan data, the LSFS data, and cylindrical rod wake data, respectively. Figure 19 shows a wake profile from the UPS fan rotor at two downstream locations, for 56% immersion at 7497 rpm. A typical rotor wake profile obtained from the LSFS stage is shown in Figure 20. The wake profiles from cylindrical rods of four different diameters were measured at six downstream locations in a free-jet facility in the GEAE ARL. In Figure 21, the result from a 0.063-in diameter of rod is shown. All the wake profiles shown in Figures 19 through 21 suggest reasonable agreement for any of the wake profile models, given in equations (1) through (4), and that there is good similarity between high speed (UPS), low speed (LSFS) data, and rod wake profile data..

Wake Mean Velocity Decay and Spreading: The Mani formulae (Reference 13) for the axial decay behavior of rotor wake mean velocities was modified by using the same functional form, but

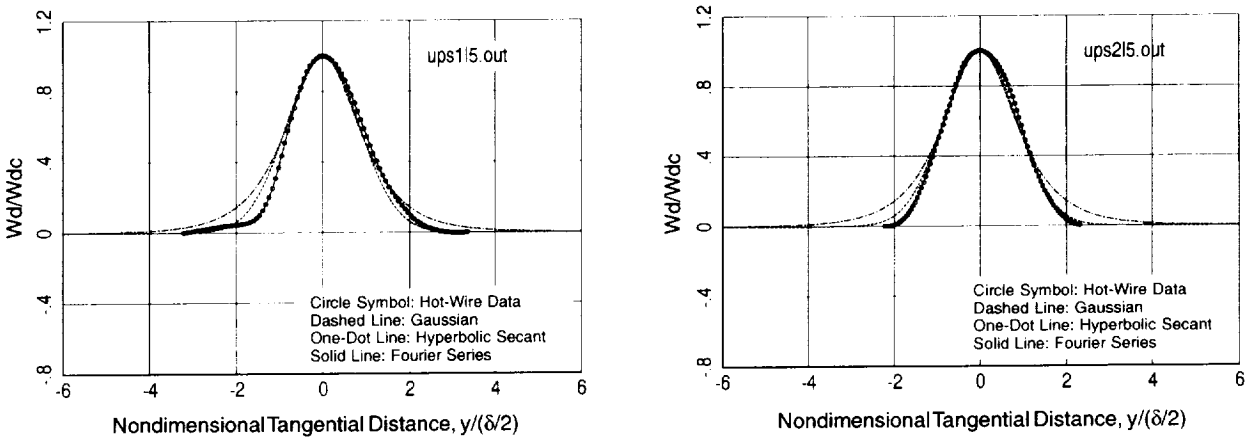

Figure 19. UPS Fan Rotor Wake Profiles at Fan Exit and OGV Inlet Downstream Locations at 56.0% Immersion with 7497 rpm

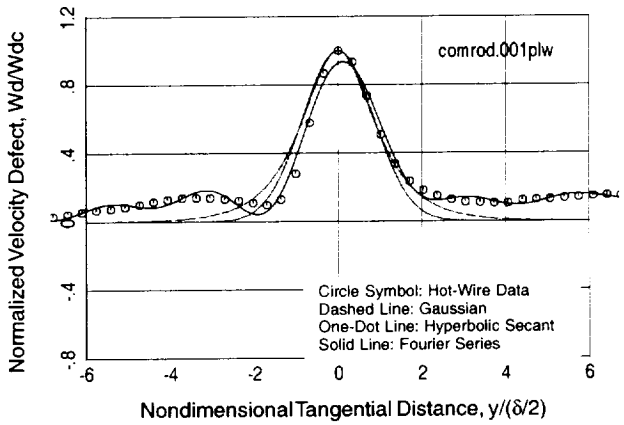

Figure 20. LSRC Rotor Wake Profiles at 50% Immersion

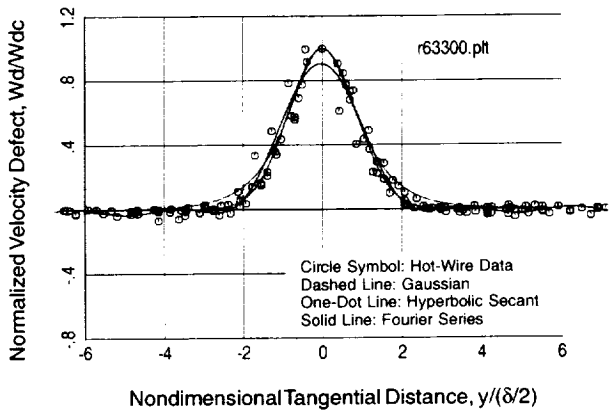

Figure 21. Wake Profiles from the Rod of 0.063-in Diameter at Six Downstream Locations

regression analysis was used on the experimental results to derive new coefficients and exponents. The original formula is given by the following:

$$\frac{U_0 - U}{U_0} = \frac{C_D c}{2\sqrt{\ell\pi\,(x + a)}} \exp\left[\frac{-y^2}{(x + a)\ell}\right] \tag{5}$$

where U_0 is the mean, free-stream velocity outside of the wake region, and U is the local velocity at point (x, y) in the wake. The airfoil chord is given by c; the virtual origin of the wake, relative to midchord, is given by a. The transverse distance from the wake centerline is given by y, and the airfoil drag coefficient is given by C_D. The downstream distance in Equation (5) is parallel to the airfoil chord with origin $x = 0$ at midchord. The wake scaling length in Equation (5) is given by the expression (Reference 10):

$$\ell = (0.68)^2 \cdot C_D \cdot c/\pi \tag{6}$$

The correlation of maximum wake defect or deficit as a function downstream distance x was obtained by fitting Equation (5) to wake profile data from the LSFS, where Equation (5) is evaluated at y=0 (the wake centerline), as follows:

$$\frac{(U_0 - U_{min})}{U_0} = 0.2057 \cdot x^{-0.3096} \tag{7}$$

This new amplitude formula was combined with the Equation (5), resulting in the following:

$$\frac{U_0 - U}{U_0} = 0.2057 \cdot x^{-0.3096} \exp\left[\frac{-y^2}{(x + a)\ell}\right] \tag{8}$$

The comparisons between Equations (5) and (8) with measured data at $x = 0.5$ inch downstream, at 50% immersion, are shown in Figure 22. The comparisons show that the empirical formula given by Equation (8) gives a much better estimate of the wake maximum defect, especially at small distances from the rotor trailing edge, although the formulation is incapable of simulating the asymmetry of the wake profile in its current form. The empirical constants in Equation (8) can be used to evaluate some of the parameters in Equation (5), and it is further deduced from comparing Equations (5) and (8) that the streamwise decay rate is not proportional to $1/\sqrt{x}$.

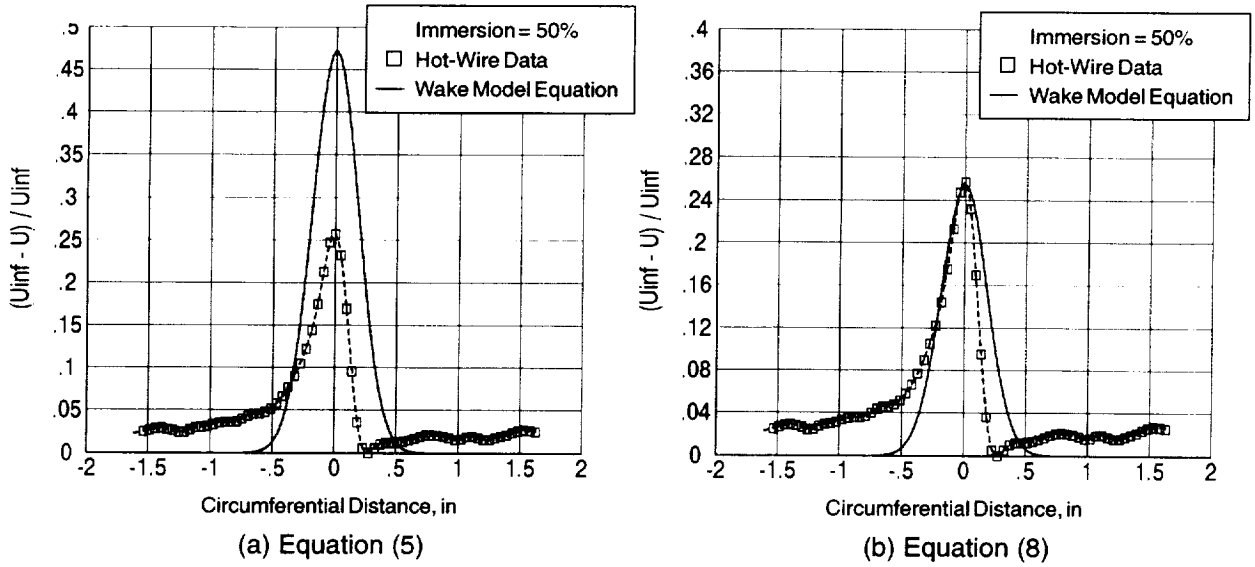

Figure 22. Velocity Correlation Comparison

Wygnanski et al. (Reference 5) give a modification of the formula in Equation (5) for the velocity decay behavior, and this expression was examined as a possible form for carrying out correlations of wake mean flow. Wygnanski's formula for mean velocity field was obtained experimentally from measurements of the wakes of several body shapes in a low-speed flow and is expressed by the modified exponential distribution:

$$\frac{U}{U_0} = 1 - \frac{u_0}{U_0} \exp(-0.637\eta^2 - 0.056\eta^4) \tag{9}$$

where: $\eta = y/L_0(x)$,
$L_0(x) = \delta/2$,
U_0 is the free-stream velocity,
$u_0(x)$ is the wake centerline velocity deficit, and
$L_0(x)$ is the length scale (half of wake width at half of u_0).

The parameters $u_0(x)$ and $L_0(x)$ are given in Reference 13 by algebraic similarity formulas with constants that can be evaluated from experimental data as follows:

$$(U_0/u_0)^2 = AX \tag{10}$$

$$(L_0/\theta)^2 = BX \tag{11}$$

where: $X = (x - x_0)/2\theta$

In these expressions, θ is the wake momentum thickness, x is the axial distance from the rotor blade trailing edge, and x_0 is a virtual origin. Note that Equations (2) and (9) give identical expressions when $\eta = 1$.

Equation (9) can be rewritten as follows:

$$\frac{U_0 - U}{u_0} = \exp(-0.637\eta^2 - 0.056\eta^4) \tag{12}$$

Also note that the wake deficit parameter u_0 in the Wygnanski formulas is the same as the the parameter W_{dc} used in the previous formulas.

3.5 Turbulence Model Correlations

The LSRC fan stage simulation data at 50% immersion was processed to evaluate the degree to which the Wygnanski parametric relationships could be used to correlate rotor wake turbulence data. Data from the four axial stations and the three throttle settings were normalized via the formulas given by Equations (10) and (11), and the results are shown in Figure 23 for wake half-width and Figure 24 for velocity deficit. A regression fit of the resulting data trends was performed, and the resulting equations obtained are given as follows.

For wake half-width, a first-order correlation formula was obtained as follows:

$$(L_0/\theta)^2 = 0.158X + 2.494 \tag{13}$$

For wake centerline deficit, the following expression was obtained:

$$(U_0/u_0)^2 = 2.133X + 7.458 \tag{14}$$

These trend lines are also shown in Figures 23 and 24. Note that Equations (13) and (14) indicate that the virtual origins of the wake centerline velocity deficit and wake half-width may not be the same, since different, nonzero constants were deduced.

Comparisons were made between hot-wire data and the wake profile correlation Equation (12) at 50% immersion. The hot-wire data were normalized by using the expression $(U_0 - U) / (U_0 - U_{min})$, and L_0 was calculated by using regression Equation (13). Comparisons show very good correlation for all the axial locations, Figure 25.

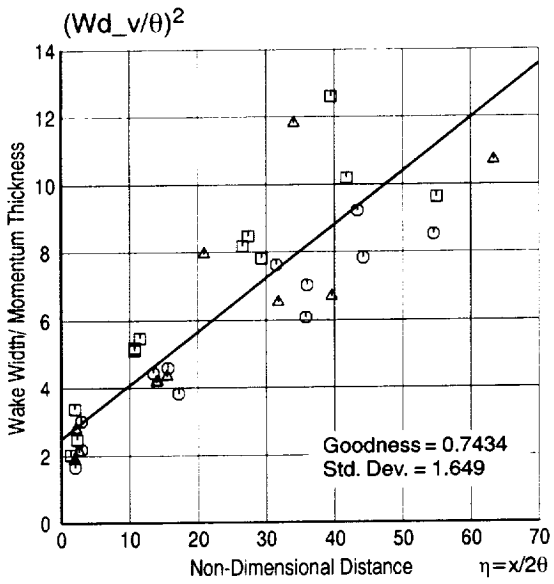

Figure 23. Wake Width Variation Along X Axis

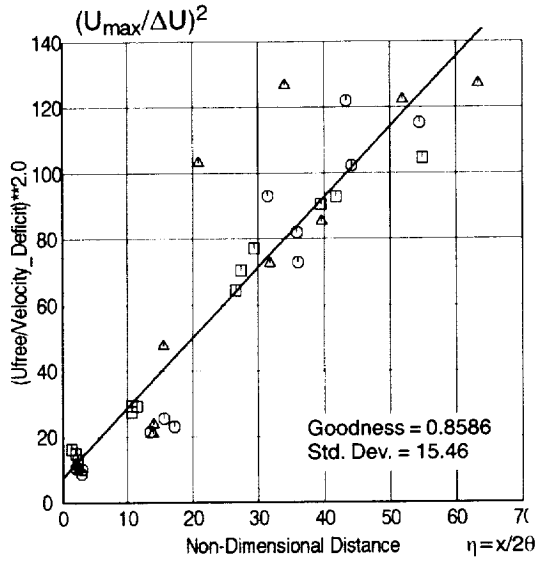

Figure 24. Velocity Deficit in the Wake Variation Along X Axis

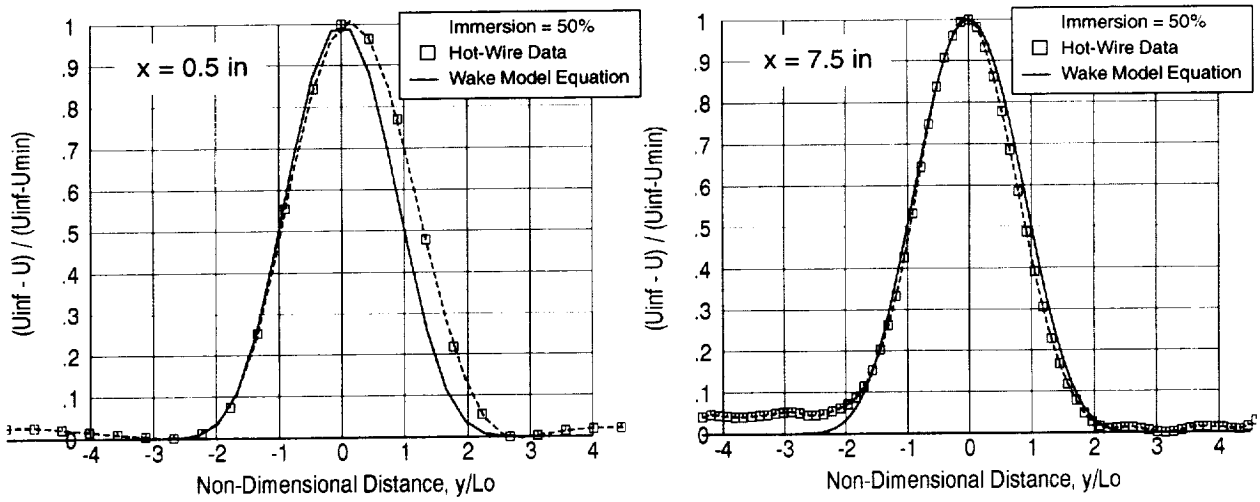

Figure 25. Mean Velocity Comparison: x = 0.5 and x = 7.5 at Throttle 30

Correlations of various turbulence parameters were developed using the LSFS data at 35, 50, and 65% immersion. These included total wake turbulence intensity (maximum and circumferentially averaged levels), and the individual component turbulence velocity amplitudes in the axial, circumferential, and radial directions. In addition, the axial length scales for the axial, circumferential, and radial components of turbulent velocity correlations were also normalized, and correlation distributions and trend lines were developed for these parameters. The correlation plots for mean velocity profile parameters are shown in Figures 23 and 24. The correlation plots for turbulence intensity and component turbulence velocity amplitudes are shown in Figures 26 through 35. The correlation plots for turbulence length scales for the three components of turbulence velocity are shown in Figures 36 through 44.

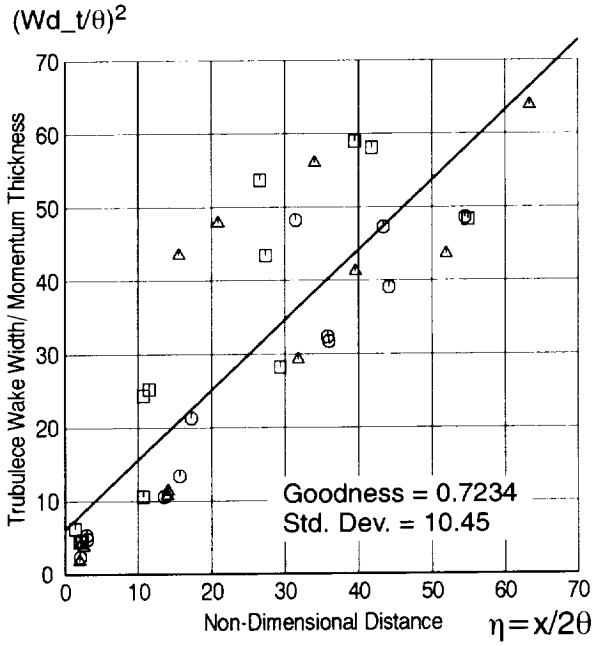

Figure 26. Turbulence Velocity Width Variation Along X Axis

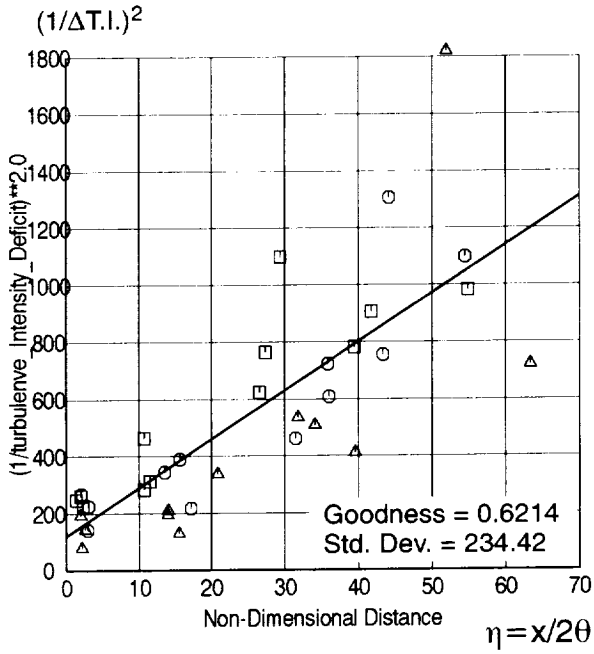

Figure 27. Turbulence Intensity Defect (Difference Between Free Stream and Wake Centerline) Along X Axis

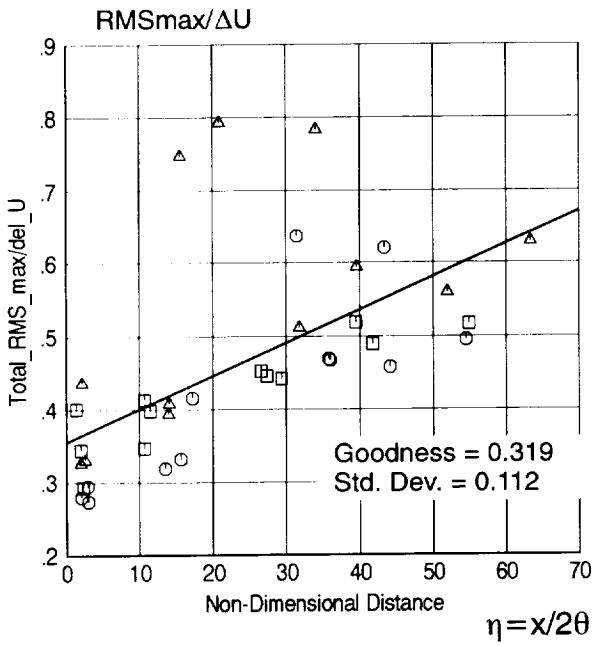

Figure 28. Total Maximum Turbulence Velocity Variation Along X Axis

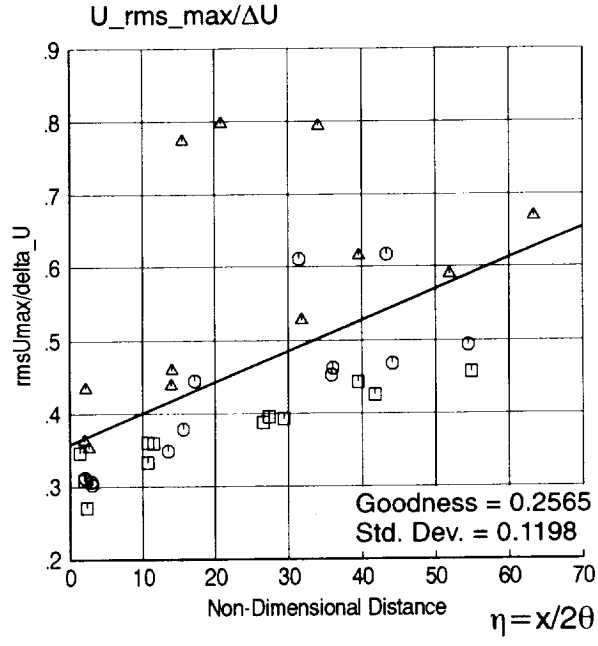

Figure 29. U-Component Maximum Turbulence Velocity Variation Along X Axis

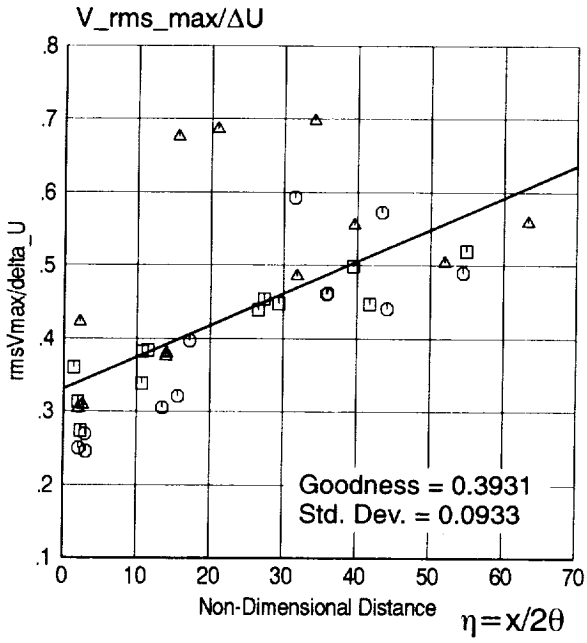

Figure 30. V-Component Maximum Turbulence Velocity Variation Along X Axis

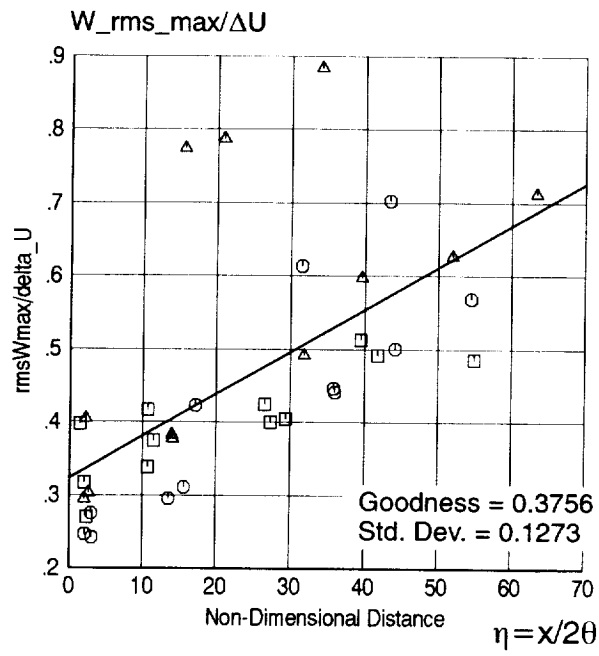

Figure 31. W-Component Maximum Turbulence Velocity Variation Along X Axis

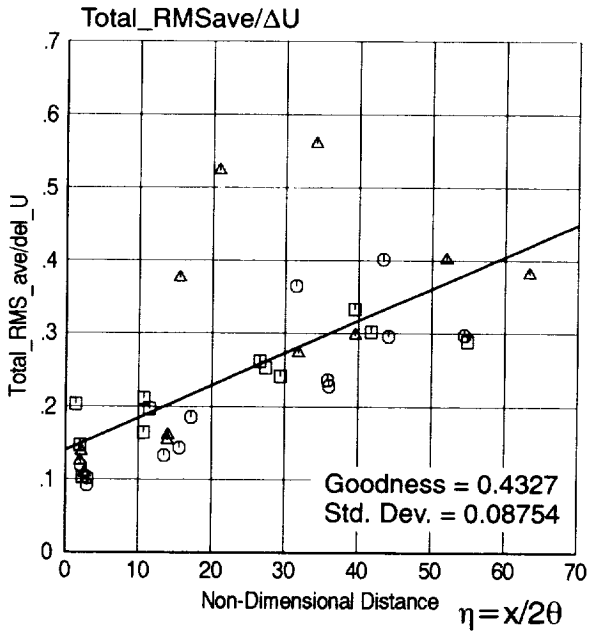

Figure 32. Total Averaged Turbulence Velocity Variation Along X Axis

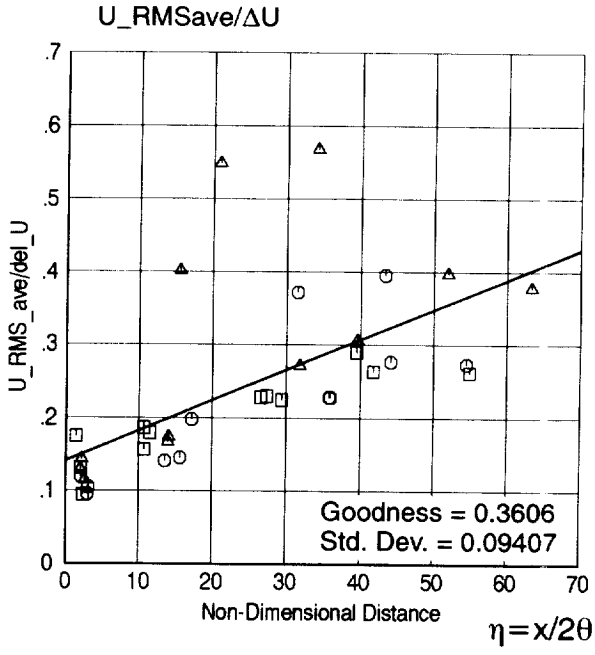

Figure 33. U-Component Averaged Turbulence Velocity Variation Along X Axis

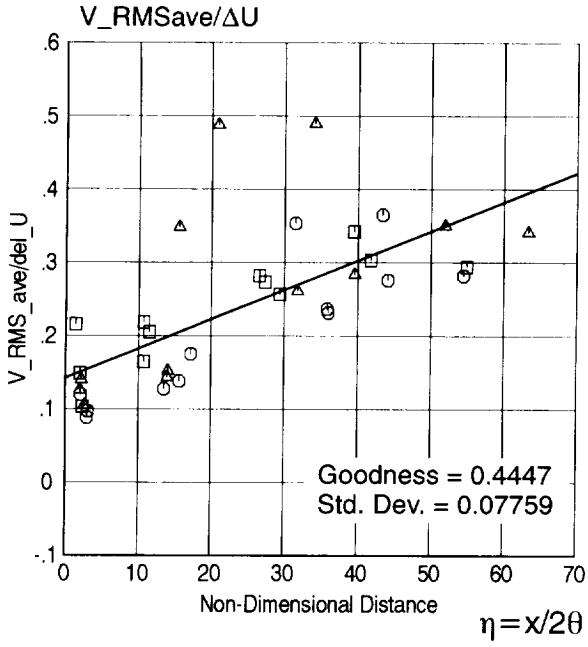

Figure 34. V–Component Averaged Turbulence Velocity Variation Along X Axis

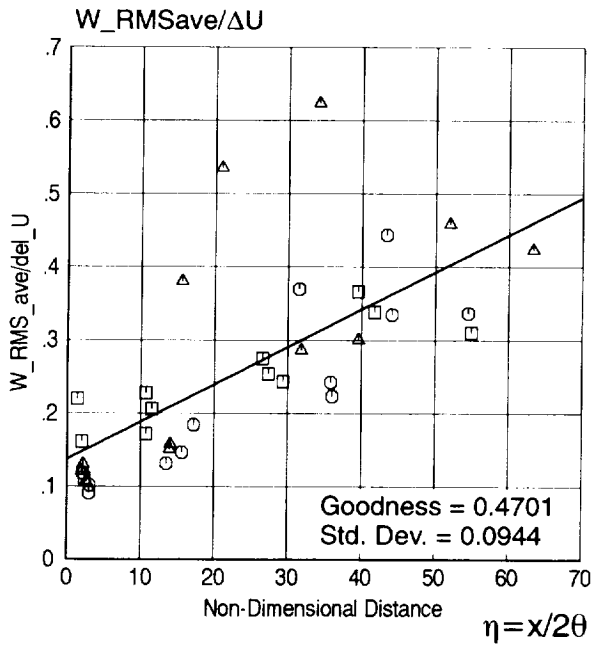

Figure 35. W–Component Averaged Turbulence Velocity Variation Along X Axis

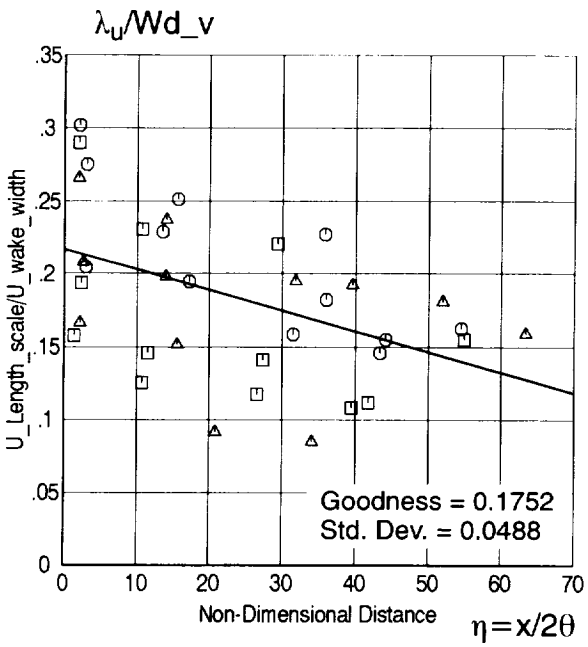

Figure 36. U-Component Length Scale Normalized by Velocity Wake Width Variation Along X Axis

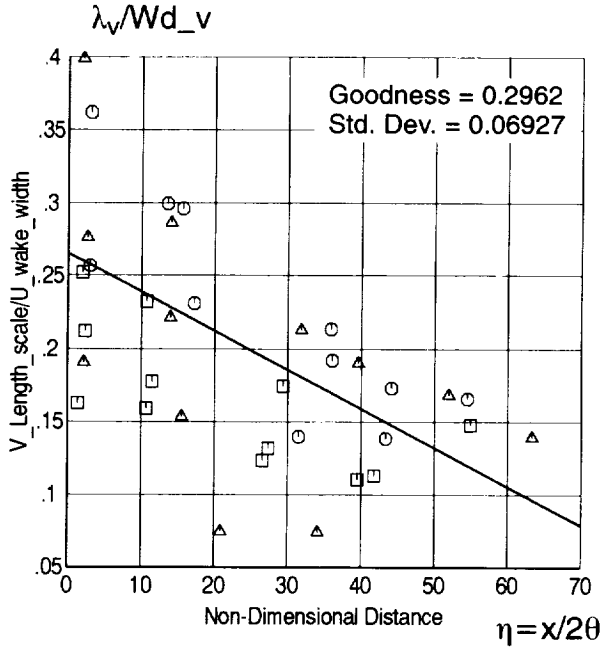

Figure 37. V-Component Length Scale Normalized by Velocity Wake Width Variation Along X Axis

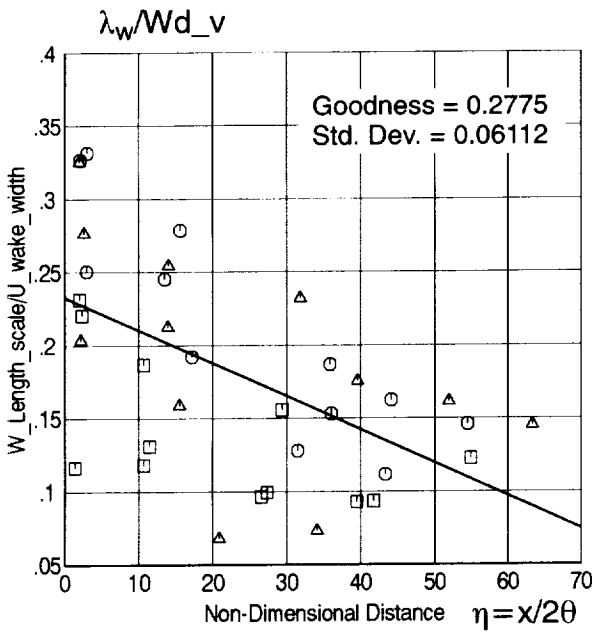

Figure 38. W-Component Length Scale Normalized by Velocity Wake Width Variation Along X Axis

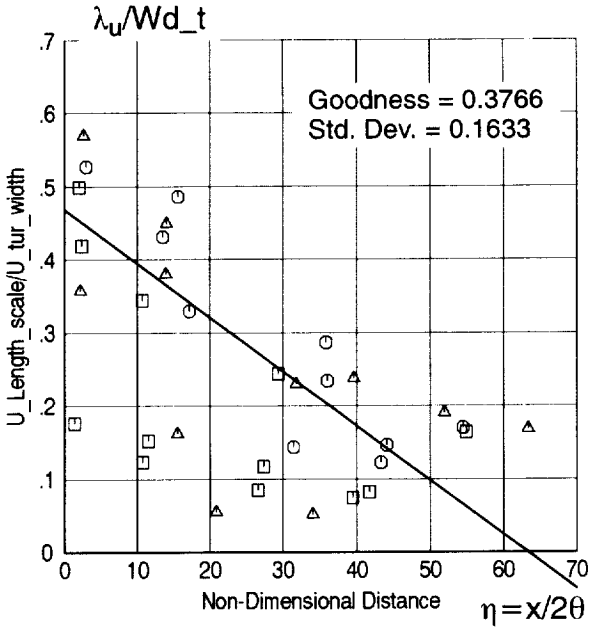

Figure 39. U-Component Length Scale Normalized by Turbulence Velocity Wake Width Variation along X Axis

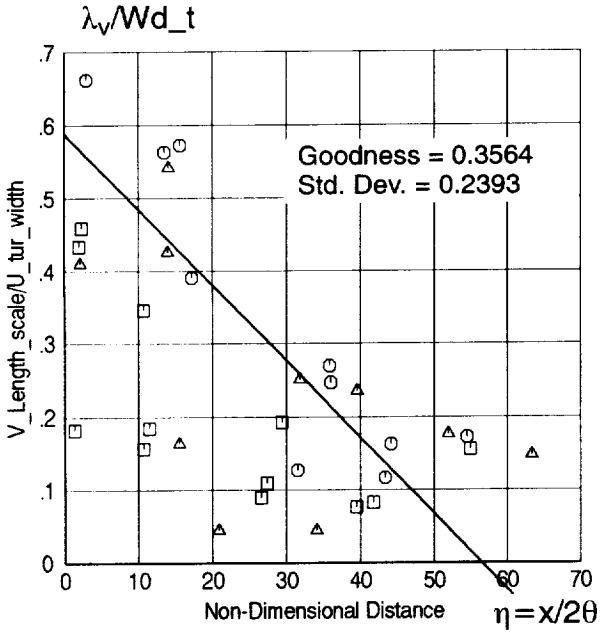

Figure 40. V-Component Length Scale Normalized by Turbulence Velocity Wake Width Variation along X Axis

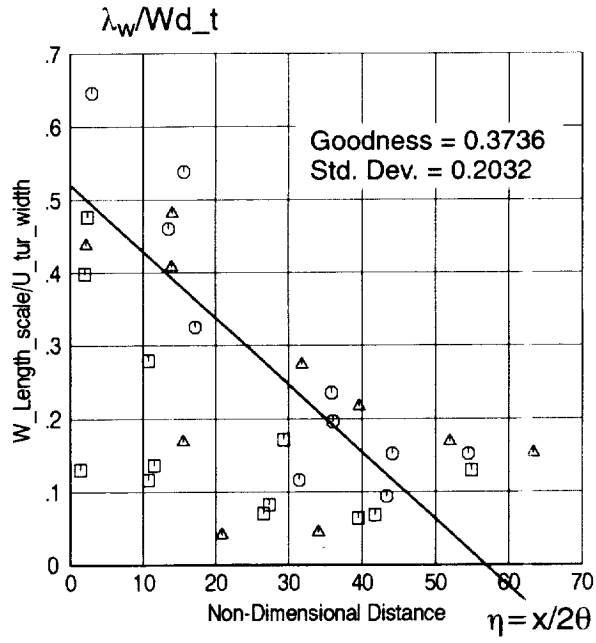

Figure 41. W-Component Length Scale Normalized by Turbulence Velocity Wake Width Variation along X Axis

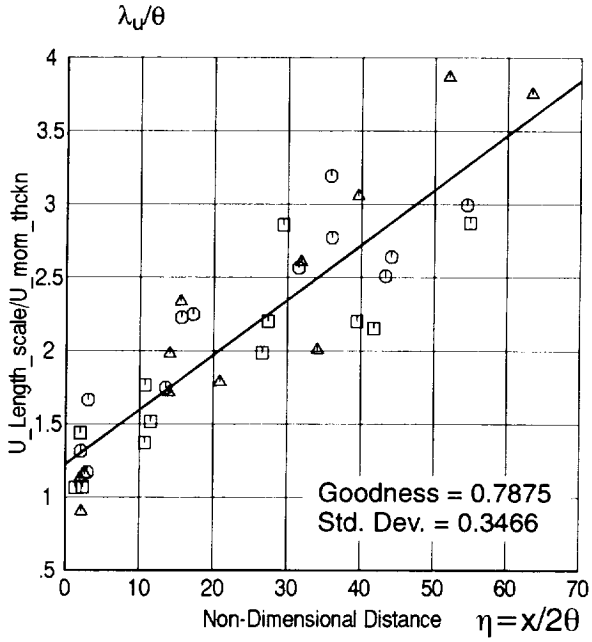

Figure 42. U-Component Length Scale Normalized by Momentum Thickness Variation Along X Axis

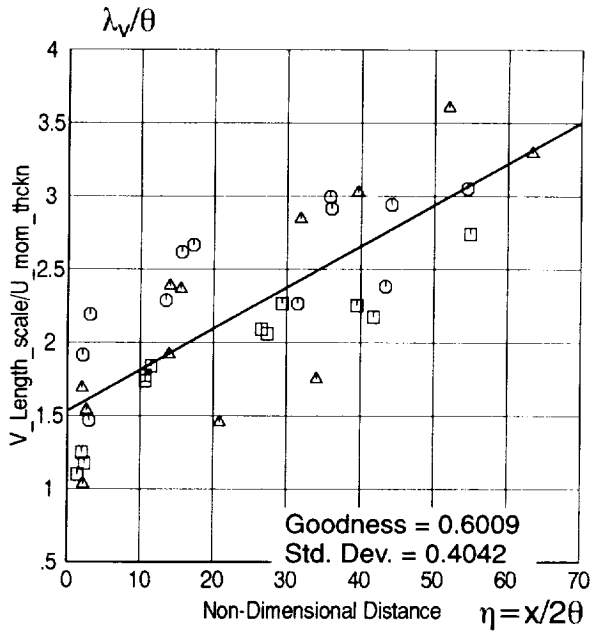

Figure 43. V-Component Length Scale Normalized by Momentum Thickness Variation Along X Axis

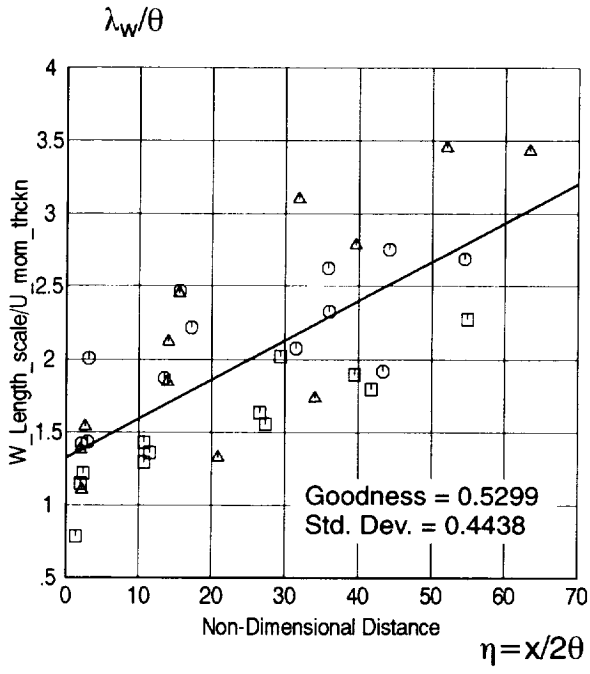

Figure 44. W-Component Length Scale Normalized by Momentum Thickness Variation Along X Axis

Plots were also made of the spanwise distribution of the various turbulence velocity length scales. These plots are shown in Figures 45 through 65. In general, there is considerable scatter near the tip end-wall region (near zero immersion). The trends appear fairly consistent along the rest of the span, for each distance downstream, until the hub end-wall is approached where again the data scatter is greater.

Figures 66 through 68, plots of overall turbulence intensity versus immersion depth, indicate that turbulence intensity does not vary significantly with downstream distance. This seems contrary to intuition, especially when looking at the normalized trends shown in Figures 28 through 35. However, the normalized trends are based on normalizing turbulence velocity root mean square (rms) amplitude by wake centerline velocity defect which, as Figure 27 shows, decreases with increasing distance downstream of the rotor. The radial profiles of turbulence intensity shown in Figures 66 through 68 are normalized by rotor exit free-stream velocity, which is approximately constant with increasing downstream distance. Hence, the wake velocity defect decays, and the turbulence intensity (as a fraction of the velocity defect) increases, but the absolute value of turbulence velocity stays approximately constant.

It is also of interest to note that the individual turbulence velocity components (Figures 33 through 35) are not significantly different from one another, indicating that, at least in the midspan region outside of the end-wall flows, turbulence is approximately isotropic. This seems also to be true for the axial length scales corresponding to each of the turbulence velocity components, although the differences are somewhat greater. It was found that the axial length scales correlated best when normalized by the local wake momentum thickness as shown in Figure 42. The correlations were found to be very weak when normalized by either wake mean velocity half-width, wake turbulence profile half-width, or blade-to-blade circumferential spacing.

Linear regression lines for the various turbulence and mean velocity profile parameters are also shown in all figures for correlation. The resulting regression line equations are listed in Table 6. Also listed in Table 6 are the data correlation regression line standard deviation and "goodness of fit," equivalent to the square root of the classical R2 statistics parameter. The resulting regression lines were used to predict the mean velocity and turbulence properties of the UPS fan described in Section 3.2.1, page 19. These comparisons are shown in Figures 69 and 70. It can be seen that the regression equations based on the low-speed fan simulation stage data are consistent with the high-speed UPS fan results.

3.6 Final Aeroacoustic Turbulence Prediction Model

Based on the results discussed in Section 3.5, the following correlation equations are recommended for estimating fan rotor wake mean velocity and turbulence velocities and scales, given the rotor chord, rotor, section drag coefficient or trailing edge momentum thickness, the mean velocity profile velocity defect is expressed as (see Figure 24, page 38):

$$\left(\frac{U_0}{u_0}\right)^2 = 2.133\left(\frac{x}{2\theta}\right) + 7.458 \tag{15}$$

Mean velocity profile wake half-width (see Figure 23, page 38):

$$\left(\frac{L_0}{\theta}\right)^2 = 0.158\left(\frac{x}{2\theta}\right) + 2.494 \tag{16}$$

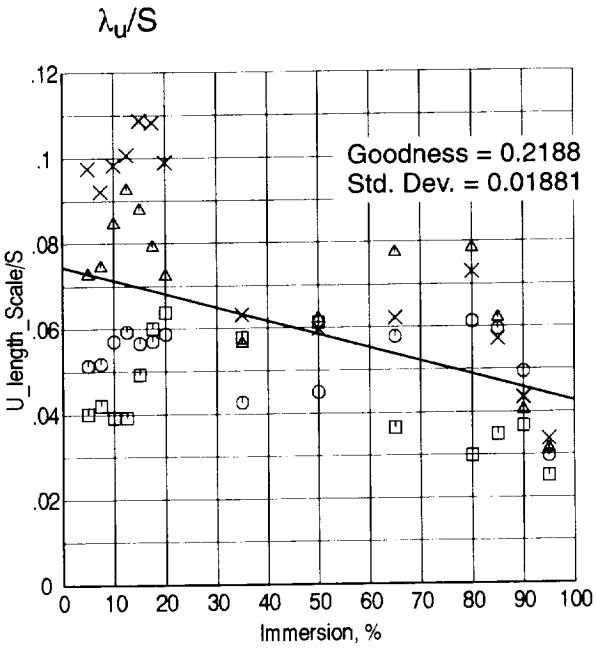

Figure 45. U-Component Length Scale Normalized by BB Spacing Variation Along Radial Direction for Throttle 45

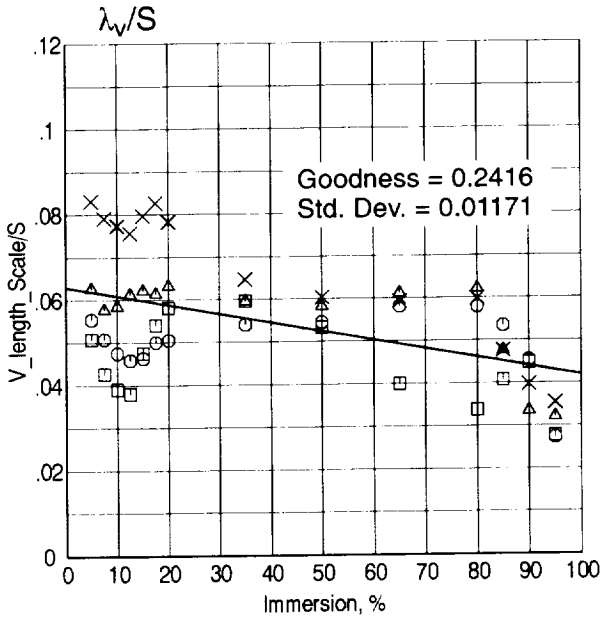

Figure 46. V-Component Length Scale Normalized by BB Spacing Variation Along Radial Direction for Throttle 45

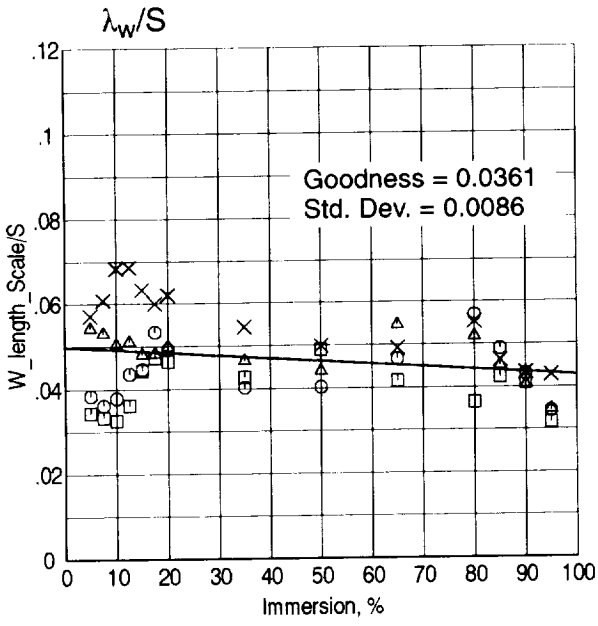

Figure 47. W-Component Length Scale Normalized by BB Spacing Variation Along Radial Direction for Throttle 45

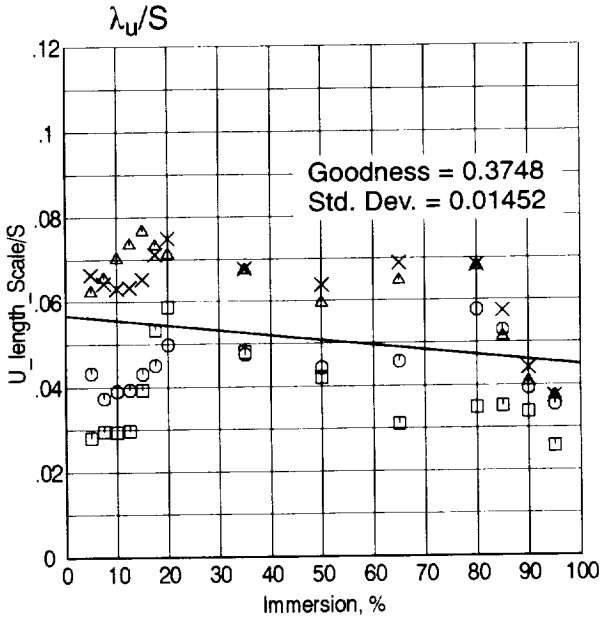

Figure 48. U-Component Length Scale Normalized by BB Spacing Variation Along Radial Direction for Throttle 30

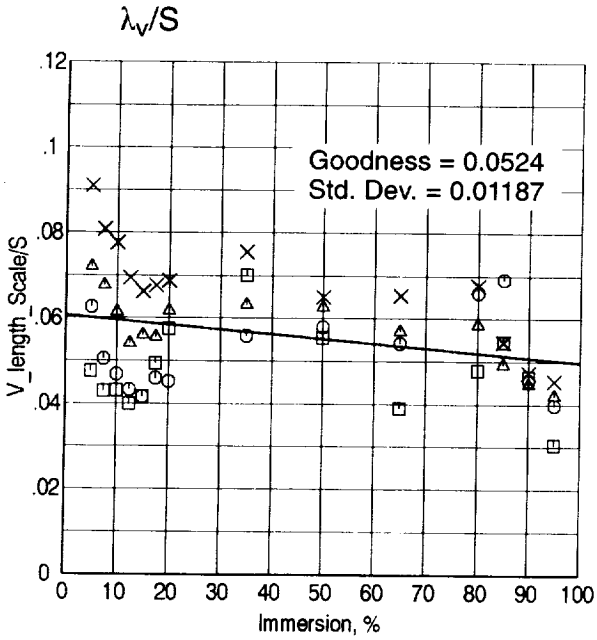

Figure 49. V-Component Length Scale Normalized by BB Spacing Variation Along Radial Direction for Throttle 30

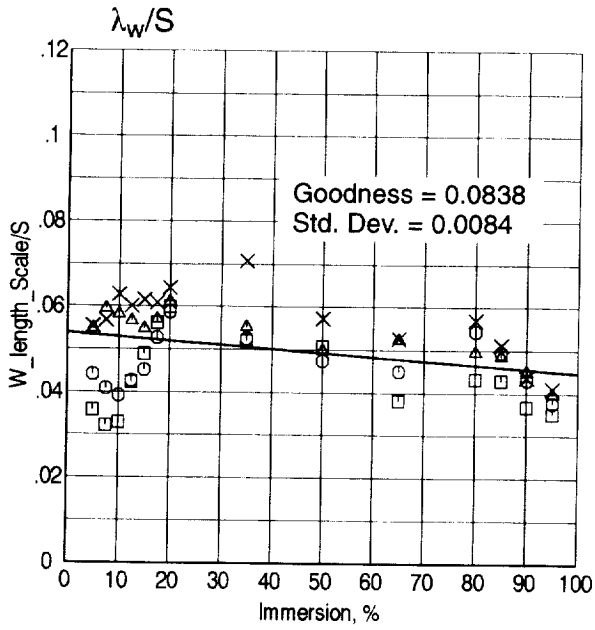

Figure 50. W-Component Length Scale Normalized by BB Spacing Variation Along Radial Direction for Throttle 30

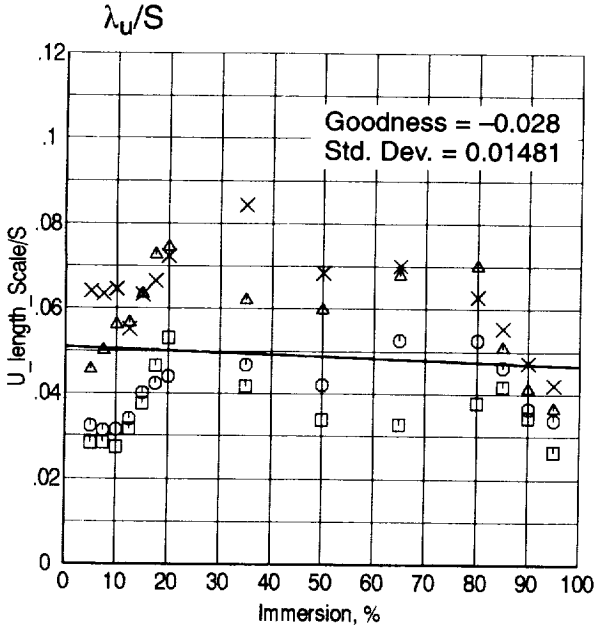

Figure 51. U-Component Length Scale Normalized by BB Spacing Variation Along Radial Direction for Throttle 26

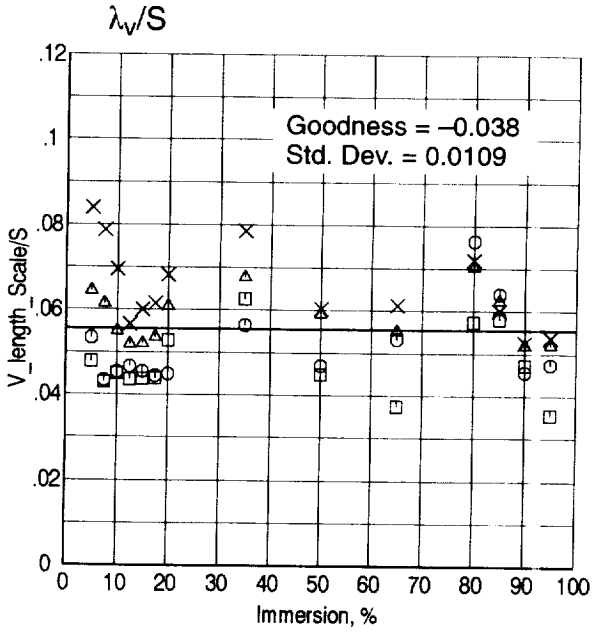

Figure 52. V-Component Length Scale Normalized by BB Spacing Variation Along Radial Direction for Throttle 26

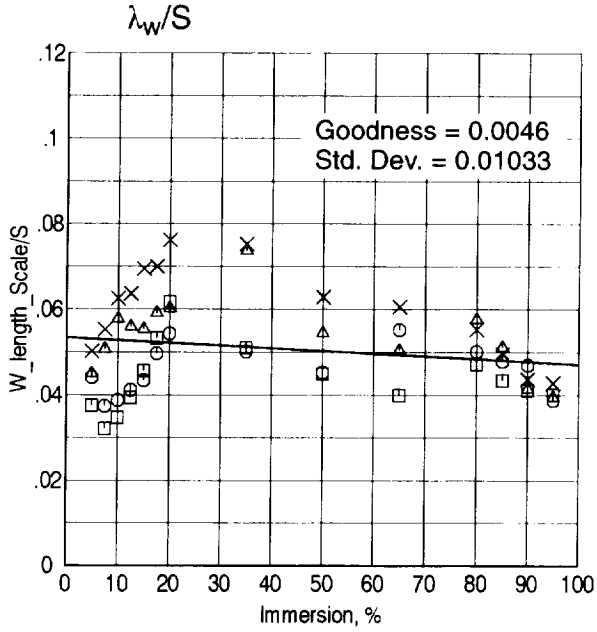

Figure 53. W-Component Length Scale Normalized by BB Spacing Variation Along Radial Direction for Throttle 26

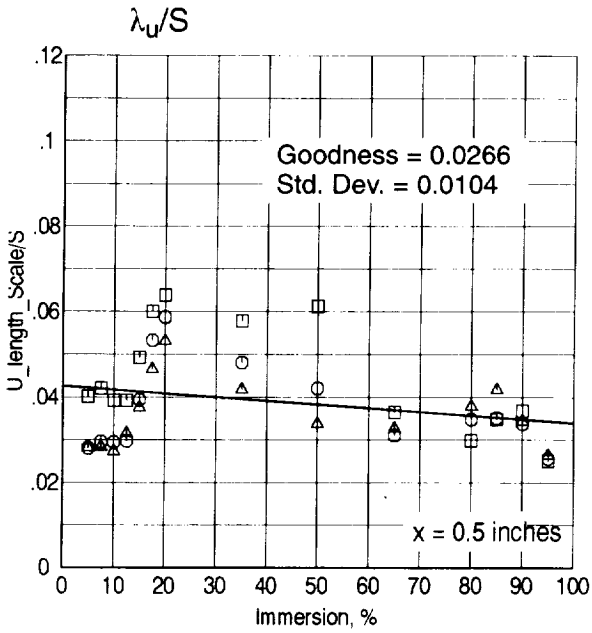

Figure 54. U-Component Length Scale (Throttle 45, 30, and 26) Normalized by BB Spacing Variation Along Radial Direction at x = 0.5

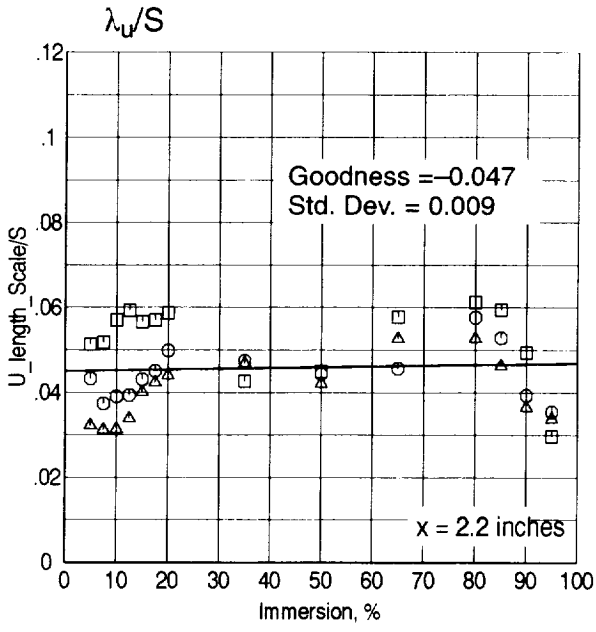

Figure 55. U-Component Length Scale (Throttle 45, 30, and 26) Normalized by BB Spacing Variation Along Radial Direction at x = 2.2

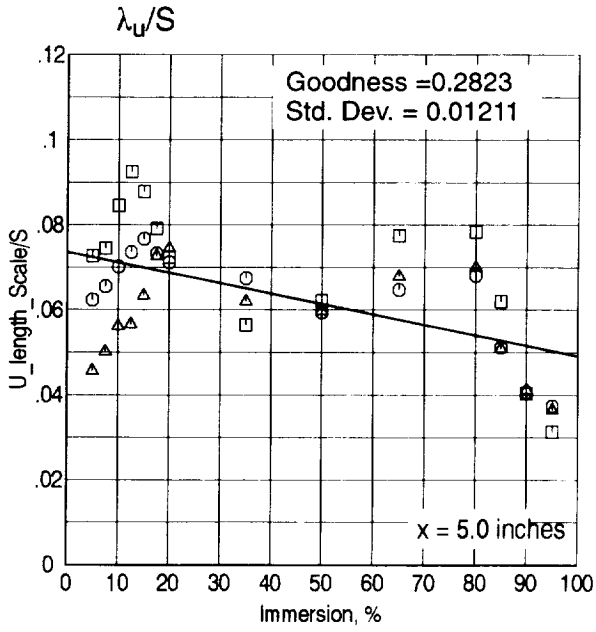

Figure 56. U-Component Length Scale (Throttle 45, 30, and 26) Normalized by BB Spacing Variation Along Radial Direction at x = 5.0

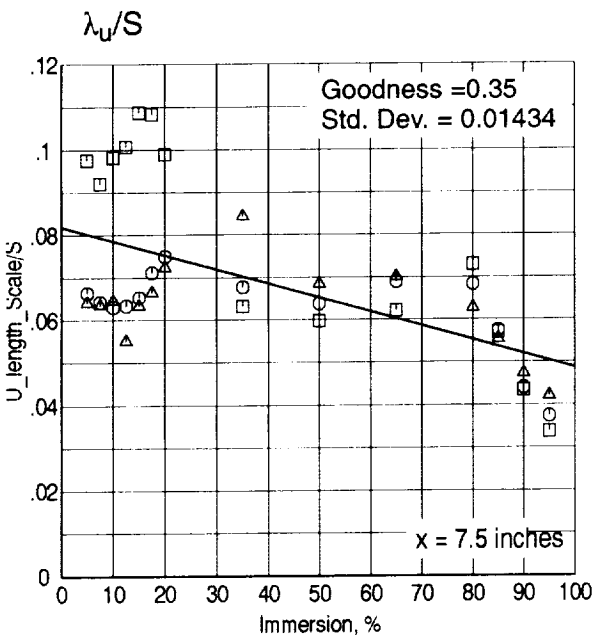

Figure 57. U-Component Length Scale (Throttle 45, 30, and 26) Normalized by BB Spacing Variation Along Radial Direction at x = 7.5

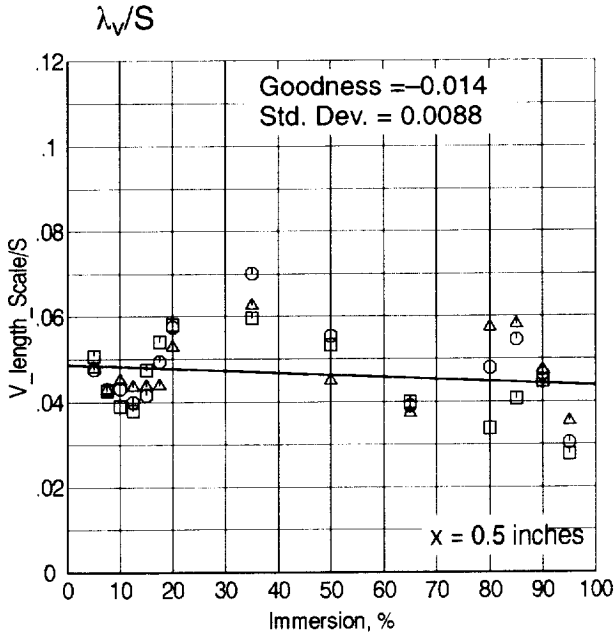

Figure 58. V-Component Length Scale (Throttle 45, 30, and 26) Normalized by BB Spacing Variation Along Radial Direction at x = 0.5

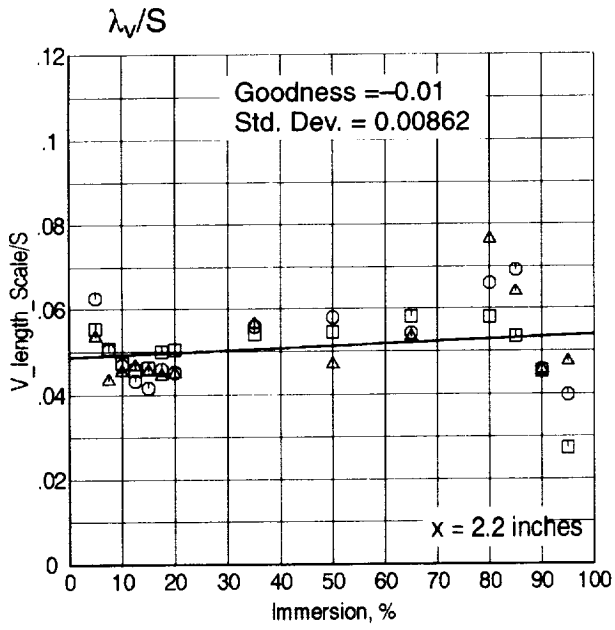

Figure 59. V-Component Length Scale (Throttle 45, 30, and 26) Normalized by BB Spacing Variation Along Radial Direction at x = 2.2

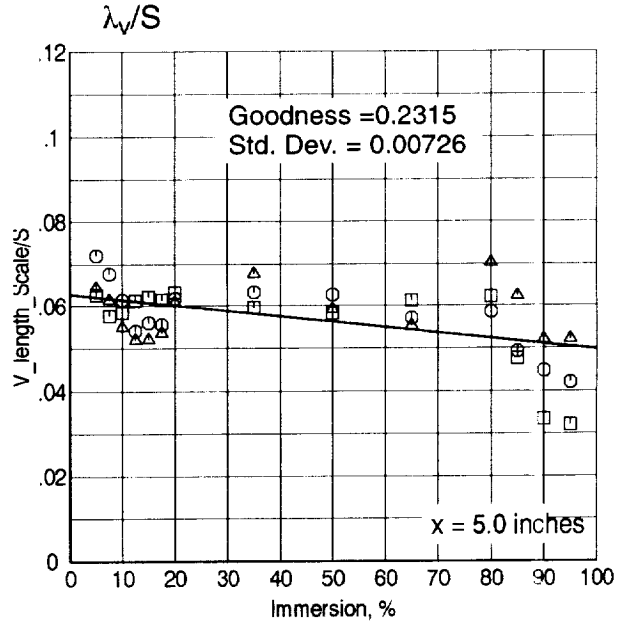

Figure 60. V-Component Length Scale (Throttle 45, 30, and 26) Normalized by BB Spacing Variation Along Radial Direction at x = 5.0

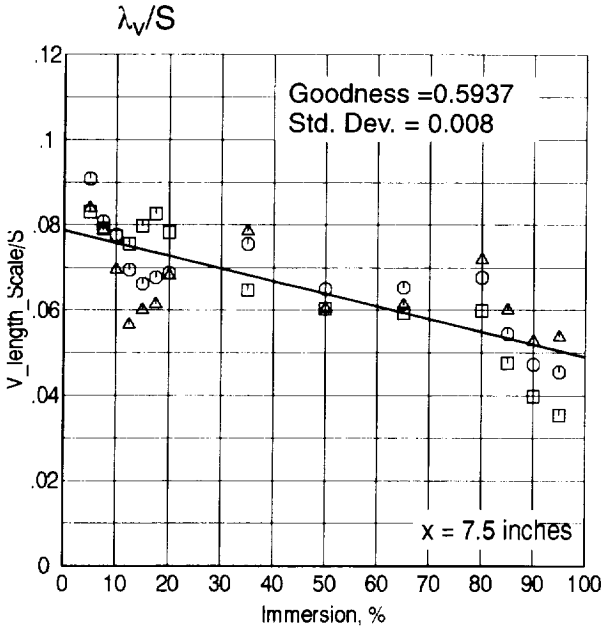

Figure 61. V–Component Length Scale (Throttle 45, 30, and 26) Normalized by BB Spacing Variation Along Radial Direction at x =7.5

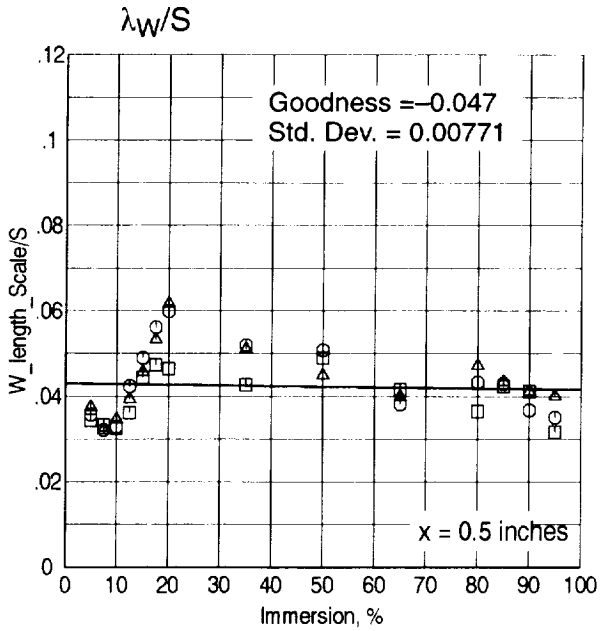

Figure 62. W–Component Length Scale (Throttle 45, 30, and 26) Normalized by BB Spacing Variation Along Radial Direction at x =0.5

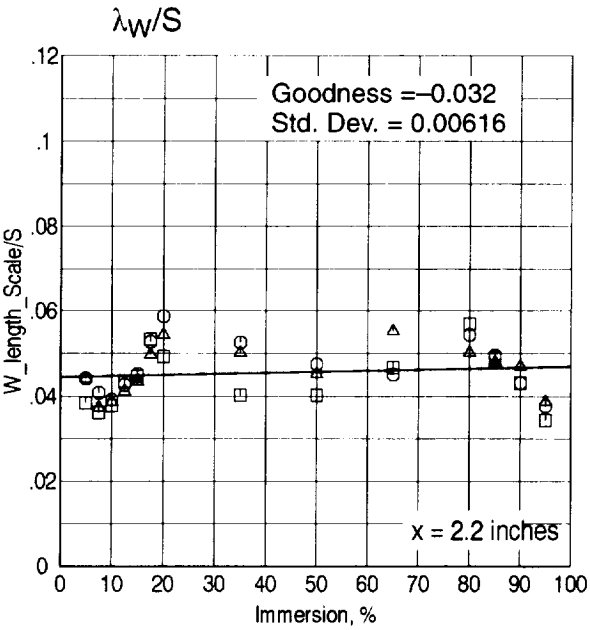

Figure 63. W–Component Length Scale (Throttle 45, 30, and 26) Normalized by BB Spacing Variation Along Radial Direction at x =2.2

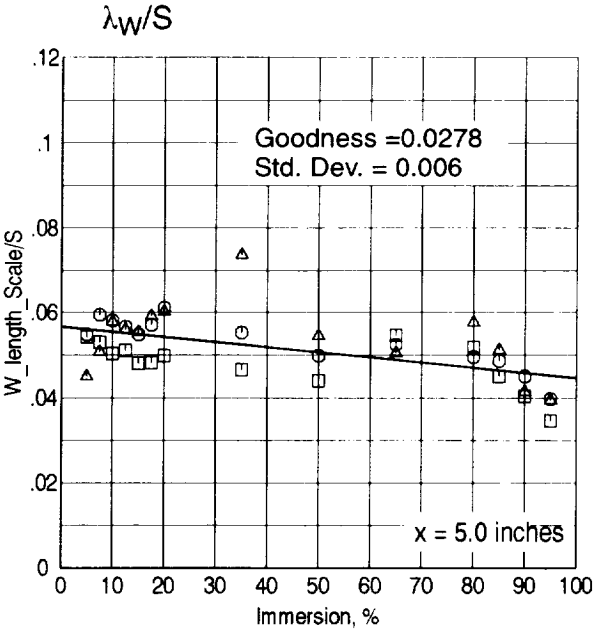

Figure 64. W–Component Length Scale (Throttle 45, 30, and 26) Normalized by BB Spacing Variation Along Radial Direction at x =5.0

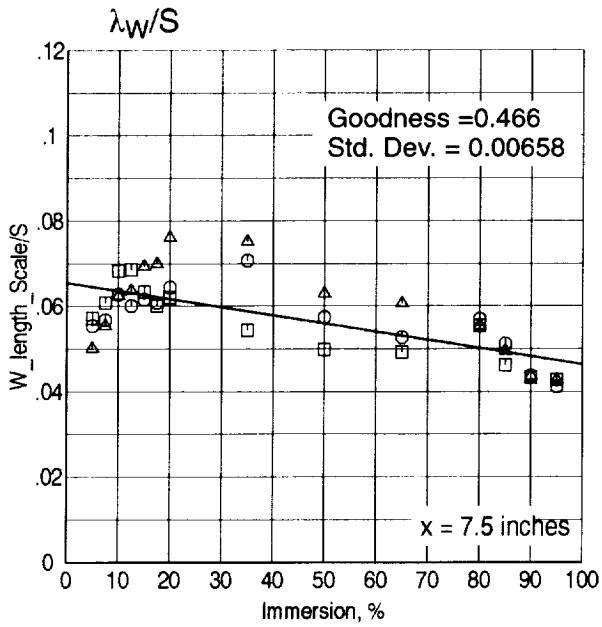

Figure 65. W–Component Length Scale (Throttle 45, 30, and 26) Normalized by BB Spacing Variation Along Radial Direction at x =7.5

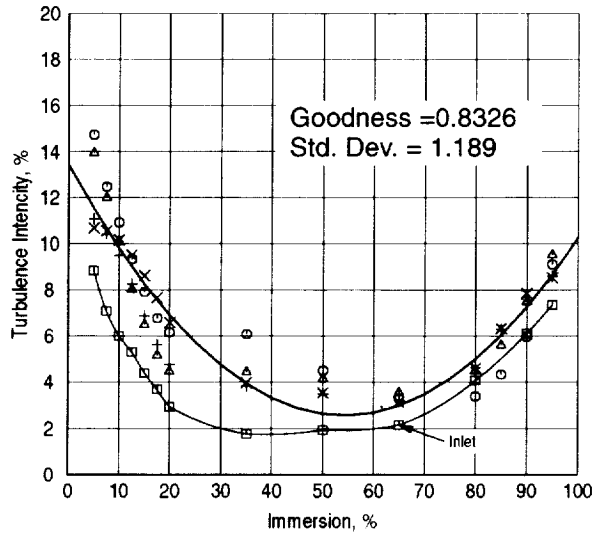

Figure 66. Turbulence Intensity Distribution at Various Downstream Locations Along Immersion for Throttle 45

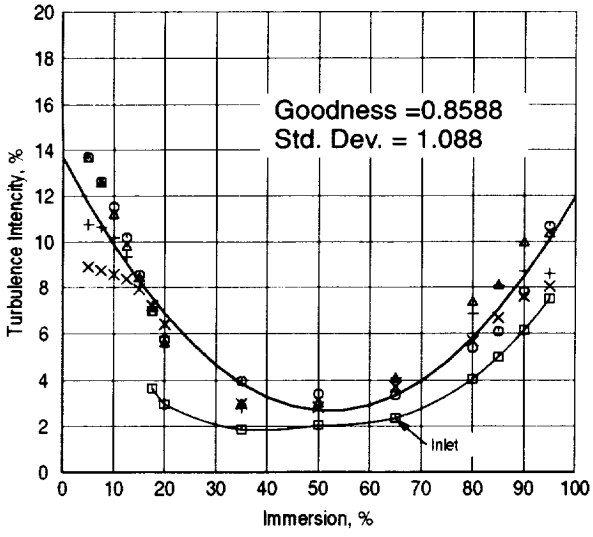

Figure 67. Turbulence Intensity Distribution at Various Downstream Locations Along Immersion for Throttle 30

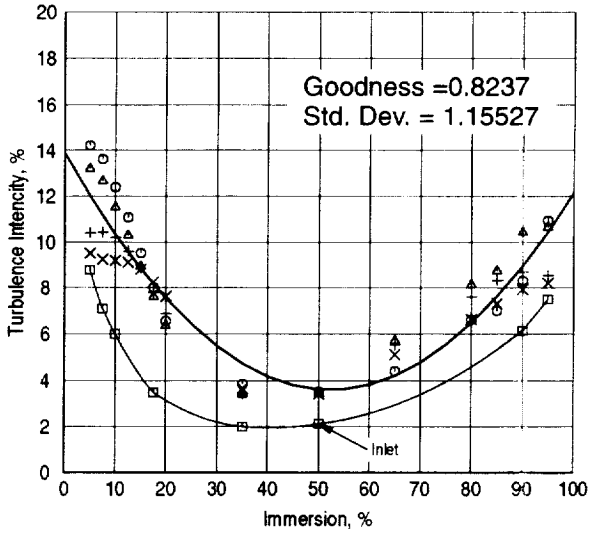

Figure 68. Turbulence Intensity Distribution at Various Downstream Locations Along Immersion for Throttle 26

Table 6. Regression Line Equations

Figure	Equation: y = ax + b		Goodness	Standard Deviation
	a	b		
23	0.1579	2.4946	0.7434	1.6949
24	2.133	7.458	0.8586	15.46
26	0.9521	6.0965	0.7234	10.45
27	17.02	119.93	0.6214	234.42
28	0.452×10^{-2}	0.3553	0.319	0.112
29	0.423×10^{-2}	0.358	0.2565	0.1198
30	0.436×10^{-2}	0.3306	0.3931	0.0933
31	0.576×10^{-2}	0.3233	0.3756	0.1273
32	0.4417×10^{-2}	0.1402	0.4327	0.08754
33	0.413×10^{-2}	0.1412	0.3606	0.09407
34	0.40×10^{-2}	0.1423	0.4447	0.07759
35	0.511×10^{-2}	0.1371	0.4701	0.0944
36	-0.141×10^{-2}	0.217	0.1752	0.0488
37	-0.267×10^{-2}	0.2655	0.2962	0.06927
38	-0.226×10^{-2}	0.2329	0.2775	0.06112
39	-0.74×10^{-2}	0.4687	0.3766	0.1633
40	-0.104×10^{-1}	0.5889	0.3564	0.2393
41	-0.9155×10^{-2}	0.5209	0.3736	0.2032
42	0.375×10^{-1}	1.223	0.7875	0.3466
43	0.282×10^{-1}	1.532	0.6009	0.4042
44	0.269×10^{-1}	1.3225	0.5299	0.4438
45	-0.32×10^{-3}	0.0745	0.2188	0.01881
46	-0.211×10^{-3}	0.063	0.2416	0.0117
47	-0.707×10^{-4}	0.0499	0.0361	0.0086
48	-0.1205×10^{-3}	0.05678	0.3748	0.01452
49	-0.109×10^{-3}	0.0606	0.0524	0.01187
50	-0.9117×10^{-4}	0.0538	0.0838	0.0084
51	-0.4328×10^{-4}	0.05101	−0.028	0.01481
52	0.1848×10^{-6}	0.0558	−0.038	0.0109
53	-0.6326×10^{-4}	0.05347	0.0046	0.01033
54	-0.8652×10^{-4}	0.04258	0.0266	0.0104
55	0.1795×10^{-4}	0.04503	−0.047	0.009
56	-0.2442×10^{-3}	0.07361	0.2823	0.01211
57	-0.3324×10^{-3}	0.0819	0.35	0.01434
58	-0.498×10^{-4}	0.04873	−0.014	0.0088
59	0.5125×10^{-4}	0.04871	−0.01	0.00862
60	-0.13×10^{-3}	0.06273	0.2315	0.00726
61	-0.2977×10^{-3}	0.07876	0.5937	0.008
62	-0.1388×10^{-4}	0.04293	−0.047	0.00771
63	0.2475×10^{-4}	0.0444	−0.032	0.00616
64	-0.12×10^{-3}	0.05664	0.0278	0.006
65	-0.1911×10^{-3}	0.06552	0.466	0.00658

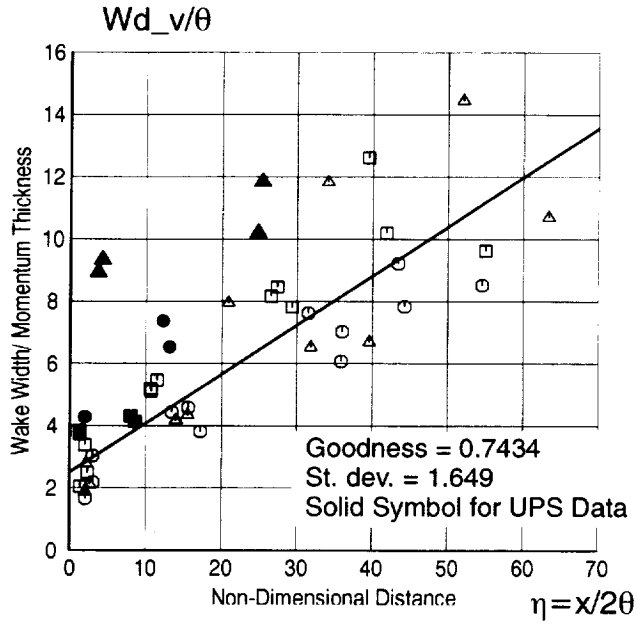

Figure 69. Wake Width Variation Along X Axis for LSFS and UPS Data

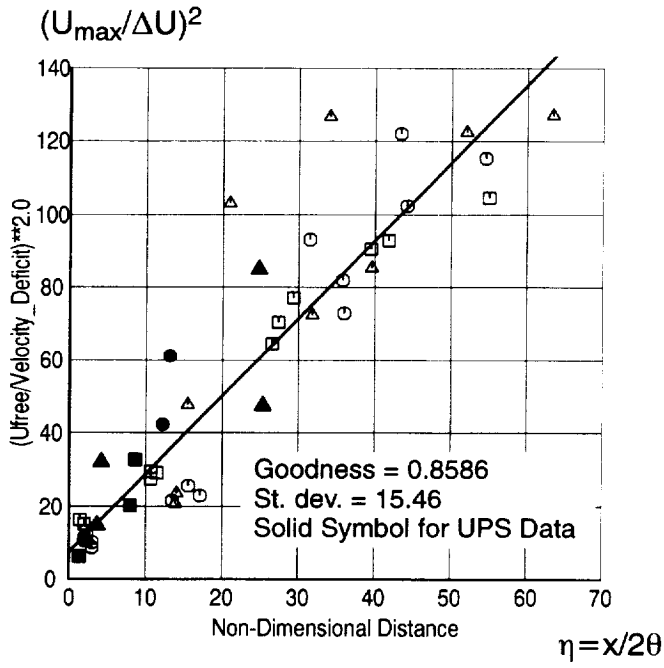

Figure 70. Velocity Deficit in the Wake Variation Along X Axis for LSFS and UPS Data

Total wake rms turbulence velocity, circumferentially averaged (see Figure 32, page 40):

$$\frac{V'}{u_0} = 0.004417\left(\frac{x}{2\theta}\right) + 0.1402 \tag{17}$$

Axial component of turbulence rms velocity, circumferentially averaged (see Figure 33, page 40):

$$\frac{u'}{u_0} = 0.004132\left(\frac{x}{2\theta}\right) + 0.1412 \tag{18}$$

Circumferential component of turbulence rms velocity, circumferentially averaged (see Figure 34, page 41):

$$\frac{v'}{u_0} = 0.004005\left(\frac{x}{2\theta}\right) + 0.1423 \tag{19}$$

Radial component of turbulence rms velocity, circumferentially averaged (see Figure 35, page 41):

$$\frac{w'}{u_0} = 0.005114\left(\frac{x}{2\theta}\right) + 0.1371 \tag{20}$$

Axial length scale for axial turbulence velocity (see Figure 42, page 43):

$$\frac{\lambda_u}{\theta} = 0.03746\left(\frac{x}{2\theta}\right) + 1.223 \tag{21}$$

Axial length scale for circumferential turbulence velocity (see Figure 43, page 43):

$$\frac{\lambda_v}{\theta} = 0.02816\left(\frac{x}{2\theta}\right) + 1.532 \tag{22}$$

Axial length scale for radial turbulence velocity (see Figure 44, page 43):

$$\frac{\lambda_w}{\theta} = 0.02691\left(\frac{x}{2\theta}\right) + 1.3225 \tag{23}$$

The parameter x is the axial distance downstream of the rotor trailing edge. In Equations (15) through (23), the wake trailing-edge momentum thickness can be approximated by the section drag coefficient, where c is the blade chord, through the approximate relation:

$$\theta \simeq C_d \cdot \frac{c}{2} \tag{24}$$

The above Equations (15) through (23) for rotor wake mean velocity profile and turbulence parameters were used to compute input for the fan broadband noise codes developed in Section 4, page 58, as well as for the earlier version of the broadband noise model reported in Reference 4. Cases were run back-to-back with this new wake model and with the previous wake model (referred to as the "old wake model") described in Reference 11 and partially described in Subsection 3.4.4 and Equation (5). The scale-model GEAE UPS fan was used as the configuration for these comparative calculations, as described in References 2 and 3. Predictions of fan rotor/stator interaction broadband noise were made for both the "old" and "new" wake models, using the "old" and "new" broadband noise prediction codes, where the "old" broadband noise code refers to that reported in Reference 4, and the "new" broadband noise model refers to the code developed in this program and documented in Section 4.

Predicted inlet and exhaust sound power level (PWL) spectra at four fan tip speeds were compared and are shown in Figures 71 through 74, respectively, for the four fan tip speeds of 720, 895, 1100 and 1275 ft/s — corresponding to approximate community noise conditions of approach, cutback, full power takeoff, and growth takeoff, respectively. The fan is a 22-bladed, wide-chord, modern design with 54 outlet guide vanes spaced approximately 2.4 axial tip chords downstream of the rotor. The fan tip diameter is 22 in.

Figure 71 illustrates the results for the approach power condition, at a tip speed of 720 ft/s. Shown in this figure are sound power spectra (PWL) versus 1/3-octave band frequency. Four graphs are shown, corresponding to the dipole component, the quadrupole component, and the inlet and exhaust radiation for each of these sources. The solid lines correspond to the old wake model; the dashed lines correspond to the new wake model. The curves with plus-sign points correspond to the new broadband noise code, called SDIR, developed in this program. The curves without symbols correspond to the old broadband noise code, called GS, reported in Reference 4. All predictions in Figure 71 are for stator-generated noise produced by rotor/wake turbulence interaction.

It can be seen that the new wake model significantly increases the high-frequency noise, and the difference in predictions diminishes as frequency decreases. Also the new broadband noise code (designated as SDIR in Figure 71) shows a much greater sensitivity to the difference in wake models than does the old broadband noise code (designated as GS in Figure 71). The difference for the SDIR code at high frequencies is about twice that of the GS code results. It can be observed that the exhaust noise is predicted to be higher than the inlet noise, by about 5 to 10 dB at the peak noise frequencies, and the difference is observed to be greater for the dipole component. It is also observed that the quadrupole component peak noise levels are predicted to be on the order of 10 dB higher than the dipole component peak noise levels. A final observation is that the new broadband noise code (SDIR) predicts less low-frequency noise than does the old code (GS).

Corresponding comparisons for the cutback case are shown in Figure 72. The increase in predicted noise levels due to the new wake model are larger and occur at low frequencies as well, at least for the inlet-radiated noise. Again, exhaust noise is predicted to be higher than the inlet noise, by about 10 dB, and the quadrupole noise is predicted to be higher than the dipole noise, also by about 10 dB.

The takeoff and growth takeoff cases are shown in Figures 73 and 74, respectively. For these cases, because the rotor relative Mach numbers were supersonic, the new broadband noise code had difficulty for certain streamlines in calculating certain acoustic noise source parameters. This was subsequently resolved (as described in Section 4), but the code fixes were not made in time to affect this analysis. Therefore only the old broadband noise code (GS) results are shown in Figures 73 and 74. Based on the results shown in Figures 71 and 72, the wake model change effects were about the same for either code, so the results shown in Figures 73 and 74 should still be qualitatively the same for the new broadband noise code (SDIR).

In Figure 73, for the takeoff condition, the new wake model have small impact on predicted noise levels for either inlet or exhaust radiation and for either dipole or quadrupole components.

For the growth takeoff power case, Figure 74, the effect of the new wake model is qualitatively the same, but the magnitude of the changes is larger, more like that observed for approach and cutback. No physical explanation has been found for the relative insensitivity to the wake model changes at the takeoff condition, compared with the changes observed at the other three conditions.

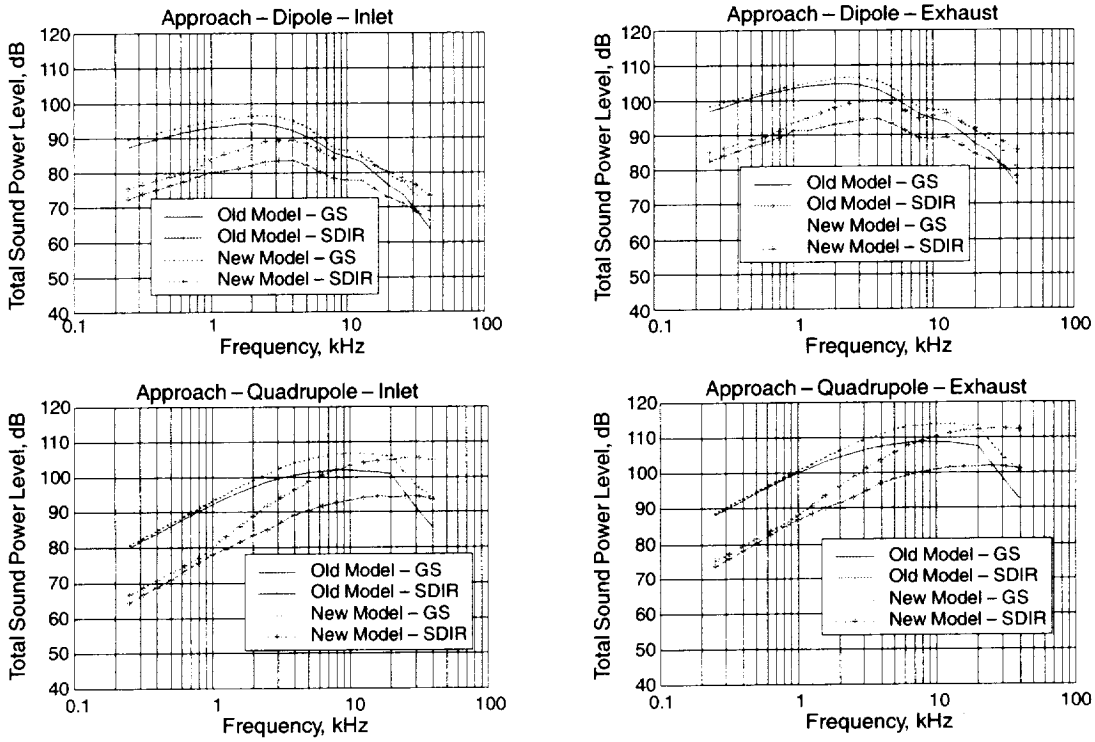

Figure 71. Comparison of New vs. Old Wake Model Stator-Generated Broadband Noise Predictions at Approach Power

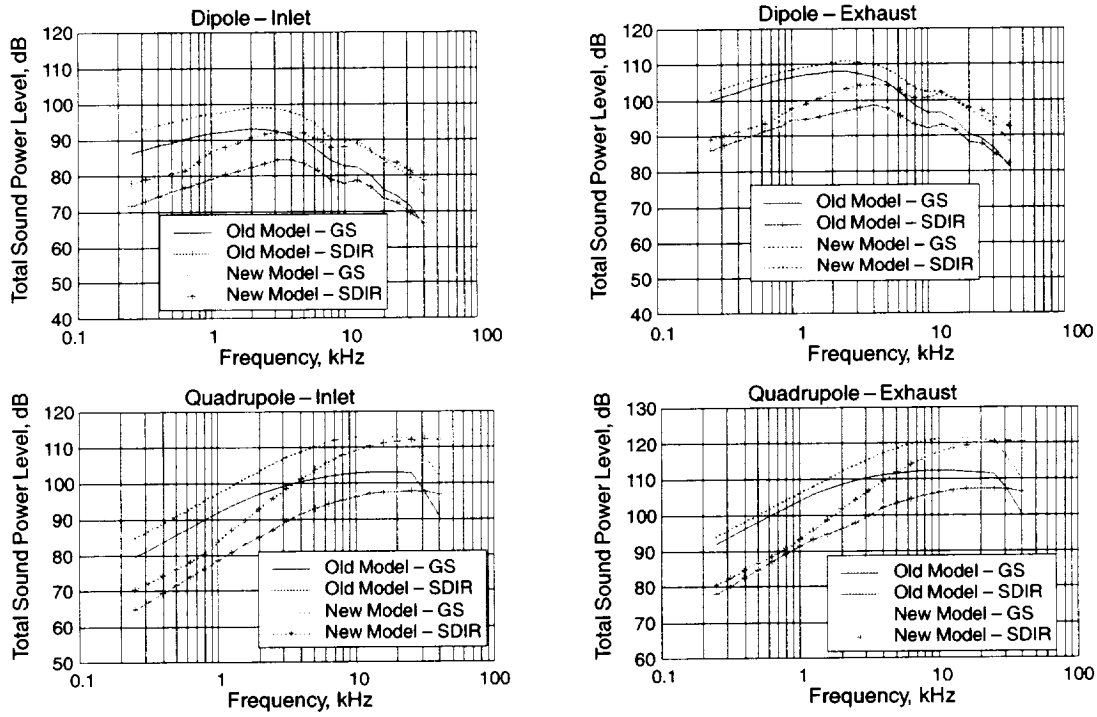

Figure 72. Comparison of New vs. Old Wake Model Stator-Generated Broadband Noise Predictions at Cutback Power

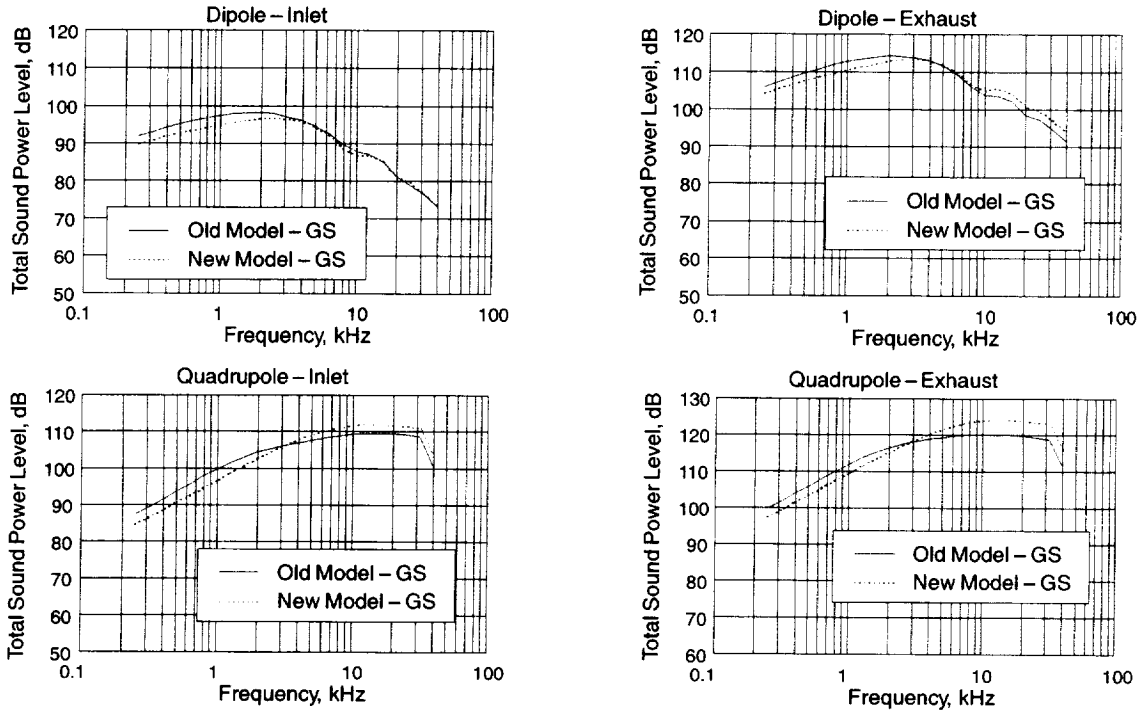

Figure 73. Comparison of New vs. Old Wake Model Stator-Generated Broadband Noise Predictions at Takeoff Power

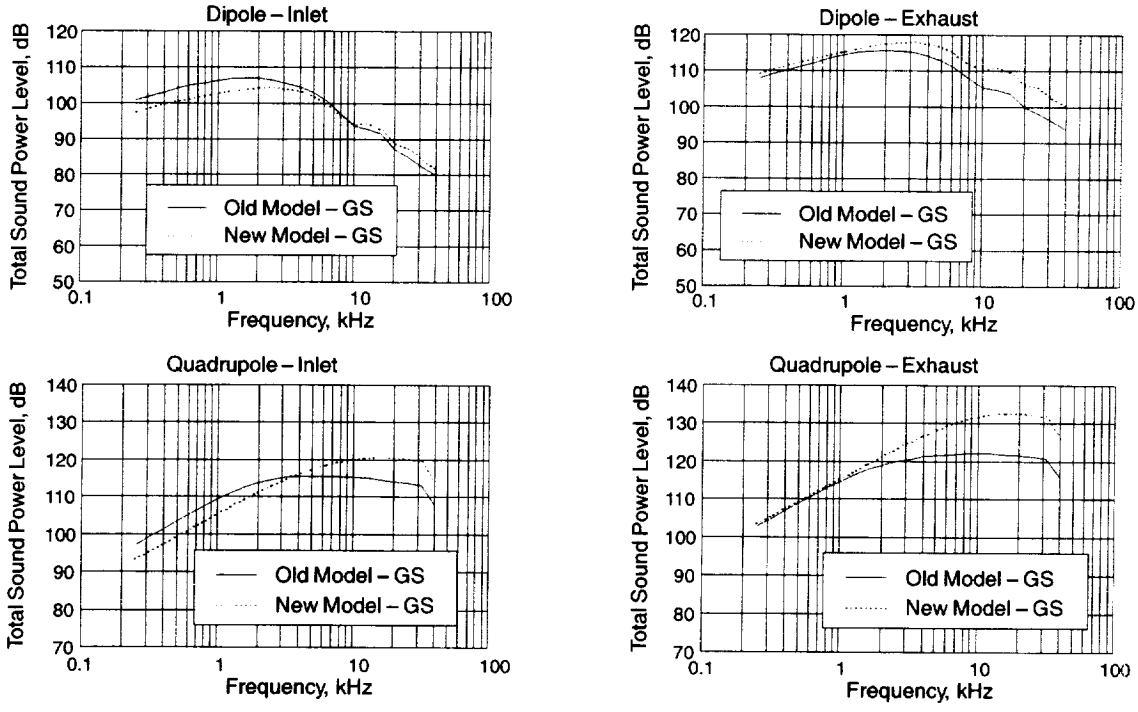

Figure 74. Comparison of New vs. Old Wake Model Stator-Generated Broadband Noise Predictions at Growth Takeoff Power

The wake model key turbulence input parameters to the broadband noise codes (either GS or SDIR) are the stator inlet axial turbulence intensity, the stator inlet axial length scale, the ratio of tangential-to-axial length scale at the stator inlet, and the ratio of tangential-to-axial turbulence velocity at the stator inlet. For the GEAE UPS fan test cases shown in Figures 71 through 74, the old and new wake model inputs are compared in Figure 75. These inputs are normalized and plotted vs. streamline number from tip to hub, and the normalized values were used for all speeds shown in Figures 71 through 74. The axial turbulence intensity for the new model is seen to be higher over most of the annulus height for the new model, consistent with the higher noise levels predicted for the new model. The axial length scales are not very different, except near the tip (streamline number 1). The length scale ratio is about 40% higher for the new model, and the turbulence velocity ratios for the two models are nearly the same, being close to unity over much of the annulus height.

How the new wake model will impact the prediction accuracy of the new fan broadband noise code (SDIR) is discussed in Section 4.

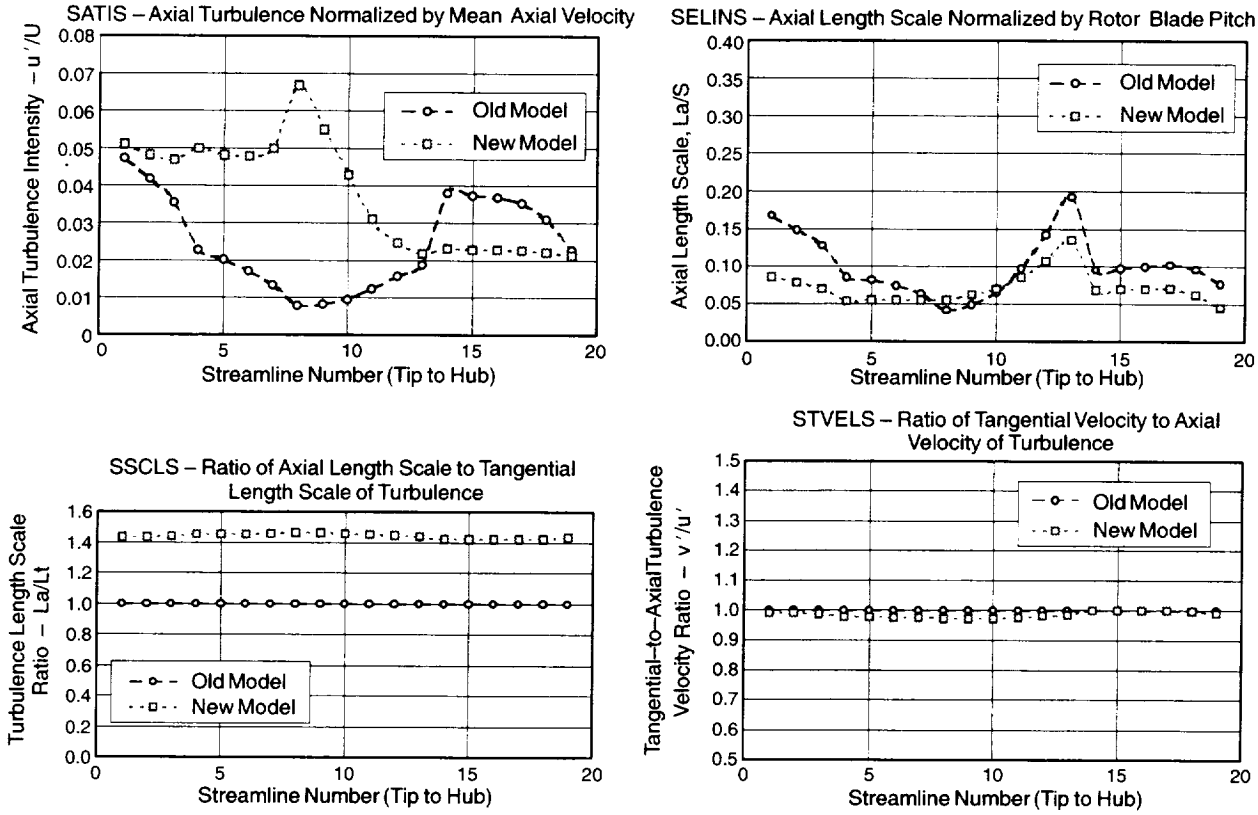

Figure 75. New vs. Old Turbulence Model Predicted Stator Inlet Turbulence Properties for GEAE UPS Fan Stage Used as Input for Broadband Noise Predictions

4.0 Fan Broadband Noise Model Development

4.1 Objectives and Approach

This section documents five areas of activity that constituted the principal efforts to improve the GEAE fan broadband noise model.

- The role of dipoles and quadrupoles in the interaction of a shear wave with a loaded compressor rotor
- Three-dimensional effects model
- Directivity model
- Anisotropic turbulence model
- Blade/vane self-noise

A fundamental CFD based study is described in Section 4.2, page 58, aimed at clarifying the role of quadrupole and dipole source mechanisms in fan noise. A case of a single shear wave interacting with a blade row with loading was studied. Two-dimensional (2D) CFD was used. The conclusion of this study is that under conditions of high pressure ratio (approaching 1.2 in this particular example) frequencies exceeding three times blade-passing frequency (BPF), quadrupole noise is a significant fraction of the total forward-radiated noise.

In Section 4.3, page 88, the extension of the basic GEAE fan noise model (Reference 16) to include 3D effects is described. The decomposition of the 3D annular duct model using Fourier Bessel analysis into a sequence of 2D problems is described. The complexities introduced by the need to use Bessel-functions-based spanwise eigenfunctions is described. The section concludes with an assessment of the adequacy of the methods currently being used to calculate the blade-row locked flowfields (due to steady lift on the blade row).

Directivity effects are discussed in Section 4.4, page 91. A simplified procedure for predicting directivity based on a frequency parameter and cut-off ratio of the duct mode of interest is outlined. In Section 4.5, page 94, the ability to construct an adequate anisotropic turbulence model is demonstrated. In Section 4.6, page 95, self-noise from a blade row (the noise as would be emitted with no incoming turbulence) is discussed, and the development of improvements to the current GEAE model (based on work reported by Mugridge, Reference 17) is detailed. Finally, in Section 4.7, page 117, the revised GEAE fan broadband noise model incorporating the results of all the new developments under the present contract is applied to 10 cases of experimental data from scale-model fans.

4.2 Role of Dipoles and Quadrupoles in the Interaction of a Shear Wave with a Loaded Compressor Rotor

4.2.1 Introduction

Ever since Lighthill's classic work (References 18 and 19), aeroacoustic noise sources have been described in terms of basic multipole elements: monopoles, dipoles, and quadrupoles. In particular, Lighthill showed that sound radiated by fluid motion in regions away from solid surfaces is best described as due to quadrupole noise sources. Early extensions of Lighthill's work to include solid surfaces (for instance Curle, Reference 20, and the review by Crighton, 1992, Reference 21) showed that, in addition to quadrupole sources, flow around a solid surface also includes dipole sources.

While the existence of both dipole and quadrupole noise sources for flows around solid surfaces is clear from aeroacoustic theory, what has not been clear is whether the quadrupole sources radiate enough energy to be significant in the farfield as compared to the dipoles. Since dipole sources involve less phase cancellation, they inherently radiate more efficiently than quadrupole sources (see for instance the basic review of Crighton 1975, Reference 22), and many researchers have speculated that dipole sources dominate, when they exist. This view has been challenged over the years by other researchers (Ffowcs–Williams and Hawkings, 1969, Reference 23). In the field of turbomachinery, Morfey (Reference 24) showed theoretically how quadrupoles could dominate dipoles in certain cases. Furthermore, recent work using direct numerical simulations (DNS) by Wang, Lele, and Moin (References 25 and 26) has investigated quadrupole noise in boundary layers and in the wakes of airfoils.

In the development of a noise-prediction model for broadband fan noise, it it is necessary to select the nature of the acoustic sources and to develop models for the strengths of the sources. Given the basic confusion as to whether or not quadrupoles are important, we decided to try and answer the question of the relative importance of dipoles and quadrupoles by using computer simulations of relevant model problems. We considered the sound radiated by the interaction of a shear wave with an isolated, 2D, loaded compressor rotor blade row. This is an often-studied model problem; see Peake and Kerschen (Reference 27) for a recent review of the literature. Our interest is to examine the relative role of dipoles and quadrupoles and the effect on the radiated sound of frequency and blade loading.

Our approach is to compute the radiated sound directly and then compare the directly obtained sound to the dipole and quadrupole components predicted by acoustic theory where the source terms for the acoustic theory are evaluated using data from the numerical simulations. This approach, comparing directly computed sound to the evaluation of acoustic theory based on the directly computed acoustic sources, is similar to the approach used in jet noise by Mitchell, Lele, and Moin (References 28 and 29).

In Section 4.2.2 the physical model problem is described, and in Section 4.2.3, page 61, an overview of the computational procedure is provided. In Section 4.2.4, page 62, a description of how we use acoustic theory to determine the relative strengths of the dipoles and quadrupoles is given. In Section 4.2.10, page 72, the cases considered are summarized, and the results of study are presented in Section 4.2.11, page 73. Conclusions are offered in Section 4.2.14, page 87.

4.2.2 Description of Problem

In this study, we consider the interaction of a small-amplitude shear wave (or vortical disturbance) with a loaded compressor blade row. The amplitude of the shear wave is assumed to be sufficiently small that it can be viewed as an unsteady, linear disturbance imposed on a steady, nonlinear base flow. Thus the nonlinear flow can be described separately from the description of the imposed shear wave disturbance.

The flow and geometry were taken to be 2D and inviscid. Although three-dimensionality (of both the flow and geometry) and viscous effects can be very important for turbomachinery noise, the fundamental question of the relative importance of dipoles versus quadrupoles can be adequately addressed without the extra complications.

Figure 76 is a schematic of the base flow, which is the steady airflow through the blade row. The velocity in the absolute frame is denoted by v and the velocity in the relative frame by w. The uniform

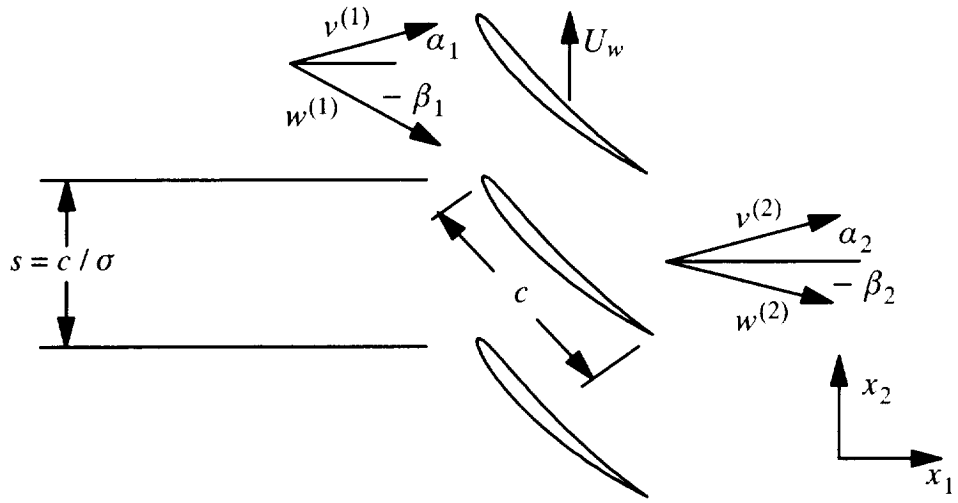

Figure 76. Schematic of Steady Flow Through the Blade Cascade

flow upstream of the cascade is station (1) and the uniform flow downstream is station (2). The chord length (c) and blade spacing (s) are related by the solidity (σ). To solve for the flow in the cascade, upstream total pressure and temperature in the absolute frame (p_{t1}, T_{t1}), wheel speed U_w, upstream flow angle α_1, and downstream static pressure p_2 must be specified. In order to examine the effect of loading on the radiated noise, the loading was varied by varying the exit static pressure (p_2) while all other parameters were fixed. All cases considered had axial flow at the inlet, that is, $\alpha_1 = 0$.

The airfoils have a circular arc mean-line with the NACA 65 series thickness distribution:

$$\frac{t}{t_{\max}} = \left(\frac{1.0}{0.2}\right)(0.29690\sqrt{z} - 0.12600z - 0.35160z^2 + 0.28430z^3 - 0.10360z^4) \quad (25)$$

where z is fractional distance along the mean-line of the blade. The coefficient of the fourth-order term was modified from 0.10150 to 0.10360 in order to avoid a cusp at the trailing edge. NACA 65 series airfoils are described in Abbot and van Doenhoff (Reference 30). The blades are completely defined by the thickness ratio t_{max}/c, stagger angle ζ, and camber angle θ.

In deciding which cases to consider, a velocity vector analysis code that analyzed the flow based on the upstream total pressure and temperature, downstream static pressure, and downstream relative flow angle was used. Once a desired flow configuration was established, the camber and stagger angles of the blade were determined by solving the equations:

$$\theta = \beta_2 + \delta - \beta_1 \quad (26)$$

$$\zeta = \frac{1}{2}(\beta_2 + \delta + \beta_1) \quad (27)$$

where δ is the deviation angle. Carter's rule, as described in Cumpsty, section 4.5 (Reference 31), was used to estimate the deviation angle, $\delta = \delta(\zeta, \sigma)$. Equations (26) and (27) were solved using a simple iterative procedure.

Now that the base flow has been introduced, the unsteady shear waves that propagate from upstream of the blades towards the blades are described. The shear waves have the form:

$$w'_{\text{shear}} = \hat{w}\, e^{-i\omega t}\, e^{ik_s \cdot x} \quad (28)$$

and are governed by the equations:

$$k_s \cdot \hat{w} = 0 \tag{29}$$

$$\omega = k_s \cdot w^{(1)} \tag{30}$$

In the present study, only disturbances that are being convected in the direction of the mean flow (that is, $k_s \cdot v^{(1)} = 0$) are considered. This means, under the assumption that the upstream flow is purely axial in the absolute frame, that the shear waves are given by:

$$k_{s1} = 0\,; \quad k_{s2} = -\frac{2\pi n}{s} \tag{31}$$

where n is the harmonic ($n = 1, 2, 3, \ldots$) of the shear wave. The temporal frequency is given by:

$$f = \frac{\omega}{2\pi} = n \times bpf = n\left(\frac{\sigma U_w}{c}\right) \tag{32}$$

where *BPF* is the "blade-passing frequency," and the velocity components are given by:

$$\hat{w}_1 = 1\,; \quad \hat{w}_2 = 0 \tag{33}$$

where the amplitude of the axial component is arbitrary (so we have set it equal to unity).

When the shear wave interacts with the blades, the radiated noise will consist of discrete acoustic modes in the regions upstream and downstream of the blades. The acoustic pressure is given by a summation of normal modes:

$$\hat{p}(x;\omega) = \sum_m \hat{p}_m^{\pm} e^{ik_1^{m\pm}x_1} e^{ik_2^m x_2} \tag{34}$$

where the plus sign is used for waves traveling downstream of the blades and the minus sign is used for waves traveling upstream. The allowed tangential wave numbers are interconnected with the tangential wavenumber of the incident shear waves via:

$$k_2^m = k_{s2} + \frac{2\pi}{s} m \tag{35}$$

The axial wavenumber (k_1^m) is related to the temporal wavenumber (ω) and tangential wavenumber (k_2^m) via the dispersion relationship of the convective wave equation, see Equation (61). For a given temporal wave number, only a few acoustic modes propagate; the rest are evanescent waves. The plane-wave mode, which is the mode for which $k_2^m = 0$ and corresponds to $m = n$, always propagates. The existence of discrete acoustic modes in a blade row is very similar to acoustic modes in hard-wall ducts, see Morse and Ingard, Chapter 9 (Reference 32) for an elementary discussion.

Although all the cases considered create multiple acoustic modes, we will focus our attention exclusively on the plane-wave mode.

4.2.3 Overview of the Computational Code and Procedure

All the computations reported in the study were obtained using a GE proprietary code, TACOMA, written to provide numerical solutions to the steady and unsteady flow in a single, passage of a blade

row. TACOMA can solve both the steady, nonlinear Euler equations and the unsteady, linearized Euler equations. Aspects of TACOMA are described in Holmes, Mitchell, and Lorence (Reference 33).

The algorithm for solving the nonlinear Euler equations is unremarkable and is essentially that of Jameson and Arone (References 34, 35, and 36). In brief, the Euler equations are discretized using a second-order-accurate, finite-volume scheme. The solution is advanced towards steady state using a four-stage Runge–Kutta time-marching scheme. Convergence is accelerated by using local time stepping and multigrid. Numerical smoothing is provided by the standard, blended second/fourth-order smoother driven by a second order pressure switch in each grid direction.

The Euler equations are linearized by numerical discretization for a single time harmonic mode. The solution algorithm is similar to that used for the nonlinear equations. Of particular note is that TACOMA employs the exact Giles 2D nonreflecting boundary conditions (Reference 37).

Because the CFD solver can be run in nonlinear and linear modes, use in the present study closely parallels the description of the problem given in Section 5. First, TACOMA is used to calculate the base flow for a given geometry, upstream absolute flow angle, upstream total pressure and temperature, and downstream static pressure. Then TACOMA is run with a linear disturbance (the shear wave) imposed at the inlet boundary. After the linearized solution is found, the amplitudes of the upstream- and downstream-propagating pressure waves are calculated as are the source terms needed for the acoustic prediction method to be discussed in Section 4.3.

It has been remarked in the literature (Crighton, Reference 38) that there are many impediments to application of numerical methods to direct computation of noise. The present problem is amenable to numerical means for a number of reasons:

- The acoustic wavelength, which can be readily estimated as $\lambda/c = 1/(\sigma M_w)$, is comparable to the blade chord since the solidity for all the case considered is 1 and the wheel speed Mach number is either 0.5 or 0.65. As a result, the computational domain need only extend a few chord lengths upstream and downstream in order to capture the farfield. Furthermore, since the acoustic wavelengths are comparable to the chord length of the blade, the numerical grid requirements imposed by the acoustic waves and by the blade geometry are not dissimilar.
- Since the Mach numbers in the relative frame are typically larger than 0.5, the radiated acoustic waves are sufficiently energetic to be distinguishable from numerical errors.
- Because we are solving for a single frequency in a flow with a known periodicity in the x_2 direction, exact nonreflecting boundary conditions can be applied. The ability to construct exact boundary conditions is a direct consequence of the modal decomposition that can be performed for small disturbances imposed on a uniform flow; see for instance Equation (35).

Although second-order-accurate finite-volume or finite-difference schemes traditionally exhibit poor resolution of wave propagation characteristics, we avoided problems by using very fine grids (a luxury afforded by the 2D nature of the problem). Furthermore, many of the results were obtained on two different grids to verify grid independence.

4.2.4 Dipole/Quadrupole Decomposition

Having described the cases considered and the computational code and procedure, we now discuss how to use nearfield data available from the computations to determine the dipole and quadrupole

strengths. It would be desirable to merely decompose the directly computed sound to determine the dipole and quadrupoles. One might conceive of a plan to perform this decomposition based on examination of the farfield directivity. However, such a plan is not feasible in the present case since the existence of discrete acoustic modes means that all fundamental sources (monopole, dipole, quadrupole, etc.) give rise to acoustic fields with the same directivity. In other words, the dipole gives rise to a plane wave, and the quadrupole gives rise to a plane wave, and there is no way to tell which part of the plane wave is from which type of source by examining the farfield data.

Since examination of the farfield is not sufficient, a procedure based on examination of the nearfield data must be developed. Our approach is to use acoustic theory to predict the farfield sound. As will be shown shortly, acoustic theory predicts the existence of monopole, dipole, and quadrupole sources. If the total prediction is in good agreement with the directly computed sound, then the predicted dipole and quadrupole strengths may be used to judge relative importance.

The acoustic theory considered is an extension of Lighthill's result (References 18 and 19) for a uniformly moving medium with embedded stationary surfaces:

$$\rho'(x;t) = \int\int T_{ij}\frac{\partial^2 G}{\partial y_i \partial y_j}dyd\tau + \int\int F_i\frac{\partial G}{\partial y_i}dS(y)d\tau + \int\int H\frac{DG}{D\tau}dS(y)d\tau \qquad (36)$$

The derivation of Equation (36) is given in Section 4.2.5. The first term is the quadrupole, the second term is the dipole, and the last term is the monopole. As will be discussed later, the monopole term is zero for the two dimensional cases considered herein. Equation (36) is developed for a moving medium with a uniform velocity. This creates two complications. First, a Green's function for a moving medium with cascade style periodic boundaries is needed. Second, a methodology must be developed to deal with the fact that a blade cascade does not have an obvious uniform velocity about which to base the acoustic theory.

The first difficulty is a matter of solving an appropriate wave equation. This is done in Section 4.2.6. The second difficulty is more fundamental, and approximations must be made. Clearly the regions upstream and downstream of the blades can each be well described as a uniform moving medium. The crux of the problem is that, as a consequence of flow turning, which is an essential feature of a subsonic compressor rotor, these upstream and downstream moving mediums are not the same. Our resolution of this difficulty is to replace the gradual flow turning due to the blade by two actuator disks located at the leading and trailing edges. This allows us to view the flow field as consisting of three regions of uniform flow: (1) upstream region, (2) blade region, and (3) downstream region. Our acoustic prediction procedure solves Equation (36) using the uniform velocity field in the blade region. The acoustic waves are then transmitted/reflected through the actuator disks. Formally, this procedure is only accurate if the acoustic waves are very long compared to the chord length of the blades, a restriction that does not hold in the cases considered. However, the amount of flow turning is small enough that the actuator disks model appears adequate.

An additional complication also needs to be addressed. For a moving medium, dipole and quadrupoles sources, in addition to generating acoustic waves, generate shear waves that are converted to acoustic waves by interactions with the actuator disks. For the problem considered in this study, there is no mechanism for the generated shear waves to be converted into plane acoustic waves. Thus, we do not have to account for the shear waves in the sections that follow. However, the inclusion of the shear waves would not change the basic strategy used — it merely requires an extension of the model used to transmit/reflect waves through the actuator disks.

In Section 4.2.5, the extended form of Lighthill's result is developed, and in Section 4.2.6, page 66 an appropriate Green's function is derived. Section 4.2.7, page 68, discusses how the flow is broken into the three regions. In Section 4.2.8, page 69, we discuss how the acoustic prediction in the blade region is performed, concentrating on the nature of the acoustic sources. Finally, in Section 4.2.9, page 71, a procedure is developed for transmitting the acoustic waves predicted by acoustic theory in the blade region through the actuator disks.

4.2.5 Derivation and Solution of Lighthill's Acoustic Analogy in a Moving Medium that Contains a Moving Surface, using the Method of Ffowcs–Williams

Our goal in this section is to develop a form of Lighthill's equation valid for a moving medium that contains a moving surface. We will follow the approach first used by Ffowcs–Williams and Hawkings (Reference 39), see also Ffowcs–Williams' Chapter 11 in Crighton et al. (Reference 21) and Brentner and Farassat (Reference 40). However, our use of generalized functions and derivatives is more similar to that of Farassat (Reference 41) and Myers and Farassat (Reference 42) than the approach used by Ffowcs–Williams.

We start with the continuity and momentum equations expressed for perturbations (not necessarily small) from a uniform, steady flow with velocity $\overline{u}_i$ and density $\overline{\rho}$:

$$\frac{\partial \rho'}{\partial \tau} + \overline{u}_j \frac{\partial \rho'}{\partial y_j} + \frac{\partial}{y_j}(\rho u'_j) = 0 \tag{37}$$

$$\frac{\partial \rho u'_i}{\partial \tau} + \overline{u}_j \frac{\partial \rho u'_i}{\partial y_j} + \frac{\partial}{\overline{y}_j}(\rho u'_j u'_i) = \frac{\partial \sigma_{ij}}{\partial y_j} \tag{38}$$

where the stress tensor is $\sigma_{ij} = -p\delta_{ij} + \tau_{ij}$ where τ_{ij} are the viscous stresses.

We introduce a scalar function $f(y)$ defined such that $f \geq 0$ when y is a point in the fluid and $f < 0$ when y is a point inside the surface. We also require f to be defined such that ∇f is equal to the surface normal, $\hat{n}$ when $f = 0$. Furthermore, we do not allow the surface to deform or rotate, thus

$$\left[\frac{\partial f}{\partial \tau}\right]_{f=0} + v_j \left[\frac{\partial f}{\partial y_j}\right]_{f=0} = 0 \tag{39}$$

where v_j is the velocity of the surface. Equation (39) implies that $\partial f/\partial \tau = -v_n$ when evaluated on the surface.

Next, we define generalized functions akin to the fluid variables. For instance, the generalized function form of ϱ is

$$\tilde{\rho}(y) = \begin{cases} \rho(y) & \text{if } f(y) \geq 0 \\ 0 & \text{if } f(y) < 0 \end{cases} \tag{40}$$

In order to transform Equations (37) and (38), we use the relationship:

$$\frac{\tilde{\partial}\tilde{\phi}}{\partial s} = \frac{\partial \phi}{\partial s} + [\phi]^+ \frac{\partial f}{\partial s}\delta(f) \tag{41}$$

where $[\phi]^+$ is the value of ϕ on the surface. See Farassat (Reference 41) for more details on this use of generalized functions and derivatives.

Upon transformation using generalized functions and derivatives, the continuity equation becomes,

$$\frac{\tilde{\partial}\tilde{\rho}'}{\partial\tau} + \bar{u}_j\frac{\tilde{\partial}\tilde{\rho}'}{\partial y_j} + \frac{\partial}{y_j}(\rho\tilde{u}'_j) = (\bar{u}_n - v_n)[\rho']^+\delta(f) + [\rho u'_j]^+ n_j\delta(f) \tag{42}$$

and the momentum equations become,

$$\begin{aligned}\frac{\tilde{\partial}\rho\tilde{u}'_i}{\partial\tau} + \bar{u}_j\frac{\tilde{\partial}\rho\tilde{u}'_i}{\partial y_j} + \frac{\tilde{\partial}}{y_j}(\rho\tilde{u}'_j u'_i) - \frac{\tilde{\partial}\tilde{\sigma}_{ij}}{\partial y_j} &= (\bar{u}_n - v_n)[\rho u'_i]^+\delta(f) \\ &\quad + [\rho u'_i u'_j - \sigma_{ij}]^+ n_j\delta(f)\end{aligned} \tag{43}$$

At this point, we will drop the tildes, without any loss of clarity, and proceed to develop a wave equation by subtracting the spatial derivative of Equation (43) from the total derivative, $\bar{D}/D\tau = \frac{\partial}{\partial\tau} + \bar{u}_j\frac{\partial}{\partial y_j}$, of Equation (42). This yields an inhomogeneous convective wave equation:

$$\begin{aligned}\left(\frac{\bar{D}^2}{D\tau^2} - \bar{a}^2\nabla^2_{(y)}\right)\rho' &= \frac{\partial^2 T_{ij}}{\partial y_i\partial y_j} \\ &\quad - \frac{\partial}{\partial y_i}\left((\bar{u}_n - v_n)[\rho u_i']^+\delta(f) + [\rho u_i' u_j' - \sigma_{ij}]^+ n_j\delta(f)\right) \\ &\quad + \frac{\bar{D}}{D\tau}\left((\bar{u}_n - v_n)[\rho']^+\delta(f) - [\rho u_i']^+ n_i\delta(f)\right)\end{aligned} \tag{44}$$

where
$$T_{ij} = \rho u_i' u_j' + (p' - \bar{a}^2\rho')\delta_{ij} - \tau_{ij} \tag{45}$$

Equation (44) is similar to Lighthill's equation but with the addition of several terms on the right-hand side that deal with the effect of the surface.

We next solve Equation (44) by use of an appropriate Green's function. Transferring the resulting derivatives to the Green's function, and restricting volume intregrals to surface integrals due to the $\delta(f)$ terms, yields:

$$\rho'(x;t) = \int\int T_{ij}\frac{\partial^2 G}{\partial y_i\partial y_j}dyd\tau + \int\int F_i\frac{\partial G}{\partial y_i}dS(y)d\tau + \int\int H\frac{DG}{D\tau}dS(y)d\tau \tag{36}$$

The "source" functions T_{ij}, F_i, and H are evaluated at (y, τ) and the Green's function is evaluated at $(x - y, t - \tau)$. The source term in the second integral is:

$$F_i = (\bar{u}_n - \bar{v}_n)\rho u_i' + (\rho u_i' u_j' - \sigma_{ij})n_j \tag{46}$$

For an impermeable surface this reduces to:
$$F_i = p' n_i - \tau_{ij} n_j \tag{47}$$

which is the force exerted by the surface on the fluid. The source term in the third integral is:

$$H = -(\bar{u}_n - v_n)\rho' - \rho u'_i n_i = -(\bar{u}_n - v_n + u'_n)\rho + \bar{\rho}(\bar{u}_n - v_n) \tag{48}$$

which for a impermeable surface reduces to: $H = \bar{\rho}(\bar{u}_n - v_n)$ (49)

The interpretation given to the three terms are that H represents a monopole term related to the mass displacement caused by the solid object, F_i is a dipole noise source caused by the force exterted on the fluid by the surface, and T_{ij} is a quadrupole source caused by the unsteady stresses in the volume of the fluid. The monopole term is only present if the surface is accelerating.

In developing Equation (36), any Green's function could be used. However, if the free space Green's function is used, then the acoustic boundary conditions on the surface, $\partial p/\partial n = 0$, are not enforced. This means that the solution does not account for the effects of reflection and scattering of sound by the solid surface. For a solid body with dimensions much smaller than an acoustic wavelength, this may well be appropriate.

It could be pointed out that if the pressure term in F_i was known exactly — that is, if it contained the acoustic and aerodynamic pressure fluctuations — then the solution (36) would automatically account for the effect of the acoustic boundary conditions even with use of a free-space Green's function. However, since exact knowledge of the source terms is unlikely, it is fair to state that if the effects of reflection/scattering are important then the correct Green's function should be employed. Green's functions that account for acoustic boundary conditions on the surface are only available for extremely simple geometries.

Goldstein Chapter 4 (Reference 43) develops the same result. However, he starts with Lighthill's equation expressed for a moving medium and then manipulates the surfaces integrals introduced by the classical solution of the wave equation using fluid dynamics relationships. The end result is the same as that obtained by the approach used herein.

4.2.6 Green's Function of a Moving Medium Subject to Cascade-Style Periodic Boundary Conditions

We need to find the solution to:

$$\left[\left(\frac{\partial}{\partial t} + \bar{u}_j\frac{\partial}{\partial x_j}\right)^2 - \bar{a}^2\nabla^2\right]G(x,y;t) = Q$$
$$= e^{-i\omega_0 t}\delta(x_1 - y_1)\sum_l\left[\delta(x_2 - y_2 - ls)e^{il\psi}\right] \tag{50}$$

where $\bar{u}$ is a known velocity of the moving medium and ψ is the phase lag, in radians, between individual point sources that are separated by the cascade spacing, s, in the x_2 direction.

Our approach to solving for ϕ' will be to take Fourier transforms in space and time and solve the resulting equations in Fourier space. To this end, the temporal Fourier transform pair is defined as:

$$f(t) = \int_L \hat{f}(\omega)e^{-i\omega t}\,d\omega \qquad \hat{f}(\omega) = \frac{1}{2\pi}\int f(t)e^{i\omega t}\,dt \tag{51}$$

where the contour L in the complex ω plane is located an infinitesimal distance above the real ω axis. Similarly, the transform pair in the x_1 direction is defined as:

$$f(x_1) = \int_F \tilde{f}(k_1) e^{ik_1 x_1}\, dk_1 \qquad \tilde{f}(k_1) = \frac{1}{2\pi}\int f(x_1) e^{-ik_1 x_1}\, dx_1 \tag{52}$$

where the contour F is the real k_1 axis. In the x_2 direction, a Fourier series is used:

$$f(x_2) = \sum_m f_m e^{ik_2^m x_2} \qquad f_m = \frac{1}{s}\int f(x_2) e^{-ik_2^m x_2}\, dx_2 \tag{53}$$

where $m = \ldots, -2, -1, 0, 1, 2, \ldots$ and where $k_2^m = \frac{1}{s}(\psi + 2\pi m)$. The temporal Fourier transform of Equation (50) is:

$$\left[(-i\omega + \bar{u}_j \frac{\partial}{\partial x_j})^2 - \bar{a}^2 \nabla^2\right] \hat{G}(x,y;\omega) = \hat{Q}(x,y;\omega) \tag{54}$$

where:

$$\hat{Q}(x,y;\omega) = \left[\frac{1}{2\pi}\int e^{i(\omega-\omega_0)t}\, dt\right] \times \left[\delta(x_1 - y_1) \sum_l \delta(x_2 - y_2 - ls) e^{il\psi}\right] \tag{55}$$

The term in the first bracket can be shown to be $\delta(\omega - \omega_0)$, so:

$$\hat{Q}(x,y;\omega) = \delta(\omega - \omega_0)\delta(x_1 - y_1) \sum_l \delta(x_2 - y_2 - ls) e^{il\psi} \tag{56}$$

The next step is to take the Fourier transform in the x_2 direction of Equations (54) and (56):

$$\left[(-i\omega + i\bar{u}_2 k_2^m + \bar{u}_1 \frac{d}{dx_1})^2 + \bar{a}^2 k_2^m k_2^m - \bar{a}^2 \frac{d^2}{dx_1^2}\right] \hat{G}(x_1, k_2^m, y;\omega) = \hat{Q}_m \tag{57}$$

where:

$$\begin{aligned} \hat{Q}_m(x_1, k_2^m, y;\omega) &= \frac{1}{s}\left[\int_0^s \frac{1}{s} \sum_n e^{ik_2^n(x_2 - y_2)} e^{ik_2^m x_2}\, dx_2\right] \delta(\omega - \omega_0)\delta(x_1 - y_1) \\ &= \frac{1}{s} e^{-ik_2^m y_2}\, \delta(\omega - \omega_0)\, \delta(x_1 - y_1) \end{aligned} \tag{58}$$

where in the first line of Equation (58) the Poisson summation formula (Lighthill 1962, Section 5.4 — Reference 44) was used.:

$$\sum_l \delta(x_2 - y_2 - ls) e^{il\psi} = \frac{i}{s} \sum_m \exp\left[\frac{i}{s}(\psi + 2\pi m)(x_2 - y_2)\right] \tag{59}$$

Finally, we Fourier transform in the x_1 direction:

$$D(k_1, k_2^m;\omega)\tilde{\hat{\phi}}_m = \frac{1}{2\pi s}\delta(\omega - \omega_0)\, e^{-ik_1 y_1}\, e^{-ik_2^m y_2} \tag{60}$$

where D is the dispersion relationship:

$$D = (-i\omega + i\,\bar{u}_1 k_1 + i\,\bar{u}_2 k_2^m)^2 + \bar{a}^2(k_1^2 + k_1^m k_1^m) \tag{61}$$

Solving for $\tilde{\hat{G}}_m$, we obtain:

$$\tilde{\hat{G}}_m(k_1, k_2^m, y; \omega) = \frac{1}{2\pi s} \frac{\delta(\omega - \omega_0)\ e^{-ik_1 y_1}\ e^{-ik_2^m y_2}}{D} \tag{62}$$

Now that a solution for $\tilde{\hat{G}}_m$ has been found, the various Fourier transforms need to be unwrapped. Starting with the inverse Fourier transform in k_1, we obtain:

$$\hat{G}_m(x_1, k_2^m, y; \omega) = \frac{1}{2\pi s}\ \delta(\omega - \omega_0)\ e^{-ik_2^m y_2} \int_F \frac{e^{-ik_1(x_1 - y_1)}}{D}\ dk_1 \tag{63}$$

The integral can be evaluated by closing the contour and then considering the singular points. For $x_1 > y_1$, the contour is closed in the upper half of the complex k_1 plane; for $x_1 < y_1$, the contour is closed in the lower half plane. For given m and ω, there are two values of k_1 where D has a simple zero, $k_1^{m\pm}$. The plus is to be used for $x_1 > y_1$. Because our choice of the contour L is such that ω has a small positive imaginary component, the k_1^{m+} solution has a small positive imaginary component; likewise, k_1^{m-} has a small negative imaginary component. Thus, the solution becomes:

$$\hat{G}_m(x_1, k_2^m, y; \omega) = \frac{\frac{i}{s}\delta(\omega - \omega_0)\ e^{-ik_2^m y_2}\ e^{ik_1^{m\pm}(x_1 - y_1)}}{\pm \left[\frac{\partial D}{\partial k_1}\right]_{k_1^{m\pm}}} \tag{64}$$

Next, the solution is unwrapped in the x_2 direction:

$$\hat{G}(x, y; \omega) = \frac{i}{s}\delta(\omega - \omega_0) \sum_m \frac{e^{ik_1^{m\pm}(x_1 - y_1)}\ e^{ik_2^m(x_2 - y_2)}}{\pm \left[\frac{\partial D}{\partial k_1}\right]_{k_1^{m\pm}}} \tag{65}$$

Last, we inverse Fourier tranform in time (closing the contour in the lower half of the complex ω plane) to get the final answer:

$$G(x, y; t) = \frac{ie^{-i\omega_0 t}}{s} \sum_m \frac{e^{ik_1^{m\pm}(x_1 - y_1)}\ e^{ik_2^m(x_2 - y_2)}}{\pm \left[\frac{\partial D}{\partial k_1}\right]_{k_1^{m\pm}}} \tag{66}$$

Where D is given by Equation (61).

4.2.7 Decomposition of the Flow into Three Regions

Figure 77 is a schematic of the multiregion decomposition. Flows in the upstream and downstream regions (denoted as stations 1 and 2) are determined by mass-averaging the relative Mach number and relative flow angle obtained from the steady-state CFD solution at the inlet and exit of the

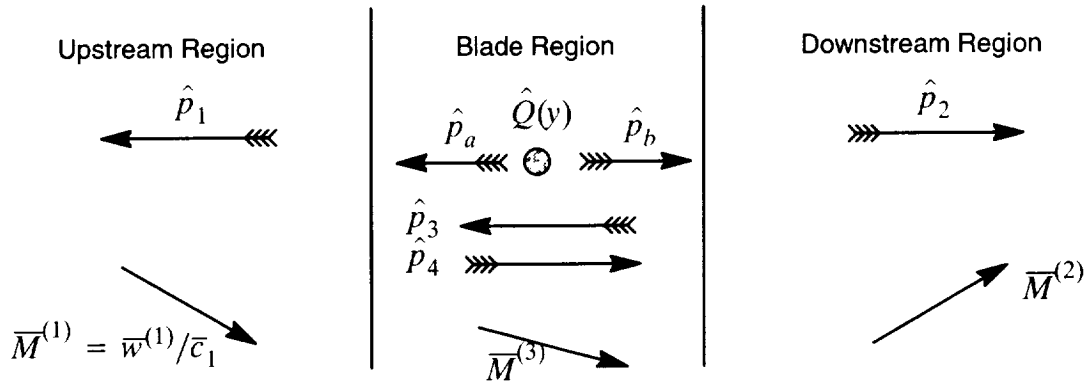

Figure 77. Schematic of Multiregion Decomposition

computational domain. Since the relative total temperature and total pressure are also known, we have sufficient information to determine all other fluid mechanical properties.

The uniform flow in the blade region is arbitrary. We choose it by first requiring the flow angle to be at the average flow angle (Cumpsty, page 138 — Reference 31):

$$\tan\beta_3 = \frac{1}{2}(\tan\beta_1 + \tan\beta_2) \tag{67}$$

The blade-region average Mach number is then calculated via an iterative procedure such that the mass flow in the blade region is the same as in the upstream and downstream regions. At this point the flow in all three regions is completely specified. Although not needed in the present study, the forces on the actuator disk can be calculated from considering conservation of momentum.

4.2.8 Acoustic Prediction in Blade Region

As discussed earlier, the relevant acoustic theory is an extension of Lighthill's equation:

$$\rho'(x;t) = \int\int T_{ij}\frac{\partial^2 G}{\partial y_i \partial y_j}dyd\tau + \int\int F_i\frac{\partial G}{\partial y_i}dS(y)d\tau + \int\int H\frac{DG}{D\tau}dS(y)d\tau \tag{36}$$

where the velocity of the moving medium is given by $\overline{u} = \overline{w}^{(3)}$. Since the computations are performed for a single temporal wavenumber, it is more convenient to work with the Fourier transform in time of Equation (36) that, upon neglecting the monopole term (which we will show to be unimportant), becomes:

$$\hat{\rho}(\boldsymbol{x};t) = \int \hat{T}_{ij}\frac{\partial^2 \hat{G}}{\partial y_i \partial y_j}dy + \int \hat{F}_i\frac{\partial \hat{G}}{\partial y_i}dS(y) \tag{68}$$

The relevant Green's function is Equation (64) where m is taken such that $k_2^m = 0$; that is, the plane-wave mode.

The monopole term is given by Equation (49) and for a stationary surface reduces to:

$$H = \overline{\rho}\,\overline{u}_n \tag{69}$$

Since the medium is not accelerating, H is constant and thus does not contribute to the farfield. Consequently, the monopole contribution to the sound is zero. The dipole source strength is given by Equation (47) and for an inviscid flow reduces to:

$$\hat{F}_i = \hat{p} n_i \tag{70}$$

This term is neither zero nor steady; thus, the dipole contributes to the farfield. The surface integral evaluation uses the same surface discretization used by the CFD computations.

The quadrupole term is given by Equation (45) and for an inviscid flow simplifies to:

$$T_{ij} = \rho w_i' w_j' + (p' - \bar{a}^2 \rho')\delta_{ij} \tag{71}$$

The second term is small since:

$$d(p - \bar{a}^2 \rho) = \frac{\rho a^2}{C_p} ds + (a^2 - \bar{a}^2) d\rho \tag{72}$$

where s is the thermodynamic entropy. Since entropy is constant for an inviscid flow and since the speed of sound does not vary much in the domain, the second term in Equation (71) is neglected. The velocity perturbations in the remaining term consist of three terms:

$$w' = W(y) + w'(y;\tau) - \overline{w}^{(3)} \tag{73}$$

The first term is for the nonlinear, steady flow that is found when the CFD solver is run without the linear perturbation. The second term is the unsteady, linear velocity perturbation calculated by the CFD solver as the unsteady response of the flow to an imposed shear wave. The third term is the imposed uniform velocity of the blade region. Substituting Equation (73) into Equation (71), taking a temporal Fourier transform, ignoring density variations, retaining only terms linear in $\hat{u}$, and restricting our attention to $\hat{T}_{11}$, which is the only component of the Lighthill stress tensor that can generate plane acoustic waves, we obtain:

$$\hat{T}_{11} = 2\bar{\rho}_3 \left(W_1 - \overline{w}_1^{(3)}\right) \hat{w}_1 \tag{74}$$

Upstream and downstream of the blades, W_1 approaches a uniform value that is different from $\overline{w}_1^{(3)}$. As a result, the Lighthill source terms have an infinite extent. Even though the source terms have infinite extent, the regions upstream and downstream of the blades do not radiate noise. The problem of source terms of infinite (or at least large) extent is not new. Mitchell, Lele, and Moin (Reference 29) discuss it in the context of jet noise, and Wang, Lele, and Moin (Reference 25) discuss it in the context of isolated airfoils. We avoid the problem by approximating Equation (74) with:

$$\hat{T}_{11} = 2\left(\rho(y) W_1(y) - \bar{\rho}_3 \overline{w}_1^{(3)}\right) \hat{w}_1(y;\omega) \tag{75}$$

This formulation exploits conservation of mass to ensure that the source terms decay to zero upstream and downstream of the blades.

With reference to Figure 77, the solution of Equation (68) determines the waves denoted by $\hat{p}_a$ and $\hat{p}_b$. The topic of the next section is how to determine $\hat{p}_1$ and $\hat{p}_2$.

4.2.9 Transmission of Acoustic Waves through Actuator Disks

With reference to Figure 77, once $\hat{p}_a$ and $\hat{p}_b$ are known, let us denote by Tr_{31} and R_{31} the transmission and reflection coefficients between region 3 (blade) and region 1 (upstream). We can then state the following relationships:

$$\hat{p}_1 = Tr_{31}(\hat{p}_a + \hat{p}_3) \qquad \hat{p}_4 = R_{31}(\hat{p}_a + \hat{p}_3) \tag{76}$$

and similarly:

$$\hat{p}_2 = Tr_{33}(\hat{p}_b + \hat{p}_4) \qquad \hat{p}_3 = R_{32}(\hat{p}_b + \hat{p}_4) \tag{77}$$

Given the reflection and transmission coefficients, Equations (76) and (77) can be solved for $\hat{p}_1$ and $\hat{p}_2$, in terms of $\hat{p}_a$ and $\hat{p}_b$.

In order to find the reflection and transmission coefficients, it is sufficient to consider an acoustic wave (1) being transmitted (3) and reflected (2) by a single actuator disk, see Figure 78.

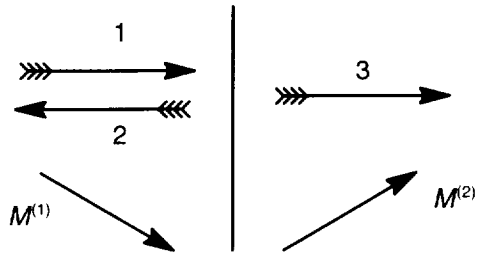

Figure 78. Wave Reflection and Transmission Through a Single Actuator Disk System

However, before proceeding, we need to settle some issues of nomenclature. We will only be considering plane acoustic waves of the form:

$$p'(y;\tau) = \hat{p}e^{-i\omega\tau}e^{ik_1^{n\pm}y_1} \tag{78}$$

where the n superscript denotes which region (1 or 2) and the plus superscript indicates downstream-propagating waves. The velocity of the acoustic wave is denoted by:

$$w'(y;\tau) = \left(f^{n\pm}\hat{p}\right)e^{-i\omega\tau}e^{ik_1^{n\pm}y_1} \tag{79}$$

where:

$$f^{n\pm} = \frac{k^{n\pm}/\bar{\rho}_n}{\omega - k^{n\pm}\cdot\bar{w}_n} \tag{80}$$

In order to find the amplitude of waves 2 and 3 given the amplitude of wave 1, we require mass:

$$\Delta(\rho w)' = 0 = \Delta\left[\bar{\rho}w' + \bar{w}\frac{p'}{c^2}\right] \tag{81}$$

and momentum:

$$\Delta(\rho w^2 + p)' = 0 = \Delta\left[(1+\bar{M}^2)\hat{p} + 2\bar{\rho}\,\bar{w}w'\right] \tag{82}$$

to be conserved. Consider mass conservation in more detail:

$$\left[\bar{\rho}_1 f_1^{1+} + \frac{\overline{w}_1^{(1)}}{\bar{a}_1^2}\right]\hat{p}_1 e^{ik_1^{1+}y_1} + \left[\bar{\rho}_1 f_1^{1-} + \frac{\overline{w}_1^{(1)}}{\bar{a}_1^2}\right]\hat{p}_2 e^{ik_1^{1-}y_1} = \left[\bar{\rho}_2 f_1^{2+} + \frac{\overline{w}_1^{(2)}}{\bar{a}_2^2}\right]\hat{p}_3 e^{ik_1^{2+}y_1} \tag{83}$$

and consider momentum:

$$\left[(1 + \overline{M}^{(1)^2}) + 2\bar{\rho}_1 \bar{u}_1^{(1)} f_1^{1+}\right]\hat{p}_1 e^{ik_1^{1+}y_1} + \left[(1 + \overline{M}^{(1)^2}) + 2\bar{\rho}_1 \bar{u}_1^{(1)} f_1^{1-}\right]\hat{p}_2 e^{ik_1^{1-}y_1} = \left[(1 + M_1^{(2)^2}) + 2\bar{\rho}_2 \bar{u}_1^{(2)} f_1^{2+}\right]\hat{p}_3 e^{ik_1^{2+}y_1} \tag{84}$$

Equations (83)-(84) can be solved to find $Tr = \hat{p}_3/\hat{p}_1$ and $R = \hat{p}_2/\hat{p}_1$.

4.2.10 Cases Considered

We considered three distinct cases. In the first two cases, data were taken at several points along a constant-speed line set by varying the back pressure. When choosing the configuration, a design point was chosen: the upstream relative flow angle (β_{dp}) for which the blade should have zero leading-edge incidence. The location of the design point, the solidity, and the desired exit relative flow angle (β_{exit}) were then used to design the blade. The geometric and flow parameters that describe these cases are listed in Table 7. The blades are shown in Figure 79.

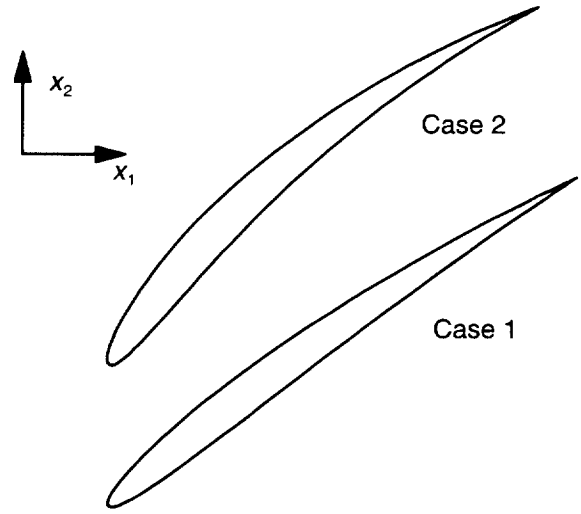

Figure 79. Blade Shapes for Cases 1 and 2

Table 7. Geometric Parameters for Cases 1 and 2

Case	ξ	θ	σ	t_{max} / c	β_{dp}	β_{exit}	$M_w = U_w / a_{1t}$
1	–43.41	13.18	1.0	0.07	–50	–45	0.50
2	–48.31	33.38	1.0	0.07	–65	–45	0.65

The third case was designed to overcome some shortcomings discovered in cases 1 and 2. In particular, it will be shown later that regions of supersonic flow developed near the leading edge as the incidence angles increased. The resulting shock wave introduced an additional noise source that made the results more difficult to interpret. Furthermore, due to inviscid separation (caused by numerical viscosity), we were unable to get a very large variation of the loading parameter $Pr - 1$,

where Pr = cascade total pressure ratio. To deal with these difficulties, a flow configuration and speed line were determined, but then four blades were designed with the intent that each blade would cover a different portion of the speed line with three points where the geometries overlap. The geometric parameters are listed in Table 8, and the blade shapes are shown in Figure 80.

Table 8. Geometric Parameters for Case 3

Geometry	ξ	θ	σ	t_{max}/c	β_{dp}	β_{exit}	U_w/a_{1t}
1	–45.00	0.00	1.0	0.07	–45	–45	0.5
2	–48.40	13.80	1.0	0.07	–55	–45	0.5
3	–51.50	25.00	1.0	0.07	–64	–45	0.5
4	–52.5	31.50	1.0	0.07	–68	–45	0.5

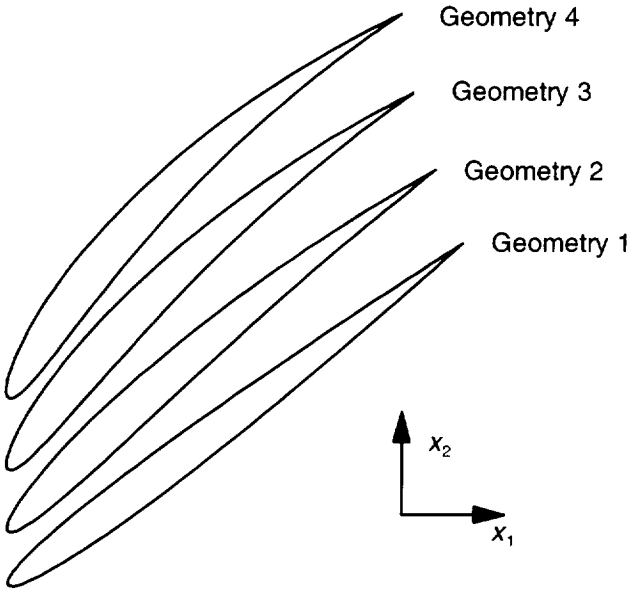

Figure 80. Blade Shapes for Case 3

The computational grids for all cases extended to approximately two chords upstream of the leading edge and approximately two chords downstream of the trailing edge. The results presented for cases 1 and 2 were obtained using a grid with 64 points in the tangential direction and 320 points in the axial direction. Comparing the results to other grids for the same cases, it is felt that these grids are very accurate for the base flow and are accurate for frequencies one and two times the blade passing frequency. For case 3, a grid with 128 points in the tangential direction and 640 points in the axial direction was used. It is felt that this grid is accurate for one to four times the blade passing frequency.

The working fluid is air with γ (ratio of specific heats) = 1.4.

4.2.11 Results

We start by considering some aspects of nonlinear, steady flow. Figure 81 is a compressor map of the three cases. Pressure ratio is defined as the ratio of the downstream to upstream absolute total pressures. Note the three overlapping points on the operating map for case 3 marked by the arrows.

The difference between "design intent" and the actual performance is due to inaccurate predictions of the deviation angles used in choosing the camber and stagger. The actual and predicted deviation angles (δ) are shown in Figure 82. The difference between design intent and the achieved flow is immaterial to this study and only noted for curiosity's sake.

Figures 83 and 84 show the relationship between loading and incidence angle. For case 3, this is a complicated relationship due to the four different geometries used. Once again, note that three values of the pressure ratio are achieved using two different incidences. Figure 85 shows the maximum Mach number in the relative frame for cases 1 and 2. For either large or small incidence these cases develop localized regions of supersonic flow near the leading edge with an associated shock. The relative Mach number for case 3 is always subsonic. In fact, a desire to have a case with a large range of loading without regions of supersonic flow was a prime motivation for the construction of case 3 using four different geometries. The lift coefficient is shown in Figure 86 and is defined as:

$$C_L = \frac{L}{\frac{1}{2}\rho_m W_m^2 c} \tag{85}$$

where the lift per span (L) is the component of the force acting perpendicular to the average flow direction β_m, where the average flow is defined by:

$$\begin{aligned} \rho_m &= (\rho_1 + \rho_2)/2 \\ W_m &= (\rho_1 w^{(1)} + \rho_2 w^{(2)})/(2\rho_m) \end{aligned} \tag{86}$$

Note that the results for cases 1 and 3, which have the same wheel speed, collapse along the same line.

We now turn our attention to the unsteady flow. The unsteady lift coefficient $\hat{C}_L$ normalized by the incidence angle variation $\hat{i}$ and further normalized by 2π.:

$$\frac{\hat{C}_L}{2\pi\hat{i}} = \frac{\hat{L}}{\frac{1}{2}\rho_m W_m \hat{u} \sin\beta_m} \tag{87}$$

is shown in Figures 87, 88, and 89. A theory for the unsteady lift coefficient for incompressible flow over isolated flat-plate airfoils is due to Sears (Goldstein Chapter 3, Reference 43) who showed that the normalized lift coefficient is given by what has become known as the Sears' function:

$$\frac{\hat{C}_L}{2\pi\hat{i}} = S\left(\frac{\omega c}{2W_m}\right) \tag{88}$$

For low frequencies, the Sears' function approaches unity. We note two things about the normalized unsteady lift coefficient. First, it is relatively insensitive to loading. This suggests that extensions to include the effect of loading, such as due to Horlock (Reference 45), may not be necessary. Second, the unsteady response of the blades is reduced as the frequency increases.

Although many acoustic modes may be present, we will only present results for the plane-wave mode. For cases 1 and 2 which were run for $f = 1 \times BPF$ and $f = 2 \times BPF$, most of the acoustic power radiated to the farfield is contained in the plane-wave mode. For case 3, which was run for higher frequencies, the plane-wave mode is not necessarily the dominant acoustic mode. This is illustrated

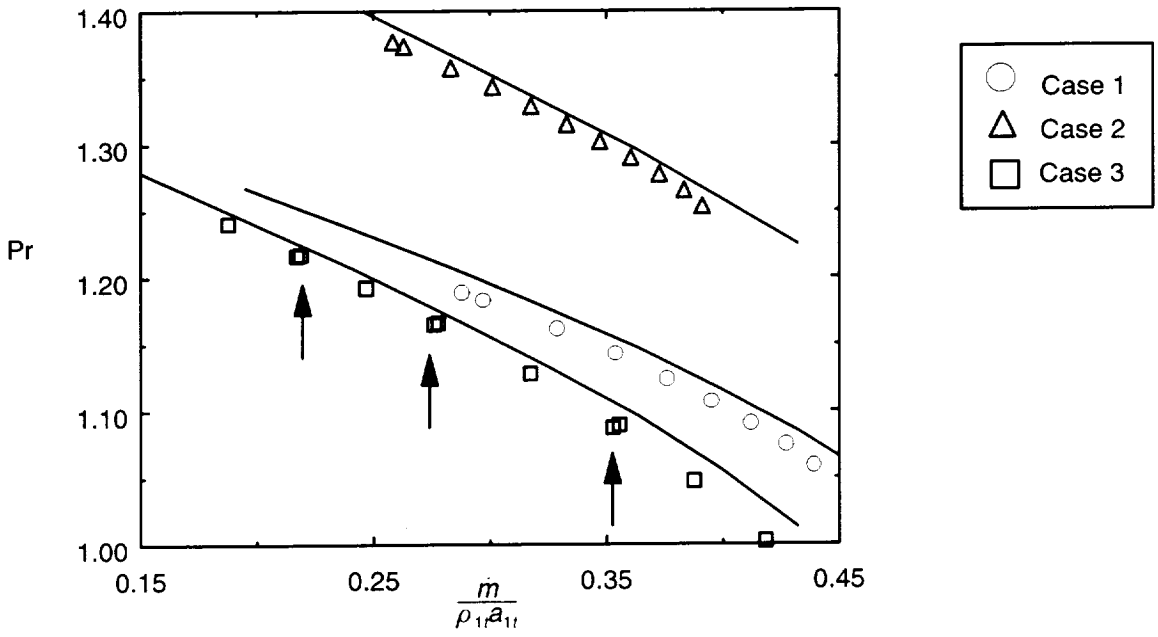

Figure 81. Compressor Map for Cases 1, 2, and 3 *The solid lines represent design intent.*

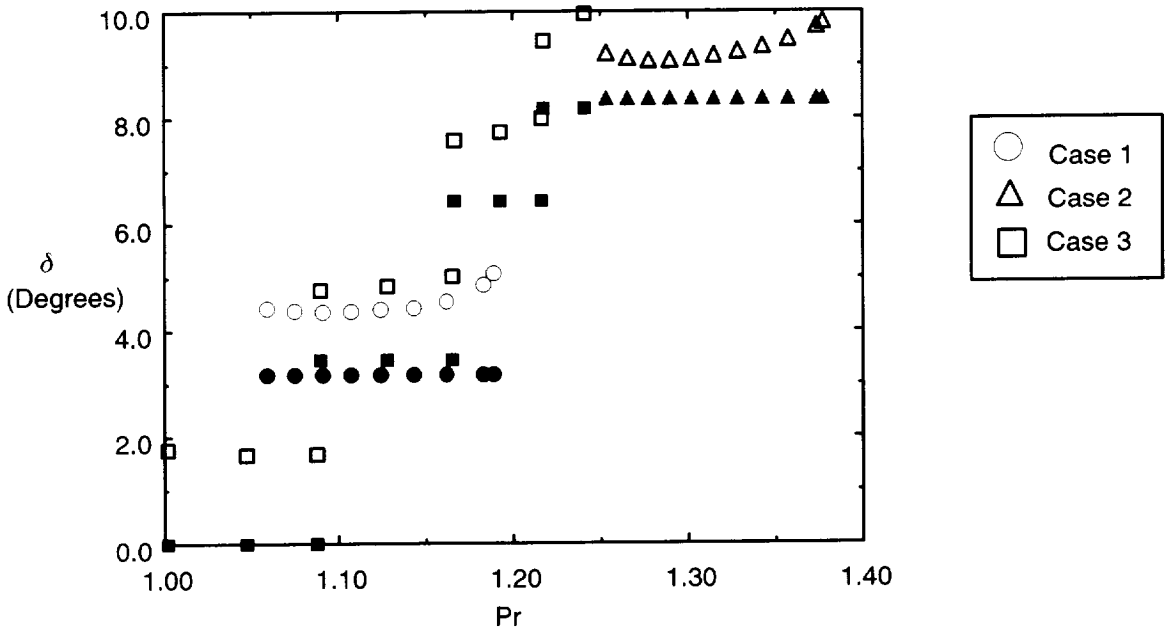

Figure 82. Deviation Angles for Cases 1, 2, and 3 *Open symbols are the actual deviation angles; filled symbols are the predicted angles.*

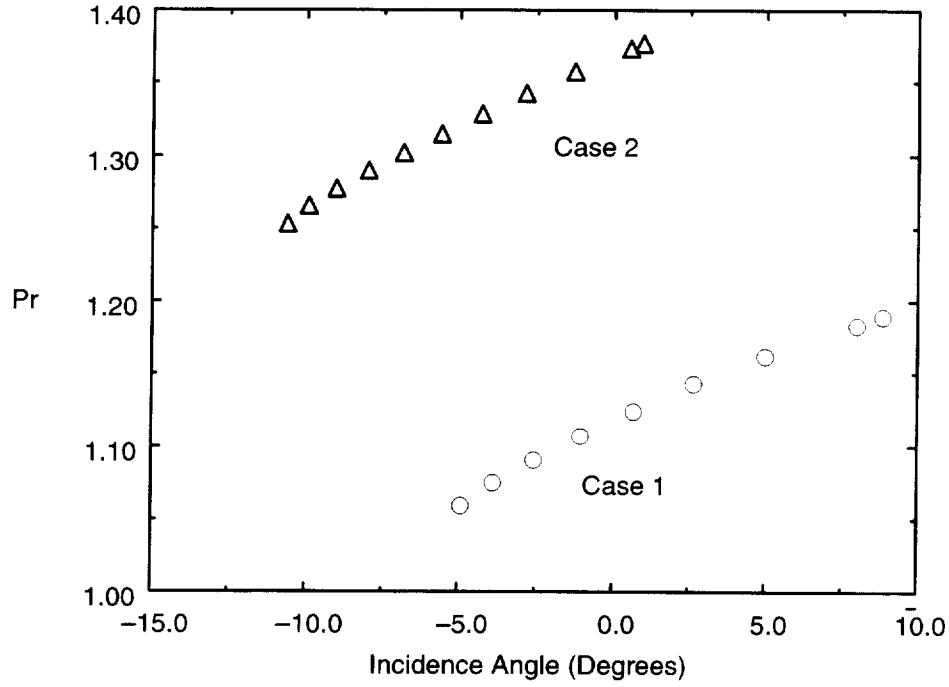

Figure 83. Effect of Incidence Angle on Pressure Ratio for Cases 1 and 2

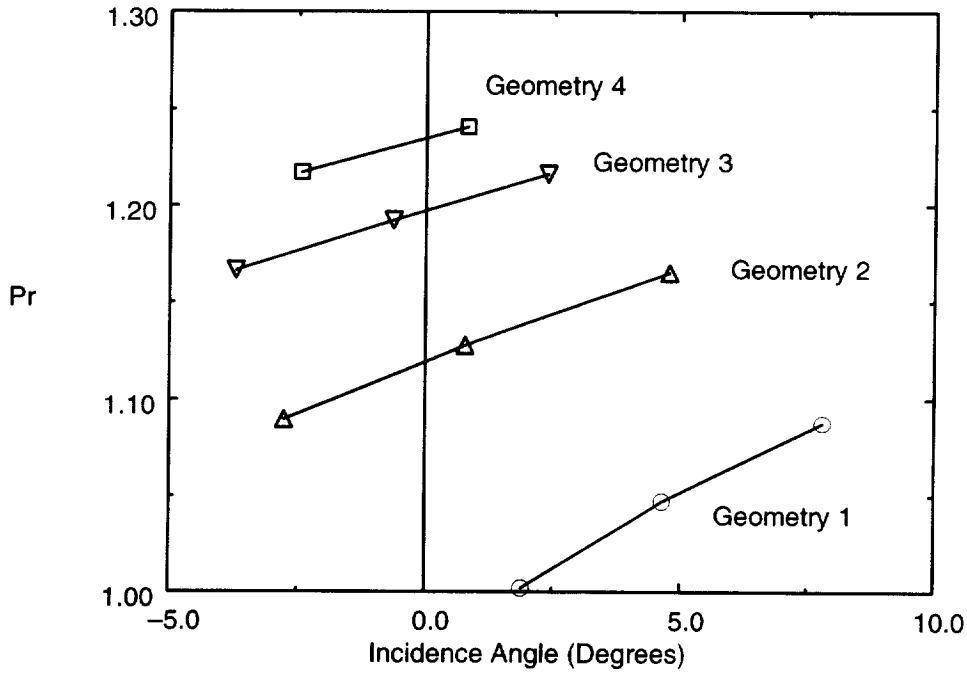

Figure 84. Effect of Incidence Angle on Pressure Ratio for Case 3

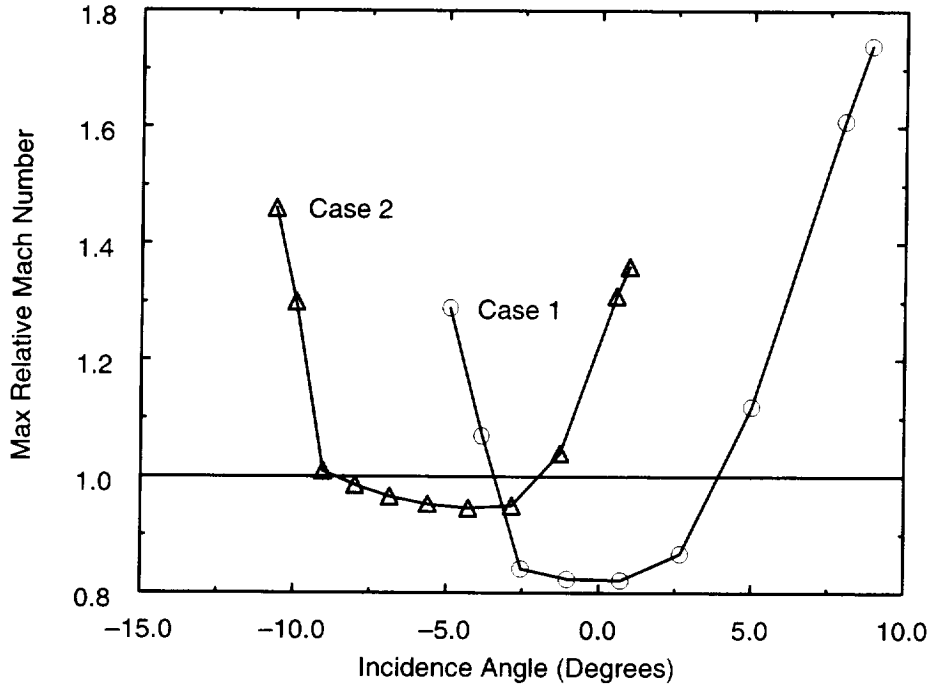

Figure 85. Maximum Relative Mach Number for Cases 1 and 2

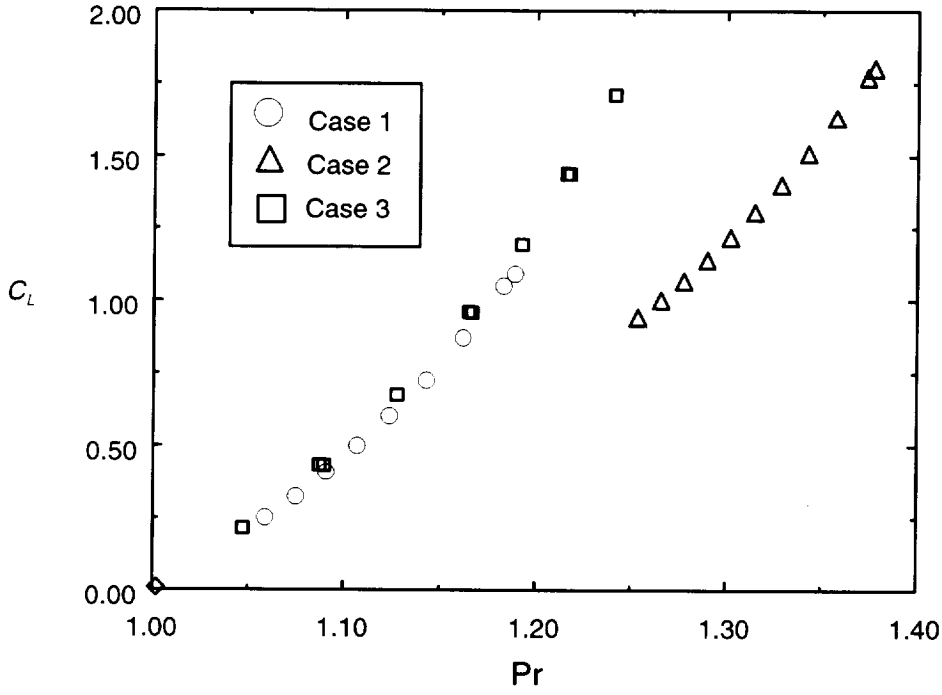

Figure 86. Lift Coefficient for Each Case

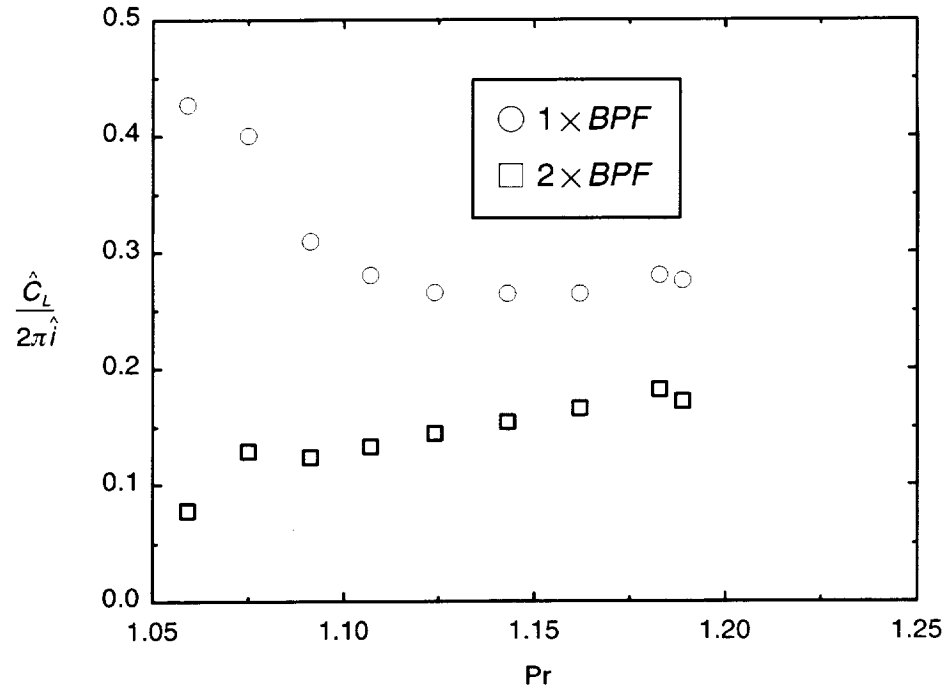

Figure 87. Normalized Unsteady Lift Coefficient for Case 1

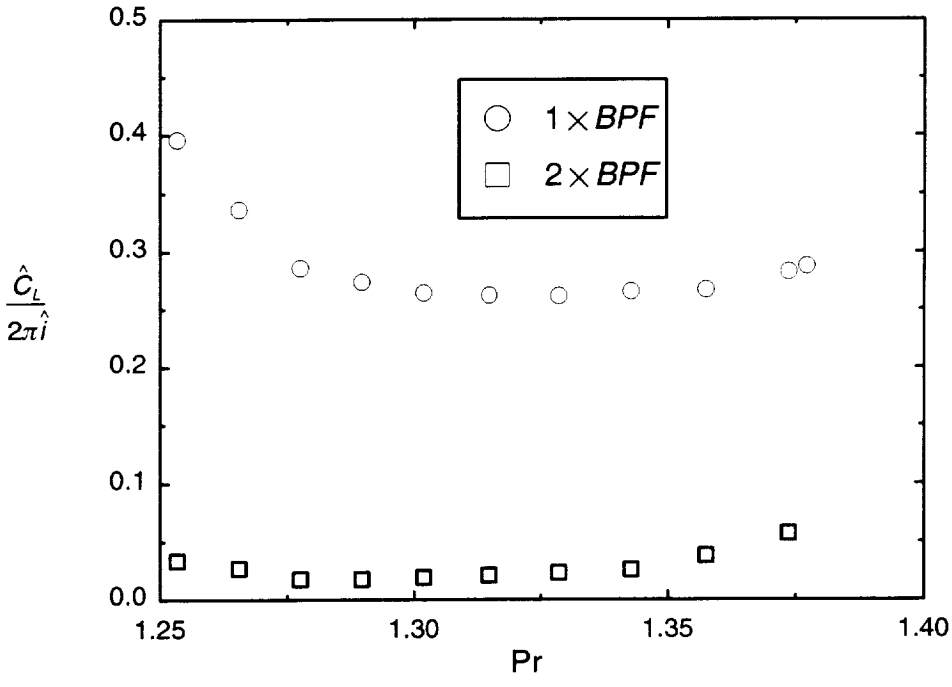

Figure 88. Normalized Unsteady Lift Coefficient for Case 2

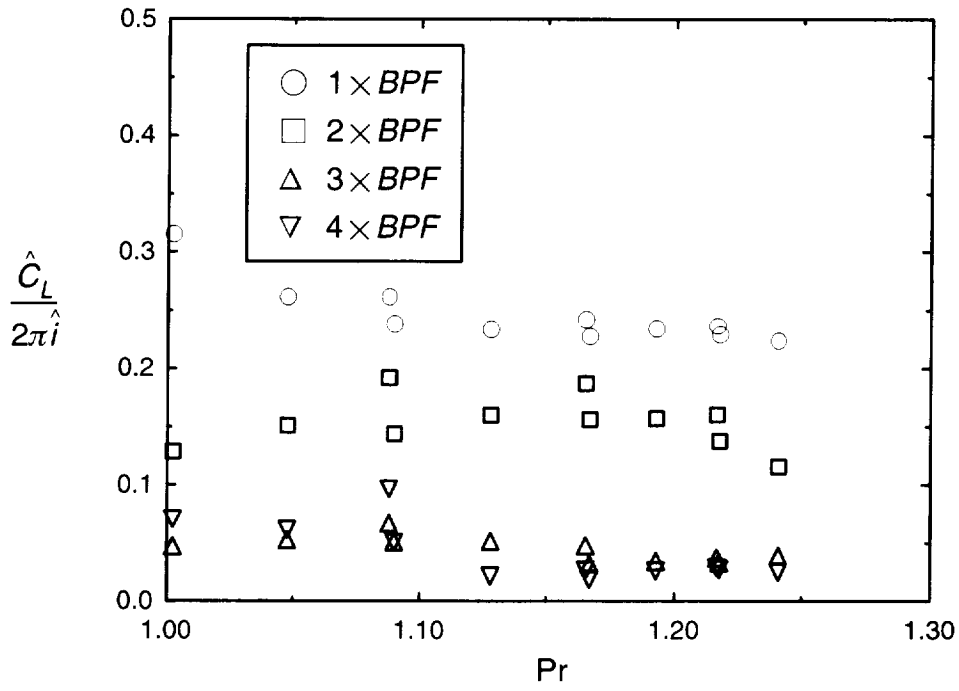

Figure 89. Normalized Unsteady Lift Coefficient for Case 3

in Figure 90 which shows the fraction of the total acoustic energy radiated by plane-wave mode. For $f = 1$ and $2 \times BPF$, most of the energy is in the plane-wave mode. However, at $f = 3$ and $4 \times BPF$, considerable energy exists in higher order modes. Section 4.2.12 documents our definition of acoustic intensity and power.

The directly computed sound is compared to the predicted dipole and quadrupole components in Figures 91, 92, and 93. In these plots, the vertical axis is acoustic efficiency — defined as the power radiated either upstream of downstream divided by the power in the imposed shear wave:

$$\eta_a = \frac{\hat{I}_m \cdot n_1}{\frac{1}{2}\rho_1 w_1^{(1)} w'_s} \tag{89}$$

where $\hat{I}_m$, is defined in Section 4.2.12 and m corresponds to the plane-wave mode.

Considering cases 1 and 2 first, we note that the dipole mostly dominates the quadrupole; however, there are exceptions. Consider the results for the upstream-propagating acoustic wave. At low loading (Pr), the quadrupole strength is significant. In fact for case 1, the quadrupole component of the noise is the same magnitude as the dipole component for $f = 2 \times BPF$. Presumably, the quadrupole sources are enhanced by the existence of a shock near the leading edge. Recall from Figure 85 that the flow in case 1 is locally supersonic for the three data points with lowest loading. For case 2, the quadrupole noise is a sufficiently large fraction of the dipole noise at low loading for $f = 2 \times BPF$ that it impacts the total radiated sound. Recall that the two data points at lowest loading are also locally supersonic for case 2.

Note that acoustic efficiency increases with increased loading and, except for the data points at low loading (which contain the complication of additional shock noise), the quadrupole noise increases

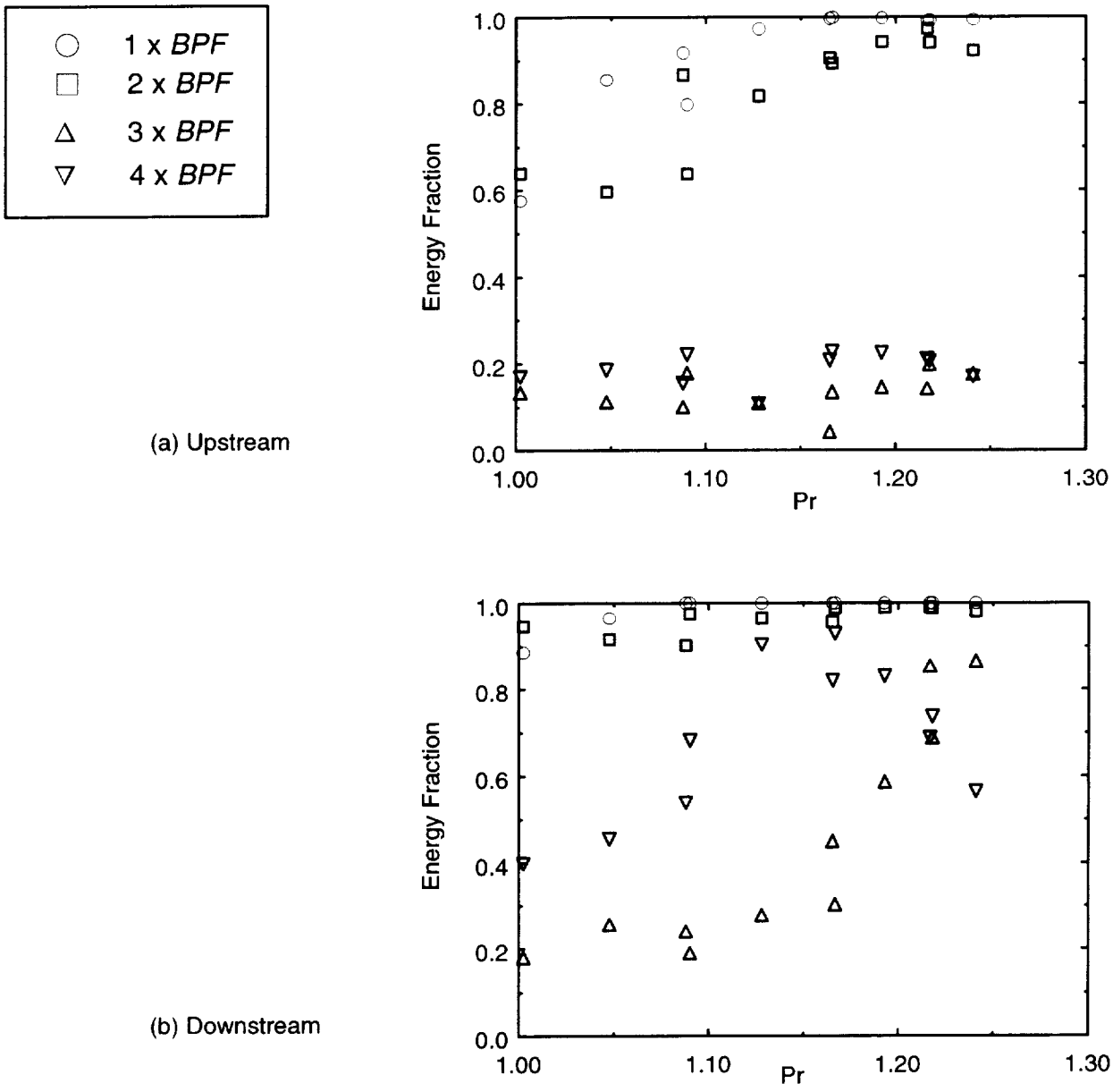

Figure 90. Fraction of Acoustic Power Radiated at the Plane-Wave Mode for Case 3

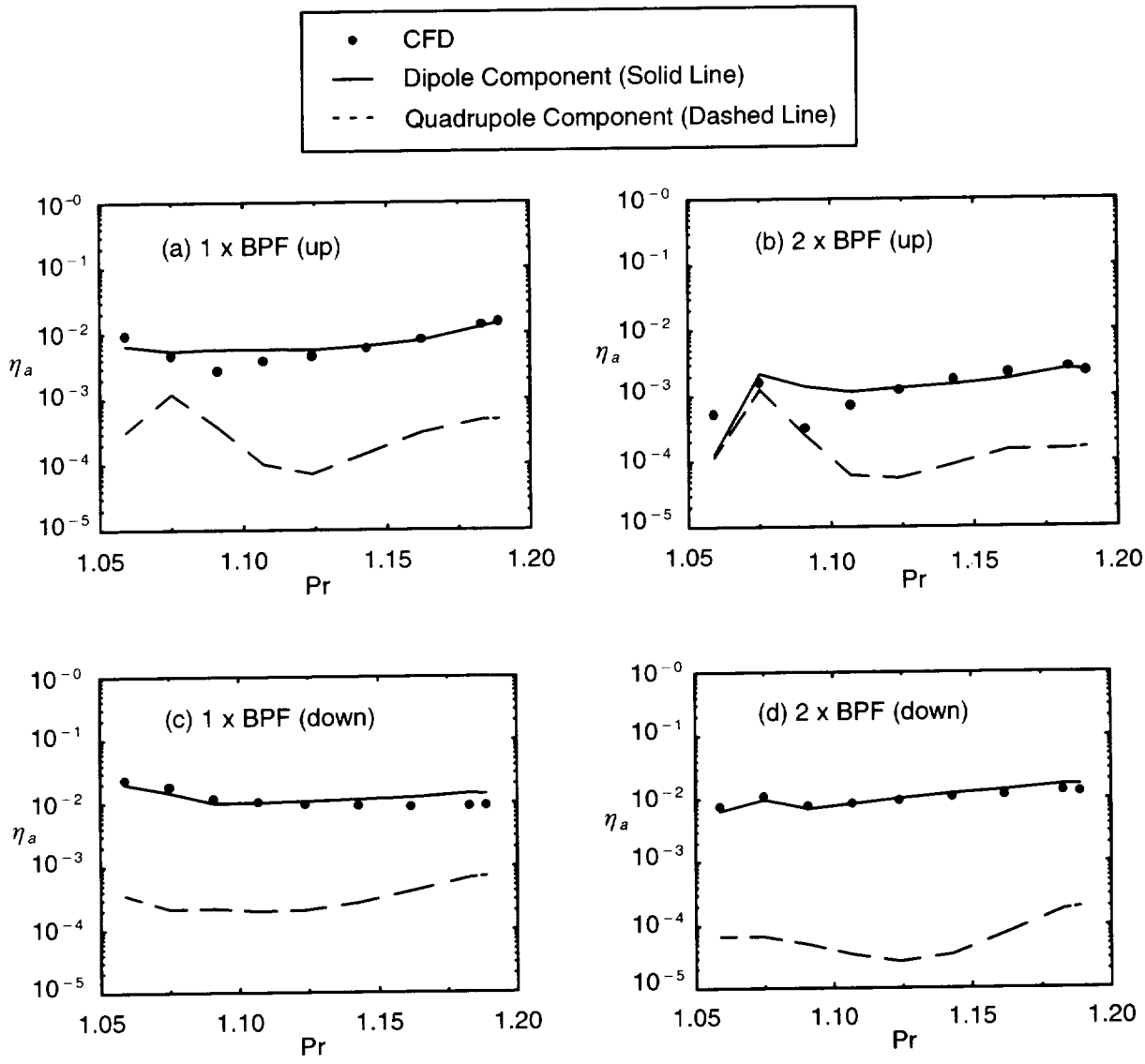

Figure 91. Acoustic Efficiency for Case 1

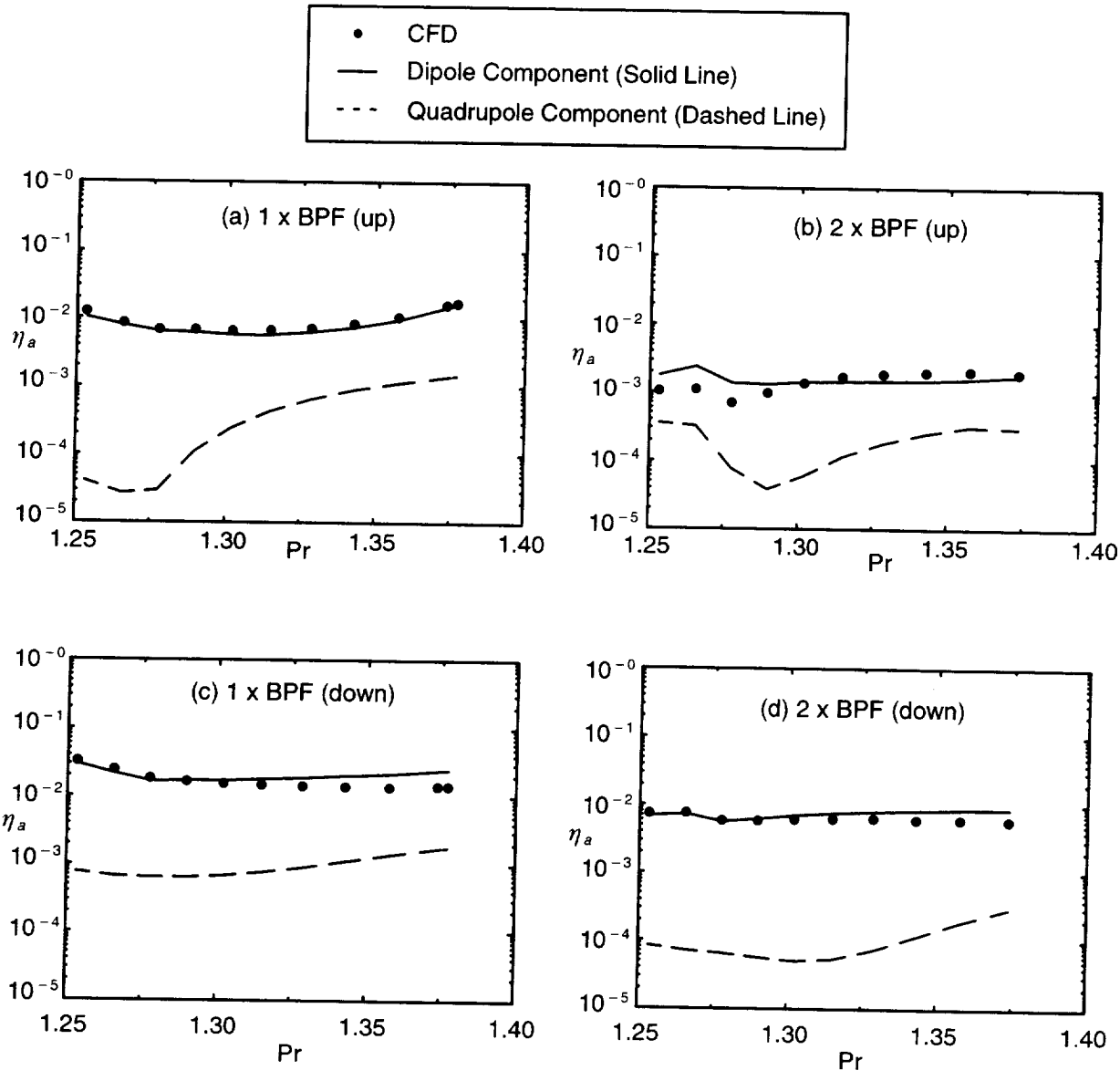

Figure 92. Acoustic Efficiency for Case 2

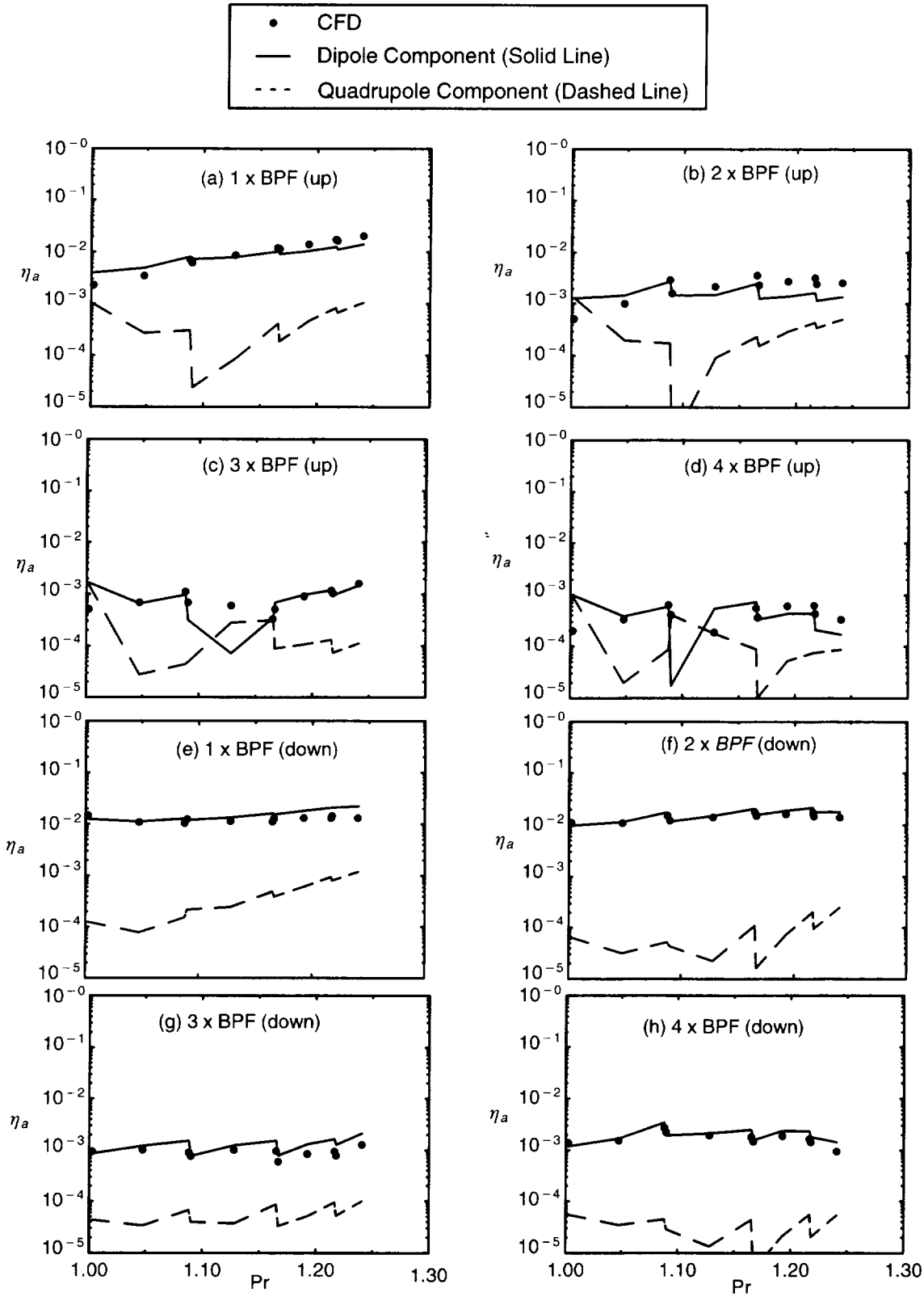

Figure 93. Acoustic Efficiency for Case 3

faster than the dipole noise. In other words, quadrupoles becomes more important as loading is increased. Furthermore, the dipole noise is a stronger function of frequency (it decreases as the frequency increases) than the quadrupole. This observation is supported by the theory of Morfey (Reference 24) to be discussed later. Additionally, the downstream noise is entirely dominated by the dipoles. It is not surprising that the dipoles would be relatively more important downstream when it is realized that the ratio of the quadrupole to dipole is roughly:

$$\frac{k_1 k_1 \hat{T}_{11}}{k_1 \hat{F}_1} = \frac{\hat{k} T_{11}}{\hat{F}_1} \tag{90}$$

Since $k_1^- < k_1^+$, the dipole is anticipated to be relatively more important downstream.

Examining the results for case 3 reveals trends similar to those observed in cases 1 and 2. Of note is that at the highest two frequencies, 3 and 4 $\times$ *BPF*, the noise radiated upstream by the dipole and quadrupole sources is similar. By examining the three operating points where two blade designs were considered, it is clear that the choice of blade geometry can impact the total radiated noise, the dipole noise, and the quadrupole noise. Generally, the quadrupole noise is more sensitive to blade geometry than the dipole. It is suspected that differences in leading-edge incidence drives this sensitivity. Presumably the quadrupole sources near the leading edge are stronger for a blade design with large incidence, positive or negative, as compared to a blade designed to give zero incidence flow. Although the three-dimensional quadrupole source distribution was available, time did not permit this valuable diagnostic resource to be examined.

Figure 94 demonstrates that our results are relatively independent of grid resolution. In this figure, the acoustic efficiency for case 3 is compared to the results obtained using a computational mesh with half as many grid points in both of grid directions. The comparison suggests that the case 3 results are grid independent for $f = 1$ to 3 $\times$ *BPF* and only slightly grid dependent for $f = 4 \times$ *BPF*.

Figure 95 shows the dipole and quadrupole noise predicted by the theory of Morfey (Reference 24), summarized in Section 4.2.13, page 87, for case 3. The Morfey predictions only depend on simple parameters of flow ,such as the flow upstream of the cascade and the lift coefficient of the blade. The predictions from Morfey's theory are larger than the directly computed noise, shown in Figure 93, by about two orders of magnitude. This is likely due to the fact that Morfey made the assumption of acoustical compactness. Note that the acoustic theory developed herein made no assumptions about acoustical compactness. Simple experiments with our prediction model did reveal that assuming acoustic compactness increases the level of the predicted sound radiated by both the dipole and quadrupole sources.

Despite a prediction of the radiated sound that is too large, Morfey's theory does support some of the trends observed in our results. First, Morfey's theory shows that the dipole strength varies like $1/n$, but the quadrupole has no frequency dependence (recall that $f = n \times$ *BPF*). This is consistent with our results which showed that the dipole noise was more sensitive to frequency than the quadrupole noise. Second, Morfey's theory shows that the sound increases with increased loading, as was also observed in our results.

Finally, Morfey's theory reveals that the quadrupole noise becomes relatively more important than the dipole noise as loading increases — a trend also noted above.

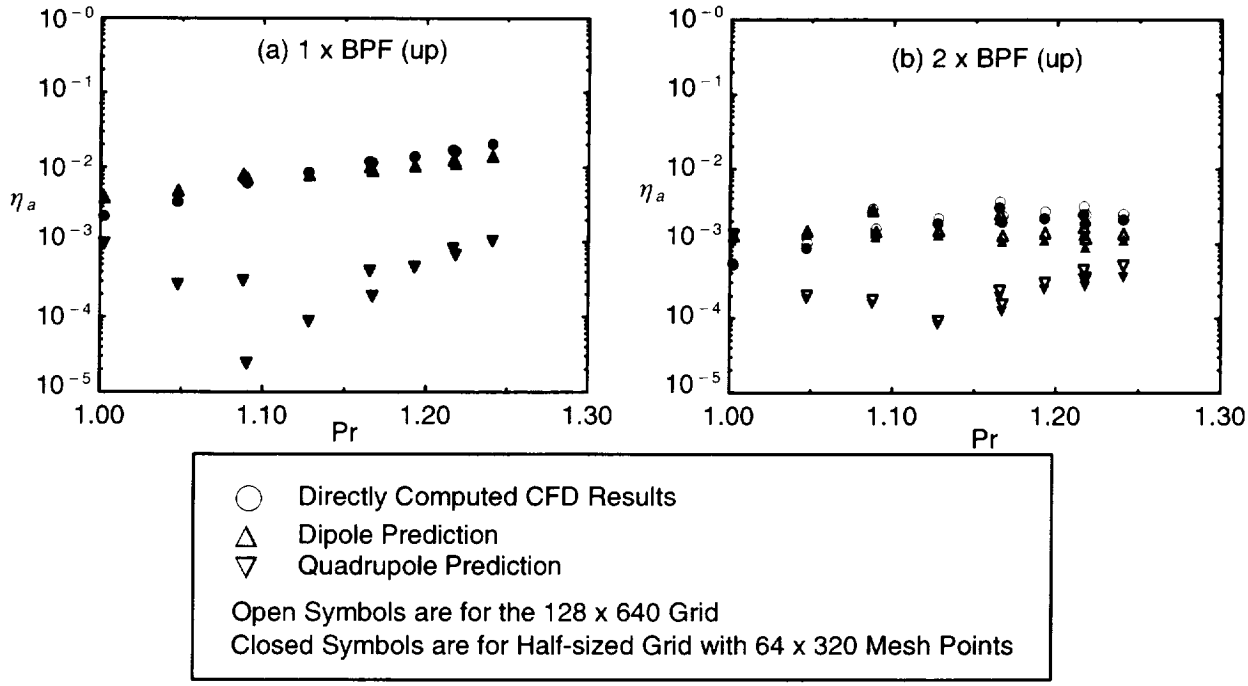

Figure 94. Demonstration of Grid Independence for Case 3

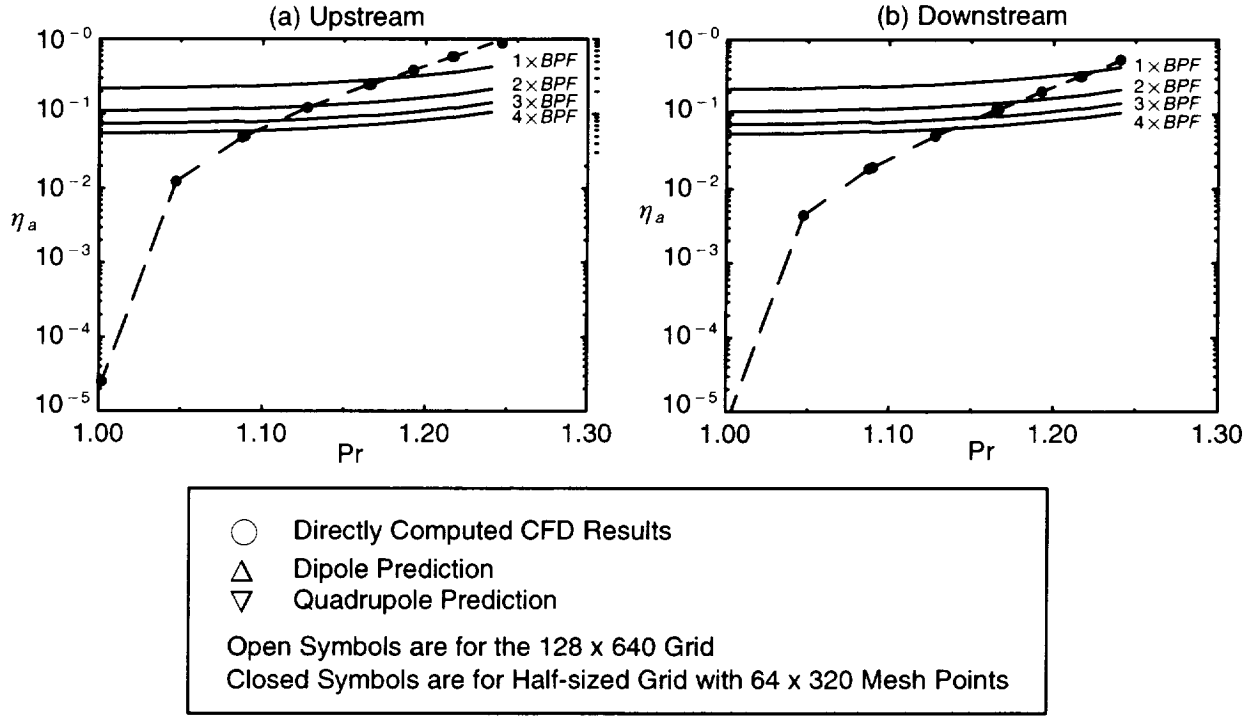

Figure 95. Predictions of Dipole (Solid Line, Frequency as Marked) and Quadrupole (Dashed Line with Solid Circles) Strengths using the Theory of Morfey (Reference 24) as extended by Mani (Reference 11)

4.2.12 Definition of Acoustic Intensity

In a medium moving at uniform, constant velocity $\bar{u}$, the acoustic intensity is given instantaneously by (Goldstein, Section 1.7.2, Reference 43):

$$I(x;t) = \left(\frac{p'}{\bar{\rho}} + u' \cdot \bar{u}\right)(\bar{\rho}u' + \rho'\bar{u}) \tag{91}$$

The primes denote acoustic disturbances. The average acoustic power radiated by a region of space bounded by a surface S is:

$$\mathcal{P} = \int_S \bar{I} \cdot \hat{n}\, dS \tag{92}$$

where the overbar denotes a time average. We consider acoustic disturbances to be a combintation of normal modes, that is:

$$p'(x;t) = \mathrm{Re} \sum_m \hat{p}_m e^{-i\omega t} e^{ik_m \cdot x} \tag{93}$$

If we express the intensity as: $$I = P \times V \tag{94}$$

then $$\bar{I} = \frac{1}{2}\mathrm{Re} \sum_{m_1} \sum_{m_2} \hat{P}^*_{m_1} \hat{V}_{m_2} e^{i(k_{m_1} - k_{m_2}) \cdot x} \tag{95}$$

For turbomachinary, an orthogonality principles holds, so we can express:

$$\bar{I} = \sum_m \frac{1}{2}\mathrm{Re}\hat{P}^*_m \hat{V}_m = \sum_m \hat{I}_m \tag{96}$$

The intensity for a given mode $\hat{I}_m$ is our desired result. By use of Equation (91), we have:

$$\hat{I}_m = \frac{1}{2}\mathrm{Re}\left[\frac{\hat{p}^*_m}{\hat{\rho}_m} + \hat{u}_m \cdot \bar{u}\right]\left(\bar{\rho}\hat{u}_m + \hat{\rho}_m\bar{u}\right) \tag{97}$$

Using acoustic relationships, we know that:

$$\hat{\rho}_m = \frac{\hat{p}_m}{c_0^2} \qquad \hat{u}_m = \frac{\hat{p}_m}{\bar{\rho}}\frac{k_m}{\omega_m^s} \qquad \omega_m^s = \omega - k_m \cdot \bar{u} \tag{98}$$

so we are able to express the intensity as: $$\hat{I}_m = \frac{1}{2}\frac{|\hat{p}_m|^2}{\bar{\rho}}\left(1 + \frac{k_m \cdot \bar{u}}{\omega_m^s}\right)\left[\frac{k_m}{\omega_m^s} + \frac{\bar{u}}{c_0^2}\right] \tag{99}$$

From the wave equation we know that $\omega_m^s = c_0|k_m|$, which gives our final result:

$$\hat{I}_m = \frac{1}{2}\frac{|\hat{p}_m|^2}{\bar{\rho}c_0}\left(\frac{\omega}{\omega_m^s}\right)\left(\frac{k_m}{|k_m|} + \bar{M}\right) \tag{100}$$

where $\bar{M} = \bar{u}/c_0$.

4.2.13 The Theory of Morfey

Morfey (Reference 24) considered the dipole and quadrupole sound radiated by a rotor in response to an axial velocity disturbance where the tangential wavelength was equal to the blade spacing. The strength of the disturbance is given by ϵ, defined as:

$$\epsilon = \sqrt{2}\frac{w_1'}{\overline{w}_1} \tag{101}$$

Morfey's results have been extended by in this program for axial disturbances with tangential wavelength equal to an integer multiple, say n, of the blade spacing. The results presented below reflect these extensions along with corrections for some typographical errors in Morfey's paper.

The acoustic intensity predicted by Morfey for the dipole is:

$$\frac{I_d}{\overline{\rho}\,\overline{a}^3} = \frac{1}{8n}\,\epsilon^2\sigma\overline{M}_1^4 f(\beta) \tag{102}$$

where:

$$f(\beta) = \sin\beta\left(\tan\beta - \frac{C_L}{\pi}\right)^2 \tag{103}$$

The acoustic intensity for the quadrupole is:

$$\frac{I_q}{\overline{\rho}\,\overline{a}^3} = \frac{1}{4}\,\epsilon^2\,\sigma^2\,C_L^2\,g(\beta,\overline{M}_1)\,\frac{\overline{M}_1^6}{1 \pm \overline{M}_1{}^2} \tag{104}$$

where:

$$g(\beta,\overline{M}_1) = \frac{\sin^2\beta}{\cos^4\beta}\left[1 - \frac{\overline{M}_1^2}{1 \pm \overline{M}_1}\tan^2\beta\right]^2 \tag{105}$$

This result is independent of n. The plus sign is to be used when evaluating the quadrupole strength downstream of the blades, and the minus sign is to be used upstream. In evaluating I_d and I_q, we interpreted all flow quantities to be evaluated in the uniform medium upstream of the blades.

4.2.14 Summary and Conclusions

The results reported herein provide some answers to the fundamental question investigated in this study: quadrupole noise be deemed as important as, or even more important than, dipole noise? Our results, supported by Morfey (Reference 24), show that quadrupole noise becomes increasingly important as the frequency and loading increase. We also demonstrate that blade shape has a strong impact on radiated noise, with the quadrupole component being more sensitive than the dipole component. This strongly supports the use and development of quadrupole noise models for fan broadband noise prediction.

It is also appropriate to comment on the usefulness of the approach taken in this study. We were able to use computation methods to answer directly a vexing question of aeroacoustics. Computational tools were used to provide complete data for the radiated sound but also to provide all the information needed for aeroacoustic theory. This style of accurate computations applied to carefully chosen model problems can provided a wealth of insight into noise and noise generation, much like the use of computations has advanced our understanding of turbulence (Moin and Mahesh, Reference 46).

4.3 Three-Dimensional Effects Model

The basic approach used to develop a "3D Effects" model is to exploit the idea that the 3D problem of noise generation in an annular duct (of constant inner and outer radii), carrying a uniform axial flow due to a specified source distribution, can be reduced by Fourier Bessel decomposition (in the radial coordinate) to a sequence of two-dimensional problems. The implications of this decomposition (and how it is performed) are described herein. The subsequent solution of the 2D problems and details of source estimation are adopted entirely from prior GE work in references from Mani (References 16, 11, and 47) and Gliebe (Reference 48).

There is an inherent difficulty in constructing a 3D model of broadband noise when turbulence is the noise source. This arises from the fact that turbulence spectra and correlation functions are much easier to construct in the case of spatially homogeneous turbulence. Isotropy (or lack thereof) is another issue, but (to a limited extent) anisotropy is easier to account for than inhomogeneity, so we would prefer to deal with homogeneous turbulence. In a duct, turbulence cannot be homogeneous, particularly in the radial directions, since the duct, while axisymmetric, is constrained by inner and outer walls at fixed radii. A less severe issue, from the lack of homogeneity point of view, is the fact that in the tangential direction, one (strictly speaking) requires periodicity every 360° rather than homogeneity. It is not possible within the scope of the present effort to rigorously allow for both sources of inhomogeneity, but an approximate formulation is employed.

In terms of the radial direction, the following approximation is adopted. The duct annulus is broken up into several annular strips as shown in Figure 96. Each strip has a radial extent equal to the spanwise integral length scale of the turbulence. Within each strip, we assume the turbulence to be completely correlated and the turbulence in each strip is assumed to be completely uncorrelated from that in any other strip. This then permits us to evaluate noise from each strip separately in full 3D terms, and then add up the power spectra from each strip in a mean square sense. This approximation permits tractable 3D treatment, allows for specification of spanwise length scales and yet allows complete "2D" turbulence inputs in the blade-to-blade cylindrical surface. The only disadvantage of the formulation is that final answers are not independent of the manner in which strips are chosen — hardly surprising since choice of radial strips does correspond to specification of spanwise length scales.

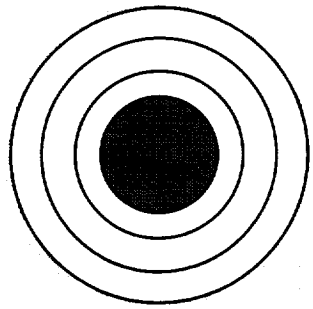

Figure 96. Annulus Broken Into Strips for 3D Effects Model

To implement this formulation while retaining the code infrastructure (set up to implement a "two-dimensional strip" approach) we adopt the following procedure (full details will be given but it may be useful to provide a synopsis first). First, the frequency of interest is selected; we then consider one radial mode order at a time. All possible radial mode orders that are cut-on are considered. For each frequency and radial mode order, we consider a range of tangential wave numbers and associated radial eigenfunctions which are cut-on. By Fourier Bessel analysis, a "three-dimensional" correction factor is derived that relates two-dimensional "strip theory" to the true three-dimensional annular situation. This correction factor depends on radial and tangential order and the spanwise extent of the strip. Finally, the broadband noise contribution from each strip

is evaluated one radial mode at a time, integrating over all tangential wavenumbers above cut-off. For a fixed tangential (acoustic) wavenumber, an infinite series of tangential and axial wavenumbers of the turbulence spectrum due to the "haystacking" phenomenon is involved.

The explicit steps are as follows.

Step 1 – We start with a specified frequency of interest or equivalent, by the wave number "k." Also, the strip $c \le r \le d$ is being considered with inner radius of duct denoted by $r = a$ and outer radius by $r = b$.

Step 2 – Consider one radial mode order at a time. We only consider effects of uniform, subsonic, axial flow at Mach number M. Then with n denoting a radial index, we need to consider a range of:

$$n = 0 \quad \text{to} \quad n = k\,(b-a)/\left(\pi\sqrt{1-M^2}\right) \tag{106}$$

in order to consider modes above cut-off. Let:

$$k_n^2 = [k^2 - n^2\pi^2(1 - M^2)/(b - a)^2] \tag{107}$$

The range of possible tangential acoustic wave numbers is from

$$-k_n/\sqrt{1 - M^2} \qquad \text{to} \qquad k_n/\sqrt{1-M^2}$$

If the transverse spacing between the blades in the annular strip under consideration is d and k_{ys} denotes the acoustic tangential wave number, then we need to consider a range of tangential turbulence wave numbers $k_{yt} = k_{ys} + 2\pi\ell/d$ where ℓ ranges from $-\infty$ to ∞. For the case of scattering by a stator, the corresponding axial wave number of the turbulence would be k/M, but for a rotor the shift by multiples of blade passing frequency needs to be accounted for.

Step 3 – For each transverse acoustic wave number k_{ys} a good approximation to the transverse eigenfunction $\phi_{mn}{}^{(r)}$ is:

$$\phi_{mn}(r) = J_m(k_{mn}r)\,Y'_m(k_{mn}a) - Y_m(k_{mn}r)\,J'_m(k_{mn}a) \tag{108}$$

Where $m = k_{ys}(a+b)/2$ and $k_{mn}^2 = k_{ys}^2 + n^2\pi^2/(b - a)^2$ (109)

Step 4 – For a source perfectly correlated for $c \le r \le d$ but uncorrelated with sources lying in other strips, we first note that for each radial mode order n we can (rigorously) solve a "two-dimensional" problem in the strip $c \le r \le d$ governed by the reduced acoustic wave number k_n and turbulence and blade-row properties appropriate to that blade row in that strip. In the true annular case, such a solution would be modified by the Fourier Bessel coefficient:

$$C_{mn} = \int_c^d r\phi_{mn}(r)dr \Big/ \int_a^b r\phi_{mn}^2(r)dr \tag{110}$$

In the conventional two-dimensional strip theory, the two-dimensional solution would radiate through an area (except for a factor of 2π) given by $(d^2 - c^2)/2$. In the annular case, the correct factor would be:

$$C_{mn}^2 \int_a^b r\phi_{mn}^2(r)dr \tag{111}$$

Thus we may introduce a correction factor $f3D$ that is a function of k_{ys} $(a + b)/2$ (or m) and n (and a, b, c, d):

$$2C_{mn}^2 \int_a^b r\phi_{mn}^2(r)dr \,/\, (d^2 - c^2) \tag{112}$$

or

$$f3D = \frac{2\left[\int_c^d r\phi_{mn}dr\right]^2}{\left[\int_a^b r\phi_{mn}^2(r)dr\right](d^2-c^2)} \tag{113}$$

Multiplying the previous strip theory results by $f3D$ (with the strip theory calculation done for the reduced acoustic wavenumber k_n) is a formal, convenient way of using prior work based on strip theory and a multiplicative factor $f3D$ to deduce the required three-dimensional results. On the one hand, the convenience is only formal since $f3D$ needs to be calculated for each radial order, each k_{ys}, and each strip, but viewing the 3D case in this fashion has helped preserve coding developed for implementation of strip theory.

It is also clear that, in principle, the order of the Bessel functions in ϕ_{mn} (r), such as m, should be an integer, but in this formulation it is not. Again this reflects an approximation induced by inability to ensure that the turbulence correlations are actually periodic in the azimuthal direction and not homogeneous as assumed herein. In view of this and the approximations used in k_{mn}, it was found that the normalizing integral in the denominator of the expression for C_{mn} was best computed numerically by Simpson's rule and not from end-point values as is possible (in principle) if exact forms (that is, integer orders and exact eigenvalues) were employed.

A couple of additional comments are in order concerning calculation of 3D effects. When frequencies on the order of 10 kHz and fans 10–11 feet in diameter are considered, it can be shown that very high-order Bessel functions (400 plus) and high arguments are involved. Computing these involves using appropriate asymptotic formulae including distinctions based on whether argument exceeds order or vice versa. In an earlier version, the radial eigenfunctions were sought to be simplified by using trigonometric forms — explicitly the form: $\cos [n\pi (r-a) / (b-a)]$. This form is a very poor approximation to ϕ_{mn} based on Bessel functions when large orders are involved; hence, the approach fails for high-frequency noise. We mention this because other studies have used this simplification which we believe is inadequate for high-frequency broadband noise. The approximation for k_{mn} used herein, on the other hand, seems quite adequate even for large m, n.

4.3.1 Acoustic Treatment Effects

We briefly outline implementation of an approximate, ray-based method suggested in Rice (Reference 49) for analysis of the effects of duct treatment.

At a given frequency with acoustic wavenumber k, corresponding to a radial mode order n, the acoustic mode has wavenumbers in the radial tangential and axial directions as follows:

Radial wave number = $n\pi / (b-a)$ with: $k_n^2 = k^2 - n^2\pi^2(1 - M^2) / (b - a)^2$ (114)

a range of tangential wave numbers k_{ys} is possible from $-k_n/\sqrt{1 - M^2}$ to $k_n/\sqrt{1-M^2}$.

It will be convenient to let: $k_{ys} = k_n \sin\theta/\sqrt{1 - M^2}$ (115)

where $-\pi/2 < \theta < \pi/2$.

The axial wavenumber corresponding to downstream/upstream propagation is:

$$\alpha = (-kM \pm k_n \cos\theta) / (1 - M^2) \quad (116)$$

The square root sum of the squares of the above three wavenumber components is $k - \alpha M$, or:

$$(k \mp Mk_n \cos\theta) / (1 - M^2) \quad (117)$$

From here on, Rice's approximate method of evaluating treatment effects proceeds as follows. The direction cosines of the normal to wavefronts vector (defining the direction of the phase velocity) has axial and radial components:

$$(dc)_{ax} = \alpha / (k - \alpha M) \quad (118)$$

and

$$(dc)_{rad} = n\pi / [(b - a)(k - \alpha M)] \quad (119)$$

Thus, if the projection of the phase velocity is inclined at angle ϕ_y to the radial direction in the axial/radial plane:

$$\cos(\phi_y) = (dc_{rad}) / \left[(dc)_{rad}^2 + (dc)_{ax}^2\right]^{1/2} \quad (120)$$

and

$$\sin(\phi_y) = (dc_{ax}) / \left[(dc)_{rad}^2 + (dc)_{ax}^2\right]^{1/2} \quad (121)$$

If the projection of the group velocity of the mode makes an angle ψ_x with the axial direction in the axial radial plane:

$$\tan(\psi_x) = (dc)_{rad} / [(dc)_{ax} + M] \quad (122)$$

The number of bounces N that the ray makes with the outer wall over an axial length L is:

$$N = L \tan(\psi_x) / 2(b - a) \quad (123)$$

The sound absorption A per bounce at the outer wall (where the specific acoustic resistance and reactance are assumed to be R, X at the frequency of interest) is given by Equation (34) of Rice (Reference 49) as:

$$A = \frac{(R^2 + X^2)\cos^2\phi_y (1 + M\sin\phi_y)^2 - 2\theta\cos\phi_y (1 + M\sin\phi_y) + 1}{(R^2 + X^2)\cos^2\phi_y (1 + M\sin\phi_y)^2 + 2\theta\cos\phi_y (1 + M\sin\phi_y) + 1} \quad (124)$$

The power absorption over N bounces is A^N.

In this model, the absorption is infinite at cut-off (when $\psi_x = \pi/2$).

4.4 Directivity Model

A detailed report on directivity models suitable for fan broadband and core noise, authored by E.J. Rice, has been provided by Hersh Acoustical Engineering Inc. who performed this task under

subcontract to GEAE. Their complete report is replicated as an Addendum to this document. Salient information germane to fan broadband noise is summarized in this subsection.

Farfield noise models and computer codes have been developed for the radiation of broadband random noise from the fan inlet and exhaust ducts and the core engine nozzle. These models have been developed to be used in conjunction with turbomachinery broadband noise generation models that define acoustic power generation in the duct as distributed as a mode cut-off ratio distribution and as a function of noise frequency. The models transform the in-duct acoustic power distribution into the farfield radiation field either on a constant radius or sideline distance. The inlet radiation model includes the influence of the bellmouth used in static tests or the inlet lip used for wind-tunnel tests, and the results should be adequate for either of these cases. The aft duct cases include the effect of the nozzle area change and the jet slip layer on propagation and radiation of the internally generated broadband noise. A new termination transmission loss model has been developed to determine the reflection of sound at the exits of the inlet and exhaust ducts. Acoustic power has been conserved even for the difficult aft-radiation cases where the radiation angle is drastically altered by the shear layer. The radiation models are intended to be approximate but adequate representations for noise radiation where very rapid calculations are needed for a multitude of cases.

The broadband random noise radiation models developed here are intended to be reasonably accurate and provide extremely fast computational capability. This speed is required because extremely large numbers of duct modes can propagate in modern turbofan engines at the high frequencies usually encountered with turbomachinery broadband noise. The noise radiation models are intended to be used in conjunction with noise source models which predict the broadband noise generation in the engine ducts in terms of a convenient modal representation such as the modal cut-off ratio power distribution.

A key requirement for a useful broadband random noise radiation model is the availability of a fairly simple multimodal radiation capability. The concept of the multimodal radiation directivity without a steady flow was introduced by Saule and Rice (Reference 50) using a simple, flanged-duct, modal radiation directivity. This concept was further simplified when Rice (Reference 51) showed that the flanged-duct radiation expression could be approximately expressed as a function only of the mode cut-off ratio and the sound frequency, and an approximate equation for broadband radiation was developed using these concepts. A radiation model for the aircraft engine inlet which includes steady flow was presented by Rice et al. (Reference 52) and fully developed by Rice and Sawdy (Reference 53) to incorporate the multimodal properties of the noise source in the duct, the attenuation of the noise field due to duct wall treatment, the termination reflection, and the resulting farfield radiation. Unfortunately, the early work used the preservation of modal phase velocity vector angle through the inlet velocity gradients. The results of this model appeared to fit the experimental data in spite of this physically unattractive assumption. The forward beaming of the inlet bellmouth provided a roughly compensating error. This was recently corrected by Rice (Reference 54) by incorporating the preservation of modal group velocity vector angle through the inlet velocity gradients and providing a model for the bellmouth effect on the inlet farfield noise radiation directivity.

Numerical sound propagation codes have been reported such as those developed by Horowitz et al. (Reference 55) and Eversman et al. (Reference 56). These numerical codes, based on finite-element analysis within and just outside of the duct, can more adequately handle duct area variation, inlet lip shape, and velocity variations than the earlier analytical models. Since concentration of effort was for some time on the engine tone noise consisting of only a few modes, at least in flight, these

numerical codes were excellent for calculating the radiation of these individual duct modes. However, for broadband noise, many modes must be considered. Although this is possible with a finite-element code, it is more practical to use simplified, yet surprisingly accurate, approximate radiation models to perform the multitude of calculations that are necessary. Nallasamy (Reference 57) recently reported modal sound radiation results for the geometry and test conditions of the NASA Lewis ANC fan facility using the Eversman finite-element code. The results have been very useful since they appear to validate the inlet group velocity vector angle preservation and also that the mode cut-off ratio alone determines the angular position of the farfield radiation principal lobe peak. These results were used to confirm the accuracy of the simplified model used for the broadband noise radiation method developed here.

The modal cut-off ratio radiation model has also been extended to fan aft noise radiation by Rice and Saule (Reference 58) for single- and multiple-mode radiation. The single-mode approximate radiation results agreed well with the results of Savkar (Reference 59) using the Wiener–Hopf method. The approximate broadband radiation directivity calculations agree with the shape of the experimental results.

For all of the approximate radiation calculations mentioned above, the agreements noted were in directivity shape only. The results were moved up or down as required to obtain the best superposition possible. For the models needed in this program, more than just shape agreement was necessary. Since broadband random noise acoustic power is to be calculated in the fan or core duct and the results are to be tested by observation of farfield acoustic power directivity, acoustic power must be conserved passing through the apertures and surrounding flow fields. The sound pressure level in the farfield for a mode or a group of modes characterized by mode cut-off ratio depends on acoustic power (watts) and the area (ft^2) subtended by the principal radiation lobe (approximately). The principal lobe width depends on sound frequency, and the area is also a function of radiation angle. Evaluation of this area is complicated for aft radiation because the propagation angle is a function of mode cut-off ratio and the angle change caused by refraction through the jet shear layers.

As part of this acoustic power conservation, a new termination transmission loss model was developed to assess the reflection loss at the inlet lip or nozzle exit. This improved termination loss model is a function of mode cut-off ratio and sound frequency and replaces previous models which included cut-off ratio only.

The theory detailed in the Addendum has been incorporated into three computer codes to calculate the farfield radiation directivity produced by a multimodal noise source. The three codes are specialized for noise propagation from the fan inlet, fan exhaust duct, and aft core duct. These codes are intended to be used with broadband noise source generation models that predict acoustic power as a function of mode cut-off ratio and frequency. The radiation codes then take the acoustic power past the particular aperture and into the farfield and include the new model developed to predict the termination transmission loss with flow at the bellmouth or nozzle termination.

The single-mode radiation theory has been fairly well validated for inlet noise radiation using both experimental data and numerical calculations. The multimodal radiation results should be a straightforward extension of this single-mode theory. Thus, the inlet multimodal radiation models should be quite adequate. Aft-radiation models have not been so well validated because experimental data for the radiation of internal noise through a jet shear layer are not so common. Some exist for plane-wave radiation through jets up to about 200-ft/s velocity. The refraction model for the plane wave has been modeled to agree with these limited data. The methods used to model the aft radiation have

had limited single-mode validation through comparisons to some analytical results using a Wiener–Hopf technique. Thus, the aft radiation models are believed to be reasonably accurate for initial use and can easily be modified if necessary.

4.5 Anisotropic Turbulence Model

The anisotropic turbulence model used in this study is the same as the one employed in Gliebe and Kerschen (Reference 48). It is based on homogeneous axisymmetric turbulence with direction 1 denoting the streamwise direction (assumed to be the axis of symmetry) and directions 2, 3 denoting directions transverse to the stream. Further "3" is used to denote the spanwise direction.

If $R_{ij}\ (\bar{r})$ denotes the velocity correlation between velocity components i and j between two points separated by $\bar{r}$, the spectrum function Φ_{ij} is defined as the spatial, three-dimensional Fourier transform of R_{ij} as:

$$\Phi_{ij}\ (\bar{k}) = \frac{1}{8\pi^3} \int_{-\infty}^{\infty} R_{ij}(\bar{r}) \exp[-i\bar{k} \cdot \bar{r}\ ]d\bar{r} \tag{125}$$

The two-dimensional spectrum function $\Phi_{ij}\ (k_1, k_2)$ is defined as the integral of $\Phi\ (\bar{k})$ over $-\infty < k_3 < \infty$. It can be easily shown that Φ_{ij} is the two-dimensional Fourier transform of $R_{ij}\ (\bar{r})$ where $\bar{r}$ lies entirely in the 1, 2 plane; that is, no spanwise separation between the points at which the correlation is defined. Specifically:

$$\phi_{ij} = \frac{1}{4\pi^2} \int_{-\infty}^{\infty} R_{ij}\ (x_1, x_2, 0) \exp[-i\ (k_1 x_1 + k_2 x_2)]\ dx_1 dx_2 \tag{126}$$

The same forms for $\phi_{ij}\ (k_1, k_2)$ as defined in Equation (16) of Gliebe and Kerschen (Reference 48) are used herein; namely, with streamwise and transverse fluctuations of u_a and u_t and corresponding length scales of ℓ_a and ℓ_t we have:

$$A_0^2 = 1 + k_1^2\, \ell_a^2 + k_2^2\, \ell_t^2 \tag{127}$$

then with $\mu = u_\tau / u_\alpha$ and $\lambda = \ell_a / \ell_t$ we have:

$$\phi_{11} = \ell_a \ell_t u_a^2 (3k_2^2\, \ell_t^2 + A_0^2) / (4\pi A_0^5) \tag{128}$$

$$\phi_{22} = \ell_a \ell_t u_a^2 (3k_1^2\, \ell_a^2 / \lambda^2 + A_0^2\, [2\mu^2 - 1/\lambda^2]) / (4\pi A_0^5) \tag{129}$$

$$\phi_{12} = 3\ell_t^2 u_a^2 (k_1 \ell_a)(k_2 \ell_t) / (4\pi A_0^5) \tag{130}$$

These spectra have the property that:

$$\int_0^{\infty} R_{11}\ (r, 0, 0,)\ dr = u_a^2\, \ell_a \qquad \text{and} \qquad \int_0^{\infty} R_{22}\ (0, r, 0,)\ dr = u_t^2\, \ell_t \tag{131}$$

so that ℓ_a and ℓ_t are the integral length scales of the turbulence in the axial and tangential directions.

The direct use of these relations, however, needs the measurement of the two-point correlations R_{22} $(0, r, 0)$. We can circumvent this by noting that:

$$\int_0^\infty R_{22}(r,0,0,)\,dr = \pi \int_{-\infty}^{\infty} \phi_{22}(0,k_2)\,dk_2 \tag{132}$$

Integration of Equation (132) requires only measurement of the single-point autocorrelation R_{22} (r, 0, 0) $u_t^2 \ell_{ta}$. With the present forms of assumed spectral function ϕ_{22}, we have:

$$\ell_{ta} / \ell_a = 1 - 1/(2\mu^2 \lambda^2) \tag{133}$$

By single-point measurements, we can thus establish u_a, u_t, and ℓ_a directly (also $\mu = u_t / u_a$) and ℓ_{ta}. By the above relation, we can calculate λ and hence completely determine the four needed parameters u_a, u_t, ℓ_t, and ℓ_a for the assumed anisotropic turbulence spectrum solely by single point measurements.

Gliebe and Kerschen noted (Reference 48) that nonnegativity of ϕ_{22} requires that $\lambda^2 \geq 1 / (2\mu^2)$. Since we do not measure λ directly, the above requirement translates to:

$$0 < (\ell_{ta} / \ell_a) < 1 \tag{134}$$

This requirement seems to be easily met in all the single-point measurements of ℓ_{ta} and ℓ_a that we have examined.

4.6 Fan Broadband Self-Noise Prediction Model

4.6.1 Introduction

Recent studies and assessments of the modeling of aircraft engine fan broadband source noise have identified several key mechanisms thought to be important contributors to the total fan broadband noise spectrum. The currently favored physical mechanisms include the following:

1. Inlet end-wall boundary layer turbulence interaction with the rotor tip (ITRI)
2. Rotor wake turbulence interaction with the downstream stators (RWSI)
3. Rotor tip end-wall turbulence interaction with the downstream stators (RTSI)
4. Rotor hub end-wall turbulence interaction with the downstream stators (RHSI)
5. Rotor blade surface boundary layer and trailing-edge noise (RSN)
6. Stator vane surface boundary layer and trailing-edge noise (SSN)

Mechanisms 1 through 4 are thought to be the major contributors, but the self-noise mechanisms 5 and 6 could be setting a "floor" for the total fan broadband noise spectrum and thus may limit the noise benefit achievable through developing technologies for reducing mechanisms 1 through 4.

It is important, if possible, to quantify the self-noise mechanisms for fan broadband noise generation to the same degree of sophistication, detail, and complexity as the turbulence interaction mechanisms (1–4). This would allow more accurate assessment of the benefits of reducing the various interaction mechanisms and provide insight into the proximity of the "self-noise floor." A physics-based understanding of self-noise generation may also provide insight on how to reduce it and therefore increase the fan broadband noise reduction potential. The physical modeling of rotor and stator self-noise is the subject of this study.

4.6.2 Objectives and Approach

The objective of the work reported herein was to develop a quantitative prediction method for fan rotor and stator self-noise that is theoretically consistent with the turbulence/blade-row interaction models currently being developed, such as those in References 11, 12, 47, 60, and 61. By "theoretically consistent" we mean that the modeling assumptions and formulation approach are about the same and/or to the same level of approximation.

The approach taken was to build upon the fan rotor self-noise formulations suggested by Sharl and (Reference 62) and expanded upon by Mugridge and Morfey (References 17 and 63). The model proposed by Mugridge and Morfey is based on the physical mechanism of airfoil-surface boundary layer pressure fluctuations producing noise, especially at the airfoil trailing edge, where the upper and lower surface boundary layers meet and form an airfoil wake. It is suggested in (Reference 17) that strong correlation occurs at the trailing edge between the upper and lower surface pressure fluctuations resulting in a trailing-edge unsteady loading or force fluctuation related to the boundary layer turbulent pressure spectra near the trailing edge. A similar approach was proposed by Brooks and Marcolini (Reference 64) for airfoils to quantify the noise produced by aircraft wings.

The Mugridge and Morfey formulation, however, contains many simplifying assumptions and approximations for the purpose of arriving at a scaling law or parameter-dependence relationship. Although the resulting formulation gives guidance on the sensitivity of fan rotor self-noise to various operating and geometric parameters such as tip speed, flow coefficient, blade chord, etc., it is still a relatively crude formulation compared to the formulations available and being developed for turbulence/blade-row interaction (TBRI). For example, the Mugridge–Morfey model uses an empirical spectrum shape function that is only dependent on fan parameters in the sense of scaling of the peak frequency — the shape itself is invariant. There is no connection between the airfoil or rotor blade surface pressure turbulent spectrum characteristics and the result acoustic spectrum. Secondly, the model does not contain the effects of duct acoustics; for example, no accounting for propagating and nonpropagating wavenumber energy is included.

The approach taken herein is to review and critique the Mugridge–Morfey formulation in detail, to identify each simplifying assumption in the formulation, and to extend or improve the model formulation as required to achieve consistency with the TBRI formulations where possible. As part of this process, it is instructive to take a typical TBRI model problem — say, for example, inlet turbulence/rotor interaction — and compare the equivalent Mugridge–Morfey modeling approach with the more exact approaches documented in References 11, 12, 47, 60, and 61, to draw out the parallels between the self-noise and TBRI noise models. This, as we shall see, sheds some light on the necessary improvements required in the Mugridge–Morfey approach to achieve compatibility with the favored TBRI models.

4.6.3 The Mugridge–Morfey Model for Rotor Self-noise

Using the compact, dipole, unsteady force acoustic modeling approach developed by Sharl and (Reference 62), Mugridge (Reference 17) begins with the following expression for the radiated acoustic power from an airfoil with an unsteady, random, spanwise loading:

$$W = \frac{1}{12\pi\rho c^3}\left\langle \frac{dL}{dt} \right\rangle h\ell_s \tag{135}$$

where W = acoustic power

ϱ = flow ambient density

c = flow ambient speed of sound
L = unsteady lift on the airfoil (force per unit span)
t = time
h = airfoil span
ℓ_s = spanwise unsteady lift correlation length

The correlation length ℓ_s is assumed to be much smaller than the span, $\ell_s \ll$ h. The spectral density equivalent of Equation (135) is given by the following:

$$\frac{dW}{d\omega} = \frac{1}{12\pi\rho c^3}\left[\omega^2 G_L(\omega) \cdot h\ell_s(\omega)\right] \tag{136}$$

where G_L = airfoil-surface unsteady loading spectrum.

The total power radiated from the airfoil is the sum of the radiation from (h/ℓ_s) uncorrelated regions, each with spanwise extent ℓ_s. Source compactness requires $\ell_s \ll \lambda$ and that the half-chord of the airfoil $b \ll \lambda$, where λ is the acoustic wavelength of the sound.

Mugridge (Reference 17) next makes the assumption that most of the acoustic energy at a given observed frequency is concentrated in a narrow band of acoustic wavenumbers k_x, given by:

$$k_x = \omega/U_c \tag{137}$$

where U_c is the turbulent eddy convection speed over the airfoil surface, typically somewhat less than the flow speed U. The wavenumber bandwidth is assumed to be approximately 1/3-octave.

Next, the unsteady pressure on the airfoil surface is assumed to have the form:

$$p = P(y) \cdot \exp[i(\omega t - k_x x)] \tag{138}$$

Equation (138) is a "convected wave" form. The function $P(y)$ represents the spanwise loading distribution, assumed to be independent of the chordwise distance x. By integrating Equation (138) over the chord length from $x = -b$ to $x = +b$, an expression for the unsteady lift function $L(y,t)$ can be obtained, as follows:

$$L(y,t) = \int_{-b}^{+b} p(x,y,t)\,dx = P(y) \cdot e^{i\omega t} \int_{-b}^{+b} e^{-ik_x x}\,dx \qquad \text{or}$$

$$L(y,t) = P(y) \cdot e^{i\omega t} \int_{-b}^{+b} \left[\cos(k_x X) - i \cdot \sin(k_x x)\right] dx = b \cdot P(y)\left[\frac{2\sin(k_x b)}{k_x b}\right] e^{i\omega t} \tag{139}$$

Thus the unsteady loading $L(y, t)$ is just a factor $[\sin(k_x b)] / (k_x b)$ times the unsteady pressure field on the airfoil surface. The mean-square spectrum of $L(y, t)$ is therefore expected to be proportional to the unsteady pressure spectrum $G_p(\omega)$, with a factor equal to the average of the square of the above factor over the wavenumber band. This factor is defined as $F(k_x b)$, as follows:

$$F(k_x b) = \frac{1}{\Delta k_x} \int_{k_{xl}}^{k_{xu}} \left[\frac{\sin(k_x b)}{(k_x b)}\right] dk_x \tag{140}$$

where the upper and lower limits of integration k_{xu} and k_{xl} correspond to the upper and lower frequency limits of the 1/3-octave band around the center frequency k_x and Δk_x is the bandwidth $(k_{xu} - k_{xl})$.

Mugridge gives the final result of this integration and factorization as follows:

$$G_L(\omega) = (2b)^2 F(k_x b) \cdot G_p(\omega) = \frac{(2b^2)}{2(k_x b)^2} G_p(\omega) = 2\left(\frac{U_c}{\omega}\right)^2 G_p(\omega) \tag{141}$$

This expression (141) is obviously an approximation for the integral in (140) and therefore should be examined for the possibility of developing a more exact expression.

Mugridge (Reference 17) then employs an empirical expression for the boundary layer surface pressure fluctuation spectrum $Gp(\omega)$, as follows:

$$G_p(\omega) \cong 10^{-3} \rho^2 \delta^* U^3 \tag{142}$$

where δ^* is the airfoil trailing-edge displacement thickness, and this expression is valid over the frequency range: $0.02 \leq \omega\delta^*/U \leq 0.6$.

Combining the results of Equations (140), (141), and (142) into Equation (136), the following expression for acoustic power is obtained:

$$\frac{dW}{d\omega} = \frac{1}{12\pi\rho c^3}\left[\omega^2 \cdot 2(U_c/\omega)^2 \cdot 10^{-3} \rho^2 \delta^* U^3 h \ell_s(\omega)\right] \tag{143}$$

Mugridge then argues that the factor of 2 in Equation (141) should be dropped, since blade chord does not appear in (141), suggesting that the net loading is an edge effect produced by termination of the net loading at the leading and trailing edges. Since the boundary layer is negligible at the leading edge, and since we are evaluating boundary layer nonuniformity and unsteady effects, the leading-edge contribution should be negligible. Hence, Mugridge drops the factor of 2 in Equations (141) and (143), taking only half of the integral given by Equation (140).

Mugridge goes on to suggest that, for typical unseparated boundary layers,

$$U_c \cong 0.8U \qquad \text{and} \qquad \ell_s \cong 2U/\omega \tag{144}$$

Upon dropping the factor of 2 and incorporating the approximations given by Equation (144), the following expression for the sound power spectrum is obtained:

$$\omega \frac{dW}{d\omega} \cong \frac{10^{-4}}{3}\left[\frac{\rho h \delta^* U^6}{c^3}\right] \tag{145}$$

Note that the constant $10^{-4}/3$ comes from combining all the constants in Equations (143) and (144) as follows:

$$\frac{2 \cdot (0.8)^2}{12 \cdot \pi} \cdot 10^{-3} \cong \frac{2 \cdot (4/5)^2}{2 \cdot 6 \cdot 3.2} \cdot 10^{-3} \cong \frac{16 \cdot 10^{-3}}{25 \cdot 6 \cdot (32/10)} \cong \frac{10^{-3}}{150 \cdot (2/10)} \cong \frac{10^{-4}}{3} \tag{146}$$

Mugridge then states that, for a fan rotor with B blades, with chord $2b$, the displacement thickness at the rotor blade trailing edges may be approximated by (for both upper and lower surfaces) the following expression:

$$\delta^* \cong 2\Theta \cong 2 \cdot C_d b \tag{147}$$

Then, defining the inlet relative Mach number as $M_{rel} = U/c$, Equation (145) can be rewritten in terms of Equation (147) as follows:

$$\omega \frac{dW}{d\omega} \approx \frac{10^{-4}}{3} \rho \cdot c^3 B \cdot A_b M_{rel}^6 C_d \tag{148}$$

Equation (147) comes from assuming that the boundary layer form factor $H = \delta^*/\Theta = 2.0$ at the trailing edge and then using the relationship between momentum thickness and drag coefficient that $C_d = \Theta/b$. In Equation (148), the additional parameters introduced have the following definitions:

A_b = $2bh$ = blade planform area
C_d = airfoil drag coefficient
Θ = wake trailing-edge momentum thickness

Note that Equation (148), although it is a 1/3-octave band acoustic power level, has no direct dependence on frequency. This is primarily because of the simplifying assumptions made during the course of the formulation. It shows a definite dependence on airfoil relative Mach number, planform area, and drag coefficient, but the spectral shape is lost in the approximations. Mugridge did, however, provide an empirical procedure based on analysis of experimental information, for the spectral shape, based on the reference or peak frequency (also empirically derived). The spectral shape prediction procedure is computed from the reference frequency f_0, given by the following:

$$f_0 = \frac{U}{20 \cdot (2b) \cdot C_d} \tag{149}$$

For the frequency range $f_0 < f < 2f_0$, the sound power is given by Equation (148) but multiplied by the 1/3-octave band ratio $\Delta f/f = 0.231556$. The constant in Equation (148) then becomes $7.718 \times 10^{-6} \cong 8 \times 10^{-6}$. For frequencies in the range $2f_0 < f < 4f_0$, Mugridge suggests that the spectrum falls off at the rate of 3 dB per octave. For frequencies in the range $f > 4f_0$, the fall-off rate is 8 dB per octave. Finally, for frequencies in the range $f < f_0$, the fall-off rate is 3 dB per octave.

Mugridge further proposes a correction for tip-clearance effects which simply adds a correction to the drag coefficient to account for the additional drag due to tip-clearance secondary flows. This correction is given by the following:

$$\Delta C_d = \frac{9}{4}\left(\frac{\sigma^2}{1+q}\right) \cdot C_L^{3/2}\left(\frac{U_{rel}}{U_{tip}}\right)^3 \cdot \frac{\delta'}{\varphi^2} \tag{150}$$

where q = Hub-to-tip ratio
δ' = Tip clearance/span ratio
φ = U_{ax}/U_{rel}
σ = Rotor tip solidity (chord/spacing)

Equations (148) and (149) can then be used to predict the broadband noise of a fan rotor caused by the airfoil boundary layer turbulence or self-noise.

The above prediction method was programmed into a Microsoft EXCEL spreadsheet for the purpose of exploring and understanding the model and identifying limitations. The prediction method can also be applied to stators, with the replacement of the relative Mach number into the rotor by the

absolute Mach number into the stator. Then the relative contributions of rotors versus stators to the total fan broadband self-noise can, at least on a preliminary basis, be evaluated.

4.6.4 The Mugridge–Morfey Model for Rotor Incident Turbulence Noise

For incident turbulence interacting with a rotor, the sound power spectrum for a fan rotor with B blades is also represented by Equation (136), as follows:

$$\frac{dW}{d\omega} = \frac{B}{12\pi\rho c^3}\left[\omega^2 G_L(\omega) \cdot h\ell_s(\omega)\right] \tag{151}$$

Mugridge gives the following expression for $G_L(\omega)$ in the case of turbulence interacting with a rotor:

$$G_L(\omega) = (2\pi\rho bU)^2 K_L G_{vv}(\omega) \tag{152}$$

where $G_L(\omega)$ is the unsteady blade lift spectrum, K_L is a lift response function, and $G_{vv}(\omega)$ is a turbulence spectrum function. The Lift response function K_L, analogous to the square of the "Sears Function," is given by Mugridge as follows:

$$K_L = \frac{1}{(1 + 2\pi k_1)}\left[1 - \frac{1}{2H_L}(1 - e^{-2H_L})\right] \tag{153}$$

where $$H_L = \frac{h}{2b}\left[k_1^2 + \frac{2}{\pi^2}\right]^{1/2} \qquad \text{for } k_1 > 2 \tag{154}$$

Here, $k_1 = \omega b/U$, and H_L is a spanwise correlation factor that takes into account the lack of spanwise coherence when the blade encounters a three-dimensional gust such as produced by incident turbulence. The factor $1/(1 + 2\pi k_1)$ is the square of the two-dimensional, incompressible, flat-plate, isolated airfoil Sears function approximation. In principle, this factor can be replaced by the compressible, two-dimensional response functions of Osborne (low-frequency) and Amiet (high-frequency). Note that Mugridge has a qualifier that the validity of Equation (154) is restricted to "high" frequencies, that is, $k_1 > 2$.

Substituting Equation (152) into (151) and rearranging terms, the following expression for incident turbulence noise is obtained:

$$\frac{dW}{d\omega} = \frac{\pi}{6}(B \cdot A_b) \cdot k_1^2 \cdot (\ell_s/b)(\rho c) \cdot M_{rel}^4 \cdot K_L \cdot G_{vv}(\omega) \tag{155}$$

The turbulence spectrum function $G_{vv}(\omega)$ was not defined in References 60 and 17, but we can derive it as a limiting form of the turbulence spectrum functions in Mani's theory, Reference 11.

The isotropic turbulence spectrum given by Mani (Reference 11) for isotropic turbulence is as follows for a rotor consisting of flat-plate blades aligned with the flow, having an in-flow axial Mach number M_a, a transverse (rotational) Mach number M_t, and a flow angle (equal to the stagger angle of the blade row) given by $\alpha_r = \tan^{-1}(M_t/M_a)$:

$$G_{vv}(k_x, k_y) = \tag{156}$$

$$\left[\frac{u'^2\lambda_f^2}{4\pi}\right]\left[\frac{(1 + 3\cos^2\alpha_r)k_x^2\lambda_f^2 + 1}{(1 + k_x^2\lambda_f^2 + k_y^2\lambda_f^2)^{5/2}} + \frac{6(\sin\alpha_r\cos\alpha_r)k_x\lambda_f k_y\lambda_f}{(1 + k_x^2\lambda_f^2 + k_y^2\lambda_f^2)^{5/2}} + \frac{(1 + 3\sin^2\alpha_r)k_y^2\lambda_f^2 + 1}{(1 + k_x^2\lambda_f^2 + k_y^2\lambda_f^2)^{5/2}}\right]$$

where λ_f is the longitudinal ($u'u'$) correlation integral length scale, k_x is the unnormalized wavenumber in the x direction, and k_y is the wavenumber in the cascade rotational speed direction y, as shown in the sketch of Figure 97. Equation (156) is integrated over all tangential wavenumbers k_y to obtain the total turbulence spectral energy impinging on the cascade. Mani (Reference 11) shows that this integration should be done over the range of k_y values that yield propagating (nondecaying) pressure waves, corresponding to the cut-off limits for the cascade/duct system at each turbulence gust frequency. Equation (156) already contains an integral over spanwise (z direction) wavenumber space, and it assumes that the spanwise turbulence correlation length scale is also equal to λ_f.

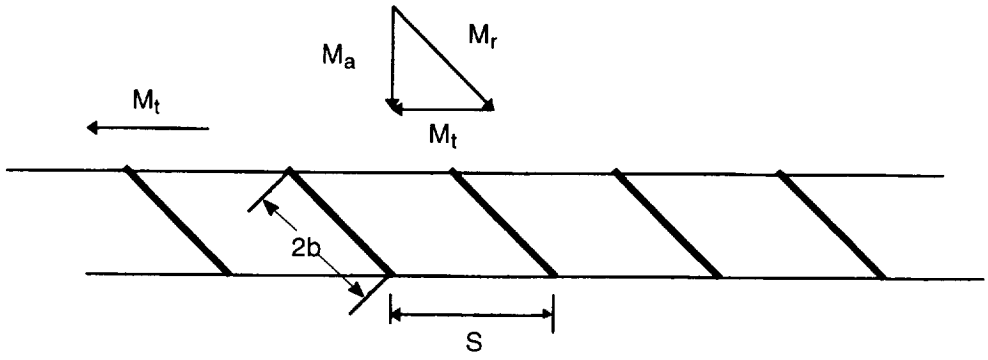

Figure 97. Flat-Plate Cascade Rotor Geometry and Aerodynamic Vector Diagram

For an isolated airfoil, as assumed by Mugridge (Reference 17), Equation (156) is simplified because we can set $\alpha_r = 0$ and let the integration be carried out over all values of k_y, since there is no cascade/duct cut-off effect. The resulting single-airfoil approximation is then given by:

$$G_{vv}(k_x) = \left[\frac{u'^2\lambda_f}{2\pi}\right]\frac{1 + 3k_x^2\lambda_f^2}{(1 + k_x^2\lambda_f^2)^2} \tag{157}$$

In this approximation, $k_I = k_x$ and Equation (157), in combination with Equation (155), can be used to predict blade-row turbulence interaction noise power spectra, consistent with the self-noise formulation given by Equations (148) through (150). This allows us to assess the relative contributions of the two mechanisms for typical fan configurations and thus estimate the importance of addressing self-noise as a floor to further broadband noise reduction. A Microsoft EXCEL spreadsheet model for Equations (155) and (157) was developed for the purpose of evaluating each of the mechanisms, and this model was used to carry out the mechanisms contribution analysis described in the next section. The above formulations neglect spanwise variations in flow and geometric parameters, which is not too bad an assumption for the end-wall-related mechanisms. For the rotor-wake/stator mechanism, however, a spanwise strip integration can be carried out, taking into account the (approximate) spanwise variations in flow Mach number, flow angle, and geometry.

4.6.5 Sample Estimates of Self-Noise Contributions to Fan Broadband Noise

The self-noise and blade-row interaction formulas given by Equations (148) through (157) were used to estimate the relative contributions of key mechanisms 1–6 (listed on page 95) for a typical

fan stage for a high-bypass engine. Relevant fan stage geometry and operating conditions are listed in Table 9.

Table 9. Sample Case Fan Operating Conditions for Mechanisms Contribution Assessment

Fan Diameter = 22.0 inches, Blade Number = 22, Vane Number = 54			
Condition	**Approach**	**Cutback**	**Takeoff**
Axial Mach Number M_a	0.2846	0.4310	0.5539
Tip Mach Number M_t	0.6311	0.8608	1.0301
Blade Passing Frequency *BPF*	2750	3750	4490
Tip Lift Coefficient C_L	0.3164	0.3579	0.3948

Estimates were made of rotor-in-flow/turbulence interaction, rotor-wake/stator interaction, rotor self-noise, and stator self-noise. Fan broadband noise characteristics were computed using Equations (148) through (157) at conditions corresponding to typical approach, cutback, and full-power takeoff. For rotor-wake/stator interaction noise, a spanwise integration was carried out, using a 20-stream-tube or strip subdivision of the annulus. The annulus axial Mach number was assumed to be constant, as was the rotor total pressure rise. A simplified spanwise variation in stator vector diagrams was computed based on these assumptions. Figure 98 shows the self-noise spectra for both rotor and stator at each of these conditions. Figure 99 shows the interaction noise spectra for each of the rotor and stator interaction noise mechanisms, again at all three conditions.

Also shown in Figures 98 and 99 are measured acoustic power spectra. It is observed in Figure 98 that the Mugridge self-noise model considerably overpredicts the measured data. It also predicts that rotor self-noise is considerably greater (over 20 dB) than stator self-noise. Further, it can be seen that the predicted interaction noise total power spectra (Figure 99) are in fairly good agreement with the measurements, with some overprediction in the middle frequency range at the two lower tip speeds. It is to be expected that the Mugridge–Morfey model would overpredict measured data because it does not take into account duct cut-off effects. The results shown in Figure 99 also indicate that the high-frequency range is consistently underpredicted.

Figures 98 and 99 indicate several interesting trends, keeping in mind that the results are for a simplistic, isolated-airfoil, approximation model:

- Rotor self-noise has the highest peak levels.
- Stator self-noise has the lowest levels.
- Rotor-wake/stator interaction has the highest levels at high frequencies.
- End-wall boundary layer turbulence/rotor interaction has high levels compared to rotor-wake/stator interaction, but the latter is still higher.
- Rotor self-noise peaks at lower frequencies than stator self-noise and is, on the average, about 20 dB higher than stator self-noise.
- The peak self-noise levels shown in Figure 98 are predicted to be substantially higher than either the measured data or the total interaction noise peak spectra shown in Figure 99.

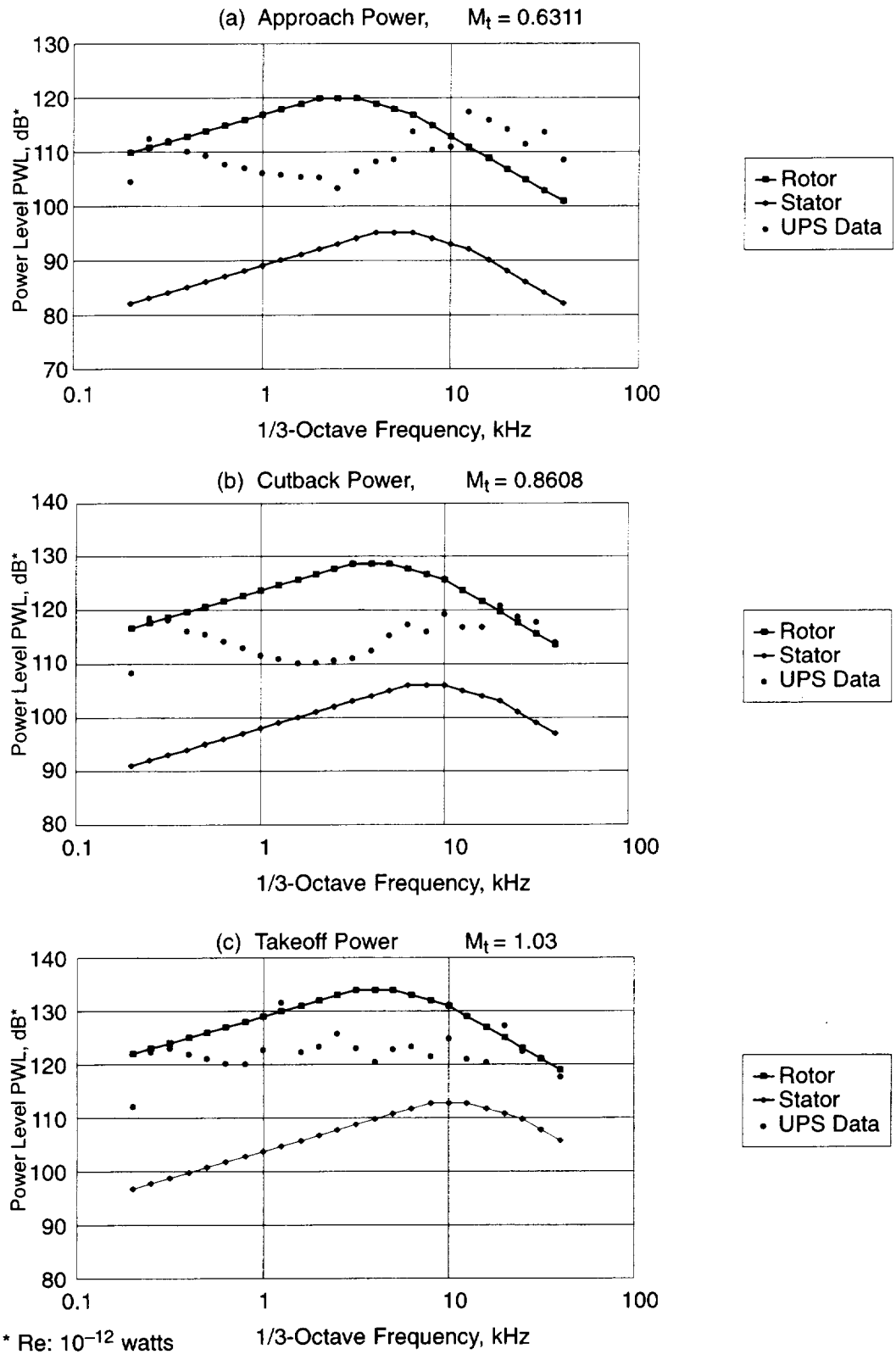

Figure 98. Predicted Self-Noise Components Using Mugridge Model for UPS Fan Stage

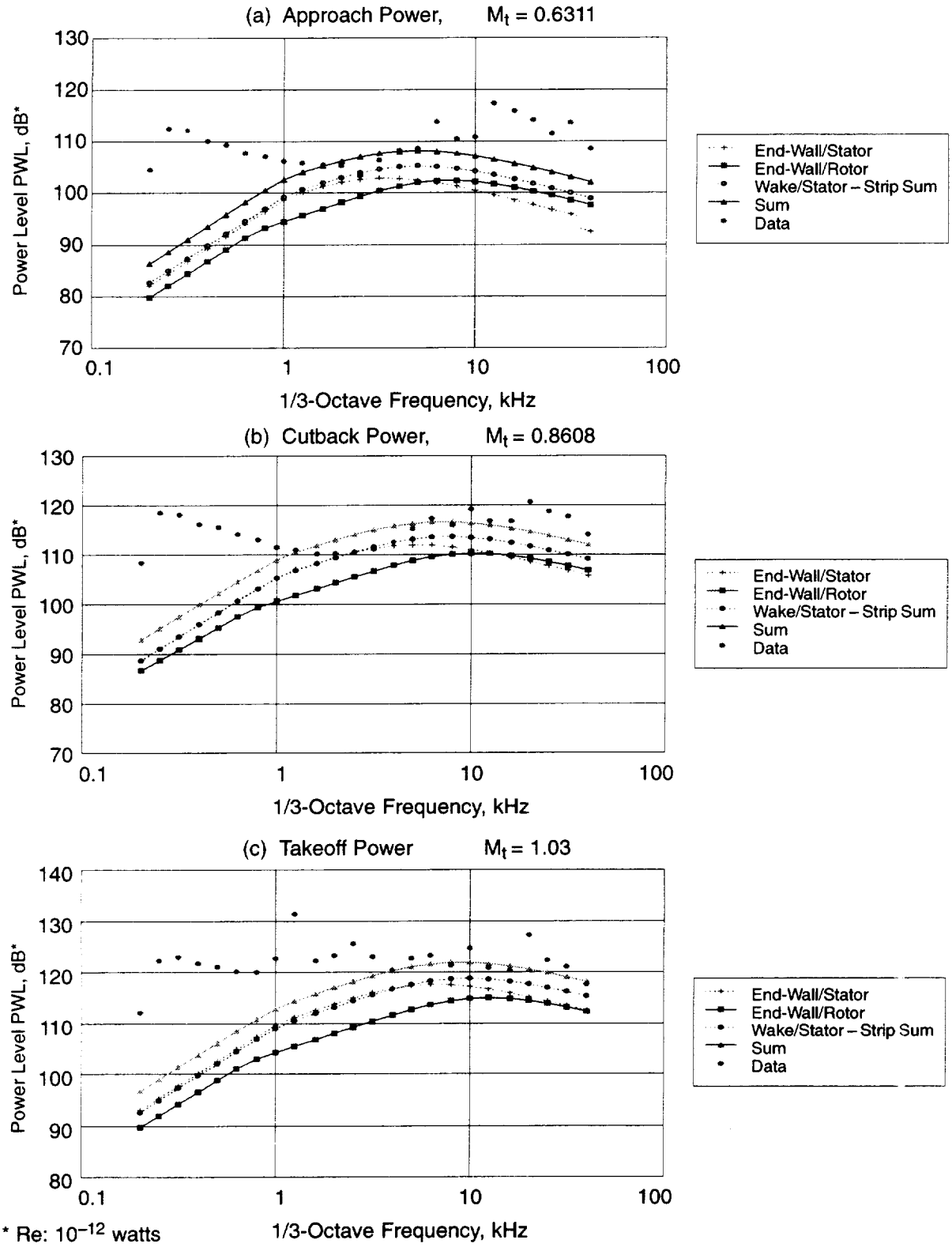

Figure 99. Sample Case Fan Turbulence/Blade-Row Interaction Estimates: Mugridge–Morfey Method

Keeping in mind the simplistic formulation methodology, these examples nevertheless imply that at least rotor self-noise may be a significant contributor to fan broadband noise and that rotor-wake/stator interaction is at least as important as inflow boundary layer turbulence-rotor interaction as a significant blade row interaction mechanism. In the following subsections, the simplifying assumptions of the Mugridge–Morfey self-noise model formulation are examined and, where possible, eliminated via improvements or less stringent assumptions. Further, extensions to include cascade effects and to include spectral shape analytically rather than empirically are also developed.

4.6.6 Self-noise Model Improvements

4.6.6.1 Chordwise Loading Model Improvements:

The chordwise loading formulations described above and expressed in Equations (138) through (141) can be improved and some of the assumptions relaxed. First, the derivation of Equation (141) from (140) is useful to recover because it will clarify an important simplifying assumption inherent in Mugridge's formulation. The integration in Equation (140) was carried out numerically over a one-third octave interval centered about a given normalized wavenumber $k_x b$, for a range of $k_x b$ corresponding to 0.01 to 100. Results of the computations are shown in Figure 100. Low wavenumber and high wavenumber asymptotes can be discerned with oscillatory behavior in midrange wavenumbers. The results are shown in Figure 100 as $10 \log_{10} [I(k_x b)]$, where $I(k_x b)$ is defined by the relation:

$$F(k_c b) = \frac{1}{\Delta(k_x b)} \int_{x_l}^{x_u} \left[\frac{\sin(x)}{x}\right]^2 dx = \frac{1}{\Delta(k_x b)} I(k_x b) \tag{158}$$

The upper and lower limits of integration for $F(k_x b)$ are defined by Equation (140) and correspond to 1/3-octave band limits about the center value $k_x b$.

The low-wavenumber asymptote, from a linear curve fit of the numerical results shown in Figure 100 over the range $0.001 \leq k_x b \leq \times 0.1$ is as follows:

$$10 \log_{10}[I(k_x b)] = -6.3840 + 0.99958[10 \log_{10}(k_x b)] \tag{159}$$

The high-wavenumber asymptote, again from a linear regression curve fit of the numerical results shown in Figure 100 over the range $10 \leq \times k_x b \leq \times 1000$, is as follows:

$$10 \log_{10}[I(k_x b)] = -9.8104 + 0.97909[10 \log_{10}(k_x b)] \tag{160}$$

It can also be shown, through taking the limits of Equation (140) as $k_x b \rightarrow 0$, that the low wavenumber asymptote is analytically given by:

$$10 \log_{10}[I(k_x b)] = -6.3534 + 1.0[10 \log_{10}(k_x b)] \tag{161}$$

Similarly, through taking the limits of Equation (140) as $k_x b \rightarrow \infty$, the high-wavenumber asymptote is analytically given by:

$$10 \log_{10}[I(k_x b)] = -9.3634 + 1.0[10 \log_{10}(k_x b)] \tag{162}$$

In order to obtain Equation (162), it was assumed that, for high wavenumbers, many "cycles" of the factor sin (x) in the integrand of Equation (158) occur over the integration interval $\Delta k_x b = a k_x b$ and

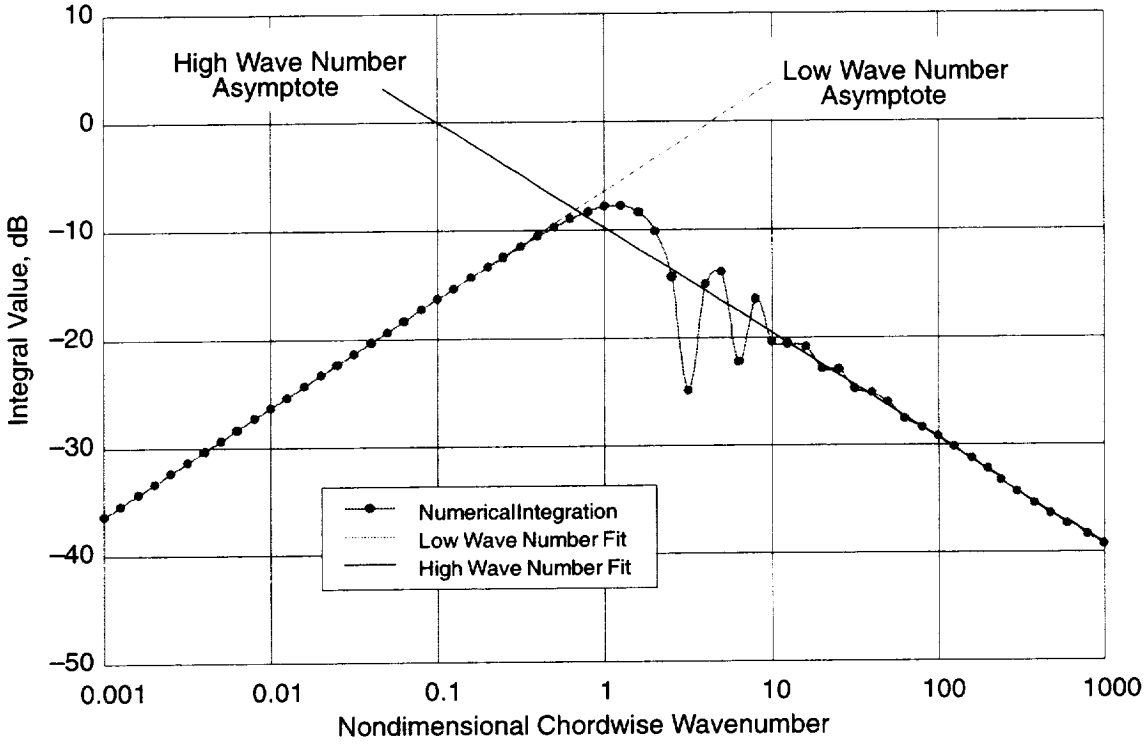

Figure 100. Chordwise Loading Integral Versus Chordwise Wavenumber: Rectangular Loading Distribution

that the integrand can therefore be approximated by the average value of $\sin^2(x)$ over one cycle, times the number of cycles. The number of cycles is approximately given by $N_C \cong \alpha(k_x b) / 2\pi$, and the denominator of the integrand is approximated by its value at the center of the interval.

The first constant in Equation (161) is analytically given by $10 \log_{10}(\alpha)$, where $\alpha = 0.231556$, the 1/3-octave bandwidth coefficient. Similarly, the first constant in Equation (162) is given by $10 \log_{10}(0.5\alpha)$. It can be seen that the numerical results, Equations (160) and (161), are in substantial agreement with the analytically derived asymptotic limits, Equations (161) and (162). Substituting Equations (161) and (162) into Equation (141), the asymptotic limiting forms for the corresponding unsteady lift spectrum $G_L(\omega)$ become as follows.

For low wavenumbers, $k_x b \to 0$:

$$I(k_x b) = \alpha(k_x b) \qquad F(k_x b) = 1 \qquad G_L(\omega) = (2b)^2 G_p(\omega) \tag{163}$$

For high wavenumbers, $k_x b \to \infty$:

$$I(k_x b) = \frac{0.5\alpha}{k_x b} \qquad F(k_x b) = \frac{0.5}{(k_x b)^2} \qquad G_L(\omega) = \frac{(2b)^2}{2(k_x b)^2} G_p(\omega) \tag{164}$$

Thus it can be seen, comparing with Equation (141), that the Mugridge formulation is an asymptotic high-wavenumber approximation and the approximation can be removed by using the numerical integration of Equation (140). Alternatively, the asymptotic approximations of Equations (163) and (164) can be used in each of the respective ranges of $k_x b$. In fact, the asymptotic regression fits shown in Figure 100 give a reasonable approximation, even in the midrange of $k_x b$ values.

In Figure 100 the oscillatory behavior in the midrange of wavenumbers around $k_x b \cong 1$ is attributable to the singularities associated with sin $(x) = 0$, which occur when $k_x b$ is an integer multiple of π. Thus the first "dip" in Figure 100 occurs at $k_x b = \pi$, the second at 2π, etc. until the bandwidth substantially exceeds π. The bandwidth exceeds π when $\alpha k_x b > \pi$ or when $k_x b > (\pi/\alpha) = 13.567$. It can be observed in Figure 100 that indeed the first two "dips" occur at $k_x b \cong 3.14 = \pi$ and at $k_x b \cong 6.3 = 2\pi$ and that the "waviness" of the curve diminishes above $k_x b \cong 40$, which is equivalent to about 1.5 "cycles" per bandwidth.

One insight gained in examining limiting forms and comparing with numerical integration results was identification of the particular approximations made by Mugridge in the original formulation for self-noise. Hence, the assumptions could be relaxed to provide a more general formulation not restricted to high wavenumbers.

An additional assumption made by Mugridge is that of a uniform or "rectangular" chordwise loading distribution, as indicated by Equation (138). Suppose, however, we assume a nonuniform, linear loading distribution of the form:

$$p(x, y, t) = P(y, t) \cdot Q(x) \cdot e^{i\omega t} \tag{165}$$

where $Q(x) = A \cdot (x + b) \cdot e^{ik_x x}$.

Thus $p(-b, y, t) = 0$, and $p(+b, y, t)$ is the trailing-edge loading. We can define the function $P(y, t)$ as the trailing-edge loading or unsteady pressure difference so that, from Equation (165), the constant $A = 1 / (2b)$. We thus have a linear variation in unsteady pressure loading which is zero at the leading edge and increases linearly to the trailing edge value $P(y, t)$. This intuitively seems a more realistic model for unsteady loading chordwise behavior associated with self-noise which, as was put forth by Mugridge, comes from the pressure fluctuations in the airfoil surface boundary layer. It can be speculated that these pressure fluctuations are negligible at and near the leading edge, where the boundary layer is thin and possibly laminar, and grows in some fashion to a more or less maximum value at the trailing edge where the boundary layers then merge into the downstream wake. We can now invoke the same process as was done for the uniform loading assumption, including looking at the limiting forms for small and large wavenumbers, and establish a more realistic formulation for the unsteady lift spectrum function.

Following the same process used to derive Equation (139), the unsteady lift on an airfoil due to unsteady differential surface pressure fluctuations of the form given by Equation (165) can be written as follows:

$$L(y, t) = P(y) \cdot (i\omega t) \cdot f(k_x b) \tag{166}$$

where

$$f(k_x b) = f_1(k_x b) + f_2(k_x b) \tag{167}$$

$$f_1(k_x b) = \frac{1}{2b} \int_{-b}^{b} x \cdot \exp(-ik_x x)\, dx \tag{168}$$

and

$$f_2(k_x b) = \frac{1}{2b} \int_{-b}^{b} b \cdot \exp(-ik_x x)\, dx \tag{169}$$

Thus $f_2(k_x b)$ is just half the uniform-loading integral. The term $f_1(k_x b)$ represents a first-order correction to the uniform-loading case, as will be discussed later in the derivation. The integral for $f_2(k_x b)$ can be written down from Equation (139) as follows:

$$f_2(k_x b) = \frac{1}{2}\left[2b\frac{\sin(k_x b)}{(k_x b)}\right] \tag{170}$$

This is to be compared with Equation (139), which has the same form but without the factor of 1/2. Carrying out the integration of Equation (168), we obtain the following:

$$f_1(k_x b) = -ib\left[\frac{\sin(k_x b)}{(k_x b)^2} - \frac{\cos(k_x b)}{(k_x b)}\right] \tag{171}$$

The mean-square unsteady lift spectrum, as discussed in the derivation of Equations (140) and (141), is proportional to the square of $f(k_x b)$ averaged over the proportional 1/3-octave bandwidth whose midpoint is defined by $k_x b$. From Equations (166) through (170), it can be shown that the mean-square unsteady lift spectrum is given by the following, where the square of $f(k_x b)$ is obtained by multiplying by its complex conjugate:

$$G_L(\omega) = (2b)^2 \cdot F(k_x b) \cdot G_p(\omega) = [f(k_x b)]^2_{Avg} \cdot G_p(\omega) \tag{172}$$

where $[f(k_x b)]^2 =$

$$b^2\left\{\left[\frac{\sin(k_x b)}{(k_x b)}\right]^2\left[\frac{\sin(k_x b)}{(k_x b)^2}\right]^2 - 2\cdot\left[\frac{\sin(k_x b)\cdot\cos(k_x b)}{(k_x b)^3}\right] + \left[\frac{\sin(k_x b)}{(k_x b)}\right]^2\right\} \tag{173}$$

It can be seen that for the linear or "triangular" loading distribution, Equations (172) and (173) yield an unsteady lift spectrum similar to that for the uniform or "rectangular" loading distribution given by Equation (140) but with additional terms. Recall that, in the discussion following Equation (143), Mugridge argues that his formulation for uniform loading distribution should be reduced by a factor of ½ to account for the presumption that the model should have no leading-edge contribution, only a contribution from the trailing edge; therefore, he somewhat arbitrarily took only half of the formulated value. In the above linear loading model, the leading term in Equation (173) is just the uniform loading distribution term but smaller by a constant factor of ¼. With the linear loading assumption, there is no need to invoke an arbitrary division by a factor of 2 to "eliminate" the leading-edge contribution to the formulation. Equation (173), however, has to be integrated (or averaged) over the bandwidth $\alpha(k_x b)$, as suggested by Equation (172).

The integrations for Equation (173) were carried out numerically, and the results expressed in terms of the function $I(k_x b)$, as was done for the uniform-loading model. Further, limiting forms for the function $I(k_x b)$ were derived for the extreme cases of $k_x b \to 0$ and $k_x b \to \infty$. The numerical results are shown in Figure 101. Additionally, linear regression fits of the numerical results were carried out, and the resulting limiting forms for low and high wavenumber were developed. These agreed with the analytic limiting forms, as seen by the Equations and accompanying discussion in the following paragraphs.

The low-wavenumber asymptote, from a linear curve fit of the numerical results shown in Figure 100 over the range $0.001 \leq k_x b \leq 0.1$, is as follows:

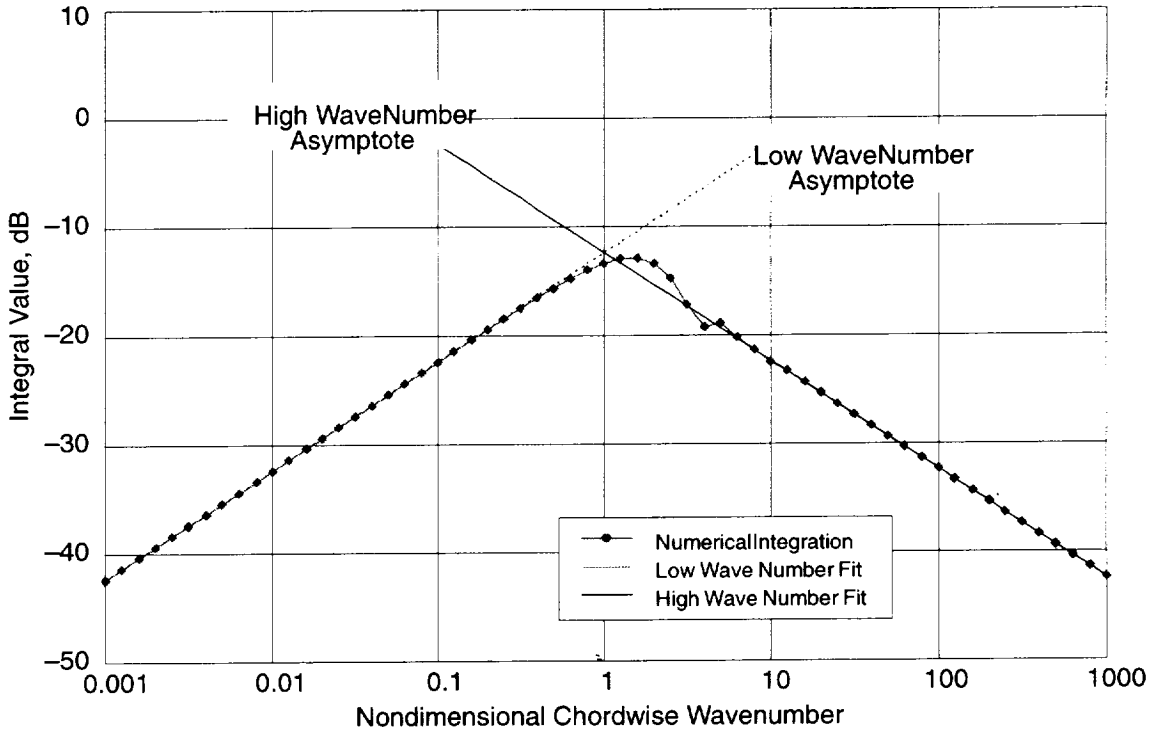

Figure 101. Chordwise Loading Integral Versus Chordwise Wavenumber: Linear Loading Distribution

$$10\log_{10}[I(k_x b)] = -12.401 + 0.99972[10\log_{10}(k_x b)] \quad (174)$$

The high-wavenumber asymptote, again from a linear regression curve fit of the numerical results shown in Figure 100 over the range $10 \leq \times k_x b \leq 1000$, is as follows:

$$10\log_{10}[I(k_x b)] = -12.3178 + 1.00045[10\log_{10}(k_x b)] \quad (175)$$

It can also be shown, taking the limits of Equation (140) as $k_x b \rightarrow 0$, that the low-wavenumber asymptote is analytically given by:

$$10\log_{10}[I(k_x b)] = -12.374 + 1.0[10\log_{10}(k_x b)] \quad (176)$$

Similarly, through taking the limits of Equation (140) as $k_x b \rightarrow \infty$, the high-wavenumber asymptote is analytically given by:

$$10\log_{10}[I(k_x b)] = -12.374 + 1.0[10\log_{10}(k_x b)] \quad (177)$$

Figure 101 shows that the asymptotic formulae of Equations (174) and (175) give a reasonable representation of the numerical integration results over the entire wavenumber spectrum if Equation (174) is used for $k_x b < 1$ and Equation (175) is used when $k_x b > 1$. It is easily shown that the crossover point of Equations (174) and (175) is at $k_x b = 1$. Compared to the uniform-loading distribution results shown in Figure 100, the linear loading wavenumber spectrum shape has significantly less oscillatory wiggles in the midrange of wavenumbers, no doubt as a result of having additional terms that have different "zeros" than the leading term and thus "fill in" the spectrum dips.

The resulting asymptotic forms can therefore be recommended for use in the original self-noise Equation (136), instead of the Mugridge simplifications. Equations (178) and (179) below summarize the recommended expressions to be used for the unsteady lift spectrum in Equation (136).

For low wavenumbers, $k_x b \rightarrow 0$ ($k_x b < 1$):

$$I(k_x b) = \frac{1}{4}a(k_x b) \qquad F(k_x b) = \frac{1}{4} \qquad G_L(\omega) = \frac{1}{4}(2b)^2 G_p(\omega) \tag{178}$$

For high wavenumbers, $k_x b \rightarrow \infty$ ($k_x b > 1$):

$$I(k_x b) = \frac{0.5a(k_x b)}{4}\left[\frac{2}{(k_x b)^2} + \frac{1}{(k_x b)^4}\right]$$

$$F(k_x b) = \frac{0.5}{4}\left[\frac{2}{(k_x b)^2} + \frac{1}{(k_x b)^4}\right] \tag{179}$$

$$G_L(\omega) = \frac{(2b)^2}{8}\left[\frac{2}{(k_x b)^2} + \frac{1}{(k_x b)^4}\right] G_p(\omega)$$

In practice, as is seen from comparing the regression fitted expressions of Equations (174) and (175) with the numerical results, only the first term of Equations (179) is really needed when $k_x b \gg 1$, as the second term is an order of magnitude smaller for high values of wavenumber.

4.6.6.2 Trailing-Edge Surface Pressure Spectrum Improvements

The trailing-edge surface pressure spectrum function $G_p(\omega)$ in Equations (178) and (179) was approximated by Equation (142) in the Mugridge formulation and has no dependency on frequency over the range of nondimensional frequencies (normalized by boundary layer trailing-edge displacement thickness and free-stream velocity) indicated following Equation (142). If this function can be quantitatively defined with a realistic, technically defensible frequency dependence, then (with the refinements in chordwise loading wavenumber dependence) it may be possible to produce a semi-analytic model for the self-noise spectrum shape without resorting to the totally empirical Mugridge shape functions introduced in the discussion around Equation (149).

The Mugridge approximation for $G_p(\omega)$ given by Equation (142) was estimated from airfoil surface unsteady pressure measurements discussed by Mugridge in Reference 65. Mugridge discussed at length how the airfoil data presented in that reference did not correspond very well to similar measurements made by previous investigators. Further, his data did not collapse when normalized using previous practice. In References 66 and 67, Willmarth and Wooldridge normalized unsteady pressure spectra by using free-stream velocity, density, and boundary layer displacement thickness, as follows:

$$G_p^*(\omega^*) = \frac{G_p(\omega)}{\rho^2 \delta^* U^3} = f\left(\frac{\omega \delta^*}{U}\right) \tag{180}$$

The normalized unsteady pressure power spectral density G_p^* typically collapses to a common spectral shape when plotted versus normalized frequency $\omega\delta^*/U$ on a log-log scale for various

free-stream velocities. However, Mugridge found two distinct spectral shapes for the two free-stream velocities tested. He attributed this to the transducer size being too large relative to the wavelengths being measured but was unsuccessful in reconciling these results even when the transducer size corrections were introduced, and his results still seemed to give much higher spectral levels than those of other investigators. Equation (142) represents a somewhat arbitrary average value of all the results given in Reference 65, with no attempt to define a spectral shape.

Additional data of this type were reported by Schloemer in Reference 68. Schloemer measured unsteady pressure fluctuation spectra on a flat plate in a wind tunnel, with opposite-wall geometry variations designed to impose positive and negative pressure gradients. Schloemer showed significant changes in the unsteady pressure spectrum with adverse pressure gradient, relative to a zero pressure gradient, and his zero pressure gradient data were shown to agree well with those of Willmarth, References 66 and 67.

A more recent study reported by Blake et al., Reference 69, included measurements of the unsteady pressure spectrum in the vicinity of the trailing edge of both a blunted-trailing-edge airfoil and a sharp-trailing-edge airfoil. These measurements, especially those of the sharp-trailing-edge configuration, compare favorably with those of Schloemer in Reference 68. Blake et al. used the wake thickness just downstream of the airfoil trailing edge as the normalizing length scale, rather than local boundary layer displacement thickness, as was done in References 65 through 68, so a direct comparison is not easily done based on the information provided in Reference 69. However, the low-frequency asymptotic behavior is constant with decreasing frequency, the level being comparable to that obtained by Schloemer for the case of adverse pressure gradient.

Taken all together, the data on trailing-edge unsteady pressure spectra were found to be reasonably represented by the following expression, when the adverse-pressure-gradient data of Reference 68 and the sharp-trailing-edge data of Reference 69 are favored as being most representative of fan blade and vane trailing edges:

$$G_p^*(\omega^*) \cong \frac{A_0}{[1 + A_1(\omega^*)^2]^{5/2}} \tag{181}$$

where $A_0 = 10^{-4}$ and $A_1 = 0.5$ were found to give the best fit with the cited data. This trend is illustrated in Figure 102. Referring to Equations (178) through (180), the following formula is recommended for substitution into Equations (178) and (179):

$$G_p(\omega) = \rho^2 \cdot \delta^* \cdot U^3 \cdot G_p^*(\omega^*) \tag{182}$$

where G_p^* is given by Equation (181). Equations (181) and (182) now replace Equation (142), and there is no restriction on the applicable normalized frequency range for $\omega\delta^*/U$.

4.6.6.3 Convection Speed Improvements

Mugridge (Reference 17) assumed that the convection velocity U_c used to define the streamwise wavenumber k_x in Equation (137) is equal to $0.8U$, where U is the free-stream velocity. In Reference 65, however, Mugridge estimated the convection speed to be about $0.7U$, based on hot-wire cross-correlation measurements in the boundary layer on the surface of the airfoil. In Reference 68, Schloemer made similar measurements using surface pressure transducers on a flat plate with positive, zero, and negative pressure gradients. He found that convection speed relative to local

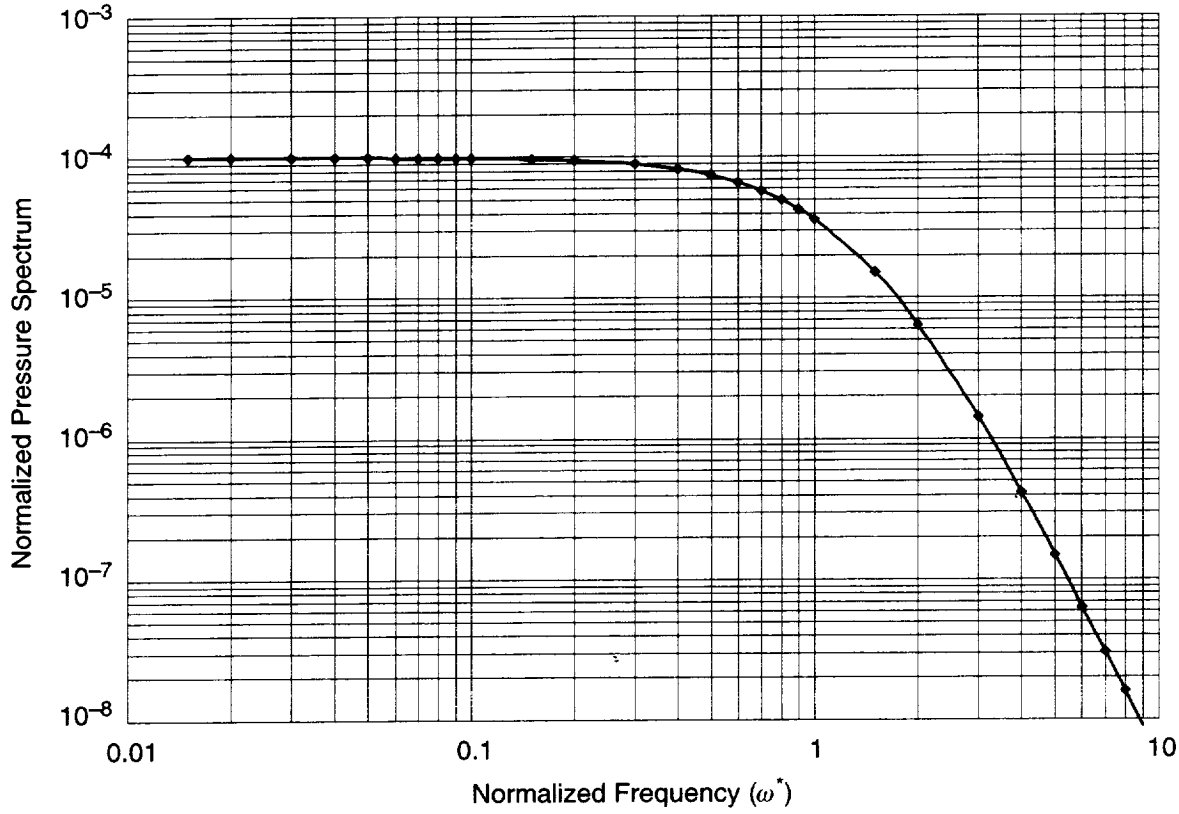

Figure 102. Airfoil Unsteady Surface Pressure Spectrum Model Derived from Data in References 65 through 68

free-stream velocity varied with normalized frequency $\omega\delta^*/U$, although there was significant scatter or spread in the data trends. In particular, convection velocity deduced from transducer pair crosscorrelations seemed to stratify with separation distance between transducer pairs in the longitudinal or streamwise direction.

Nevertheless, some clear trends were evident from Schloemer's data, including the following:

- Convection velocity relative to free-stream velocity decreases as pressure gradient increases.
- Convection velocity relative to free stream velocity decreases with increasing normalized frequency $\omega^* = \omega\delta^*/U$.

If we again take the data for adverse pressure gradient as typical or representative of flow conditions at or near the trailing edge of an airfoil or cascade of airfoils, then the convection velocity can be reasonably represented by the expression:

$$\frac{U_c}{U} = \frac{B_0 + B_1 \cdot \omega^*}{1 + B_2 \cdot \omega^*} \tag{183}$$

where $B_0 = 0.75$, $B1 = 0.6$, and $B_2 = 1.333$. This expression is illustrated in Figure 103.

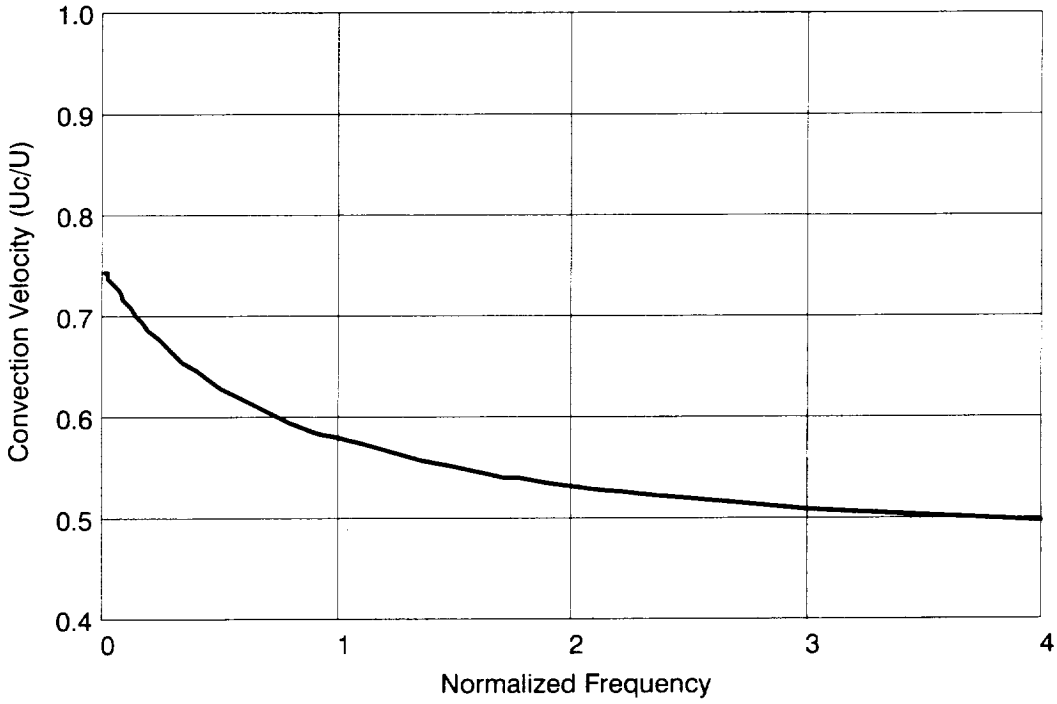

Figure 103. Airfoil Surface Turbulent Eddy Convection Velocity Correlation Model, Based on Data from References 65 through 68

4.6.6.4 Length Scale Model Improvements

Schloemer, Reference 68, speculated that turbulent boundary layer pressure fluctuations were caused by turbulent velocity fluctuations in the boundary layer and that the size of convecting turbulent eddies in the boundary layer are roughly equal to twice the distance from the wall where the boundary layer mean local velocity is equal to the eddy convection speed. Schloemer also estimated the longitudinal microscale (average dimension of the smallest eddies), using parabolic approximations to measured autocorrelation functions, and found the microscale is approximately 12.5% of the boundary layer thickness for zero pressure gradient, 18% for favorable pressure gradient, and 14% for adverse pressure gradient cases.

Blake et al. (Reference 69) reported estimates of the spanwise integral length scale that vary with unsteady pressure spectrum frequency, based on exponential curve fits to spanwise coherence spectra. For low normalized frequencies, the spanwise integral length scale was approximately equal to the wake half-width at the trailing edge. For normalized frequencies above and below $\omega\delta_w/U \cong 1$, the length scale decreases with increasing frequency approximately as follows:

$$\begin{aligned} &\text{for } \omega\delta_w/U < 1 && \ell_s \cong \delta_w \\ &\text{for } \omega\delta_w/U > 1 && \frac{\ell_s}{\delta_w} \cong \frac{1}{(\omega\delta_w/U)} \end{aligned} \qquad (184)$$

Mugridge, Reference 17, estimated spanwise correlation length for unsteady pressure fluctuations to be approximately twice the boundary layer thickness δ^*, based on spanwise crosscorrelations. In

order for this observation to be compatible with Equation (184), the boundary layer thickness must be approximately half the wake half-width, or inversely the wake half-width must be approximately twice the boundary layer thickness. This is probably a reasonable relationship, since the wake half-width is measured some distance (albeit small) downstream of the trailing edge, while the boundary layer thickness of interest is that located some small distance upstream of the trailing edge. Hence, we can reasonably replace δ_w by $2\delta^*$ in Equation (184).

In summary, we can place Equation (144) in the Mugridge self-noise formulation by Equations (183) and (184).

4.6.6.5 Cascade Effects Refinement

Glegg, Reference 70, developed a theoretical relationship between the trailing-edge noise generated by an isolated airfoil and that produced by a cascade of airfoils. The theory quantifies the additional scattering, by adjacent airfoils in the cascade, of the sound produced at one airfoil. Glegg assumed a linear cascade of flat-plate airfoils and derived an expression for a modal correction factor to the isolated single-airfoil case. This correction factor is a function of cascade airfoil spacing and stagger as well as frequency and wavenumber components. The correction factor exhibits oscillatory behavior as a function of frequency and adds as much as 6 dB to the isolated airfoil level at certain frequencies. It was also found to be relatively insensitive to free-stream Mach number.

An approximate, asymptotic expression was given by Glegg for this correction factor as follows:

$$C_m \simeq 1 - e^{2i\zeta_m h} \tag{185}$$

where h is airfoil spacing normal to chord and

$$\zeta_m = \sqrt{[(\omega + \gamma \cdot U)/c_0]^2 - \gamma^2 - \nu^2} \tag{186}$$

where γ is the wavenumber in the chordwise direction and ν is the wavenumber is the spanwise direction. This correction factor applies to the acoustic sound pressure, so the square of C_m must be applied to the sound power.

To this point, we have not addressed modal distributions for self-noise, although this was touched upon in discussing Equation (156) and blade-row/turbulence interaction. In order to use Equation (185), we need to address an integration over spanwise and tangential or normal-to-chordwise direction wavenumbers γ and ν. Thus, we need an expression for the contribution of C_m to the sound power level over the wavenumber intervals $-\infty < \gamma < \infty$ and $-\infty < \nu < \infty$. The square of C_m is given by the following:

$$C_m^2 = [1 - \cos(2 \cdot \zeta_m h)]^2 + [\sin(2 \cdot \zeta_m h)]^2 \tag{187}$$

The trend of C_m with $\zeta_m h$ is shown in Figure 104 for two "cycles" of the parameter $2\zeta_m h$. This trend closely resembles that described by Glegg, Reference 70, for specific values of γ, ν and M as a function of normalized frequency ωh/U. For the purposes of 1/3-octave analysis, however, it may be reasonable to assume that, for each 1/3-octave band, the average of Equation (187) over the repeating interval of 2π is a good approximation. It turns out that this average is just 2.0, which means that, to this level of approximation, the cascade effect is to increase the isolated airfoil estimate by a factor of 2, independent of the cascade geometry or normalized frequency.

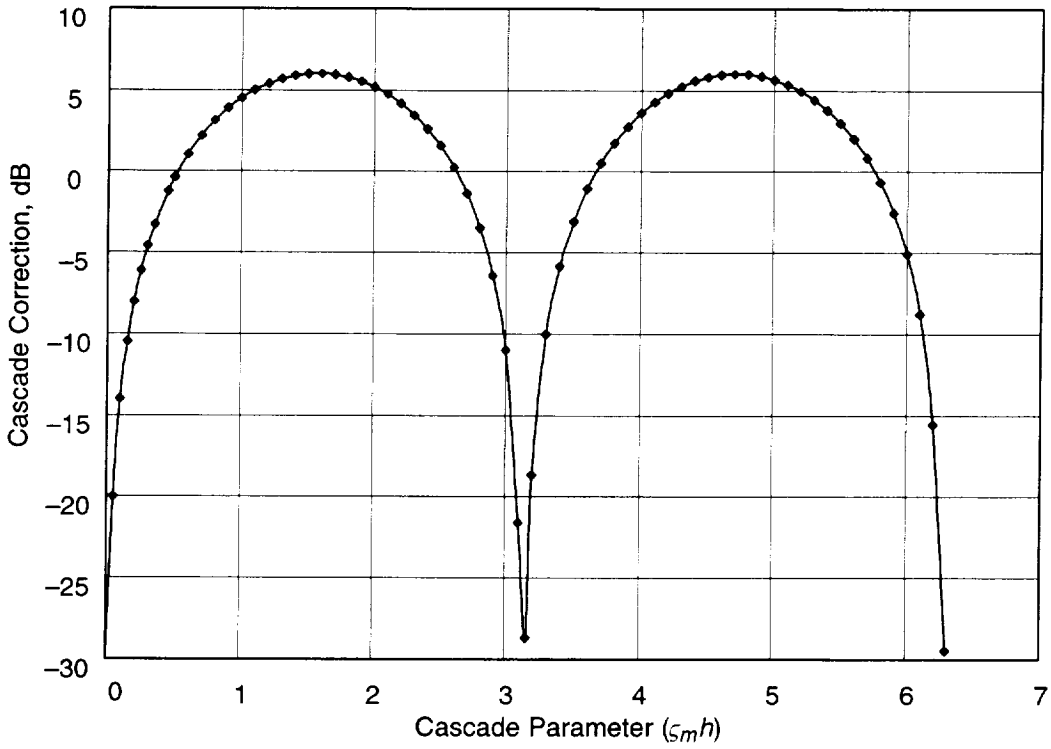

Figure 104. Cascade Effect on Self-Noise Produced by Trailing-Edge Unsteady Loading

4.6.7 Predicted Effects of Improvements on Self-Noise Model

The modifications described above were incorporated into the original Mugridge self-noise model, and the cases given in Figures 98 and 99 were recomputed. The resulting self-noise prediction differences are shown in Figure 105. Also shown in these Figures are the experimental data. It can be seen that the above improvements have considerably reduced the predicted self-noise levels.

It should be noted that the original Mugridge model, which was used to generate the results shown in Figure 98 (page 103), used rotor tip relative Mach number for computing rotor self-noise. In both sets of results in Figure 105, however, a root-mean-square (rms) radius value of rotor rotational Mach number was used to compute the noise levels. Comparing the results in Figure 98 with the "old method" results in Figure 105, it can be seen that the stator levels were not significantly affected by this difference in rotor speed (on the order of 1 to 2 dB). For the rotor self-noise, however, this change in rotor speed definition (rms radius value instead of tip radius value) reduces the peak levels by about 10 dB. The intent in changing this definition for rotor speed was to reflect that rotor (and stator) self-noise is generated all along the span, and the rms radius value represents an average value over the blade or vane length.

It also can be seen that the spectral shape is predicted quite well (in the sense that the shape is consistent with the previously derived experimental correlation of Mugridge) without resorting to empirical spectrum shape formulae as described on page 99 following Equation (149). It is also observed that the self-noise of the rotor is still predicted much higher than that of the stator. Further, the rotor and stator peak frequencies are different, as was derived by Mugridge, with the rotor self-noise peak frequency being lower.

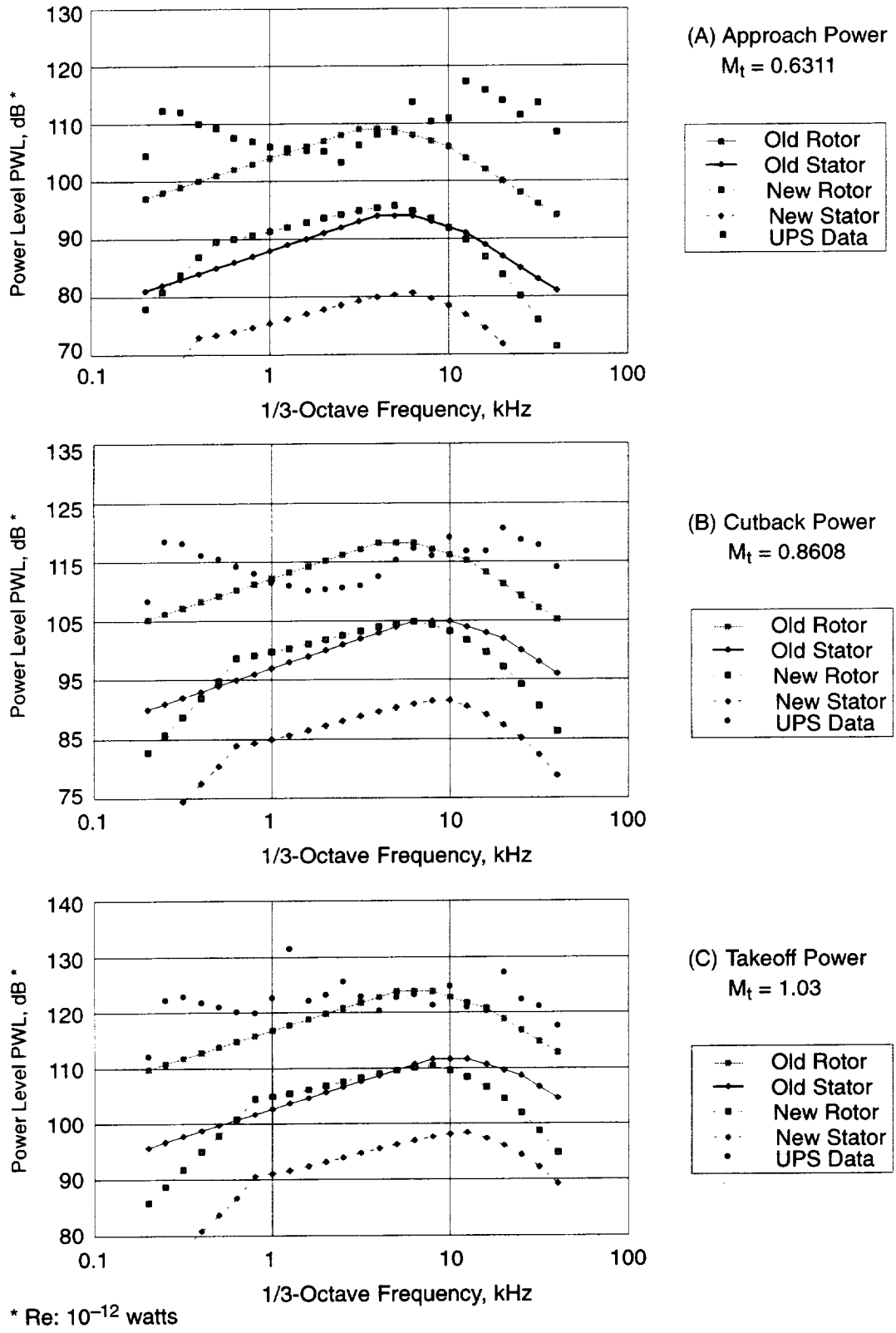

Figure 105. New Versus Old Self-Noise Model Comparisons for UPS Fan Stage

It is not possible, without specially designed experiments, to validate the self-noise model directly, since typical fan noise spectra contain both interaction sources and the self-noise sources. However, it can be said that, at least for the data set used herein, the old Mugridge self-noise model definitely overpredicts, and the improvements developed herein do not. From the results shown in Figures 99 and 105, it would appear that stator self-noise does not contribute significantly to the overall fan broadband noise. Rotor self-noise, however, probably does contribute to some extent, most likely in the middle frequency range between *BPF* and 2 or 3 × *BPF*. For the UPS data examples, this corresponds to the range of 3 to 10 kHz.

4.7 Theory/Data Comparisons

Theory/data comparisons for 10 fan cases for acoustic data are discussed in this section. In 6 of the 10 cases, turbulence data were available to exercise the theory and code developed in Section 4.3, page 88. In the remaining four cases, no such information was available. Hence, 3D Reynolds averaged Navier–Stokes CFD codes were used to deduce some of the turbulence information needed. In 4.7.1, the CFD usage is described. In 4.7.2, the noise predictions and comparisons with farfield noise data are discussed.

4.7.1 CFD for Fan Broadband Noise Prediction

Turbulence is a vital input into aircraft engine fan broadband noise prediction codes. Two principal sources of fan broadband noise are the inlet turbulence impinging on the fan and the turbulence generated by the fan and impinging on the outlet guide vanes (OGV's). Analytical noise prediction tools typically require, at minimum, the radial distributions of circumferentially averaged turbulence kinetic energy and turbulence length-scale information. These radial profiles are needed at two primary axial stations: the fan face and the OGV leading edge. Since turbulence is often anisotropic, the Reynolds stress tensor and a measure of anisotropy of the turbulent eddy sizes are also desirable.

Traditionally, the required turbulence data have been obtained experimentally, most often using hot-wire probes. Obtaining turbulence data behind a transonic fan is difficult, time-consuming, and expensive, and these data are often not available for making noise predictions early in the engine design process where they have a better chance of being able to impact the final design.

CFD can serve as an alternative to experimental measurements in supplying necessary turbulence data for fan broadband noise-prediction codes. It offers the possibility of being able to predict turbulence properties directly from geometry definitions. This makes it much easier to conduct parametric studies early in the design process.

In this work, CFD was used to predict turbulence data that were then used as input into the fan broadband noise codes. Four operating points for which experimental noise data were available from the UPS were simulated numerically. For each operating point, two separate calculations were made.

The first calculation was at the engine inlet consisting of the interior and exterior surfaces of the nacelle. This simulation, which captured the turbulence generated in the inlet and centerbody boundary layers, was performed using the NASA code CFL3D. From this calculation, radial turbulence profiles were extracted at the fan-face axial station.

The second calculation was of a single fan blade passage. This calculation included the engine splitter and a domain extending downstream to the OGV leading-edge station. This simulation,

which captured the turbulence generated by the fan, was performed using the GE proprietary code TACOMA. From this calculation, radial turbulence profiles were extracted at the OGV leading edge axial station.

The remainder of this section describes in greater detail the processes followed and the results obtained. First, the UPS facility is briefly described and the parameter values for the four operating points are given. Next, the inlet simulations are discussed. The computational grids are shown, the CFL3D code is described, and the resulting solutions are presented. Finally, the single-passage fan blade simulations are discussed, the computational grids are illustrated, the TACOMA code is described, and the resulting solutions are presented.

4.7.1.1 Universal Propulsion Simulator (UPS)

For this work, the predictive capabilities of the fan broadband noise prediction codes were assessed against experimentally measured noise data from the UPS. This subsection briefly describes the UPS rig and the values of some key parameters for the four operating points at which the noise comparisons were made.

The UPS rig is an experimental test vehicle representative of a modern, high-bypass, ducted-fan, aircraft engine. It includes a nacelle, inlet, fan, booster, OGV's, and exhaust system, as shown schematically in Figure 106. The nacelle is a conventional design with 3° of inlet droop. The noise data in this work were taken using a fan blade representative of a modern, wide-chord design. This fan has a diameter of 22-inches and consists of twenty-two blades. The 100% speed condition for this fan is approximately 12,644 rpm. The booster in the UPS consists of a first-stage stator and rotor, a second-stage stator, and a set of deswirl vanes. The UPS OGV configuration incorporates 54 vanes.

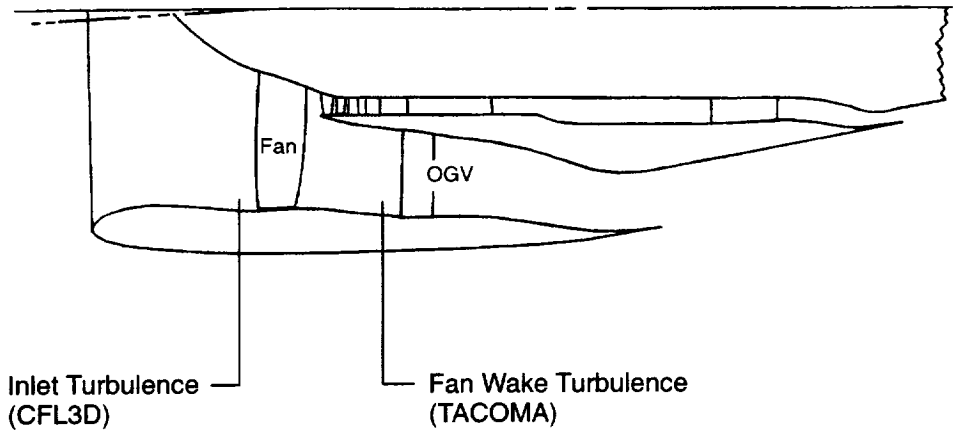

Figure 106. Universal Propulsion Simulator (UPS) Schematic

For this work, four operating points were chosen at which to compare analytical noise predictions with measured noise data. The four points are designated approach, cutback, takeoff, and high takeoff. Some pertinent parameter values for these four operating conditions are listed in Table 10.

Table 10. UPS Key Operating Parameters

Parameter	Approach	Cutback	Takeoff	High Takeoff
Percent Speed	64.0	76.4	94.3	104.4
Fan Speed (RPM)	8096.8	9655.2	11926.2	13200.3
Total Mass Flow (lbm/s)	67.619	81.627	97.932	105.563
Bypass Ratio	8.670	8.413	7.987	7.793
Inlet Total Pressure (psi)	14.984	14.982	14.742	14.635
Inlet Total Temperature (°R)	504.0	504.9	511.0	513.0

4.7.1.2 Inlet Analysis

To provide a description of the turbulence impinging on the fan, CFD simulations were performed on the UPS inlet geometry. Radial profiles of circumferentially averaged turbulence kinetic energy at the fan face were then extracted from these solutions and used as input in the fan broadband noise prediction codes. In the remainder of this subsection, the computational grids employed are shown, the CFD simulation is described, and results for the four operating points are presented.

Computational Grid – A three-dimensional CFD model of the UPS inlet was constructed as shown in Figure 107. It was only necessary to model half the geometry, due to left/right symmetry. The computational grid consisted of three grid blocks as shown in Figure 108. One grid block was upstream of the fan face, one downstream, and a third in the external flow region. In this way, the fan-face axial station was on a planar grid block boundary that facilitated postprocessing of the flow quantities at this location. To prevent the annulus from choking at the high engine mass flows, the

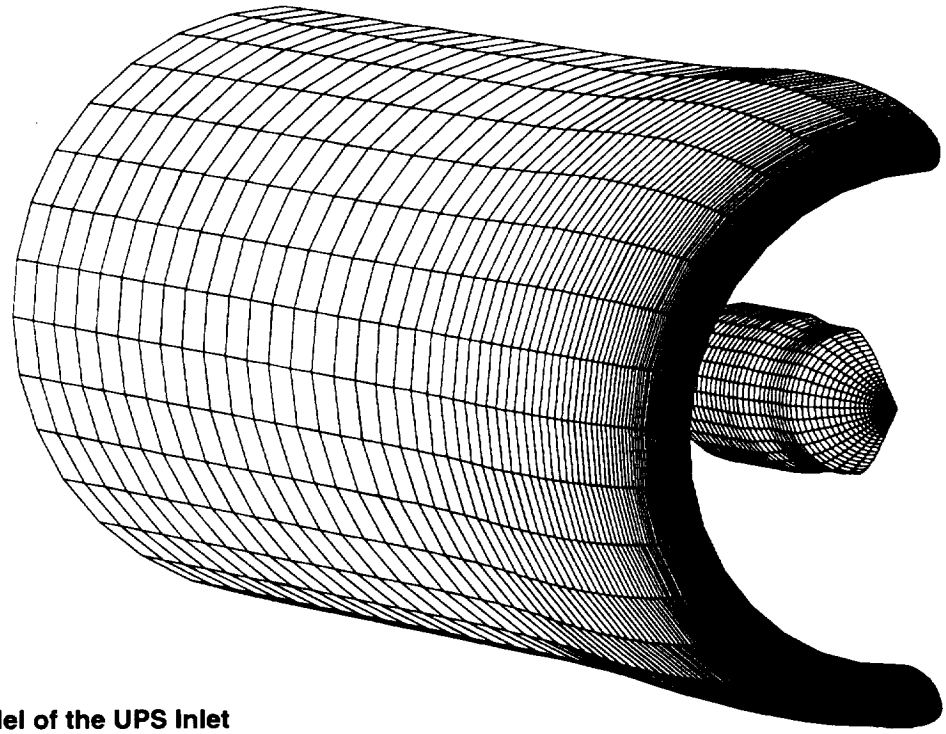

Figure 107. CFD Model of the UPS Inlet

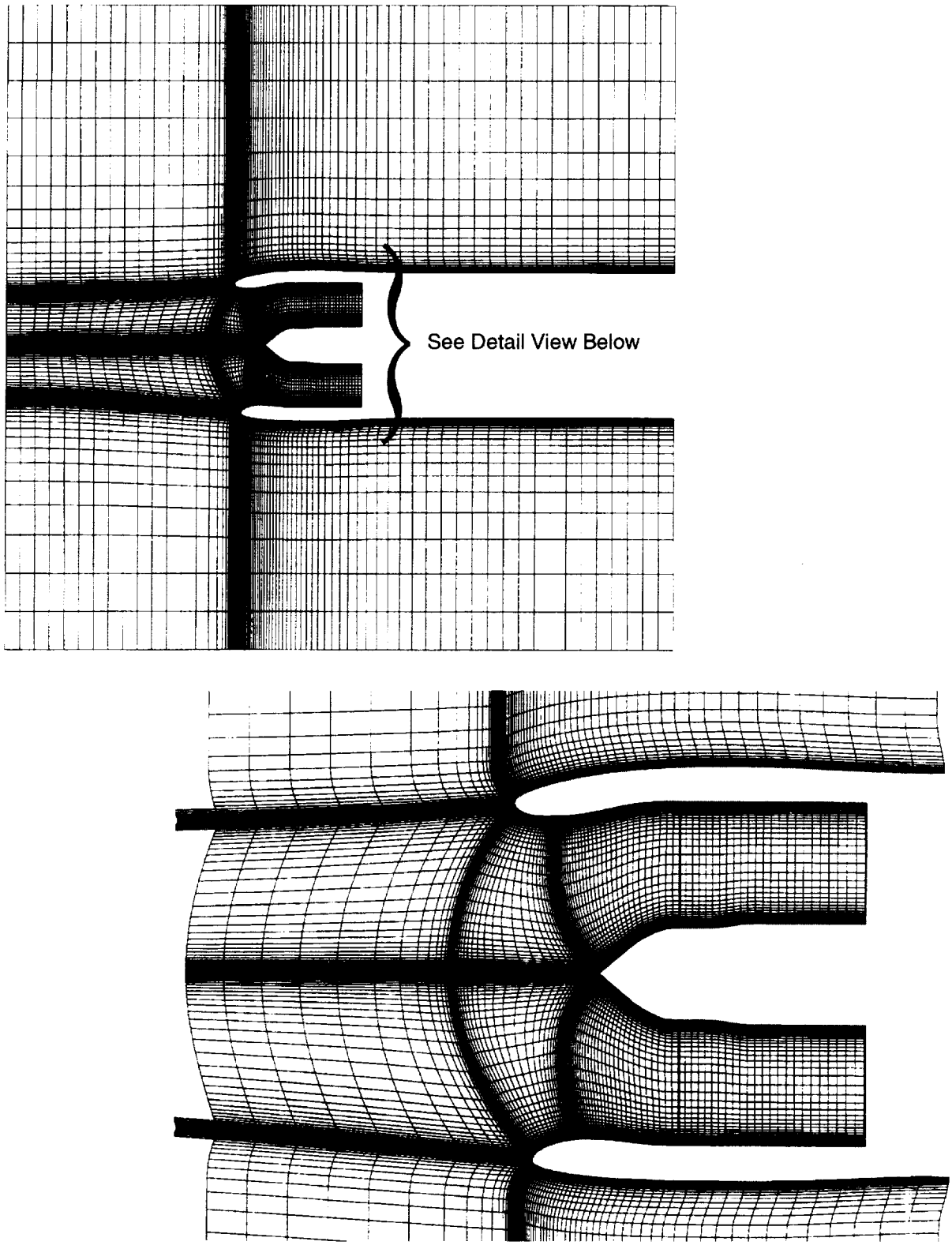

Figure 108. Computational Grid for the UPS Inlet CFD Simulation

centerbody was reduced in radius beginning downstream of the fan-face station. This is explained further in the discussion of CFD simulations below. The sizes of the three grid blocks are given in Table 11. Overall, the grid consisted of 262,400 cells. A fine grid was used in the radial direction in order to resolve the nacelle and centerbody boundary layers. Sufficient resolution was used to permit solving the turbulence model all the way to the wall without the need for wall functions.

Table 11. Dimensions of Grid Blocks for Inlet Simulation

Grid Block	Axial	Circumferential	Radial
Upstream of Fan	88	16	100
Downstream of Fan	24	16	100
External	100	16	52

CFD Simulations – NASA code CFL3D version 5.0 was used to perform the CFD simulations of the inlet. This code solves the thin-layer form of the three-dimensional, compressible, Reynolds-averaged Navier–Stokes equations using a cell-centered, finite-volume formulation. The spatial discretization chosen was Roe's flux-difference splitting with an upwind-biased, higher-order-accurate ($\varkappa$ = 1/3) MUSCL (References 71 and 72) reconstruction. The Wilcox $k-\omega$ turbulence model was used (Reference 73). The flow at the inlet boundary was assumed to have zero free-stream turbulence. Since a very fine boundary layer mesh was employed, the turbulence model was solved all the way to the wall — obviating the need for wall functions. The calculations were performed at a free-stream Mach number of 0.25 and a 3° angle of attack to simulate the experimental test conditions at which the noise data were taken.

Each of the four operating points was simulated by adjusting the static pressure at the fan flow exit in order to match the experimental engine mass flow. Lacking a more detailed description, the static pressure was assumed to be uniform at the fan flow exit boundary. The effect of this assumption on the flow at the fan face was minimized by choosing the fan flow exit station to be several passage heights downstream of the fan face. Also, this approximation is consistent with the use of a modified centerbody. As mentioned in the discussion of computational grid above, the centerbody radius was modified (reduced) downstream of the fan face station to prevent the flow in the annulus from choking at high mass flows in the absence of the work input from the fan (which was not modeled).

Results – Figure 109 shows Mach number contours on the symmetry plane for the four operating points. The slight mismatches in the contours at the fan face grid block boundary are artifacts from postprocessing the cell-centered solution to the vertices, for visualization. At the high takeoff operating point, the flow becomes slightly supersonic as it accelerates around the lip of the nacelle. On the lower lip, this supersonic zone terminates in a weak shock. The boundary layer development on the nacelle and centerbody walls is clearly apparent. Overall, the inlet flow is well behaved under these operating conditions.

For the purposes of noise prediction, turbulence intensity is of most interest. The turbulence intensity (in percent) is defined as:

$$I = 100\frac{\sqrt{\frac{1}{3}\overline{u_i' u_i'}}}{\|u\|} = 100\frac{\sqrt{\frac{2}{3}k}}{\|u\|} \tag{188}$$

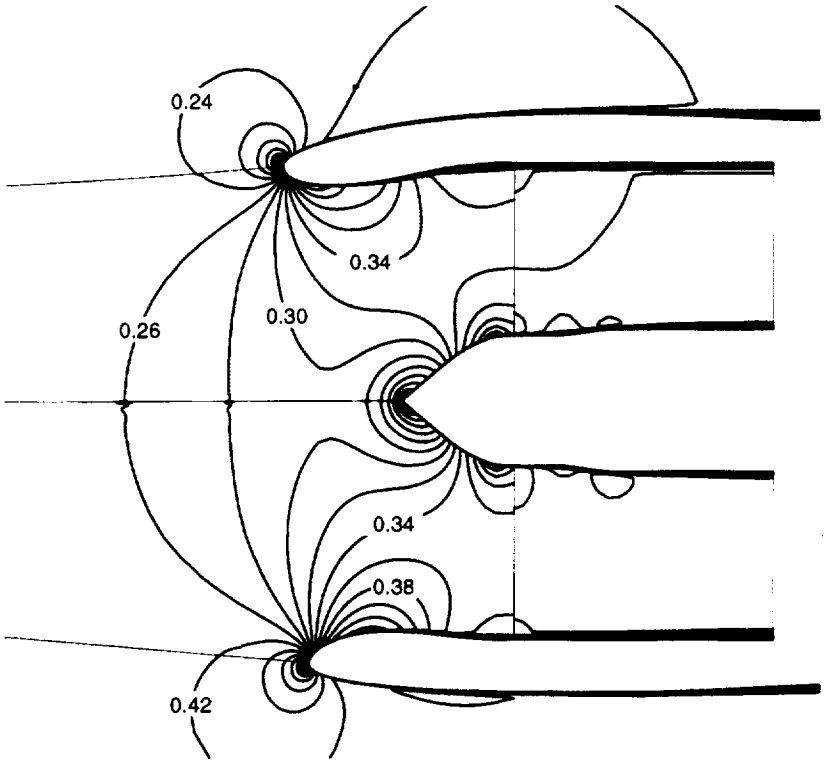

(a) Approach

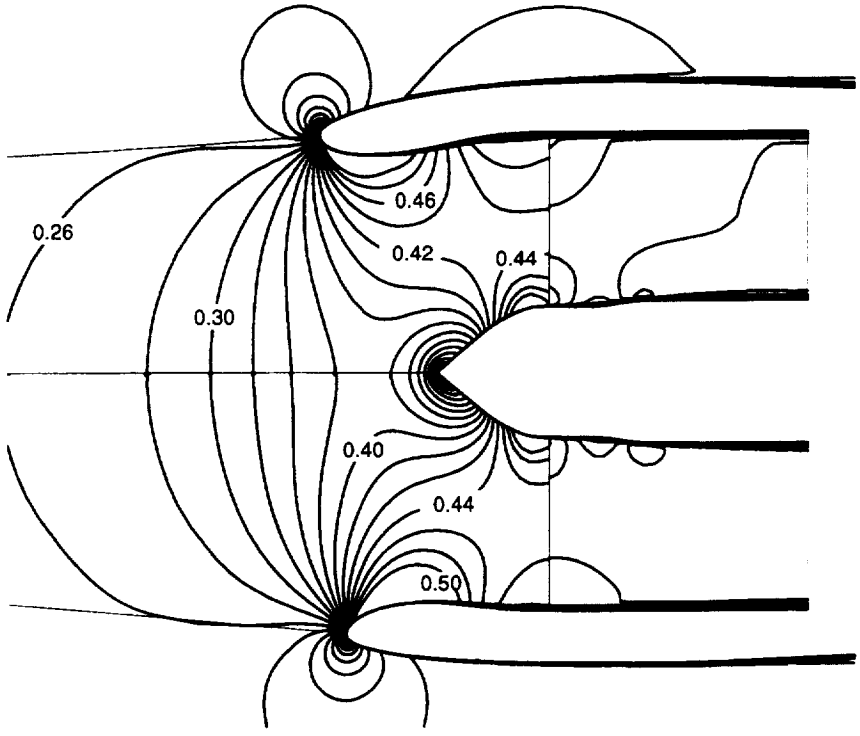

(b) Cutback

Figure 109. Mach Number Contours on the Symmetry Plane

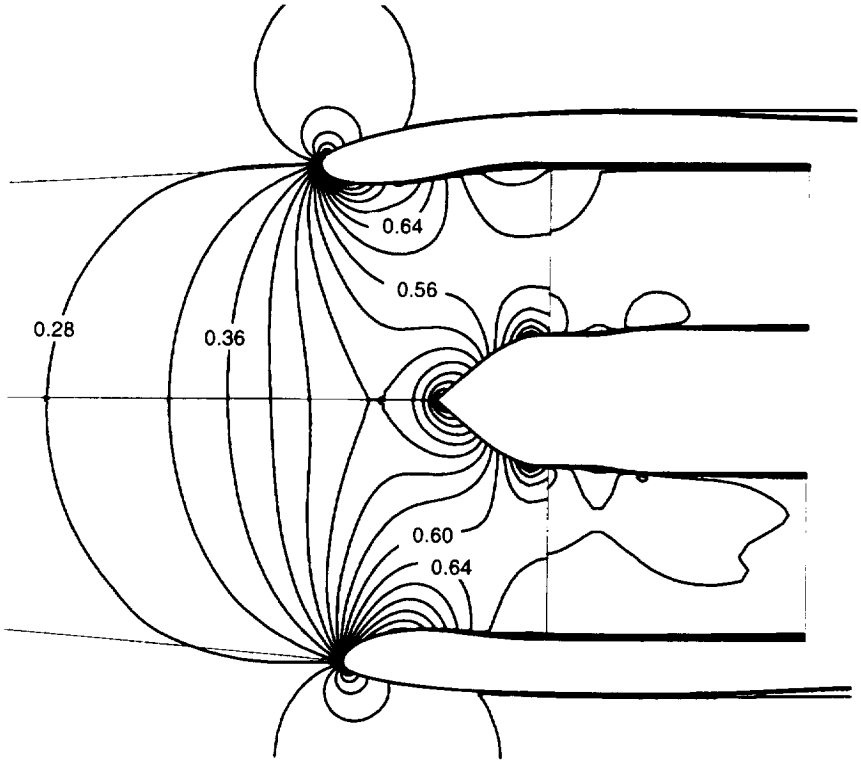

(c) Takeoff

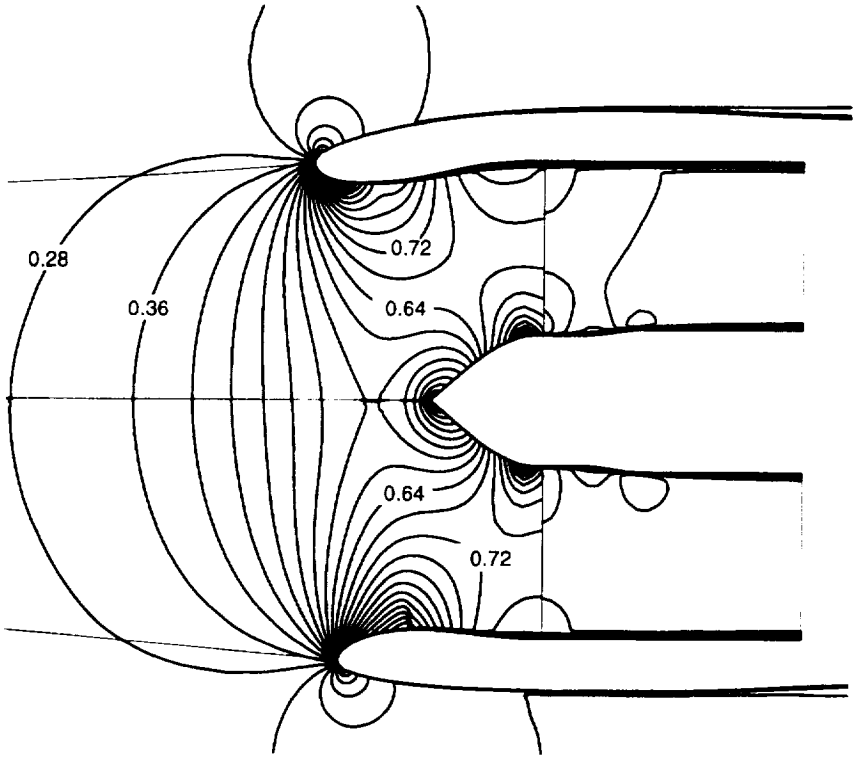

(d) High Takeoff

Figure 109. Mach Number Contours on the Symmetry Plane (Concluded)

where u is the (local) mean velocity, u_i' is the fluctuating velocity, and k is the turbulence kinetic energy. The turbulence intensity is easily computed from the CFD solution since the turbulence model solves for k directly. Figure 110 shows contours of the turbulence intensity on the symmetry plane for the high takeoff operating point. The results for the other three operating points look similar. As mentioned above, the free-stream turbulence intensity was set to zero for these simulations. Turbulence generation can be seen in the developing nacelle and centerbody boundary layers.

For each of the four operating points, the turbulence intensity at the fan-face axial station was then circumferentially averaged to obtain a radial profile. These radial profiles are shown in Figure 111. Here the radial coordinate has been nondimensionalized by the fan tip radius. Figure 111(a) shows the full radial profile from the centerbody to the fan tip. The centerbody boundary layer is seen to be very thin. Although the turbulence intensity peaks there at around 16%, this turbulence is not a significant source of broadband noise due to the relatively low rotational velocity of the hub.

Figure 111(b) is an enlarged view of the turbulence intensity in the tip region. Due to the high fan tip speed, this turbulence does make a significant contribution to the broadband noise. The turbulence intensity is highest at the approach operating point, peaking around 11%. The turbulence intensity is slightly lower at the other three operating points. At cutback, there is a fairly broad region in which the turbulence intensity is around 8.5%. The profiles at takeoff and high takeoff are similar, with the turbulence intensity increasing slightly to just over 9%.

4.7.1.3 Fan Duct Analysis

Another primary source of fan broadband noise is turbulence from the fan impinging on the outlet guide vanes. CFD simulations at the four operating points of the UPS fan were performed to predict the turbulence intensity at the OGV leading-edge axial station. In the remainder of this subsection, the CFD model formulation is described, the computational grid is shown, the CFD simulations and the code employed are discussed, and results from the numerical simulations at the four operating points are presented.

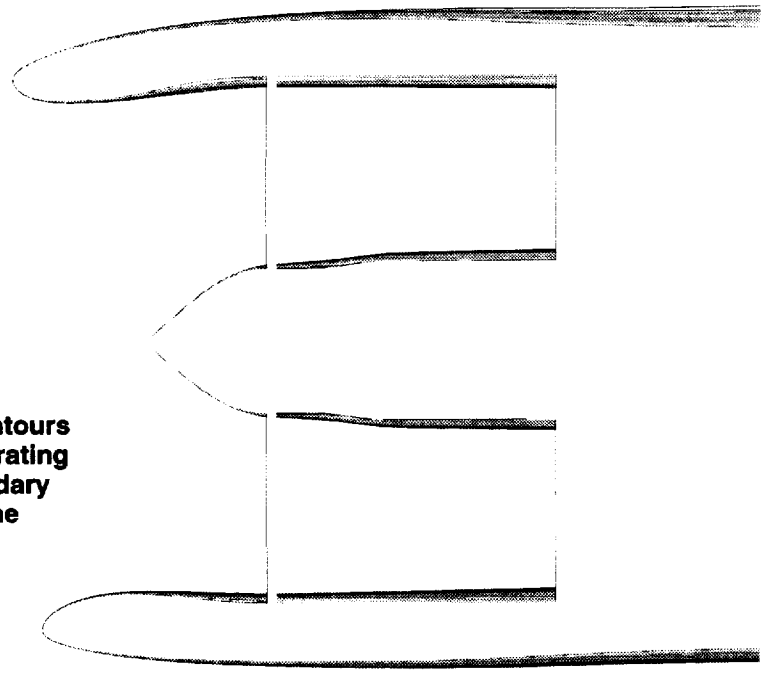

Figure 110. Turbulence Intensity Contours for the High Takeoff Operating Point Showing the Boundary Layer Development on the Nacelle and Centerbody

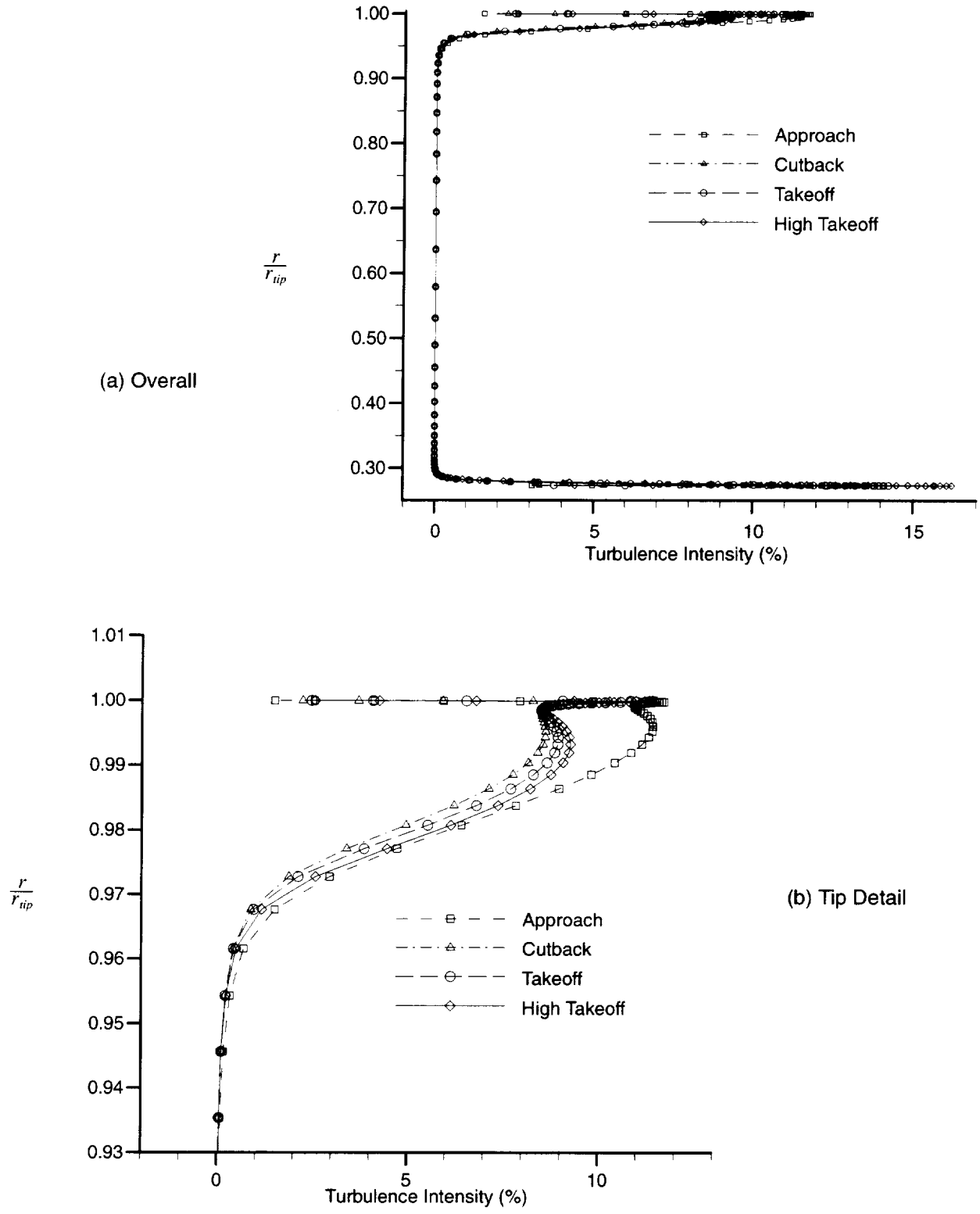

Figure 111.. Radial Profiles of Circumferentially Averaged Turbulence Intensity at the Fan-Face Axial Station, from UPS Inlet CFD Simulations

Computational Grid – As is standard in turbomachinery simulations, flow is computed in a frame of reference rotating with the fan. The flow in this rotating reference frame is assumed to be steady and periodic from one blade passage to the next. Under these assumptions, the CFD model need only consist of a single fan blade passage. The full three-dimensional CFD model used in this work is shown in Figure 112. Two fan blade passages are shown for clarity, although only one passage was actually used in the simulations. The model consists of the fan blade, the hub and casing, surfaces, and the engine splitter. The tip gap between the fan tip and the casing surface has been included in the model.

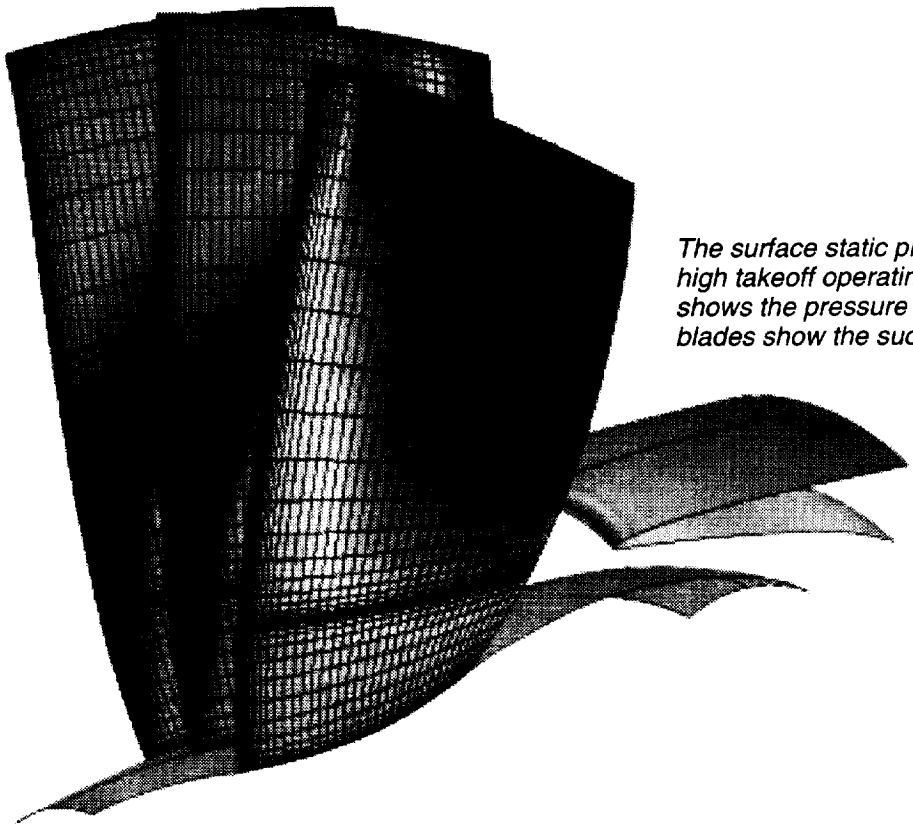

The surface static pressures are shown at the high takeoff operating point. The front fan blade shows the pressure surface; the other two blades show the suction surface.

Figure 112. UPS Fan CFD Model Showing Two Fan Blade Passages, the Engine Splitter, and the Hub Surface

Figure 113 is a meridional view of the computational grid employed for the UPS fan simulations. Arrows indicate the locations of the four axial stations (fan leading edge, fan trailing edge, splitter leading edge, and OGV leading edge) at which the turbulence quantities were postprocessed. The mesh has 124 cells in the axial direction: 36 upstream of the fan leading edge, 52 between the fan leading and trailing edges, and 36 downstream of the fan trailing edge. There are 48 cells in the radial direction: 44 along the blade and 4 in the tip gap (16 in the core and 32 in the fan bypass duct). The mesh has 64 cells in the circumferential direction. Overall, there are 380,928 computational cells in the mesh. Grid refinement studies were performed in which the number of axial cells downstream of the fan trailing edge was increased to 64 and the number of circumferential cells was increased to 96. Only slight differences in the solutions were observed.

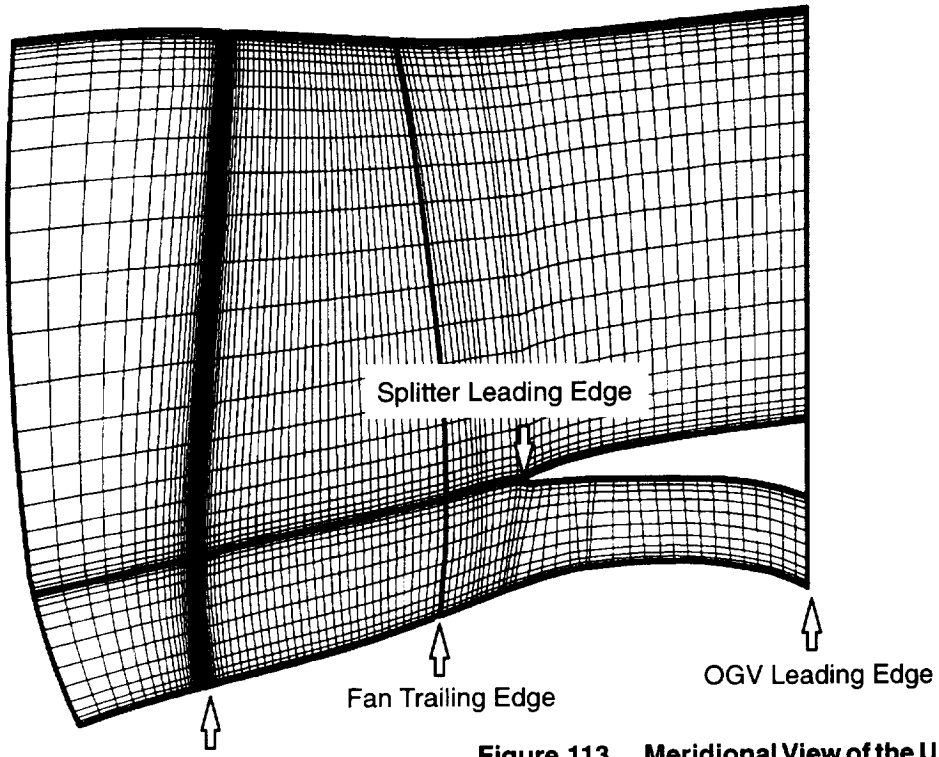

Turbulence intensity is evaluated at the four axial stations indicated.

Figure 113. Meridional View of the UPS Fan Grid Showing the Fan Blade and the Engine Splitter

Figure 114 shows the blade-to-blade mesh at the hub, pitch (mid-span), and tip. Since there is a fairly wide stagger angle variation, a special effort was made to align the mesh downstream of the fan with the anticipated blade wake. This helped prevent the wake from being excessively smeared by numerical dissipation due to oblique alignment with the grid. This was especially important in this application since the OGV leading-edge axial station on which the turbulence quantities are desired is located several blade chords downstream of the fan trailing edge.

CFD Simulations – The CFD simulations of a single passage of the UPS fan were performed using the proprietary GE code TACOMA. This code solves the full three-dimensional compressible Reynolds-averaged Navier–Stokes equations using a cell-centered, finite-volume method in a frame of reference rotating with the fan. All spatial derivatives are discretized using central differences. Artificial dissipation in the form of blended second and fourth differences is added to maintain numerical stability. Steady solutions are obtained by marching an (arbitrary) initial condition forward in pseudo-time using a multistage Runge–Kutta method. Multigrid is used to accelerate the convergence to a steady state. The fluid turbulence is simulated using the Wilcox (Reference 73) $k-\omega$ turbulence model with wall functions.

The boundary conditions used are straightforward. The no-slip condition is imposed on all walls. In the relative frame, the engine splitter and casing surfaces are moving at the wheel speed while the blade and hub surfaces are stationary. At the inlet boundary, the absolute total pressure, absolute total temperature, absolute tangential velocity (equal to zero), and r–z flow angle are specified. Two turbulence parameters are specified at the inlet. One is the turbulence intensity which, combined with a reference inlet velocity, is used to determine the inlet turbulence kinetic energy. The other is the eddy viscosity to molecular viscosity ratio, μ_t/μ, which sets the turbulence length scale. For these

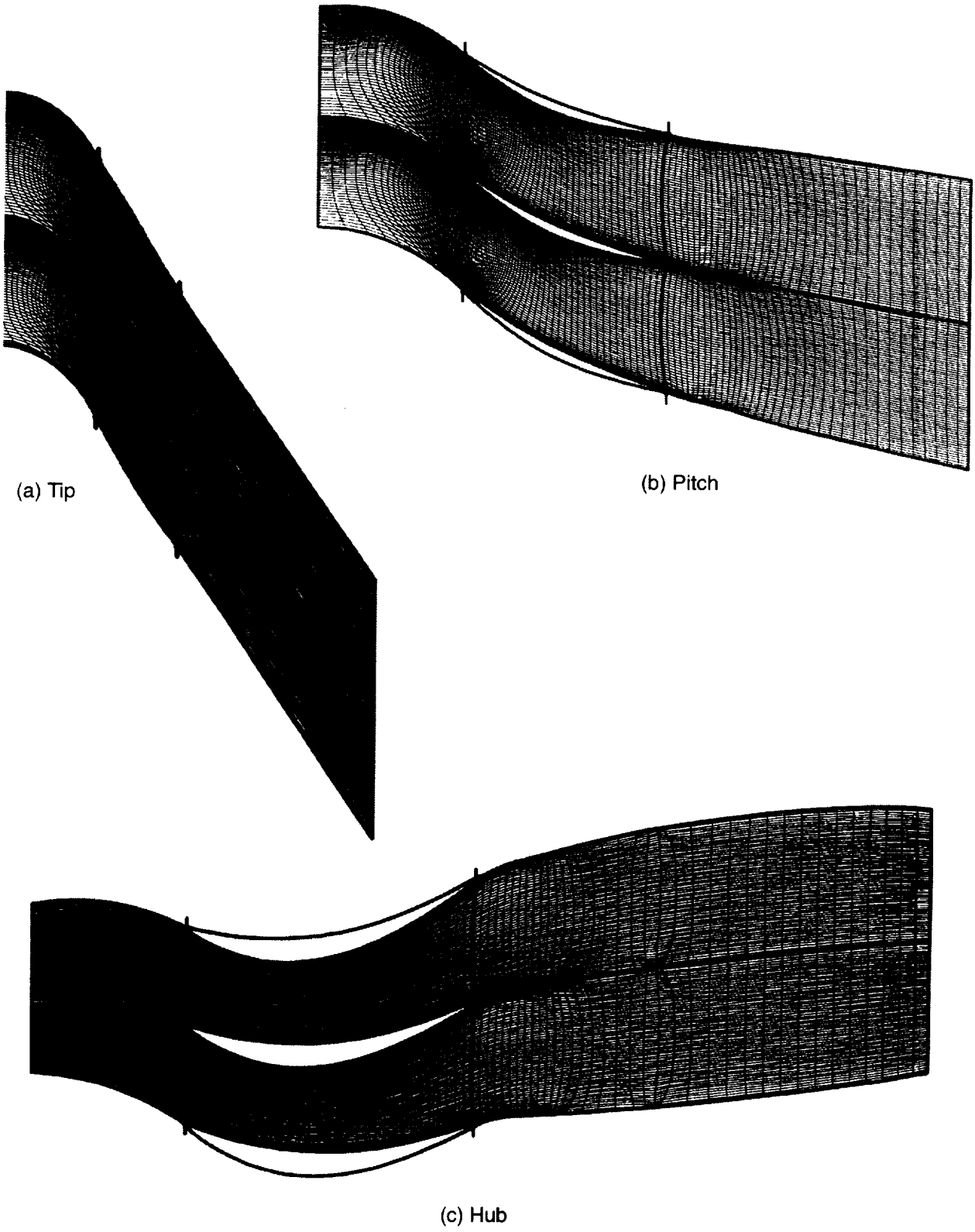

Figure 114. UPS Fan Grid at Three Radial Locations *Two fan blade passages are shown.*

simulations, the inlet turbulence intensity is taken to be 1%, and the inlet eddy viscosity to molecular viscosity ratio is taken to be 100. The sensitivity of the results to these values is described in the next discussion. At the exit, midpassage static pressures in the core and fan bypass duct are specified in order to match the experimental total mass flow and bypass ratio. Since the flow at the exit is swirling, radial equilibrium is used to extend these "pivot" pressures along the span.

Results – Figure 115 shows the turbulence intensity at 85% of the tip radius for the four operating points of the UPS fan. At this radius, turbulence intensity is highest at the approach operating point with values slightly over 10% in most of suction-side boundary layer and the near wake region. As the wake spreads downstream, peak turbulence intensity decays, diminishing to about 7% at the OGV leading-edge station. The turbulence intensity is lower at the cutback and takeoff operating points since there is less production in the suction-side boundary layer. At the high takeoff operating point, there is a region of high turbulence intensity on the suction surface toward the rear of the blade. The reason for this will be apparent momentarily. Figure 116 shows turbulence intensity contours at 95% of the tip radius. Overall, these plots are similar to the previous ones at the 85% tip radius location. The main differences are slightly lower turbulence intensities at the approach condition and higher intensities at the high takeoff condition.

Figure 117 is a cross-stream plot of the turbulence intensity at the splitter leading-edge axial station for the four operating points. At the approach condition, the turbulence intensity is slightly over 10% along most of the span of the fan. The turbulence intensity is somewhat lower at the cutback condition and lower yet at the takeoff condition. In the tip region, at the high takeoff operating point, a region of high turbulence intensity appears that does not exist at the lower power settings.

Figure 118 sheds light on the reason for this increased turbulence intensity by showing comparison of the takeoff and high takeoff flow fields at 95% of the tip radius. The plots on the left show the relative Mach number for these two power settings; the corresponding turbulence intensity plots are shown on the right. At the takeoff setting, the fan is unstarted with a detached bow shock in front of the blade. Under these conditions, flow remains attached where the shock contacts the suction surface of the blade. At the high takeoff condition shown in the lower plots, the fan is started with a normal passage shock. In this case, the shock is stronger and induces a boundary layer separation where it contacts the suction surface. This region of recirculating flow causes an increase in the turbulence intensity, as seen in the plot on the lower right.

Figure 119 shows circumferentially averaged radial profiles of the turbulence intensity at the four axial stations: fan leading edge, fan trailing edge, splitter leading edge, and OGV leading edge. Results for the four operating points are shown on each plot. The radial coordinate in the plots has been made nondimensional by dividing by the tip radius. At the fan leading-edge station shown in Figure 119(a), the profiles are nearly uniform. Although for all operating points a nominal turbulence intensity of 1% was prescribed at the inlet boundary, some (minor) level differences are seen at this station. The turbulence intensity at the high takeoff and takeoff conditions is very nearly 1%, while it is about 1.5% at the cutback setting and 2% at the approach setting. These differences are due to the way in which the inlet turbulence intensity was computed from the reference inlet velocity.

Figure 119(b) and (c) shows the evolution of these inlet profiles as the flow passes through the fan and exits the computational domain at the OGV leading-edge station. At the approach setting, the turbulence intensity increases, especially near midspan and near the tip, reaching approximately 4% at the OGV leading edges. The cutback operating point follows a similar behavior, although to a lesser degree. At the takeoff condition, the turbulence intensity increases from approximately 1%

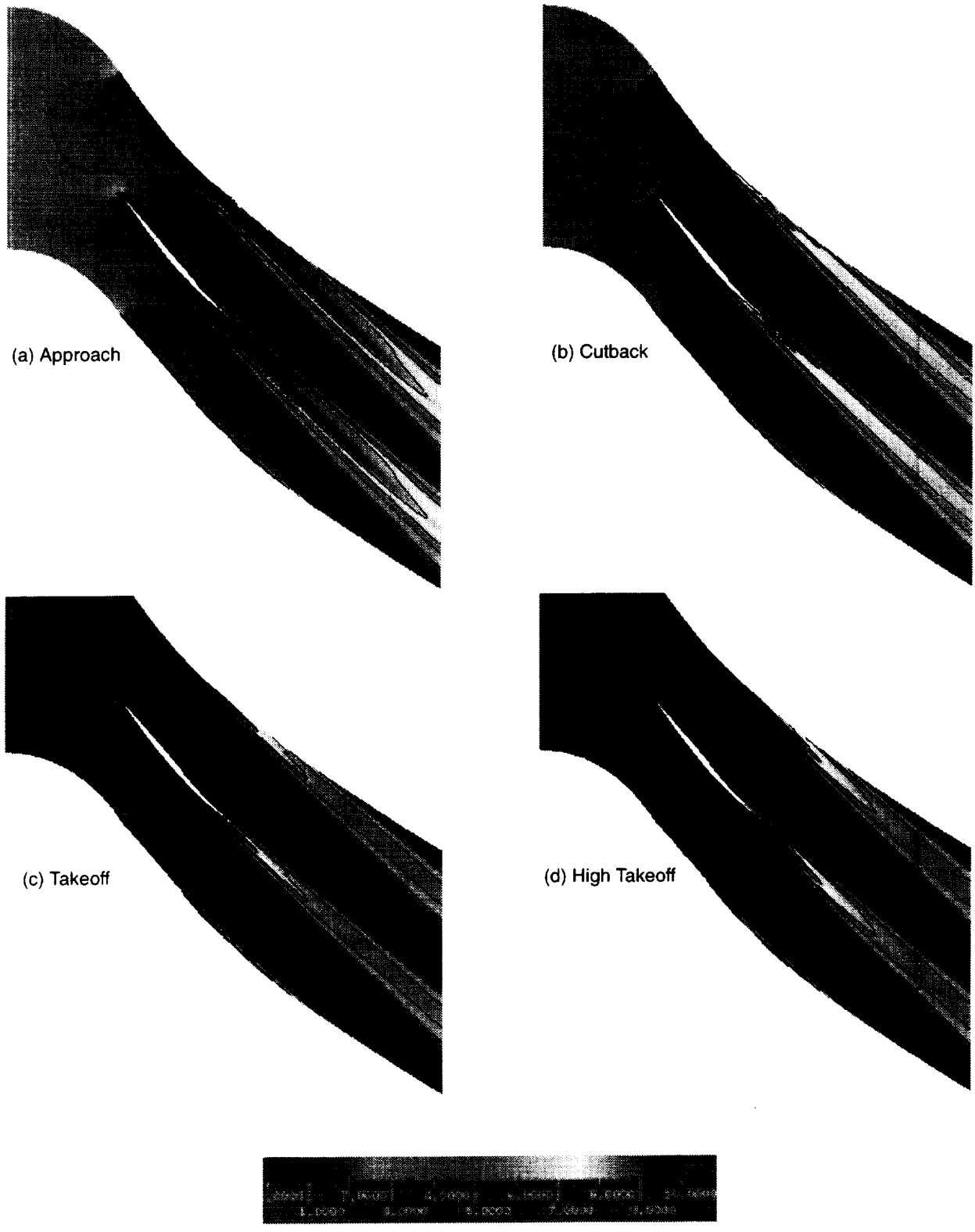

Figure 115. Turbulence Intensity at 85% Tip Radius for the Four Operating Points of the UPS Fan

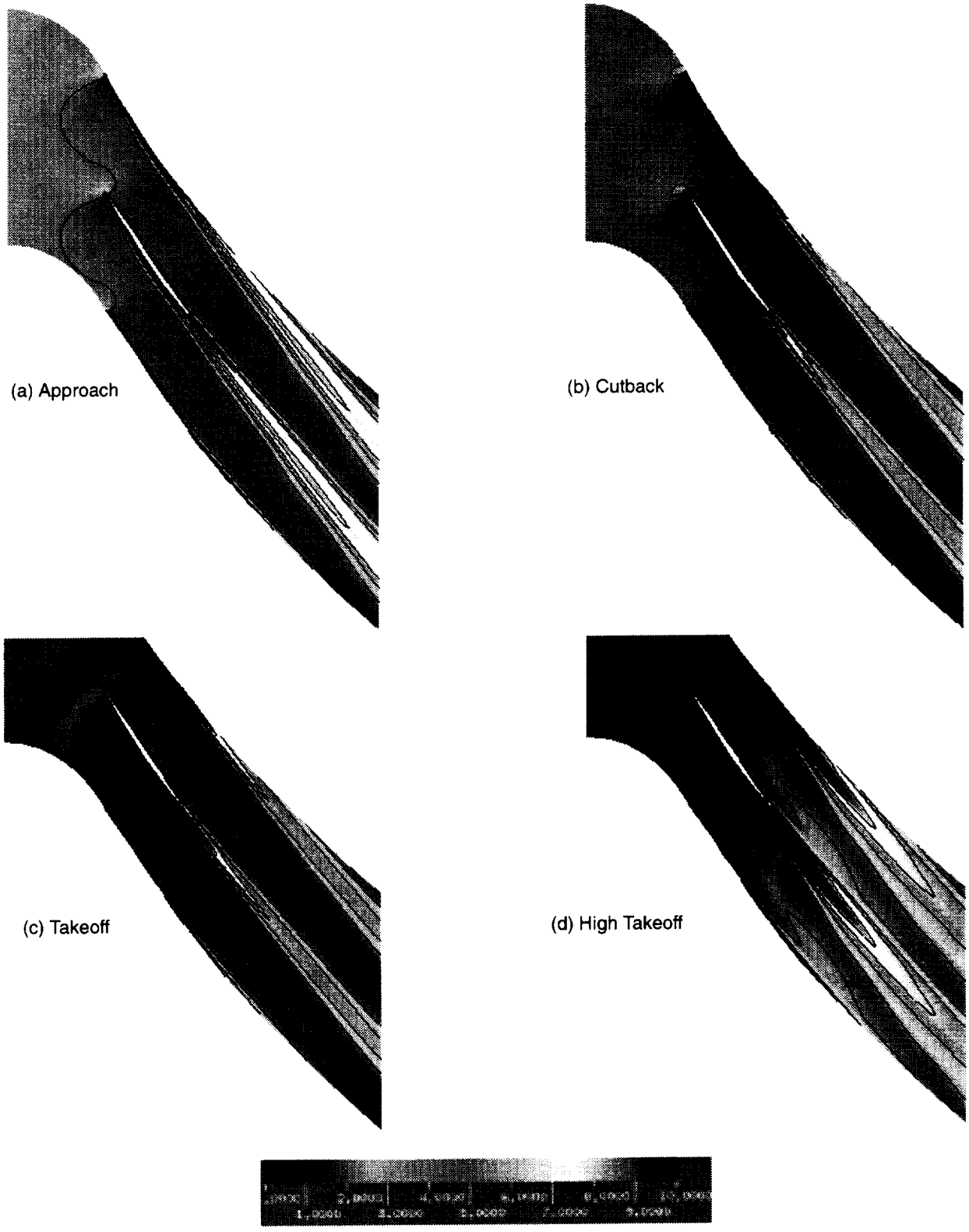

Figure 116. Turbulence Intensity at 95% Tip Radius for the Four Operating Points of the UPS Fan

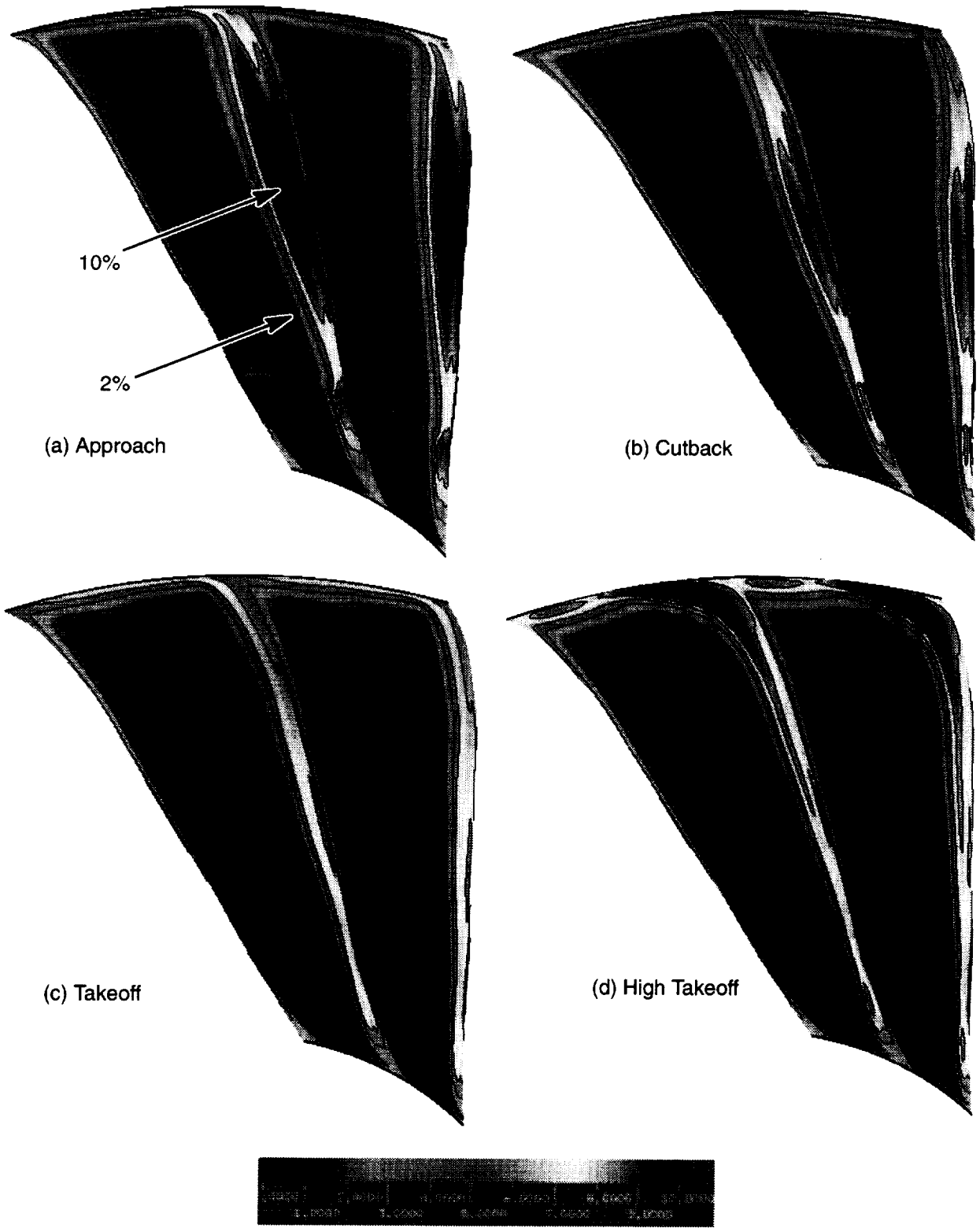

Figure 117. Cross-Stream Plot of Turbulence Intensity at the Splitter Leading Edge Axial Station for the Four UPS Fan Operating Points *Two fan blade passages are shown.*

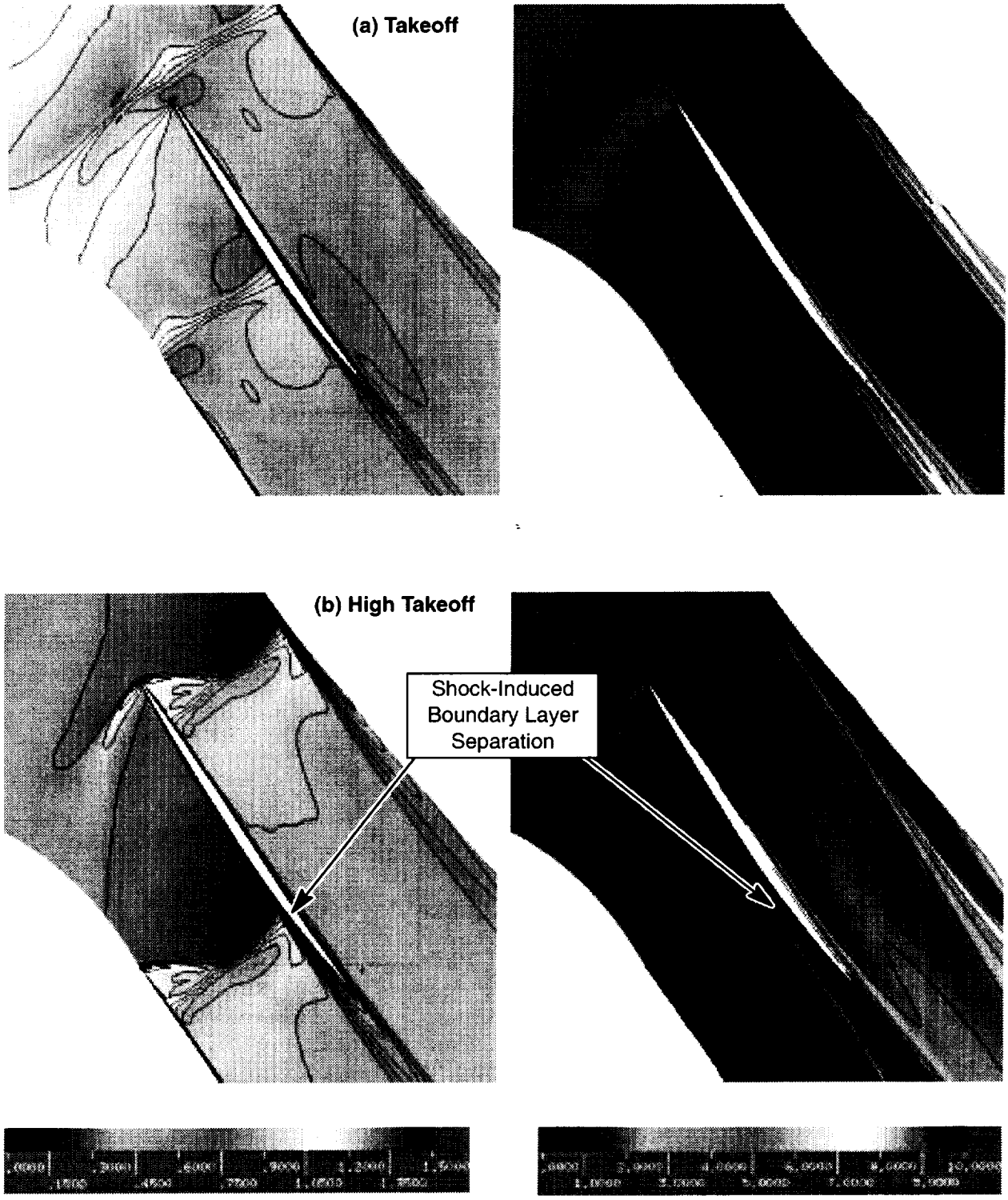

Figure 118. A Comparison of Relative Mach Number and Turbulence Intensity Contours at 95% of the Tip Radius for the UPS Fan Takeoff and High Takeoff Operating Points
Shock-induced boundary layer separation is responsible for the higher turbulence in the tip region at the high takeoff condition.

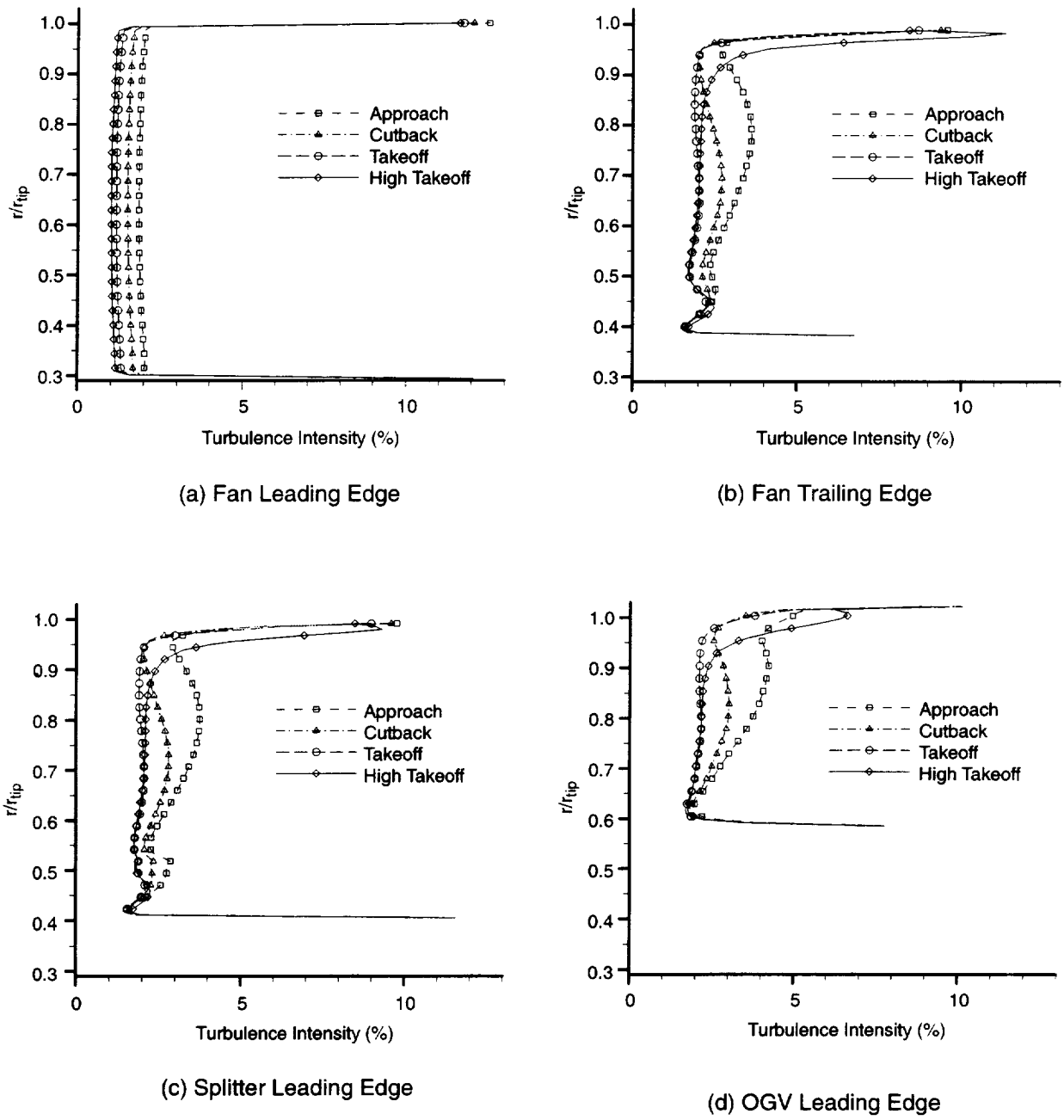

Figure 119. Radial Profiles of Circumferentially Averaged Turbulence Intensity at the Four Axial Stations from the UPS Fan CFD Simulations

to 2% as the flow passes through the fan, but then it remains fairly flat at this level except very near the tip. At the high takeoff condition, there is a similar increase across the fan. However, the effect of the shock-induced boundary layer separation toward the blade tip is clearly evident.

Effect of Turbulence Inlet Parameter – Since the precise level of turbulence at the inlet to the fan is not always known, a study was conducted to assess the effects of varying the turbulence inlet parameters on the predicted turbulence intensity profiles. All the results described in the previous discussion assumed 1% inlet turbulence intensity and an inlet eddy viscosity to molecular viscosity ratio of 100. To assess the effects of these values on the results, additional calculations were performed at the approach and high takeoff operating points.

A two-factor, two-level DOE (design of experiments) approach was used to systematically explore the parameter space. The two factors varied were the inlet turbulence intensity and the inlet eddy viscosity to molecular viscosity ratio. For each of these factors, two levels — one low (L) and one high (H) — were chosen. The chosen turbulence intensity levels were 1% and 2%; the chosen viscosity ratio levels were 100 and 200. A full factorial DOE exercising each of the four possible parameter permutations (LL, LH, HL, and HH) was then used to explore the parameter space.

The results of the DOE at the approach operating point are shown in Figure 120. Note that the first curve in these plots is the "baseline" result shown earlier. Figure 120(a) shows the circumferentially averaged radial profile of the turbulence intensity at the fan leading edge. At that station, the profiles are quite uniform, as expected, but the levels differ slightly from those specified at the inlet boundary. As explained previously, this discrepancy is due to the way the inlet turbulence intensity values are computed from the reference inlet velocity. Nevertheless, two distinct levels are apparent, roughly 2% and 3%. Figure 120(b) shows the corresponding profiles at the OGV leading edge. At that station, the profiles all appear similar and vary in level by only about 0.5%. So, despite the differences at the inlet, the results at the OGV leading edge do not change significantly.

Figure 121 shows the results of the DOE at the high takeoff operating point. Turbulence intensities at the fan leading edge are much closer to those specified at the inlet due to a better correspondence between the actual inlet velocity and the reference inlet velocity. Again, the results at the OGV leading-edge station appear quite similar, with differences in level less than those at the inlet.

4.7.2 Theory Data Comparisons: Acoustic Data

The 3D broadband noise prediction code has the following features:

- It allows for both dipole and quadrupole noise sources calculated as described by Mani (Reference 16) in each radial strip.
- The radial strips are chosen to conform to estimated spanwise correlation length scales of the incident turbulence.
- The 3D effects are calculated assuming that sources within each strip are completely correlated and sources in the strip are completely uncorrelated from those in other strips.
- The noise from each strip is calculated by considering a "top hat" profile of dipole and quadrupole sources in each strip (in the radial direction). Fourier–Bessel decomposition in the radial direction (applied to such "top hat" distributions) is used to decompose the full 3D problem into a sequence of "reduced" 2D problems to which the inlet-turbulence/blade-row noise calculation procedures of prior GE analyses are applied.

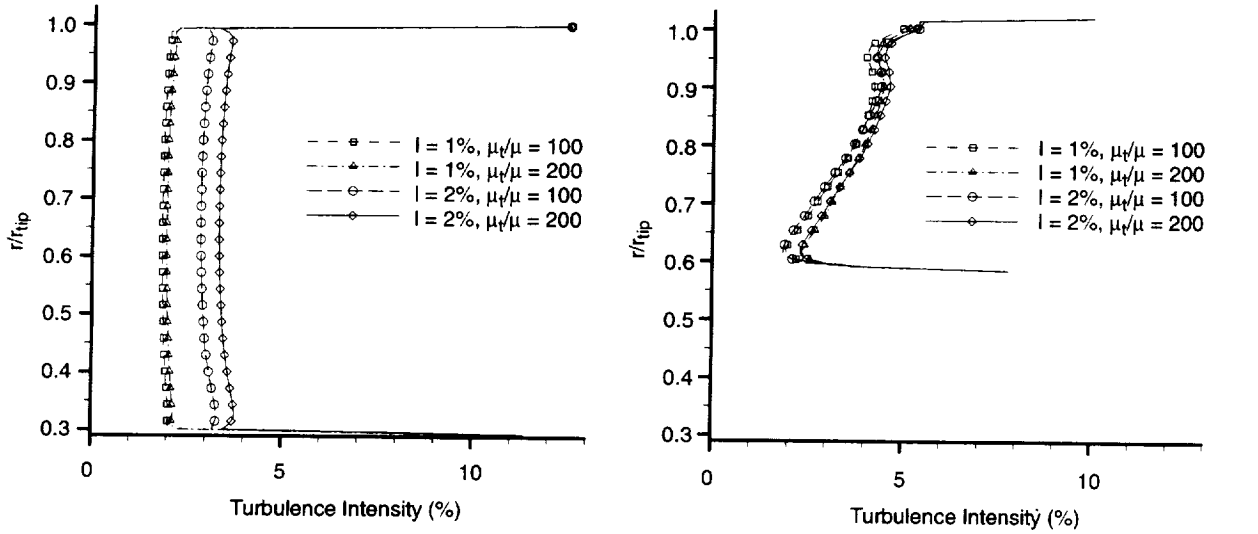

(a) Fan Leading Edge

(b) OGV Leading Edge

Figure 120. Results from Turbulence Inlet Parameter Sensitivity Study for the Approach Operating Point

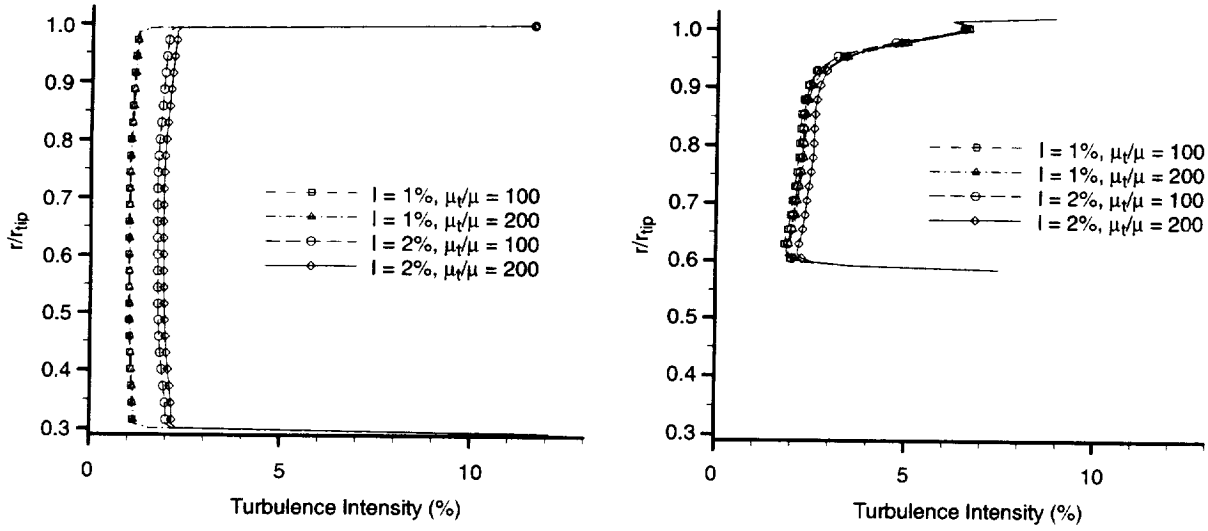

(a) Fan Leading Edge

(b) OGV Leading Edge

Figure 121. Results from Turbulence Inlet Parameter Sensitivity Study for the High Takeoff Operating Point

- Anisotropic turbulence is characterized by arbitrary streamwise and cross-stream intensities and length scales (in each radial strip). A four parameter description of inlet turbulence is adopted. Chordwise source noncompactness effects (as discussed in Reference 16 for dipole noise as well as for calculation of blade row locked potential flow fields) are included.
- Using a highly simplified actuator disk model (Reference 16), transmission loss of upstream-generated noise from vanes through the rotor and of downstream-generated noise from the rotor through the vanes is calculated. If for a particular strip, the rotor operates with supersonic inlet relative Mach number, all the vane generated upstream noise is assumed to be reflected.
- The directivity in each 1/3-octave-band based on cut-off ratio is calculated as described in Section 4.4 and the Addendum report. This model was developed by Hersh Acoustical Engineering (Rice) under subcontract to GE in the present program.
- The effects of acoustic treatment are included by means of the simple ray model of Rice outlined in Section 4.3 and detailed in the Addendum. While reasonable attenuations are predicted by this approach using realistic wall impedance for the various frequencies, no theory/data comparisons are presented in this report for this aspect of the model.

The computer program developed in this study has been applied to 10 cases, as listed in Table 12.

In the case of the Boeing data (Reference 74), turbulence and aerodynamic data were kindly supplied by Boeing. In the case of the GE experiments, 3D Reynolds-averaged Navier–Stokes (k–ε) CFD codes (as described earlier) were used to deduce turbulence incident on the rotor and stator. Turbulence was assumed to be isotropic and, since the current CFD is unable to yield integral length scales, Boeing 18-inch fan measurements of length scales were scaled and interpolated to enable calculations for the GEAE fan.

Table 12. Broadband Noise Code Validation Test Cases and Parameters

Fan Designation and Test Point	Tip Diameter, Inches	Tip Mach Number	1/3 Octave Band BPF	Hub/Tip Ratio	Total Pressure Ratio, Pitch
Boeing 18-in: 55% Speed, Low Load	17.93	0.637	35	0.4	1.115
Boeing 18-in: 55% Speed, High Load	17.93	0.637	35	0.4	1.133
Boeing 18-in: 70% Speed, Low Load	17.93	0.806	36	0.4	1.195
Boeing 18-in: 70% Speed, High Load	17.93	0.811	36	0.4	1.23
Boeing 18-in: 100% Speed, Low Load	17.93	1.165	37	0.4	1.464
Boeing 18-in: 100% Speed, High Load	17.93	1.161	37	0.4	1.557
Ups Fan, Approach (GE)	22	0.69	35	0.3	1.18
UPs Fan, Cutback (GE)	22	0.82	36	0.3	1.32
UPS Fan, Takeoff (GE)	22	0.98	36	0.3	1.47
UPS Fan, High Takeoff (GE)	22	1.07	37	0.3	1.62

Figures 122 through 124 show the theory/data comparisons for inlet and exit power spectra in the 1/3-octave bands of most interest (given that a scale-model fan is being tested). In these figures, in addition to the total theoretical prediction, the constituent elements of the theoretical prediction

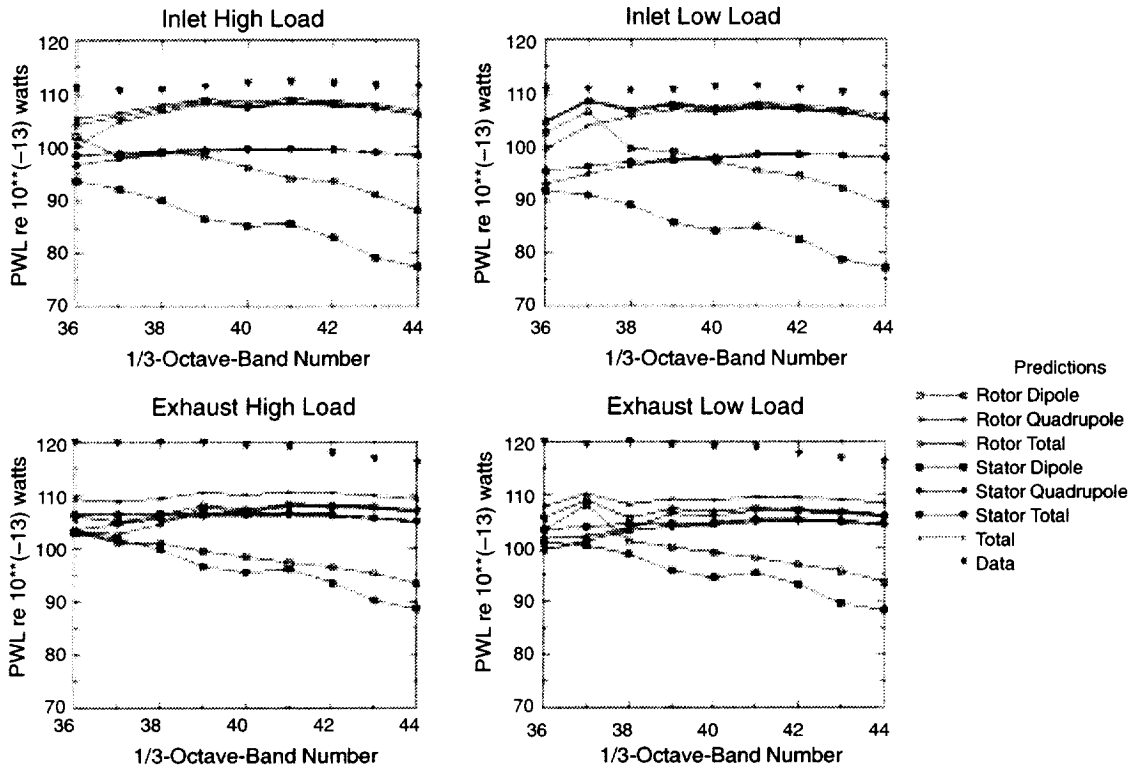

Figure 122. Boeing 18-in Fan, 55% Speed *Separate contributions to total theoretical shown.*

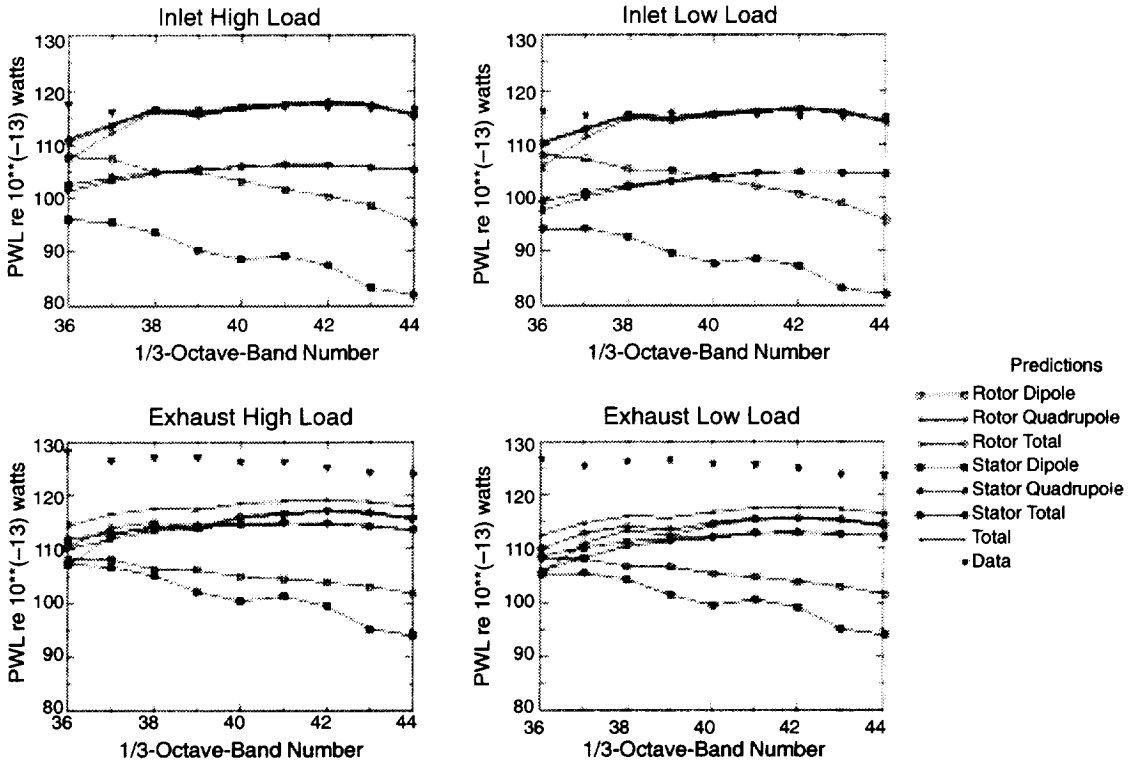

Figure 123. Boeing 18-in Fan, 70% Speed *Separate contributions to total theoretical shown.*

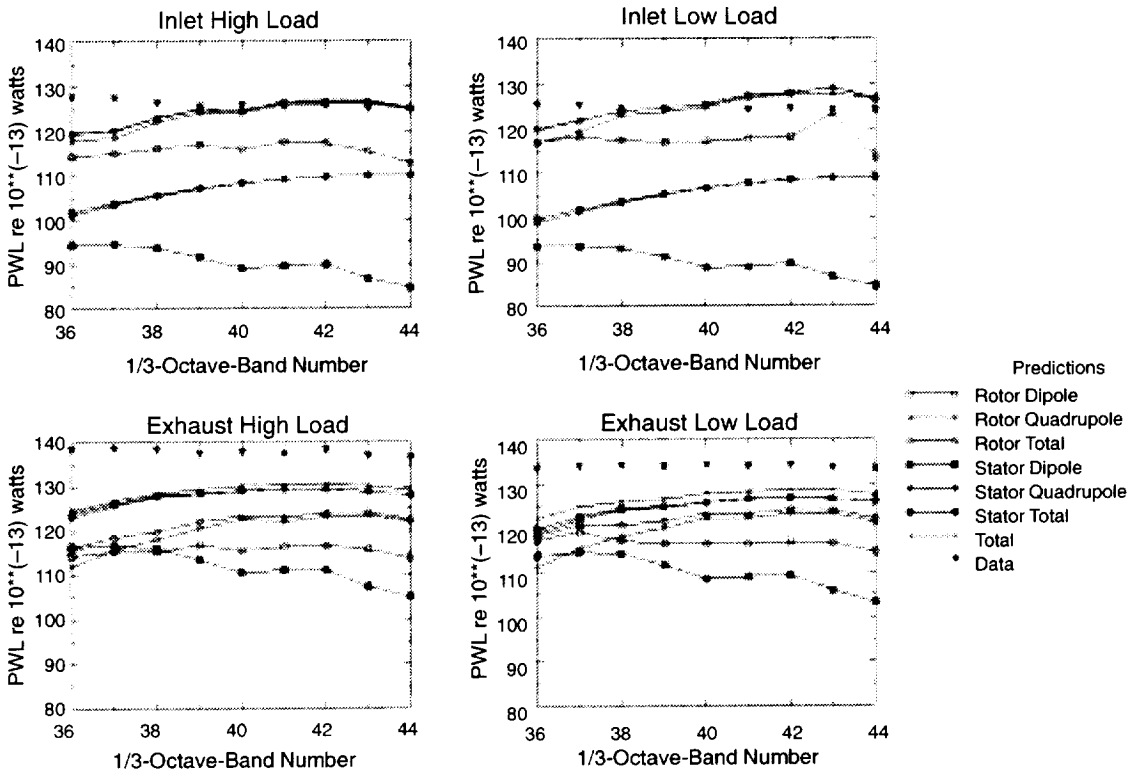

Figure 124. Boeing 18-in Fan, 100% Speed *Separate contributions to total theoretical shown.*

(rotor noise and stator noise) and within each case (dipole and quadrupole noise contributions) are shown. Concerning the noise constituents, on the inlet, rotor noise dominates — especially as the stator noise is attenuated in passing through the rotor. On the exhaust, the contributions of rotor and stator are (predicted to be) more nearly equal. Indeed, at 100% speed, stator noise contributions to exhaust noise exceed that of the rotor. The quadrupole noise is dominant, particularly at the higher frequencies and for the inlet. The quadrupole-to-dipole ratio appears higher for stators than for rotors because typically stators are more highly loaded (higher lift coefficient) than rotors.

Now consider the comparisons to data. The inlet predictions are roughly in accord with the data, but the exhaust noise is underpredicted significantly (by about 5 to 10 dB). In the case of 100% fan speed with inlet relative Mach numbers supersonic at the fan rotor tip, an alternative method of calculating rotor-locked potential flow fields at the rotor tip as contrasted to the shock-based method described in Mani (Reference 16) was employed. The alternate method is to carry out a potential flow calculation linearizing about the flowfield aft of the rotor. Since the discharge relative Mach number is invariably subsonic, no difficulties associated with divergent integrals as described in Reference 16 arise. The noise predicted by this linearization is the one that is employed in Figure 124.

Concerning the exhaust noise, there have been suggestions that the Boeing 18-inch fan noise facility has spurious sources in the exhaust due to presence of support struts at least up to around 4 kHz (octave band number 36).

In Figures 125 and 126, we examine effects of blade loading (or pressure ratio) at fixed speed. In this instance, the effects are well predicted for both inlet and exhaust noise, especially for the 55% and 70% speed cases. Small loading effects are measured and predicted. On one hand, loading

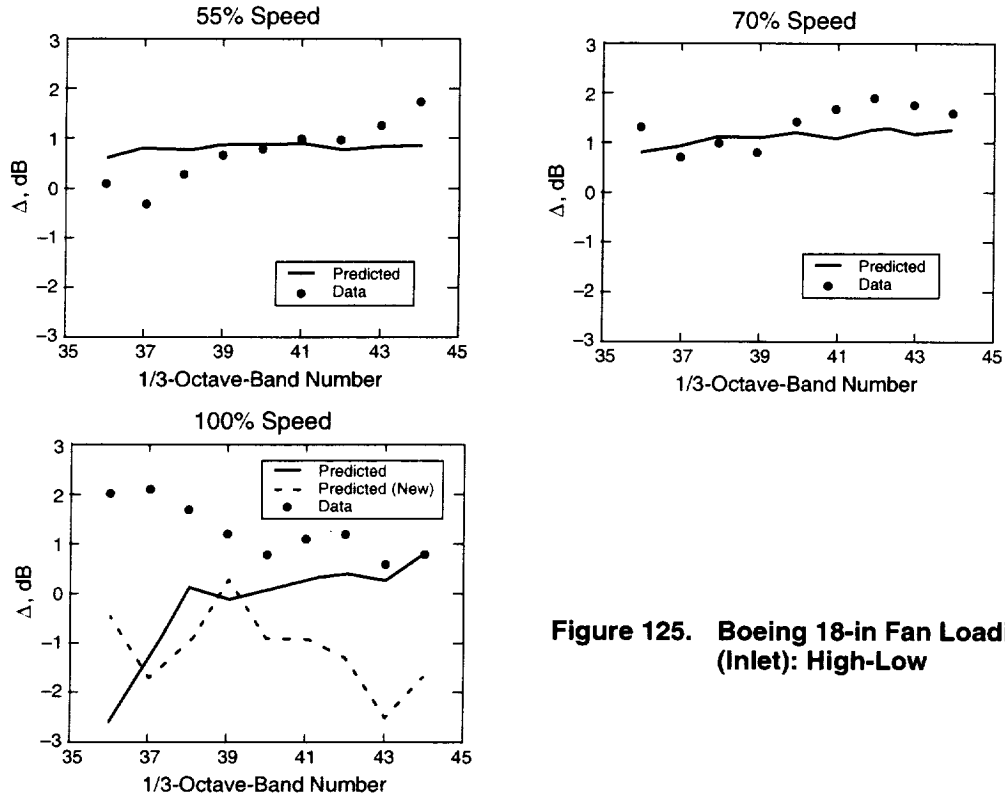

Figure 125. Boeing 18-in Fan Loading Effects (Inlet): High-Low

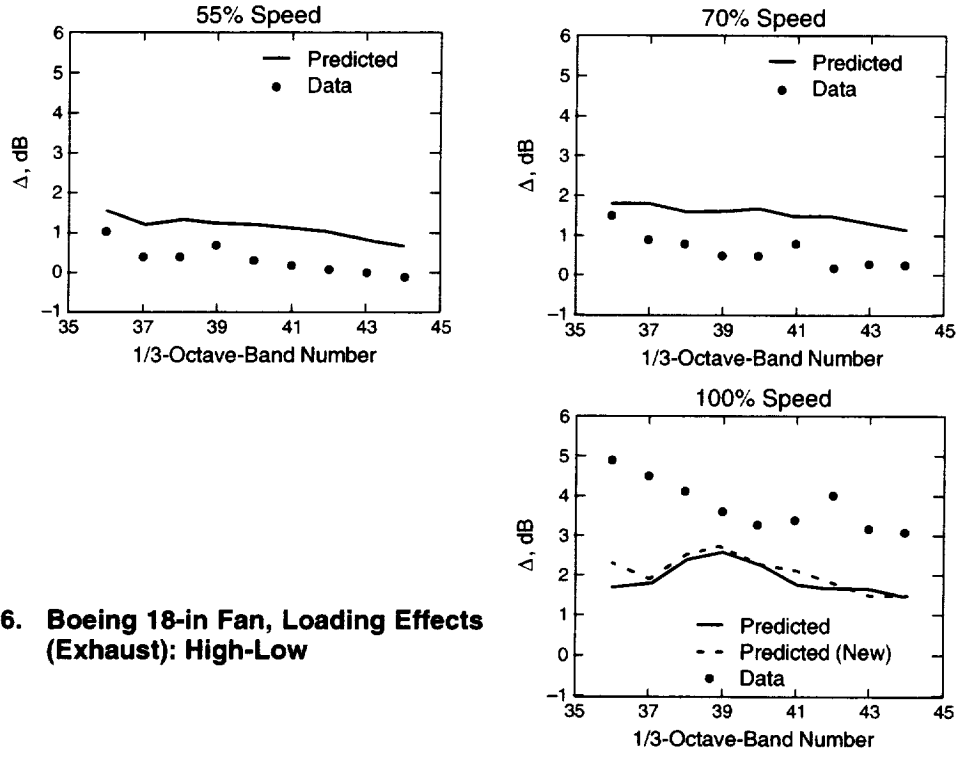

Figure 126. Boeing 18-in Fan, Loading Effects (Exhaust): High-Low

increases the strengths of the sources — both quadrupole and dipole, but the fan flow drops as loading increases, thus partially offsetting the gain in source strength.

In Figure 127, the effect of tip speed at the high load is evaluated. Again good agreement is indicated, especially with the new approach to rotor locked flowfield evaluation at the supersonic exit relative Mach number (at the tip) condition.

In Figure 128, comparison with the GE 22-inch fan (UPS) data are shown for the total noise power spectra. It appears that there is somewhat better agreement between the theory and data than that of the Boeing data. In Figure 129, as contrasted to Figure 128, we have recalculated the noise by subdividing the outermost tip strip in the case of Figure 128 into two strips — each one-half the radial extent of the single strip used in Figure 128. This approach amounts to halving the spanwise correlation length used to calculate noise in the tip region. The predictions (compared to Figure 128) are biased towards the higher frequencies. The agreement with data is of the same extent as in Figure 128. Figures 128 and 129 do indicate a weakness of the current prediction method: the results depend on choice of spanwise strips. This result is not surprising since we assume that the spanwise partitioning is according to the spanwise length scales.

In Figure 130 the predicted sound pressure level directivity of the sound is compared with prediction. Except for the sharp diminution due to the refraction by the exhaust jet predicted by the theory, agreement (at 20-ft sideline) is reasonable.

4.8 Conclusions and Recommendations

The 2D CFD study based on unsteady, linear, harmonic Euler approaches validates the concept of increasing prominence of quadrupole sources in the case of a blade row interacting with incoming turbulence as frequency and blade loading increase, particularly for inlet noise. It would be useful to extend the calculations to higher wheel tip Mach numbers and higher pressure ratios than were considered herein.

Three-dimensional effects modeling presents some challenges in an annular duct due to the need to consider Bessel functions of high order. Without consideration of an annular duct, noise is likely to be overestimated. We have not found a satisfactory formulation based on homogenous turbulence wherein the results are insensitive to choice of strips in the spanwise direction.

It appears quite adequate to parameterize the acoustic power based on cut-off ratio, and improvements may not be needed in the area of prediction of directivity for broadband noise. However, the bulk of theory/data assessments conducted here are for the PWL spectrum, and there is a need to evaluate directivity predictions further.

A very satisfactory representation of anisotropic turbulence is shown to be feasible, and the four parameters needed to achieve the representation are deducible from single-point turbulence measurements.

Modifications were made to the semiempirical broadband self-noise model of Mugridge. The Mugridge empirical spectrum shape assumption was eliminated, and a direct calculation of spectral shape is based on key rotor and stator airfoil turbulence properties at the trailing edge. The model improvements result in much lower self-noise levels than originally predicted, consistent with the observations that interaction noise sources dominate the measured spectra. Direct verification of the self-noise component, however, requires specialized experiments.

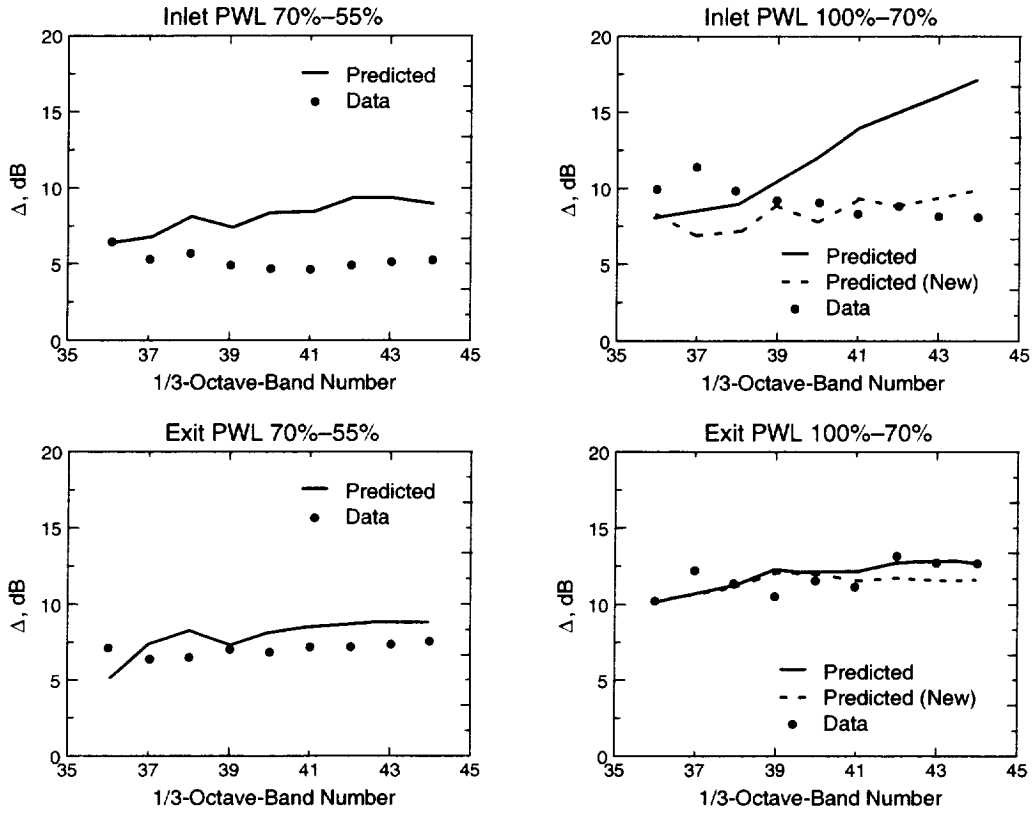

Figure 127. Boeing 18-in Fan, Speed Effects (High Load)

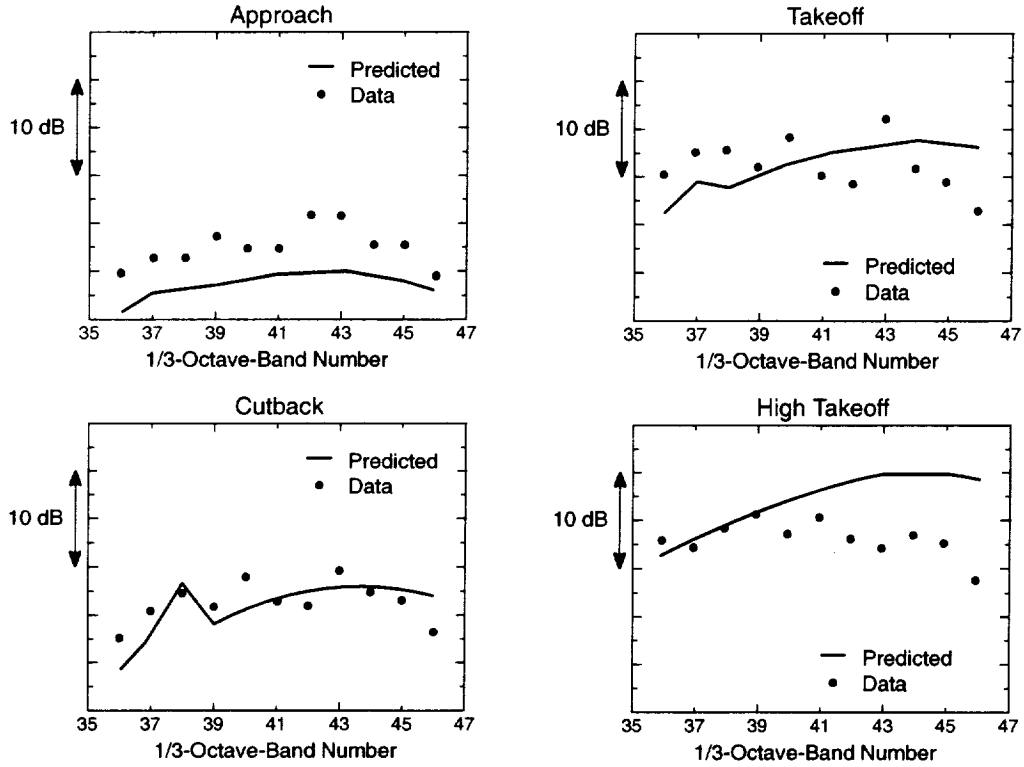

Figure 128. UPS Total Noise: Relative PWL in dB

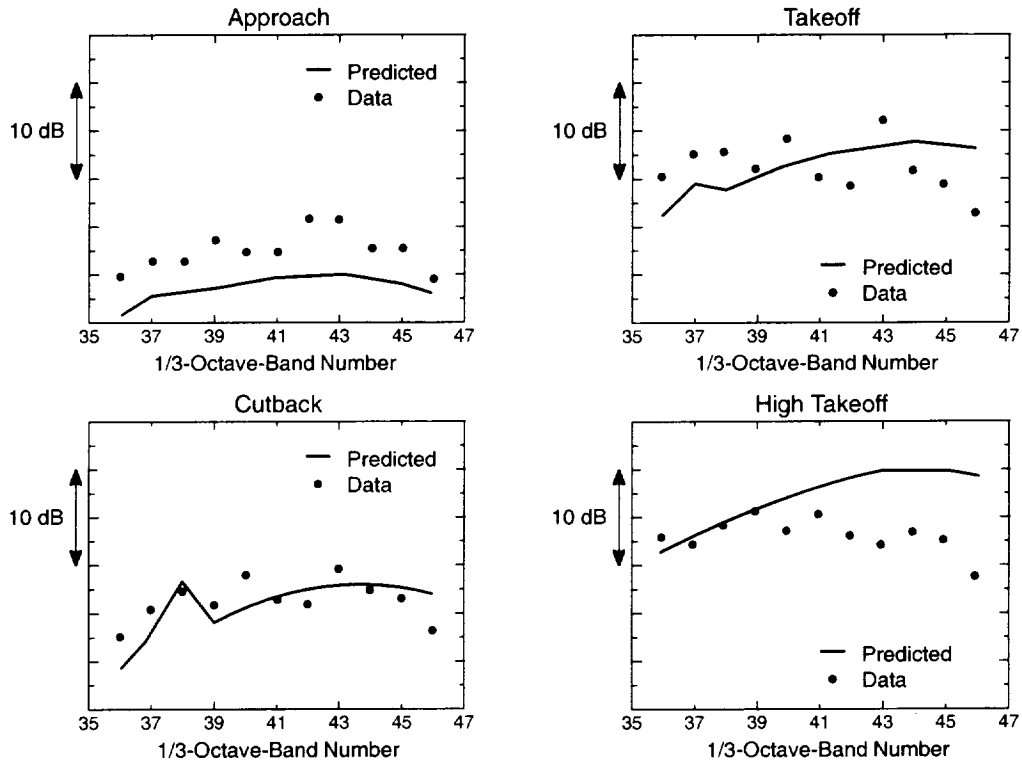

Figure 129. UPS Total Noise: Relative PWL in dB (1 Extra Strip at Tip)

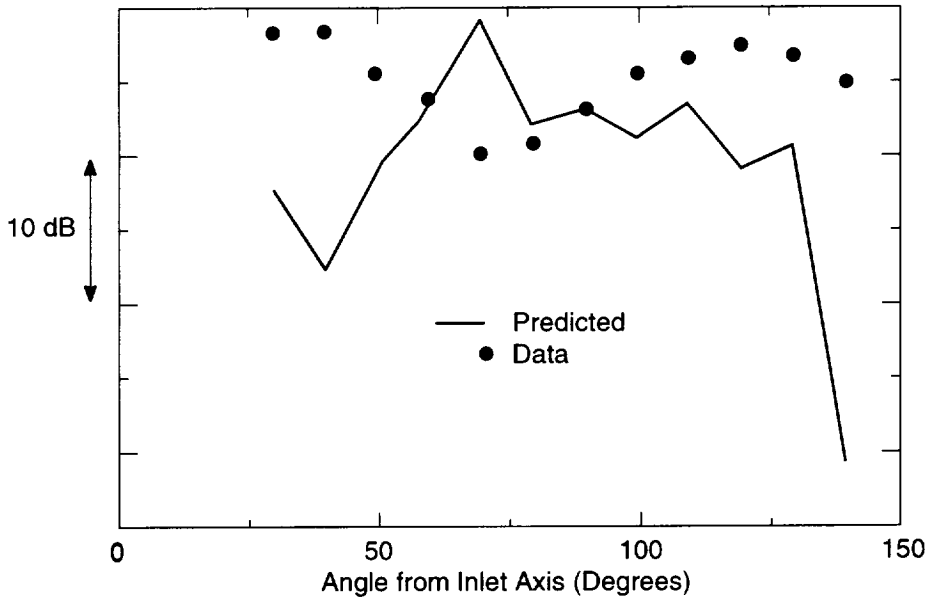

Figure 130. UPS Directivity at Approach, 16 kHz; Relative SPL at 20-ft Sea Level

Three-dimensional, Reynolds-averaged, Navier–Stokes (RANS) is a useful tool in broadband noise prediction, and it is an essential element if predictions are to be made prior to acquiring wake flow survey measurements. Length scales needed to predict noise are not currently available in any obvious sense from the RANS results, and this area needs further evaluation. The theory/data comparisons for 10 cases evaluated provide reasonable agreement given possible sources of error. Variations of noise with tip speed and pressure ratio (at fixed speed) are well predicted. As noted earlier, the bulk of the theory/data comparisons are for the PWL spectrum, and more exploration is needed for directivity effects and effects of treated walls. The theory outlined in Section 4.3, page 88, does incorporate an approximate method of studying treated walls.

5.0 Fan MPT Noise Model Development

5.1 Introduction

Multiple pure tone (MPT) or "buzz saw" noise is generated in fans with supersonic tip speeds and occurs at the part-speed cutback condition associated with takeoff. It is a significant component of both cabin and environmental noise associated with the fan.

A typical fan map is shown in Figure 131. In the region to the left of the dashed line, the flow is unstarted; to the right it is started. The differing shock patterns for started and unstarted flow near a fan tip are illustrated in Figure 132. When the flow is unstarted, the strength and position of the upstream-running normal shock becomes very sensitive to blade geometry variations, as illustrated in Figure 133. When the flow is started, this sensitivity is greatly reduced. These geometry variations typically arise from manufacturing tolerances. Stagger angle differences of as small as 0.1° can give rise to significant MPT noise. The resulting azimuthal pressure field and subsequent Fourier decomposition for a typical fan are shown in Figures 134 and 135. It can be clearly seen that there are now discrete tones lower than the blade passing frequency.

The objective of the work presented here is to develop a model for predicting the MPT's from specified blade variations. This is described in Section 5.2, page 148. The method of running the CFD code for transonic fans is described in Section 5.3, page 148. The work presented in Sections 5.4 and 5.5, pages 149 and 157, determines the applicability of 2D or 3D CFD methods for predicting

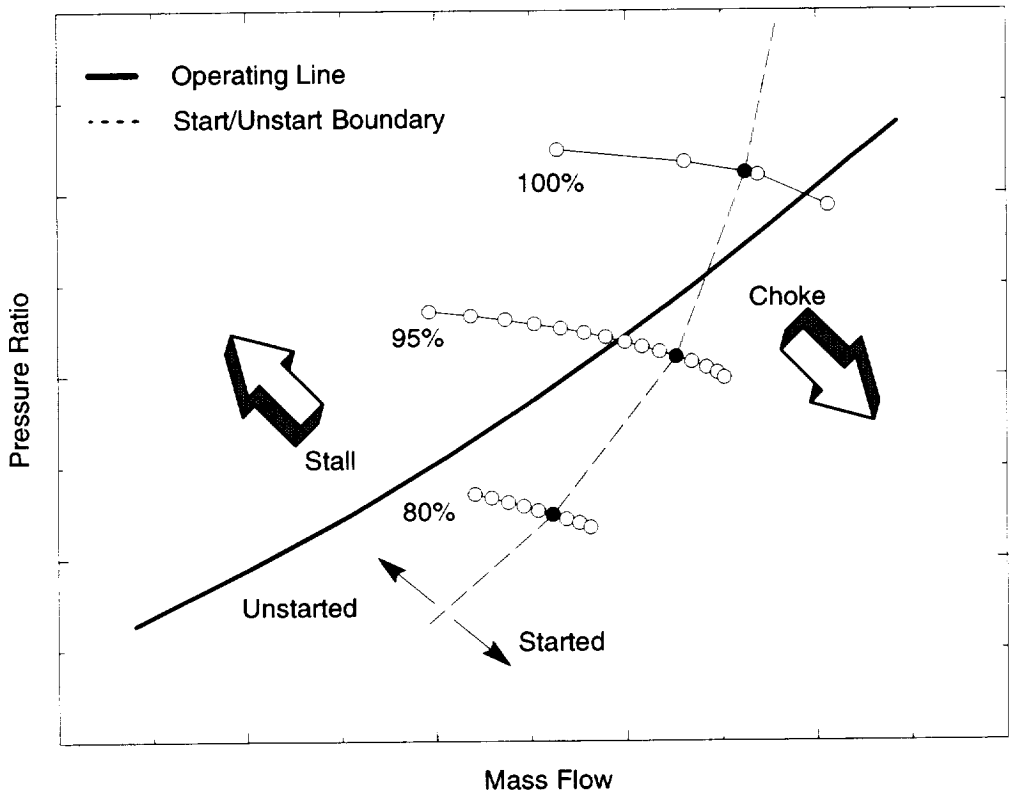

Figure 131. Typical Fan Map

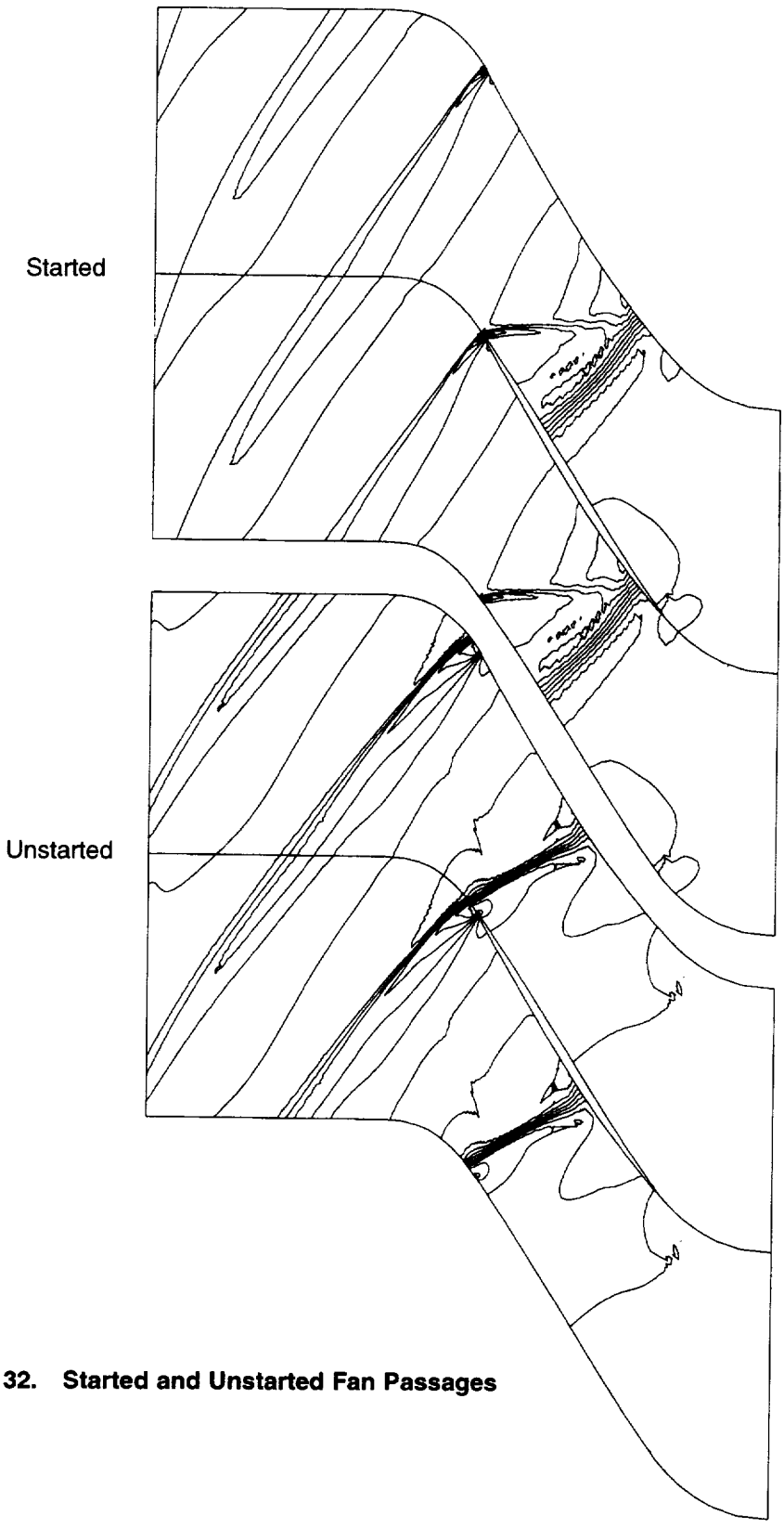

Figure 132. Started and Unstarted Fan Passages

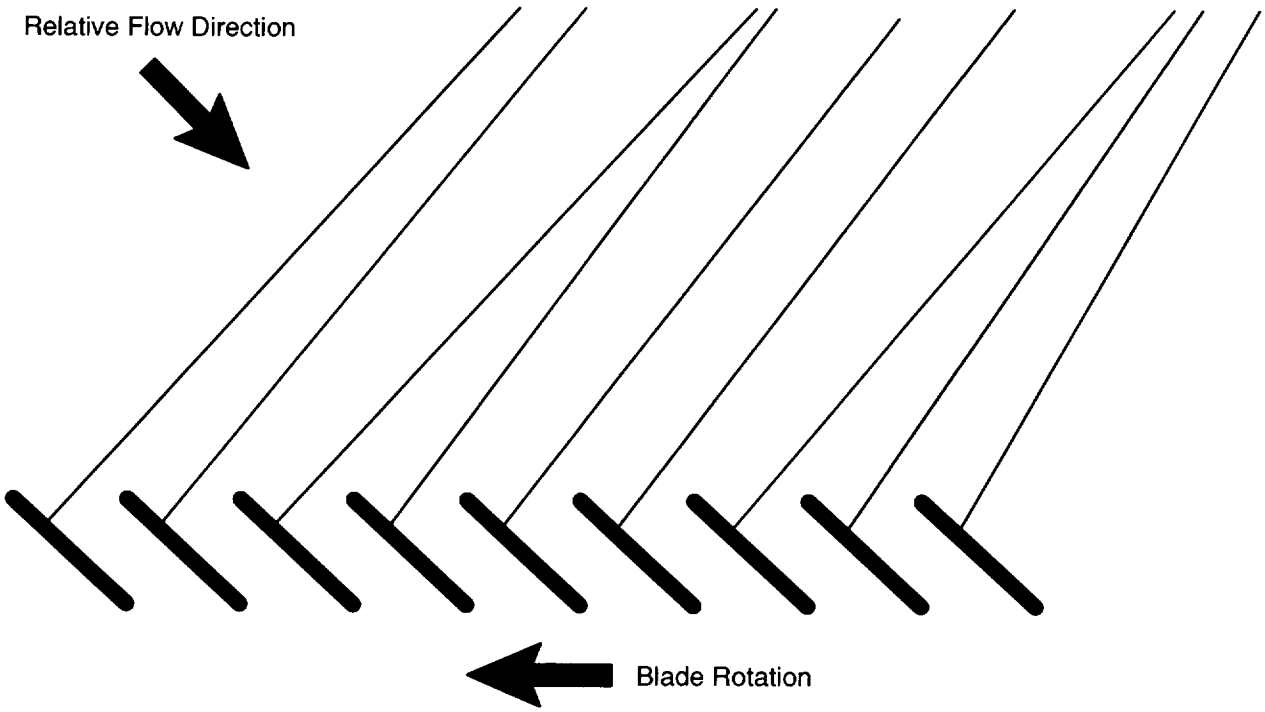

Figure 133. Schematic of Shock Structure at Fan Tip

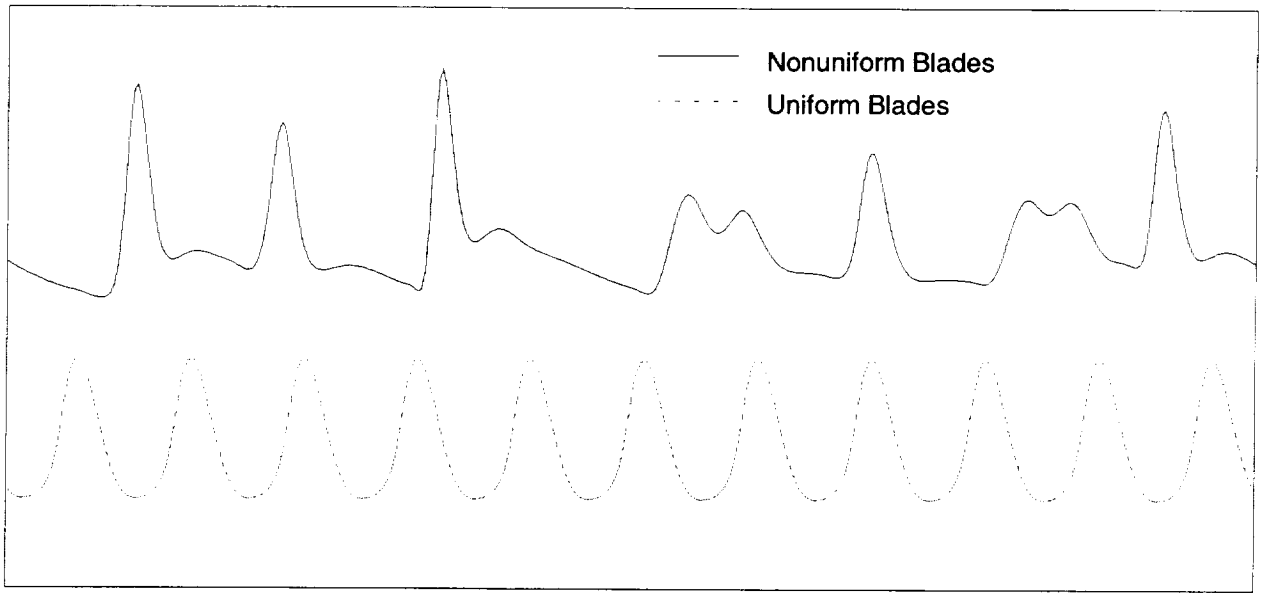

Figure 134. Circumferential Pressure Field

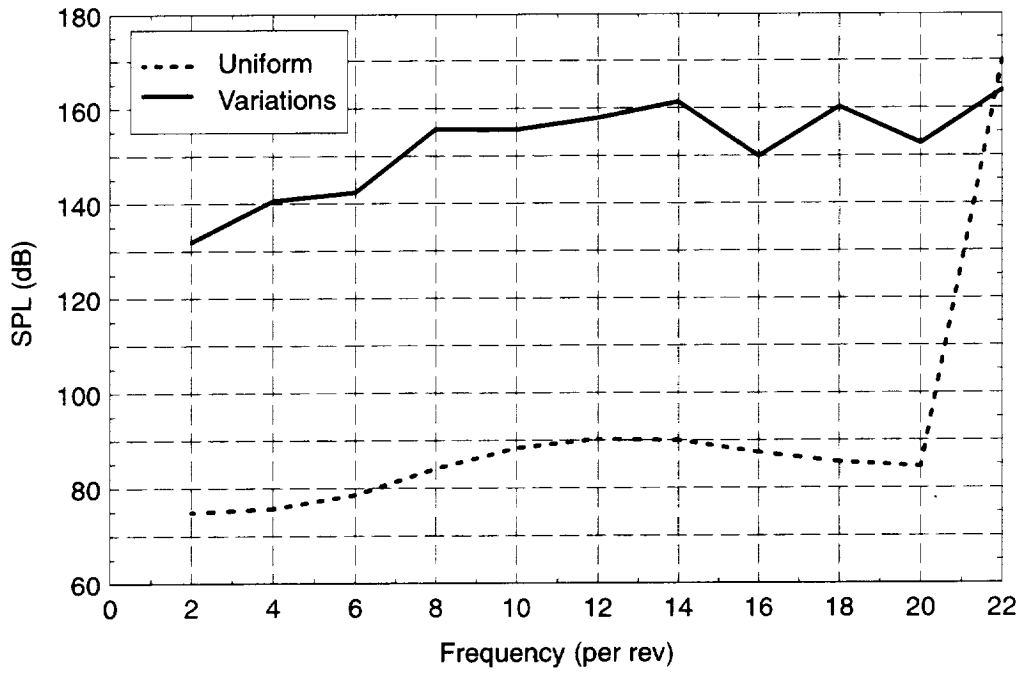

Figure 135. Fourier Modes

MPT's. For a variety of reasons, 3D methods are deemed necessary. Using the 3D CFD method, the effect of different geometry variations is examined in Section 5.6, page 166.

The generation of MPT's depends primarily on stagger and camber variations. Development of a superposition model coupled with a multipassage CFD prediction is described in Section 5.7, page 169. A circumferential pressure distribution, together with details of the geometry variations, are input to the SUPERPOSE program. The output comprises the predicted MPT spectra. Validation of this model against CFD solutions and test data is described in Section 5.8 and 5.9, pages 172 and 173. Two methods for reducing MPT noise are described and evaluated in Section 5.10, page 176.

5.2 Objectives

The objective of this effort was to develop and validate a CFD based model and associated computer code for predicting multiple pure-tone noise of fans operating at supersonic relative Mach number. The intention is to be able to predict the modal content of the azimuthal pressure field some distance upstream of the fan. It is not the intention to predict the farfield noise level.

5.3 Numerical Simulations of Fans

The operating line for a fan describes the relationship between pressure rise and mass flow as the rotational speed of the fan is changed. The accurate simulation of a fan requires that the CFD calculation is on the same operating line as the actual fan.

With an inviscid calculation, due to the lack of viscous blockage, the mass flow is usually too high at a given speed, and the back pressure of the fan is then adjusted to place the simulation on the operating line.

With a viscous calculation the back pressure still has to be adjusted to place the fan on the operating line but by a smaller amount than the inviscid calculation. The position on the operating line will

usually be closer to the test data than the inviscid prediction. Figure 136 illustrates the effect of changing the back pressure for viscous and inviscid solutions on an advanced fan typical of modern design. In this case, the viscous solution also included the effect of tip clearance and the engine splitter. Figure 137 compares the surface pressures near the tip of the fan of the two 3D CFD solutions on the operating line. The results illustrate good agreement between the inviscid and viscous solutions both in shock position and strength.

The numerical simulation of a fan can be performed in two or three dimensions. Two-dimensional solutions offer the benefit of reduced computational cost at the expense of accuracy. Sections 5.4 and 5.5, pages 149 and 157, evaluate the relative merits of two- and three-dimensional methods for predicting the MPT phenomena.

5.4 Two-Dimensional CFD Predictions

5.4.1 CFD Code description

A quasi-3D code employing the explicit solution algorithm (References 34, 35, 75, and 36) has been developed within GE (References 77, 78, and 79). It employs an unstructured, mixed mesh of triangular and quadrilateral elements with the variables stored at grid nodes. Automatic, solution-based mesh refinement is used to resolve features accurately. A multigrid solution acceleration scheme is employed.

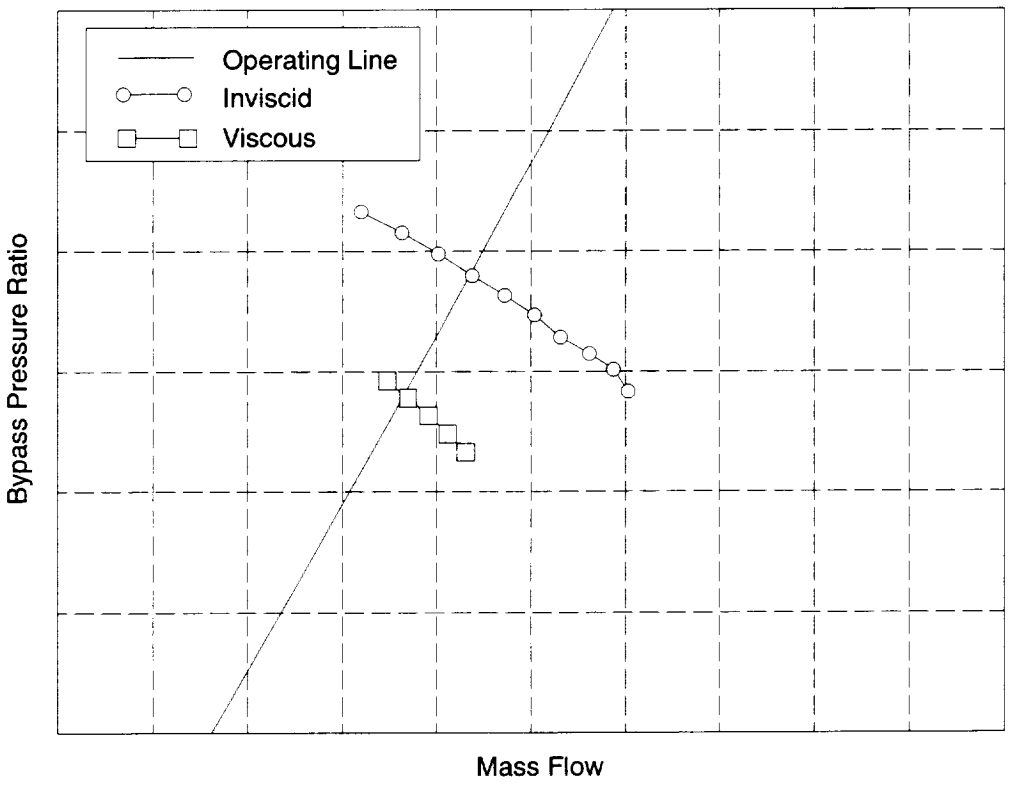

Figure 136. Constant Speed Lines for Inviscid and Viscous Solutions

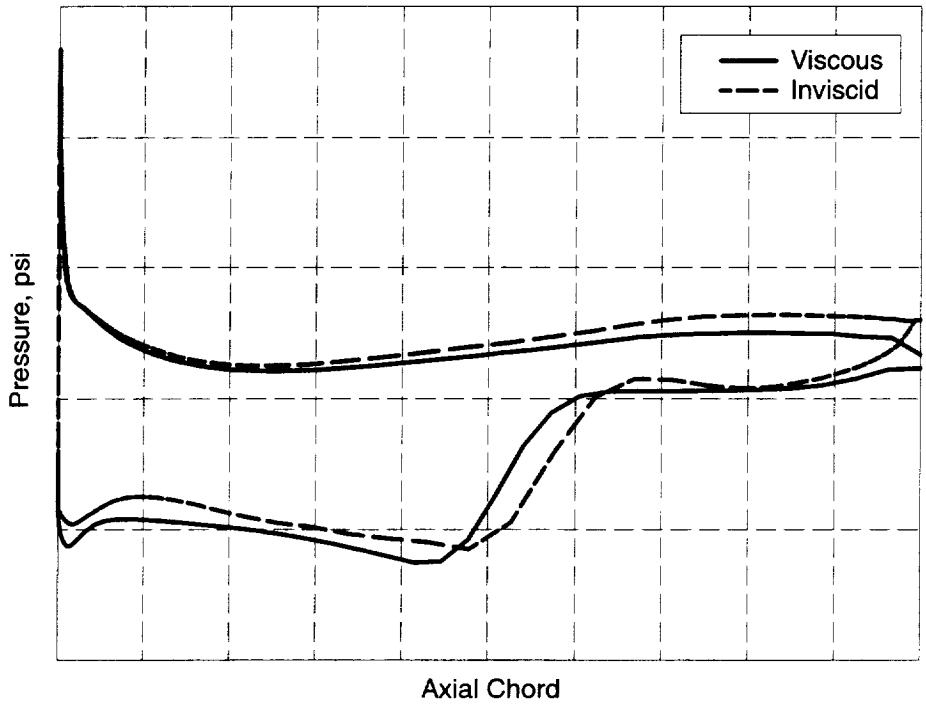

Figure 137. Surface Pressure Comparison

5.4.2 Mesh Generation

The computational mesh for multiple blade passages is built by combining meshes generated for single passages. The mesh for a single passage is generated by first modifying the geometry to reflect the change of interest; the actual mesh is then generated using an elliptic procedure.

5.4.3 Preliminary 2D Predictions of MPT Noise

Initially, the ability of the 2D CFD code to predict the MPT phenomena was investigated. A cascade of nine blades (¼ annulus) was created for a typical modern fan geometry (AF2). A random stagger change of ±0.25° was applied to each blade. The actual angle rotations are listed in Table 13.

Table 13. Blade Rotation Angles

Blade Number	Angle Rotation
1	+0.00°
2	–0.10°
3	+0.20°
4	–0.25°
5	–0.20°
6	+0.10°
7	+0.15°
8	+0.05°
9	+0.25°

A back pressure of 18.8 psi was chosen to be sure that all the passages would be unstarted. Figure 138 shows the resulting solution, and Figure 139 shows the pressure distribution on the upstream boundary for the uniform and nonuniform blade row. The associated Fourier coefficients are shown in Figure 140. Note that, since only one-forth of the annulus is considered, the minimum frequency is 4/rev. These results illustrate the ability of the 2D CFD code to qualitatively predict the MPT phenomena.

The modal content of the circumferential pressure field at various axial locations is shown in Figure 141. Near the leading edge, the largest mode is the one associated with the blade passing frequency. The relative amplitudes of the lower frequency modes increases further upstream. This illustrates the redistribution of acoustic energy from the blade passing frequency to lower frequencies.

5.4.4 Multiple Solutions

The CFD code has the ability to restart from an existing solution. This is useful when adjusting boundary conditions and helps reduce computer time requirements. This ability was used to move the single-passage solution from an unstarted to started mode by adjusting the back pressure. In doing this, it was observed that close to the pressure ratio when the fan first unstarts (exit pressure of 18.4 psi) two solutions were possible. These were obtained depending if the CFD code was started form an unstarted or started initial guess.

This multiple-solution phenomena is illustrated by the fan map in Figure 142. Here, for a range of speeds, the back pressure has been cycled between the started and unstarted flow regimes.

The effect of stagger angle variations in the non-unique solution region was examined. The same nine bladed non-uniform cascade was run but at an exit pressure of 18.4 psi. At this pressure a started and unstarted solution had been found to exist for a single passage. For the multiple-passage case, it was found that the solutions again depend significantly on the initial guess. Figure 143 illustrates the solutions for two different initial guesses. The upstream pressure distributions are shown in Figure 144 and the plot of the Fourier modes in Figure 145.

The existence of multiple solutions for a single airfoil begs the question of multiple solutions existing within the same cascade of identical airfoils; that is, is it possible to have started and

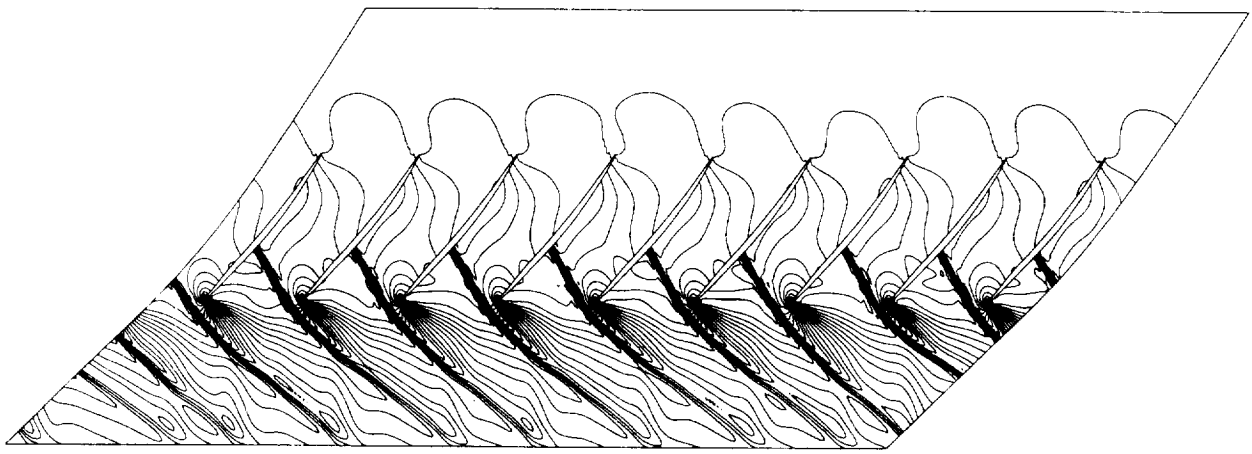

Figure 138. Isobars for Nonuniform Cascade, P_{exit} = 18.8

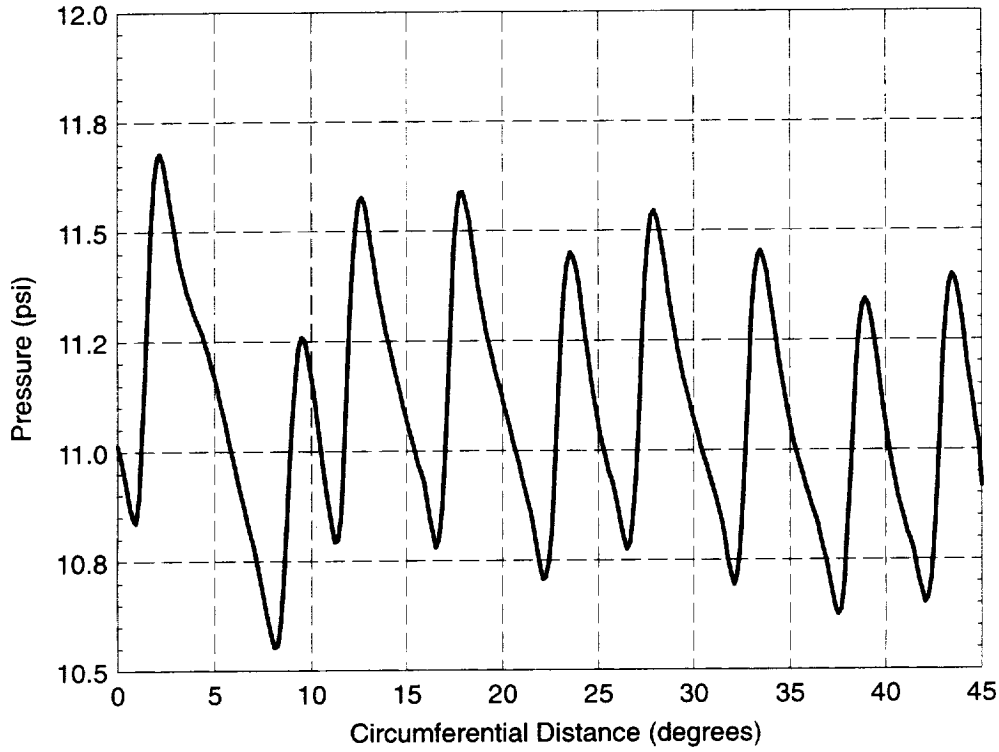

Figure 139. Pressure Distribution Along Upstream Boundary for Nonuniform Cascade, P_{exit} = 18.8

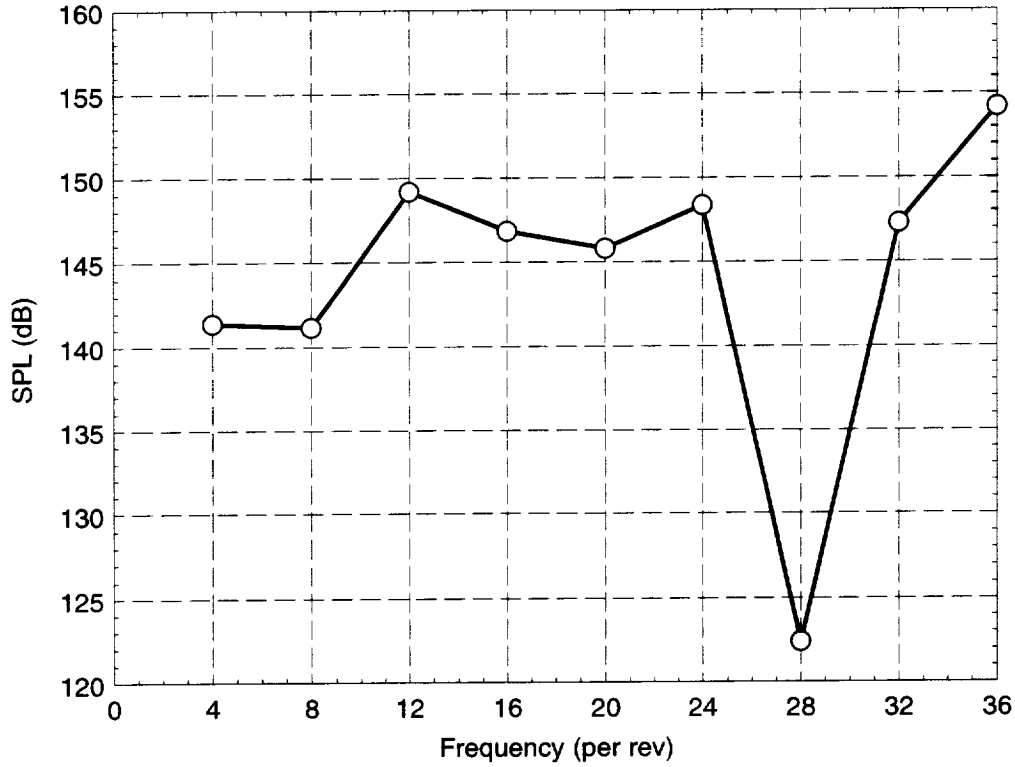

Figure 140. Amplitudes of Fourier Modes, P_{exit} = 18.8

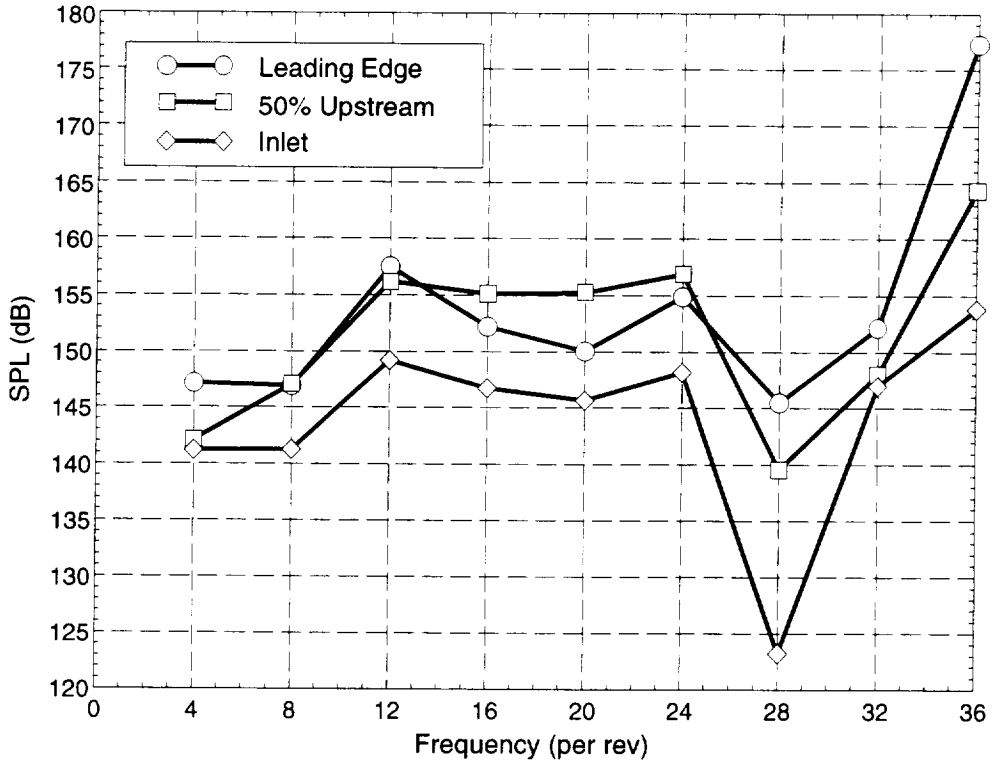

Figure 141. Development of Pressure Field, P_{exit} = 18.8

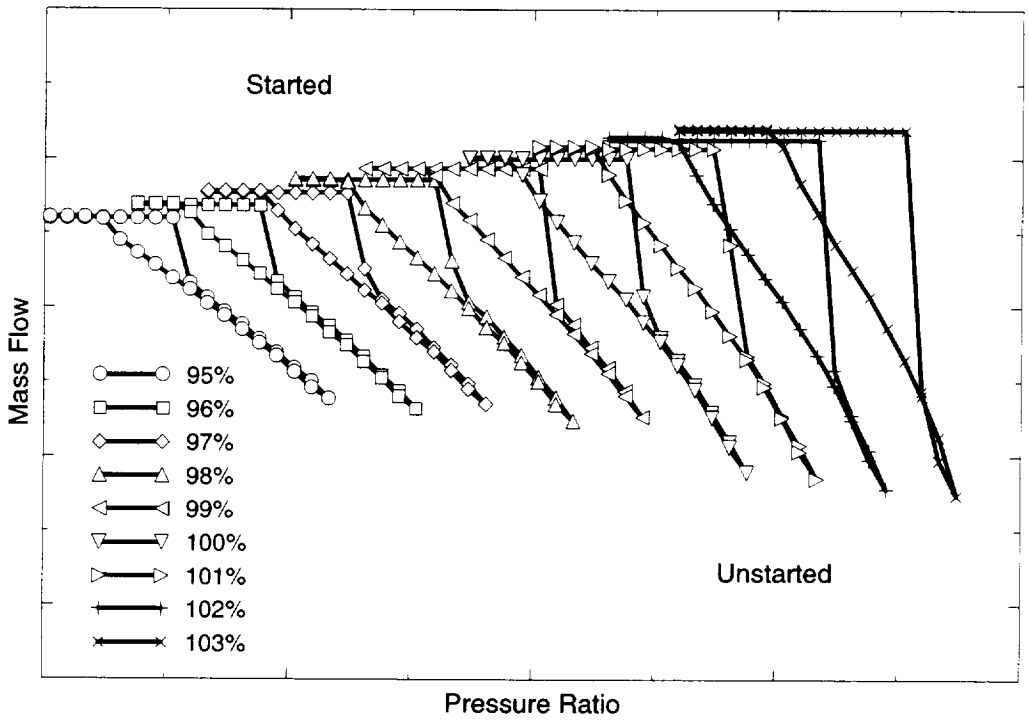

Figure 142. Hysteresis Effect for AF2

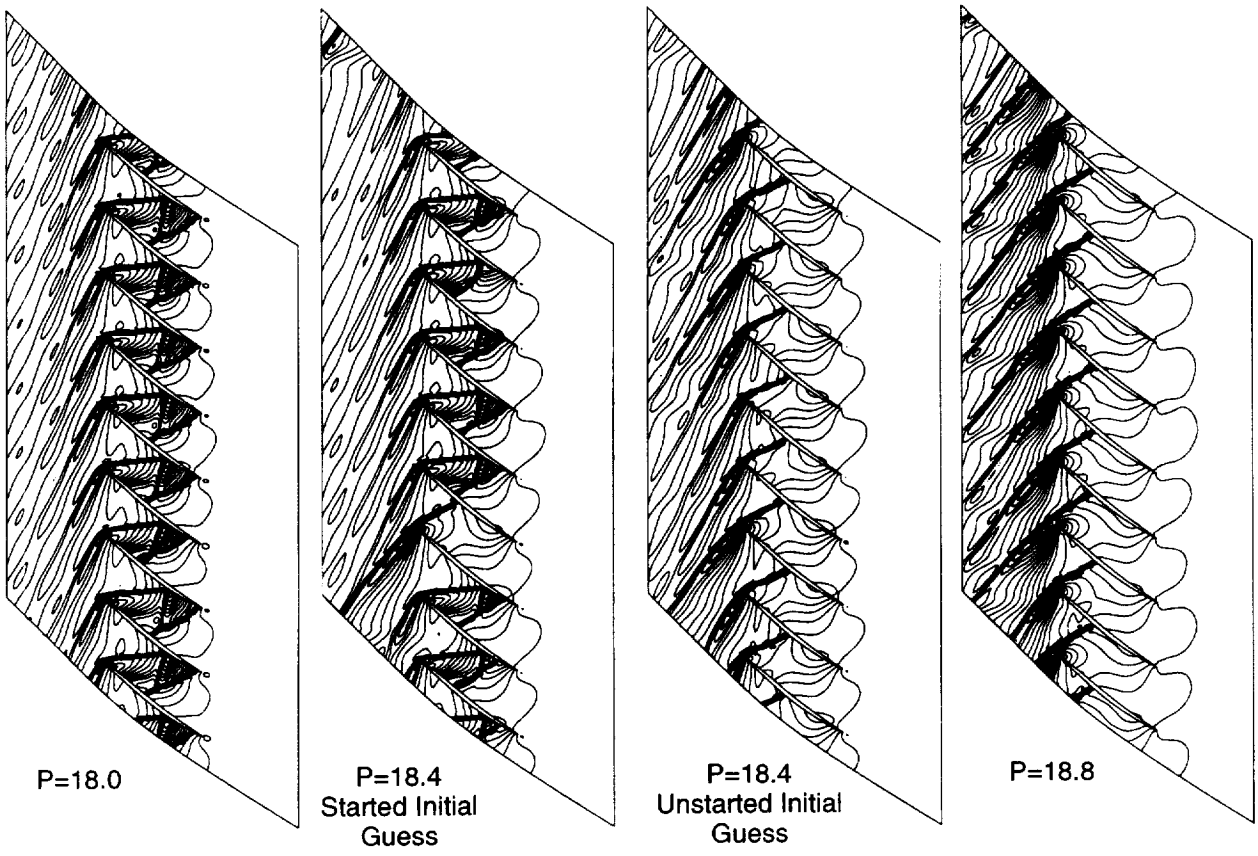

Figure 143. Effect of Initial Guess on Isobars, Nonuniform Cascade P_{exit} = 18.40

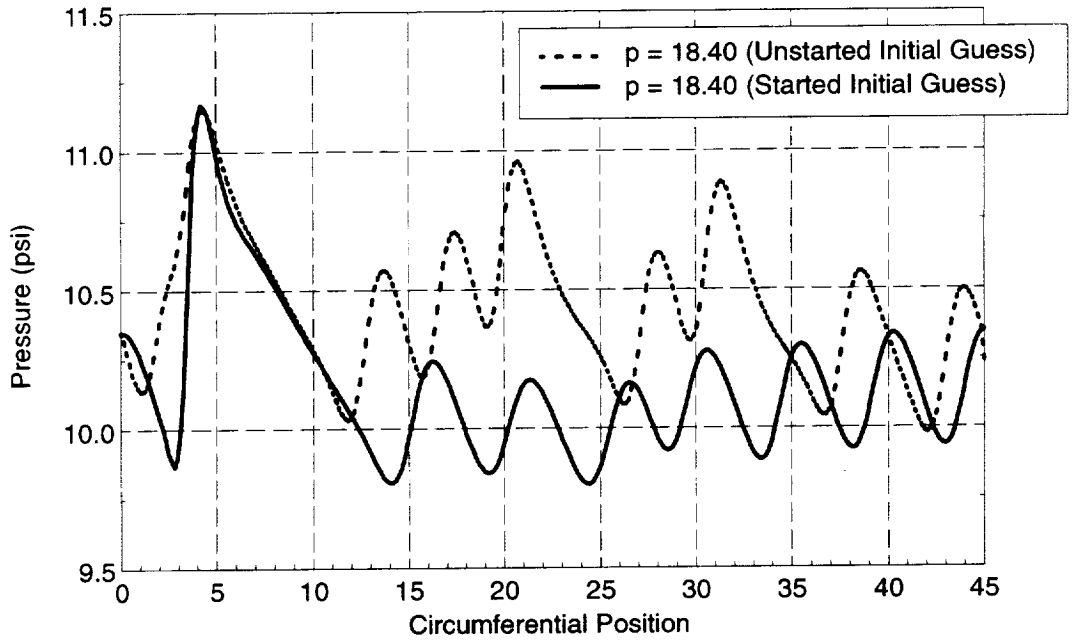

Figure 144. Effect of Initial Guess on Upstream Pressure Distribution, Nonuniform Cascade, P_{exit} = 18.4

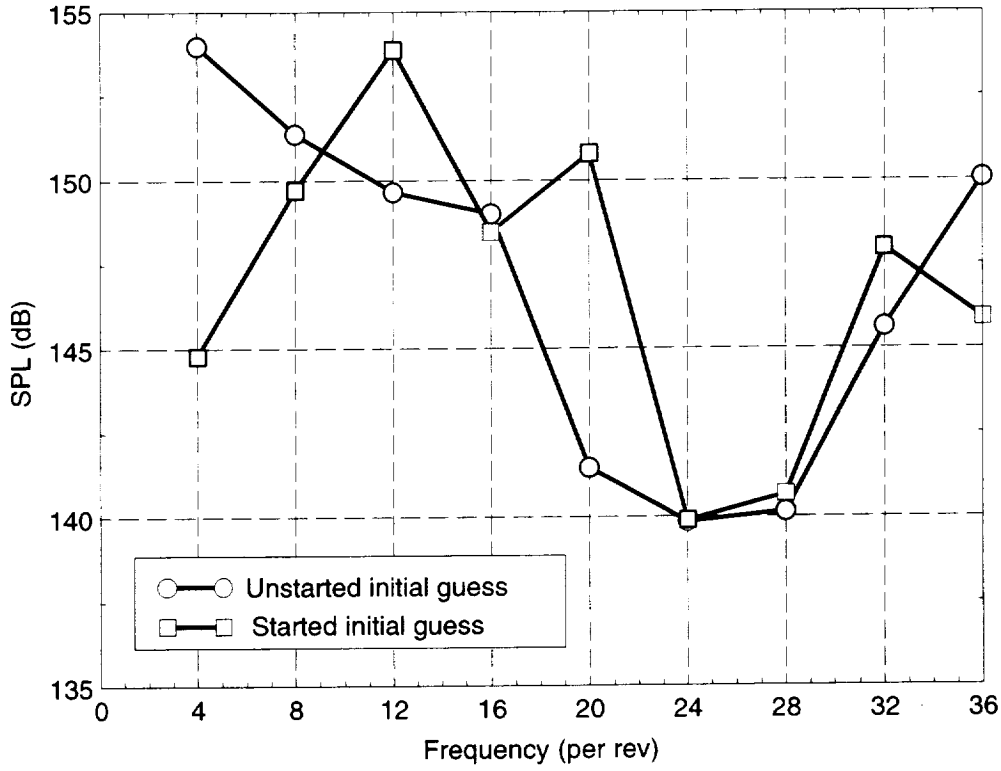

Figure 145. Effect of Initial Guess on Fourier Modes, Nonuniform Cascade P_{exit} = 18.4

unstarted passages within the same cascade? To see if this was possible, a cascade of nine identical airfoils was generated. A nonuniform exit pressure was then prescribed to force a mixture of started and unstarted passages. The resultant shock pattern is shown in Figure 146. Starting from this solution, the exit pressure was made uniform, and the solver was restarted. The resultant solution is shown in Figure 147. The plot of the amplitude of the Fourier modes is also shown in Figure 145. This demonstrates that it is possible for multiple solutions, and hence the MPT phenomena, to exist in a cascade of identical airfoils.

5.4.5 Conclusions

It may be concluded from this quasi-3D investigation that:

- The 2D CFD code can qualitatively predict the MPT phenomena.
- A new mechanism for MPT noise generation has been discovered. The generation comes form a mix of started and unstarted passages.
- Multiple solutions can exist for pressure ratios close to the start/unstart boundary.
- Due to the potential existence of multiple solutions, it is possible to generate MPT noise from a fan with identical blades.

Because three-dimensional effects may significantly affect these results and conclusions, a similar investigation is performed in Section 5.5, page 157, using a three-dimensional CFD code.

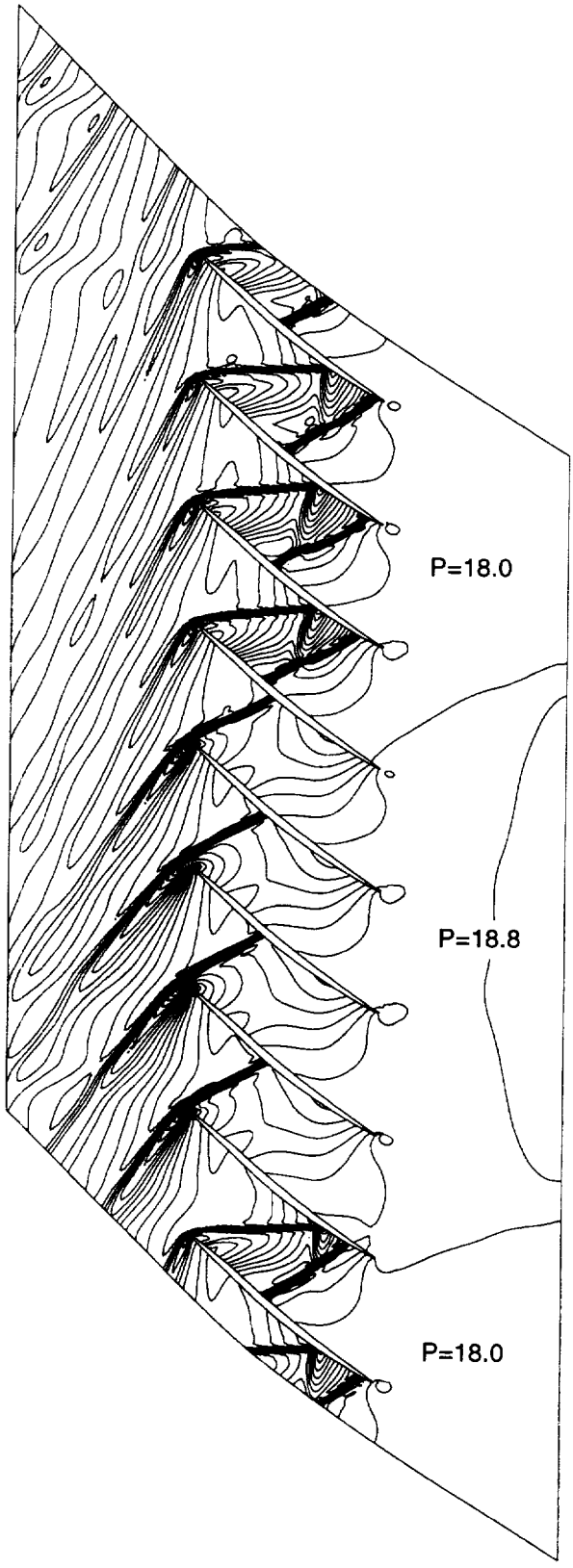

Figure 146. Nonuniform Exit Pressure

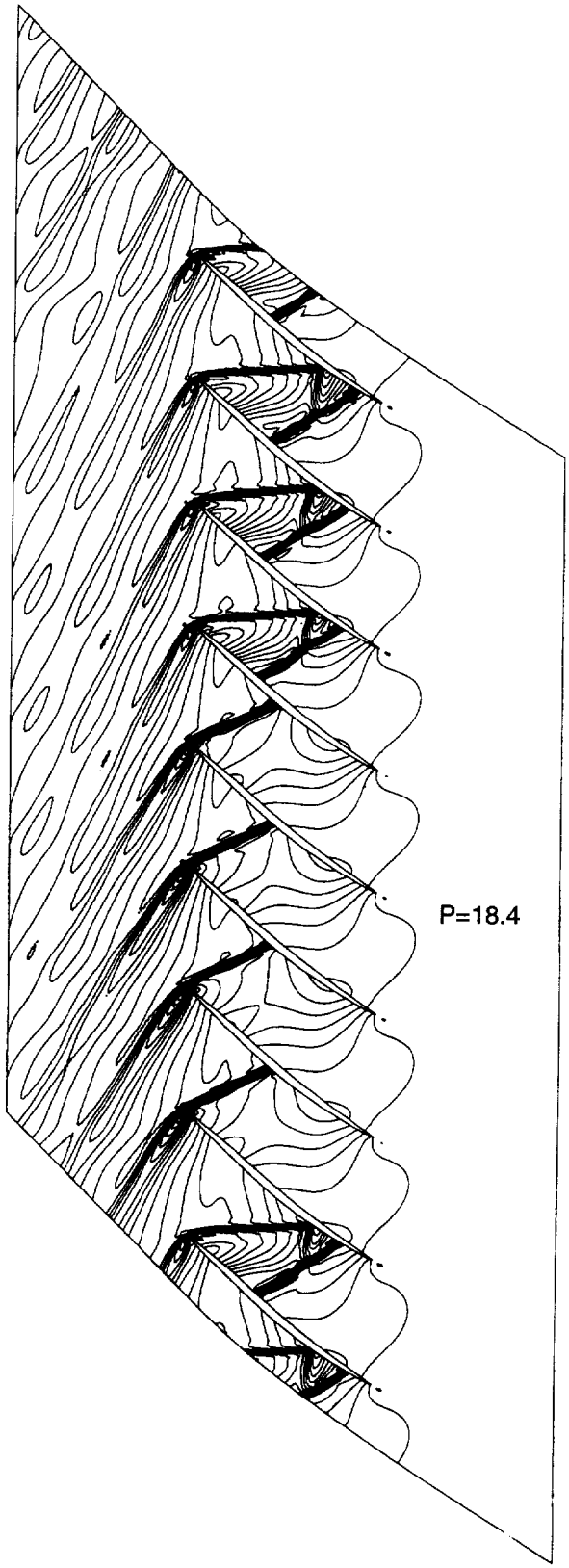

Figure 147. Uniform Exit Pressure

5.5 Three-Dimensional CFD Predictions

5.5.1 Code Description

The basic steady-flow-solution algorithm is unremarkable. It is described in References 34, 35, 75, and 36 and has been in use at GE for many years. Solutions are computed in a reference frame rotating with the blade row. Absolute flow quantities are computed in this relative frame.

A cell-centered, finite-volume scheme with central differences is used on a structured multi-block mesh of hexahedral elements.

Numerical smoothing is provided by a standard, adaptive second/fourth-order smoother driven by a second-order pressure switch in each grid direction.

The solution is obtained via a multistep Runge–Kutta explicit time-marching scheme with convergence acceleration via local time steps, residual averaging, and V-cycle or W-cycle multigrid.

5.5.2 Mesh Generation

Because a number of 3D multiple passage solutions with dissimilar blades were planned, a suitable mesh generation scheme had to be developed. Note that the change in blade shape was assumed to be uniform in the spanwise direction; thus, if a change in stagger angle of 0.2° was required then all sections were rotated 0.2°.

The algorithm begins with a single-passage mesh where the blade is in the center of the passage, as illustrated for a simple biconvex cascade in Figure 148. The blade shape is now modified by changing, for example, the stagger angle. As these changes at the leading and trailing edges may be larger than the near-wall spacing, an invalid mesh may result as shown in Figure 149. To counteract this possibility, a simple LaPlacian smoother is invoked on each spanwise grid surface to smooth the position changes on the blade surface into the mesh. The smoothed mesh is shown in Figure 150. A position change of zero is specified in the inlet, exit, and periodic boundaries. To generate the final multiple-passage mesh, a number of single-passage meshes are combined to form the final multi-block mesh. An example mesh for a three-passage case is shown in Figure 151. Typical CPU (central processor unit) time to generate an 11-passage mesh with 2,500,000 mesh points is one minute on an HP C180 workstation. Generation of the original single-passage mesh takes approximately five CPU minutes.

5.5.3 Multiple Solutions

The two-dimensional solutions showed evidence of multiple solutions as the back pressure was cycled between the started and unstarted flow regime. This phenomena was not observed in the three-dimensional solutions.

5.5.4 Viscous Effects

It was initially unclear whether or not the effects of viscosity and tip clearance were needed for accurate prediction of the MPT noise phenomena. A viscous solution requires significantly more computer resources than an inviscid calculation, adding the effects of tip clearance and the engine splitter further increases the requirements. As a number of part annulus solutions were planned, there was concern that the cost of a full viscous solution may be prohibitive.

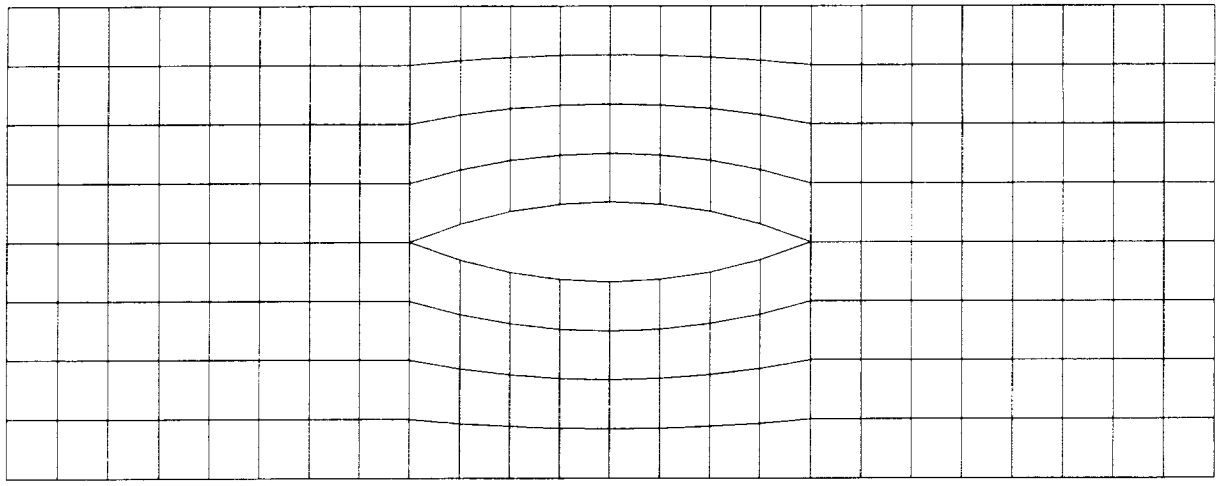

Figure 148. Initial Mesh

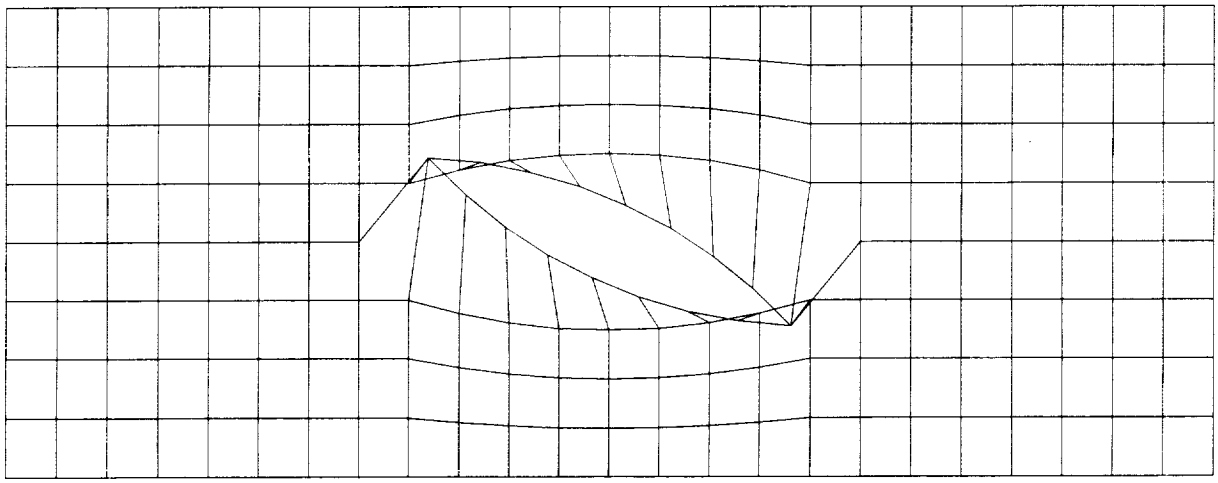

Figure 149. Modified Blade Geometry

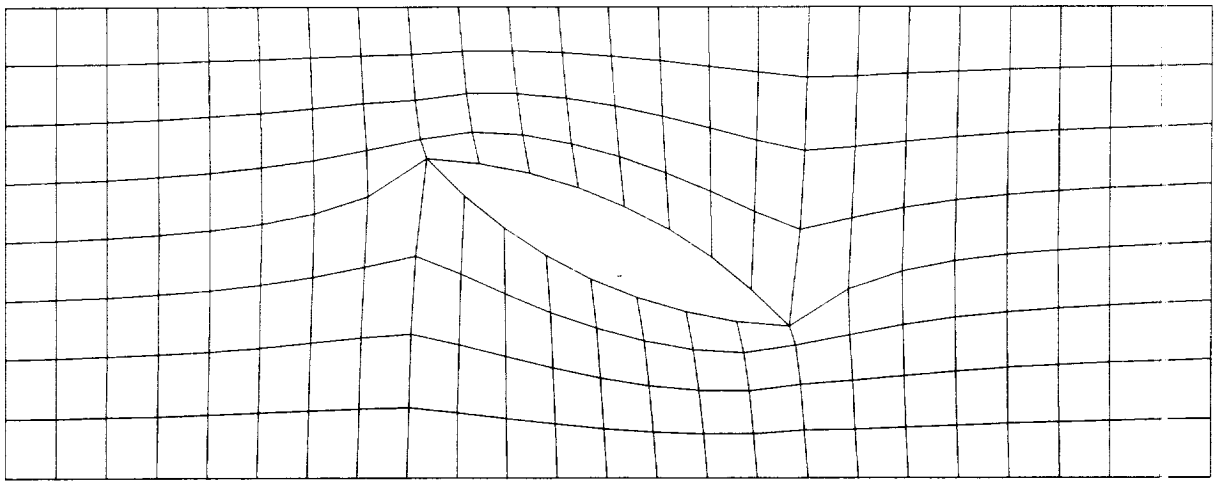

Figure 150. Smoothed Mesh

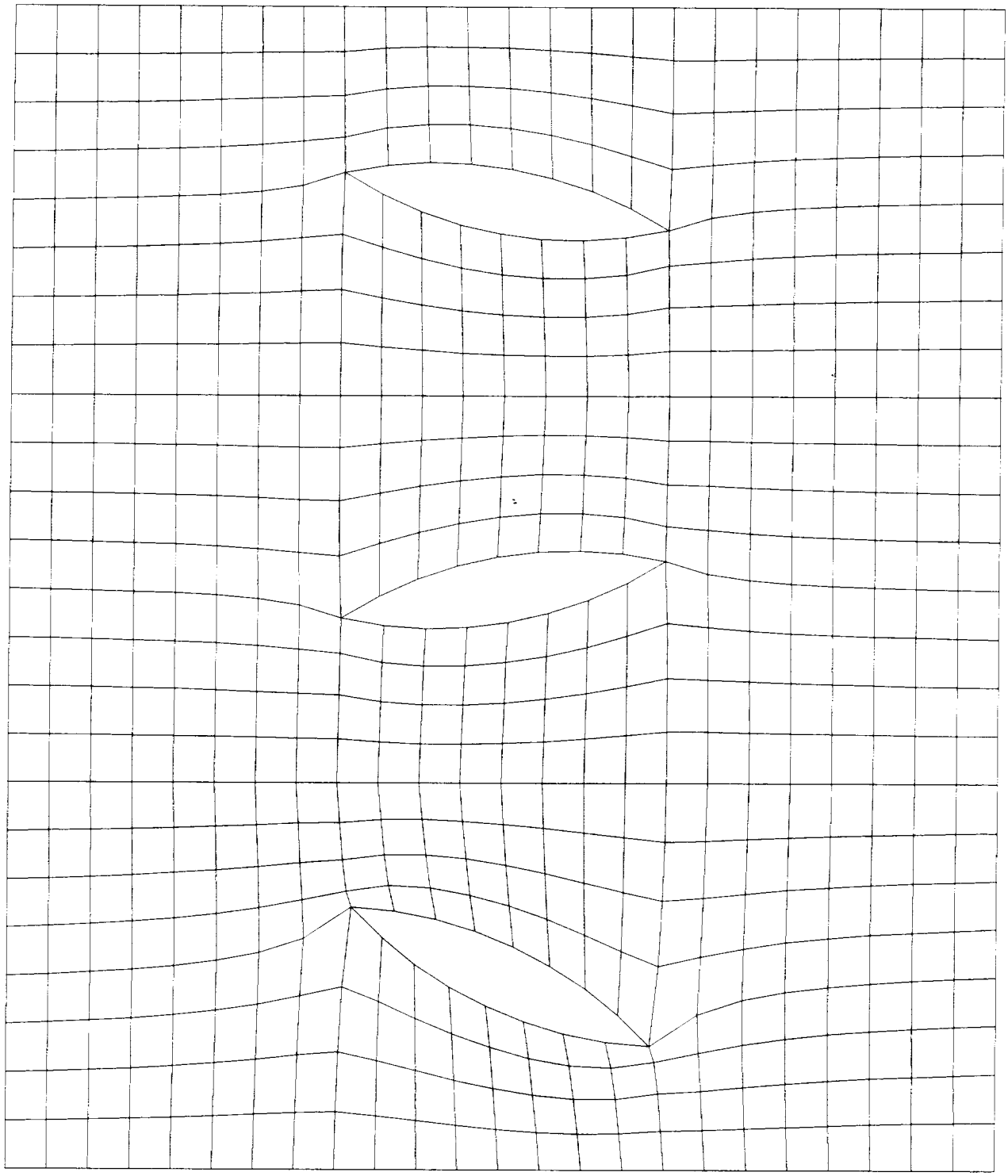

Figure 151. Combined Mesh

A test case was designed to determine whether an inviscid solution was sufficient for MPT prediction purposes. Solutions were computed for three blades where the stagger of the center blade had been adjusted by 0.2°. This case was designed to compare the sensitivity of the shock position and angle to changes in geometry. This viscous solution included the effects of tip clearance and the engine splitter. The results indicated the inviscid solution was adequate for prediction of MPT phenomena.

5.5.5 Inlet Boundary Condition

With the strong upstream-running shock, spurious reflections from the inlet boundary initially presented a problem. A variety of nonreflecting boundary conditions were tried in the CFD code, but none totally eliminated the reflection. A simple alternative strategy proved effective: a block of mesh was added to the inlet with 16 points in the axial direction and a geometrical stretching of 1.15:1 in the axial direction. As the shocks move through this mesh, they are slowly diffused and are extremely weak when they encounter the inlet boundary. Consequently, no strong reflections are generated. The effect of this boundary condition is illustrated in Figure 152.

5.5.6 Preliminary 3D CFD Predictions of MPT Noise

To assess the ability of the CFD code to capture the MPT phenomena, some preliminary multiple-passage CFD calculations were performed on representative fan geometry. The 95% speed condition

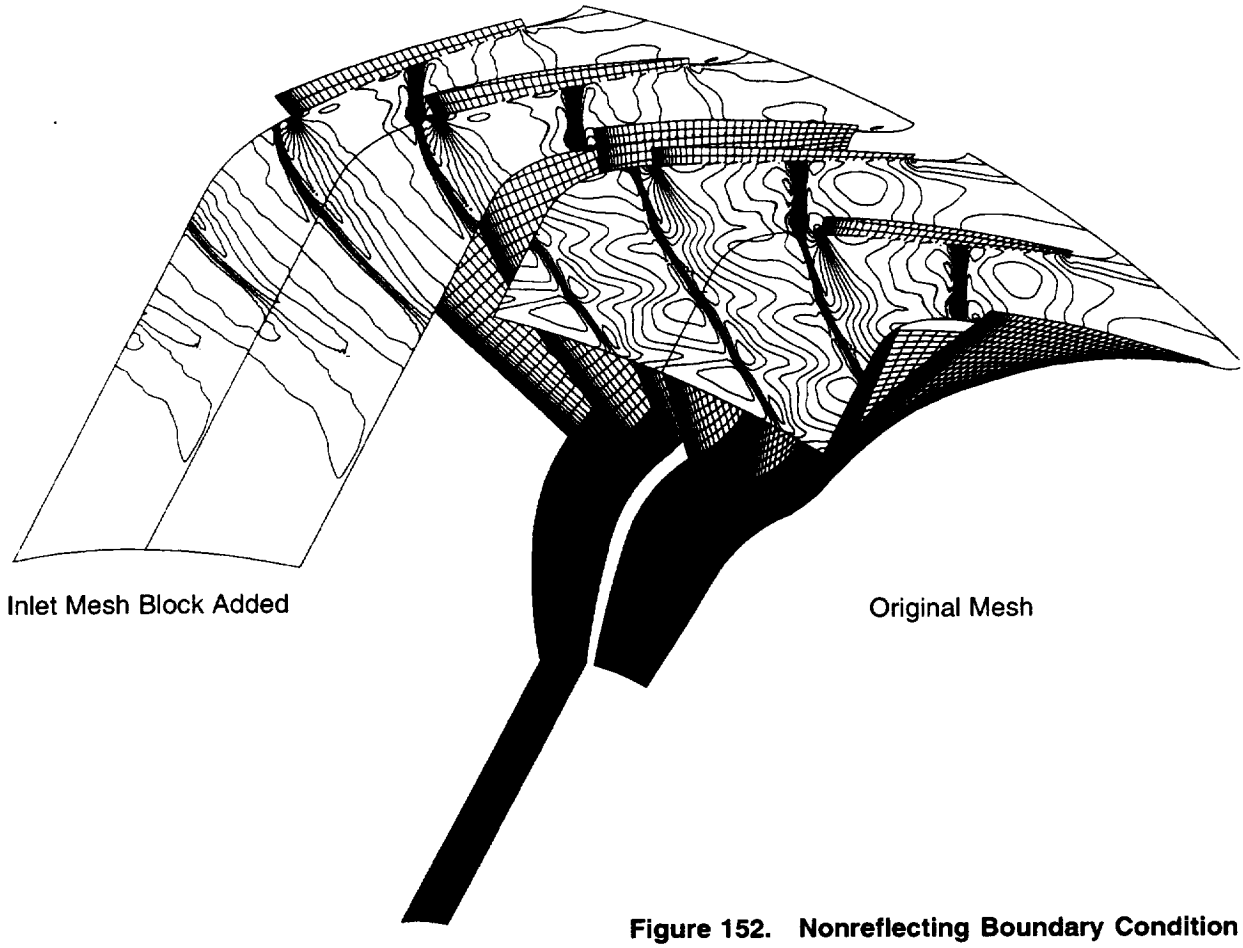

Figure 152. Nonreflecting Boundary Condition

was chosen, and back pressure was adjusted to place the numerical simulation on the operating line as described in Section 5.3, page 148. The tip relative Mach number at this condition is 1.35.

This fan (AF1) contains 22 blades, and an optimal inviscid mesh for each passage would need 222,000 mesh points to generate a mesh for the complete annulus — exceeding the computing resources available. The number of points per passage could have been reduced, but this would have degraded the solution accuracy. A mesh for half the annulus (11 blades) was tractable, so such a mesh was generated with the random variations in stagger angle (degrees) as shown in Table 14.

Table 14. Blade Stagger Angles

Blade Number	Stagger Angle
1	+0.00°
2	–0.10°
3	+0.20°
4	–0.25°
5	–0.20°
6	+0.10°
7	+0.15°
8	+0.05°
9	+0.25
10	–0.20°
11	+0.10°

The variations represent typical deviations based on available inspection data. The final mesh contained approximately 2,500,000 nodes. The flow solver required 780 Mb of memory and four CPU hours for 136 multigrid iterations on an SGI Origin 2000 (R10000) machine. For the multipassage solution, the flow solver was started from the single-passage solution at the 95% speed condition. The single-passage solution took approximately one CPU hour for 450 multigrid iterations and required 55 Mb of memory.

A view of the complete mesh and solution is shown in Figure 153. A contour plot of pressure on an unwrapped cylindrical surface near the tip of the fan is shown in Figure 154(a). The effects of the blade shape changes can be clearly seen on the angle of the shocks as they propagate upstream. The radial shock pattern is shown in Figure 155.

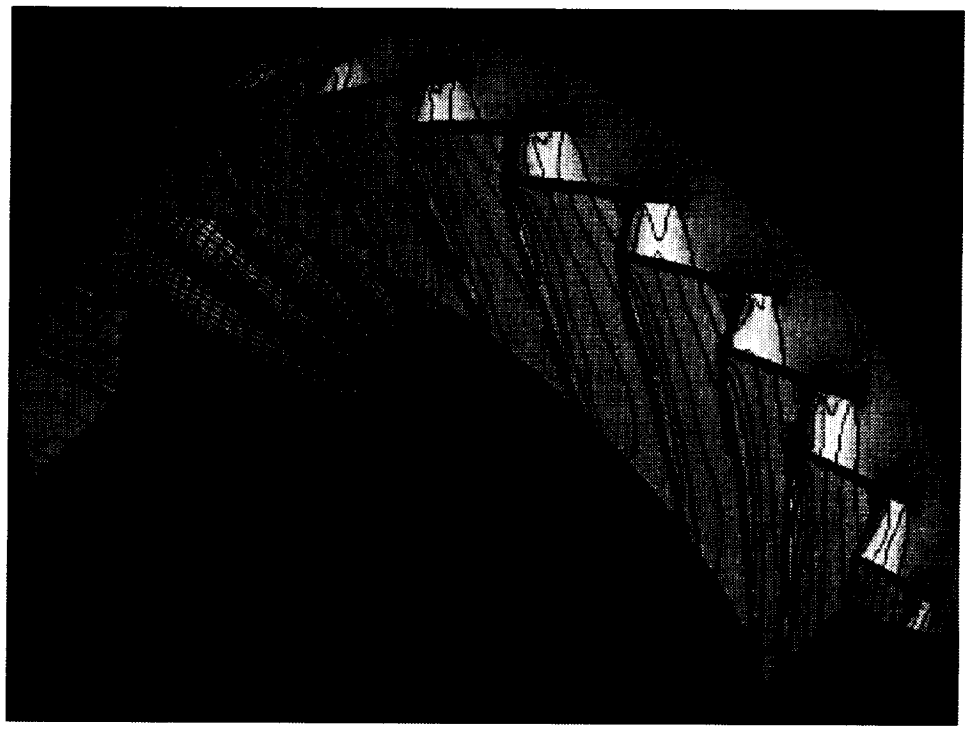

Figure 153. Overall View of 11-Blade Mesh And Solution

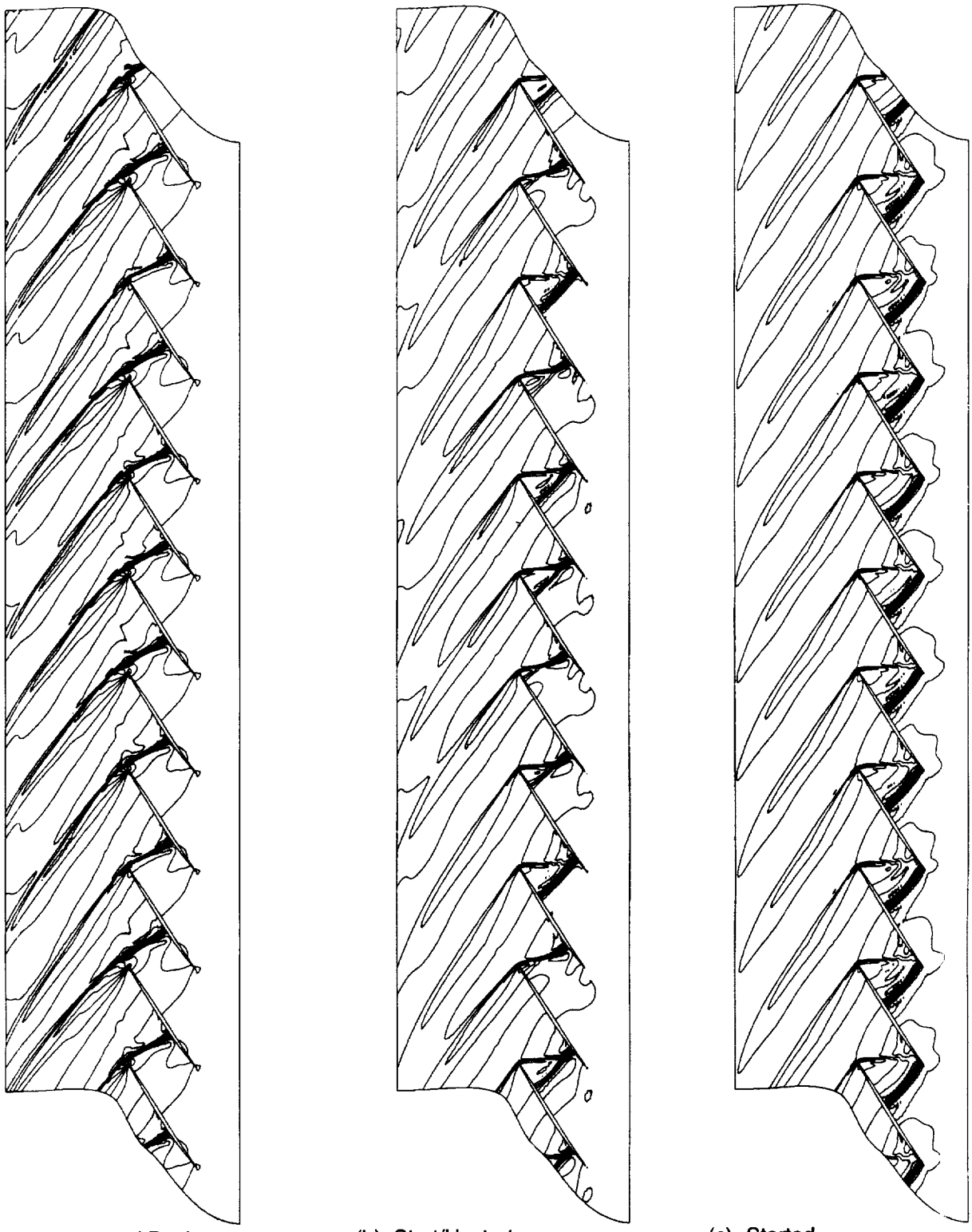

(a) Unstarted Design Condition

(b) Start/Unstart $P_{exit} = P_{exit} - 0.35$ psi

(c) Started $P_{exit} = P_{exit} - 0.65$ psi

Figure 154. Pressure Contours Near Tip for 1/2-Annulus Fan, 95% Speed

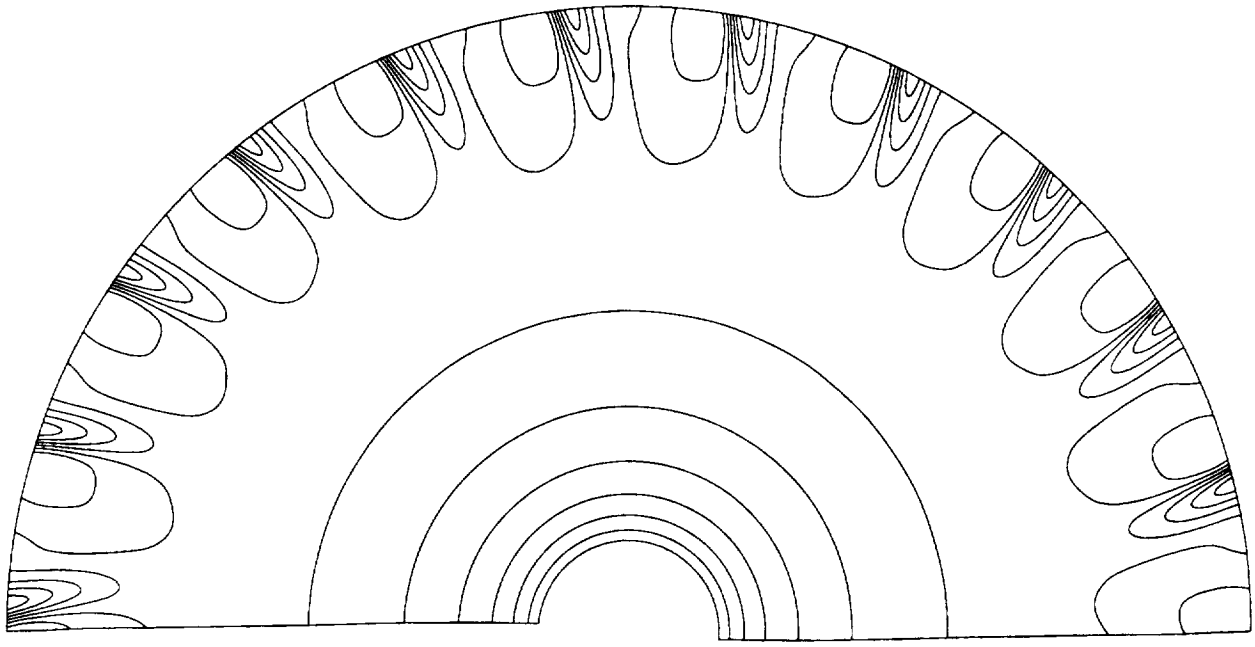

Uniform

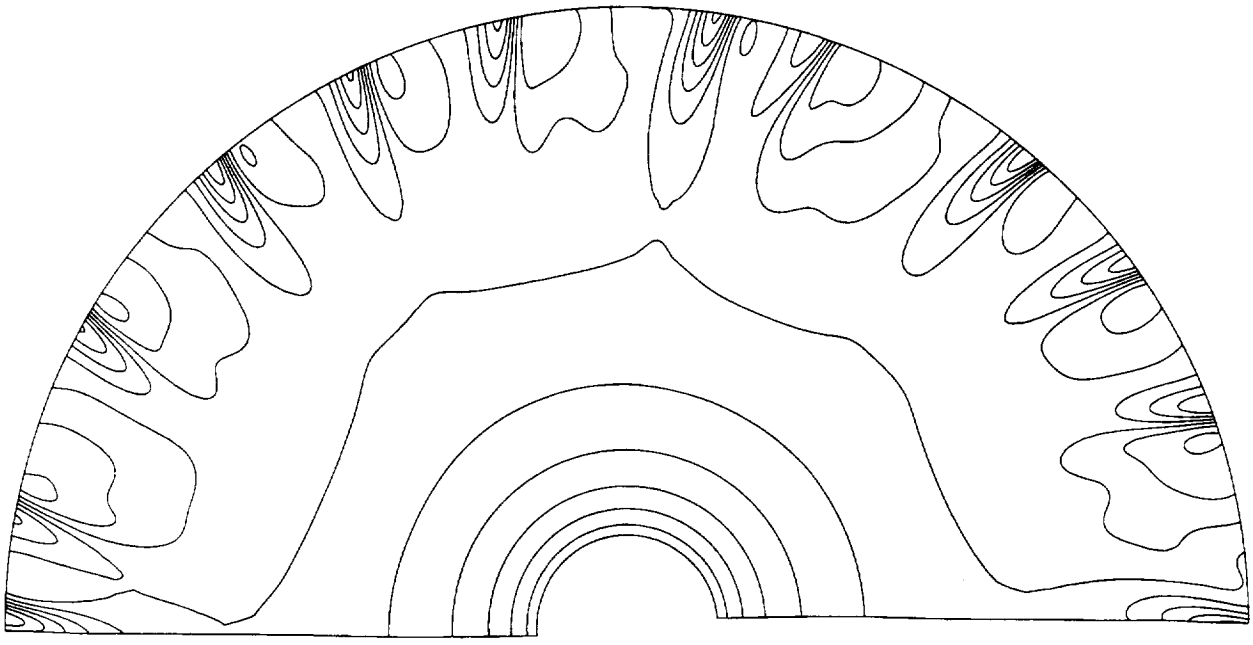

Nonuniform

Figure 155. Radial Extent of Pressure Field

Development of the upstream pressure field is illustrated in Figure 156. As expected, the spectrum near the leading edge is dominated by the blade passing frequency. The spectra further upstream show the amplitude of the component at the blade passing frequency reducing and the relative amplitudes of the lower frequency components increasing. This figure can be compared with two-dimensional results for a different fan in Figure 141.

To assess the effects of geometry changes on the shock pattern at different operating points, this case was rerun with the back pressures reduced by 0.35 and 0.65 psi to give a condition on the start/unstart boundary and a fully started case. The concern was that a case on the start/unstart boundary may rise to high MPT noise due to potentially increased sensitivities to geometry changes. The results of this exercise are shown in Figure 154 (b) and (c). The circumferential pressure 1.6 axial chords upstream of the leading edge near the tip is illustrated in Figure 157. This was the location of the kulite pressure transducer that will be used for comparisons with experimental data in subsequent sections. The resulting Fourier decomposition of the pressure field for modes below blade passing frequency is shown in Figure 158. It can be seen that the largest amplitude MPT noise signature occurs in the unstarted case. The amplitudes for the case on the start/unstart boundary are reduced, indicating no increased sensitivity on the start/unstart boundary.

The 95% speed case was run over a wider range of back pressures to further assess the effect of operating point on the MPT noise signature. The resulting spectra are shown in Figure 159. The main observation from these results is the expected sudden increase in amplitude of the MPT components as the fan unstarts.

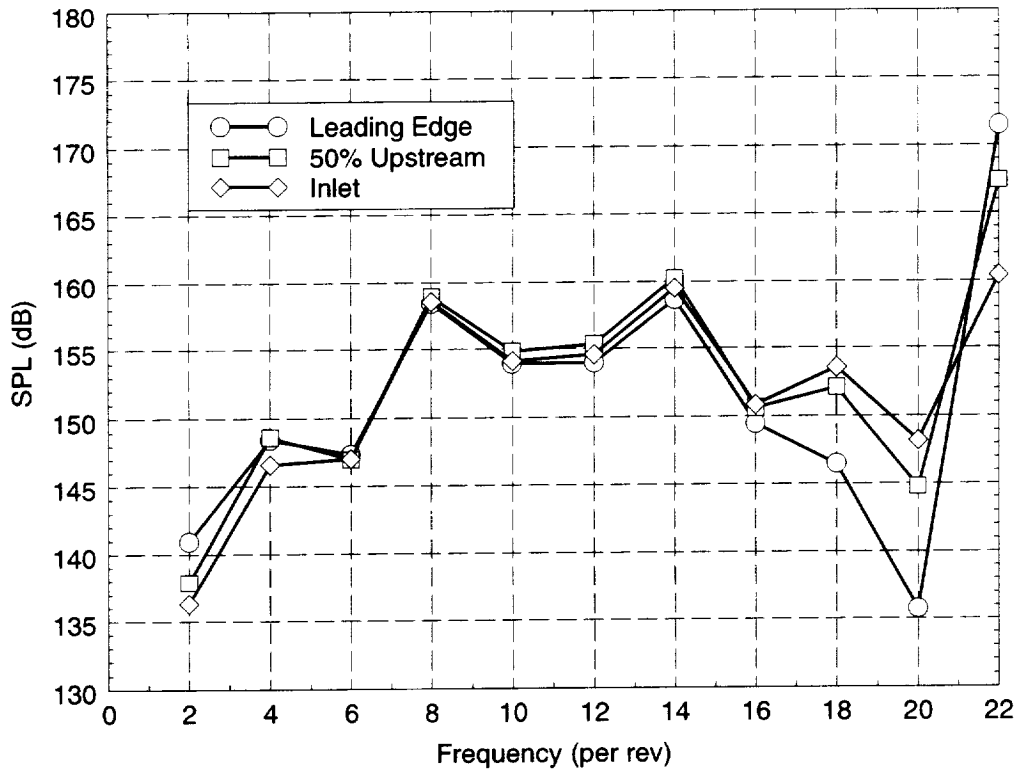

Figure 156. Development of Upstream Pressure Field

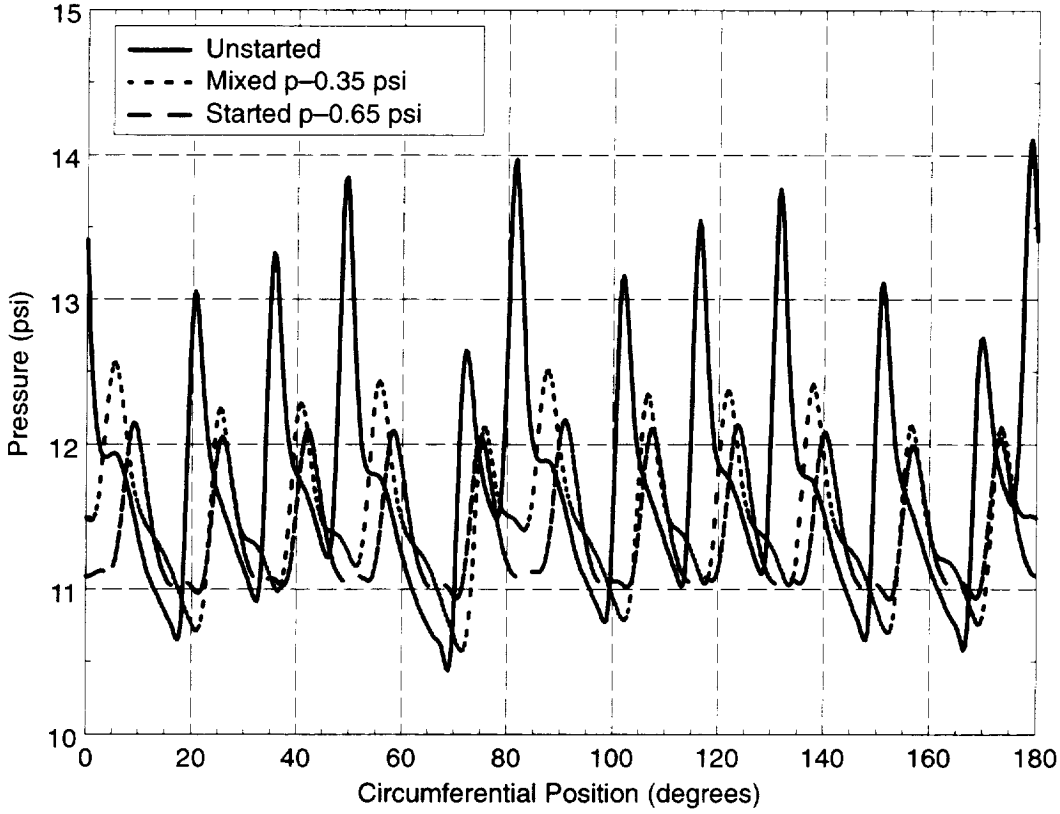

Figure 157. Comparison of Circumferential Pressure Distribution at Various Operating Points

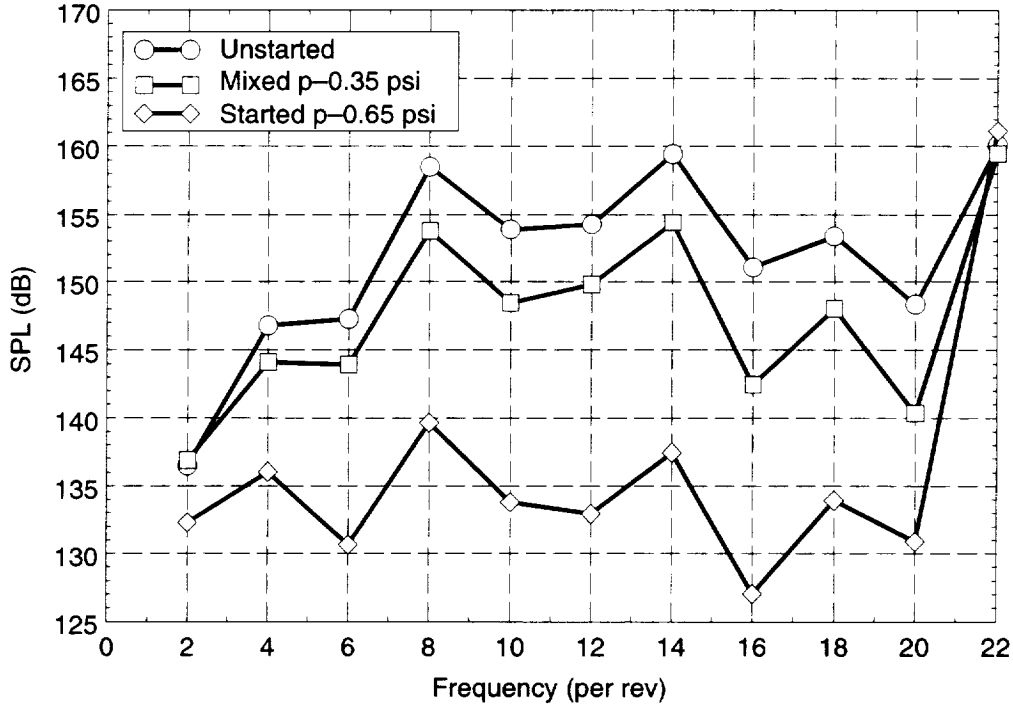

Figure 158. Amplitudes of Fourier Modes at Various Operating Points

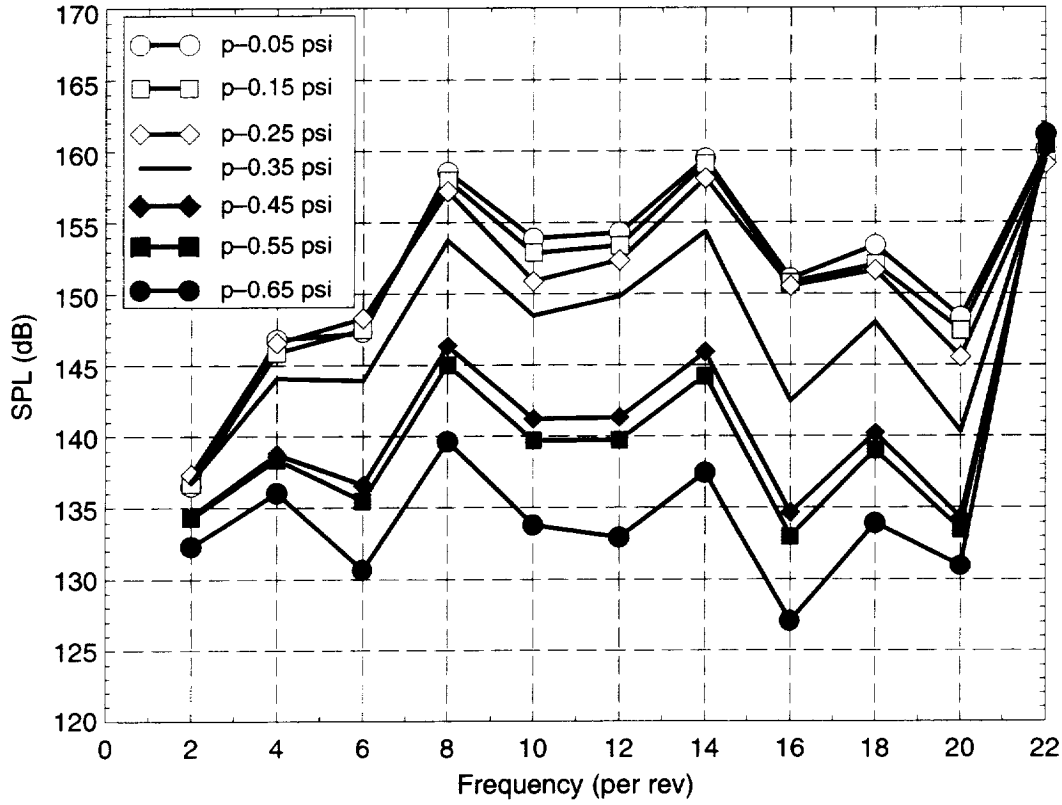

Figure 159. Comparison of Fourier Modes Over a Range of Operating Points

It can be concluded from these results that the inviscid CFD predictions show considerable promise in ability to predict the effects of small blade-shape changes on the strength and position of upstream-running shocks — the mechanism for generating MPT noise.

5.6 Effect of Typical Geometry Changes

In Section 5.5, page 157, some preliminary calculations demonstrated the ability of CFD to predict the effect of small stagger angle changes on the pressure field upstream of a transonic fan. In this section, CFD is used to assess the relative importance of other geometry changes.

The changes considered are stagger angle, camber angle, thickness, and pitch variations. A large number of runs were required, so computational requirements were minimized by considering a three-blade case where the geometry of the center blade was modified. Note that it is not sufficient to consider a single passage and modify one blade; that removes any effect of passage-to-passage area change. As will be seen later in this section, this is the dominant effect in generating MPT's.

From available inspection data for typical fan blades, changes in the four geometrical factors previously listed were inferred. The maximum change represented two standard deviations from the mean. A number of runs were made for each of these factors:

- **Stagger** – The center blade was rotated by ±0.2° (2 runs).
- **Thickness** – Blade thickness was specified at the leading edge, midchord, and trailing edge — with three possible values at each position: thick, normal, and thin (26 runs).

- **Camber** – Three values of leading- and trailing-edge camber were considered: increased, no change, and decreased (8 runs).
- **Pitch.** Two values of pitch were considered (2 runs).

The circumferential pressure distribution resulting from these changes on AF1 upstream of the leading edge is shown in Figure 160. As shown, stagger and camber have the largest and almost equal effect followed by camber changes. Changes in pitch have little or no effect.

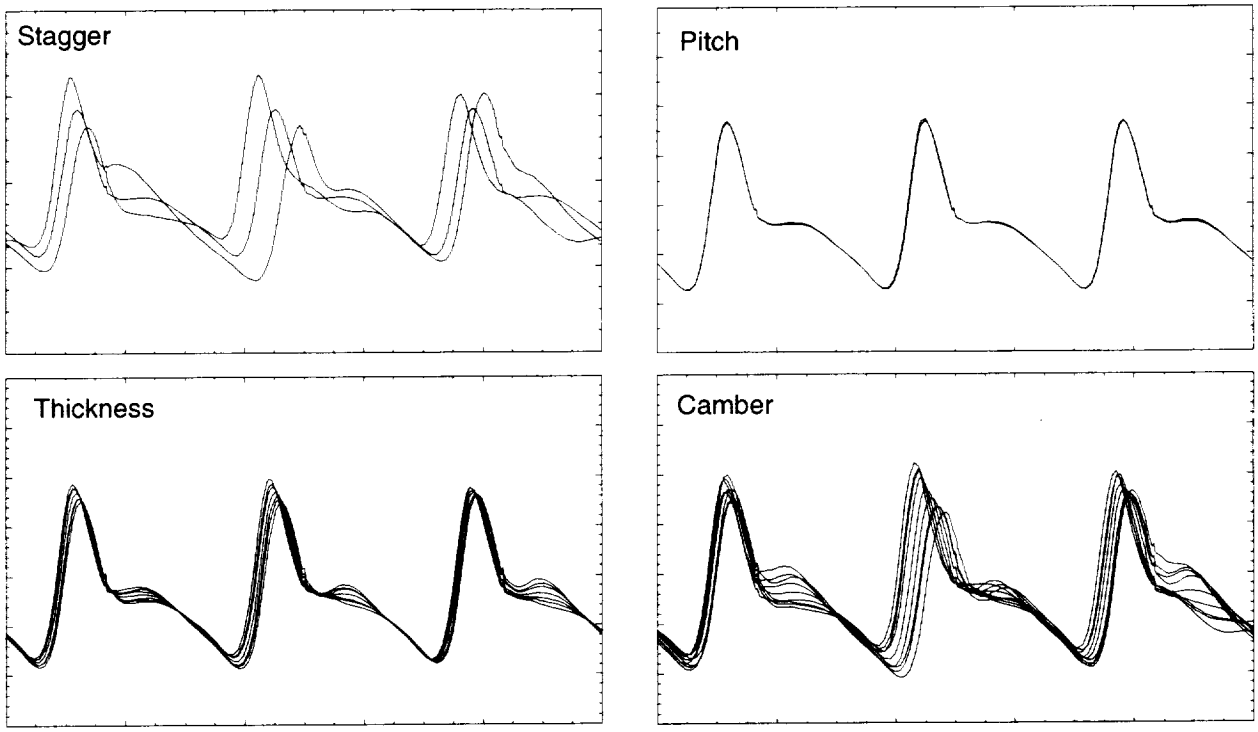

Figure 160. Circumferential Upstream Pressure from Three-Blade Case

Studying the above results, coupled with the result that changing all the blades uniformly has little effect on the upstream pressure field, leads to the conclusion that the fan must be thought of as a series of passages rather than blades. Variations in these passage shapes govern the upstream pressure field.

To study passage shape changes in more detail, a number of four-passage cases were considered where the geometry of the middle two blades, and hence the center passage, was varied. Obviously the geometry of the two adjacent passages would also be modified (but to a lesser degree). Four-passage (rather than a larger number) cases were chosen to minimize computational requirements. Subsequent studies, described in Section 5.7, page 169, varied up to 10 blades (with two adjacent blades) and demonstrated the validity of the limited solution domain. Only camber and stagger changes were considered, as these had been found to be the dominant geometrical factors.

The results for stagger changes are shown in Figure 163. The dotted line is the circumferential pressure field for identical blades. Two cases were considered; opening and closing the trailing edge. For camber changes, four cases were considered. In Figure 161 the camber on the last 50% of chord is adjusted to open and close the trailing edge with the first 50% unchanged. Figure 162 shows the

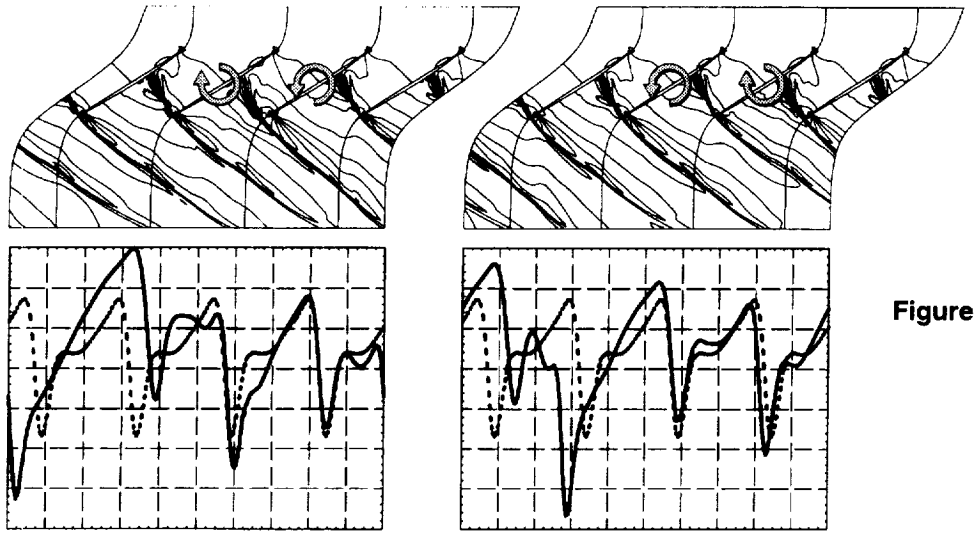

Figure 163. Stagger Changes

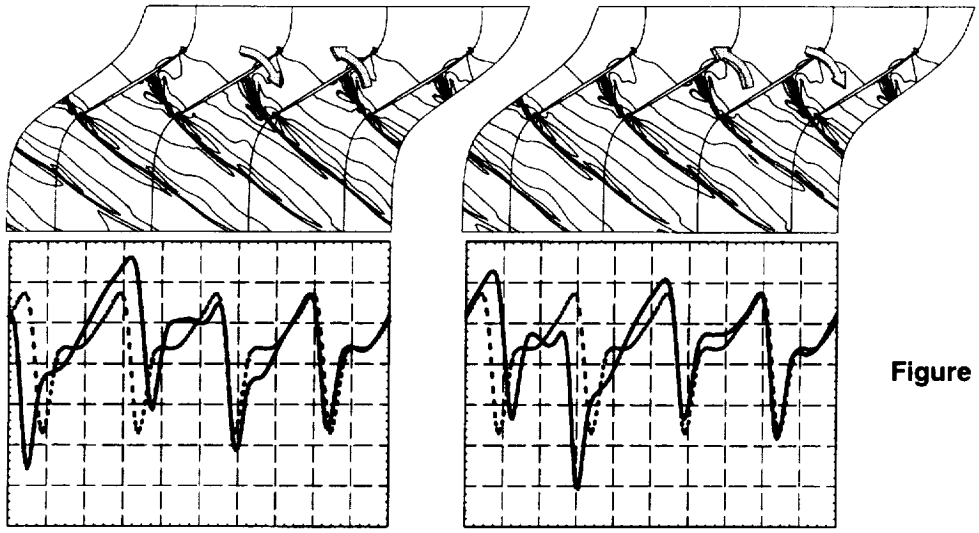

Figure 161. Trailing-Edge Camber Changes

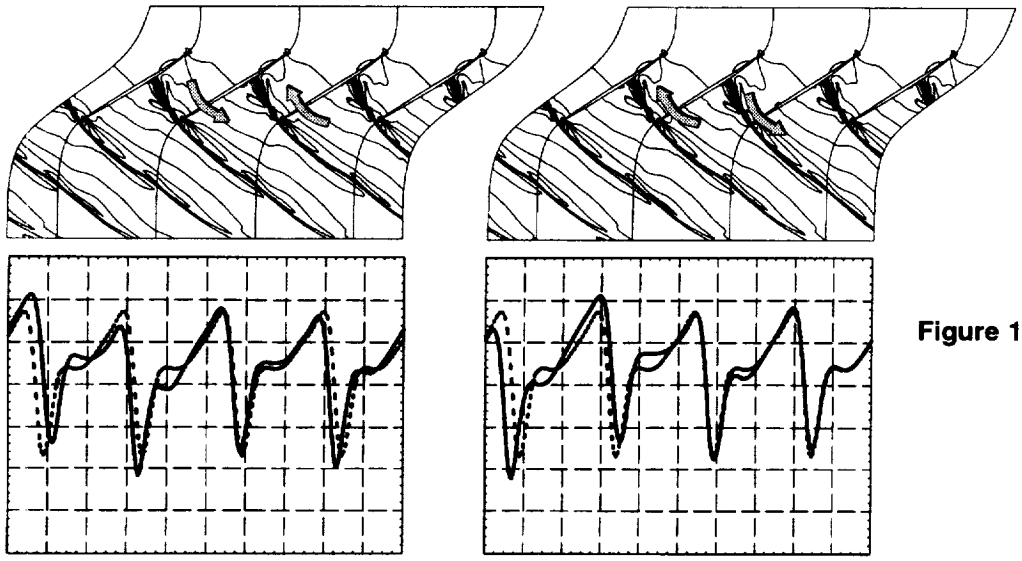

Figure 162. Leading-Edge Camber Changes

effect of adjusting the leading-edge camber. The amount by which the leading and trailing edges moved as a result of camber and stagger changes was roughly equivalent. Again the magnitude of these changes came from available inspection data.

Comparing Figures 163 and 161 shows that opening or closing the trailing edge through stagger or camber has a similar effect on the circumferential position and strength of shocks. Changes in the leading-edge shape, as shown in Figure 162, has a much smaller effect on the pressure field.

Careful examination of Figures 163 and 161 indicates that opening and closing the trailing edge has an opposite effect on the pressure field. This suggests that the changes in pressure may be linear with blade-shape changes. To test this observation, the 11-blade unstarted case described in Section 5.5, page 157, was run again with the stagger angle variations reduced by a factor of 0.5. The resulting Fourier decomposition is shown in Figure 164. The amplitudes of all the modes are reduced 5 dB, demonstrating that the pressure field is indeed linear with blade-shape changes at this running condition. A similar comparison was done at the condition on the start/unstart boundary to test the linearity hypotheses at this condition, and the results are shown in Figure 165. Here, the change in amplitude is not as constant, indicating increasing nonlinear behavior in the region.

5.7 CFD Based MPT Prediction Model

In the original statement of work, it was proposed to base the MPT prediction method on a correlation relating blade-shape changes to the MPT spectra. It was intended to develop this correlation by numerous runs of a quasi-3D CFD code and was envisioned that standard deviations of geometry variations could then be related to MPT spectra via this correlation. The approach was abandoned for two main reasons:

1. Flow in a transonic fan is highly three-dimensional and not adequately predicted by two-dimensional methods. Developing a correlation based on a 3D CFD code would be impractical due to the computer requirements.
2. The results presented earlier indicate that the MPT spectra are highly dependant on the ordering of the blades in the annulus. A standard deviation of a geometry variation is insufficient to characterize the fan.

The results presented in Section 5.6, page 166, demonstrate that the changes to the amplitudes of the Fourier modes composing the circumferential pressure distribution are linear with passage shape changes. Hence, if the effect of changing one passage on these modes can be obtained by simple superposition, the effect of any distribution of passage shapes can be quickly derived.

Obviously it is impossible to change one passage in isolation because changing the geometry of one blade affects two passages. However, if for example the stagger of one blade is modified, then one adjacent passage is closed and one opened. The resultant upstream pressure can be considered as the sum of the contributions from the changes to the two passages. The Fourier modes arising from one passage will be phase-shifted by one pitch and negated with respect to the other. It is therefore possible to obtain from the combined pressure distribution the base modes resulting from changing just one passage.

To incorporate these ideas into a useful model for prediction of MPT noise spectra, an initial multiple-passage CFD calculation is required with one blade modified. This prediction is made at the fan operating point and is under consideration. The subsequent Fourier analysis to determine the

Figure 164. Fourier Mode Amplitudes, 95% Speed, Unstarted

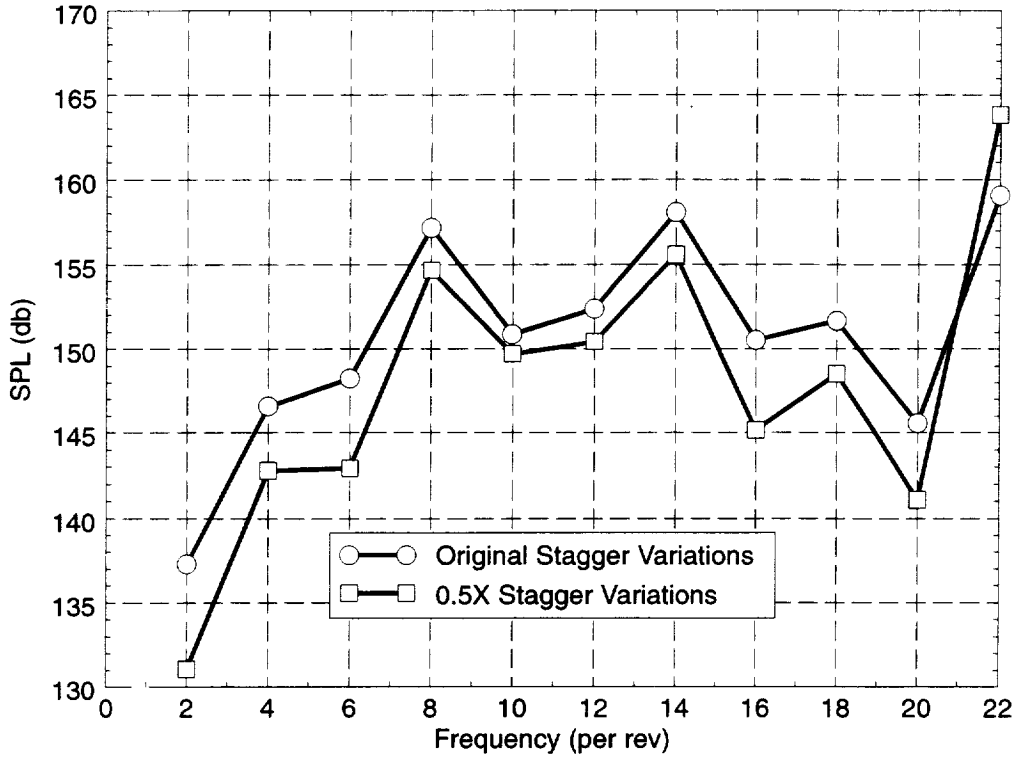

Figure 165. Fourier Mode Amplitudes, 95% Speed, Start/Unstart Boundary

base modes essentially computes the sensitivities of the Fourier modes to the geometry change in question. Using the superposition ideas, the MPT spectra for a range of geometrical variations can be computed.

It should be noted that if the geometrical variations were a combination of, say, a stagger and camber change, then the base modes would be computed for each geometrical variation. The resultant spectra would be the sum of the amplitudes of the modes arising from each geometry change.

With the multiple-passage CFD solution, periodic boundary conditions are applied between the meridional grid surfaces. The number of passages used in the multiple passage CFD solution needs to be large enough that the influence of a passage geometry change does not return via the periodic boundary to influence the passage that has been changed. To assess the region of influence of a passage change, a case with 10 passages was computed. The first five blades were rotated +0.2° and the second five –0.2°. This gives a case with two changed passages, and the results are shown in Figure 166. As expected, the results show that (due to the supersonic inlet relative Mach number) a passage shape change affects only the downstream passages. The region of influence is about three passages. This suggests that a minimum four passages are required.

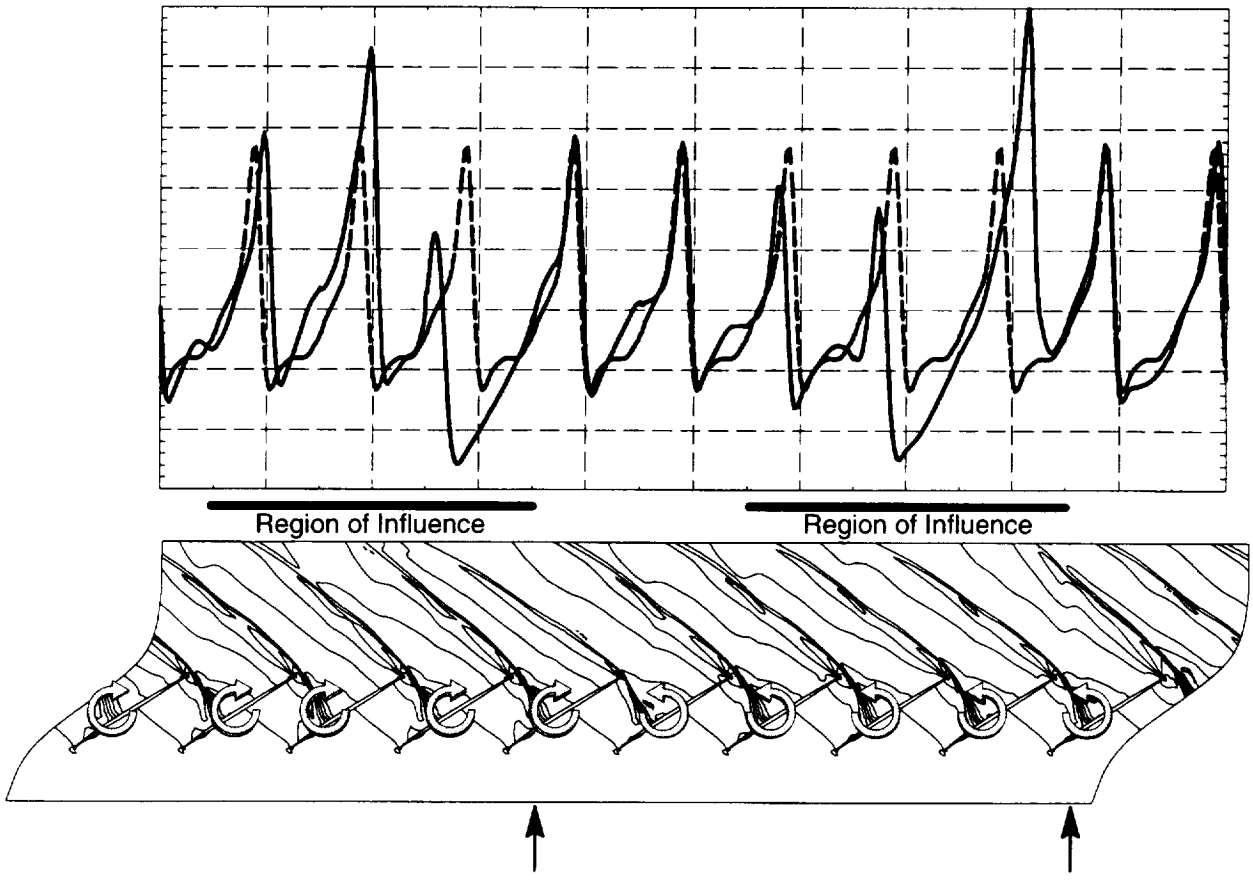

Figure 166. Circumferential Region of Influence of Passage Shape Change

Computation of the base modes is as follows. The circumferential pressure field $p(\theta)$ at the axial location of interest may be expressed as:

$$p(\theta) = p_1(\theta) + p_2(\theta) \tag{189}$$

where $p_1(\theta)$ and $p_2(\theta)$ represent the effects of the two adjacent modified passages. The Fourier series representation of $p(\theta)$ may expressed as:

$$p(\theta) = a_0 + \sum_{i=1}^{i=n} a_i cos(i\theta) + b_i sin(i\theta) \tag{190}$$

where n is the total number of passages. Similarly $p_1(\theta)$ and $p_2(\theta)$ may be expressed as:

$$p_1(\theta) = a_0^1 + \sum_{i=1}^{i=n} a_i^1 cos(i\theta) + b_i^1 sin(i\theta) \tag{191}$$

and

$$p_2(\theta) = a_0^2 + \sum_{i=1}^{i=n} a_i^2 cos(i\theta) + b_i^2 sin(i\theta) \tag{192}$$

Due to the linear nature of the system $p_2(\theta)$ may be expressed in terms $p_1(\theta)$ through a phase shift of one passage and a negation of coefficients. The relationship between the coefficients can be expressed as:

$$p_2(\theta) = a_0^1 + \sum_{i=1}^{i=n} \Big[- a_i^1 cos(i\delta\theta) + b_i^1 sin(i\delta\theta) \Big] cos(i\theta) + \Big[-a_i^1 sin(i\delta\theta) + b_i^1 cos(i\delta\theta) \Big] sin(i\theta) \tag{193}$$

where $$\delta\theta = \frac{2\pi}{n} \tag{194}$$

The relationship between the coefficients becomes:

$$\begin{pmatrix} a_i \\ b_i \end{pmatrix} = \begin{pmatrix} 1-\cos(i\delta\theta) & \sin(i\delta\theta) \\ -sin(i\delta\theta) & 1-\cos(i\delta\theta) \end{pmatrix} \begin{bmatrix} a_i^1 \\ b_i^1 \end{bmatrix} \tag{195}$$

Hence, it is a simple matter to determine the base mode coefficients ($a_i{}^1$, $b_i{}^1$) via a 2×2 matrix inversion from the coefficients derived from the multiple-passage CFD solution.

Having obtained the base mode coefficients, it is a simple matter to reconstruct the total pressure field by superposition for any distribution of geometry changes.

A computer program has been written to compute the base mode and perform the superposition. The exercise takes less than one CPU second on a HP C180 workstation.

5.8 Model Validation – 3D CFD

The objective here is to evaluate how well the superposition method can predict CFD results prior to predicting engine data. The validation case chosen was the 11-blade fan test case used previously. Three multiple-passage solutions were run with one blade modified to compute the base mode.

These contained four, six, and eight passages. A superposed prediction was then made for the 11-blade case where all the blades were different. This would enable determination of the minimum number of passages required for accurate computation of the base mode.

The MPT spectra are shown in Figure 167. Based on these results, it would appear that a six-passage solution is required for the superposition rather than four passages as postulated in Section 5.7, page 169. The blade-to-blade and circumferential pressure field for the six-passage solution are shown in Figure 168. The superposition results for the six-passage case reproduce the half-annulus CFD solution to within 2 dB over the whole frequency range. This represents excellent agreement and demonstrates that the simple superposition algorithm works extremely well.

To further test the algorithm, the other 95% speed cases at the started and start/unstart conditions were run. Figure 169 shows the comparisons at the start/unstart condition, and Figure 170 shows the comparison at the started condition. Both comparisons were based on a six-blade multiple-passage CFD prediction. Agreement between the CFD solution and superposed solution deteriorates in both cases. Although the level is not well predicted, the relative magnitudes of the modes are reasonably well predicted. In the started case, the SPL is so low that noise in the system may be beginning to overwhelm the predictions. For the case on the start/unstart boundary, the nonlinear effects observed in Section 5.6, page 166, are becoming larger and reduce the accuracy of the prediction to ±5dB.

5.9 Comparison of Predicted MPT Noise with Test Data

The inspection data obtained for the test case fan comprised measurements at approximately 25 equally spaced radial sections for each fan blade. The measurements were: tangent angle, leading-edge thickness, chord, and thickness. These measurements indicated that the geometry variations could be interpreted as primarily stagger variations. As the stagger angle did not vary significantly with radius in the tip region, stagger angle data for a section near the tip were used.

The inspection data used in this section were obtained from the fan in a "cold" state. The limited test data available indicate that cold variations are representative of the hot variations; however, this is still open to debate. It may be expected that the cold variations would be a reasonable estimate at conditions where the aerodynamic loads are similar between blades. In regions where the aerodynamic loads differ significantly between blades, near the start unstart boundary for example, then the aerodynamic loads could magnify (or diminish) the differences.

Kulite data were available for a variety of positions in the fan duct and at a variety of operating points. As supplied, the unsteady pressure from the kulite had already been processed into narrow-band frequency data. A transducer at 1.6 chords upstream of the leading edge was chosen for the comparison.

Single-passage and six-passage solutions were run. Circumferential pressure distributions at the kulite location from these two solutions were obtained. These distributions, together with the stagger angle variations near the tip from the inspection data, were input to the superpose program. The results for the 95% part-speed condition are shown in Figure 171. The agreement is in general very good with the superposition approach predicting the overall shape and amplitude of the spectrum.

To further test the algorithm, a 100% speed condition was chosen. At this condition the CFD code predicts a started flow, as opposed to unstarted for the 95% speed condition. Based on previous results, it would be expected that the amplitudes of the MPT's would diminish. The comparison is

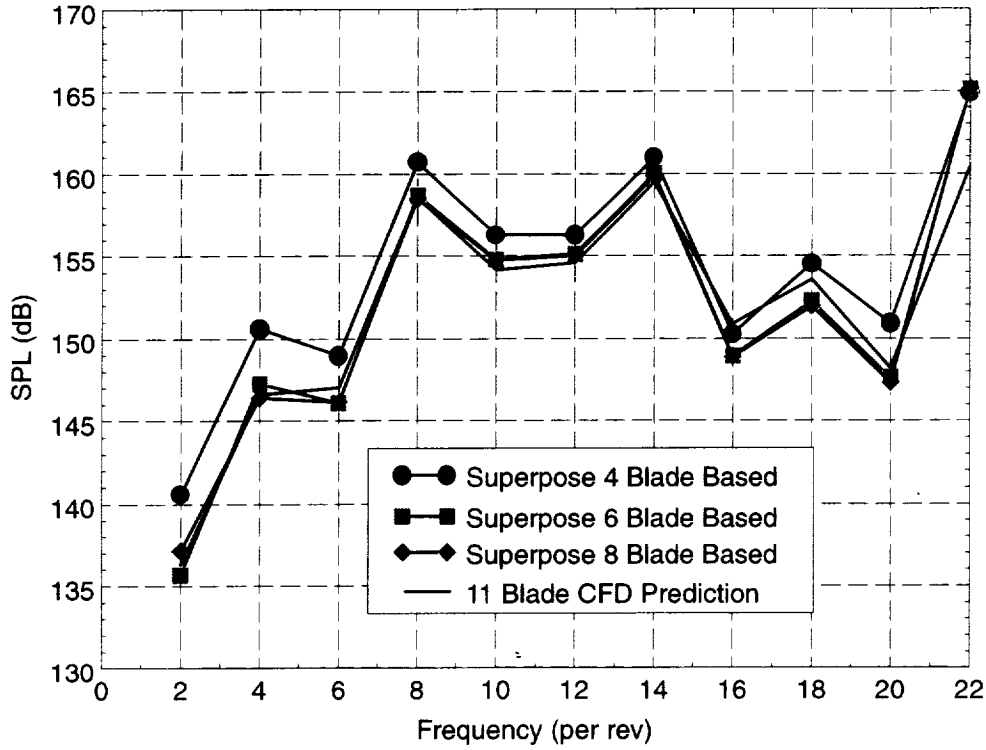

Figure 167. Comparison of CFD and Superposed Predictions at 95% Speed (Unstarted)

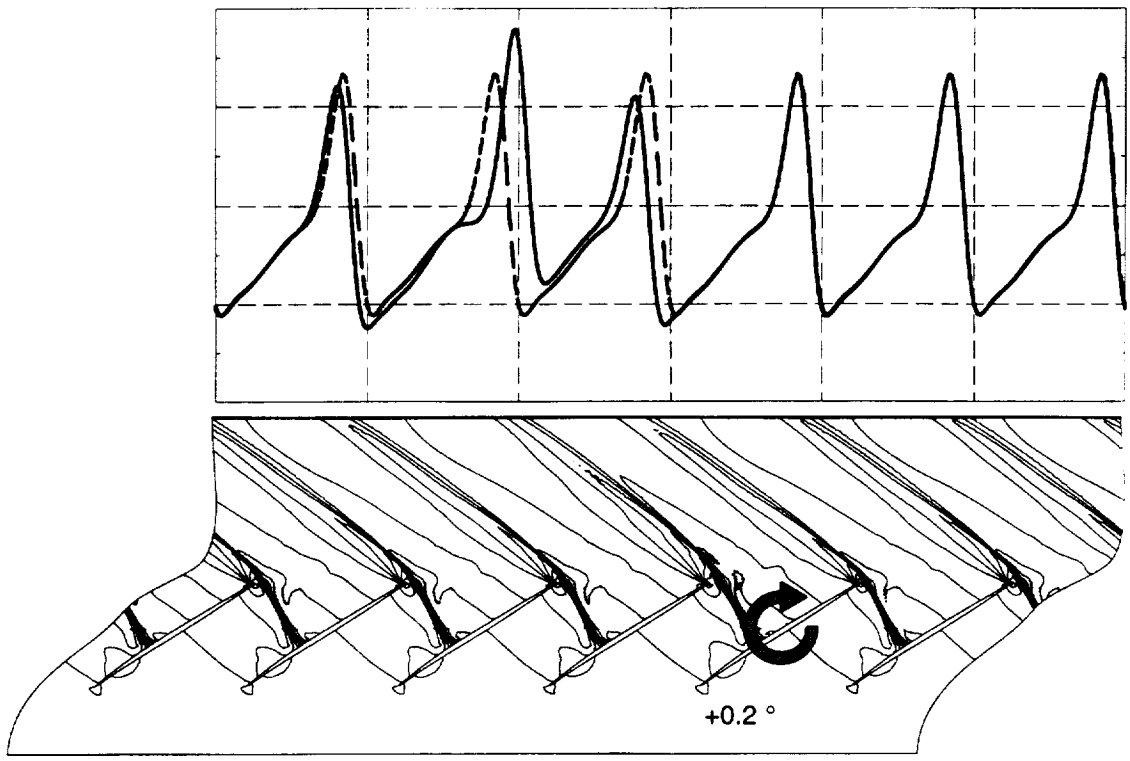

Figure 168. Six-Blade Solution

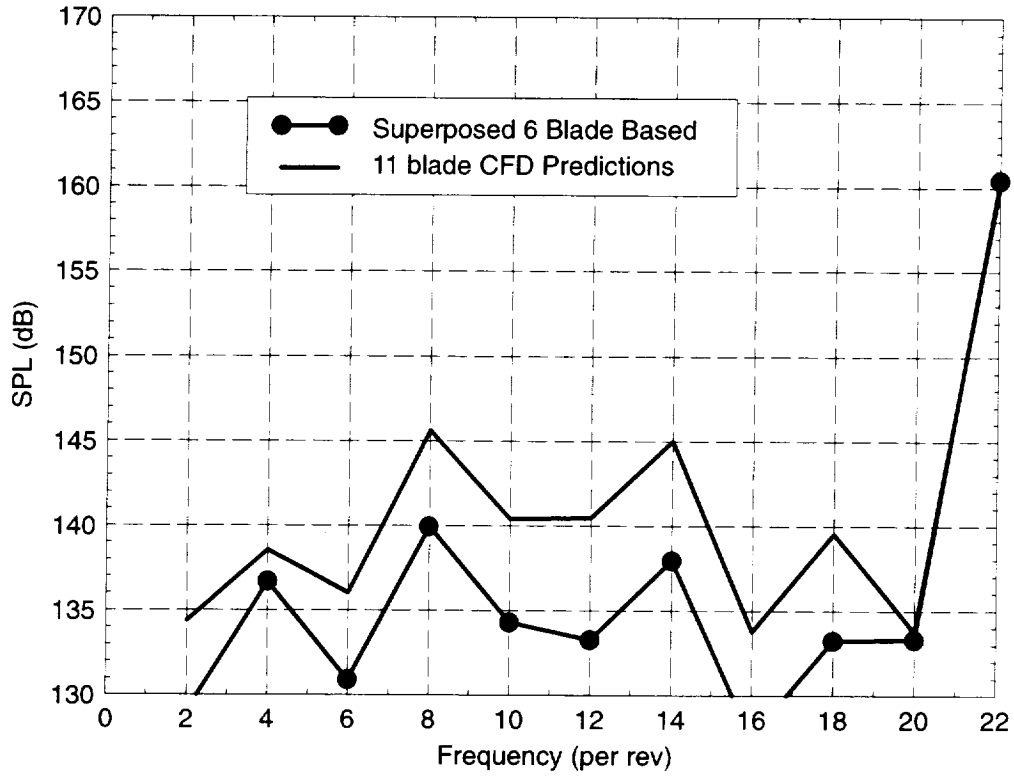

Figure 169. Comparison of CFD and Superposed Predictions at 95% Speed (Started)

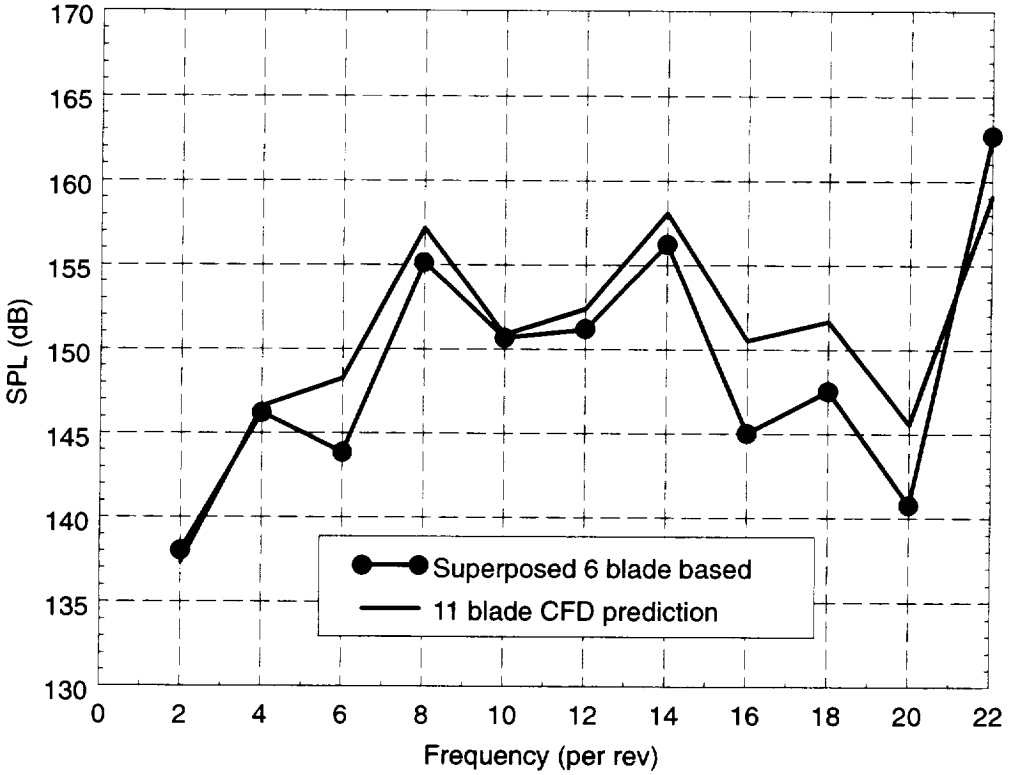

Figure 170. Comparison of CFD and Superposed Predictions for 95% Speed (Mixed)

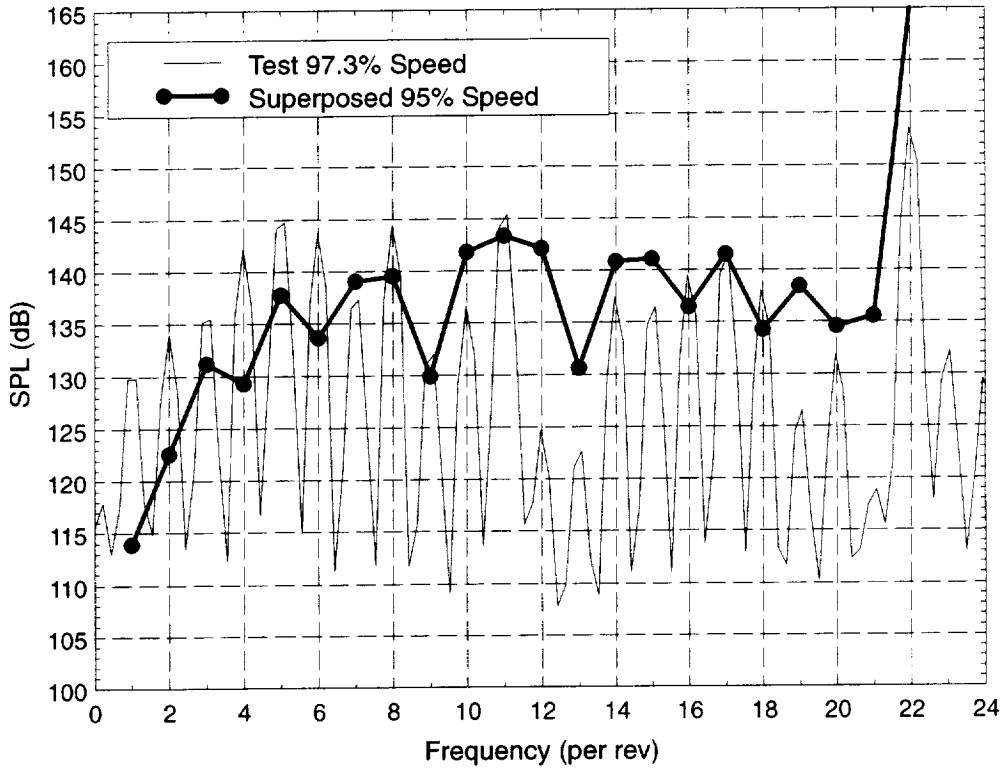

Figure 171. AF1 Superposition and Test Data Comparison at 95% Speed

presented in Figure 172. Comparing Figures 171 and 172, it can be seen that superpose predicts a reduction in amplitude of up to 5dB. The change in the test data is less clear, although agreement is still good.

5.10 MPT Noise Reduction

In this section two possible methods for reducing MPT noise are examined. In the first, the 3D shape of the blade is exploited to reduce the sensitivity of the flowfield to blade shape changes. The second method is aimed at reducing the MPT signature of a fan by shuffling the blades in the annulus.

5.10.1 Forward sweep

As shown earlier, MPT noise arises from the fan being unstarted at the tip at part-speed conditions. The position and strength of the upstream-running shocks are sensitive to blade shape changes and give rise to the MPT noise. To reduce the MPT noise the fan geometry needs to be modified to desensitize flow field to geometry variations.

One potential way to do this is to modify the blade so that the tip starts at a lower speed. This will reduce any MPT noise that occurs at this lower speed because the shocks will be weaker. The tip will now be started at the part-speed operating point and will minimize MPT noise.

One method that shows potential in achieving this is the adoption of forward sweep. To test this computationally, two fans with 24 blades designed (Reference 76) with the same operating line were analyzed. The first had a conventional straight design and the second a forward-swept design. These

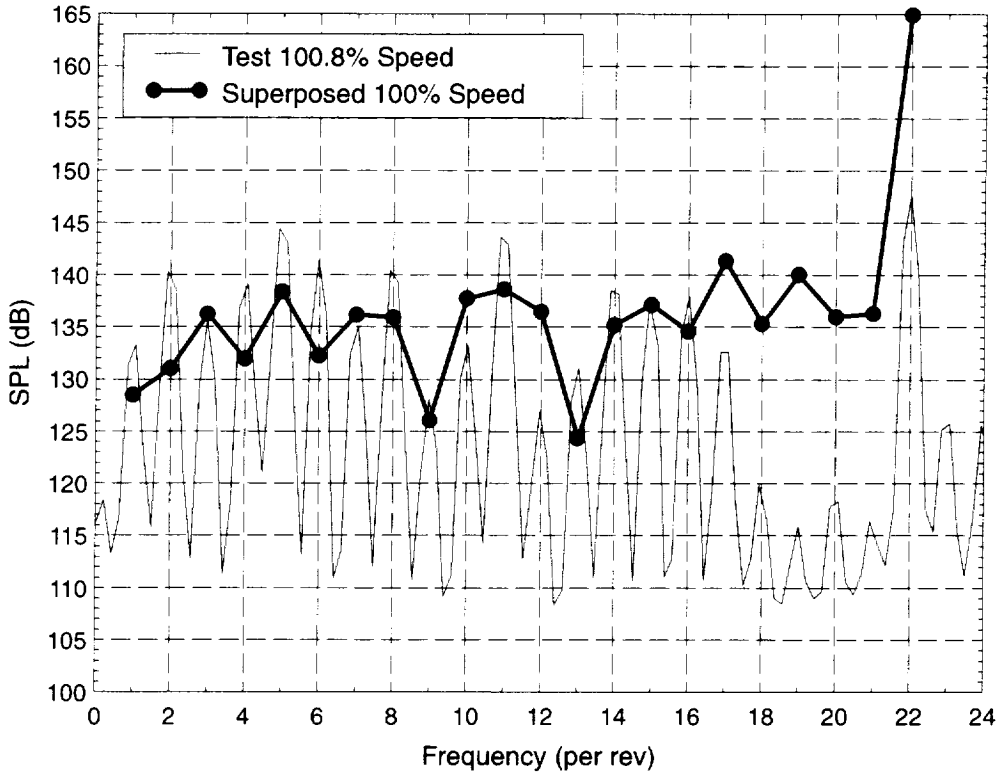

Figure 172. AF1 Superposition and Test Data Comparison at 100% Speed

are the AEC UHB forward swept rotor and the GE UHB wide-chord rotor. The shapes of these two blades are compared in Figure 174. The tip relative Mach number for both blades is approximately 1.45. It should also be noted here that forward sweep may also be beneficial by increasing efficiency and stall margin (Reference 80) though there are concerns about the structural integrity of the blades. The computationally generated fan map in Figure 173 shows that the tip starts at lower speed for the forward-swept blade than the straight blade. Based on previous arguments, a lower MPT signature would be expected. Figure 175 shows the differing tip shock patterns for a single-passage solution at the 85% speed point. It can be seen that the tip is unstarted for the straight blade and started for the forward-swept blade. Moving radially inward, the forward-swept blade unstarts while the straight blade remains unstarted.

Based on the above single-passage results, it would be expected that the forward-swept blade would have a lower MPT signature. To test this hypothesis, an 11-blade, multiple-passage simulation was run with the straight and forward-swept blades. Stagger variations similar to those used in Section 5.5, page 157, were employed. Figure 176 compares the shock patterns near the tip. Figure 177 compares the amplitudes of the fourier modes of the circumferential pressure field on the casing some distance upstream of the fan. It can be clearly seen that the forward sweep reduces the amplitudes by up to 15 dB.

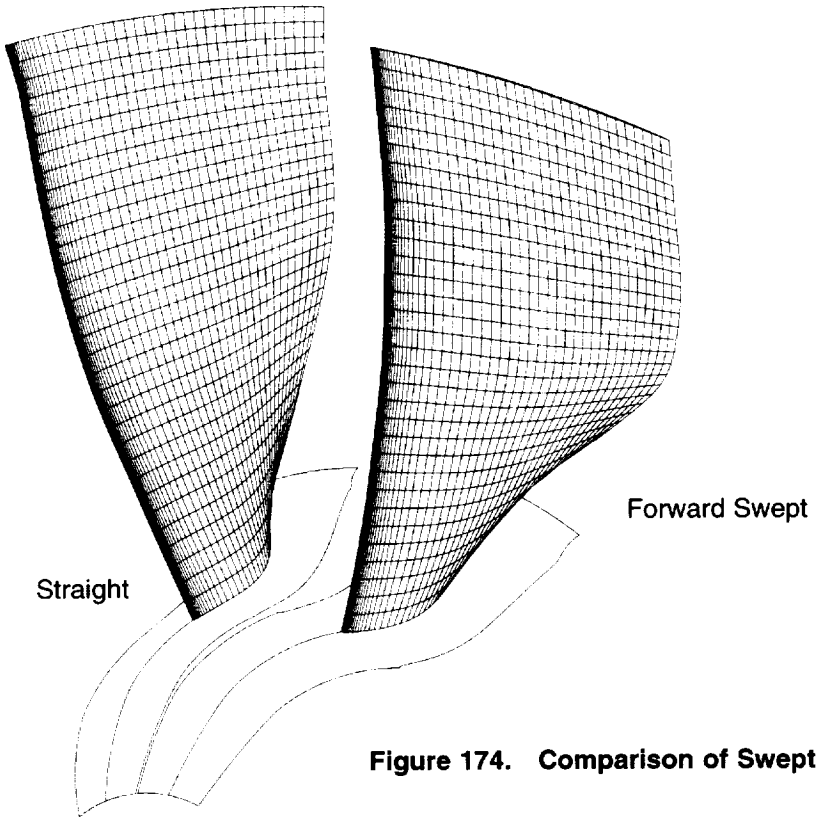

Figure 174. Comparison of Swept and Straight Geometries

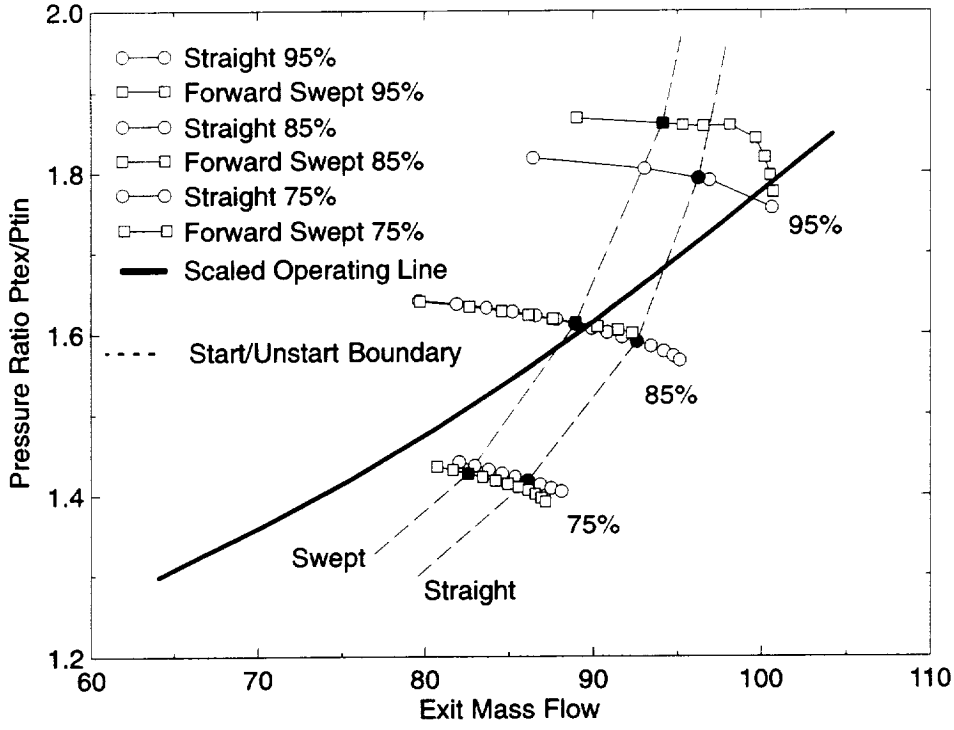

Figure 173. Fan Map for Swept and Straight Blades

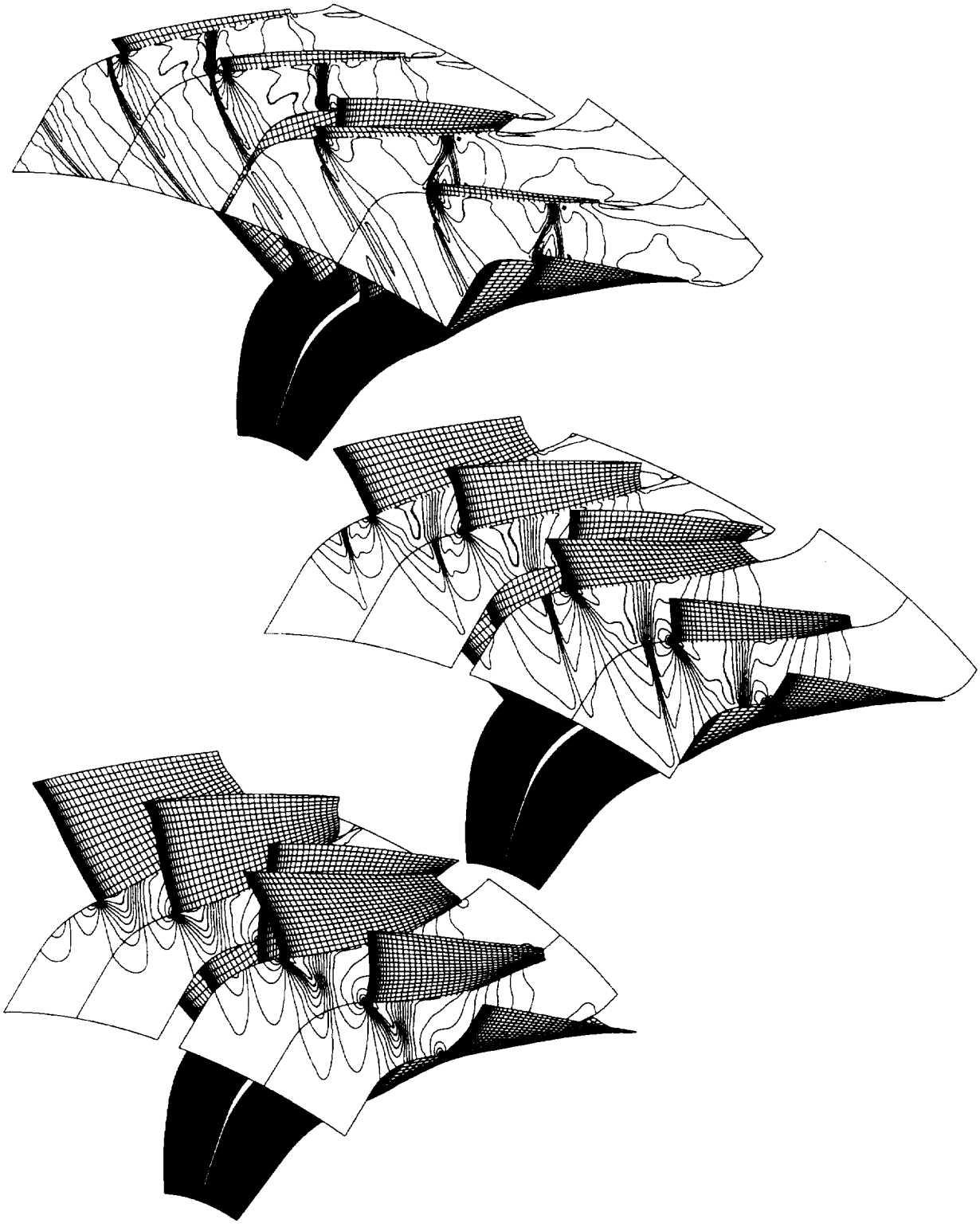

Figure 175. Comparison of Straight and Swept Blade Shock Patterns at 85% Speed (Forward Swept Right, Straight Left)

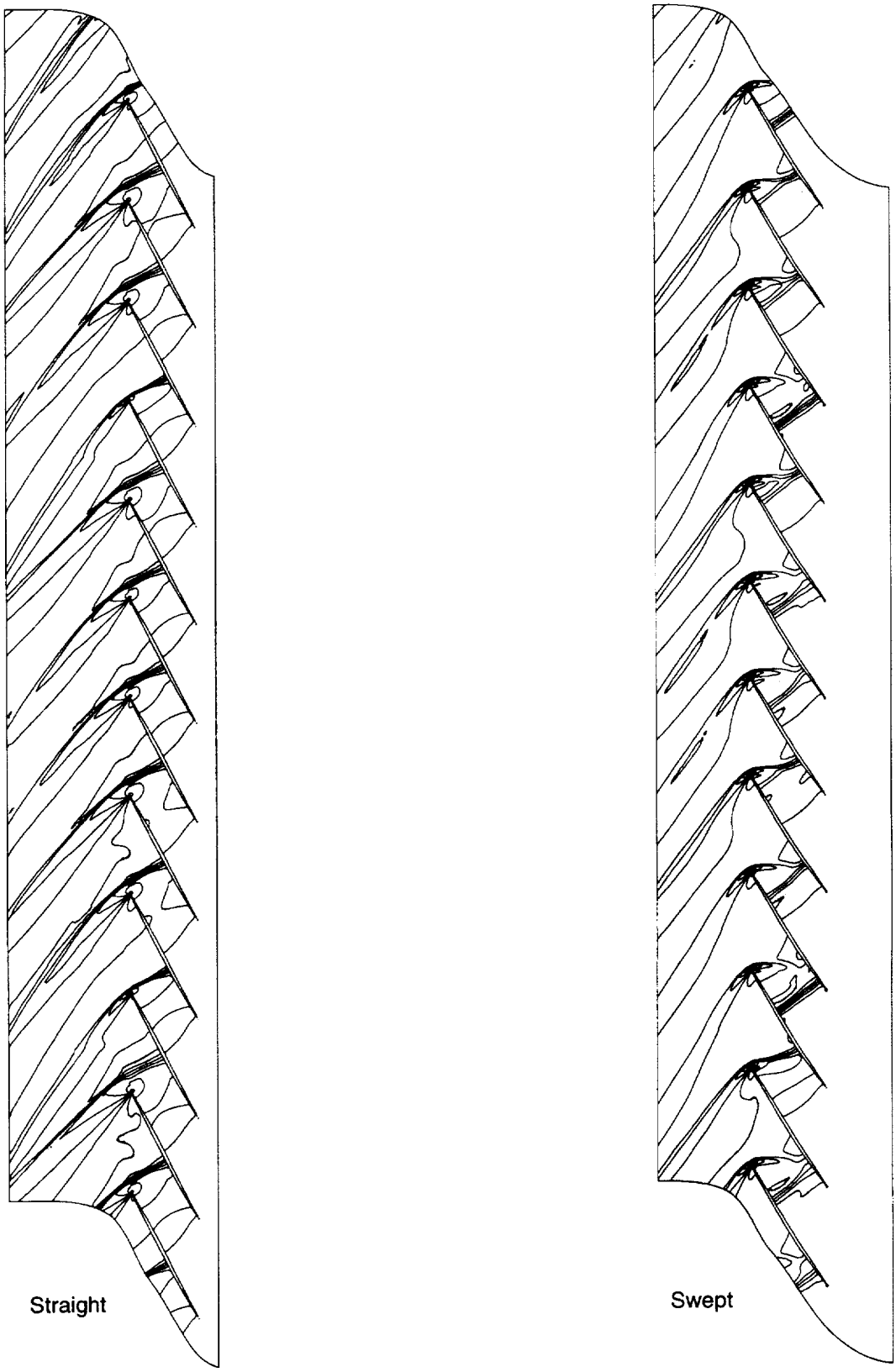

Figure 176. Comparison of Shock Structures Near Tip For Straight and Forward-Swept Blades

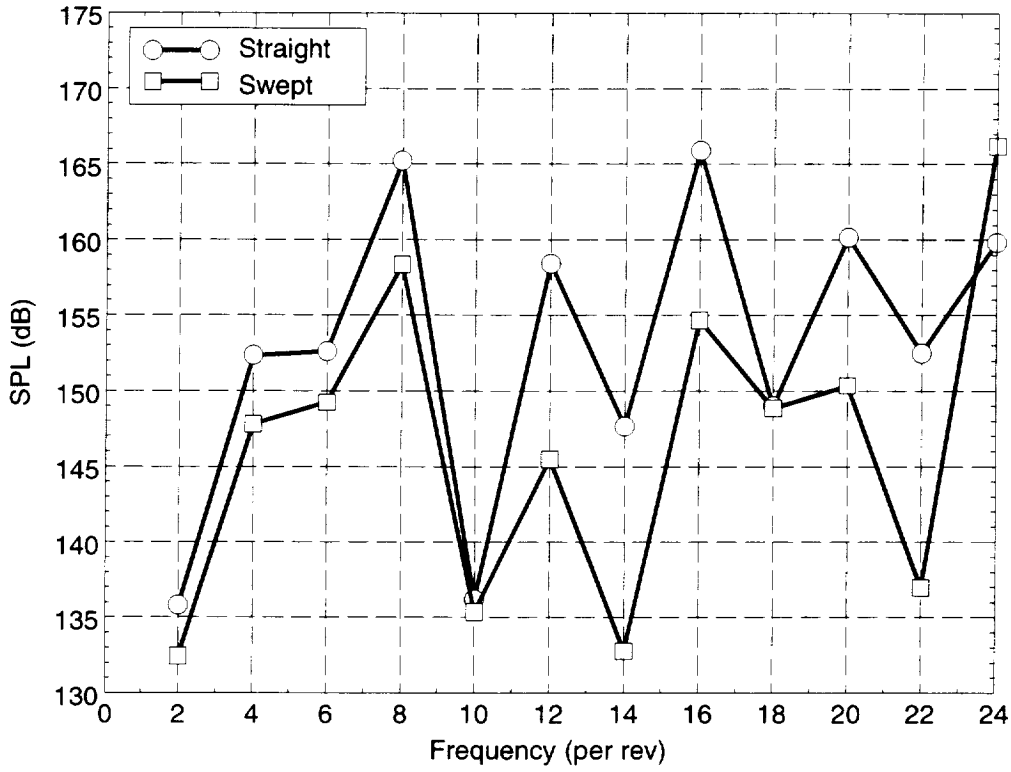

Figure 177. Comparison of Amplitude of Modes for Straight and Forward-Swept Blades

The farfield noise level will not just depend on the casing pressure field but the full radial variation. Figure 178 shows the radial pressure field some distance upstream of the fan. The radial pressure field associated with the forward-swept blade is more periodic relative to that of the straight blade. It can therefore be expected that the farfield noise arising from modes below blade passing frequency would be reduced. In addition, for the swept case the circumferential position of the shocks varies with radius, and this may also be beneficial in reducing MPT noise.

5.10.2 Blade Sorting

The CFD studies described in Section 5.6, page 166, indicate that the governing factor behind the MPT noise phenomena is the difference in geometric variations between adjacent blades rather than the variation itself.

This suggests that if the fan blades are shuffled in the annulus to minimize variations between adjacent blades then the MPT noise may be reduced. There has been some limited work in this area (Reference 81), although the patent only mentions the idea of sorting rather than any specific algorithm, probably due to commercial considerations.

If stagger angle variations $\delta\phi_i$ are considered, then it is required to minimize the following sum:

$$\sum_{i=1}^{n} |\delta\phi_i - \delta\phi_{i+1}| \tag{196}$$

where $\delta\phi_{n+1} = \delta\phi_1$ (197)

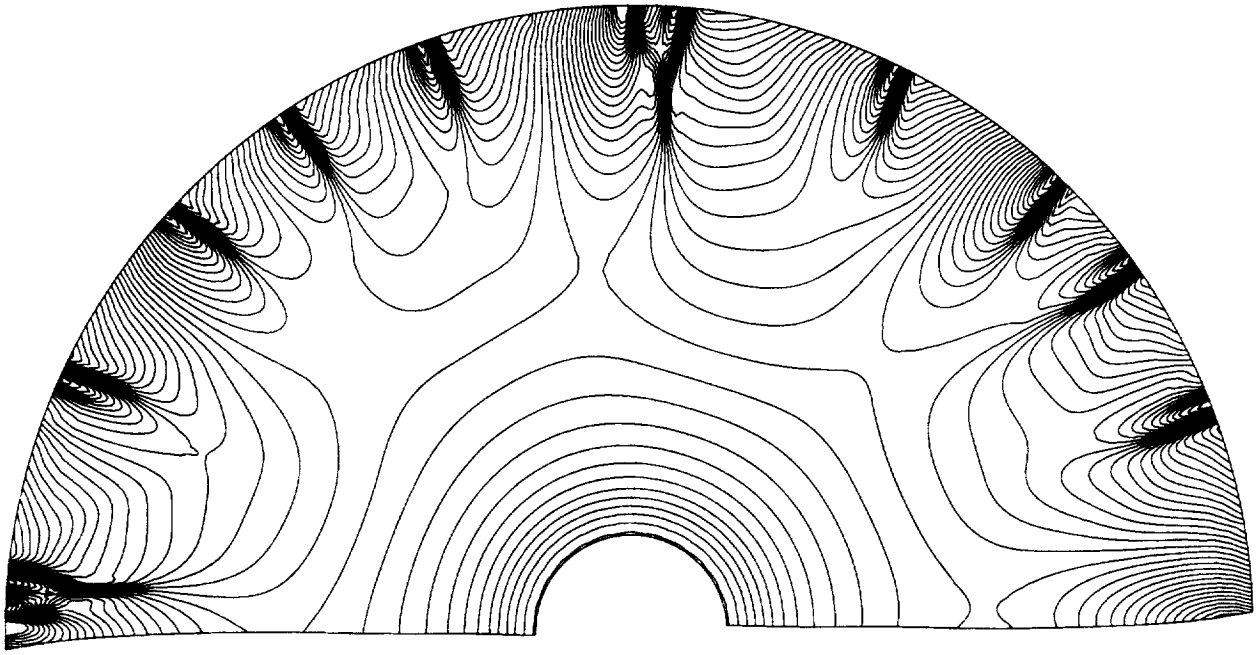

Straight Blade

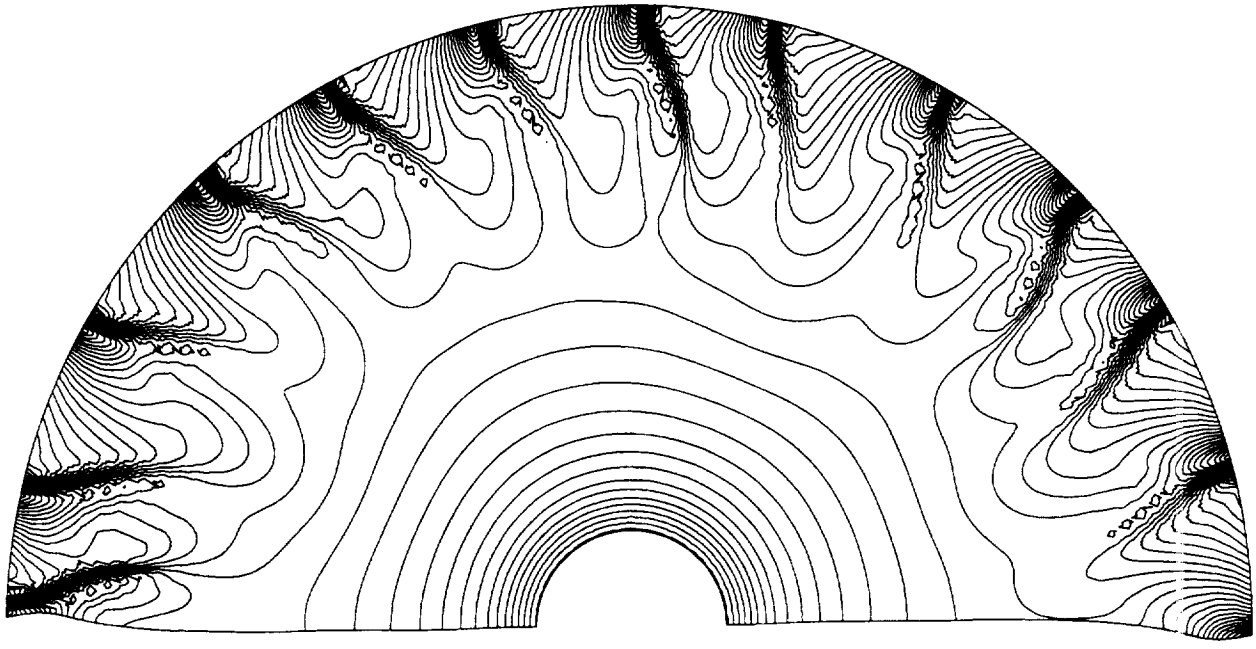

Forward Swept

Figure 178. Radial Pressure Distribution

An efficient algorithm is required to implement the required sort. Simply evaluating every possible combination is impractical. If $n = 20$, there are $n! = 2.4 \times 10^{18}$ possible combinations. Each combination requires about $2n - 1$ flops. If we assume a workstation running at 50 Mflops, evaluating every possible combination would take approximately a million years! We obviously require something more efficient.

The key to developing a more efficient algorithm is to recognize that generating the required sort is identical to the classic traveling salesman problem (TSP). Here the problem is to minimize the distance traveled for the salesman is to visit each city exactly once and return to the starting city. The blades can be thought of as cities lying on the $\delta\phi$ axis. This problem has been extensively studied, and there is much freely available software employing efficient algorithms.

To see if the idea of sorting has any merit, the half-annulus (11 blade) case for AF1 with stagger angle variations was chosen as a test vehicle. An approximate TSP algorithm was obtained, and the blades were sorted. The sort took a few seconds of CPU time. A new 11-blade mesh was generated, and the flow solver was exercised again.

Figure 179 compares the Fourier modes associated with the circumferential pressure distributions of the two solutions upstream of the leading edge. It can be seen that the amplitudes of the modes below blade passing frequency have, in general, been reduced by the sorting process — an average of approximately 3 dB. The mode at blade passing frequency has increased as a result of the sort. Sorting the blades has had the desired effect of moving the energy from the lower frequencies back towards the blade passing frequency.

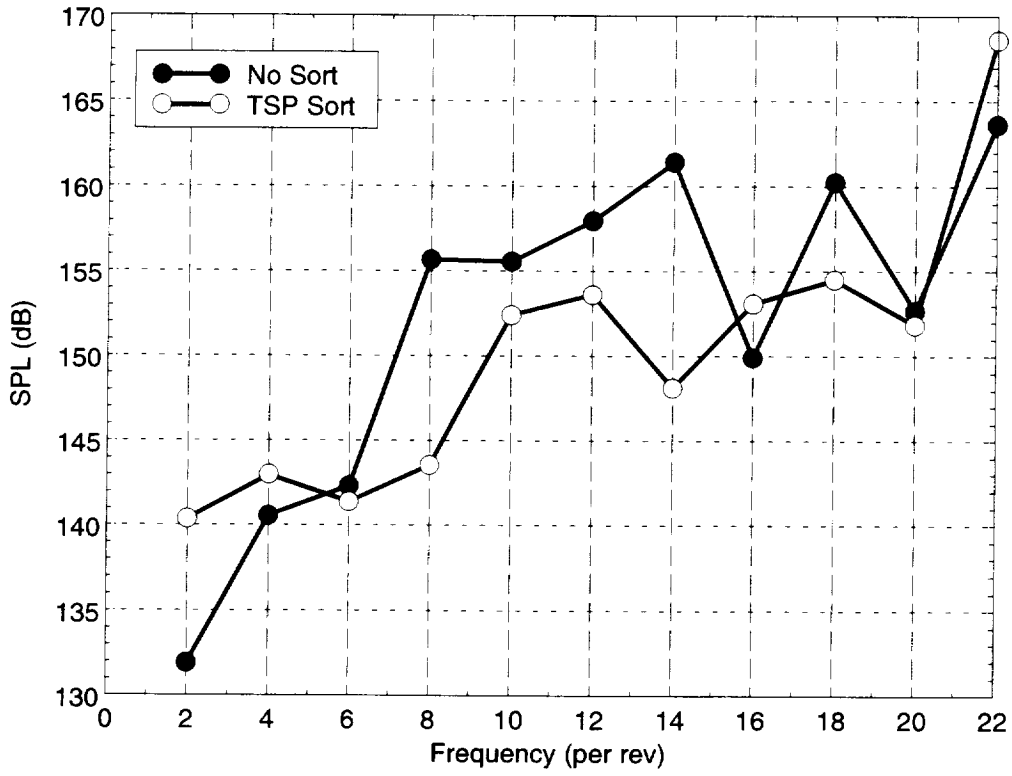

Figure 179. Comparison of Fourier Mode Amplitudes for Sorted and Unsorted Cases

The TSP sort is just one sort of many possible sorts. A number of other sorts were generated to investigate effectiveness. All were aimed at minimizing the sum of the stagger angle differences and employed a variety of algorithms. The blades were ordered as follows:

- **Original:** No sort (0.0/–0.1/0.2/–0.25/–0.2/0.1/0.15/0.05/0.25/–0.2/0.1)
- **TSP:** As described (0.0/0.1/0.2/0.05/0.1/0.15/0.25/–0.1/–0.2/–0.2/–0.25)
- **Descend:** Variations monotonically decreasing (0.25/0.2/0.15/0.1/0.1/0.05/0.0/–0.1/–0.2/–0.2/–0.25)
- **Ascend**: Variations monotonically increasing (–0.25/–0.2/–0.2/–0.1/0.0/0.05/0.1/0.1/0.15/0.2/0.25)
- **Sin:** Variations follow a sine wave (0.0/–0.1/–0.2/–0.25/–0.20/0.05/0.1/0.15/0.25/0.2/0.1)
- **Pyramid:** Variations increase, then decrease (–0.25/–0.2/0.0/0.1/0.15/0.25/0.2/0.1/0.05/–0.1/–0.20)

These sorts are shown graphically in Figure 180.

The results of these sorts on the 11-blade test case are shown in Figure 181. The pyramid and sine sorts provide the maximum reduction in the MPT modes. The maximum reduction for some modes is in excess of 25 dB! Table 15 shows the maximum and average reductions achieved by the various sorts for tones below the blade passing frequency. A negative value implies an increase in amplitude rather than a reduction. The fifth and sixth columns are the sum of the first and second differences of stagger angle.

Table 15. Comparison of Various Blade Sorts

Sort	Maximum dB	Minimum dB	Average dB	$\Sigma \lvert\delta\phi\rvert$	$\Sigma \lvert\delta^2\phi\rvert$
Original	00.0	0.00	0.00	2.4	4.4
TSP	13.3	–8.47	2.64	1.3	1.8
Descend	14.0	–8.81	4.86	1.0	1.4
Ascend	10.1	–7.36	1.21	1.0	1.4
Sine	20.8	–10.4	9.70	1.0	0.8
Pyramid	26.4	–10.4	11.7	1.0	0.9

From these CFD results, it can be concluded that the sorting of blades shows considerable promise in reducing the amplitude of the tones below blade passing frequency. It is interesting to note that the approximate TSP sort is not optimal in terms of the sum of stagger angle differences. The other four sorts are equally optimal, but all produce significantly different MPT spectra. These results imply that minimizing the sum of the stagger angle differences is necessary but not sufficient to minimize the MPT's. The exact nature of the condition to obtain a truly optimal sort is unclear. However, it may be postulated that, as the above sorts produced a desirable sort by essentially minimizing the sum of the first derivative of the stagger variations, it may be beneficial to minimize the sum of higher derivatives. The final column in Table 15 lists the sum of the second differences. Based on this consideration, the pyramid and sine sorts would be close to optimum of the sorts considered. With this small number of blades, it is possible to exhaustively search all combinations to see if there is a better minimum. Performing this search yields a second derivative minimum of 0.7, marginally better than the current optimal pyramid sort.

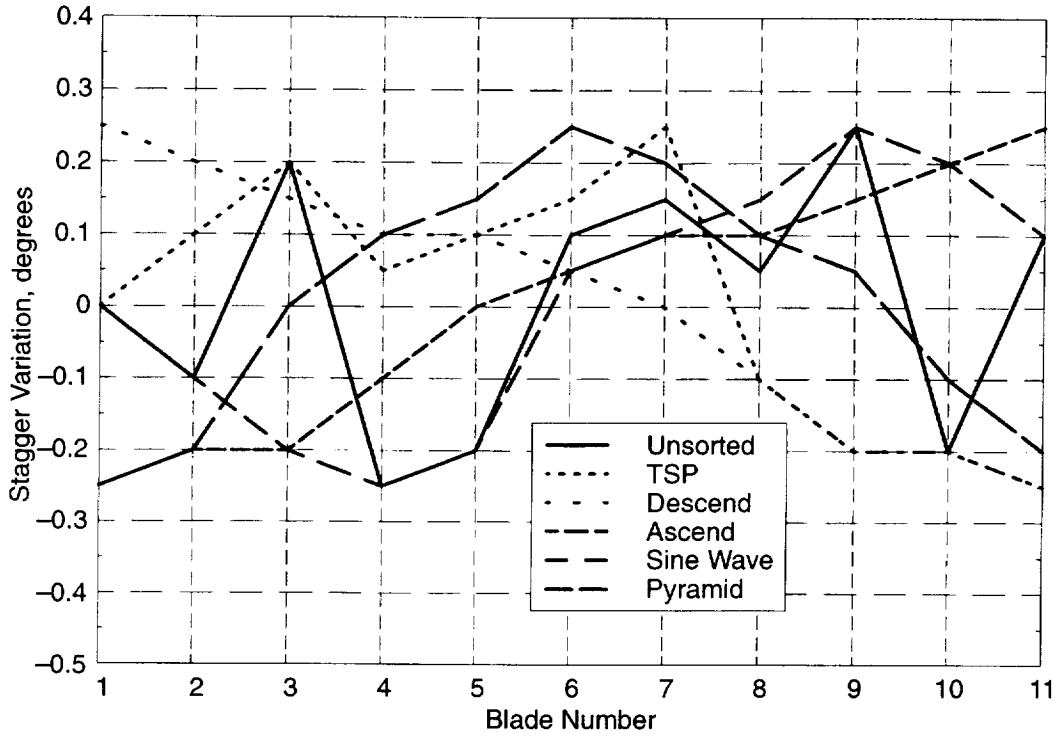

Figure 180. Comparison of Various Blade Sorts

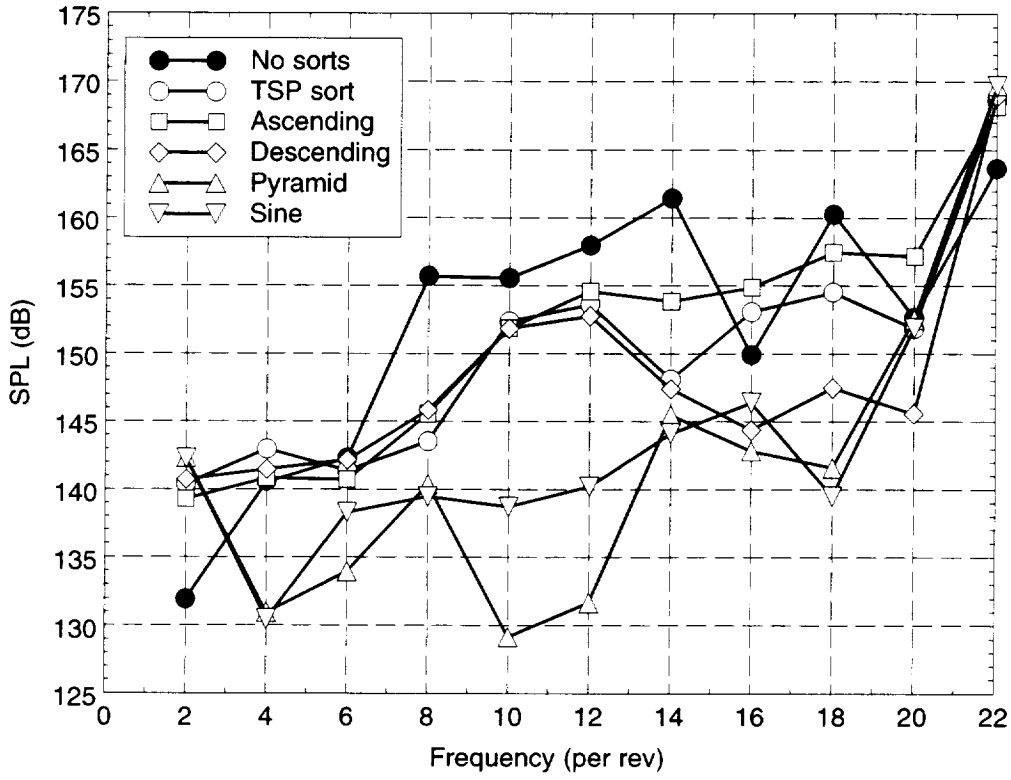

Figure 181. Comparison of the Effect of Various Sorts on Upstream Pressure Modes

In reality, it may not be possible to reorder the blades in the optimum way — due to other mechanical considerations. For example, it may not be possible to balance the fan. In addition, some sorts, for example the pyramid sort, will induce a once-per-revolution, shaft-bending moment that may be undesirable. (This arises as blades with high and low lift are grouped together.) The sorting algorithm would have to be modified with the mechanical requirements as a constraint on the reordering for noise considerations.

A final point can be made that MPT's are not necessarily all bad. The sorting ideas are aimed at pushing all the energy back into the blade passing frequency. Casing treatments can then be used to minimize this tone. However, this reduced tone will persist to the farfield. If the energy from this tone could be spread over lower frequencies by generating MPT's, then the farfield amplitude of the blade passing tone would be reduced. To gain the most benefit from this approach, a desired farfield spectrum would need to be defined based on perceived noise level. The blades could then be sorted to achieve this desired spectrum.

5.11 Summary and Conclusions

The CFD based MPT prediction method developed can quickly assess the effect on MPT spectra of geometry variations. The method requires a single three-dimensional solution to a six-passage problem where one blade has been modified to reflect the geometry variation of interest. Using this solution and a linear superposition algorithm, the MPT spectra of the complete fan may be estimated. This can be done efficiently for any distribution of geometry changes within the annulus.

A number of conclusions may be drawn from this work:

1. The amplitudes of the MPT's are governed by the flow regime the fan is operating in. If the flow is unstarted, the amplitudes will be high; if the flow is started, the amplitudes will be reduced.
2. The shape of the last 50% of chord governs the trailing-edge passage area and is the most important geometrical factor in the generation of MPT's. These shape changes can arise from stagger or camber variations.
3. Due to erroneous multiple solutions and the dominance of three-dimensional effects in fans, two-dimensional, quasi-3D solutions are inadequate for modeling MPT's.
4. A three-dimensional inviscid solution placed on the correct operating line is an adequate simulation vehicle for MPT prediction.
5. The MPT phenomena is linear and may be adequately predicted with a CFD based superposition algorithm.
6. Blade sorting and forward sweep show significant promise as methods for reducing MPT's.

6.0 Low-Emissions Core Noise Model Development

6.1 Objectives and Approach

The motivation for this study is the observation that, under conditions of low-power operation, core noise from an aircraft engine (which tends to be in the range of 400 Hz to 1 kHz for modern high-bypass turbofans) equipped with a LEC (low-emissions combustor) appears much more pronounced than from an engine equipped with an SC (standard combustor). The difference in peak SPL between the two combustor types that may be associated with core noise could be as high as 10 to 15 dB at low power operation. (The difference is virtually nonexistent at full-power.)

A key difference between LEC and an SC at low power is that some type of staged combustion (such as radially staged combustion) is employed with a LEC. Staged combustion results in much more spatially inhomogeneous heat release. The associated inhomogeneous temperature field can be a source of large temperature fluctuations, often called a "hot spot" or "entropy" wave. These hot spots, when convected through multistage turbomachinery, can generate noise in the farfield.

Section 6.2 describes an empirical correlation of combustor-related core noise developed using recent engine farfield acoustic measurements for engines that employ combustors of modern, low-emissions design. Some newer engines, particularly those employing dual-annular combustor designs, are noisier than expected in the frequency range characteristic of combustor-generated noise, at low power settings typical of landing or approach conditions. It was therefore deemed useful to collect and analyze the combustor-related noise characteristics from these newer engines and assess whether there was a consistent trend that low-emissions combustors do indeed generate higher noise levels than the older designs on which existing empirical correlations are based.

In Section 6.3, 3D CFD calculations are carried out for LEC and a SC engines operating at low power. Using the fast-chemistry "mixed is burned" model, the level of temperature fluctuations at combustor exit for the two cases are calculated. The mean temperature as well as temperature fluctuations are circumferentially averaged to obtain radially averaged information.

Section 6.4 describes an actuator-disk-based multistage turbomachinery analysis to compute noise generated aft of the turbomachinery due to the entropy waves incident on the turbomachinery. In the case of turbomachinery with all blade rows unchoked, the method of solution is essentially as has appeared in earlier literature. In the case where a blade row may be choked, other than the most downstream blade row, special treatment is needed. A spectral representation of the incident fluctuations (Fourier transform of the spatial correlation) is employed to predict the power spectra.

The 3D CFD cannot yield the length scales needed to fully characterize the temperature fluctuations. In Section 6.5 some preliminary ideas on how to estimate the needed length scales are discussed. In addition, comparisons between theory and data are presented for farfield SPL for a LEC and a SC at low power. The directivity model used to go from a power spectrum to a farfield SPL spectrum is the same as described in Section 4.4 (page 91). Full details of this directivity calculation, which is based on a partitioning of the acoustic power according to frequency and cut-off ratio, are given in a document authored by E.J. Rice and replicated as an addendum to this report. To minimize the amount of steady flow turbine aerodynamic information needed to implement the calculation, we assume the turbine aerodynamics to be in accord with a free-vortex design.

6.2 Combustor Noise Empirical Correlation

6.2.1 Introduction

The primary objective of work described in this section was to quantify the extent to which low-emissions combustors, particularly the dual-annular type, produce higher noise levels than the older, conventional combustors designed to less stringent emissions standards. A secondary objective was to evaluate the extent to which accepted combustor prediction models, in particular the method described in References 83 and 84, underpredict noise of these types of combustors and, if possible, establish an improved prediction method that accounts for some of the important design features of low-emissions combustors.

6.2.2 Approach

Static test stand farfield acoustic data taken at the GEAE Peebles Site 4D facility on several modern commercial turbofans with low-emissions combustors were collected for this study. These data included both SAC and DAC configurations of the CF6–80C2, CFM56–5B, CFM56–7B, and GE90 engines. The overall farfield noise data were first decomposed or decimated to assess contributions due to the combustor for each of the engines. Next, the data were separated into two groups: SAC and DAC. For each group, SPL correlations were developed that take into account combustor geometry, cycle conditions, spectral frequency content, and measurement angle or directivity. The resulting correlations developed from these data sets were then compared with the measured data and with existing empirical prediction models.

6.2.3 Current Empirical Prediction Model

Current GEAE design practice uses the prediction method described in References 83 and 84. That method assumes engine core (or combustor) noise spectra peak at 400 Hz, independent of combustor geometry or engine airflow; it is based on older, single-annular-type combustors and does not account for staging of the fuel injectors. A more recent combustor or core noise prediction model developed by NASA (Reference 85) takes into account combustor size and introduces multiple-lobe frequency spectra, rather than using a single spectral shape that peaks at 400 Hz. It was felt useful to investigate whether the multiple-peak frequency spectrum concept was indeed exhibited by the LEC data collected for this study.

It was speculated that, if the existing (References 83 and 84) prediction model is inaccurate in predicting the noise characteristics of LEC's, then any improved model should have the ability to take into account the following:

- Combustor geometry
- Engine cycle parameters
- Single- versus double-annular combustor design
- Fuel injector staging pattern
- Turbine nozzle loss parameters

Data analyses and subsequent development of a new combustor noise correlation method are described in the next subsection. A FORTRAN-based computer code featuring these correlations has been developed.

6.2.4 Engine Data Decomposition and Correlation

Diversitec, Inc. was subcontracted to carry out the engine data decomposition and correlate the resulting combustor-related noise levels for the data sets. Diversitec developed a decomposition or "decimation" algorithm that separated combustor noise from the total noise spectra. The "decimation" process used the method outlined in Reference 86 for identifying the contribution of fan noise and the method of Reference 87 for identifying the contribution of jet noise to the total spectrum. The process consisted of fitting fan and jet spectral shapes from References 86 and 87 to the data and then extracting the remaining noise levels as combustor noise, concentrating on part-power data in the aft quadrant where combustor noise is most likely to be a significant contributor.

The "decimated" results showed that single-annular combustors exhibit spectral noise peaks at 63, 160, and 630 Hz; the dual-annular combustors exhibit peaks at 160 and 500 Hz. Hence, the multiple-lobe frequency model proposed in Reference 85 seemed a logical approach to correlating the data. The correlations were therefore developed for the peak SPL's at each of these frequencies, for SAC and DAC engines separately.

Correlations for the SAC configurations were based on data from the CF6–80C2, CFM56–5B, and CFM56–7B engines. Correlations for the DAC configurations were based on data from the GE90, CFM56–5B, and CFM56–7B engines. The final correlation models developed from the SAC and DAC data sets are described in following subsections.

6.2.5 SAC Correlation

The single-annular combustors were found to exhibit three peak frequencies: 63 , 160, and 630 Hz. In addition, the 63-Hz data were found to peak at an observer angle 150° from the engine inlet axis, while the 160- and 630-Hz data were found to peak at 130°. Based on the above observations, a separate set of correlations was developed for each of the peak frequencies, as described below.

The computational procedure for estimating sound pressure level comprises the following steps:

Step 1: For SAC's, pick one of the three peak frequencies and the corresponding peak angle. The peak frequencies and peak angles are:

$$f_p = 63 \text{ Hz}, \alpha_p = 150°$$
$$f_p = 160 \text{ Hz}, \alpha_p = 130°$$
$$f_p = 630 \text{ Hz}, \alpha_p = 130°$$

Step 2. To calculate OASPL at a given angle (α), normalize it by α_p:

$$\alpha_n = \alpha / \alpha_p \tag{198}$$

Step 3. Use the following equations to compute normalized OASPL (OASPLN) as a function of α_n.

For the spectral peak at $f_p = 63$ Hz:

$$\text{OASPLN} = -67.8\,(\alpha_n)^2 + 141.7\,(\alpha_n) - 66.84 \tag{199}$$

For the spectral peak at $f_p = 160$ Hz:

$$\text{OASPLN} = -26.019\,(\alpha_n)^3 - 5.2974\,(\alpha_n)^2 + 93.43\,(\alpha_n) - 61.75(200) \tag{201}$$

For the spectral peak at f_p = 630 Hz:

$$\text{OASPLN} = -156.5\ (\alpha_n)^2 + 322.34\ (\alpha_n) - 164.89 \tag{202}$$

Step 4: Next, compute OASPL as a function of α using the following:

For the peak SPL at f_p = 63 Hz:

$$\text{OASPL}(\alpha) = \text{OASPLN}(\alpha_n) + \text{OASPL}(\alpha_p) + 0.40\ [\text{SPL}(\text{F}_\text{C}) - \text{SPL}(\text{T}_\text{L})] \tag{203}$$

For the peak SPL at f_p = 160 Hz:

$$\text{OASPL}(\alpha) = \text{OASPLN}(\alpha_n) + \text{OASPL}(\alpha_p) + 0.10\ [\text{SPL}(\text{F}_\text{C}) - \text{SPL}(\text{T}_\text{L})] \tag{204}$$

For the peak SPL at f_p = 630 Hz:

$$\text{OASPL}(\alpha) = \text{OASPLN}(\alpha_n) + \text{OASPL}(\alpha_p) + 0.30\ [\text{SPL}(F_C) - \text{SPL}(T_L)] \tag{205}$$

SPL(F_C) and SPL(T_L) are the combustor flow and turbine nozzle transmission-loss related effects, defined as follows:

$$\text{SPL}(F_C) = 20 \log (F_C) \tag{206}$$

$$\text{SPL}(T_L) = 20 \log (T_L) \tag{207}$$

where

$$F_C = \frac{W_3 \sqrt{T_4 - T_3}}{P_3 \cdot A_{EC}^2 \sqrt{N_f}} \tag{208}$$

$$T_L = \frac{(1 + F_T)^2}{(4L_c \cdot F_T)/(\pi \cdot h)} \tag{209}$$

$$F_T = (P_4/P_7)(T_7/T_4)^{1/2} \tag{210}$$

The turbine transmission loss effect SPL(T_L) is taken from Reference 88. Definitions of the various flow, geometry, and cycle parameters are listed in Table 16. Subscript "4" refers to combustor exit or turbine inlet conditions, subscript "3" refers to combustor inlet conditions, and subscript "7" refers to last turbine stage exit conditions. P refers to total pressure and T refers to total temperature. W_3 is the combustor airflow.

Step 5: In order to carry out computations in step 4, one needs to compute the peak overall sound pressure level, OASPL(α_p), as follows:

For f_p = 63 Hz:

$$\text{OASPL}(\alpha_p) = -20 \log (R_0) + H_{CP} \cdot (30/N_f)^{-0.225} \tag{211}$$

where

$$H_{CP} = 76.45 + 14.256 \cdot \log (CP) \tag{212}$$

and cycle parameter

$$CP = \frac{W_3 \sqrt{T_3}}{P_3} \cdot \frac{(T_4 - T_3)}{T_4} \cdot \frac{P_3}{P_0} \cdot \left(\frac{D_h}{D_e}\right)^{0.50} \tag{213}$$

Table 16. Nomenclature and Cycle Parameter Definitions

Nomenclature	Definition
AA	Air Attenuation, dB per 1000 ft, GEAE Design Practice
f_n	Normalized Frequency ($f_n = f/f_p$)
f_p	Combustor Spectral Lobe Peak Acoustic Frequency, Hz
OASPL	Overall Sound Pressure Level, dB
OASPLN	Normalized OASPL, dB
R_0	Observation Radius (150ft)
SPL	Sound Pressure Level, dB
SPLN	Normalized SPL, dB
α_n	Normalized Observer Angle Relative to Inlet Axis, α/α_p
α_p	Peak Noise Observer Angle Relative to Inlet Axis, Degrees
A_{EC}	Combustor Exit Area (Station 3.9), ft^2
D_e	Exhaust Nozzle Exit Plane Effective Diameter, ft
D_h	Exhaust Nozzle Exit Plane Hydraulic Diameter, ft
F_C	Combustor Flow Function
L_C	Combustor Nominal Length, ft
h	Annulus Height at Combustor Exit (Station 3.9), ft
N_f	Numbers of Ignited Fuel Nozzles
$N_{f\,max}$	Total Number of DAC Fuel Nozzles
P_o	Reference Ambient Pressure, psia
P_3	Combustor Inlet Pressure, psia
P_4	Combustor Exit Pressure, psia
P_7	Station 7 Turbine Exit Pressure, psia
T_3	Combustor Inlet Temperature, °R
T_4	Combustor Exit Temperature, °R
T_7	Station 7 Turbine Exit Temperature, °R
T_L	Turbine/Nozzle Acoustic Transmission Loss Parameter
W_3	Combustor Inlet Flow, lbm/s

For f_p = 160 Hz:
$$\mathrm{OASPL}(\alpha_p) = -20 \log (R_0) + H_{CP} \cdot (30/N_f)^{0.050} \tag{214}$$

where
$$H_{CP} = 108.50 + 3.31 \cdot \log (CP) \tag{215}$$

and CP is again given by Equation (213).

For f_p = 630 Hz:
$$\mathrm{OASPL}(\alpha_p) = -20 \log (R_0) + H_{CP} \cdot (30/N_f)^{0.020} \tag{216}$$

where
$$H_{CP} = 106.38 + 6.938 \cdot \log (CP) \tag{217}$$

and CP is again given by Equation (213).

Step 6: The SPL spectral shapes are computed from the following formulae.

First, compute normalized sound pressure level (SPLN) as a function of normalized frequency ($f_n = f/f_p$) as follows:

For f_p = 63 Hz: $$SPLN(f_n) = -152.70 + 295.46\,(f_n) - 145.61\,(f_n)^2 \quad (218)$$

For f_p = 160 Hz: $$SPLN(f_n) = -170.07 + 331.33\,(f_n) - 163.34\,(f_n)^2 \quad (219)$$

For f_p = 630 Hz: $$SPLN(f_n) = -147.50 + 286.40\,(f_n) - 142.31\,(f_n)^2 \quad (220)$$

Next, compute the spectra as follows:

$$SPL(\alpha, f) = OASPL(\alpha) + SPLN(f_n) + AA \cdot (R_0/1000) \quad (221)$$

where OASPL(α) is computed from Step 4, using OASPL(α_p) from Step 5 above, and SPLN(f_n) is computed from Step 6 above. *AA* is the air attenuation factor, in dB per 1000 ft, as computed by standard design practices.

6.2.6 DAC Correlation

The DAC's were found to exhibit two peak frequencies: 160 and 500 Hz. The corresponding peak observer angle (relative to engine inlet axis) was found to be fairly constant at 130°. The correlations developed for each of the peak frequencies are described below.

The procedure for estimating SPL comprises the following steps.

Step 1: For the DAC's, for either of the peak frequencies, the peak angle is 130°.

Step 2: To compute OASPL at a given angle (α), normalize it by α_p, see Equation (198).

Step 3: Use the following equation for computing normalized OASPL as a function of α_n.

For the spectral lobe with f_p = 160 Hz:

$$OASPLN = -116.95\,(\alpha_n)^2 + 235.23\,(\alpha_n) - 120.65 \quad (222)$$

For the spectral lobe with f_p = 500 Hz:

$$OASPLN = -137.59\,(\alpha_n)^2 + 283.40\,(\alpha_n) - 147.73 \quad (223)$$

Step 4: Next, compute OASPL as a function of α using the following:

For f_p = 160 Hz:

$$OASPL(\alpha) = OASPLN + OASPL(\alpha_p) + 0.45\,[SPL(F_C) - SPL(T_L)] \quad (224)$$

For f_p = 500 Hz:

$$OASPL(\alpha) = OASPLN + OASPL(\alpha_p) - 0.10\,[SPL\,(F_C) - SPL(T_L)] \quad (225)$$

In the above equations, SPL(F_C) and SPL(T_L) are combustor flow and turbine-related corrections. SPL(F_C) is as defined in Equation (206) for Step 4 of the SAC calculation procedure, but for DAC's:

$$F_C = \frac{W_3\sqrt{T_4 - T_3}}{P_3 \cdot A_{EC}^2\sqrt{20 + N_f}} \tag{226}$$

where N_f is now the number of inner-row fuel nozzles ignited.

The turbine transmission loss correction SPL(T_L) is the same as that given in Equation (207) for Step 4 of the SAC calculation procedure.

Step 5: To carry out computations in Step 4, one needs to compute OASPL(α_p), and for DAC's this correlation was developed as a function of the fuel-nozzles staging. GEAE combustor geometries, for which acoustic data were available, employ an inner row and an outer row with 20 fuel nozzles in the outer row and either 10 or 20 nozzles in the inner row, and tests were done with various sequential patterns of fuel nozzles burning/fired. The correlations therefore are for specific fuel nozzle patterns. The patterns tested fired all 20 outer-annulus nozzles, and the number and pattern of the inner row of nozzles was varied. The resulting correlations are as follows:

$$\text{OASPL}(\alpha_p) = K_{NF}\left[-20\log(R_0) + H_{CP}\left(\frac{20 + N_f}{N_{f,max}}\right)^{-X_K}\left(\frac{30}{20 + N_f}\right)^{M_f}\right] \tag{227}$$

where the exponent $M_f = 0.020$ for the spectral peak centered at $f_p = 160$ Hz, and $M_f = 0.180$ for the spectral peak centered at $f_p = 500$ Hz.

The coefficient K_{NF} and exponent X_K depend on both the spectral peak frequency and the fuel nozzle firing pattern. The following patterns were evaluated:

1. 20 outer + 20 inner firing, all inner nozzles burning
2. 20 outer + 10 inner firing (every other inner nozzle burning if there are 20)
3. 20 outer + (2×5) inner firing, 5 equally spaced pairs in the inner nozzle burning (20 inner nozzles but only 10 ignited)
4. 20 outer firing, no inner nozzles burning

The parameter constants K_{NF} and X_K for the above nozzle firing patterns are:

Firing Pattern	Peak Frequency	K_{NF}	X_K
20 + 20	160	1.20	0.25
20 + 20	500	1.00	0.25
20 + 10	160	0.98	0.25
20 + 10	500	0.90	0.25
20 + (2·5)	160	0.98	0.20
20 + (2·5)	500	0.90	0.20
20 + 0	160	1.10	0.00
20 + 0	500	0.98	0.00

The coefficient H_{CP} in Equation (227) for OASPL(α_p) is different for the two peak-frequency lobe spectra, as follows.

For f_p = 160 Hz:
$$H_{CP} = 76.45 + 14.256 \cdot \log (CP) \tag{228}$$

and
$$CP = \frac{W_3\sqrt{T_3}}{P_3} \cdot \frac{(T_4 - T_3)}{T_4} \cdot \frac{P_3}{P_0} \cdot \left(\frac{D_h}{D_e}\right)^2 \tag{229}$$

For f_p = 500 Hz:
$$H_{CP} = 110.62 + 2.997 \cdot \log (CP) \tag{230}$$

and
$$CP = \frac{W_3\sqrt{T_3}}{P_3} \cdot \frac{(T_4 - T_3)}{T_4} \cdot \frac{P_3}{P_0} \cdot \left(\frac{D_h}{D_e}\right)^{1.20} \tag{231}$$

Step 6: The SPL spectra are computed as follows:

First, compute normalized sound pressure level as a function of normalized frequency ($f_n = f/f_p$) as follows:

For f_p = 160 Hz: see Equation (219) on page 192

For f_p = 500 Hz:
$$\text{SPLN}(f_n) = -137.21 + 268.99\,(f_n) - 135.81\,(f_n)^2 \tag{232}$$

Next, compute the spectra using Equation (221) from page 192, except OASPL(α) is computed from Step 4 above, using OASPL(α_p) from Step 5 above, and SPLN(f_n) is computed from Step 6 above.

6.2.7 Prediction Model Parametric Trends and Patterns

Correlation-model trends were compared, using the above formulas, to illustrate the correlation model predicted "average" behavior, in terms of overall level as a function of cycle conditions, directivity patterns, and spectral shapes.

Examples of the predicted trend of SAC noise for peak OASPL are shown in Figures 182 through 184, as a function of the cycle parameter *CP*. These results are normalized to a distance of 1-ft radius and shown for peak OASPL for each peak frequency (63, 160, and 630 Hz) for 20, 30, and 40 fuel nozzles. It can be seen that the lowest peak-frequency OASPL (63 Hz) is the most sensitivity to changes in both CP and number of fuel nozzles (N_f). OASPL for the other two peak frequencies (160 and 630 Hz) are relatively insensitive to changes in these parameters, although the absolute levels are higher.

The DAC OASPL trends (again normalized to a 1-ft radius) are shown in Figures 185 and 186 for the two peak frequencies (160 and 500 Hz). For these example results, it was assumed that there were 20 inner and 20 outer nozzles and the outer nozzles were on for all combinations of inner nozzle ignition patterns. The DAC trends at both peak frequencies show a rather low sensitivity to CP. An interesting observation is the highest levels of noise for the case with all inner nozzles fired (20 + 20). The next highest levels are predicted for no inner nozzles fired (20 + 0). The two intermediate patterns (20 + 10) and (20 + 2×5) show the lowest levels, with very little difference between the two. These results are qualitatively consistent with the experimentally observed differences from tests of a CFM56 DAC engine.

Comparisons of the empirically derived OASPL directivity patterns were computed for SAC and DAC types using the above formulas, and these are shown in Figures 187 and 188. For the SAC, peak

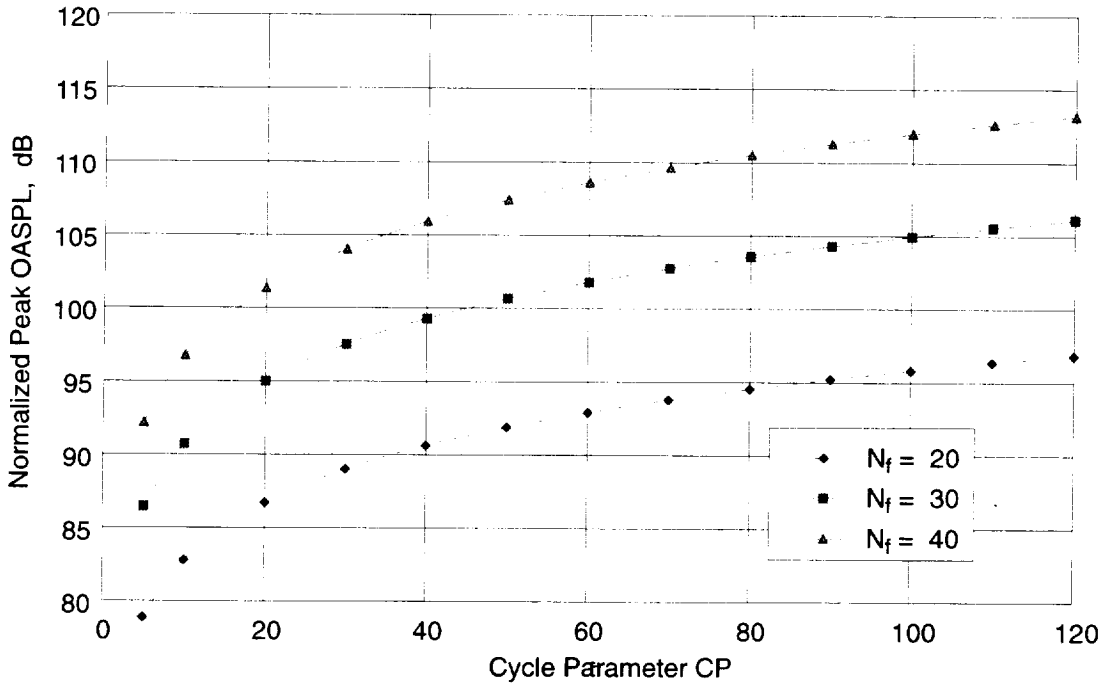

Figure 182. Peak OASPL Correlation Trends for SAC at 63-Hz Peak Frequency

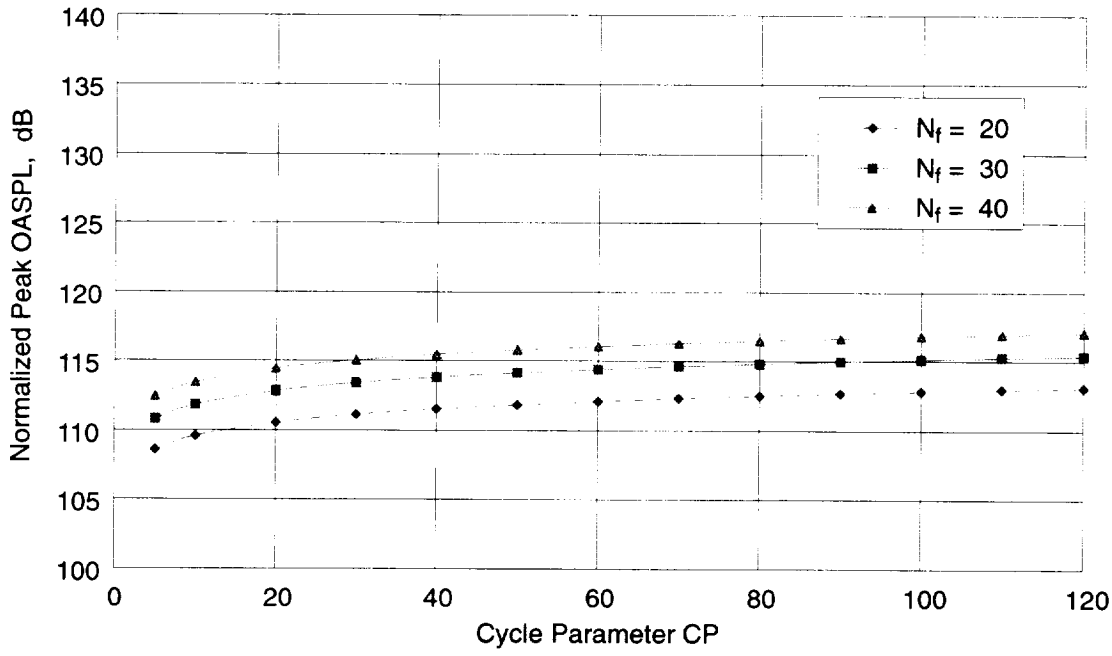

Figure 183. Peak OASPL Correlation Trends for SAC at 160-Hz Peak Frequency

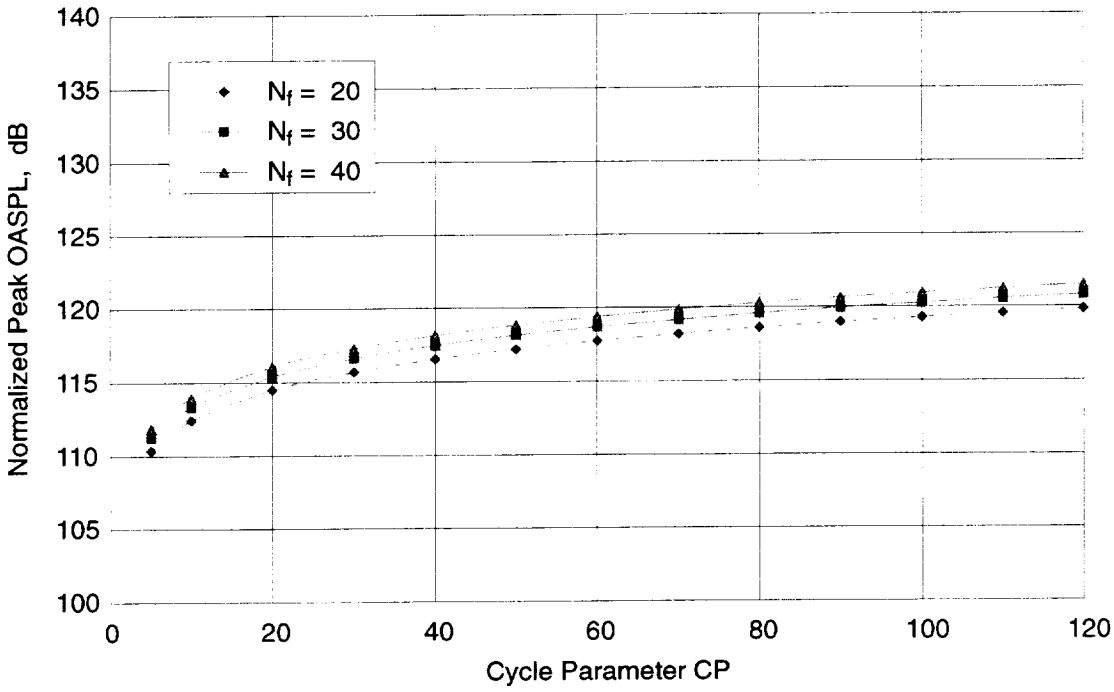

Figure 184. Peak OASPL Correlation Trends for SAC at 630-Hz Peak Frequency

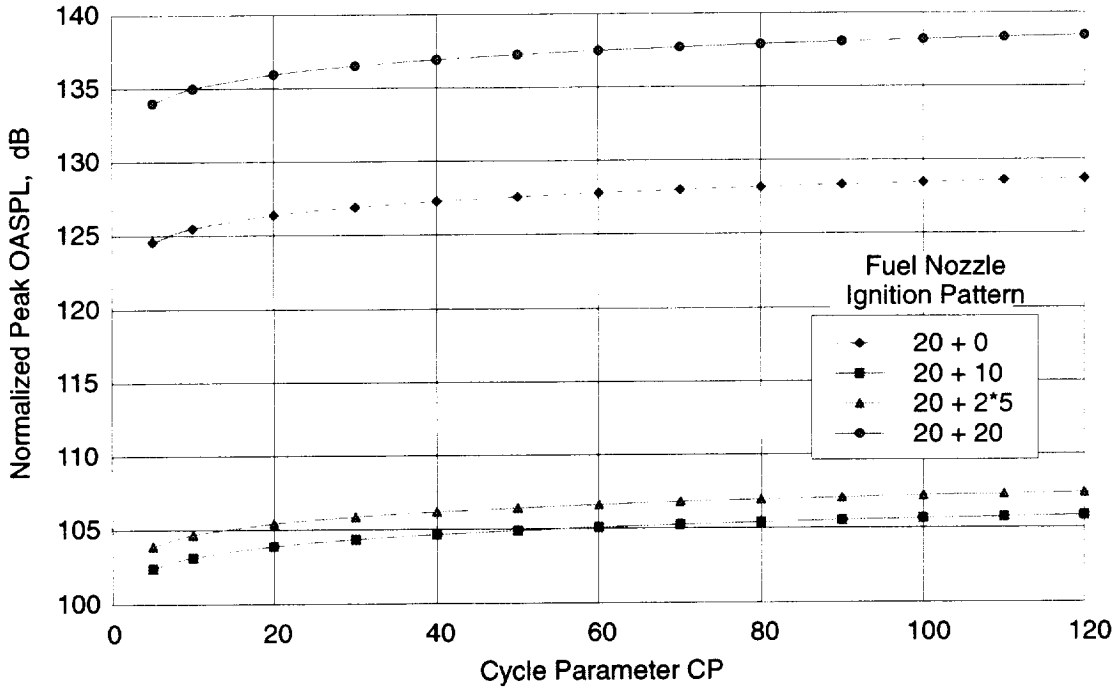

Figure 185. Peak OASPL Correlation Trends for DAC at 160-Hz Peak Frequency

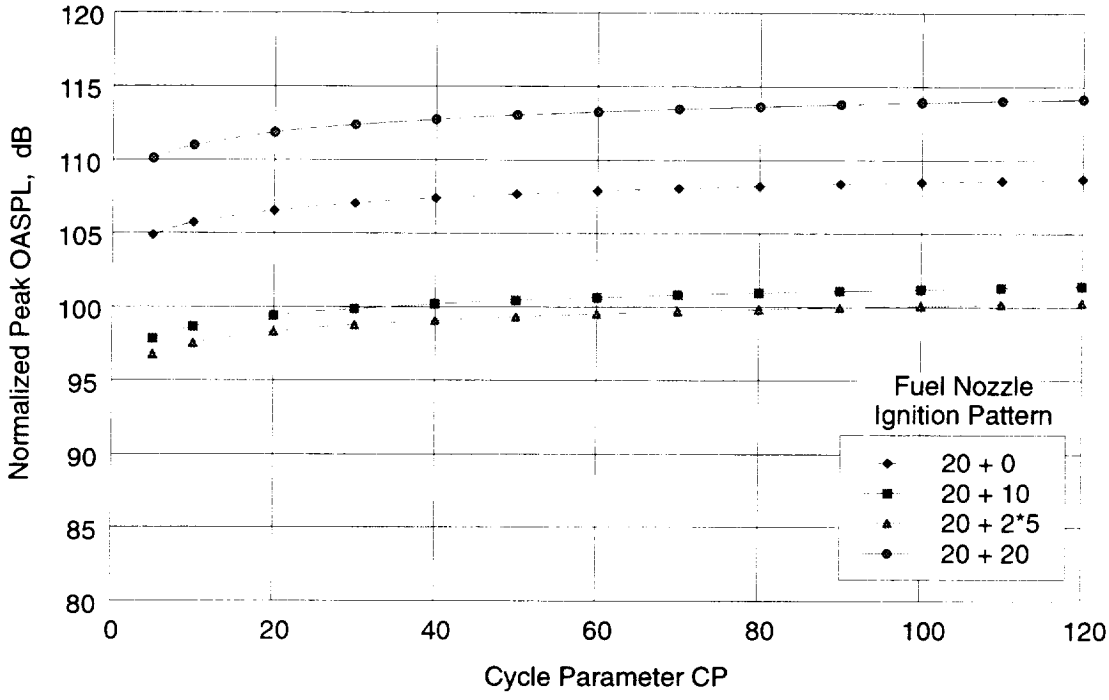

Figure 186. Peak OASPL Correlation Trends for DAC at 500-Hz Peak Frequency

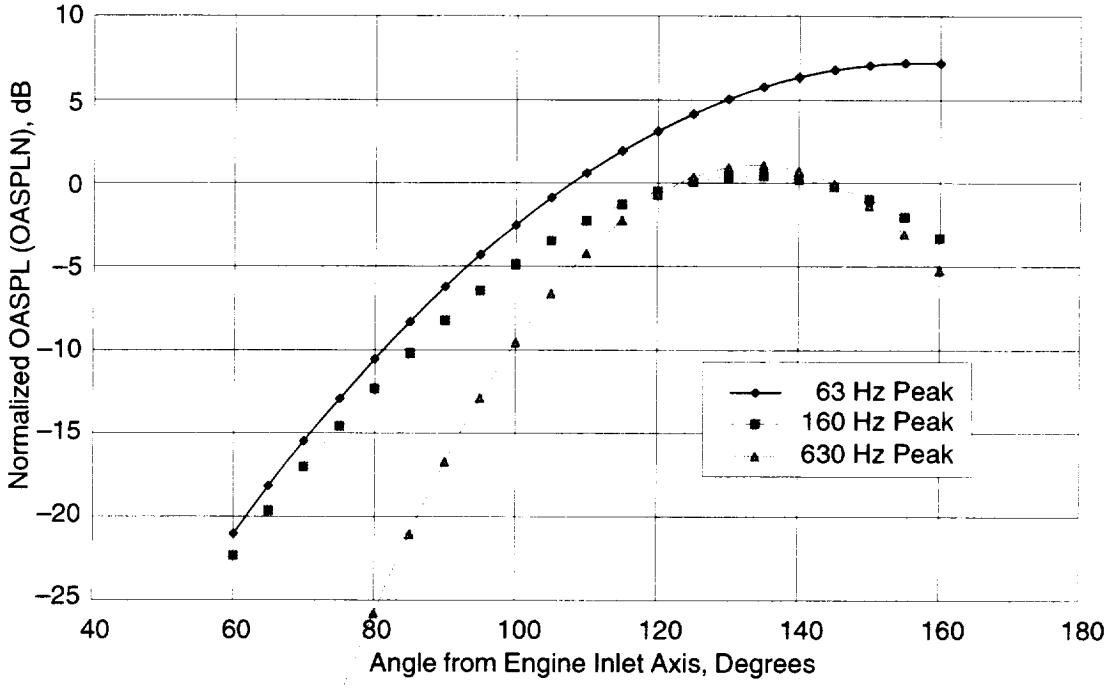

Figure 187. OASPL Directivity Trends for SAC

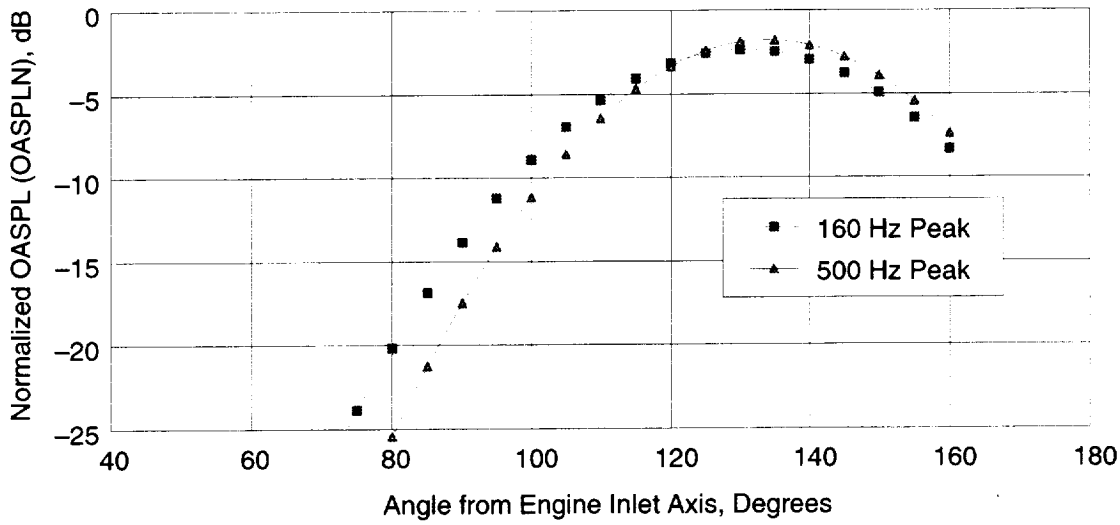

Figure 188. OASPL Directivity Trends for DAC

noise levels occur at 150° for the 63-Hz peak spectral lobe, and the spectral lobes that peak at 160 and 630 Hz have directivity peaks at 130°. Note that the 63-Hz directivity pattern does not have a peak close to zero, implying that this low-frequency peak is an additional 6 or 7 dB higher than the other two peaks. The DAC directivity patterns are similar; that is, there is no dramatic difference between the 160-Hz and 500-Hz peak patterns, and they are similar to the 630-Hz peak pattern for the SAC.

Comparisons of the empirically derived spectral shapes were computed for SAC and DAC types using the above formulas, and these are shown in Figures 189 and 190. Note that the spectral shapes as derived from the data correlation are very "peaky." That is, they are relatively narrow and do not appear to duplicate the combustor noise spectral shapes inferred from measured engine data. This observation is discussed further in the next subsection.

6.2.8 Comparison of Predictions with Data-Sample Trends

The empirical combustor noise-correlation models described above were exercised and generated predictions to compare with sample data sets. Data were compared with predictions made using the present correlation model and the older correlation model of References 83 and 84. The results are illustrated in Figures 191 through 198. These comparisons cover four engine models, for two power settings each. Power settings are denoted by the parameter CP', which is CP from Equation (213) on page 190 with the D_h/D_e factor omitted and then normalized by the exhaust nozzle area A_N.

The first comparisons are shown in Figures 191 and 192 for a CFM56 engine with a SAC. The 1/3-octave SPL spectra are shown at four observer angles: 100°, 110°, 120°, and 130°. Figure 191 shows the comparisons for a power setting corresponding to $CP' = 8.07$; Figure 192 is for a power setting corresponding to $CP' = 15.7$. Both power settings are in the range of aircraft-landing conditions, where combustor noise can be a significant contributor. The square symbols denote the actual engine data, and the circle symbols denote the old prediction method described in References 83 and 84. The current correlation model is denoted by triangle symbols. It can be seen from Figure 191 that the old method does not appear to simulate the correct peak frequencies, nor does it present a

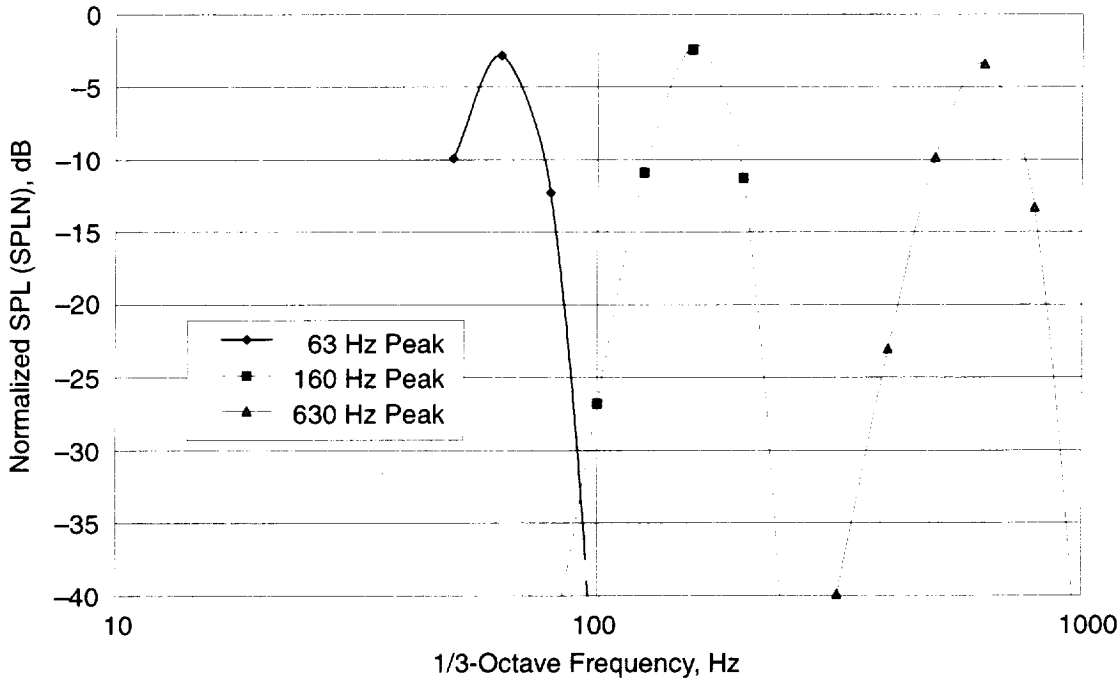

Figure 189. Normalized Spectrum Shapes for SAC

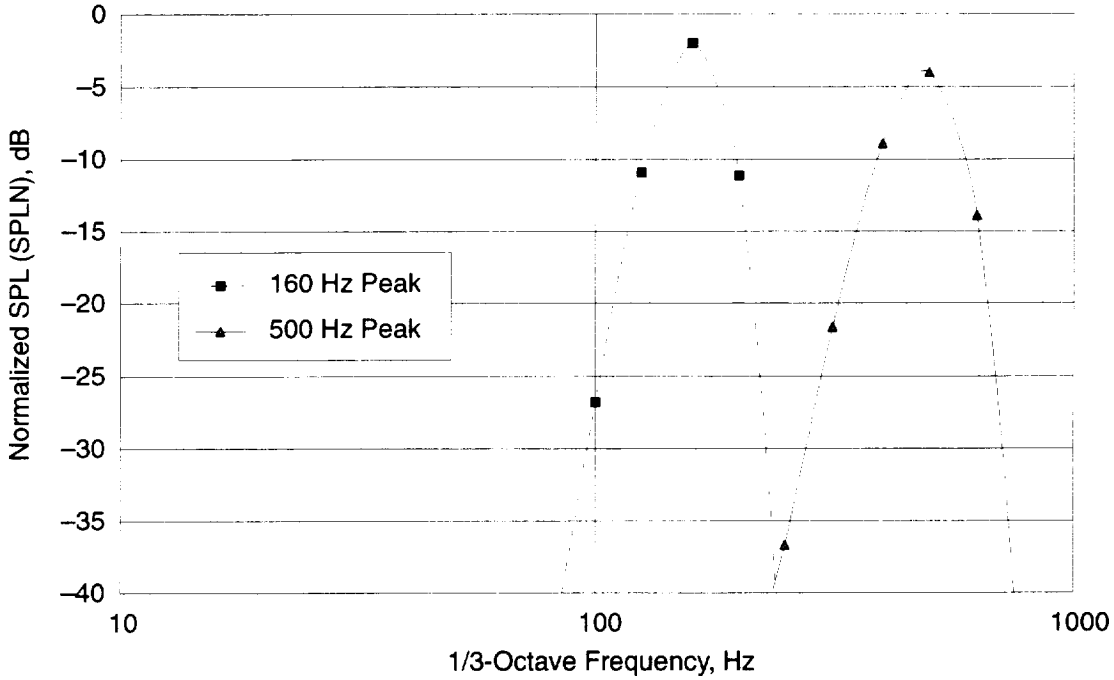

Figure 190. Normalized Spectrum Shapes for DAC

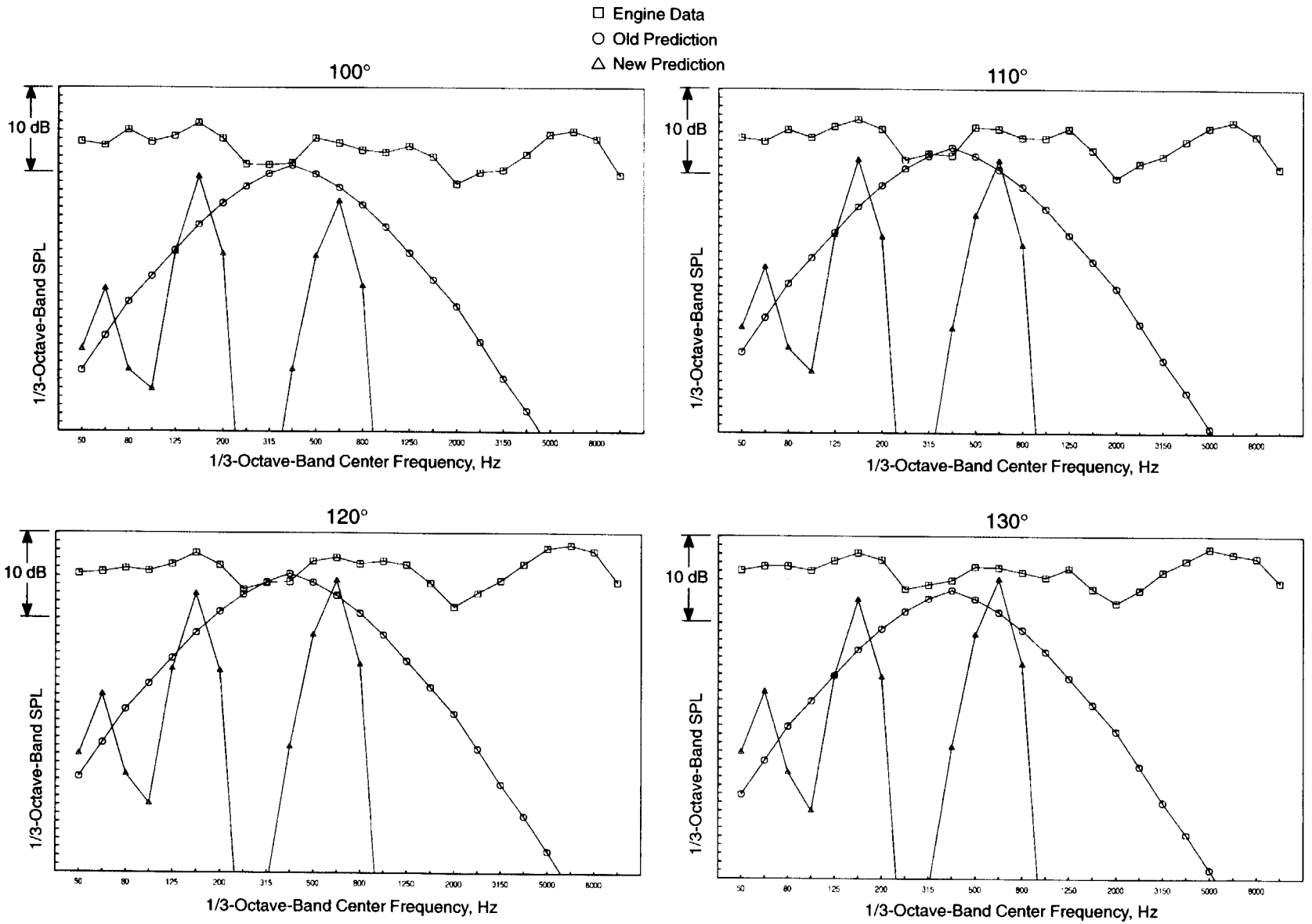

Figure 191. Comparison of Predictions with Data-Sample Trends: CFM56 SAC – CP′ = 8.07

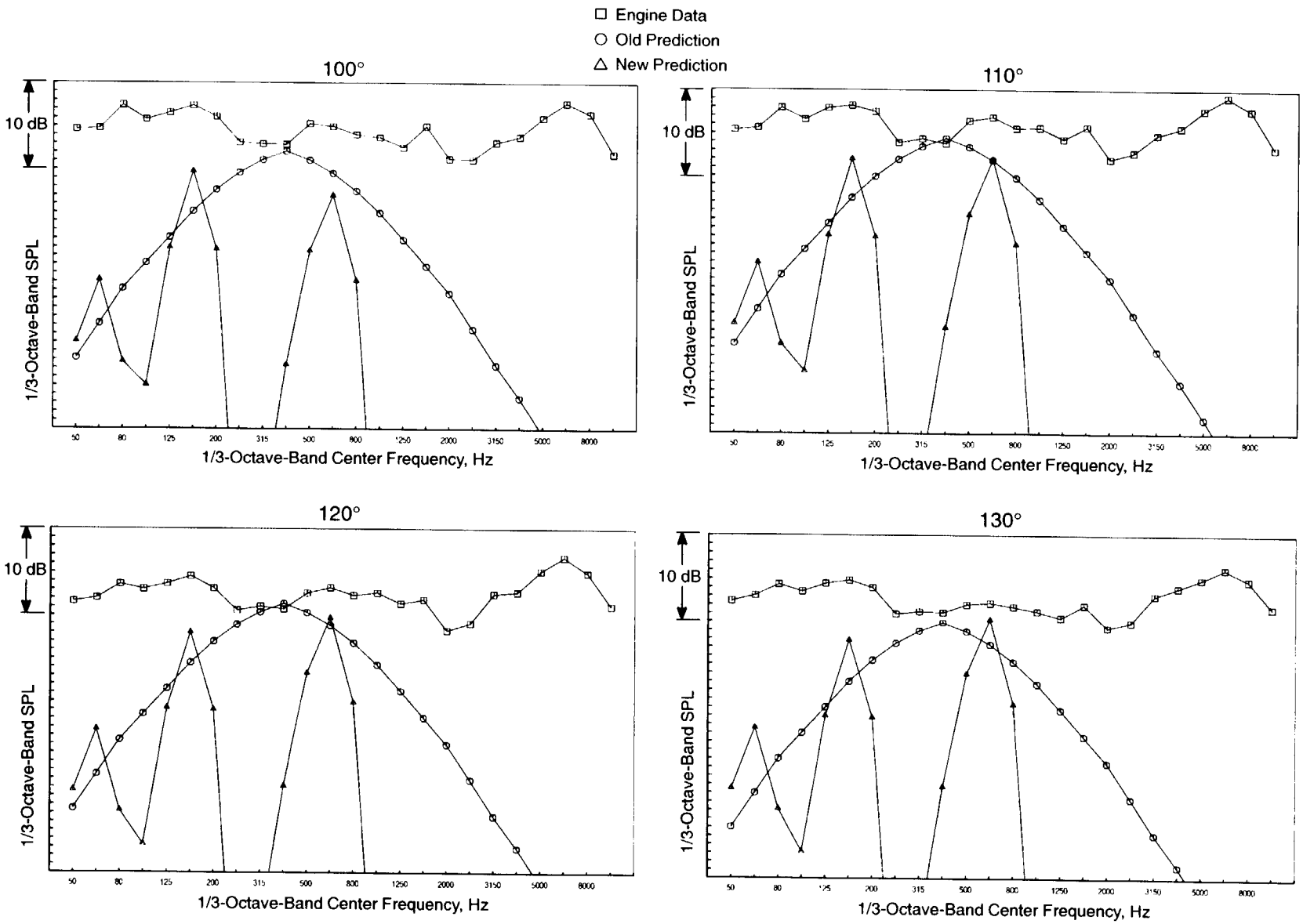

Figure 192. Comparison of Predictions with Data-Sample Trends: CFM56 SAC – CP′ = 15.7

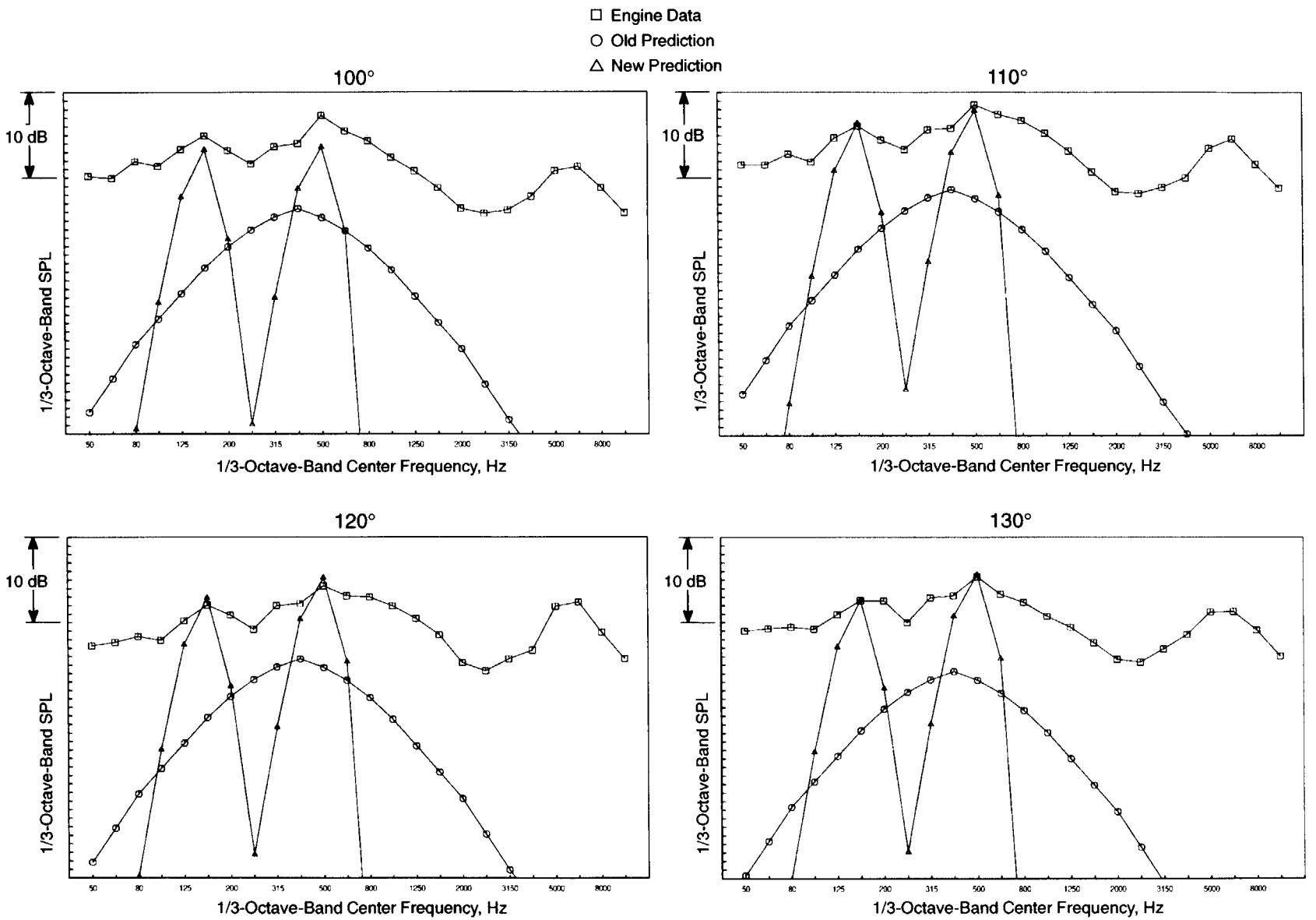

Figure 193. Comparison of Predictions with Data-Sample Trends: CFM56 DAC – CP′ = 8.8

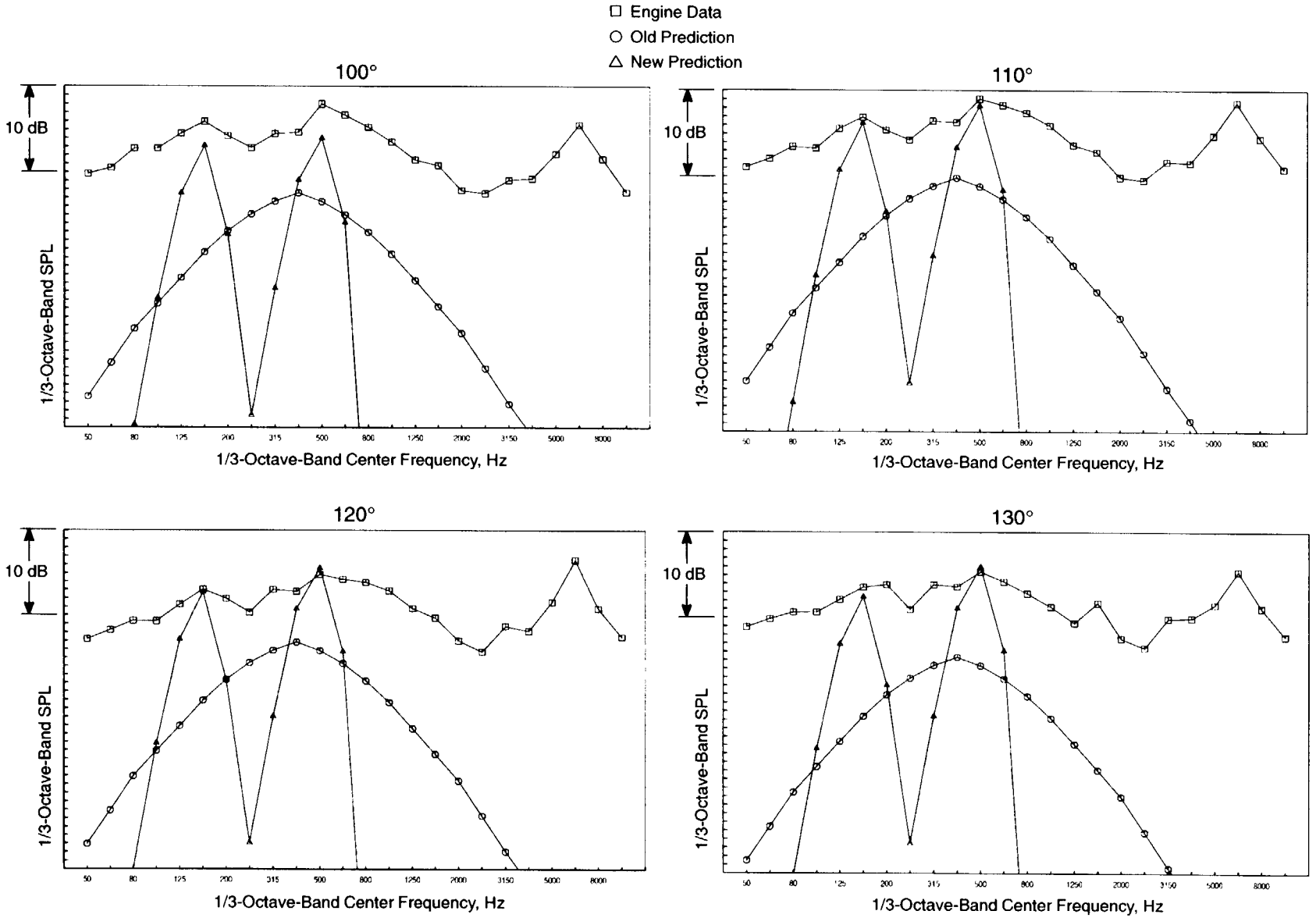

Figure 194. Comparison of Predictions with Data-Sample Trends: CFM56 DAC – CP′ = 12.9

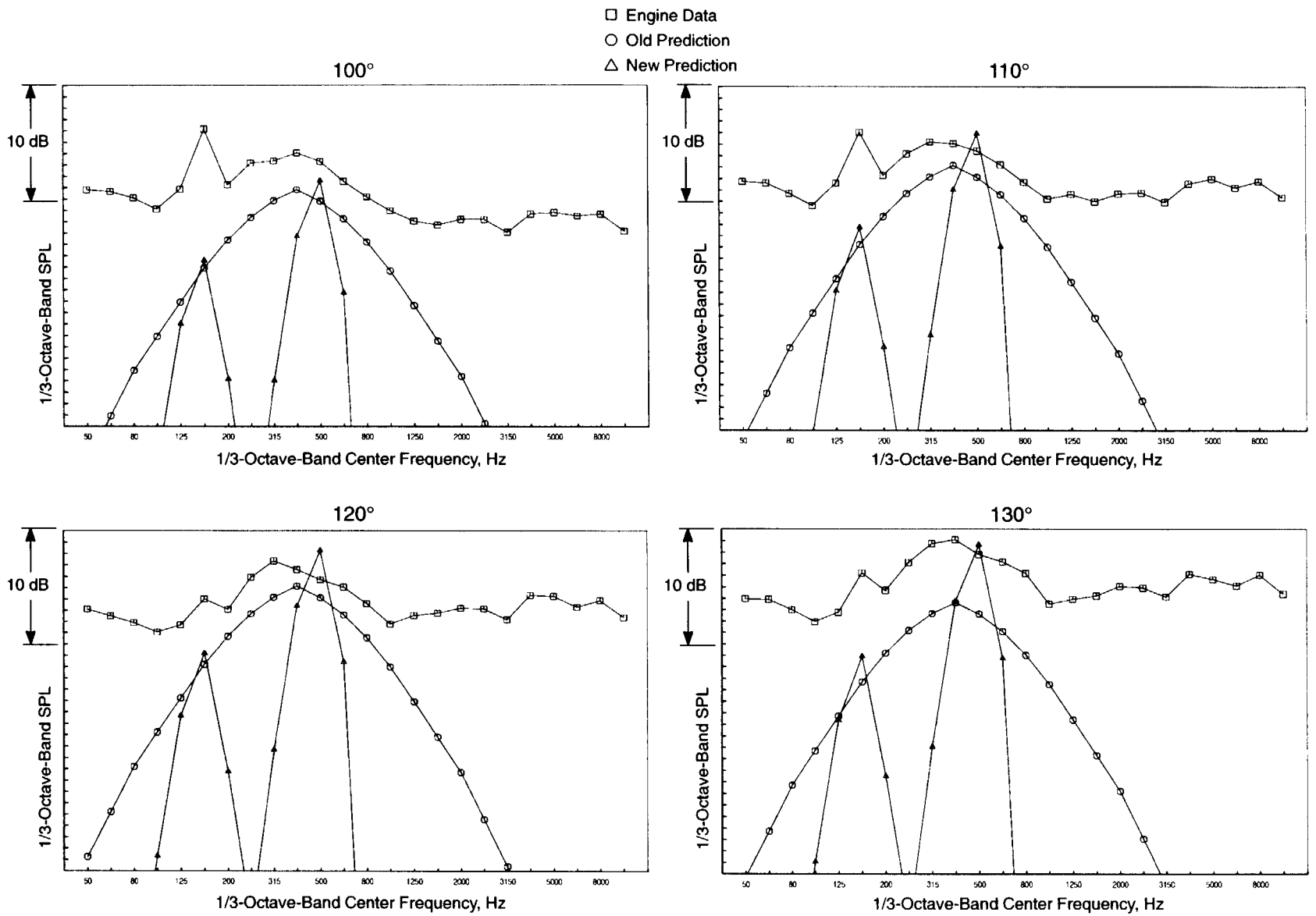

Figure 195. Comparison of Predictions with Data-Sample Trends: GE90 DAC CP′ = 14.6

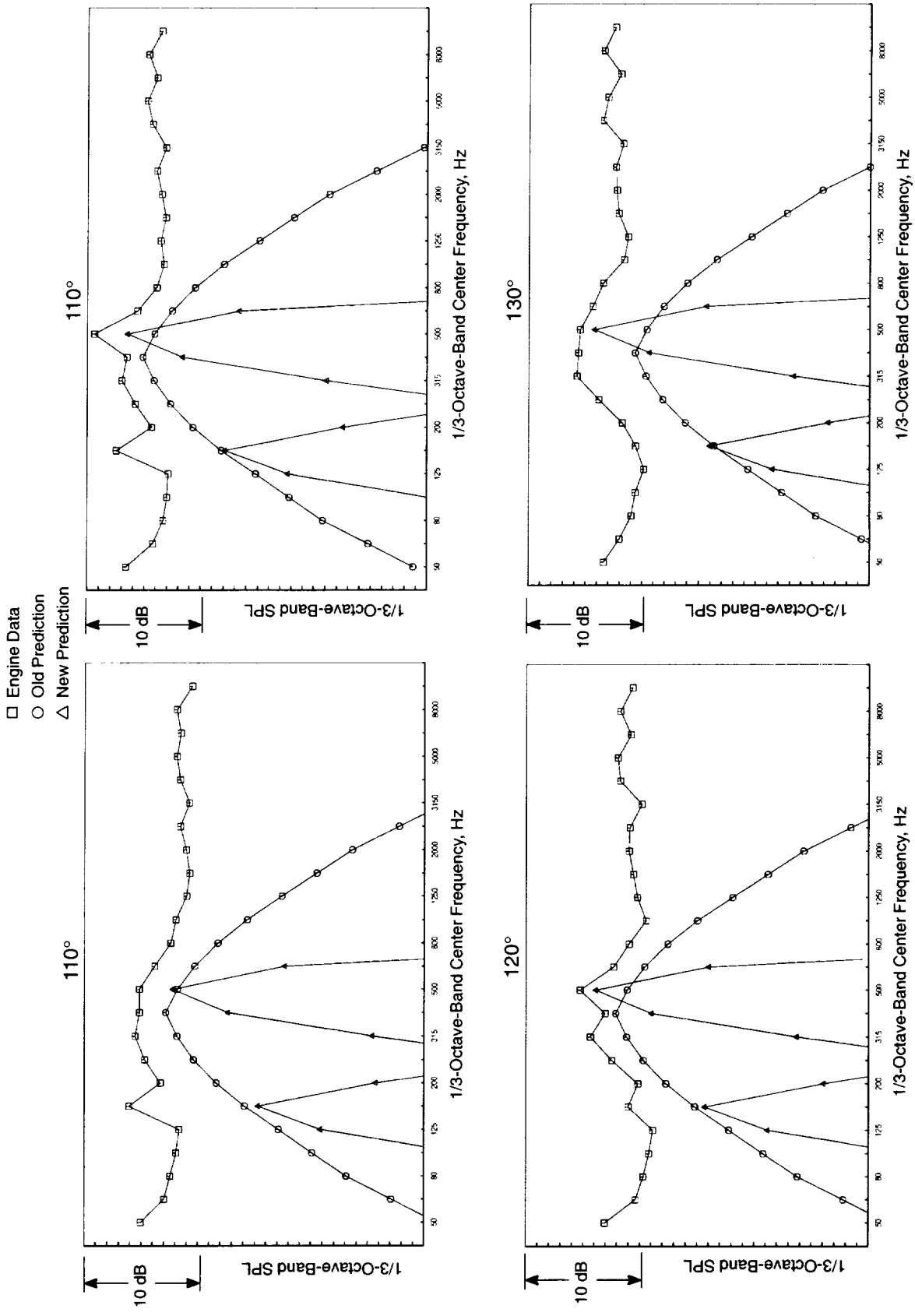

Figure 196. Comparison of Predictions with Data-Sample Trends: GE90 DAC – CP′ = 16.2

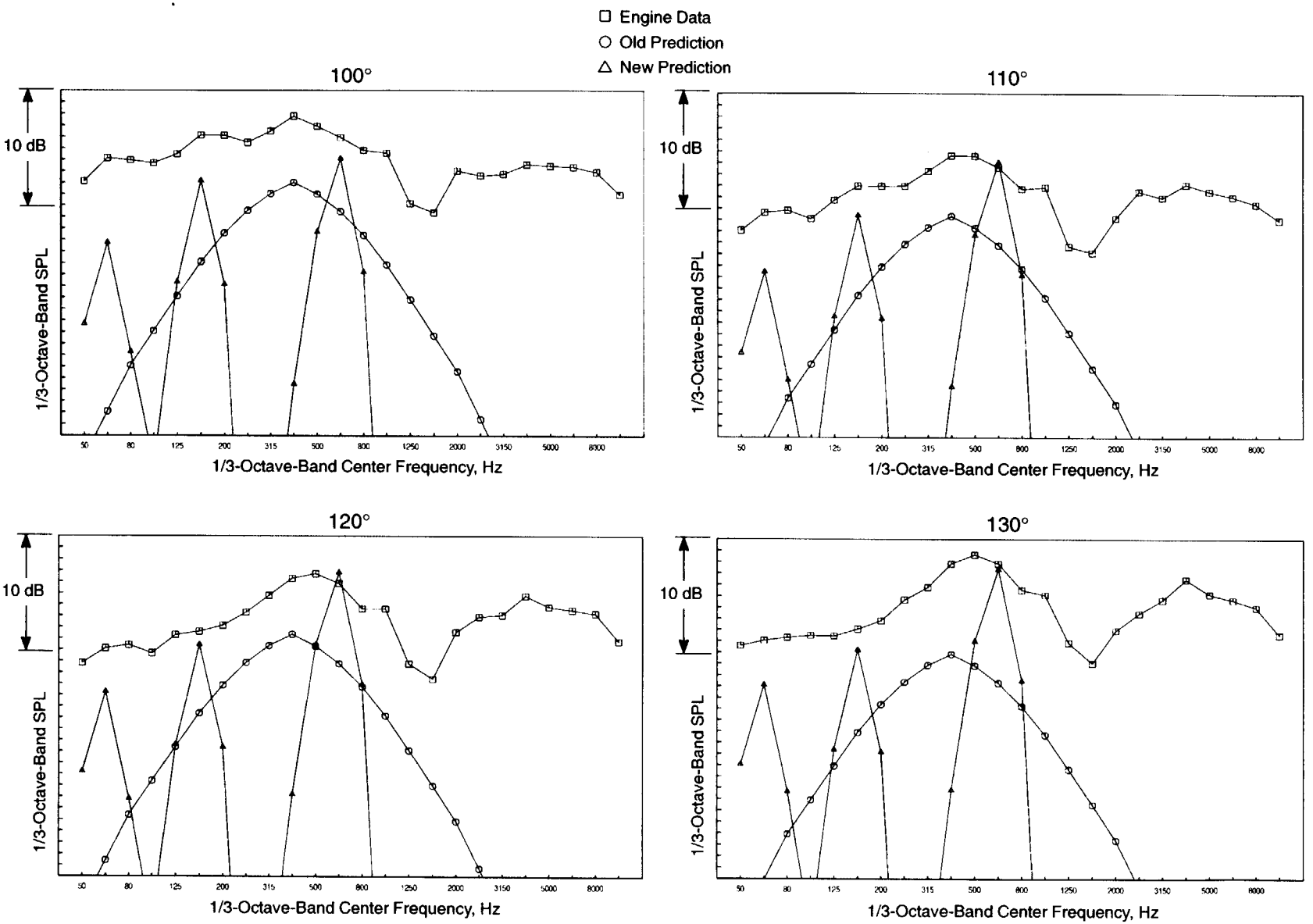

Figure 197. Comparison of Predictions with Data-Sample Trends: CF6 SAC – CP′ = 12.9

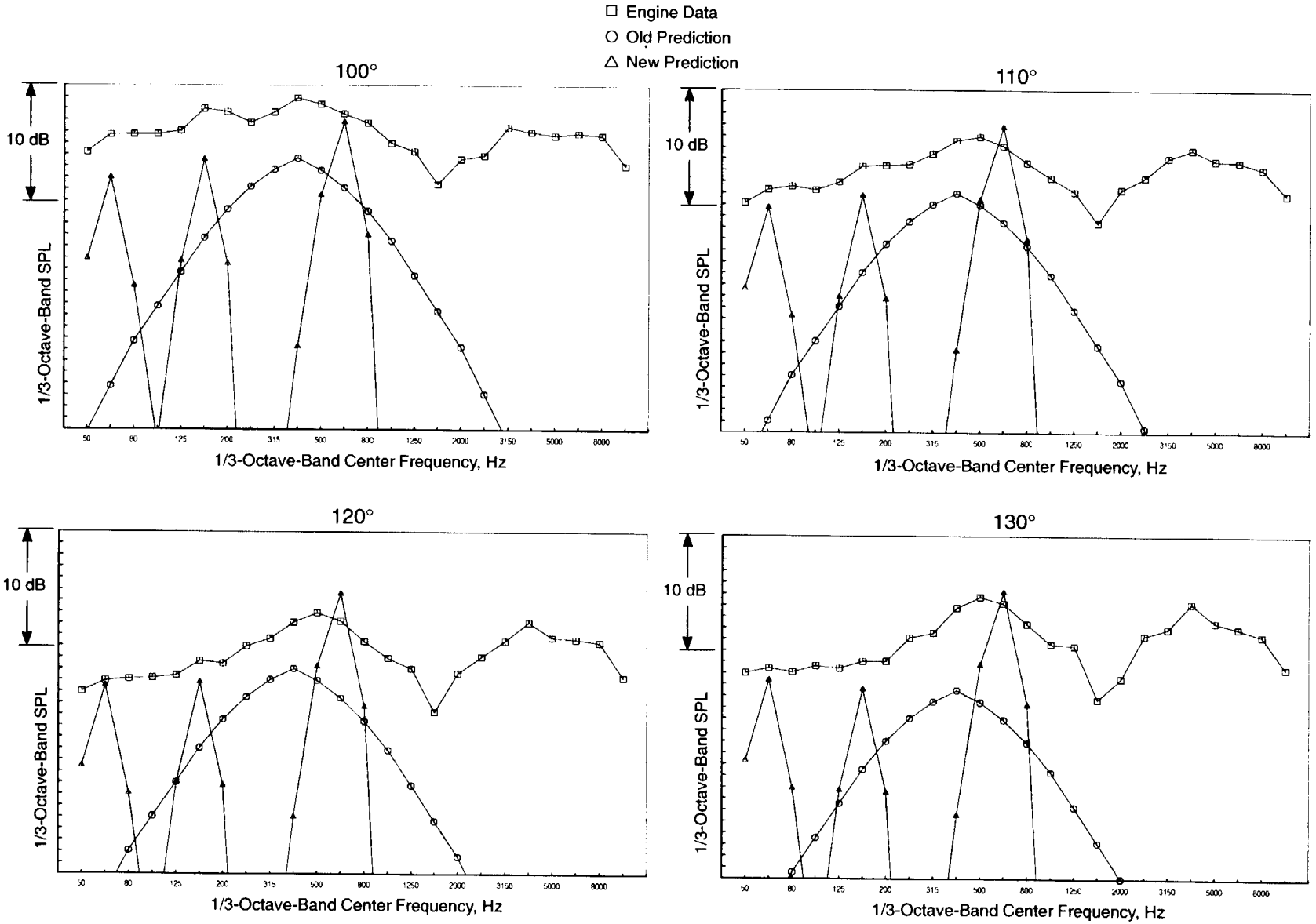

Figure 198. Comparison of Predictions with Data-Sample Trends: CF6 SAC – CP′ = 19.7

representative spectrum shape, relative to the engine data. The new correlation model, however, shows a double peak, close to where the data exhibit peaks in the spectrum, although the predicted higher peak at 630 Hz seems to be consistently one band higher than the experimental peak, which seems to occur at 500 Hz.

The second power setting ($CP' = 15.7$) comparison in Figure 192 shows similar trends, although the absolute levels are underpredicted with the new correlation, by about 5 dB on the average. It is also observed that the new correlation spectral lobes appear to be too narrow relative to the experimental data. Further, the predicted low-frequency lobe at 63 Hz seems to be predicted well below the actual engine data.

Prediction versus data comparisons for a CFM56 engine with a DAC are shown in Figures 193 and 194, corresponding to cycle parameter values of $CP' = 8.8$ and 12.9, respectively. Figure 193 shows clearly that the new correlation method does better in predicting the measured spectral peaks; the old method significantly underpredicts the measured spectra. The prediction method double-lobe behavior, with peaks at 16 and 500 Hz, appears to be consistent with the measured spectral characteristics, although again the predicted lobes (or band widths) seem too narrow relative to the measured shapes. Similar trends are shown for $CP' = 12.9$ in Figure 194, for this configuration.

Prediction versus data comparisons are shown for a GE90 engine with a DAC in Figures 195 and 196. These comparisons are for cycle parameter values of $CP' = 14.6$ and 16.2, respectively. Again, results are given at 100°, 110°, 130°, and 130° observer angles. These two figures indicate that the higher peak at 500 Hz is well predicted by the new correlation, but the lower peak at 160 Hz is underpredicted by 5 to 10 dB. The old method, on the other hand, underpredicts the data consistently by 5 to 7 dB.

Finally, prediction versus data comparisons are shown in Figures 197 and 198 for a CF6 engine with a SAC, corresponding to cycle parameter values of $CP' = 12.9$ and 19.7, respectively. The predicted peaks are close to the measured data in most cases, although the highest predicted peak seems to again be one band higher in frequency than the measured peak. For this configuration, the old method consistently underpredicts the measured peak levels by 5 to 8 dB.

Considering all the data versus prediction comparisons in Figures 191 through 198, the following observations are made relative to the new correlation method:

1. The peak-frequency lobe centered at 630 Hz for the SAC should be at 500 Hz.
2. The low-frequency lobe centered at 63 Hz for the SAC underpredicts the observed levels.
3. The predicted lobe widths are too narrow and should be broadened to give spectral lobe shapes more in line with the measured data.
4. The new correlation method at least qualitatively predicts the correct differences between the SAC and DAC noise levels.
5. The old correlation method significantly underpredicts the measured engine spectrum levels in the frequency regime where the experimental data suggest combustor noise is a significant noise source.

6.2.9 Conclusions and Recommendations

The new combustor-noise correlation model described in this section offers a significant improvement over the old correlation models currently used in practice. It at least qualitatively predicts the

effects of DAC versus SAC configuration effects — as well as the effect of fuel nozzle staging for the DAC configuration. On an absolute level basis, it appears to predict peak noise levels fairly well, while the old method consistently underpredicts the absolute levels.

This implies that the old methodology underestimates the role of combustor noise as a contributor to total propulsion system noise, at least at low power settings. Hence, the system benefits of reducing other significant sources, such as fan noise, may be overestimated.

There are some shortfalls in the new correlation that need correcting. These include a better correlation for the absolute level of the low-frequency peak level (at 63 Hz), which is currently underestimated. Further, a better spectral shape function (that is, a broader one) should be developed to better mimic actual engine measured characteristics.

6.3 CFD Analysis of Combustor Turbulence

Analyses of the SC and LEC designs was carried out using the CFD code CONCERT–3D. This is a fully elliptic, three-dimensional, body-fitted, CFD code; it has been developed extensively over the years and combines reasonable combustion models with good numerical procedures to yield comprehensive modeling capability for single- and two-phase flow predictions in practical gas turbine combustor geometries. The governing equations implemented in CONCERT–3D represent the conservation of mass and momentum in the three coordinate directions. The standard $k-\varepsilon$ turbulence model is used. The combustion model uses a conserved scalar variable for the fuel mixture fraction with assumed probability density function (PDF) and a fast-chemistry approach for the turbulence/chemistry interaction. A conservation equation is also written for fluctuation in the mixture fraction, and the fluctuation is modeled as a variance of the mixture fraction. The equilibrium density for the fuel is initially described as a function of the mixture fraction. Assuming a β PDF, and convoluting this equilibrium distribution with the PDF, a lookup table is generated that lists density as a function of the mixture fraction and its variance. Based upon the computed values of the mixture fraction and its variance, the density field is obtained from this table and used in all of the equations solved. Using a coordinate transformation, the governing equations are transformed from an arbitrarily shaped physical domain to a rectangular parallelepiped. The equations are solved in this boundary-fitted coordinate system using the SIMPLE pressure-correction algorithm.

The temperature field, the variance of the temperature field (from which the rms temperature is calculated), and the distribution of the mole fractions of species within the combustor are all obtained as a postprocessing step. In the same manner as the density, the equilibrium temperature and species mole fractions are initially described as functions of the mixture fraction. These equilibrium distributions are convoluted with the PDF to yield a second lookup table that lists the temperature, its variance, and the species mole fractions as functions of the mixture fraction and its variance. The distribution of all these quantities within the combustor are then obtained from this second lookup table using bilinear interpolation based upon the calculated values of the mixture fraction and its variance.

The structured, body-fitted CFD mesh used for the analyses is illustrated in Figure 199. Due to the geometrical symmetry (Figure 199 shows that there are 20 burners in each ring), a 1/20th sector of the combustor is modeled. It is assumed that each sector behaves exactly the same as its neighbors, thus allowing use of periodic boundary conditions at the interfaces and reducing the required number of grid points. The standard combustor design is made up of 82,500 nodes, and the low-emission

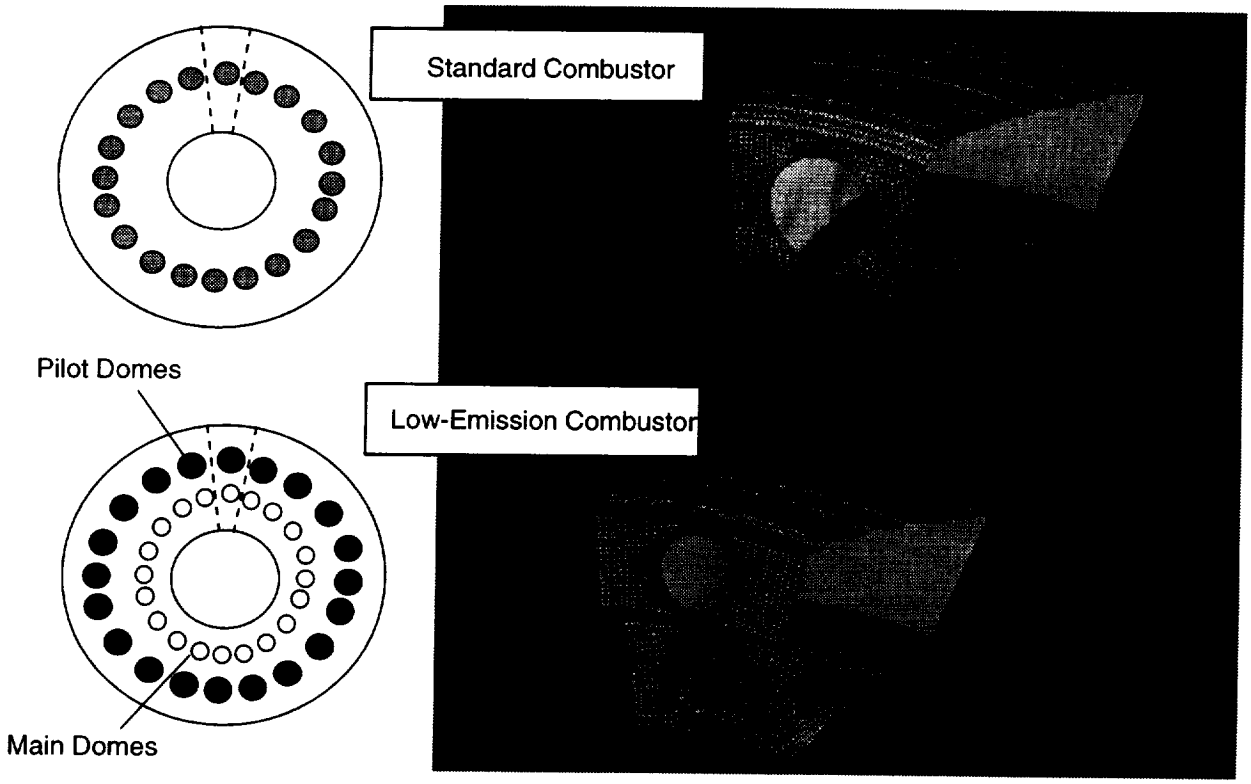

Figure 199. CFD Models of the Two Combustors Analyzed

model has 97,800 nodes. Since the noise measurements for the two designs differ most dramatically at low-power levels, only the approach condition is analyzed.

The level of grid density employed in this work was used successfully in another similar application by Gulati, et al. in 1995 (Reference 82) for a double-annular research combustor as shown in Figure 200. The adequacy of the modeling technique employed here for the standard and low-emission combustors was also validated in that application. Figures 201 and 202 compare experimental data and CFD predictions for the double-annular research combustor and reflect the adequacy of the CONCERT–3D modeling approach.

The temperature profile in Figure 202, including the inner peak in the data, is well predicted by the code. Similarly, the shape of the (normalized) rms temperature profile, with a peak in the center and sharp rise at the edges, is predicted well by the code. CONCERT–3D, however, consistently predicts lower rms values than measured. A possible reason is the turbulence model used. It is well known that the standard $k-\varepsilon$ model has certain deficiencies when applied to swirling flows. Another possible contributing factor to the discrepancies is the assumption in the code of fast chemistry in the combustion model. The predictions are overall very consistent with the data and provide a sound basis to implement CONCERT–3D in this application.

Figure 203 presents the temperature map at the exit plane of the two combustors under study. The SC design offers the more uniform temperature profile. The LEC design exhibits a significant region of cool flow owing to the inactivity of the main domes.

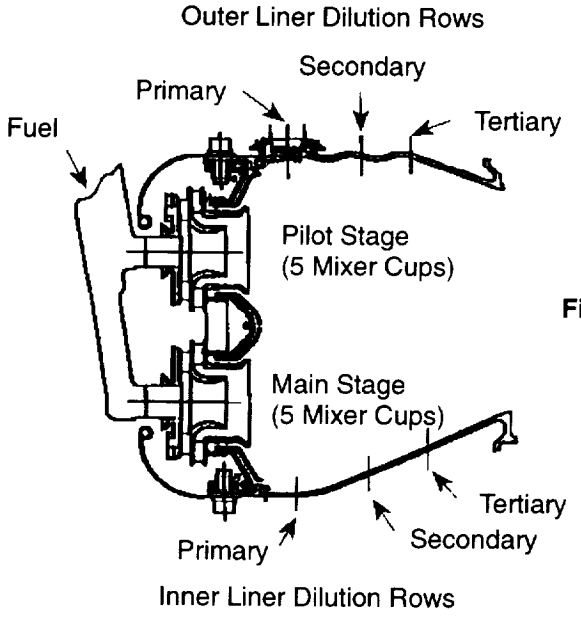

Figure 200. Schematic of Five-Cup, Double-Annular Combustor Sector Used to Validate CONCERT–3D Modeling Approach

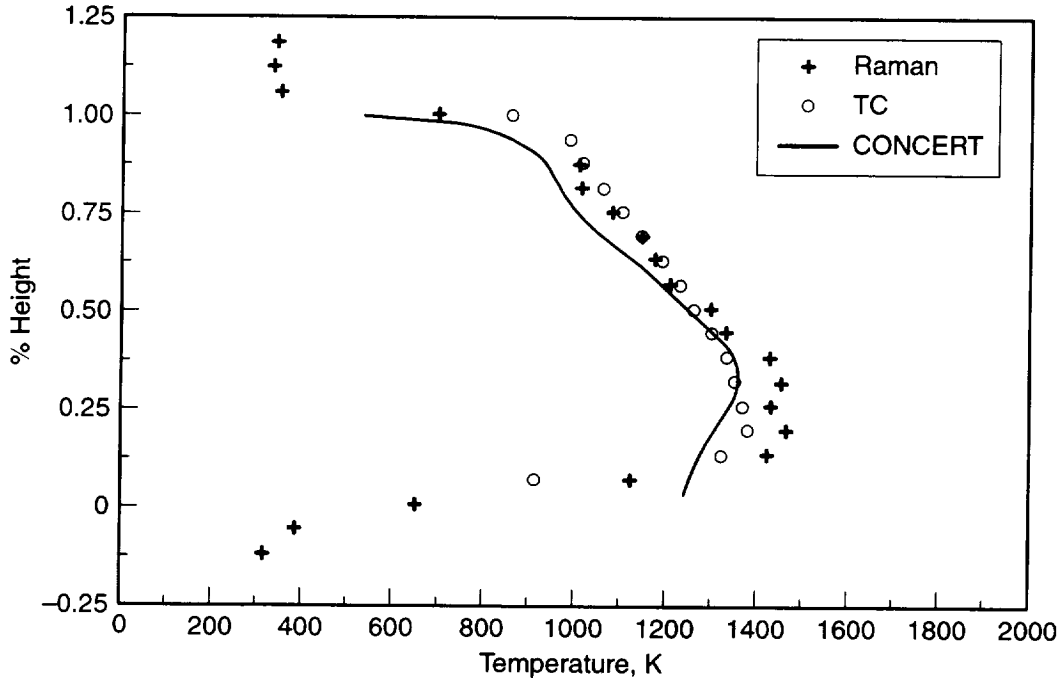

Figure 201. Comparison of Mean Temperature Profile at the Centerline of the Sector Exit Obtained with Raman Diagnostics and Thermocouple Data with CONCERT–3D Model Predic-

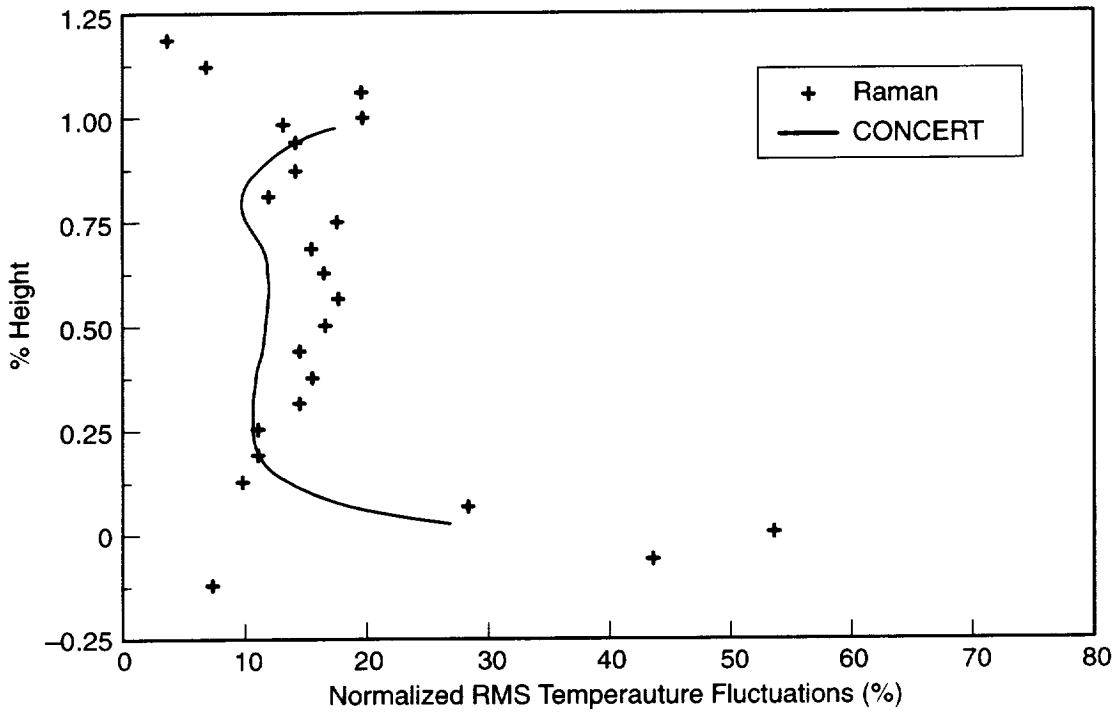

Figure 202. Centerline Profiles of Normalized RMS Temperature Fluctuations

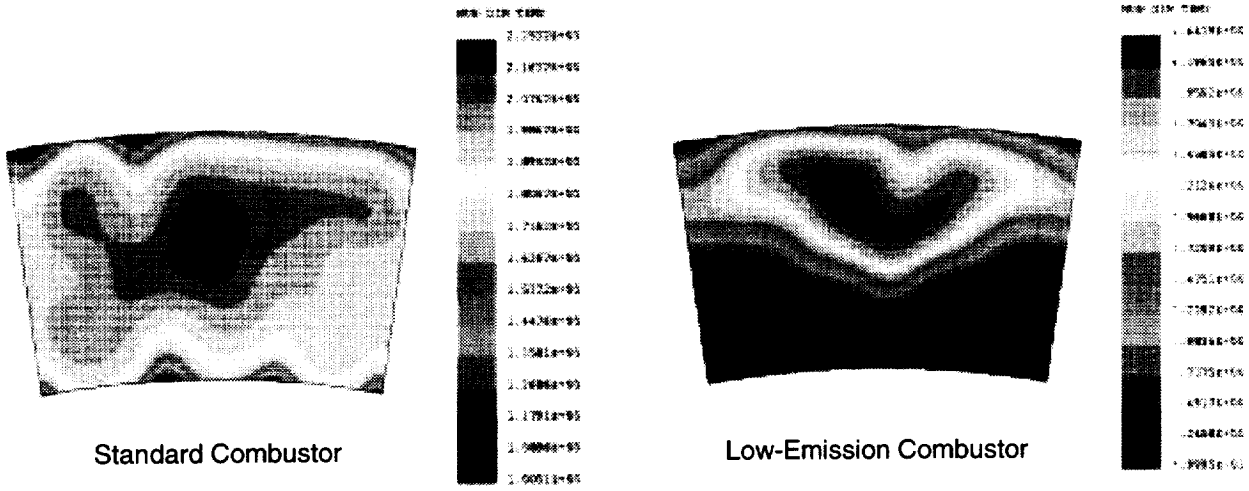

Figure 203. Normalized Temperature Maps at the Exit Plane of the Combustor

The same feature is shown in the circumferentially mass-averaged temperature plots in Figure 204. Consistent with this profile, the normalized rms temperature fluctuations at the exit plane are shown in Figure 205.

6.4 Actuator Disk Model

An actuator disk model was employed to compute the noise generated by the convection of hot spots generated at the combustor exit through multistage turbomachinery. This mechanism as a source of core noise has been discussed by Cumpsty and Marble (Reference 89). We employed a model of plane (two-dimensional) uniform flow segments changing discontinuously across blade rows (actuator disks). Such a model is valid for low-frequency noise such as whenever the wavelength of the sound substantially exceeds the chord length of or the transverse spacing between the blades. We calculate the noise produced downstream of the blade rows due to an entropy wave incident on the blade rows.

In a uniformly flowing plane flow, three wave systems are possible: (1) sound waves (both upstream- and downstream-propagating waves), (2) shear waves, and (3) entropy waves. Let the acoustic wave number be denoted by $k = \omega/c$ — where ω is the radian frequency and c is the speed of sound — and the (spatial) wave number in the tangential or y direction be denoted by k_y. Then the three wave types have the following attributes.

Consider sound waves first. The axial wave numbers corresponding to downstream and upstream wave propagation are:

$$k_x = \frac{-M_x(k - k_y M_y) \pm [(k - k_y M_y)^2 - (1 - M_x^2)k_y^2]^{1/2}}{(1 - M_x^2)} \tag{233}$$

where M_x and M_y are the axial and tangential Mach numbers of the uniform flow.

If the amplitude of a sound wave is measured by $p'/\gamma p$ where p' is the fluctuating pressure, γ the specific heat ratio, and p the mean static pressure, then the fluctuating density, axial, and tangential velocity components and temperature are:

$$\frac{\rho'}{\rho} = \frac{p'}{\gamma p} \tag{234}$$

$$\frac{u'}{c} = \frac{p'}{\gamma p}\frac{k_x}{k_0} \tag{235}$$

where $k_0 = k - k_x M_x - k_y M_y$

$$\frac{v'}{c} = \frac{p'}{\gamma p}\frac{k_x}{k_0} \tag{236}$$

and

$$\frac{T'}{T} = \frac{p'}{\gamma p}(\gamma - 1) \tag{237}$$

There are no entropy fluctuations associated with sound waves.

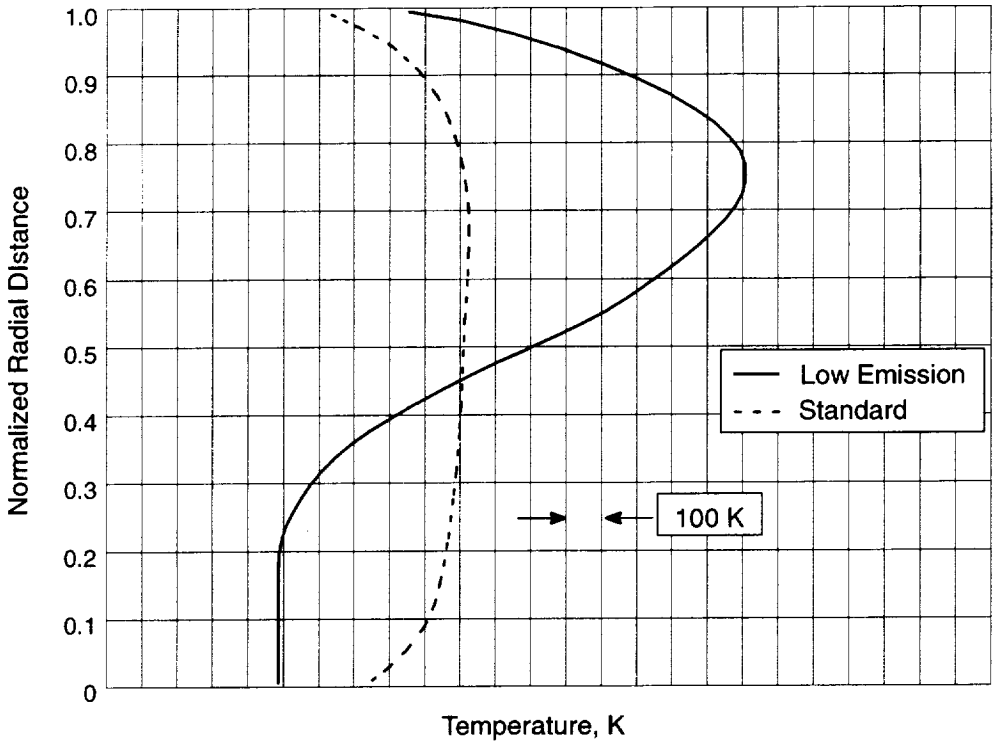

Figure 204. Radial Profile of Circumferentially Mass-Averaged Temperature at the Exit Plane of the SC and LEC under Approach Conditions

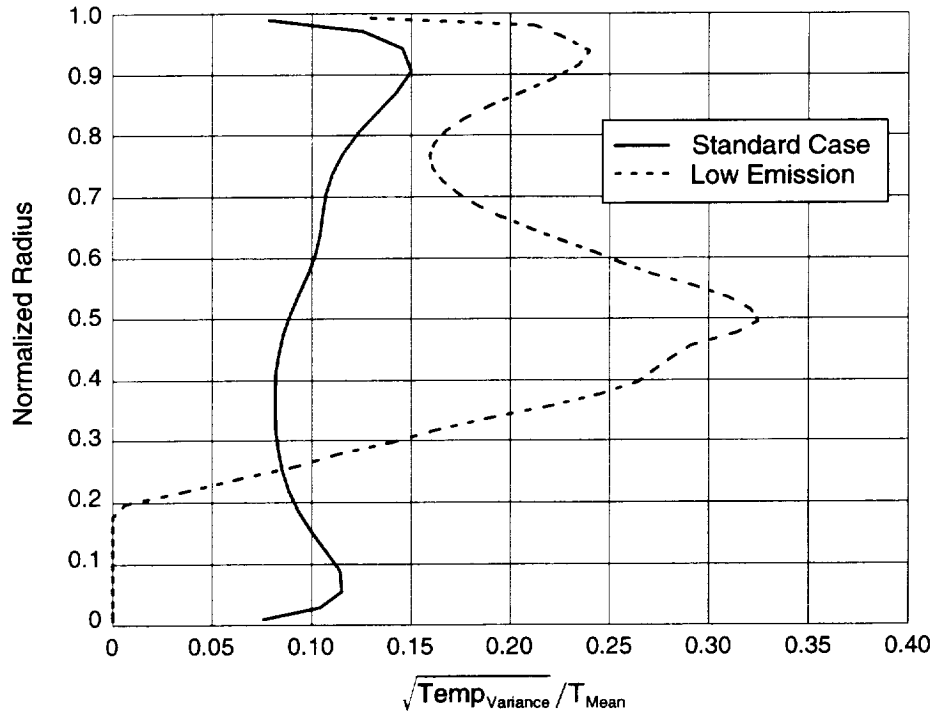

Figure 205. Normalized Standard Deviation of Temperature at the Exit Plane of the Combustors, Approach Condition

For shear waves, the axial wave number, k_{xsh} is given by:

$$k_{xsh} = k/M_x - M_y k_y/M_x \tag{238}$$

If the tangential velocity fluctuation associated with a shear wave is v', the axial velocity fluctuation is:

$$u' = -k_y v'/k_{xsh} \tag{239}$$

There are no pressure, density, temperature, or entropy fluctuations associated with shear waves.

Entropy waves are convected waves similar to shear waves and hence have the same axial wave number as shear waves. There are no velocity or pressure perturbations associated with entropy waves. If the entropy perturbation associated with an entropy wave is s' and C_p is the coefficient of specific heat at constant pressure, then density and temperature perturbations are:

$$\frac{\rho'}{\rho} = \frac{-T'}{T} = \frac{s'}{C_p} \tag{240}$$

Across blade rows, we always match the linearized axial mass flux vector, linearized stagnation enthalpy (per unit mass) relative to the blade row, and linearized entropy per unit mass.

The matching of linearized axial mass flux (given that the steady flow obeys the same mass flux conservation) yields that $(\rho'/\rho) + (u'/u)$ is continuous across a blade row.

The matching of stagnation enthalpy yields that $(C_p T' + Uu' + V_{rel}v')$ is continuous across a blade row where U and V_{rel} are mean-flow axial velocity and mean-flow tangential velocity relative to the blade row.

The entropy matching condition is the simplest of all and implies continuity of s' across the blade row and hence that entropy wave amplitudes are preserved across a blade row and thus indeed from combustor exit to turbine exit!

The fourth matching conditions depend on whether the blade rows are choked or not. If the blade rows are not choked, we assume that the unsteady flow leaves the blade row at the same angle as the steady flow which implies that $V_{rel}u' - Uv' = 0$ at the trailing edge of the blade row.

If the blade row is choked, with p_t, T_t, p_t', and T_t' denoting the mean values of the (blade row) relative mean and fluctuating total pressures and temperatures, a matching condition can be derived by noting the following constraint on the fractional axial mass flux perturbation:

$$\frac{\rho'}{\rho} + \frac{u'}{U} = \frac{p_t'}{P_t} - \frac{1}{2}\frac{T_t'}{T_t} \tag{241}$$

This condition may be applied either upstream or downstream of the blade row. Implications of the above choking conditions in terms of flow variables are to be found in equation 38 of Cumpsty and Marble (Reference 89).

Thus, if we now use the following abbreviations:

AP	Angle perturbation condition
C	Choking condition
D	Downstream-going sound wave
E	Entropy wave
EC	Entropy condition
M	Axial mass flux condition
RSE	Relative stagnation enthalpy condition
S	Shear wave
U	Upstream-going sound wave

We may describe the wave system by a column vector W whose elements are:

$$W = \begin{Bmatrix} D \\ U \\ S \\ E \end{Bmatrix}$$

Consider now a matrix upstream of a blade row (let this be the i^{th} blade row), B_{iu} whose elements (4×4) are:

	D	U	S	E
M	x	x	x	x
RSE	x	x	x	x
AP or C	0	0	0	0
EC	0	0	0	1

Likewise, downstream of a row, we can define B_{id}:

	D	U	S	E
M	x	x	x	x
RSE	x	x	x	x
AP or C	x	x	x	x
EC	0	0	0	1

In the these two matrices, an entry (for example) in column U and row RSE would contain, in terms of mean flow properties upstream and downstream of a blade row, the "influence coefficient" expressing the relative stagnation enthalpy associated with an upstream–going sound wave. Thus, the matching condition across a blade row gives the relation:

$$B_{iu} W_{ui} = B_{id} W_{di} \tag{242}$$

or

$$W_{di} = B_{id}^{-1} B_{iu} W_{ui} \tag{243}$$

If $k_{xpi(i+1)}$, $k_{xmi(i+1)}$, and $k_{xshi(i+1)}$ denote axial wave numbers for downstream sound waves, upstream sound waves, and convected waves in the space between blade rows i and $i+1$, with $g_{i\,(i+1)}$ denoting the axial distance between the midchord of blade rows i and $i+1$, we designate a diagonal transfer matrix (4×4) $S_{i(i+1)}$ whose diagonal (nonzero) elements are:

$$\exp[j\,k_{xpi(i+1)}\,g_{i(i+1)}]$$

$$\exp[j\,k_{xmi(i+1)}\,g_{i(i+1)}]$$

$$\exp[j\,k_{xshi(i+1)}\,g_{i(i+1)}]$$

and $$\exp[j\,k_{xshi(i+1)}\,g_{i(i+1)}]$$

Then the relation between W_{di} (wave system downstream of blade row i) and $W_{u(i+1)}$ (wave system upstream of blade row $i + 1$) is:

$$W_{u(i+1)} = S_{i(i+1)}W_{di} \tag{244}$$

It is clear that, by the above formalism involving repeated matrix multiplication and matrix inversion of the B_{id} matrices, we can relate W_{u1} to W_{dn} where n is the total number of blade rows. W_{u1} has one unknown element (the reflected sound wave), but the problem is "closed" by noting that W_{dn} has no reflected sound wave. For example, we assume a reflection-free termination at the end of the turbomachinery.

The above procedure works satisfactorily except in the case that there is a choked blade row that is not the last row. The problem arises because in the B_{id} matrix, for a choked case, the first three column elements of rows 1 and 3 are not linearly independent; thus, inversion of B_{id} is not possible.

In this case, if m denotes the choked row, we need to first carry the calculation up to the upstream of the m^{th} row using an upstream choking condition (as opposed to a no reflection condition) to "close" the problem and then restart the calculation (with known entropy, mass, and stagnation enthalpy fluxes) aft of the m^{th} row.

Once the (root mean square) value of the emitted (downstream-propagating) sound wave has been found, the axial component of the acoustic intensity flux vector can be found by noting that, for plane waves in a uniformly flowing medium of Mach number $\overline{M}$, the acoustic intensity flux vector is:

$$\frac{p'^2_{rms}}{\rho c}\left(\frac{k}{k_0}\right)(\overline{n} + \overline{M}) \tag{245}$$

where $k_0 = (k - M_x k_x - k_y M_y)$ and $\overline{n}$ is a unit normal to the wavefronts.

Some of the details of the noise-prediction procedure are now discussed. The axial and tangential flow Mach numbers in the duct aft of the last blade row (in each strip of mean radius a) are assumed to be M_x and M_y. The acoustic wave number here is assumed to be k_d. A range of tangential wave numbers k_y are considered such that:

$$\frac{-k_d}{[\sqrt{1-M_x^2}-M_y]} \leq k_d \leq \frac{k_d}{[\sqrt{1-M_x^2}-M_y]} \tag{246}$$

and subject to $k_y a = 2\pi m$. We assume that (given the low frequencies of interest) only plane modes exist in the radial direction. The first condition above expresses the restraint imposed by cutoff. The second restricts consideration to discrete tangential wave numbers such that the solution repeats every circumference.

The flow from the combustor exit is assumed to be purely axial at Mach number M_{xu}, and this sets the axial wave number of the temperature fluctuations at:

$$k_{xt} = k_u / M_{xu} \tag{247}$$

where k_u is the acoustic wave number of interest in the duct downstream of the combustor. If the wave number bandwidth of interest is dk_u, the corresponding wave number bandwidth k_{xt} is dk_u/M_{xu}. The tangential wave number of the spectrum of temperature fluctuations (STF) in the actuator disk model is the same as that of the acoustic spectrum, namely k_y. The STF used is one that corresponds to a correlation in the tangential direction of form:

$$\exp(-y^2/L_2^2) \tag{248}$$

where $L = 2\ell_2$ with ℓ_2 denoting the integral length scale in the tangential direction.

In the axial direction, three choices are allowed (with ℓ_1 denoting the integral length scale in the axial direction):

- Gaussian: $\exp(-x^2/L_1^2)$ with $L_1 = 2\ell_1/\sqrt{\pi}$
- Simple exponential: $\exp(-|x|/\ell_1)$
- Algebraic: $L_1^2/(L_1^2 + x^2)$ with $L_1 = 2\ell_1/\pi$

It may be noted that if $R(\bar{r})$ denotes correlation of temperature fluctuations between two points separated by $\bar{r}$, the spectrum function (STF) is defined by:

$$\Phi = \frac{1}{8\pi^3} \int R(\bar{r}) \exp(i\bar{k} \cdot \bar{r})\, d\bar{r} \tag{249}$$

where the integration is over all space and $\bar{k}$ is the vector wave number of interest in the STF.

Concerning the mean flow variables employed for the various strips in the radial direction, assume that the distribution of mean flow with radius is of the free-vortex type fore and aft of each blade row such that axial velocity, stagnation temperature and pressure, entropy constant (independent of radius), and tangential velocity vary inversely with radius.

6.5 Application to Data

This section presents some notes on the theory/data comparisons for the farfield sound pressure level spectrum for the case of engine tests of a SC and a LEC. The CFD results for these two combustors at low power are presented in Section 6.3, page 209, and radial variations of temperature fluctuations were adopted (for the two cases) from these CFD results.

The integral length scales of the temperature fluctuations in the axial and tangential direction are not available from the CFD, but Pickett has presented some discussion of likely values of these quantities (Reference 90). The discussion that follows will clarify some "trial and error" and "optimization" based studies that have resulted in some semiempirical guidance on choice of ℓ_1 and ℓ_2.

The pitch-line mean flow information (extrapolated to other radii using free-vortex concepts) needed to carry out the acoustic predictions were obtained from turbine aero designers.

A remark concerning the spectrum function Φ is in order here. Consistent with the assumption that only plane radial orders are considered (due to the low-frequency nature of core noise), we use a two-dimensional spectrum derived from Φ as:

$$\phi(k_1, k_2) = \int \Phi(k_1 k_2, k_3)\, dk_3 \tag{250}$$

where the range of integration is $-\infty < k_3 < \infty$. It can be shown that with R $(x, y, 0)$ denoting the correlation of temperature fluctuations between two points with no separation in the spanwise direction:

$$\phi = \frac{1}{4\pi^2} \int \int R \exp[-j(k_1 x + k_2 y)]\, dx\, dy \tag{251}$$

The directivity of the core noise is determined by parameterizing the power at given frequency according to cut-off ratio and using Rice's work as described in other sections and in the Addendum to this report.

In addition to the normalized rms temperature variation at the combustor exit plane, the core noise model described also requires specification of the axial and tangential length scales of temperature fluctuations. As a first attempt at extracting this information from the CFD runs, the integral length scale predicted by the k–ε model was computed in a postprocessing step as:

$$l = c_\mu \frac{k^{3/2}}{\epsilon} \tag{252}$$

where, in the standard k–ε model, $C_\mu = 0.09$.

This estimate led to length scales that were on the order of the thickness of the boundary layer and over 10 times smaller than the values recommended by Pickett (Reference 90). One alternative to resolve this inconsistency was to replace the variable C_μ with an arbitrary constant that better approximated the data. Although this is a viable approach, it will leave the other length scale unaccounted for while still introducing a constant to be optimized. Furthermore, there is no evidence to support that the desired scalar length scales must coincide with the length scales of the flow turbulence. Thus, an entirely empirical approach was taken that sought to determine the values of l_1' and l_2', where the primed quantities reflect dimensionless variables:

$$l_1' = \frac{l_1}{\bar{R}} \quad \text{and} \quad l_2' = \frac{l_2}{\bar{R}}$$

where $\bar{R}$ denotes the mean radius in the turbine passage (which is nearly constant and equal to the mean radius at the exit plane of the combustor).

The quantity to be minimized in this exercise is the relative error between the predictions and the experimental data, such as:

$$E(l_1', l_2') = \frac{1}{N} \sum_{i=1}^{N} (|\phi_{data} - \phi_{pred}|)_i \tag{253}$$

where i denotes the frequency over which data is available in the range of 200 Hz to 2 kHz and ϕ represents the experimental and predicted SPL. The aim is to find values of l_1' and l_2' such that the error $E(l_1', l_2')$ is minimized. The other inputs to the core noise model were fixed at the values predicted by the CFD codes, such as normalized temperature fluctuation at the combustor exit plane and the pitch-line mean flow information.

Following a design of experiments technique, a disciplined approach was established. Feasible ranges of variations were determined for the two length scales, and numerical experiments using the core noise model were conducted. A sample of the surface response obtained for the LEC is shown in Figure 206. The surface represents the error in dB between the experimental data and the model predictions. A clear minimum is indicated. With further refinement on the range of variation of the length scales, more numerical experiments were carried out. The results are presented in Figure 207 for the standard combustor and in Figure 208 for the low-emission design.

The tangential length scale was found to control the prediction of the overall noise level, larger tangential lengths leading to higher noise levels. The axial length scale affects primarily the general shape of the variation of the noise prediction as a function of frequency. It can be observed from Figure 207 and that the model for the SC design requires a significantly lower tangential length scale than the LEC design to enable the same level of prediction accuracy relative to the field data. The axial length scale, on the other hand, is very similar for the two designs. Figure 209 compares the model predictions to the field data. The tangential length scale for the standard combustor is 0.03; the low-emission combustor model uses a value of 0.3. The axial length scale used is 0.11 and 0.15 for the SC and LEC designs respectively. The error bars shown in Figure 209 mark a range of ±2.5 dB. In the frequency range of interest, the predictions fall within this error band, and the overall prediction error defined above is less than 2 dB.

Figure 210 is a plot comparing the mass-averaged temperature fluctuations in the tangential direction at the exit plane of the combustors. It is an attempt to understand the physical cause for the significant difference in tangential length scale between the two designs. The standard combustor design exhibits three cycles of temperature fluctuation within a single sector; whereas the LC design shows only one. Thus, denoting the number of temperature cycles in the tangential direction per periodic sector as N_c and the total number sectors (or active burners, in this case) by N_b, one can postulate a relationship to estimate the tangential length scale of temperature fluctuations:

$$l_2' = \left(\frac{1}{N_c}\right)^2 \frac{2\pi}{N_b} \tag{254}$$

For the standard combustor design Equation (254) predicts $l_2' = 0.035$. For the low-emission combustor $l_2' = 0.31$.

6.6 Conclusions and Recommendations

The results discussed in this section indicate the high plausibility of differences in temperature fluctuations (at combustor exit) being the cause of increased core noise observed at low-power operation from low-emissions combustors as contrasted to standard combustors. The mechanism that yields noise from such temperature fluctuations is the convection of "hot spots" or "entropy waves" through multistage turbomachinery. An actuator disk approach has been used to calculate the noise, and the level of temperature fluctuations was deduced using a 3D CFD approach. The higher level of temperature fluctuations associated with LEC as compared to SC at part power are due to staged combustion that results in spatially inhomogeneous heat release and, therefore, large mean temperature gradients characterized by high levels of temperature fluctuations. An aspect of the actuator disk theory is that a special treatment is needed in the case of a choked blade row that is not the last blade row.

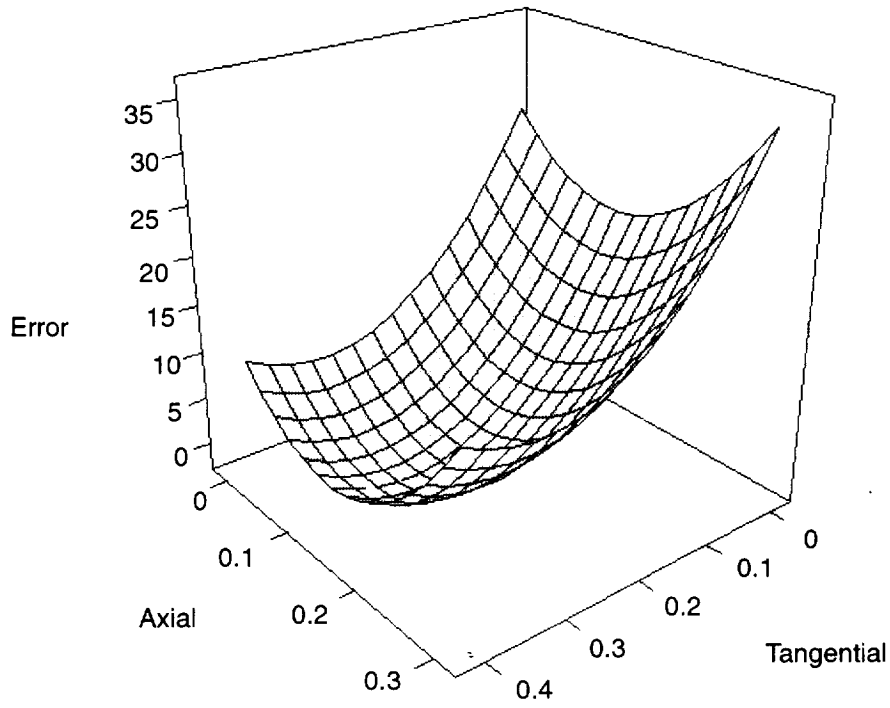

Figure 206. Error Response Surface for the Low-Emission Combustor as a Function of Axial and Tangential Length Scales

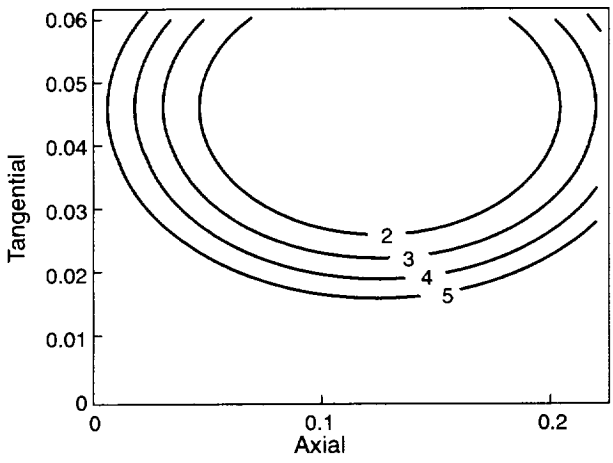

Figure 207. Contour Plot of Errors for the Standard Combustor Design

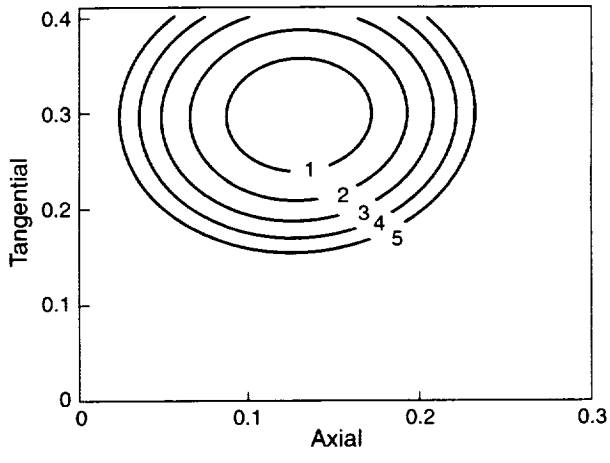

Figure 208. Contour Plot of Errors for the Low-Emission Design

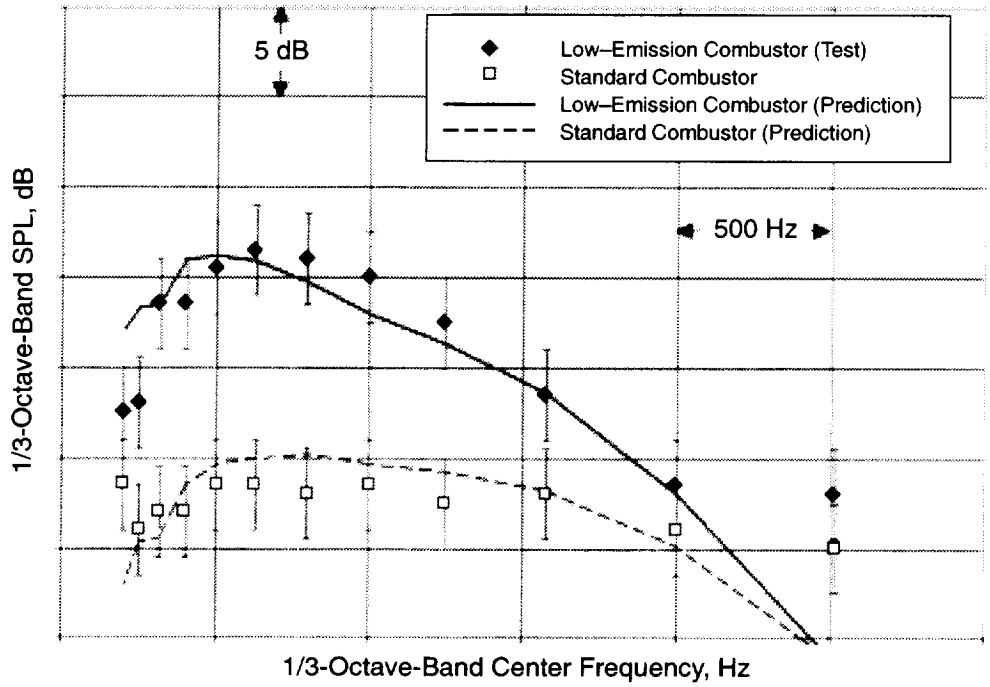

Figure 209. Comparison of Field Data and Model Predictions for Low-Emissions and Standard Combustors at Approach Conditions

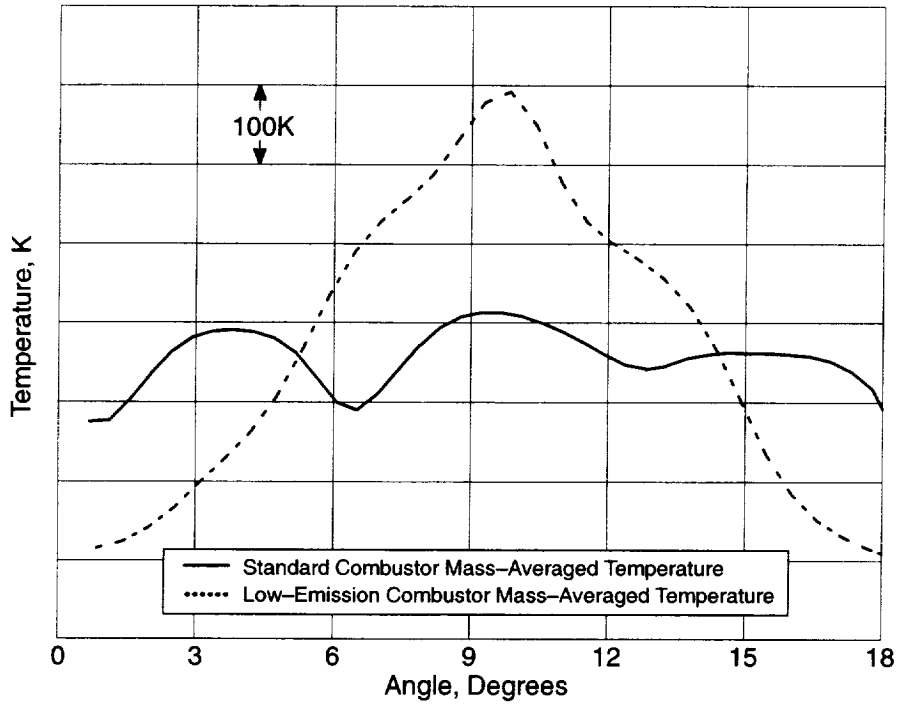

Figure 210. Comparison of Tangential Temperature Fluctuations for the Two Combustor Designs at Low-Power Conditions

Axial and tangential length scales of the "hot spots" are needed to predict the noise spectra but are not available directly from CFD. Some "semiempirical" estimates are offered concerning tangential length scales based on the circumference of the annular burner, number of burners, and the spatial inhomogeneity of mean temperature observed in the computed results (from CFD). More research is needed on how to estimate these length scales. It should be emphasized that a study as reported here would be impossible without a 3D combustor CFD code — granting that CFD currently lacks the ability to yield information on length scales. Another missing element from the results reported herein is that estimates of direct combustion noise (pressure fluctuations arising from combustion) should be made along with estimates (perhaps by using actuator disk theory) of the attenuation of direct combustor noise through multistage turbomachinery. A comparative evaluation of this source (that is, direct combustion noise plus attenuation through the turbomachinery) for LEC's and SC's is needed to (a) determine whether or not LEC's and SC's are significantly different with regard to this source at part power and (b) how (for both LEC's and SC's) this source compares with the indirect (hot spots based) mechanism considered in detail in the foregoing subsections.

7.0 References

1. Camp, T.R. and Shin, H.W., "Turbulence Intensity and Length-Scale Measurements in Multistage Compressors," ASME 94-GT-4, 1994.

2. Martens, S., Shin, H., and Gliebe, P.R., "Rotor Wake Unsteady Flowfield Hot-Wire Measurements in the Universal Propulsion Simulator (UPS) at NASA," GEAE TM97-67, March 1997.

3. Hoff, G.E. et al., "Universal Propulsion Simulator (UPS) Task Order 20 Final Report – Acoustic Calibration Test at NASA Lewis Research Center and Acoustic Treatment Scaling Evaluation," NASA Contractor Report (publication pending), May 1996.

4. Mani, R., Gliebe, P.R., and Ho, P.Y., "Fan Broadband Noise Model Development," NASA CR198457, December 1997.

5. Wygnanski, I., Champagne, F., and Marasli, B., "On the Large-Scale Structures in Two-dimensional, Small-Deficit, Turbulent Wakes", J. Fluid Mech. (1986), Vol.168, pp. 31-71.

6. Kumasaka, H.A., Martinez, M.M., and Weir, D.S., "Definition of 1992 Technology Aircraft Noise Levels and the Methodology for Assessing Airplane Noise Impact of Component Noise Reduction Concepts," Boeing Commercial Airplane Company, NASA CR 198298, June 1996.

7. Gliebe, P.R. and Kantola, R.A., "Effects of Vane/Blade Ratio and Spacing on Fan Noise, GE Aircraft Engines, NASA CR–174664, December 1983.

8. Heidmann, M.F., "Interim Prediction Method for Fan and Compressor Source Noise," NASA TM X–71763, 1975.

9. Gliebe, P.R., Janardan, B.A., and Smith, C.J., "UHB Aeroacoustic Study," NASA Contractor Informal Report, NAS3–25269 Task Order 4, July 1993.

10. Gliebe, P.R., Ho, P.Y,. and Mani, R. "UHB Engine Fan Broadband Noise Reduction Study," NASA CR198357, June 1995.

11. Mani, R., "Noise Due to Interaction of Inlet Turbulence With Isolated Stators and Rotors," J. Sound and Vibration, Volume 17 (2), pp 251–260, 1971

12. Kerschen, E.J. and Gliebe, P.R., "Noise Caused by the interaction of a Rotor with Anisotropic Turbulence," AIAA J. Vol.19, No. 6, June 1981 pp 717–723

13. Mani, R., "Noise Due to Inlet Distortion or Turbulence," NASA CR2479, 1974.

14. King, L.V., "On the Convection of Heat from Small Cylinders in a Stream of Fluid: Determination of the Convection Constants of Small Platinum Wires with Applications to Hot-Wire Anemometry," Phil. Trans. R. Soc. London, 1914, Ser. A214, pp 373–407.

15. Halstead, D., Wisler, D., Walker, G., Howard, H., and Shin, H. "Boundary Layer Development in Axial Compressors and Turbines: Parts 1, 2, 3, and 4," ASME Journal of Turbomachinery, January 1997, Vol. 119, pp 114-127.

16. Mani, R. et al., "Fan Broad Band Noise Model Development," Final Report, Contract NAS3–26617 (Task Order 33), 1995.

17. Mugridge, B.D., "Broadband Noise Generation by Airfoils and Axial Flow Fans," AIAA Paper No. 73-1018, October 1973.

18. Lighthill, M.J., "On Sound Generated Aerodynamically – I. General Theory," Proc. Royal Society, A211, pp 564–587, 1952.

19. Lighthill, M.J., "On Sound Generated Aerodynamically II – Turbulence as a Source of Sound," Proc. Royal Society, A222, pp 1–32, 1953.

20. Curle, B., "The Influence of Solid Boundaries Upon Aerodynamic Sound," Proc. Royal Society, A231, pp 505–514, 1955.

21. Crighton, D.G. et al., *Modern Methods in Analytical Acoustics,* Springer–Verlag, London, Chapter 16, 1992

22. Crighton, D.G., "Basic Principles of Aerodynamic Noise Generation," Prog. Aerospace Sci., 16, pp 31–96, 1975.

23. Ffowcs–Williams, J.E. and Hawkings, D.L., "Theory Relating to the Noise of Rotating Machinery," J. Sound and Vibration, 10, pp 10–21, 1969.

24. Morfey, C.L., "Tone Radiation From an Isolated Subsonic Rotor," J. Acoustical Society of America, 5, pp 1690–1692, 1971.

25. Wang, M., Lele, S.K., and Moin, P., "Computation of Quadrupole Noise Using Acoustic Analogy," J. AIAA, 34, pp 2247–2254, 1996.

26. Wang, M., Lele, S.K., and Moin, P., "Sound Radiation During Local Laminar Breakdown in a Low Mach-Number Boundary Layer," J. Fluid Mechanics, 319, pp 197–218, 1996.

27. Peake, N. and Kerschen, E.J., "Influence of Mean Loading on Noise Generated by the Interaction of Gusts with a Loaded Flat-Plate Cascade: Upstream Radiation," J. Fluid Mechanics, 347, pp 315–346, 1997.

28. Mitchell, B.E., Lele, S.K., and Moin, P., "Direct Computation of Mach Wave Radiation in an Axisymmetric Supersonic Jet," J. AIAA., 35, pp 1574–1580, 1997.

29. Mitchell, B.E., Lele, S.K., and Moin, P., "Direct Computation of the Sound Generated by Vortex Pairing in Axisymmetric Jets," J. Fluid Mechanics, to appear in 1999.

30. Abbot, L.H. and van Doenhoff, A.E., *Theory of Wing Sections,* Dover, New York, 1959.

31. Cumpsty, N.A., *Compressor Aerodynamics,* Addison Wesley Longman Limited, Essex London, 1989.

32. Morse, P.M. and Ingard, K.U., *Theoretical Acoustics*, Princeton University Press, 1968.

33. Holmes, D.G., Mitchel, B.E., and Lorence, C.B., "Three Dimensional Linerarized Navier-Stokes Calculations for Flutter and Forced Response," Proceedings of the 8th ISUAAT Symposium, Held September 14–18 in Stockholm Sweden, 1997.

34. Jameson, A. et al., "Numerical Solution of the Euler Equations By Finite Volume Methods Using Runge–Kutta Time-Stepping Schemes," AIAA Paper 81-1259, 1981.

35. Jameson, A., "Solution of the Euler Equations for Two Dimensional Transonic Flow by a Multigrid Method" *App. Math. and Comp.*, No. 13, pp 327–355, 1983.

36. Arnone, A., "Multigrid Methods for Turbomachinery Navier–Stokes Calculations," *Solution Techniques for Large-Scale CFD problems*, edited by Wagdi G. Habashi, John Wiley & Sons, Chichester, 1985.

37. Giles, M.B., "Nonreflecting Boundary Conditions for Euler Equation Calculations," J. AIAA, 28, pp 2050–2058, 1990.

38. Crighton, D.G., "Computational Aeroacoustics for Low Mach Number Flows," *Computational Aeroacoustics,* edited by Hardin and Hussaini, Springer–Verlag, Berlin, pp 51–68, 1993.

39. Ffowcs–Williams, J.E. and Hawkings, D.L., "Sound Generated by Turbulence and Surfaces in Arbitrary Motion," Phil. Trans. of the Royal Society, A264, pp 321–342, 1969.

40. Brentner, K.S. and Farassat, F., "Analytical Comparison of the Acoustic Analogy and Kirchhoff Formulation for Moving Surfaces," J. AIAA, 36, pp 1379–1386, 1998.

41. Farassat, F., "Discontinuities in Aerodynamics and Aeroacoustics: the Concept and Application of Generalized Derivatives," J. Sound and Vibration, 55, pp 165–193, 1977.

42. Farassat, F. and Myers, M.K., "The Moving Boundary Problem for the Wave Equation: Theory and Application," *Computational Acoustics – Algorithms and Applications*, Vol 2, Lee, D., Sternberg, R., and Schultz, M., eds, Elsevier Science Publications, 1988, pp 21–44.

43. Goldstein, M.E., *Aeroacoustics*, McGraw–Hill, New York, 1976.

44. Lighthill, M.J., *Introduction to Fourier Analysis and Generalised Functions,* Cambridge University Press, Cambridge, 1962.

45. Horlock, J. H., "Fluctuating Lift Forces on Aifoils Moving Through Transverse and Chordwise Gusts," J. Basic Engineering Series D, 90, pp 494–500, 1968.

46. Moin, P. and Mahesh, K., "Direct Numerical Simulations: A Tool in Turbulence Research," Annual Rev. Fluid Mech., 30, pp 539–578, 1998

47. Mani, R., "Isolated Rotor Noise Due to Inlet Distortion or Turbulence," NASA CR2479, 10.1974, 1974.

48. Gliebe, P.R. and Kerschen, E.J., "Analytical Study of the Effects of Wind Tunnel Turbulence on Turbofan Rotor Noise," Final Report, NAS2–10002, 1979.

49. Rice, E.J., "Modal Propagation Angles in Ducts With Soft Walls and Their Connection With Suppressor Performance," AIAA 79-0624, 1979.

50. Saule, A.V. and Rice, E.J., "Far-Field Multimodal Acoustic Radiation Diversity," NASA TM 73839, December 1997.

51. Rice, E.J., "Multimodal Far-Field Acoustic Radiation Pattern Using Mode Cut-Off Ratio," AIAA Journal, Vol. 16, pp 906–911, 1978.

52. Rice, E.J., Heidman, M.F., and Sofrin, T.V., "Modal Propagation Angles in a Cylindrical Duct with Flow and their Relation to Sound Radiation," AIAA Paper 79–0183, January 1979; also NASA TM 79030, 1978.

53. Rice, E.J. and Sawdy, D.T., "A Theoretical Approach to Sound Propagation and Radiation for Ducts with Suppressors," NASA TM 82612, May 1981.

54. Rice, E.J., "Aircraft Inlet Noise Radiation Model, Static, Flight and Bellmouth effect," AIAA Paper 96–1774, May 1996.

55. Horowitz, S.J., Sigman, R.K., and Zinn, B.T., "An Iterative Finite Element–Integral Technique for Predicting Sound Radiation from Turbofan Inlets," AIAA Paper 82–0124, January 1982.

56. Eversman, W., Parrett, A.V., Preisser, J.S., and Silcox, R.J., "Contributions to the Finite element Solution of the Fan Noise Radiation Problem," Transactions of the ASME Journal of Vibration, Acoustics, Stress, and Reliability Design, Vol 107, No. 2, pp 216–223, April 1985

57. Nallasamy, E.J. and Saule, A.V., "Far-Field Radiation of Aft Radiated Turbofan Noise," Journal of Aircraft, Vol 34, No. 3, pp 387–393, June 1997.

58. Rice, E.J. and Saulte, A.V., "Far-Field Radiation of Aft Turbofan Noise," NASA TM 81–5906, 99th Meeting of the Acoustical Society of America, Atlanta GA, April 1980.

59. Savkar, S.D., "Radiation of Cylindrical Duct Acoustic Modes with Flow Mismatch, Journal of Sound and Vibration, Vol 42, October 1975.

60. Mugridge, B.D. and Morfey, C.L., "Sources of Noise in Axial Flow Fans," J. Acoustical Soc. America, Vol. 51, No. 5, 1972, pp 1411-1426.

61. Robbins, B. and Lakshminarayana, B., "Effect of Inlet Turbulence on Compressor Noise," AIAA Journal of Aircraft, Vol. 11, No. 5, May 1974, pp 273-281.

62. Sharland, I.J., "Sources of Noise in Axial Flow Fans," J. Sound Vib., Vol. I , No. 3, 1964, pp 302-322.

63. Morfey, C.L., "Broadband Sound Radiated form Subsonic Rotors," NASA SP-304, Penn State University Symposium on Fluid Mechanics, Acoustics and Design of Turbomachinery, Part II, 1974, pp 461-485.

64. Brooks, T.F. and Marcolini, M.A., "Scaling of Airfoil Self-Noise Using Measured Flow Parameters," AIAA Journal, Feb. 1983, pp 207-212.

65. Mugridge, B.D., "Turbulent Boundary Layers and Surface Pressure Fluctuations on Two-Dimensional Aerofoils," J. Sound Vib., Vol. 18, No. 4, 1971, pp 475-486.

66. Willmarth, W.W. and Wooldridge, C.E., "Measurements of the Fluctuating Pressure at the Wall beneath a Thick Turbulent Boundary Layer," J. Fluid Mech., Vol. 14, Part 2, 1962, pp 187-210.

67. Willmarth, W.W., "Corrigendum: Measurements of the Fluctuating Pressure at the Wall beneath a Thick Turbulent Boundary Layer," J. Fluid Mech., Vol. 21, 1962, pp 107-109.

68. Schloemer, H.H., "Effects of Pressure Gradients on Turbulent-Boundary-Layer Wall-Pressure Fluctuations," J. Acoustical Soc. America, Vol. 42, No. 1, 1967, pp 93-113.

69. Blake, W.K., Gershfeld, J., and Knisely, C.W., "Trailing Edge Flows and Aerodynamic Sound," AIAA Conference Paper 88-3826-CP, 1988.

70. Glegg, S.A.L., "Airfoil Self-Noise Generated in a Cascade," AIAA Paper 96-1739, 2nd AIAA/CEAS Aeroacoustics Conference, May 6-8, 1996.

71. Roe, P.L., "Approximate Riemann Solvers, Parameter Vectors, and Difference Schemes," Journal of Computational Physics, Vol 43, 1981.

72. van Leer, B., "Towards the Ultimate Conservative Difference Scheme. V. A Second-Order Sequel to Godunov's Method," Journal of Computational Physics, Vol 32, 1979.

73. Wilcox, D.C., "Reassessment of the Scale Determining Equations for Advanced Turbulence Models," AIAA Journal, Vol 26, No. 11, 1988, pp 1299–1310.

74. Ganz, W.U. et al., "Boeing 18-Inch Fan Rig Broad Band Noise Test," NASA CR208704, September 1998.

75. Martinelli, L. and Jameson, A., "Validation of a multigrid Method for the Reynolds Averaged Equations," AIAA Paper 88-0414, 1988.

76. Delaney, B. et al., "Design and Test of Fan/Nacelle Models," NAS3–27720 AoI 14.1, Publication Pending.

77. Holmes, D.G. and Connell, S.D., "Solution of the 2D Navier Stokes–Equations on Unstructured Adaptive Grids," AIAA-89-1932, 1989.

78. Holmes, D.G., Lamson, S.H., and Connell, S.D., "Quasi-3D Solutions for Transonic Viscous Flows by Adaptive Triangulation," ASME 88-GT-83, 1988.

79. Connell, S.D., Holmes, D.G., and Braaten, M.E., "Adaptive Unstructured 2D Navier-Stokes Solutions on Mixed Quadrilateral/Triangular Meshes," ASME paper 93-GT-99, 1993.

80. Wadia, A.R., Szucs, P.N., and Crall, D.W., "Inner Workings of Aerodynamic Sweep," IGTE Florida, Paper No. ASME 97-GT-401, 1997.

81. Schwaller, J.G. and Newby, D.R., "Arrangement for Minimizing Buzz Saw Noise in Bladed Rotors," U.S. Patent No. 4,732,532, March 22, 1988.

82. Gulati, A. et al., "Effect of Dilution Air on the Scalar Flowfield at Combustor Sector Exit," Journal of Propulsion and Power, Vol. 11, No. 6, November 1995.

83. Kazin, S.B. et al., "Core Engine Noise Control Program," GEAE DOT/FAA Contractor Report, FAA–RD–74–125, Vol. III, August 1974.

84. Matta, R.K., Sandusky, G.T., and Doyle, V.L., "GE Core Engine Noise Investigation – Low Emission Engines," GEAE FAA Contractor Report FAA–RD–77–4, February 1977.

85. von Glahn, U. and Krejsa, E., "Correlation of Core Noise Obtained by Three-Signal Coherence Techniques," NASA TM83012, November 1982.

86. Heidmann, M. F., "Interim Prediction Method For Fan and Compressor Source Noise," NASA TMX–71763, 1979.

87. Anon, "Gas Turbine Jet Exhaust Noise Prediction," SAE Report ARP876, 1978.

88. Mathews, D.C. and Rekos, N.F., Jr., "Prediction and Measurement of Direct Combustion Noise in Turbopropulsion Systems," AIAA *Journal of Aircraft*, Vol. 14, No. 9, September 1977, pp 850–859.

89. Cumpsty N.A. and Marble, F.E., "The Interaction of Entropy Fluctuations with Turbine Blade Rows: A Mechanism of Turbojet Engine Noise," Proc, R. Soc. Lond, 357 323–344, 1977.

90. Pickett, G.F., "Core Engine Noise Due to Temperature Fluctuations Convecting Through Turbine Blade Rows," AIAA, 75–528, 1975.

Addendum
Broadband Noise Radiation Models for Aircraft Engines

This addendum is a report prepared by Edward J. Rice of Hersh Acoustical Engineering Inc. under subcontract to GEAE, replicated herein by inserting scanned raster images of the original pages.

FINAL REPORT

BROADBAND NOISE RADIATION MODELS FOR AIRCRAFT ENGINES

Prepared by:

Edward J. Rice, Consultant

AEROACOUSTIC CODES DEVELOPMENT AND VALIDATION

SUBTASK 2. FAN BROADBAND NOISE

SUBTASK 2.3 DIRECTIVITY MODEL DEVELOPMENT

(Purchase Order No. 200-18-14C43924)

May 21, 1998

Submitted to:

Dr. Phillip R. Gliebe
Manager, Turbomachinery & Engine System Acoustics
GE Aircraft Engines
One Neumann Way, A411
Cincinnati, OH 45215-1988

SUMMARY

Far-field noise radiation models and the related computer codes have been developed for the radiation of broadband random noise from an aircraft engine. These include the radiation from the fan inlet and aft duct, and the engine core duct. These models have been developed to be used in conjunction with turbomachinery broadband noise generation models which define the acoustic power generation in the duct as distributed among the duct modes or as a mode cut-off ratio distribution and as a function of noise frequency. The models transform the in-duct acoustic power distribution into the far-field radiation field either on a constant radius or sideline distance. The inlet radiation model includes the influence of the bellmouth used in static tests or the inlet lip used for wind-tunnel tests and the results should be adequate for either of these cases. The aft duct cases include the effect of the nozzle area change and the jet slip layer on the propagation and radiation of the internally generated broadband noise. A new termination transmission loss model has been developed to determine the reflection of the sound at the exits of the inlet and the aft ducts. Acoustic power has been conserved even for the difficult aft radiation cases where the radiation angle is drastically altered by the shear layer. The radiation models are intended to be approximate but adequate representations for the noise radiation where very rapid calculations are needed for a multitude of cases.

CONTENTS

ILLUSTRATIONS

ILLUSTRATIONS (Cont)

INTRODUCTION

The broadband random noise radiation models developed here are intended to be reasonably accurate and provide extremely fast computational capability. This speed is required since extremely large numbers of duct modes can propagate in modern turbofan engines at the high frequencies usually encountered with turbomachinery broadband noise. The noise radiation models are intended to be used in conjunction with noise source models which predict the broadband noise generation in the engine ducts in terms of the duct modes or other convenient modal representation such as the modal cut-off ratio power distribution.

The key to the broadband random noise radiation models is the availability of a fairly simple multimodal radiation capability. The concept of the multimodal radiation directivity without a steady flow was introduced by Saule and Rice[1] using a simple flanged duct modal radiation directivity. This concept was further simplified when Rice[2] showed that the flanged duct radiation expression could be approximately expressed as a function only of the mode cut-off ratio and the sound frequency and an approximate equation for broadband radiation was developed using these concepts. A radiation model for the aircraft engine inlet which included steady flow was presented by Rice[3] et al. and fully developed by Rice and Sawdy[4] to incorporate the multimodal properties of the noise source in the duct, the attenuation of the noise field due to wall mounted noise suppressors, the termination reflection, and the resulting far-field radiation. Unfortunately the work of references 3 and 4 used the preservation of modal phase velocity vector angle through the inlet velocity gradients. The results of this model appeared to fit the experimental data in spite of this physically unattractive assumption. The forward beaming of the inlet bellmouth provided a roughly compensating error. This was recently corrected by Rice[5] by incorporating the preservation of modal group velocity vector angle through the inlet velocity gradients and providing a model for the bellmouth effect on the inlet far-field noise radiation directivity.

Numerical sound propagation codes have been reported such as those developed by Horowitz[6] et al. and Eversman[7] et al. These numerical codes based upon finite element analysis within and just outside of the duct can more adequately handle duct area variation, inlet lip shape, and velocity variations than the earlier analytical models. Since concentration of effort was for some time on the engine tone noise consisting of only a few modes at least in flight, these numerical codes were excellent for calculating the radiation of these individual duct modes. However, now it appears that broadband noise may be the limiting noise source and many modes will have to be considered. Although this is possible to accomplish with a finite element code, it is more practical to use simplified, yet surprisingly accurate, approximate radiation models to perform the multitude of calculations that will probably be necessary. Nallasamy[8] has recently reported modal sound radiation results for the geometry and test conditions of the NASA Lewis ANC Fan Facility using the Eversman finite element code. These results have been very useful since they appear to validate the inlet group velocity vector angle preservation and also that the mode cut-off ratio alone determines the angular position of the far-field radiation principal lobe peak. These results will be used later to confirm the accuracy of the simplified model used for the broadband noise radiation method developed here.

The modal cut-off ratio radiation model has also been extended to fan aft noise radiation by Rice and Saule[9] for both single and multiple mode radiation. The single mode approximate radiation results agreed well with the results of Savkar[10] using the Wiener-Hopf method. The approximate broadband radiation directivity calculations agreed with the shape of the experimental results.

For all of the approximate radiation calculations mentioned above, the agreements noted were in directivity shape only. The results were moved up or down as required to obtain the best superposition possible. For the models produced in this program, more than just shape agreement was necessary. Since broadband random noise acoustic power is to be calculated in the fan or core duct and the results are to be tested by observation of far-field acoustic power directivity, acoustic power must be conserved passing through the apertures and surrounding flow fields. The sound pressure level in the far-field for a mode or a group of modes characterized by mode cut-off ratio depends upon the acoustic power (Watts) and the area (ft^2) subtended by the principal radiation lobe (approximately). The principal lobe width depends upon sound frequency and the area is also a function of radiation angle. This area is complicated for the aft radiation since the propagation angle is a function of mode cut-off ratio and also of the angle change caused by refraction through the jet shear layers. As part of this acoustic power conservation, a new termination transmission loss model was developed to adequately assess the reflection loss at the inlet lip or nozzle exit. This improved termination loss model is a function of mode cut-off ratio and sound frequency and replaces the previous model of reference 2 which included cut-off ratio only.

Some of the background material for this report has been obtained from reference 5. This reference should be consulted to supplement the model development presented here.

NOISE RADIATION MODELS

Background

The concept of group and phase velocity vector propagation angle is essential to the development that follows and will thus be defined here for later use. The development of a simple radiation model for the inlet broadband noise requires an assumption of the preservation of group velocity propagation angle. The sound produced by the fan and propagating in the inlet has an environment of high speed flow opposing the direction of sound propagation. As the sound reaches the inlet opening, the flow velocity rapidly changes with distance due to the external static environment or at least changes magnitude due to the flight velocity being different than the internal inlet flow velocity. There are analytical solutions for the radiation of sound from a duct opening for zero flow or for uniform flow everywhere. However, no solution exists when the external velocity is different from the inlet velocity. To obtain a reasonably simple expression for the far-field radiation of the noise from the inlet, assumptions must be made about some directivity quantity of the noise field. Two propagation vectors can be defined in the duct to represent the direction of sound travel. These vectors are shown in Figure 1. The phase velocity is normal to the wave front and represents the progression of the wave into the local medium. When the steady flow velocity, cM_D, is added (for this inlet case subtracted) to the phase velocity a second vector, the group velocity, results as shown in Figure 1. The group

velocity is the more fundamental of the two and represents the direction of acoustic power propagation. The expression for the group velocity is:

$$\cos \psi_x = \sqrt{1 - M_D^2} \; \frac{\sqrt{1 - 1/\xi_D^2}}{\sqrt{1 - M_D^2(1 - 1/\xi_D^2)}} \tag{1}$$

The phase velocity is given by:

$$\cos \varphi_x = \frac{-M_D + \sqrt{1 - 1/\xi_D^2}}{1 - M_D\sqrt{1 - 1/\xi_D^2}} \tag{2}$$

which are derived in Rice[3] et al. The x subscript is included to show that the angles are measured relative to the axial coordinate. The D subscript refers to "Duct" as in duct Mach number M_D. The steady flow Mach number, M_D, should be inserted in the equations as a negative number for an inlet since the flow opposes the direction of sound propagation. The mode cut-off ratio used in the above equations is given by:

$$\xi_D = \frac{\pi \eta}{\alpha\sqrt{1 - M_D^2}} \tag{3}$$

and the frequency parameter, η = fD/c where f is the frequency, D is the duct diameter, and c is the speed of sound. The hardwall duct Eigenvalues are given by α.

No analytical solution exists to describe the propagation of sound through the velocity gradients of the inlet opening. Wiener-Hopf type solutions exist for no flow and for uniform flow inside and outside of the inlet (references 11,12) and for a tube of flow separated from the external flow by a slip layer (reference 10). This latter solution is excellent for the aft radiation since the jet does resemble this situation, but it is not relevant to an inlet flow. To obtain a model for the inlet radiation directivity it might be assumed that either the phase or group velocity are preserved in passing through the velocity gradients of the inlet. The phase velocity was selected in references 3 and 4 since the results appeared to agree with the inlet experimental data even though the assumption was not physically appealing. The experimental data contained a strong inlet bellmouth effect that masked the fact that the group velocity vector angle preservation was the better assumption. Later a fundamental ray tracing study was conducted by Cho and Rice[13] and this showed conclusively that the group velocity vector must be preserved. The inlet radiation model was corrected and thoroughly discussed in reference 5. The numerical calculations of Nallasamy[8] also reinforce the group velocity choice. He found that the angle of the principal lobe of radiation for a duct mode does not depend upon the external flow velocity which is also the result for the simplified model when group velocity vector angle is preserved.

It is useful to have equations relating the phase and group velocity vector angles. These relations can be expressed as (phase to group):

$$\cos\psi_x = \frac{\cos\varphi_x + M_D}{\sqrt{1 + M_D^2 + 2M_D\cos\varphi_x}} \tag{4}$$

and (group to phase),

$$\cos\varphi_x = -M_D\sin^2\psi_x + \cos\psi_x\sqrt{1 - M_D^2\sin^2\psi_x} \tag{5}$$

Radiation Equations without Steady Flow

The inlet radiation equations will be developed in steps and the results left in blocks which can then be easily assembled into the computer codes. This will keep the equations fairly simple and easy to understand and will more clearly illustrate the normalization used here. The basic radiation equation used here is the flanged duct equation as modified by Saule[14] to provide equal energy per mode equalization. This equation is,

$$P_0^2 = \frac{\sqrt{1 - 1/\xi_0^2}\,\sin^2\psi_0\,[J_m'(\pi\eta\sin\psi_0)]^2}{[1 - (m/\alpha)^2][1/\xi_0^2 - \sin^2\psi_0]^2} \tag{6}$$

The subscript 0 is used in equation 6 to signify that the equation was of course derived for zero Mach number, no-flow. P_0^2 is the far-field pressure squared, ξ_0 is the mode cut-off ratio given by equation 3 with $M_D = 0$, m is the mode lobe number, and ψ_0 is the angle measured from the inlet axis. Saule and Rice[1] compared the results of calculations using equation 6 to the more accurate Wiener-Hopf solutions using Savkar's[10] code. The results compared very favorably particularly for the principal lobe or radiation. Equation 6 was thus judged to be sufficiently accurate and quite simple to use.

A further simplification of equation 6 for the far-field pressure-squared will be made to make the radiation model more usable when modal cut-off ratio power distribution is used rather than actual individual duct mode acoustic power. This approximate far-field acoustic pressure-squared equation developed by Rice[2] is given by,

$$P_0^2 = \frac{2\sin\psi_0\sqrt{1 - 1/\xi_0^2}\,[\sin[\pi\eta(\sin\psi_0 - 1/\xi_0)]]^2}{\pi^2\eta[1/\xi_0^2 - \sin^2\psi_0]^2} \tag{7}$$

The main advantage of equation 7 is that it does not contain explicit modal information in terms

of lobe numbers or radial orders but does still represent the modal information through the mode cut-off ratio. Some approximate properties of the principal lobe of radiation can easily be determined from equation 7. The approximate peak radiation occurs by taking the limit of the indeterminate right side of equation 7 when the argument of the numerator sine function is zero. The result is,

$$\sin \psi_{0P} = 1/\xi_0 \tag{8}$$

Thus for no-flow, the angle of the radiation peak is a function only of the mode cut-off ratio. The minima or zeroes of the principal lobe of radiation occur when the numerator sine function argument equals $\pm\pi$. The result is,

$$\sin \psi_0^{\pm} = 1/\xi_0 \pm 1/\eta \tag{9}$$

where the - represents the principal lobe zero nearer the axis and the + nearer the sideline. The width of the radiation lobe around the peak is a function only of sound frequency. Of course this type of information can be obtained from equation 6 also, but the roots of the Bessel function derivative are used rather than $\pm\pi$.

Plane wave radiation which peaks on the axis is not very important for engine inlet radiation but it is crucial for the exhaust noise radiation since it is refracted off the axis and may be critical for perceived sideline noise. The approximate radiation equation 7 is not valid for plane wave radiation. A comparable approximate radiation directivity equation for plane wave radiation can be obtained by applying limits to equation 6. Let m = 0 and $\xi_0 \to \infty$, and approximate the Bessel function with the sine function to yield:

$$P_o^2 = \frac{\sin^2(\pi \eta \sin \psi_O)}{4 \sin^2 \psi_O} \tag{10}$$

Equation 10 provides an adequate approximation to equation 6. Both have the same peak value on the axis. The Bessel function of equation 6 has its first zero at the argument of 3.8317 while the first zero of the sine function of equation 10 is at an argument equal to π.

Modification of Radiation Model to Include Uniform Flow

The conversion of the radiation equation from no flow to uniform flow everywhere will proceed as in reference 4 using the transformations presented in references 11, 12, and 15. In equation 6, 7 or 10 replace $\sin\psi_0$ by,

$$\sin \overline{\psi} = \frac{\beta \sin \psi_D}{\sqrt{1 - M_D^2 \sin^2 \psi_D}} \tag{11}$$

Replace η by $\bar{\eta} = \eta/\beta$, and ξ_0 by $\bar{\xi} = \xi_0/\beta$ where,

$$\beta = \sqrt{1 - M_D^2} \tag{12}$$

where again the subscript D indicates a duct referenced quantity. Also as needed later, replace $\cos\psi_0$ by,

$$\cos\bar{\psi} = \frac{\cos\psi_D}{\sqrt{1 - M_D^2 \sin^2\psi_D}} \tag{13}$$

In addition, for an inlet flow, equation 6, 7 or 10 must be multiplied by,

$$H_D = \frac{(1 - M_D\cos\psi_D)}{(1 - M_D\cos\psi_P)} \tag{14}$$

where the radiation principal lobe peak angle is given by,

$$\cos\psi_P = \frac{\beta\sqrt{1 - 1/\xi_D^2}}{\sqrt{1 - M_D^2(1 - 1/\xi_D^2)}} \tag{15}$$

For an exhaust flow, $M_D > 0$, use $H_D = 1$. Note that the quantity H_D of equation 14 is different than that of references 4, 11, 12, and 15 since it has been normalized by its value at the principal lobe peak ($H_D = 1$, at $\psi_D = \psi_P$). This is convenient since the final equation will remain approximately normalized if each multiplier is normalized as the equation is built up.

The final multiplier for equation 6, 7 or 10 was proposed by Sawdy[16] to remove the pressure doubling effect at the flange to better simulate the unflanged duct radiation model. This was developed by Rice and Sawdy[4] into the factor,

$$G_D = \frac{[\,1 + \cos\psi_D/\sqrt{1 - M_D^2\sin^2\psi_D}\,]^2}{[\,1 + \sqrt{1 - 1/\xi_D^2}\,]^2} \tag{16}$$

which has already been normalized by the value at the radiation principal lobe peak. Note that between 0 and 90° the numerator of equation 16 varies by a factor of four which is just right to remove the pressure doubling at the wall at 90°.

The equations for radiation from a sharp edged (simulated unflanged) duct with uniform flow everywhere are now complete. To summarize, the no-flow flanged duct radiation equations have

been presented by either equation 6, 7 or 10. For uniform flow use the convective transformations of equations 11-13. Finally use the multiplying factors of equations 14 and 16 for an inlet flow or just equation 16 for an exhaust flow. The equations will not be combined into a final equation as was done in reference 4. This final equation would be quite formidable and unnecessarily confusing. This radiation model is intended to be used as a computer code in which the final result can be built up by separately defined multiplying factors. Any final equation would be further complicated by the bellmouth or inlet lip effect for an inlet or by refraction for an exhaust flow.

Radiation Model Results Compared to Experimental Data

Radiation directivity calculations using the model defined by equation 6 were made using the same input conditions as used by Ville and Silcox[17] for their no-flow radiation experiments. One of their experiments involved the measured radiation of a single duct mode from an unflanged duct. The present model is compared to this data in Figure 2 for the lowest radials of the one and six lobed modes. The agreement is seen to be excellent. The peak angle and the breadth of the radiation pattern are predicted very well. For the six lobed mode, the radiation near the inlet axis is probably not associated with the direct radiation but is probably associated with the low level background or reflections. This excellent agreement with data provides confidence that this simple radiation model can provide good results for inlet far-field radiation directivities requiring very rapid results for multiple calculations. Of course to this point the theory has been validated only for no-flow with a sharp thin inlet lip. Further validation of the approximate radiation theory will be presented later after the effect of the inlet bellmouth has been presented.

Radiation Equation Normalization, No-flow

Under most circumstances the normalization of the radiation equation for a duct mode is not of much interest. Usually not enough is known about the relative power of the modes to make use of a normalized radiation equation. For single mode theory-data comparisons the directivity shape and peak location are usually of interest so the curves are simply moved up and down until they match the best. However, for multimodal radiation such as for broadband noise which is of interest here, the relative power of the modes must be considered and a normalized radiation equation must be used. To check the normalization of equation 6, it was area weighted and numerically integrated from 0 to 90^{o} using 1800 angle increments. The integrated acoustic power is expressed in decibels with an integrated value of unity being expressed as zero decibels. The results are shown in Figure 3 as a function of radiation principal lobe location. For no-flow the principal lobe is located according to $\sin\psi_0 = 1/\xi_0$. The normalization is seen to be quite good over most of the angle range. About a three decibel error can occur for the modes ($\xi_D \to \infty$) that propagate near the inlet axis. For the sideline near ninety degrees a large error can occur and this is caused by the first term in the numerator of equation 6 which approaches zero as cut-off ratio approached unity. A reduction in calculated acoustic power, as calculated for Figure 3, of about three decibels should be expected since an integration from 0 to 90^{o} captures only about half of a principal lobe peaking at 90^{o}. An empirical multiplier for equation 6 was developed to correct the above error and is given by,

$$N_0 = \frac{2\,[\,0.7/\eta + \sqrt{1 - 1/\xi_0^2}\,]}{1 + 0.7/\eta} \tag{17}$$

Note that this multiplier is intended to replace the factor $\sqrt{1 - 1/\xi_o^2}$ in equation 6 or 7 and it remains finite as $\xi_O \to 1$. Using equation 17 to replace the square root term in the approximate equation 7 and integrating the far-field radiation from 0 to 90° provides the results shown in Figure 4. The normalization is seen to be excellent over most principal lobe peak angles. As mentioned earlier, near 90° the principal lobe must be considered to extend beyond 90° and at this stage of the model development the radiation equations are defined only to 90°. Thus about half of the power is missed with this integration. The correlation represented by equation 17 could be improved but it is considered to be sufficient for the present purposes.

Radiation Equation Normalization with Uniform Flow

The next stage in the far-field radiation model development is to alter the far-field pressure to account for the change in radiation angle when the case of uniform flow everywhere is considered. The incremental far-field acoustic power over a small angle on the spherical surface is given by:

$$dE = 2\,\pi\,r^2\,P^2\,\sin\psi\,d\psi \tag{18}$$

where r is the radius to, ψ the angle of, and P the acoustic pressure at the far-field point. Using equation 11 the angle shift due to uniform flow is given by:

$$\sin\psi_O = \frac{\beta \sin\psi_D}{\sqrt{1 - M_D^2 \sin^2\psi_D}} \tag{19}$$

where ψ_O and ψ_D are the radiation angles with no-flow and uniform flow everywhere at Mach number M_D, and $\beta = \sqrt{1 - M_D^2}$. Conserving acoustic power between the no-flow and uniform flow cases yields;

$$\frac{P_D^2}{P_O^2} = \frac{\sin\psi_O}{\sin\psi_D}\,\frac{d\psi_O}{d\psi_D} \tag{20}$$

The differentiation of equation 20 is made using equation 19 and results are evaluated at the principal lobe peak to yield:

$$\frac{P_D^2}{P_O^2} = \frac{[\,1 - M_D^2(\,1 - 1/\xi_D^2)\,]^{3/2}}{\beta} \tag{21}$$

where again the mode cut-off ratio is given by equation 3. Equation 21 represents the adjustment that must be made to either equation 6, 7 or 10 to maintain the normalization (unity integral 0 to 90^{o}) when the no-flow radiation equations are extended to uniform flow everywhere. Considerable additional modifications must be made to account for an inlet or exhaust flow, but it will be useful to summarize the model at this stage of development in the next section.

Normalized Far-field Radiation Model with Uniform Flow Everywhere

As previously mentioned the far-field radiation model equations can become extremely complex if an attempt is made to put all of the adjustments together in a single expression. The equation shown below for radiation with uniform flow is the last expression that will be generated here, since it is already quite complex, and further modifications will be made step wise only in the computer codes. The normalized far-field radiation pressure starting with the approximate equation 7 and incorporating the refinements defined above is:

$$P_D^2 = C \frac{2Q \sin^2 [\pi \eta (Q - \frac{1}{\beta \xi_D})]}{\pi^2 \eta \beta^2 [\frac{1}{\beta^2 \xi_D^2} - Q^2]^2} \tag{22}$$

where the terms C and Q are given by:

$$C = \frac{2[0.7/\eta + \sqrt{1 - 1/\xi_D^2}]}{1 + 0.7/\eta} \frac{[1 - M_D^2(1 - 1/\xi_D^2)]^{3/2}}{\beta} \tag{23}$$

and,

$$Q = \frac{\sin \psi_D}{\sqrt{1 - M_D^2 \sin^2 \psi_D}} \tag{24}$$

The squared acoustic pressure of equation 22 must then be multiplied by H_D and G_D from equations 14 and 16 for inlet flows and by just G_D for exhaust flows.

Equation 22 (with its multipliers) was area weighted and integrated from the axis to 90^{o} to check the acoustic power normalization when the flow velocity was changed. Figure 5 shows the results as uniform steady flow Mach number was varied from -0.8 (inlet) to +0.8 (exhaust). The results are seen to be excellent with the largest error, over the angle range studied, being less than 0.25 dB. For these calculations only cut-off ratios were used that allowed full radiation principal lobes (lobe not extending into aft quadrant) to avoid the deletion of significant acoustic power. The frequency parameter $\eta = 30$ was used to allow sufficiently narrow lobes (see equation 9) so that the sideline could be approached with these full lobes.

The far-field radiation model has now been developed to a sufficient degree of accuracy that it can be extended to multimodal inlet and exhaust radiation cases. The method to describe the distribution of acoustic power among the many modes will be developed next.

Distribution of Acoustic Power Using Mode Cut-off Ratio Method

A convenient method of assigning acoustic power among the modes is available using the modal density function and relations derived from this function. The modal density function for the circular duct modes was derived by Rice[18] and is defined by:

$$D = \frac{2}{\xi_D^3} \tag{25}$$

where again the modal cut-off ratio is defined by equation 3. When equation 25 is integrated between two values of ξ_D the fraction of the total modes between these limits is determined as would be expected from a density function. The actual number of modes, which would also be a function of frequency, can also be estimated using the expressions of reference 18, but this is not important for the present discussion. The boundaries of N bins with equal number of modes in each bin can be determined from the integration of equation 25 to be represented by:

$$\frac{1}{\xi_j^2} = \frac{1}{\xi_{j-1}^2} - \frac{1}{N} \quad , \quad j = 1, 2, \ldots, N \tag{26}$$

where the boundaries can be found by recursion or with some manipulation the boundaries can be determined directly from:

$$\xi_j = \sqrt{\frac{N}{N+1-j}} \quad , \textit{ also } \quad \overline{\xi_j} = \sqrt{\frac{N}{N+\frac{1}{2}-j}} \tag{27}$$

where the second term ($\overline{\xi_j}$) is the average value of the cut-off ratio in the bin with half of the modes greater and half of the modes smaller than this average value. The first bin lower boundary is $\xi_1 = 1$, mode cut-off, and the last bin is bounded by $\xi_N = N^{1/2}$ and infinity. It is convenient when working with modes to use the expression:

$$j = 1 + N\left(1 - \frac{1}{\xi_D^2}\right) \tag{28}$$

which must be rounded down to an integer. Equation 28 determines which of the N cut-off ratio bins into which to put the acoustic power given the mode cut-off ratio ξ_D.

Sound Pressure Level in the Far-field for Multiple Modes

The user must load the cut-off ratio bins discussed in the previous section with the proper acoustic power as determined by a noise source model. The acoustic power is then radiated to the far-field as might be summarized by the expression:

$$P_F^2(\eta,\psi) = \frac{8.364\,\rho c}{r^2} \sum_j W(\eta,\xi_j) T(\eta,\xi_j) F(\eta,\xi_j,\psi) \qquad (29)$$

where ρ and c are the density and speed of sound of the surrounding air in lb_m/ft^3 and ft/sec respectively, and r is the distance to the far-field point in feet. W is the acoustic power in Watts in the j^{th} cut-off ratio bin, T is the transmission loss coefficient of the aperture (inlet or exhaust nozzle), and F is the normalized radiation directivity function as given for example by equation 22. The acoustic pressure is in Newtons/m^2.

Some comment should be made about equation 29 since use of this expression is crucial to the calculation of the broadband noise multimodal radiation directivity. The broadband noise is by its nature randomly generated. The random flow structures interacting with the blades, vanes or other structures are uncorrelated and can be expected to generate duct modes that are uncorrelated with each other. Thus the acoustic powers can be added as in equation 29. Also although equation 29 might be considered as a random addition of the acoustic power of these random modes, an additional simplification has been made in summing over the cut-off ratio bins rather than the modes. Rice[2] has shown, and it can be seen from equation 7, that duct modes of similar mode cut-off ratio will propagate similarly to the far-field. This is at least true for the principal lobe of radiation which carries most of the acoustic power. The side lobes will differ among different modes of similar mode cut-off ratio, but this is not important here. The principal lobes of other modes will dominate the acoustic power directivity at the position of the side lobes of any particular mode. Thus the computational benefit of sorting the acoustic power into the cut-off ratio dependent bins is used here. For example, for high frequencies, thousands of modes might be able to propagate, but they can adequately be handled by using perhaps ten to one hundred bins.

After the far-field pressure-squared has been calculated for the summation of all of the modes or all of the mode cut-off ratio bins, the sound pressure level is calculated using:

$$SPL(\eta,\psi) = 10 Log_{10}[P_F(\eta,\psi)] + 93.9794 \qquad (30)$$

where the reference pressure $2x10^{-5}$ Newtons/m^2 has been used.

Note that P_F and SPL are shown as functions of frequency parameter and far-field angle. Each calculation cycle of the computer codes will provide the multimodal sound pressure level at all of the far-field angles. For each frequency of interest, new information on the distribution of acoustic power as a function of mode cut-off ratio must be specified and the calculations must

then be repeated. A large number of calculations may thus be necessary depending upon the frequency range and resolution required. It is thus clear that proper simplifications and approximations are very useful to make the potentially huge number of calculations possible.

There is one final subject that is common to all of the radiation calculations before they are specialized to fan inlet and aft duct and core duct. This is the concern about radiation beyond the flange (90^o), a region for which the flanged duct theory is not technically valid.

Radiation Model for Angles Greater than Ninety Degrees

All of the flanged duct far-field radiation models (equations 6, 7 or 10) are valid only up to the flange at 90^o. If used beyond 90^o, the far-field pressure is seen to be symmetrical around 90^o. Thus another principal lobe would occur in the back quadrant which would be unacceptable. From the results of Nallasamy[8], it is seen that there is generally a gentle fall-off of acoustic pressure beyond the principal lobe peak that might be fit to an exponential fall-off. Also it appears that the radiation pressure is symmetrical over a small angle around the peak at least up to the argument of $\pi/2$ for the $\sin^2$ term in equation 22. The following methods were selected to obtain the smooth roll-off beyond the principal lobe peak and into the aft quadrant.

Non-plane Waves. For the non-plane wave modes, as expressed by equation 22, four regions had to be considered to cover all of the possibilities with two being high frequency and two low frequency regions. Let the equation 22 $\sin^2$ argument be called Arg in the following.

Region 1. $\eta \geq \beta/[\,2\,(\,1 - 1/\xi_D\,)]$. The angle ψ_D is less than 90^o at which Arg = $\pi/2$. The slope of P_D^2 is fit at this angle to an exponential function that can be used back beyond the principal lobe peak and into the back quadrant if necessary. If $\xi_D \to 1$, the peak approaches 90^o and the required frequency parameter would be very large for the lobe to be contained within the front quadrant and region 2 is required.

Region 2. $\eta \geq \beta\xi_D/2$. The fitting angle ψ_D is less than the peak and is obtained at Arg = $-\pi/2$. An exponential function can then be fit at ψ_D and, by assuming symmetry, used back beyond the principal lobe peak and into the back quadrant.

Region 3. Low frequency region with the peak greater than 60^o. An exponential function is fit at half the peak angle and, again by assuming symmetry, used back beyond the principal lobe peak and into the back quadrant.

Region 4. Low frequency region with the peak angle less than 60^o. An exponential function is fit at 80^o and used back beyond the principal lobe peak and into the back quadrant.

Plane Waves. The extension of the plane wave radiation beyond the flange is simpler than for the non-plane wave since the peak is always on the axis. The exponential fit is made for the $\sin^2$ argument equal to $\pi/2$ for $\eta \geq \beta/2$. For lower frequencies, the fit is made at $\psi = 90^o$. The exponential function is then extrapolated into the back quadrant if required.

Note that the duct dimension, frequency parameter, Mach number and mode cut-off ratio used in the above calculations are those at the exit planes. For an inlet this is the radiation plane of the bellmouth and the nozzle exit (or beyond if not properly expanded) for the exhaust duct.

The duct termination transmission loss coefficient, $T(\eta,\xi_D)$, in equation 29 will now be developed.

Acoustic Power Transmission Coefficient for the Duct Terminations

The calculation of far-field acoustic power is of interest here, and this is determined by the source production and the loss of power anywhere along the propagation path. A simple acoustic power transmission coefficient was presented by Rice[2] which was a high frequency approximation and a function only of the mode cut-off ratio. A complete form of the coefficient developed in reference 2 will be presented here. This expression also contains the frequency parameter. This acoustic power transmission coefficient expression is believed to be new and the expression of reference 2 is a limiting case of this new expression.

Acoustic Power Transmission Coefficient

The development begins with the acoustic pressure for a single mode in the duct which can be expressed by:

$$P = e^{i\omega t - im\theta}\left[e^{-i\omega k_x' x} + R_P e^{i\omega k_x' x}\right] J_m\left(\alpha_{mn}\frac{r}{r_D}\right) \tag{31}$$

where the first term in brackets represents the wave propagating in the positive axial direction, the second in the negative axial direction. The number of pressure lobes in the circumferential, θ, direction is given by m, r_D is the duct radius and ω is the radian frequency. R_P is the pressure reflection coefficient. For uniform mean flow the acoustic velocity vector is given by:

$$\bar{v} = i\frac{\nabla P}{\rho\,\omega\,Q}, \quad Q^{\pm} = 1 - M_D\frac{k_x^{\pm}}{k} \tag{32}$$

and the axial propagation wave number is determined by:

$$(a)\quad \frac{k_x^{\pm}}{k} = \frac{-M_D \pm \tau}{1 - M_D^2}, \qquad (b)\quad \tau = \sqrt{1 - 1/\xi_D^2}, \qquad (c)\quad k = \frac{\omega}{c} \tag{33}$$

The acoustic power intensity equation can be obtained from Goldstein[19] and when reduced to the case of uniform axial flow, the axial acoustic power intensity is

$$I_x = (1 + M_D^2) P v_x + \frac{M_D}{\rho_O c_O} P^2 + \rho_O c_O M_D v_x^2 \tag{34}$$

where the subscripts on density (ρ_O) and sonic speed (c_O) are used just to distinguish them as the zero order or steady terms as opposed to the perturbation (acoustic) terms. The duct termination impedance for a duct mode can be defined as:

$$\zeta_x = \frac{P}{\rho_O c_O v_x} = \theta + i\chi \tag{35}$$

which will be defined later for the individual duct modes. From equations 31 and 32 the axial impedance for a duct mode in an infinite length duct can be derived as:

$$\zeta_{x,\infty} = \frac{1 - M_D \tau}{\tau - M_D} \tag{36}$$

where again τ is defined by equation 33b. The pressure reflection coefficient of equation 31 can be derived as:

$$R_P = \frac{(1 + M_D \tau)}{(1 - M_D \tau)} \frac{[(\tau - M_D)(\theta + i\chi) - 1 + M_D \tau]}{[(\tau + M_D)(\theta + i\chi) + 1 + M_D \tau]} \tag{37}$$

The extremely important duct termination transmission coefficient to be used in equation 29 is defined as the ratio of the acoustic power transmitted through the duct termination divided by the incident acoustic power. After considerable manipulation of the above equations, this termination transmission coefficient can be expressed as:

$$T(\eta, \xi_D) = \frac{I_{x,trans}}{I_{x,incid}} = 4\tau \frac{[(\theta + M_D)(\theta M_D + 1) + M_D \chi^2]}{[\theta(\tau + M_D) + M_D \tau + 1]^2 + \chi^2 (\tau + M_D)^2} \tag{38}$$

T is expressed as a function of frequency parameter and mode cut-off ratio. Frequency dependence occurs through the termination impedance terms θ and χ. These terms also contribute to the mode cut-off ratio dependence as also does τ as seen from equation 33. The acoustic power reflection coefficient (as contrasted to pressure) can be expressed as:

$$R_E = \frac{I_{x,refl}}{I_{x,incid}} = \frac{[\theta(\tau - M_D) + M_D \tau - 1]^2 + \chi^2 (\tau - M_D)^2}{[\theta(\tau + M_D) + M_D \tau + 1]^2 + \chi^2 (\tau + M_D)^2} \tag{39}$$

As must be true, $T + R_E = 1$. The relationship between the pressure and acoustic power reflection coefficients can be expressed as:

$$R_E = \frac{(1 - M_D\tau)^2}{(1 + M_D\tau)^2} R_P R_P^* \qquad (40)$$

where the superscript * indicates the complex conjugate.

There are some interesting special cases which must be used in the computer code and which may be more familiar. For the special case of the plane wave for which $\xi_D \to \infty$ and $\tau \to 1$,

$$T(\eta) = \frac{4}{(1 + M_D)^2} \frac{[\theta(1 + M_D^2) + M_D(\theta^2 + \chi^2 + 1)]}{[(\theta + 1)^2 + \chi^2]}, \quad \textit{plane wave} \qquad (41)$$

T is now seen to be only a function of frequency through termination resistance θ and reactance χ. Likewise the plane wave acoustic power reflection coefficient is given by:

$$R_E = \frac{(1 - M_D)^2}{(1 + M_D)^2} \frac{[(\theta - 1)^2 + \chi^2]}{[(\theta + 1)^2 + \chi^2]}, \quad \textit{plane wave} \qquad (42)$$

It is readily seen from equations 41 and 42 that in the high frequency limit where $\theta \to 1$ and $\chi \to 0$, then $T \to 1$ and $R_E \to 0$ as required.

Going back to equation 38 for the general acoustic power termination transmission coefficient, if the high frequency results, $\theta \to 1$ and $\chi \to 0$, are inserted, then the special case is obtained as:

$$T(\xi_D) \approx \frac{4\tau}{(\tau + 1)^2}, \quad \textit{high frequency} \qquad (43)$$

This is the limiting case as reported by Rice[2] which is only a function of mode cut-off ratio. This has proved to be an extremely useful result, but it is too limited for the purposes of this program. A study of the aft radiation shows that the plane wave must be considered and equation 43 is not valid for the plane wave at low frequencies.

Note that for all of the equations derived above, the duct Mach number, M_D, should be considered relative to the positive x axis. For an inlet, the Mach number is negative. For an aft duct (fan or core) the Mach number is positive.

For the computer codes developed here, the acoustic power duct termination transmission coefficients expressed by equations 38 and 41 will be used. Equation 41 is used for the special case of the plane wave and equation 38 is used for all other modes or mode simulations (cut-off

ratio partitions). The use of these equations requires the definition of the termination impedance which will be developed next.

Duct Termination Impedance

The duct termination impedance presented below was obtained from the sparse information that was readily available. Improvements to this part of the broad band noise radiation codes can easily be made, if desired, as improved information is obtained. It is believed that the following expressions will be sufficiently adequate for the purposes of this study.

The termination impedance for the plane wave was obtained from Morse[20] as the radiation impedance of a rigid piston in a wall. Morse provides high and low frequency limits for the impedance components and a table of calculated results. Curve fits of these results were made using functions that preserved the high and low frequency limits for the radiation resistance and reactance. The result for the plane wave radiation resistance is:

$$\theta_{PW} = 1 + X_1 e^{-0.325226 X_1} - e^{-0.101669 X_2}, \qquad plane\ wave \tag{44}$$

where the frequency functions used were,

$$X_1 = \frac{\pi^2 \eta^2}{2}, \qquad X_2 = \eta^{5.7848} \tag{45}$$

The result for the plane wave radiation reactance is:

$$\chi_{PW} = \frac{8\eta}{3} e^{-3.57433 X_3} + \frac{B X_4^2}{1 + B X_4^3}, \qquad plane\ wave \tag{46}$$

where the frequency functions and constant used were,

$$X_4 = \frac{\pi^2 \eta}{2}, \qquad X_3 = \eta^{1.95729}, \qquad B = 0.023567 \tag{47}$$

The empirical curve fits of equations 44 and 46 for the resistance and reactance of the plane wave are compared to the tabulated values of Morse[20] in Figures 6 and 7. The fit of the data is seen to be excellent and the impedance expressions for the plane wave are as good as can be obtained at this time.

The duct termination radiation impedance for the non-plane wave modes is somewhat more complicated than that of the plane wave. For the non-plane wave the radiation impedance is a

function of frequency and mode cut-off ratio as was also shown for the radiation directivity earlier. Morfy[21] provided calculations of radiation efficiency (resistance) and collapsed the results using a very useful grouping of the variables that can be redefined as:

$$\gamma = \pi \eta \left(1 - \frac{1}{\xi_D} \right) \tag{48}$$

Zorumski[22] made radiation impedance calculations for radial orders of the axisymmetric modes which can be used to estimate the dependence upon mode cut-off ratio. His results for the radiation resistance and reactance of the 0,1 and 0,2 modes (m,n of equation 31) are plotted in Figures 8 and 9 with the ordinate expressed by the variable of equation 48. This variable is seen to collapse the Zorumski[22] results much like the results shown by Morfy[21]. Note that the magnitudes for the two modes are not exactly the same. For the resistance plots of Figure 8, the 0,2 mode resistance was reduced by a 0.8 factor. For the reactance plots of Figure 9 the (0,2) mode reactance was multiplied by 0.72. There was insufficient information to correlate the influence of radial order on the amplitudes of the radiation resistance and reactance for the non-plane modes. The correlations that follow must be considered as approximations particularly for the higher order modes.

The duct termination radiation resistance for the non-plane wave modes are approximated by:

$$\theta_N = 1 + 0.5\, e^{-0.5338(\gamma - 1.5)^2}, \qquad \gamma \geq 1.5, \qquad \underline{non}\text{-}planewave \tag{49}$$

and,

$$\theta_N = 1.5\, e^{-0.2124(\gamma - 1.5)^2}, \qquad \gamma \leq 1.5, \qquad \underline{non}\text{-}plane\ wave \tag{50}$$

the definitions being split above and below a value of γ=1.5. The duct termination radiation reactance for the non-plane wave modes are approximated by:

$$\chi_N = 1.135\, e^{-0.29(\gamma + 0.18)^2}, \qquad all\ \gamma, \qquad \underline{non}\text{-}plane\ wave \tag{51}$$

These radiation impedance correlations must be considered as approximate interim equations. They are all based upon no-flow calculations. If better information becomes available, new relationships can easily be incorporated into the broadband multimodal far-field radiation codes.

This concludes the discussions of elements that are general to the multimodal radiation of the broadband noise from the aircraft engine. Next the features that are specific to the inlet and aft broadband radiation models will be developed starting with the inlet radiation.

INLET NOISE FAR-FIELD RADIATION

The approximate single mode far-field radiation model will now be extended to be valid for the engine inlet by addition of the effect of the inlet bellmouth. Results will then be compared to a special set of data for a JT15D engine with rods ahead of the rotor to produce a single mode and to numerical radiation calculations using the geometry and conditions of the NASA Lewis ANC Fan Facility.

Inlet Bellmouth Influence on Far-field Radiation

The generation of the model begins by using a result from Cho and Ingard[23,24] that a mode can retain its identity and stay intact without significant scattering or reflection as it passes through a duct area change provided the duct change is sufficiently gradual. The group velocity vector is assumed to remain in the same direction unaffected by flow velocity change once it leaves contact with the inlet and bellmouth. However, as the mode passes from the inlet duct through the gradual bellmouth area change, a profound change can occur to the group velocity vector due to the duct dimension change and the resulting mode cut off ratio increase. This can be shown by the illustration in Figure 10. A near cut off mode with group velocity vector at nearly 90^{o} to the inlet axis is shown entering the bellmouth. This near cut off mode mainly bounces back and forth between the duct walls and if it could radiate directly it would go to near 90^{o} in the far field. As the mode progresses in the bellmouth the growing radial dimension causes the mode cut off ratio to increase, as seen by equation 3, which causes the group velocity vector, given by equation 1, to decrease its angle to more toward the inlet axis. In the limit as $\xi_D \to \infty$, equation 1 shows the group velocity vector angle to approach zero (propagation on the axis). At some axial location in the bellmouth, the group velocity angle will equal the bellmouth wall slope and the sound will no longer be constrained by the bellmouth and thus will escape to the far-field. The sound will propagate to the far field with a peak at this latter angle, not to be further changed by flow or surroundings. The lobed diffraction pattern determined by the final dimensions will accompany the sound radiation and this radiation pattern is calculated using the circular flanged duct radiation model defined by equations 6 to 16. Exactly where the sound emanates from as it releases from the bellmouth is determined by the radial center of pressure defined as a radius $F^{*}r_B$ where r_B is the bellmouth radius and F is an empirical factor in the model. F is given by:

$$F = 1 - 0.1(\xi_D - 1), \quad for \ 1 \le \xi_D \le 2.5 \tag{52}$$

$$F = 0.85, \quad for \ \xi_D > 2.5 \tag{53}$$

Thus the factor F varies between 0.85 and 1 and is certainly a candidate for refinement since it is an empirical factor based upon limited data.

The calculation outlined above is performed in a subroutine by a one-pass incremental march from the inlet duct out through the bellmouth or inlet lip region. The calculation proceeds as follows. A convenient bellmouth or inlet lip shape is chosen so that the local radius and wall

slope can be easily defined at each length along the inlet. An ellipse is convenient and often used for actual hardware. The mode Eigenvalue (or mode cut-off ratio), sound frequency, duct diameter and Mach number define the initial conditions for the calculation. At each increment in length in the bellmouth a larger radius, smaller Mach number, larger mode cut-off ratio and thus smaller group velocity vector angle (measured from the inlet axis) are obtained. At each of these length increments the wall slope angle is increasing from the initial angle of zero. Since the bellmouth or inlet lip slope goes from zero to ninety degrees, somewhere in the bellmouth the wall slope is equal to the group velocity vector angle as modified by the center of pressure consideration discussed above. When this match occurs the mode is considered released from the inlet to radiate to the far-field as governed by the local conditions at the release point. For a single mode, equations 6, 7 or 10 can be used as modified by equations 11 to 16. For the multimodal radiation inlet code as delivered under this program, equation 22 is used for each cut-off ratio partition or bin and the results are summed as shown by equation 29.

Inlet Radiation Model Results Compared to Engine Inlet Static Tests

An experiment was performed, as reported by Heidmann[25] et al., at NASA Lewis in the late 70's to help define engine far-field radiation . An inlet configuration was used providing a sound radiation experiment involving the simplest possible case of a single duct mode of sound produced by placing 41 rods in front of the 28 rotor blades which produces a spinning mode pattern with 13 lobes. The first radial of this 13 lobed pattern is the only propagating mode at sufficiently low rotor speeds. The inlet radiation model is compared to this JT15D single mode radiation data from Heidmann[25] et al. in Figure 11 for five engine speeds. The agreement is seen to be excellent over the entire speed and thus mode cut off ratio range. For the higher speeds, the mode cut-off ratio is sufficiently high and the propagation angle sufficiently small that the bellmouth does not have much influence on the radiation. The large bellmouth influence comes at the lower speeds where the cut-off ratio is nearer unity and the bellmouth has a large effect on the radiation pattern. The inputs for the radiation model were the same as the experimental conditions of reference 25 and include the inlet flow Mach number and bellmouth shape.

Inlet Radiation Model Results Compared to Numerical Calculations

Nallasamy[8] has provided some useful far-field radiation calculations using the finite element code of Eversman and Danda Roy[26]. The calculations were made for the geometry and conditions of the NASA ANC Fan Facility. This 4 foot diameter fan stage has 16 blades, 14 vanes, a design speed of 1886 rpm with 0.35 tip Mach number and an inlet mach number of M_D = 0.08. The bellmouth ellipse has an axial length of 10.8 inches and a radial dimension of 3.6 inches. At blade passage frequency (BPF) only the m,n (circumferential, radial mode order) mode 2,0 of rotor stator interaction is expected to propagate. At 2BPF the m,n = 4,0 and 4,1 interaction modes propagate. At 3BPF the m,n = 6,0, 6,1 and 6,2 interaction modes propagate. In Figures 12 to 17 the Nallasamy[8] radiation calculations for all of these modes are compared to the inlet model developed in this program. Specifically, equation 6 as modified by equations 11 to 16 and the bellmouth modification procedure were used. The agreement between the more exact finite element calculations and the approximate calculations is quite remarkable. The

location of the peak and the principal lobe breadth are faithfully reproduced by the approximate inlet radiation approach. The actual level match was not attempted since the acoustic power levels in the duct were not used. The mode cut-off ratios and the estimated principal lobe peak angle are shown on the Figures. The peak angle was estimated from $\sin\psi_P = 1/\xi_D$ since the flow Mach number effect is very small. None of examples have a sufficiently low cut-off ratio to provide near sideline radiation and thus large bellmouth effect. The largest bellmouth effect occurs for the 6,2 mode shown if Figure 17. The peak appears to be at around 55^o with the expected radiation peak without the bellmouth to be at about 64^o. The finite element calculations of Figure 17 show some interesting additional results. These numerical results show side lobe peaks almost exactly at the angles where the 6,2 mode calculation shows zeros. This is exactly what would be expected if the lower order radial modes 6,0 and 6,1 were also present. Apparently the finite element calculation for a higher order radial mode contains termination scattering into the lower order radials as might be expected.

Inlet Far-field Radiation for the Plane Wave Mode

Before the multimodal radiation from the inlet is discussed, the plane wave radiation is introduced because of its unique radiation properties. The plane wave radiation peaks on the inlet axis as can be seen from equation 10 which peaks at $\psi_O = 0$ where the equation is indeterminate (0/0) but has a limit $\pi^2\eta^2/4$. Figure 18 shows the far-field radiation for a sharp edged inlet for several values of frequency parameter from $\eta = 20$ to 0.45. For high frequency, the very narrow principal lobe of radiation is seen to have a very high value of sound pressure level (SPL). This high SPL is due to the very small area covered by the principal lobe. Since all the radiation directivities shown have 100 Watts of acoustic power, the SPL must be high to account for this small area. As seen in Figure 18, as the frequency is reduced and the principal lobe of radiation spreads out, the peak SPL is greatly reduced. Also as the frequency is reduced, the termination loss increases as shown on the legend and the SPL is further reduced.

Inlet Multimodal Far-field Radiation

The far-field for all of the modes together will now be considered. The sample problems shown here will be a simulation of equal acoustic power per mode. As discussed earlier, the cut-off ratio bins or partitions that were set up had equal numbers of modes in them as determined by the integration of the modal density function. If the modes have equal acoustic power per mode, there is also equal acoustic power per bin. Typically 100 or 200 bins are used with the highest cut-off ratio bin being reserved for the plane wave energy. If 100 Watts total are used, the plane wave has 1 or 1/2 Watt assigned to it. This is of course an artifice of the sample problem. The ultimate user will assign whatever value the noise source generation model predicts for the particular modes or cut-off ratio bin. With this artifice in mind, the multimodal far-field radiation directivity for a sharp edged inlet is shown in Figure 19. 200 cut-off ratio bins are used so the least acoustic power in the plane wave mode is 0.5 Watt. Several other power levels for the plane wave are also shown, up to 5 Watts, to illustrate the extreme sensitivity of the radiation directivity to the plane wave acoustic power at this high frequency. Even though the plane wave has only 0.5 to 5 Watts out of the 100 Watts it stands far above the other mode radiation near the axis. The extra power for the plane wave was pulled from the adjacent cut-off ratio bins since

this was computationally convenient. The dip in the radiation directivity at around 10^{o} is caused by this power transfer but it has no physical relevance.

The multimodal equal acoustic power per mode far-field radiation directivity for a low frequency ($\eta = 0.5$) is shown in Figure 20 for a sharp edged inlet. The radiation directivity is much smoother and shows a dip at the inlet axis since the plane wave principal lobe of radiation has broadened out at this low frequency. Two radiation directivities are shown. The upper curve shows the results if the assumed power distribution in the inlet duct is radiated to the far-field through the sharp edged inlet lip without any termination loss. The lower curve presents the radiation directivity if the duct termination loss model (described earlier in this report) was applied at the sharp edged inlet lip. Particularly large far-field losses occur near the sideline where near cut-off modes tend to dominate. The overall sound power loss of the termination for this sample problem was -8.85 decibels.

The influence of inlet bellmouth size on the multimodal far-field radiation is shown in Figure 21. Again an equal acoustic power per mode simulation is used. Several bellmouth sizes are shown from none (sharp edge) to a radial dimension equal to the radius of the duct. The dimension b is the radial distance from the duct radius out to the bellmouth highlight. This is the minor chord of the 2:1 ellipse assumed for each of these calculations. The lower curve shown in Figure 21 is for the sharp edged inlet lip which suffers the largest termination loss. The upper curve is the result for no termination loss. It is seen that as the bellmouth is enlarged, the termination loss is greatly reduced. A large bellmouth is good if the goal is to determine the inlet generated power by measurement of the far-field acoustic power. However, flight hardware may be better simulated by the case of $b/D = 0.083$ which has a 6 inch bellmouth or inlet lip.

The multimodal samples shown here are for illustrative purposes only. Equal acoustic power per mode may or may not simulate the broadband noise of the fan inlet but this assumption is irrelevant to the purposes of this report. The important thing here is that a preliminary tool has been developed that will aid in describing the transfer of the inlet duct multimodal acoustic power out to the far-field where measurements can more easily be made and where the effect of this noise is sensed by the observer. The internal acoustic power distribution among the modes or within the mode cut-off partitions must be defined by the user operating a noise source generation model.

AFT DUCT NOISE FAR-FIELD RADIATION

For the engine inlet, the propagation of sound through the transition from the high velocity duct flow to the lower velocity ambient flow through the accelerating potential flow region presented a challenge which was solved satisfactorily using approximate solutions and reasonable assumptions. Fortunately for the inlet case sufficient experimental data was available to check the approximate solutions. The aft radiation problem differs in several respects. The dominant physical phenomenon, refraction through the shear layer, is amenable to solution by ray acoustics and by physical acoustics using the Wiener-Hopf method (reference 8). There are not many results available to check the radiation model output. Assumptions must be made regarding the propagation in the nozzle and the radiation normalization or acoustic power conservation.

Special consideration must be given to the plane wave radiation since the on-axis principal lobe of radiation is split and refracted toward the sideline. In this section each element will be treated serially in the propagation path.

Acoustic Power in the Aft Duct

As in the inlet case, it is expected that the user will load the acoustic power into the cut-off ratio partitioned bins as defined by equations 26 or 27. The model is structured to start at the nozzle entrance with modes at a cut-off ratio of unity or larger. As will be seen in the next section, it appears that for the high flow velocities encountered in aircraft engines the nozzle could enhance the propagation of modes that are decaying along the straight section of the aft duct. These slightly cut-off modes will not be considered here and the error in this neglect is probably insignificant. These evanescent modes would probably be well attenuated by the duct acoustic liner, but it is also possible that they are produced at the end of or after the liner. These modes may suffer internal reflection within the jet and if they do escape the jet they would propagate forward into the inlet quadrant and would be reduced due to the large sideline distance.

Acoustic Propagation Assumptions in the Nozzle

The actual analysis of the sound propagation within the nozzle is beyond the scope of study of this program but this propagation must be accommodated using some reasonable assumptions. The steady flow within the nozzle is assumed to be a one-dimensional flow of an ideal gas. With the proper initial conditions and nozzle geometry an iterative solution is performed to obtain the flow conditions at the nozzle exit. As in the inlet bellmouth, the results of Cho and Ingard[23,24] are used to assume that each mode stays intact without scattering within the reasonably gentle contraction of the nozzle. The cut-off ratio of each mode is altered as it passes through the nozzle as can be seen from equation 3. If there were no flow, the cut-off ratio would be decreased since usually the diameter is reduced at the nozzle exit and thus the frequency parameter is reduced. Without flow the nozzle could cut-off modes that are just above cut-off. However, the Mach number term in the denominator of equation 3 is dominant for the usual high flow velocities in an aircraft engine. For example, by accelerating from a Mach number of 0.6 in the aft duct to a nozzle exit Mach number of 0.9, the cut-off ratio is increased by a factor of 1.84 by the Mach number term in equation 3. This phenomenon thus has a tendency to increase propagation within the nozzle and reduce the termination reflection at the nozzle exit. This would also favor a radiation shift toward the axis, but the refraction shift will overpower this as will be seen in the next section.

When the nozzle exit conditions are determined, the modified frequency parameter and mode cut-off ratio for each cut-off ratio bin are determined. Using the nozzle exit conditions, the termination transmission coefficient for each bin is determined from equations 38 or 41. If the nozzle flow has not been properly expanded, the jet conditions (velocity, sonic speed, diameter) are calculated for the ambient pressure.

Sound Refraction Through the Jet Slip Layer

If the conditions within the jet as it emerges from the nozzle were existent everywhere, the sound would radiate according to equation 22 for non-plane wave modes or for plane waves according to equation 10 as modified by equations 11 to 16. However, as shown in Figure 22 the sound waves are refracted at the jet slip layer. The relations between the wave vectors on the two sides of the slip layer are shown in Morse and Ingard[27] to be:

$$\frac{c_1}{\cos\varphi_1} + V_1 = \frac{c_2}{\cos\varphi_2} + V_2 \tag{54}$$

or,

$$\cos\varphi_2 = \frac{\cos\varphi_1}{\frac{c_1}{c_2} + \left(\frac{c_1}{c_2} M_1 - M_2\right)\cos\varphi_1} \tag{55}$$

where c, V, M and ϕ are the speed of sound, flow velocity, Mach number, and sound phase velocity vector angle. The subscripts 1 and 2 represent conditions on the jet side and the surroundings side of the jet slip layer. Some special cases are of interest. When $\phi_1 = 0$, the shadow region boundary in the surrounding region is defined by:

$$\cos\varphi_{2S} = \frac{1}{\frac{c_1}{c_2}(1 + M_1) - M_2} \tag{56}$$

As an example, let $M_1 = 0.9$, $M_2 = 0$ and $c_1 = c_2$, then $\phi_{2S} = 58.2^{\circ}$ from the jet axis or 121.8° from the inlet axis. Sound will get into this shadow zone by diffraction which will be greater at the lower frequencies. This diffraction into the shadow zone will be accommodated in this model by the principal lobe width effect especially due to the plane wave radiation. Complete internal reflection occurs when $\phi_2 = 180^{\circ}$, or back on the jet side of the slip stream:

$$\cos\varphi_{1R} = \frac{-\frac{c_1}{c_2}}{1 - M_2 + \frac{c_1}{c_2} M_1} \tag{57}$$

Again using the above example, $\phi_{1R} = 121.8^{\circ}$ and any wave propagating in the jet flow environment with a phase velocity vector angle relative to the jet axis greater than this value will experience complete internal reflection and not propagate to its place in the far-field. Note that the angles describing the refraction of sound through the jet slip layer are all phase velocity

vector angles while the acoustic power propagation is determined by the group velocity vector. The use of these vectors and their interrelationships to develop the far-field radiation will now be presented.

Aft Duct Radiation Procedure Summary

After the flow and propagation conditions are established for the jet the radiation procedure can be carried out. Although there is no longer a duct present to strictly define a frequency parameter and mode cut-off ratio, it is useful to maintain these concepts to define the radiation angles as the wave enters the jet region. The Mach number M_1 and entering cut-off ratio ξ_1 define the group velocity vector angle ψ_1 using equation 1 and the phase velocity vector angle ϕ_1 using equation 2. Note that the x and D subscripts have been dropped in favor of the region 1 subscript as shown in Figure 22. The phase velocity vector angle ϕ_2 in the surrounding region 2 can then be defined by equation 55. The group velocity vector angle ψ_2 in the surrounding region 2 can also then be defined using ϕ_2 and the surrounding Mach number M_2 in equation 4.

With the group velocity vector angles calculated, the refraction effect on the far-field radiation directivity can be readily estimated. The group velocity vector angles, which represent the location of the principal lobes of radiation for any mode or group of modes with similar effective cut-off ratio, have been rotated through the angle very simply expressed as:

$$\Delta\psi = \psi_2 - \psi_1 \qquad (58)$$

It is next assumed that the entire radiation directivity, for example as expressed by equation 22 for the non-plane wave modes, also is rotated by this same angle. This should provide fairly good results since for a multimodal radiation directivity, the principal radiation lobes will dominate the sound pressure level.

The calculation procedure can now be summarized. As described earlier, the acoustic power is sorted into the several cut-off ratio bins back in the exhaust duct. Again the bin boundaries and average cut-off ratio for each bin are defined by equations 26 and 27. A loop is performed on these cut-off ratios. For each cut-off ratio the previously described modifications in the nozzle into the jet are performed, the rotation of the directivity pattern is determined, and the pressure-squared at each far-field angle is calculated and then summed (at each angle) as the cut-off ratio loop progresses. This procedure is expressed symbolically by equation 29. The far-field pressure-squared are calculated both with and without the nozzle exit termination loss. The values without the termination loss are area weighted and integrated over all angles to calculate the total power. This is then checked against the total modal input power back in the duct to determine any small error. Any error is then used to correct the pressure-squared with the transmission loss which is of course the value of interest. Equation 30 is then used to calculate the far-field sound pressure level at each angle. This procedure assumes the use of a properly normalized modal radiation directivity which will be covered next.

Aft Duct Radiation Normalization for Non-plane Wave Modes

The normalization (unity power integral over far-field) developed earlier for uniform flow everywhere will no longer hold for aft radiation since the principal lobe of radiation has been moved to a new angle and thus different far-field area. Equation 20 still holds, but since the principal lobe of radiation has been rotated without a lobe width change, the differential area terms in equation 20 can be dropped. The multiplier used to insure proper normalization is:

$$P_2^2 = \frac{\sin\psi_1}{\sin\psi_2} P_1^2 \qquad (59)$$

Equation 59 is valid only for non-plane waves which always have the principle lobe located off-axis. For the special case of the plane wave that radiates on the axis for uniform flow (region 1) special consideration must be given to the normalization which will be treated later.

With the normalization factor of equation 59 applied to the rotated radiation directivity, the far-field power is integrated from the aft axis to the angle where the rotated flange would be located. As discussed in a previous section, the approximate directivity equation is valid only to the flange and the exponential fall-off beyond the flange had not been applied at the time of this normalization determination. The results of this integration of far-field acoustic power are shown in Figure 23. Three jet Mach numbers (M_1 = 0.9, 0.6 and 0.3) with four frequency parameters (η = 5, 10, 15, and 20) at each Mach number providing a wide range of directivity rotation due to refraction and several radiation principal lobe widths. The deviations of results for most of these calculations are seen to be quite small, about 0.5 dB. The larger deviations near mode cut-off are probably due to the principal radiation lobe peaking near the flange, and the integration of power only to the flange misses about half the power.

Aft Radiation of the Plane Wave Duct Mode

The plane wave duct mode radiating out through the jet slip layer presents a very difficult radiation normalization problem in comparison to the non-plane waves. For the latter, P^2 is always zero on the axis and a complete lobe can be identified centered at the principal lobe peak and the entire lobe can be rotated using equation 55 and 59 to describe the refraction effect. The first inclination is to rotate the axially located principal lobe off the axis as determined by equation 56 (same as equation 55 with $\phi_1 = 0$) and then account for the area difference by some other method than equation 59. Observation of experimental plane wave radiation out through a fairly low speed jet reported by Plumblee and Dean[28] and Plumblee[29] et al is convincing that the above approach would provide a lobe with about twice the proper principal lobe width. The approach used, as inferred from the reference 28 and 29 results, to model the aft plane wave radiation is shown schematically in Figure 24. The radiation is seen to peak on the jet axis for no-flow. As the jet velocity is increased to 50, 100, and 200 ft/sec, the principal lobe peak moves to higher angles as defined by equation 56 and labeled as ψ_2 on Figure 24. Notice that the lobe is being split in two as the peak moves to higher angle but the first zero of the principal lobe, $\psi_{1,0}$ remains constant for the lower jet velocities. Finally at a jet velocity such that $\psi_2 = \psi_{1,0}/2$, the

lobe is frozen and further increases in jet velocity move the entire principal lobe to higher angles according to equation 56. The above can be expressed mathematically as follows. Set the argument of the sine function in equation 10 (augmented by equation 11 for flow) equal to π which will yield the lobe zero in medium 1 to be:

$$\sin\psi_{1,0} = \frac{1}{\sqrt{\eta^2 + M_1^2}} \tag{60}$$

To keep the lobe zero constant after an angle shift, an effective frequency parameter (η_{EF}) can be defined which will reduce the lobe width just enough so that with the angle rotation ($\Delta\psi = \psi_2$) the lobe zero will not change. This effective frequency parameter can be expressed by:

$$\sin(\psi_{1,0} - \psi_2) = \frac{1}{\sqrt{\eta_{EF}^2 + M_1^2}} \tag{61}$$

Which can be solved for the effective frequency parameter. This radiation lobe reduction continues until $\psi_2 = \psi_{1,0}/2$ where the limiting frequency parameter is reached expressed by:

$$\eta_{EF,LIM} = \sqrt{\sin^{-2}(\frac{\psi_{1,0}}{2}) - M_1^2} \tag{62}$$

The results of the above model are expressed in Figure 25. The three lower velocity curves (up to 200 ft/sec) simulate the conditions of some plane wave data in references 28 and 29 and match these results fairly well. The calculations were extended to 1000 ft/sec to illustrate the progressive refraction of the plane wave radiation due to the jet slip layer.

The above model works well at sufficiently high frequencies such that $\psi_{1,0} \leq 90^o$. Below this frequency the principal lobe broadens and must be extended into the next quadrant using the exponential fall-off described for the inlet radiation. A transition must be made back from η_{EF} to η. This fairly rapid transition is made by using:

$$\eta_{USE} = \eta_{EF} - (\eta_{EF} - \eta)e^{-(\frac{\eta}{\eta_{90}})^2}, \quad \eta_{90} = \beta_1 = \sqrt{1 - M_1^2} \tag{63}$$

where η_{USE} is the value of the frequency parameter used to define the lobe width.

Normalization of the Plane Wave Radiation Directivity with Jet Refraction

The normalization of the refracted plane wave radiation lobe is accomplished by using area ratios which are subtended by the principal lobe with and without refraction. Refer to Figure 24 to visualize these subtended areas. If the media 1 extended everywhere, the far-field area subtended by the principal lobe would be:

$$A_1 = 2\pi r^2(1 - \cos\psi_{1,0}) \tag{64}$$

where the zero of the plane wave radiation principal lobe ($\psi_{1,0}$) was given by equation 60. In the surrounding media, the far-field area subtended by the refracted principal lobe would be:

$$A_2 = 2\pi r^2[1 - \cos(\psi_2 + \psi_{1,0})] , \quad if \quad \psi_2 \le \psi_{1,0} \tag{65}$$

or,

$$A_2 = 2\pi r^2[\cos(\psi_2 - \psi_{1,0}) - \cos(\psi_2 + \psi_{1,0})] , \quad if \quad \psi_2 \ge \psi_{1,0} \tag{66}$$

The normalization multiplying factors for the refracted plane wave radiation are:

$$\frac{P_2^2}{P_1^2} = \frac{A_1}{A_2} = \frac{1 - \cos\psi_{1,0}}{1 + \sin\psi_2 \sin\psi_{1,0} - \cos\psi_2 \cos\psi_{1,0}} , \quad if \quad \psi_2 \le \psi_{1,0} \tag{67}$$

or,

$$\frac{P_2^2}{P_1^2} = \frac{1 - \cos\psi_{1,0}}{2 \sin\psi_2 \sin\psi_{1,0}} , \quad if \quad \psi_2 \ge \psi_{1,0} \tag{68}$$

The above plane wave radiation directivity normalization was tested over a wide range of frequency parameter (η) and jet Mach number (M_1). Since a transition was used at $\eta = \eta_{90}$, (see equation 63) it is not surprising that an amplitude adjustment was required across this transition. An empirical relationship was determined to obtain reasonable normalization and this is:

$$C_{PW} = \frac{1}{3}[1 + \frac{5X_3}{4 + X_3}] , \quad X_3 = (\frac{\eta}{\eta_{90}})^3 \tag{69}$$

which is used as an additional multiplier along with equations 67 or 68. This is a substantial adjustment ranging from 1/3 at very low frequencies to 2 at very high frequencies. Recall that equations 67 or 68 hit a limit at $\psi_{1,0} = 90^o$ and equation 69 attempts to extend the normalization below $\eta = \eta_{90}$.

A test of the above plane wave far-field radiation normalization with jet slip layer refraction was conducted over a wide range of jet Mach number and frequency parameter. The results are shown in Figure 26. The normalization error for the aft plane wave is seen to be the largest encountered so far in all of the normalization check-outs. Up to 3 dB error is seen at the

transition frequency for the lower Mach numbers. For jet Mach numbers between 0.5 and 0.9, which is probably in the more interesting range, the error is seen to be less than 1.5 dB. These low frequencies will probably not be of much interest except for the very low frequency core radiation, perhaps combustor noise, which will probably propagate as a plane wave. This normalization could probably be improved but additional effort could not be devoted to this subject in this program. It should also be recognized that there are probably other weaknesses in the noise source model and propagation path description that are at least as large as this possible normalization error.

Aft Duct Geometry Used for Sample Problems

The geometry for the aft ducts used for the sample sound radiation that will follow is shown in Figure 27. A consideration of this geometry is must be made to set the final dimensionless variables that are essential to the radiation calculations. It is assumed that the user will (as in the sample problems) define the acoustic power in the aft duct of interest as a function of mode cut-off ratio and frequency parameter. This acoustic power distribution is then translated to the radiation region which is assumed to be the fully expanded jet. The mode cut-off ratio and frequency parameter are altered as the sound passes through the nozzle due to change in dimensions, Mach number and sonic speed (temperature). The computer codes contain subroutines that solve for the nozzle exit and jet conditions given the duct conditions and geometry. To fix the geometry variation with length the Figure 27 geometry is assumed. The core duct is assumed to be an annular duct and the nozzle exit a circle. The fan duct is assumed to be an annular duct and the nozzle exit an annulus with the contraction occurring on the outer wall only. In contrast, the NASA Lewis ANC Fan Facility uses an annular fan nozzle exit , but the area contraction occurs due to the increase of the inner diameter rather than a decrease of the outer diameter. The nozzle subroutine would have to be altered to use the current code to properly calculate the fan exhaust far-field radiation for this facility.

The duct-nozzle geometry is defined by specifying the duct outer diameter, hub-tip ratio, and the nozzle to duct area ratio.

Aft Fan and Core Far-field Radiation Model Comparison

The aft fan and core far-field radiation models are essentially the same except for those differences occurring due to the geometry differences outlined in the previous section. The core duct radiation does pass through two jet slip layers which causes two refraction processes while the fan duct radiation is refracted by only the one jet slip layer. However, when the refraction equation 54 is applied for the two slip layers of the core radiation, the intermediate fan jet conditions cancel out. Only the core jet conditions and the conditions in the surrounding medium influence the core radiation at least for the methods used in the present model. As mentioned in the previous section, the duct and nozzle geometry difference do influence the radiation so the codes are kept separate with separate nozzle calculation subroutines. The input and output variables are given slightly different terminology since it is assumed that some day the codes will be used together as subroutines in some larger code.

Aft Fan Radiation Sample Calculations

Two types of sample calculations will be shown. Single mode plane wave and multimodal equal acoustic power per mode calculations will be shown. The anticipated importance of the plane wave as possibly dominating the aft annoyance and its unique signature in the broadband directivity at least at high frequency are reasons for highlighting the plane wave radiation. Of course the purpose of these radiation models is to calculate the multimodal far-field radiation to allow extrapolation of the duct acoustic power into the far-field to estimate the annoyance. The sample multimodal calculations use equal acoustic power per mode simulation for all modes except the plane wave which has 10 Watts out of the total 100 Watts. This distribution is rather arbitrary for these sample calculations. The ultimate user can set up any power distribution desired. The current subroutines put the power into the plane wave for any cut-off ratio bin with the mode cut-off ratio greater than 3.16. Equation 27 shows that this cut-off ratio limit appears to use 10 bins, thus 1/10 of the acoustic power goes to this last mode, the plane wave.

The sample calculations of the far-field radiation for a plane wave emerging from the aft fan duct with a jet Mach number of 0.9 is shown in Figure 28. The conditions for the calculation are shown on the Figure. Several frequency parameters are used to show the influence of sound frequency on the radiation directivity. All of the directivities peak at about 120^{o} which represents the shadow zone boundary for these conditions. The high frequency sound is seen to have a very narrow lobe concentrated at the shadow zone boundary. The lower frequencies are seen to penetrate into the shadow zone simulating the low frequency diffraction effect expected for the low frequencies.

The aft fan duct multimodal simulated broadband far-field radiation directivity is shown in Figure 29. At high frequency the plane wave radiation is seen to stand out much like in the previous single mode case. As frequency is reduced the radiation directivity broadens and becomes more continuous. Note that considerable radiation radiates into the inlet quadrant. Beyond about 70^{o} the radiation is due to refracted principle lobe peaks which can be seen from the abrupt slope change for the highest frequency. Forward of 70^{o} the radiation becomes increasingly composed of the exponential extrapolation from the principle lobes and becomes increasingly in possible error.

The general shape of the multimodal radiation seen in Figure 29 shows a broad peak almost at the direct sideline at 90^{o}. This broad sideline peak is nearly independent of frequency.

Aft Core Radiation Sample Calculations

The plane wave and multimodal far-field radiation directivities for the core duct are shown in Figures 30 and 31. The high frequency plane wave radiation has a narrow peak at about 108^{o} which is the shadow zone boundary for the core radiation (compared to 120^{o} for the fan duct). Although the Mach numbers for the aft fan and core radiation problems are the same, the core jet is much hotter, the speed of sound is higher, and thus the velocity is higher and the refraction effects will be greater. Similar to the aft fan radiation, the multimodal core radiation shows a very broad peak to the near sideline which is essentially independent of frequency. The core

radiation appears to be somewhat broader and definitely shifted toward the inlet quadrant.

Again it is emphasized, that the calculations shown here are only sample calculations which are dependent upon the input assumptions. Although the equal acoustic power per mode assumption may provide results that might simulate the gross behavior of broadband noise, these are not real broadband noise calculations. The codes are developed to be used with noise source models that might adequately predict the acoustic power distribution such that the far-field radiation directivity may more adequately represent that of broadband noise.

Empirical Factors

The computer codes were written to include all of the preceding theory for the far-field radiation with the quantitative information regarding the principal lobe peak's direction, amplitude, and widths as they were altered by a bellmouth or jet slip layer refraction. This effort allowed the far-field acoustic power to come close to the duct power and hopefully provided the right relationships to describe the effect of the changes in the parameters. However, at the end the development the far-field acoustic power was integrated over the entire sphere and compared to the known input duct acoustic power. In all cases some difference was observed. Some of this error was due to the earlier power normalizations being performed only over the hemisphere where the radiation theory is technically valid. However, the final codes had to be used over the entire spherical far-field and the principal lobes of radiation were approximately extended into the back quadrant. The multiplying factors that were found to be needed for power equality will now be presented. The same names that were used in the radiation code subroutines will be used here so that they can be easily identified and altered if desired.

The inlet code has the following P^2 multiplier for the plane wave mode:

$$ACOEFPW = 0.741697 + 3.190822\,\eta^{2.650078}, \quad if \quad \eta \le 1 \tag{70}$$

and,

$$ACOEFPW = 3.932518\,\eta^{1.96285}, \quad if \quad \eta \ge 1 \tag{71}$$

The value of $\eta = fD/c$ used in equations 70 or 71 is the value at the exit of the bellmouth or inlet lip. For the inlet non-plane modes use the multiplier:

$$WATINFIX = \frac{1 + 1.9036\,X}{2.2426\,X}, \quad X = \eta^{1.08156} \tag{72}$$

where here the frequency parameter in the duct was used.

For the aft ducts, either fan or core, for the plane wave mode:

$$ACOEFPW = 1.7333 + 5.3026\,\eta^{2.2894}, \quad if \quad \eta \le 1 \tag{73}$$

and,

$$ACOEFPW = 7.0359\,\eta^{1.7737}, \quad if \quad \eta \geq 1 \tag{74}$$

For the non-plane waves the multiplier is:

$$AFPOWFAC = \frac{0.5542\,(X + 1.2750\,\eta^2)}{\eta\,X} \tag{75}$$

where,

$$X = 1 + 0.32877\,\eta^{1.7029} \tag{76}$$

The value of frequency parameter (η) evaluated for the jet condition is used in equations 73 to 76.

COMPUTER CODES - SOME INFORMATION ABOUT INPUTS AND OUTPUTS

The computer codes will not be reproduced in this final report. The recipients of the codes are mentioned in the concluding remarks and should be contacted regarding the code availability. The theory behind the contents of these codes have been thoroughly documented throughout this report. Some comments about the inputs and outputs will be made here.

Fan Inlet Code

The sample problem main program for the inlet noise calculation is named "GEINLFIN.FOR" representing that it was developed for General Electric (GE), for the fan inlet (INL) radiation, and this is the final (FIN) version (of 10). This main program is just to control the inputs and outputs for the sample problem. It inputs the required variables and calculates the acoustic power for each cut-off ratio bin for input into the main subroutine. The main program is not intended to be used except to check out the code. The user will integrate the main subroutine and the other required subroutines into their noise source generation system. For the sample problem, the main program gets the input using a namelist input from the file "AINLTDAT.INP" using the statement:

```
NAMELIST/INPUT/TTOT,PTOT,DISTANCE,DIAM,ALIP,BLIP,FMACH,FMACHS
1,WATTS,NCOF,DELANG,ETA,ISIDELN
```

The main program output is transferred to file "BBRDINLT.OUT". Among the input variables, TTOT and PTOT are the inlet flow total temperature and pressure and DISTANCE is the sideline or radial distance where the sound pressure level is to be calculated. DIAM, ALIP, and BLIP are the inlet diameter and the inlet bellmouth or lip ellipse major (axial) and minor (transverse) dimensions in inches. FMACH and FMACHS are the Mach numbers of the inlet duct flow and the flow in the surroundings (or tunnel) . WATTS is the total acoustic power (Watts) to be

divided up into the NCOF cut-off ratio bins. DELANG is the angle increment used in the far-field, often two degrees in the samples used here. One degree is the smallest angle increment to use without increasing dimensions in the codes. ETA is the frequency parameter based on duct diameter, η = fD/c. Finally, ISIDELN is a code to determine if constant sideline or radius is to be used. ISIDELN = 1 for sideline and 0 for radius. The main subroutine statement for the inlet radiation calculation is "BBRDCFIN" shown below.

```
 SUBROUTINE BBRDCFIN(TTOT,PTOT,DISTANCE,ISIDELN,DIAM,ALIP,BLIP
1,FMACHI,FMACHS,NCOF,WATTSCOF,ETAI,DELANG,NANGLE,ANGLE,SPL,SPLTL
2,WATTS,WATTRAN)
```

Only the new items are discussed here. WATTSCOF is a dimensioned variable representing the acoustic power in the many cut-off ratio bins as defined by equations 26 and 27. When using individual modes, equation 28 determines which bin receives the acoustic power of the mode. For the sample problem, the total power is equally distributed among the NCOF bins. The remaining variables are outputs. NANGLE and ANGLE are the number of angles and the angle values calculated using DELANG over 0 to 178°. SPL and SPLTL are the sound pressure levels at each angle without and with the termination transmission loss considered. These allow the evaluation of the effect of the transmission loss at each angle. WATTS and WATTRAN are the summations of the acoustics powers over all of the cut-off ratio bins both without and with the termination transmission loss being used. These allow the evaluation of the effect of the tranmission loss on total acoustic power.

The additional subroutines required for the inlet code are "LIPEF3" and "PSQGCOF". The first calculates the effect of the inlet lip or bellmouth as previously described. The second calculates the pressure-squared for non-plane modes using the cut-off ratio dependent equations.

Fan Aft Code

The sample problem main program for the aft fan noise calculation is named "GEAFTFIN.FOR". As with the inlet, this main program is just to control the inputs and outputs for the sample problem. It inputs the required variables and calculates the acoustic power for each cut-off ratio bin for input into the main subroutine. For the sample problem, the main program gets the input using a namelist input from the file "AFTDATA.INP" using the statement:

```
 NAMELIST/INPUT/TTOT,PTOT,TSUR,PSUR,DISTANCE,DDUCT,HTRAT,ANOZRAT
1,WATTS,NCOF,DELANG,FMACHD,FMACH2,ETAD,ISIDELN
```

The main program output is transferred to file "BBRADAFT.OUT". The aft fan noise input statement is very similar to the statement for the inlet with a few exceptions. There are total temperature and pressure specifications for both the jet and the surroundings. For the aft fan duct and nozzle, the duct hub-tip ratio HTRAT and the nozzle area ratio ANOZRAT are needed. The flow Mach number in the aft fan duct is specified as FMACHD and the surrounding media Mach number is FMACH2. The jet Mach number is calculated in the additional subroutine "CONOZ" which is required for subroutine operation. The main subroutine statement for the aft

fan noise radiation calculation is "BBRDCFEX" shown below.

```
 SUBROUTINE BBRDCFEX(TTOT,PTOT,TSUR,PSUR,HTRAT,ANOZRAT,DISTANCE
1,ISIDELN,DDUCT,DJET,FMACHD,FMACH1,FMACH2,NCOF,WATTSCOF,DELANG
2, ETAD,NANGLE,ANGLE,SPL,SPLTL,WATTS,WATTRAN,FMACHN,COFMIN)
```

The additional variables are the outputs jet diameter DJET, Jet Mach number FMACH1, nozzle exit Mach number, and the limiting cut-off ratio for internal reflection, COFMIN.

Core Aft Code

The sample problem main program for the core noise calculation is named "GECORFIN.FOR". As with the fan inlet and aft duct, this main program is just to control the inputs and outputs for the sample problem. It inputs the required variables and calculates the acoustic power for each cut-off ratio bin for input into the main subroutine. For the sample problem, the main program gets the input using a namelist input from the file "AFCORDAT.INP" using the statement:

```
 NAMELIST/INPUT/TTCOR,PTCOR,TSUR,PSUR,DISTANCE,DDUCTC,HTRATC
1,ANOZRATC,WATTS,NCOF,DELANG,FMACHC,FMACH2,ETAC,ISIDELN
```

The main program output is transferred to file "BBRADCOR.OUT". The input is so similar to the aft fan input that not much comment is required. Slight changes have been made to distinguish the core from the aft fan. The jet Mach number is calculated in the additional subroutine "CORNOZ" which is required for subroutine operation. CORNOZ for the core is different than CONOZ for the aft fan duct because of the different geometries which are discussed in another section. Otherwise they are the same in methodology. The main subroutine statement for the core noise radiation calculation is "BBRDCFCR" shown below.

```
 SUBROUTINE BBRDCFCR(TTCOR,PTCOR,TSUR,PSUR,HTRATC,ANOZRATC
1,DISTANCE,ISIDELN,DDUCTC,DJET,FMACHC,FMACH1,FMACH2,NCOF,WATTSCOF2
,DELANG,ETAC,NANGLE,ANGLE,SPL,SPLTL,WATTS,WATTRAN,FMACHN,COFMIN
3,CRAT)
```

Again, only minor terminology differences from the aft fan code have been made to distinguish the aft fan and core inputs. There is one additional output. CRAT is the ratio of the hot jet sonic velocity to the surrounding medium sonic velocity. It is of interest for the core because of the great difference in temperature between the two media.

INFLUENCE OF WIND TUNNEL FLOW MACH NUMBER ON ACOUSTIC PRESSURE

For a static noise test the measurement of far-field acoustic pressure is useful to directly determine the acoustic power flux. However when the measurements are performed in a wind tunnel, there are terms in the acoustic power equation that alter the relationship between acoustic pressure and acoustic power flux. For all of the theory presented in this report it was assumed that the far-field measurement point was in a static medium and the acoustic power intensity was

proportional to pressure-squared. It is useful to determine what error might be encountered if the multimodal far-field radiation model developed in this program were used and compared to wind tunnel data rather than static far-field data.

A correction for fan inlet sound pressure level measured in the wind tunnel to make the SPL comparable to static noise data was developed in this program. Note that the wind tunnel measured SPL must be reduced for the forward radiated inlet noise. This reduction is necessary since convective acoustic power effects oppose the radiated power and the SPL must increase to maintain total acoustic power. For this model the following assumptions were made.

1. The acoustic power output of the fan does not depend upon the wind tunnel flow velocity.
2. The fan inlet acoustic power group velocity vector propagation angle is not altered by the wind tunnel flow.
3. The wind tunnel velocity vector is parallel to the fan axis and does not vary over the region where the acoustic data is measured.

The acoustic power intensity equation can be obtained from reference 19 as:

$$I = p\bar{u} + \frac{p^2}{\rho_0 c_0}\overline{U_0} + \rho_0 \bar{u}\cdot\overline{U_0}\,\bar{u} + \frac{p\,\bar{u}\cdot\overline{U_0}}{c_0^2}\overline{U_0} \tag{77}$$

where the zero subscript identifies the steady flow terms. The analysis will now be specialized to the two dimensional case of a plane wave traveling obliquely to a uniform flow in the x or axial direction. Measuring the propagation angle from the axial direction, equation 77 can be expressed as:

$$I = \frac{p^2}{\rho_0 c_0}\,\frac{(1 - M_x^2)\sqrt{1 - M_x^2 \sin^2\psi_x}}{[\sqrt{1 - M_x^2 \sin^2\psi_x} - M_x \cos\psi_x]^2} \tag{78}$$

Using assumptions 1 and 2, equating acoustic power intensities for flow and no-flow gives:

$$\frac{p_M^2}{p_0^2} = \frac{[\sqrt{1 - M_x^2 \sin^2\psi_x} - M_x \cos\psi_x]^2}{(1 - M_x^2)^2\sqrt{1 - M_x^2 \sin^2\psi_x}} \tag{79}$$

This result is plotted in Figure 32. For the typical Mach number used in wind tunnel tests to simulate aircraft take-off and approach, the deviation, which is maximum near the axis, is only about 1 or 2 dB. The pressure will read high for an inlet case for the same acoustic power intensity as a no-flow case.

CONCLUDING REMARKS

This final report has presented the theory that has been incorporated into three computer codes to calculate the far-field radiation directivity produced by a multimodal noise source. The three codes are specialized for noise propagation from the aircraft fan inlet, fan exhaust duct, and aft core duct. These codes are intended to be used with broadband noise source generation models which predict the acoustic power as a function of mode cut-off ratio and frequency. The radiation codes then take the acoustic power past the particular aperture and into the far-field. A new model has been developed to predict the termination transmission loss with flow at the bellmouth or nozzle termination.

The single mode radiation theory has been fairly well validated for the inlet noise radiation using both experimental data and numerical calculations. The multimodal radiation results should be a straight forward extension of this single mode theory. Thus the inlet multimodal radiation models should be quite adequate. The aft radiation is not so well validated. Experimental data for the radiation of internal noise through a jet shear layer are not so common. Some does exist for plane wave radiation through jets up to about 200 ft/sec velocity. The refraction model for the plane wave has been modeled to agree with this limited data. The methods used to model the aft radiation have had limited single mode validation by comparison to some analytical results using a Wiener-Hopf technique. Thus the aft radiation models are believed to be reasonably accurate for initial use and can easily be modified as necessary if shown to be needed.

The computer codes have not been published with this report. Copies of the final codes will be sent to Dr. Ramani Mani and Dr. Phil Gliebe of GEAE and Dennis Huff and Dr. Edmane Envia at the NASA Lewis Research Center.

REFERENCES

1. Saule, A.V., and Rice, E.J., "Far-Field Multimodal Acoustic Radiation Directivity," NASA TM 73839, December, 1977.

2. Rice, E.J., "Multimodal Far-Field Acoustic Radiation Pattern Using Mode Cut-off Ratio," AIAA Journal, Vol. 16, pp 906-911, 1978.

3. Rice, E.J., Heidmann, M.F., and Sofrin, T.V., "Modal Propagation Angles in a Cylindrical Duct with Flow and their Relation to Sound Radiation," AIAA Paper No. 79-0183, January 1979. Also NASA TM-79030, 1978.

4. Rice, E.J., and Sawdy, D.T., "A Theoretical Approach to Sound Propagation and Radiation for Ducts with Suppressors," NASA TM 82612, May, 1981.

5. Rice, E.J., "Aircraft Inlet Noise Radiation Model, Static, Flight and Bellmouth Effect," AIAA Paper No. 96-1774, May 1996.

Technique for Predicting Sound Radiation from Turbofan Inlets," AIAA Paper No. 82-0124, January, 1982.

7. Eversman, W., Parrett, A.V., Preisser, J.S., and Silcox, R.J., "Contributions to the Finite Element Solution of the Fan Noise Radiation Problem," Trans. ASME, J. Vib., Acoust., Stress & Reliab. Des., Vol. 107, No. 2, April, 1985, pp. 216-223.

8. Nallasamy, M., "Computation of Noise Radiation from Fan Inlet and Aft Ducts," Journal of Aircraft, Vol. 34, No. 3, pp. 387-393, June 1997.

9. Rice, E.J., and Saule, A.V., "Far-Field Radiation of Aft Turbofan Noise," NASA TM 81506, Ninety-ninth Meeting of the Acoustical Society of America, Atlanta, Georgia, April, 1980.

10. Savkar, S.D., "Radiation of Cylindrical Duct Acoustic Modes with Flow Mismatch," Journal of Sound and Vibration, Vol. 42, October, 1975.

11. Lansing, D.L., Drischler, J.A., and Pusey, C.G., "Radiation of Sound From an Unflanged Circular Duct with Flow," paper presented at the 79th Meeting of the Acoustical Society of America, Atlantic City, N. J., April 21-24, 1970.

12. Homicz, G.F., and Lordi, J.A., "A Note on the Radiative Directivity Patterns of Duct Acoustic Modes," Journal of Sound and Vibration, Vol. 41, August, 1975, pp. 283-290.

13. Cho, Y.C., and Rice, E.J., "High-Frequency Sound Propagation in a Spatially Varying Mean Flow," J. Acoustic. Soc. Am., Vol. 70, No. 3, pp 860-865, September, 1981.

14. Saule, A.V., "Modal Structure Inferred from Static Far-Field Noise Directivity," AIAA Paper No. 76-574, July 1976, also NASA TM X-71909, 1976.

15. Candel, S.M., "Acoustic Radiation from the End of a Two-Dimensional Duct; Effects of Uniform Flow and Duct Lining," J. Sound Vib., Vol. 28, 1973, pp. 1-13.

16. Sawdy, D.T., "Cutoff Ratio Analysis for Predicting Inlet Liner Suppression Performance," Boeing Document No. D3-11719-1, unpublished.

17. Ville, J.M., and Silcox, R.J., "Experimental Investigation of the Radiation of Sound from an Unflanged Duct and a Bellmouth, Including the Flow Effect," NASA TP 1697, July, 1980.

18. Rice, E.J., "Modal Density function and Number of Propagating Modes in Ducts," NASA TM X-73539, November, 1976.

19. Goldstein, Marvin E., *Aeroacoustics*, McGraw-Hill International Book Company, 1976.

20. Morse, Philip M., *Vibration and Sound*, McGraw-Hill Book Company, Inc., 1948.

21. Morfy, C.L., "A Note on the Radiation Efficiency of Acoustic Duct Modes," Journal of Sound and Vibration, Vol. 9, 1969, pp. 367-372.

22. Zorumski, W.E., "Generalized Radiation Impedances and Reflection Coefficients of Circular and Annular Ducts," Journal of the Acoustical Society of America, Vol. 54, December 1973, pp. 1667-1673.

23. Cho, Y.C., and Ingard, K.U., "Closed-Form Solution of Mode Propagation in a Nonuniform Circular Duct," AIAA Journal, Vol.20, No. 1, pp 39-44, January, 1982.

24. Cho, Y.C., and Ingard, K.U., "Mode Propagation in Nonuniform Circular ducts with Potential Flow," AIAA Journal, Vol. 21, No. 7, pp 970-977, July, 1983.

25. Heidmann, M.F., Saule, A.A., and McArdle, J.G., "Analysis of Radiation Patterns of Interaction Tones Generated by Inlet Rods in the JT15D Engine," AIAA Paper No. 79-0581, March, 1979.

26. Eversman, W., and Danda Roy, I., "Ducted Fan Acoustic Radiation Including the Effects of Non-Uniform Mean Flow and Acoustic Treatment," AIAA Paper 93-4424, October, 1993.

27. Morse, Philip M., and Ingard, Uno K., *Theoretical Acoustics*, McGraw-Hill Book Company, 1968.

28. Plumblee, H.E., and Dean, P.D., "Sound Measurements within and in the Radiated Field of an Annular Duct with Flow," Journal of Sound and Vibration, Vol. 28, No. 4, pp 715-735.

29. Plumblee, H.E., Dean, P.D., Wynne, G.A., and Burrin, R.H., "Sound Propagation in and Radiation from Acoustically Lined Flow Ducts," NASA CR-2306, October, 1973.

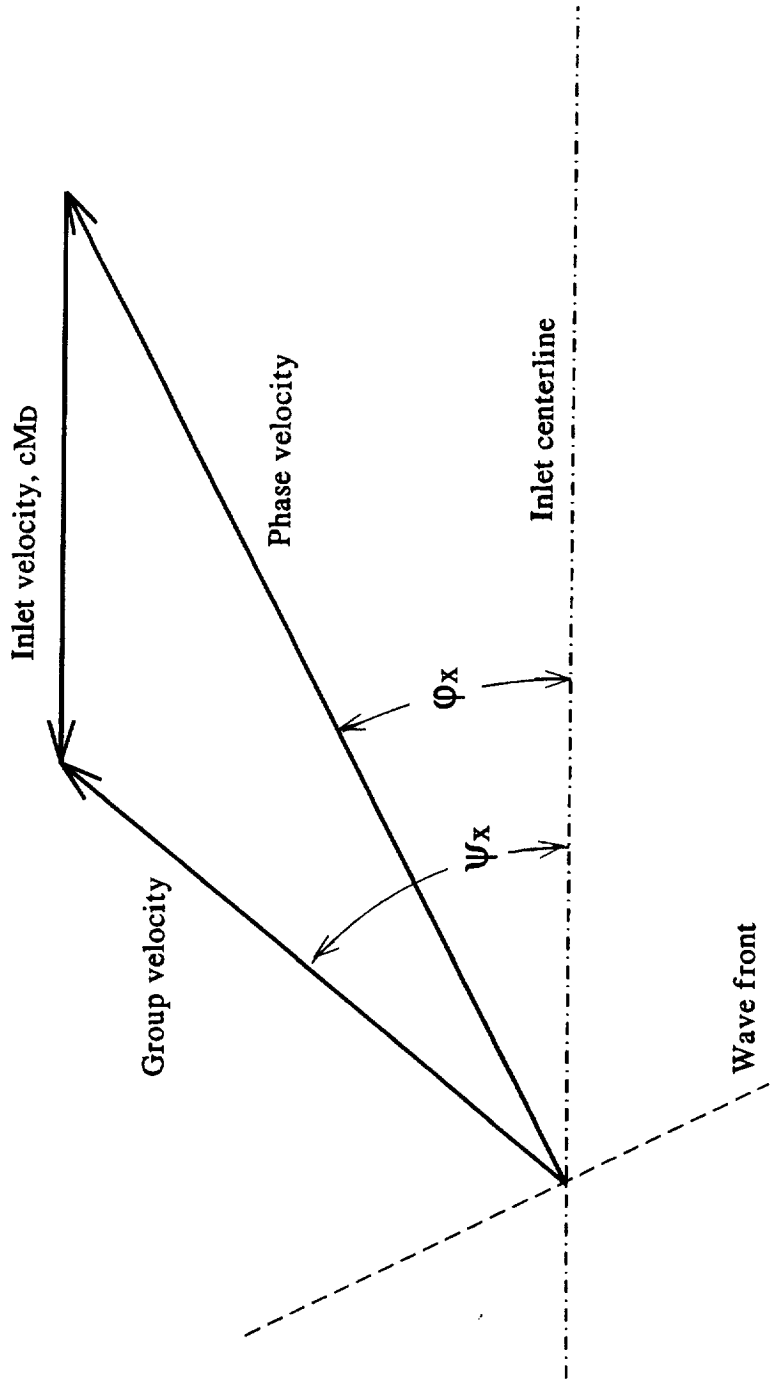

Figure 1. Acoustic propagation vectors in the inlet duct

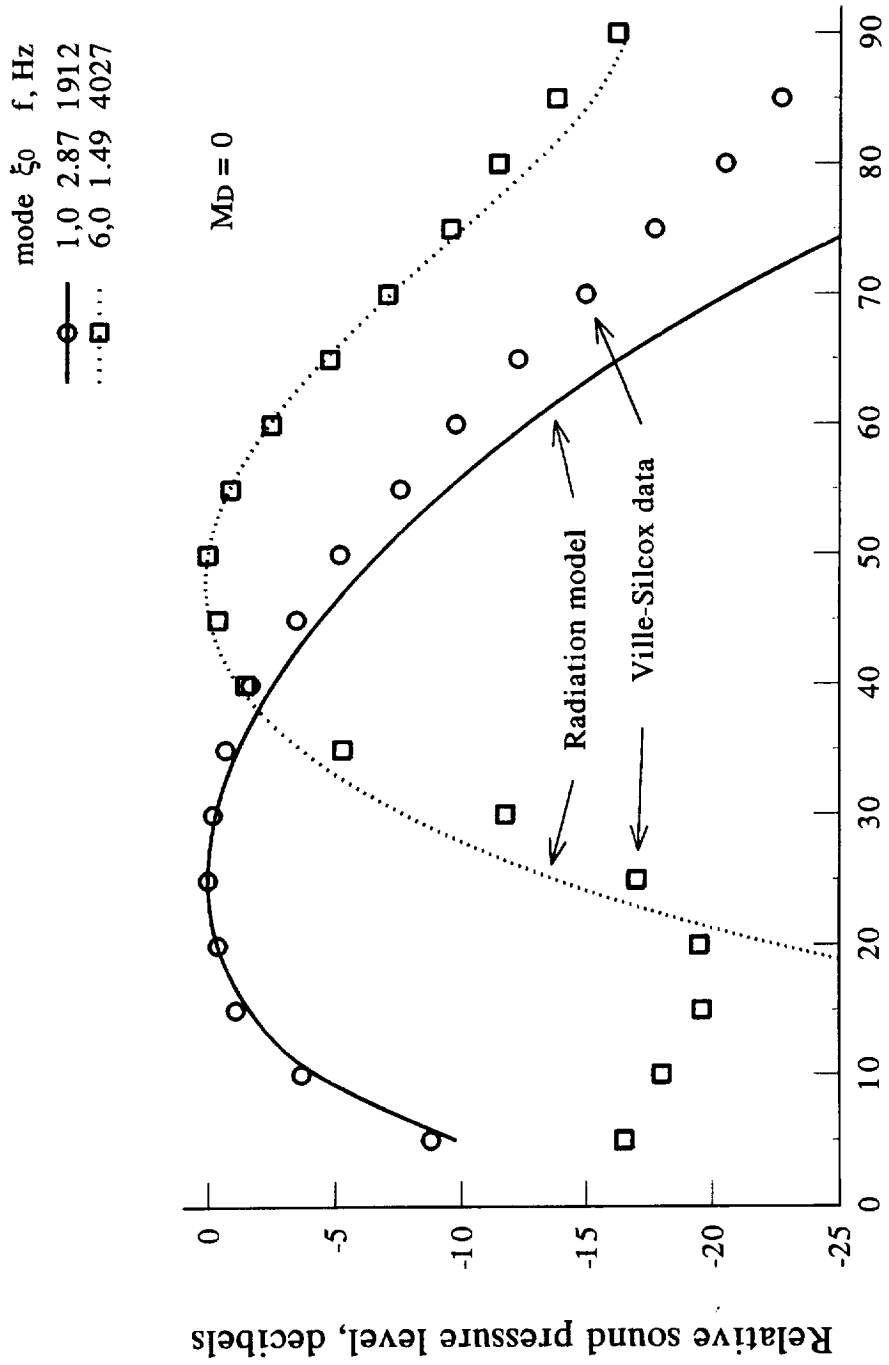

Figure 2. Unflanged duct far-field radiation data compared to model

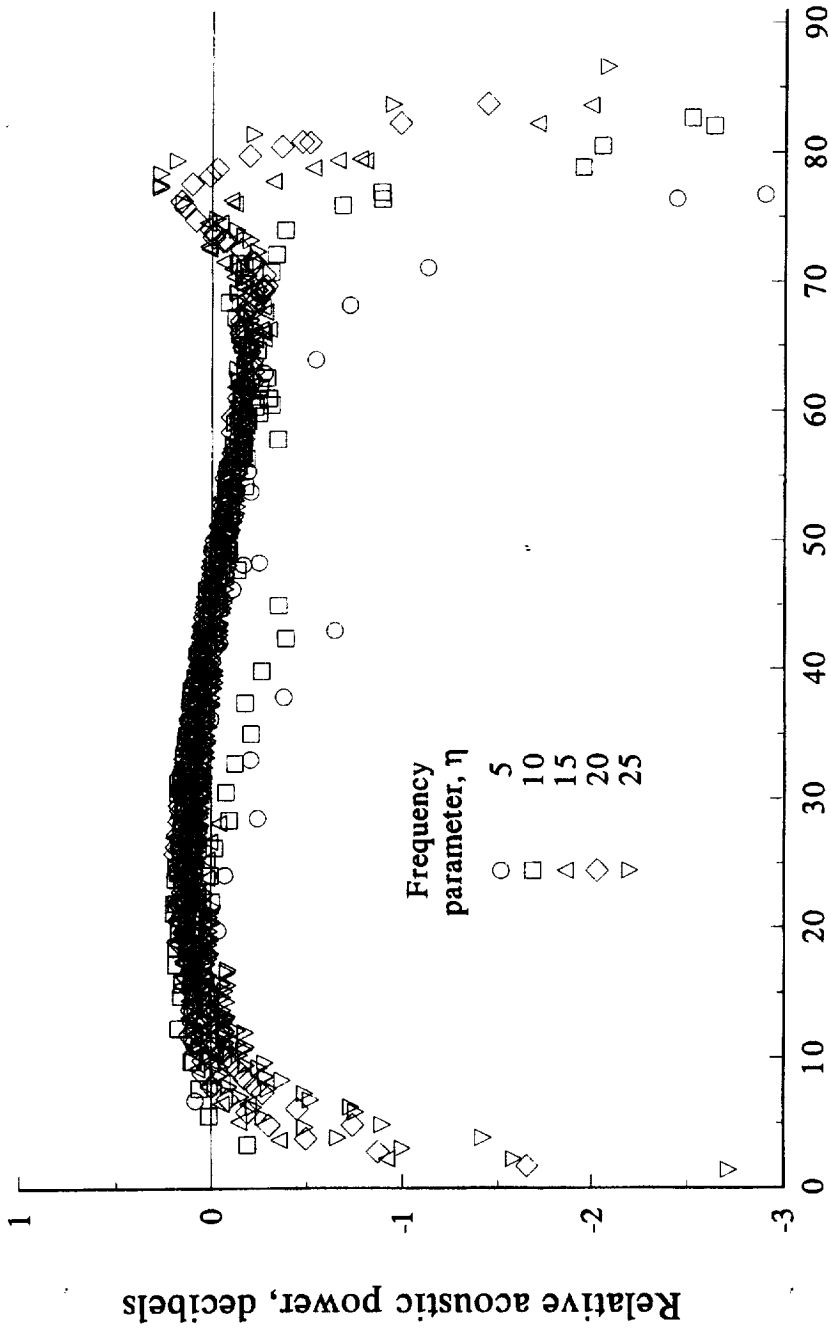

Figure 3. Integrated far-field acoustic power for propagating modes integrated over 0 to 90 degrees, no-flow, $M_D = 0$

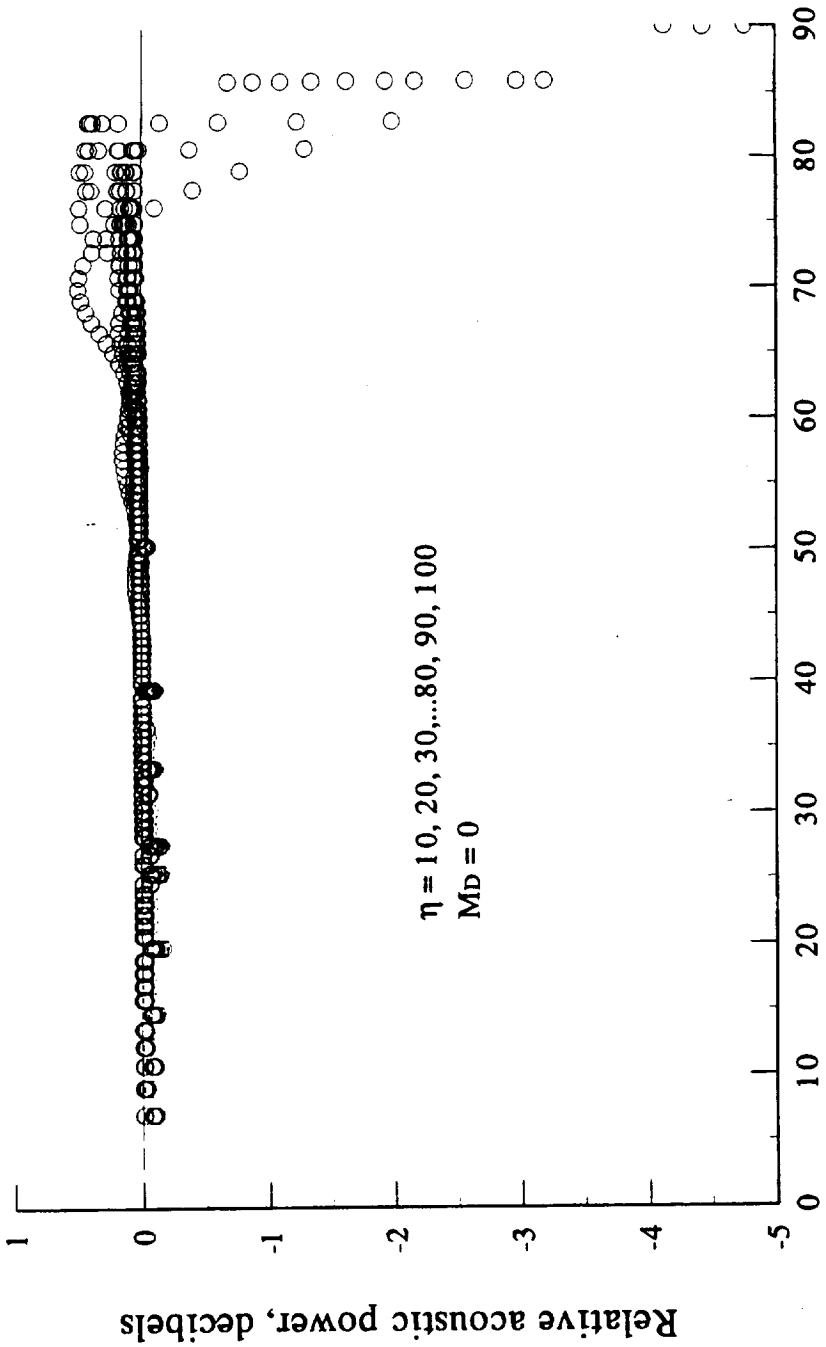

Figure 4. Integration of far-field radiation, axis to 90 degrees, no flow

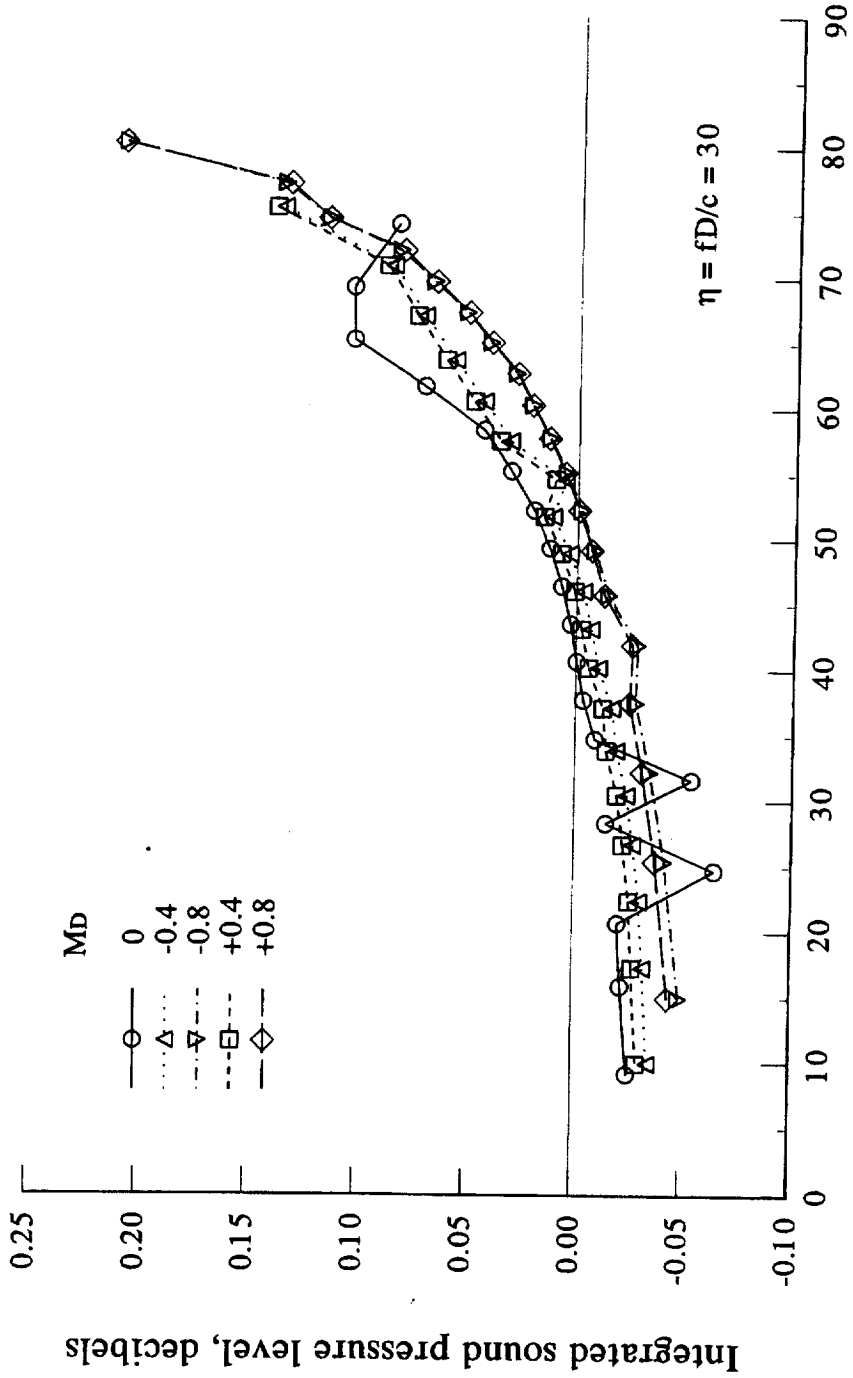

Figure 5. Integration of far-field radiation from axis to 90 degrees uniform flow Mach number varied, cut-off ratio dependent equation 22 used

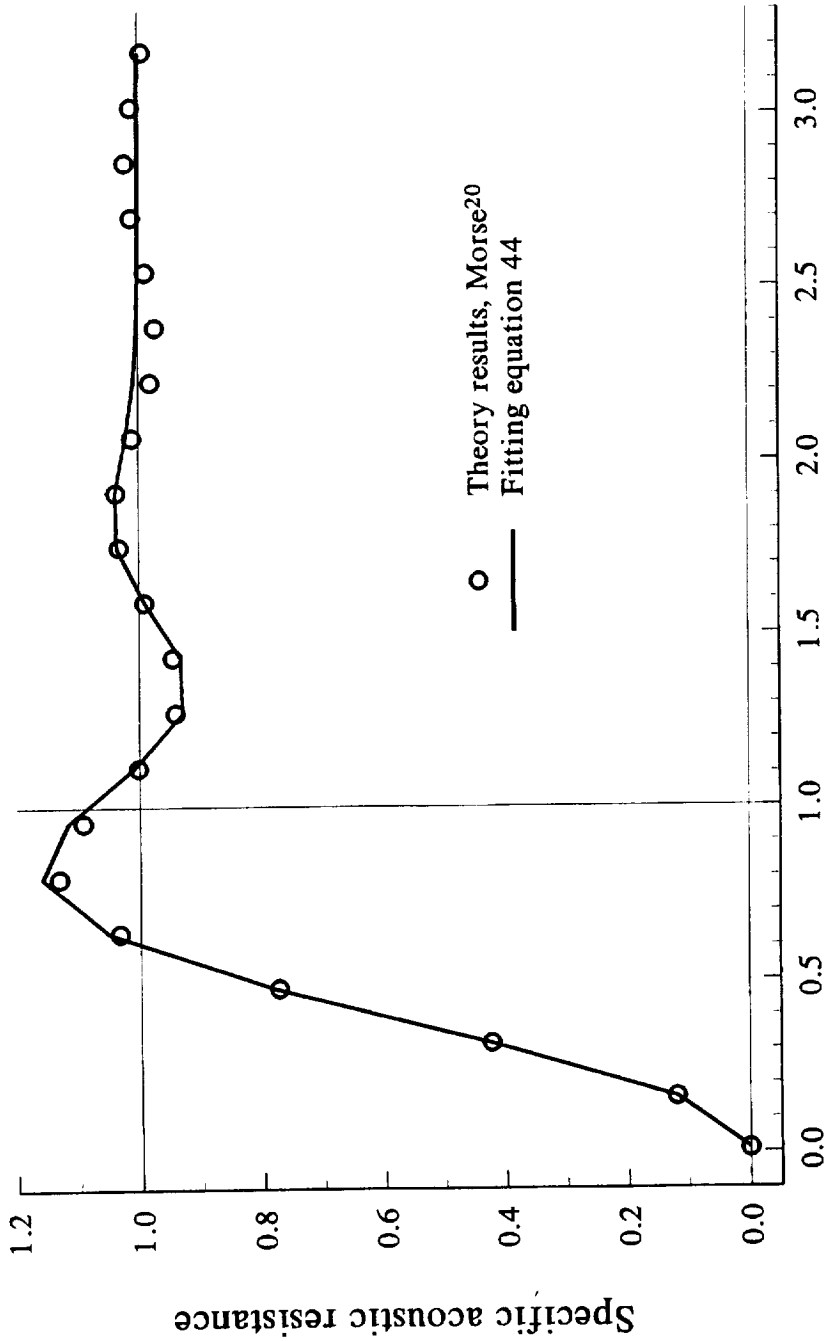

Figure 6. Radiation resistance for a piston in a wall

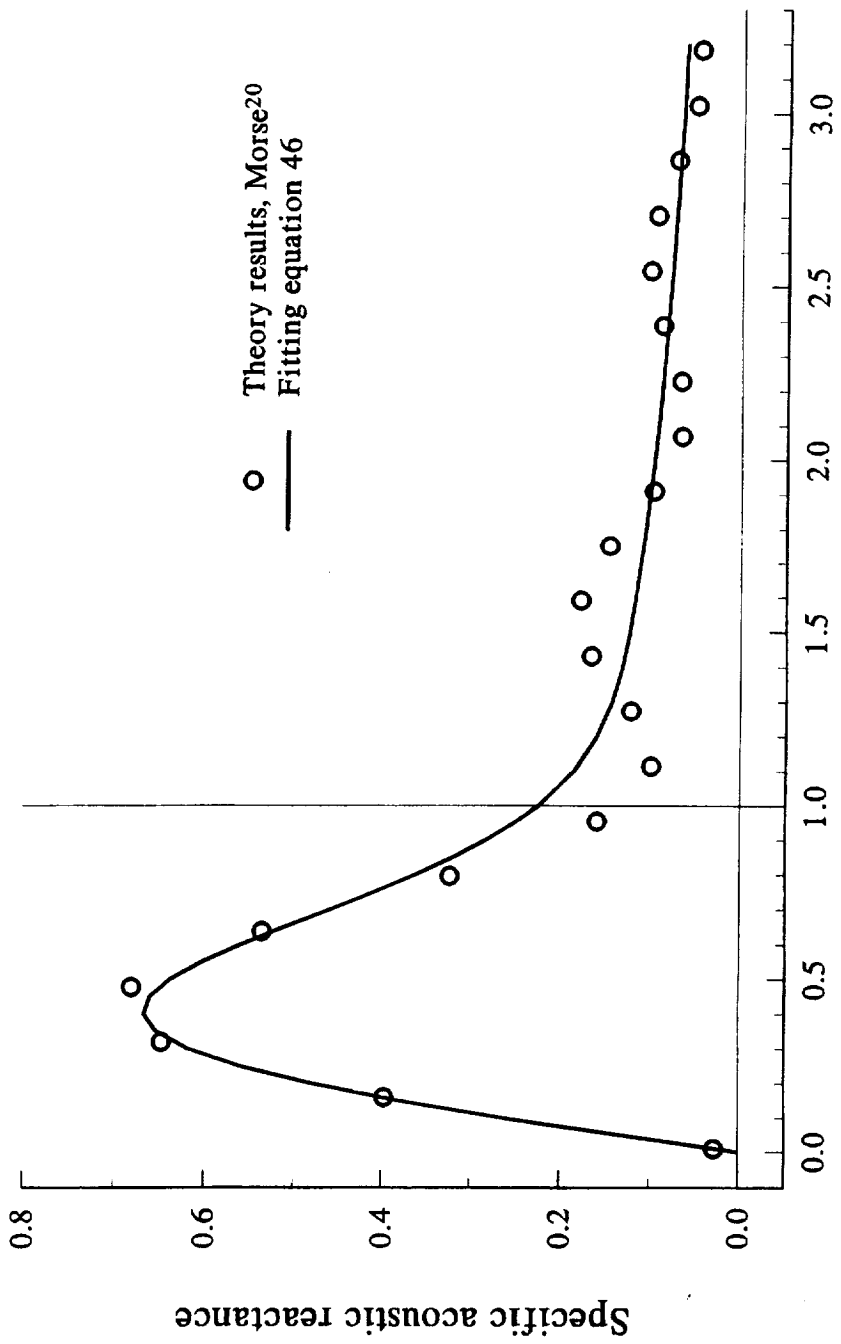

Figure 7. Radiation reactance for a piston in a wall

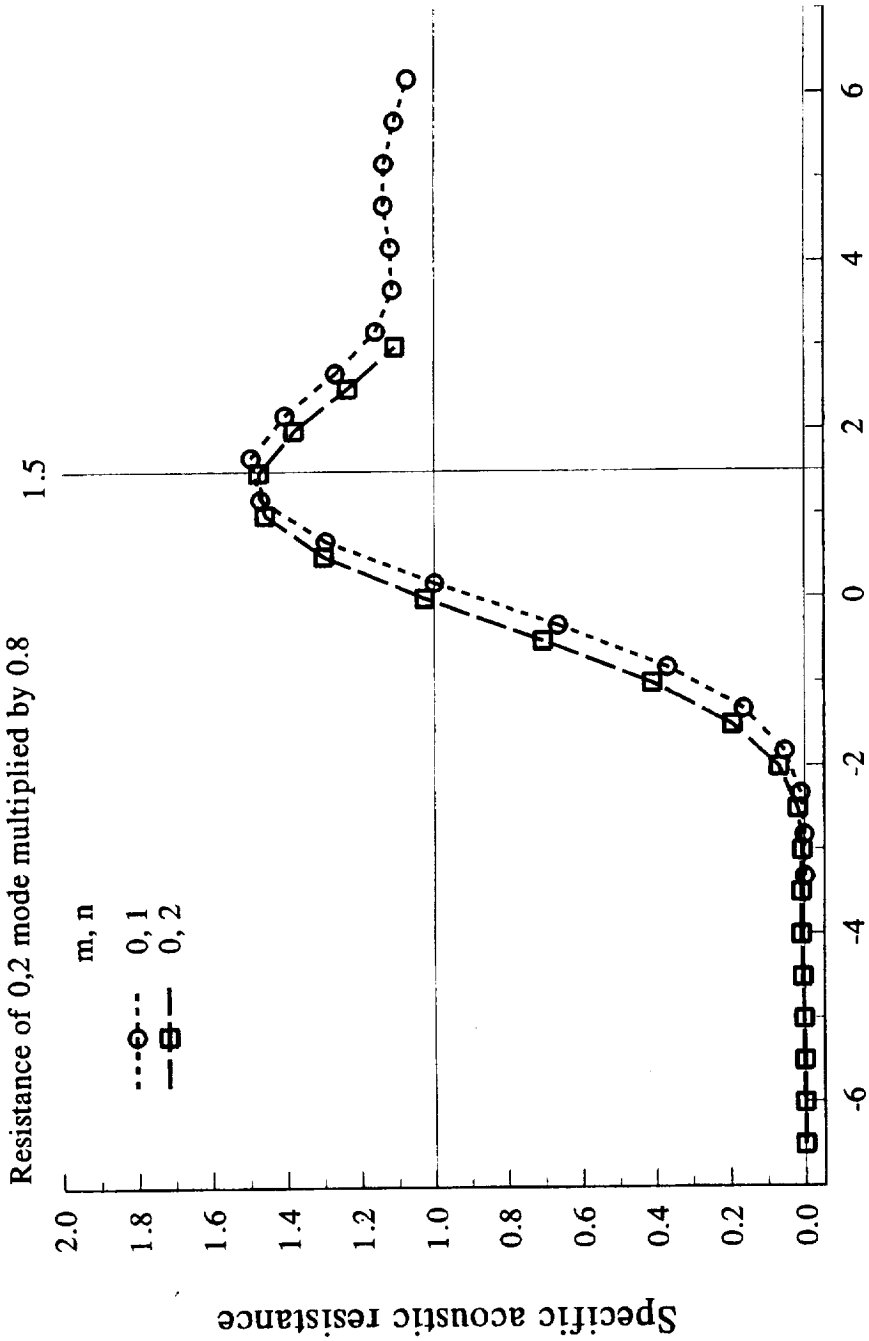

Figure 8. Radiation resistance for axisymmetric radial modes

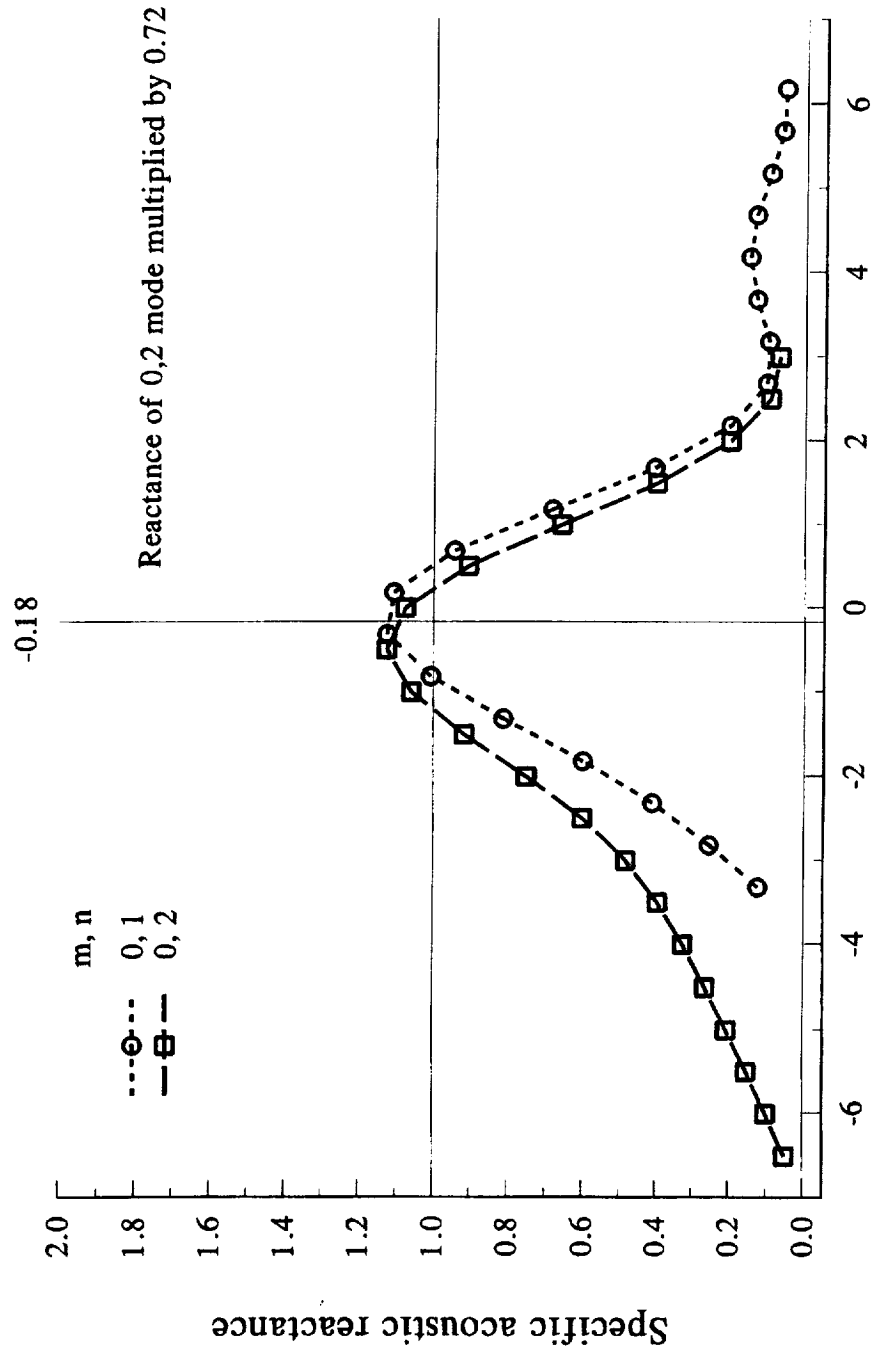

Figure 9. Radiation reactance for axisymmetric modes

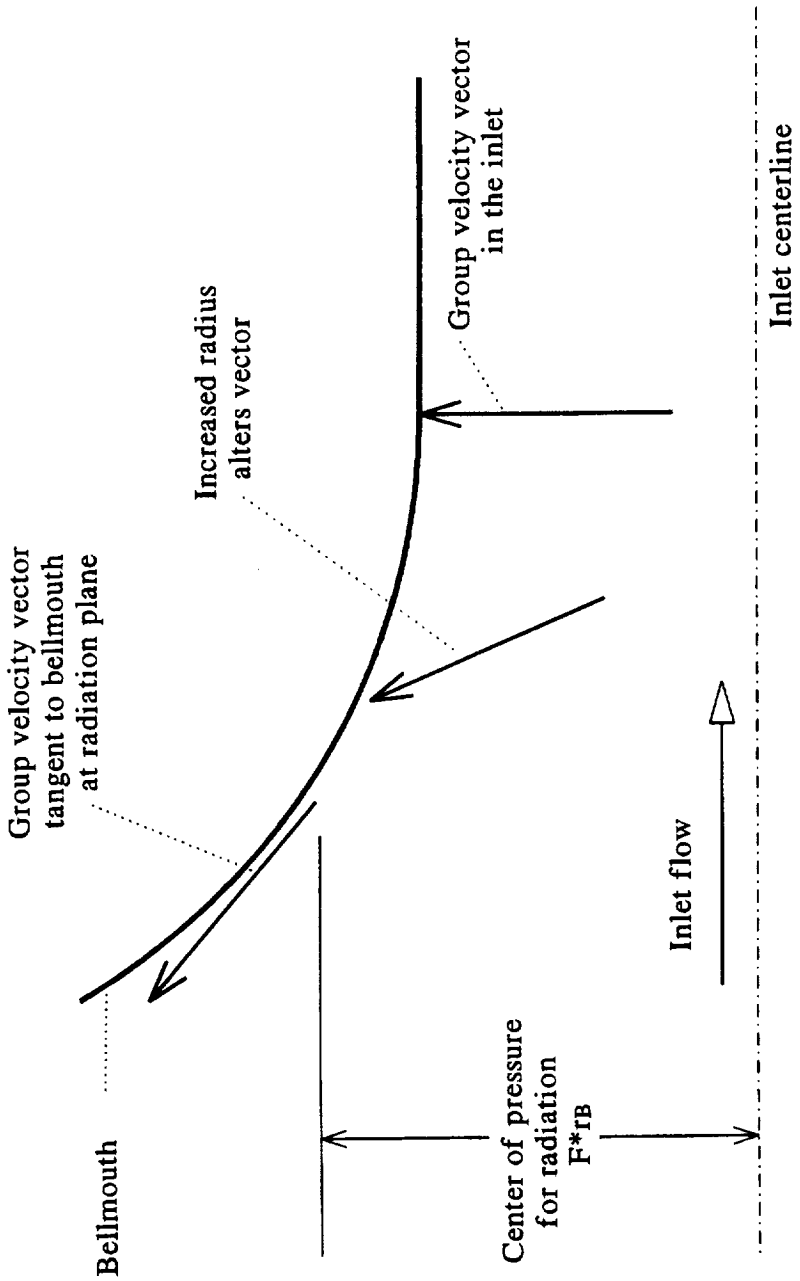

Figure 10. Group velocity vector angle variation for a mode near cut-off as the sound propagates through the bellmouth

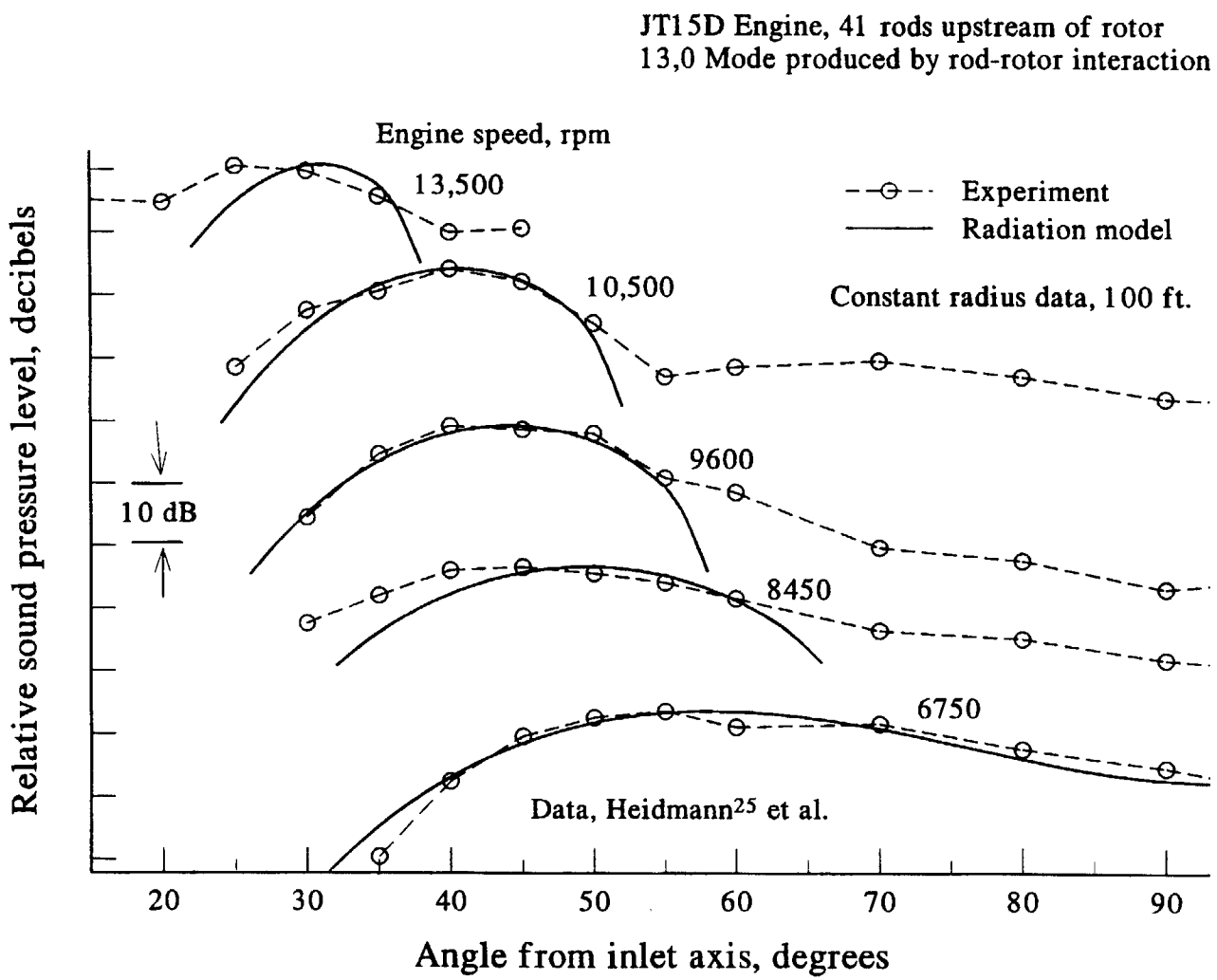

Figure 11. Noise directivity comparisons, JT15D engine inlet

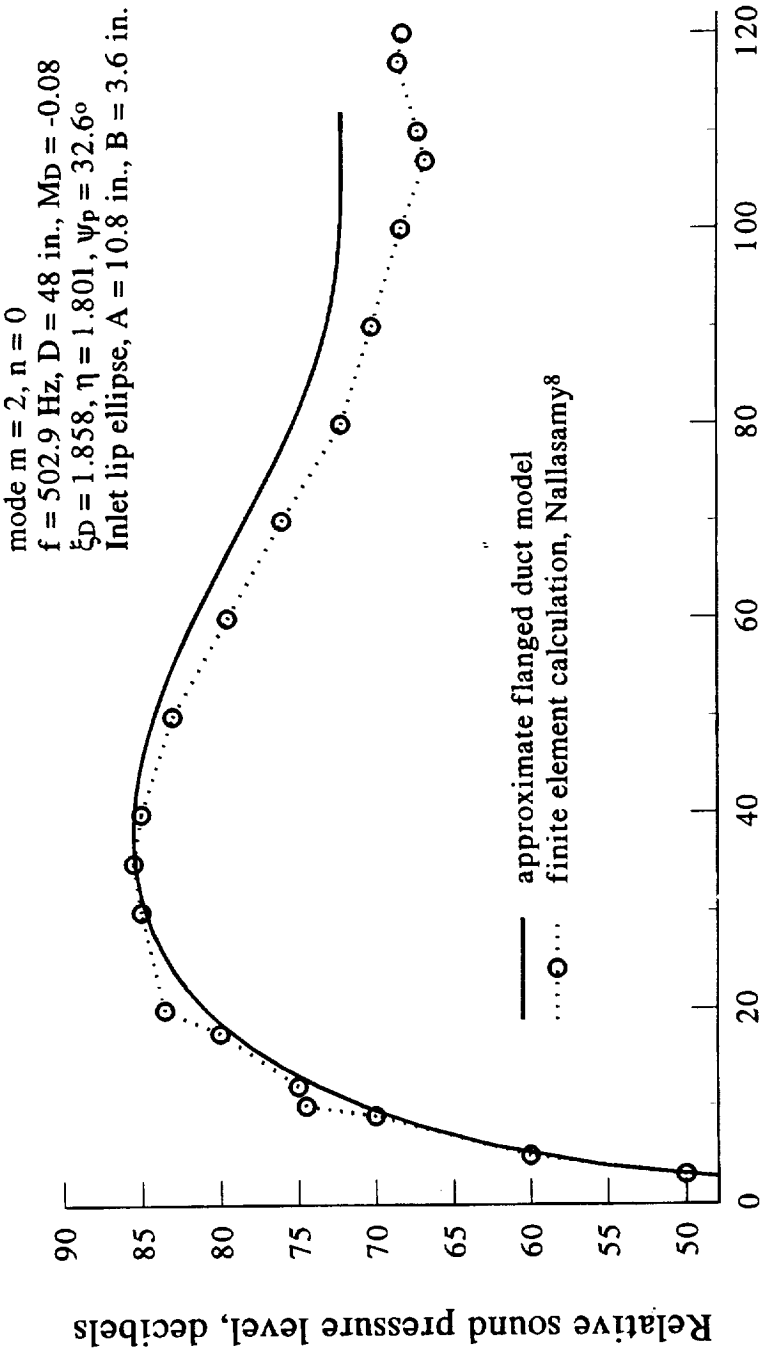

Figure 12. Comparison of far-field radiation calculations, ANC fan inlet approximate flanged duct and finite element models, mode (2,0)

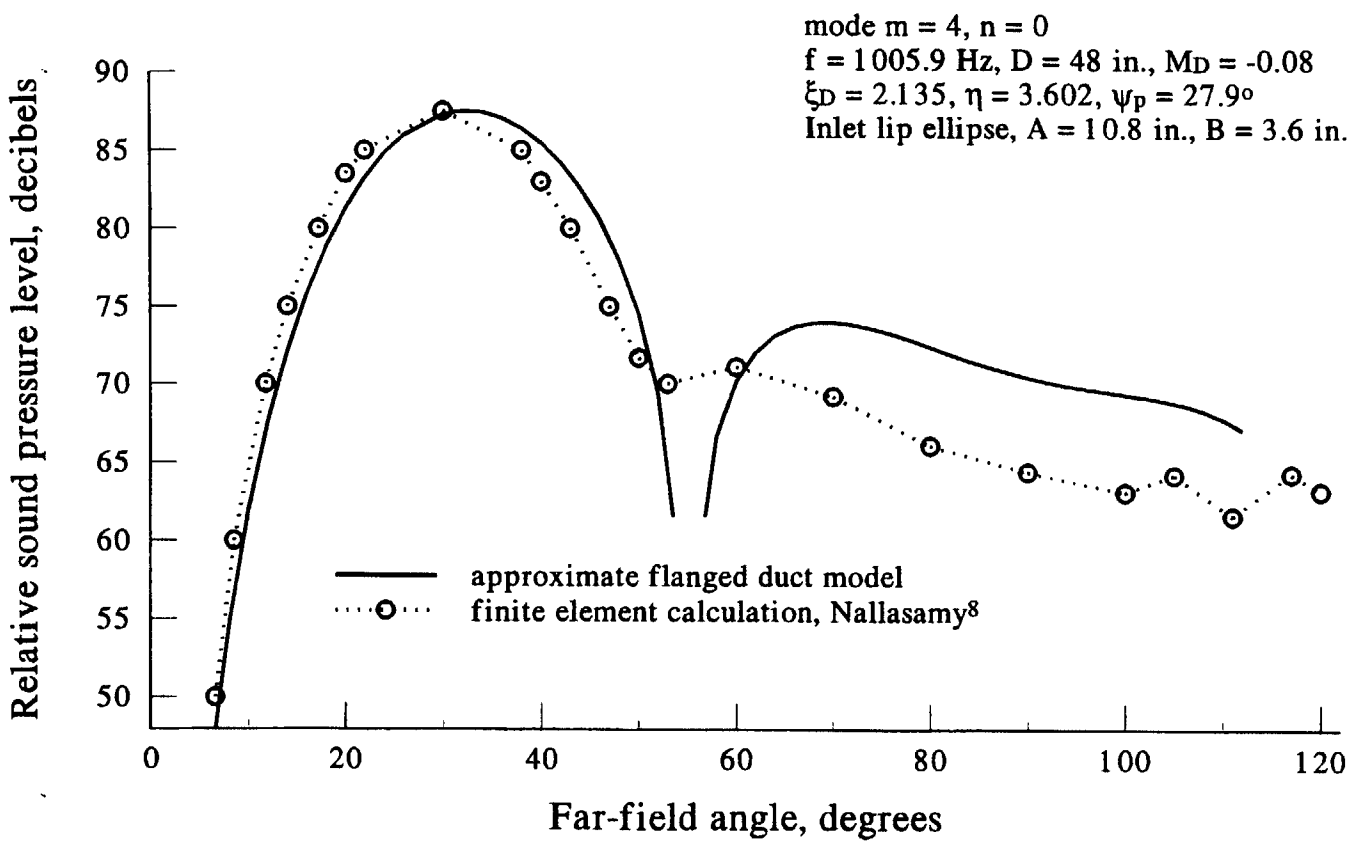

Figure 13. Comparison of far-field radiation calculations, ANC fan inlet approximate flanged duct and finite element models, mode (4,0)

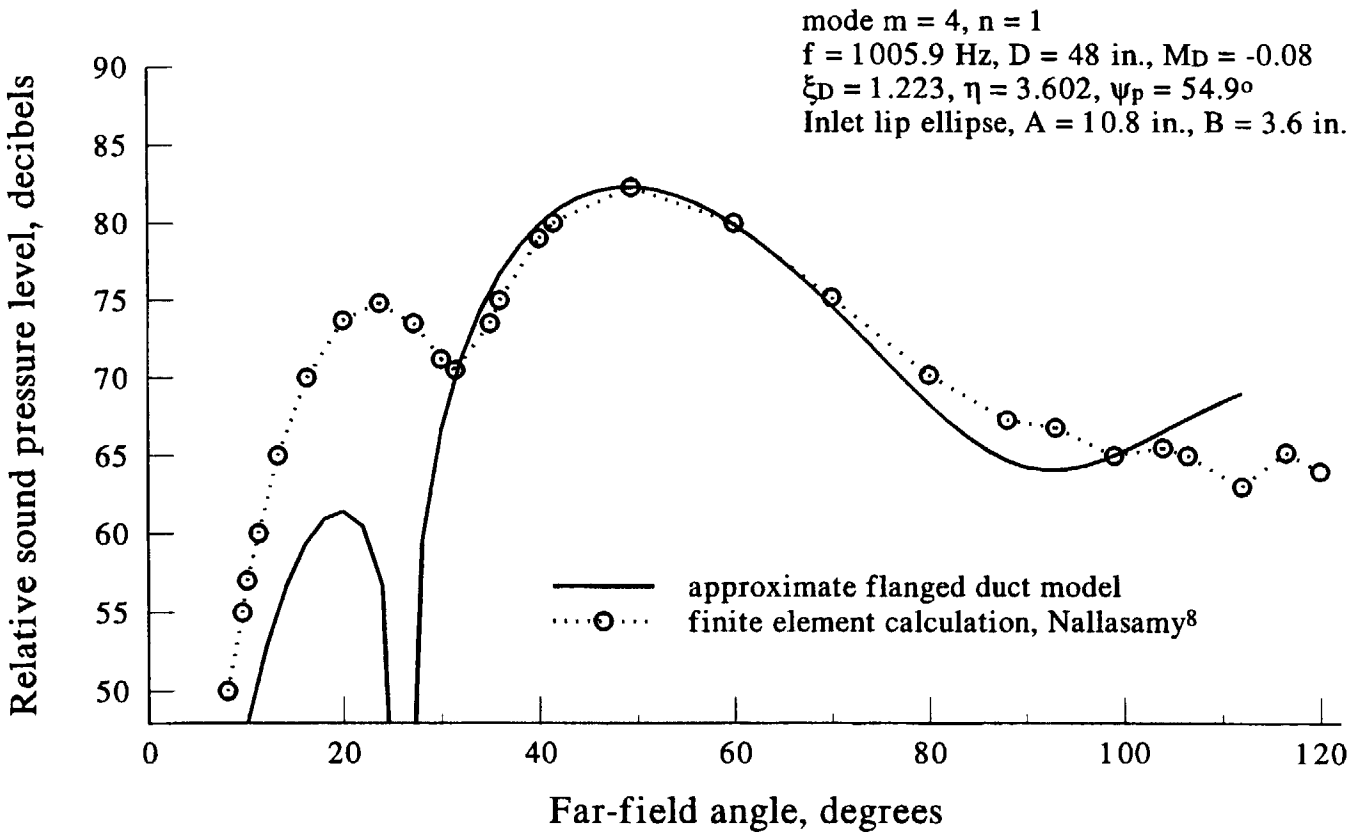

Figure 14. Comparison of far-field radiation calculations, ANC fan inlet approximate flanged duct and finite element models, mode (4,1)

Figure 15. Comparison of far-field radiation calculations, ANC fan inlet approximate flanged duct and finite element models, mode (6,0)

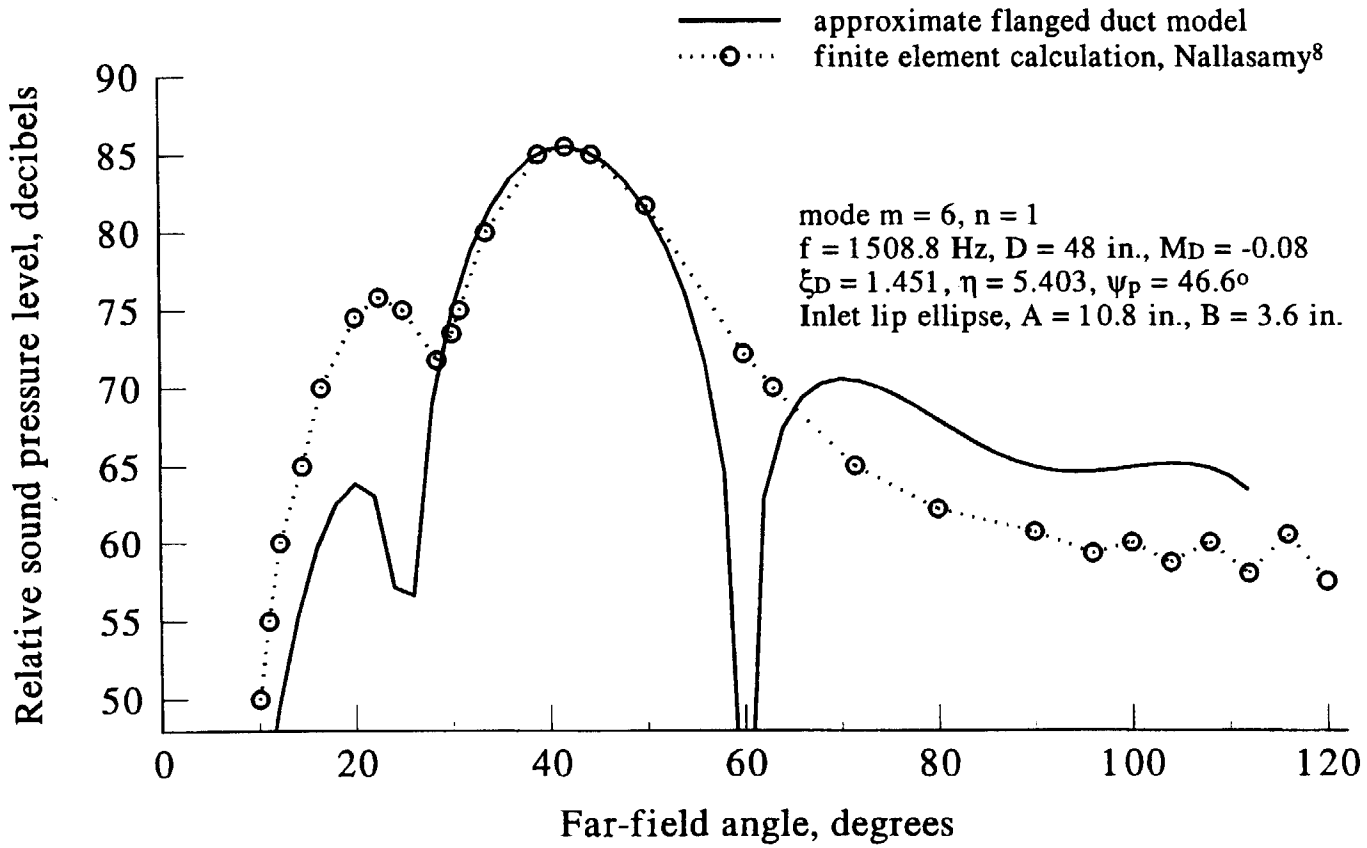

Figure 16. Comparison of far-field radiation calculations, ANC fan inlet approximate flanged duct and finite element models, mode (6,1)

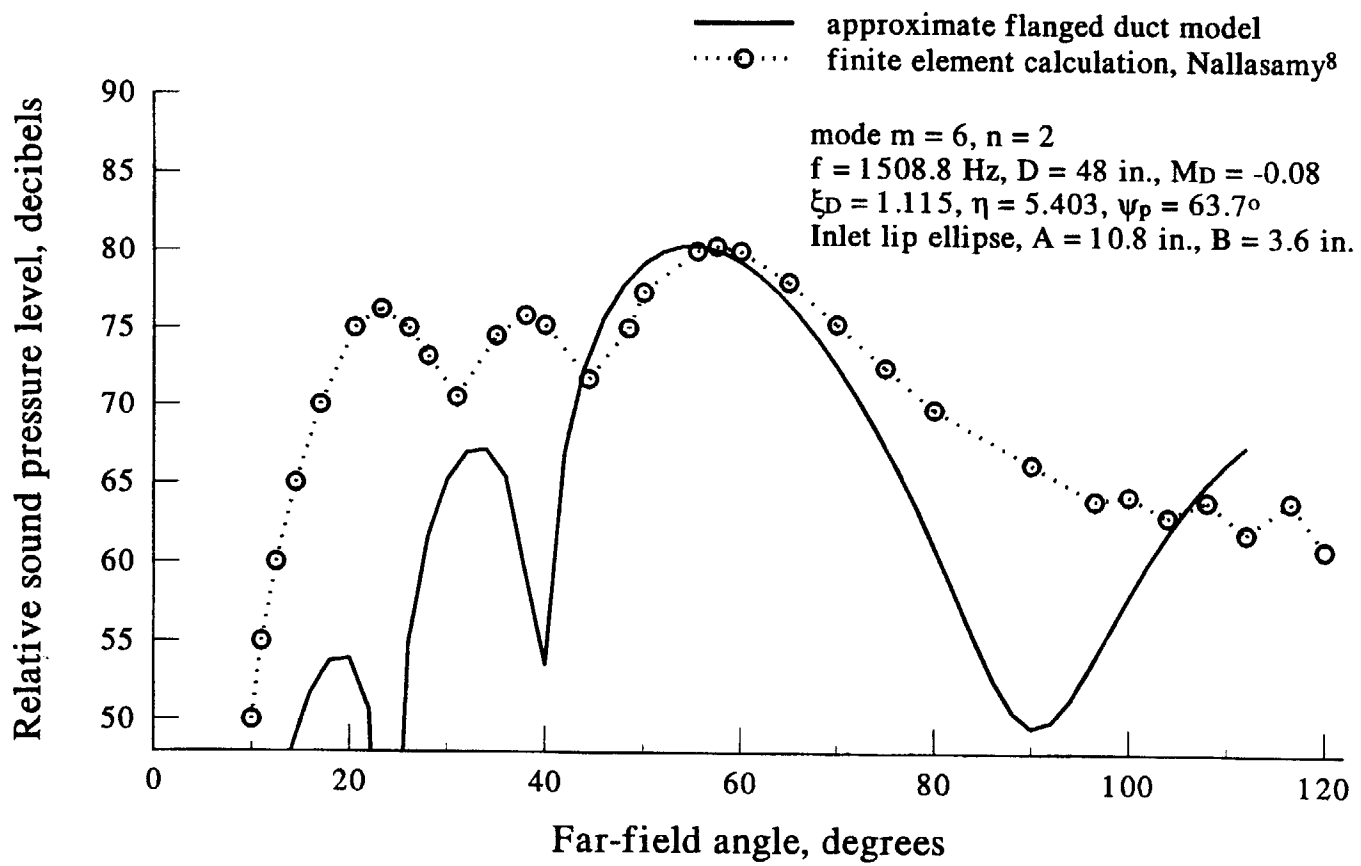

Figure 17. Comparison of far-field radiation calculations, ANC fan inlet approximate flanged duct and finite element models, mode (6,2)

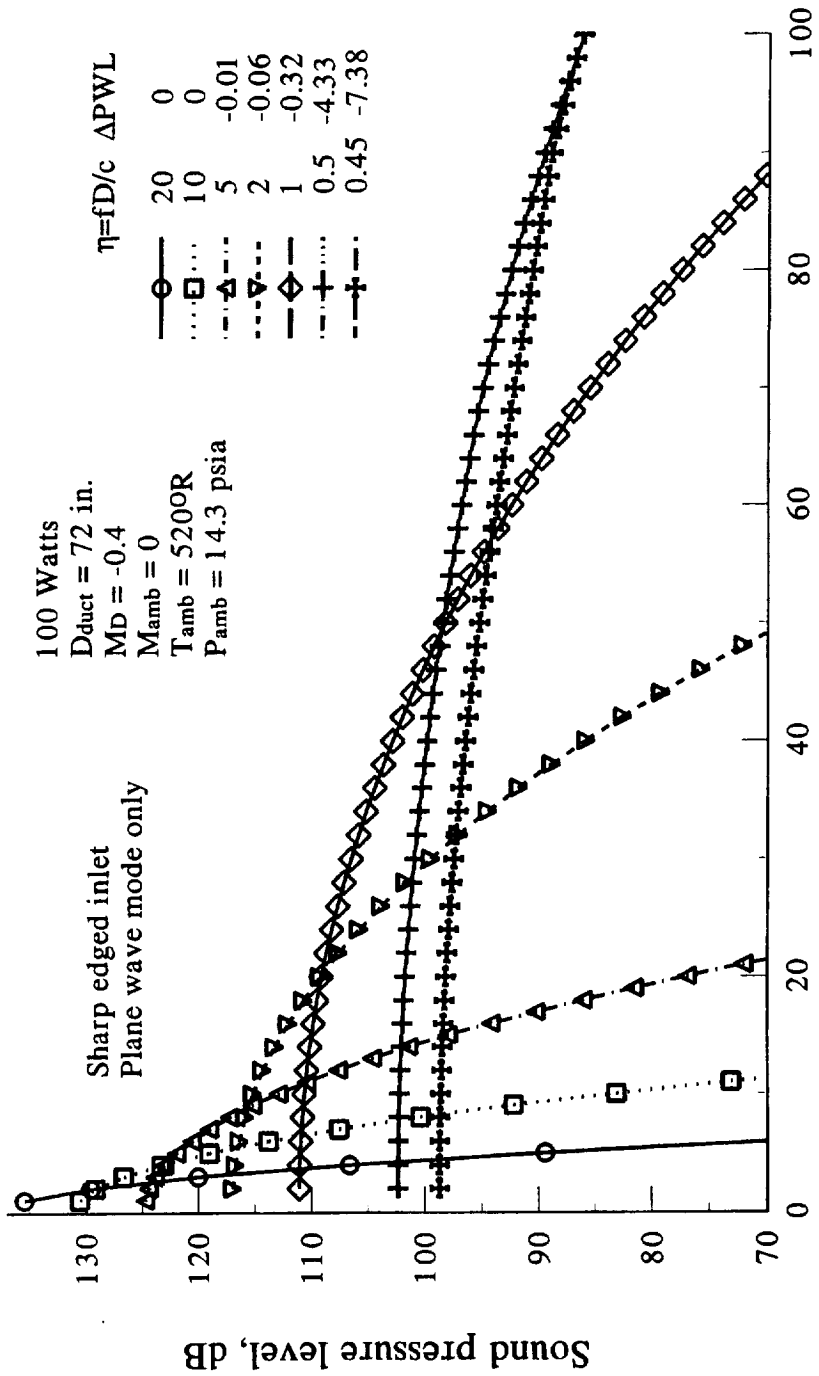

Figure 18. Fan inlet plane wave noise radiation directivities
100 ft. radius, vary frequency paramter

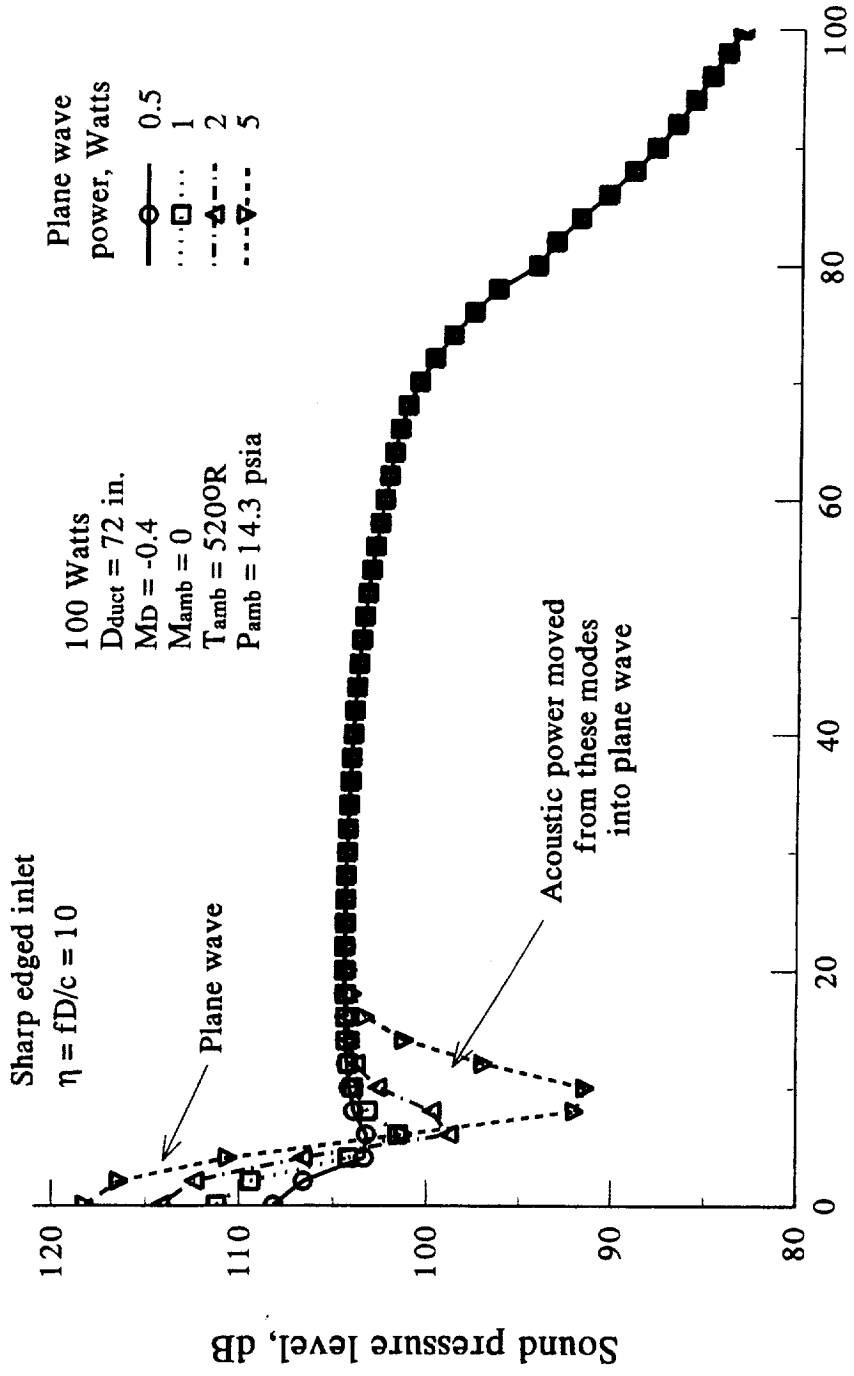

Figure 19. Fan inlet broadband noise radiation directivities, 100 ft. radius, vary acoustic power in the plane wave mode

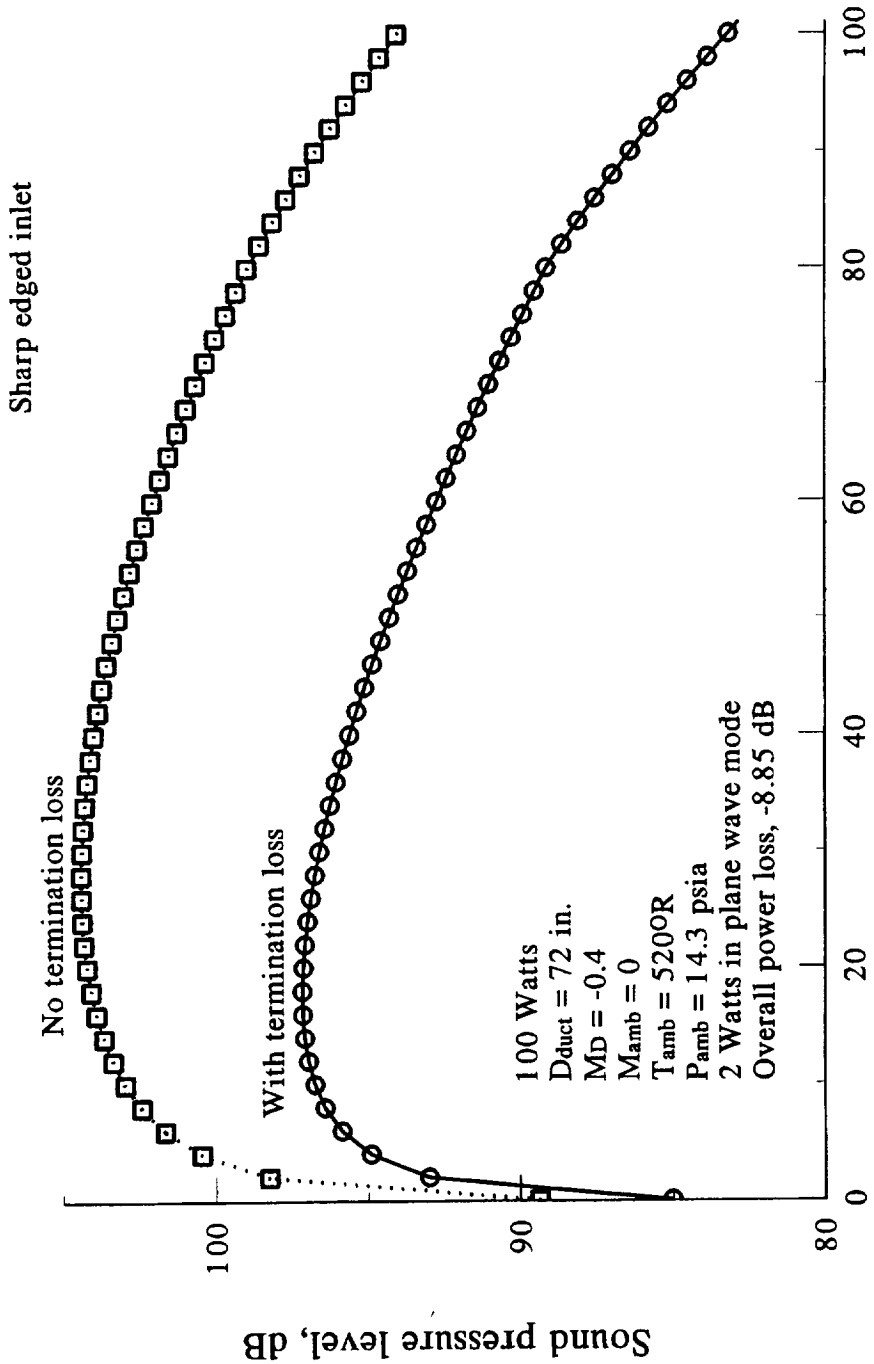

Figure 20. Fan inlet broadband noise radiation directivities, 100 ft. radius, effect of termination transmission loss at $\eta = 0.5$

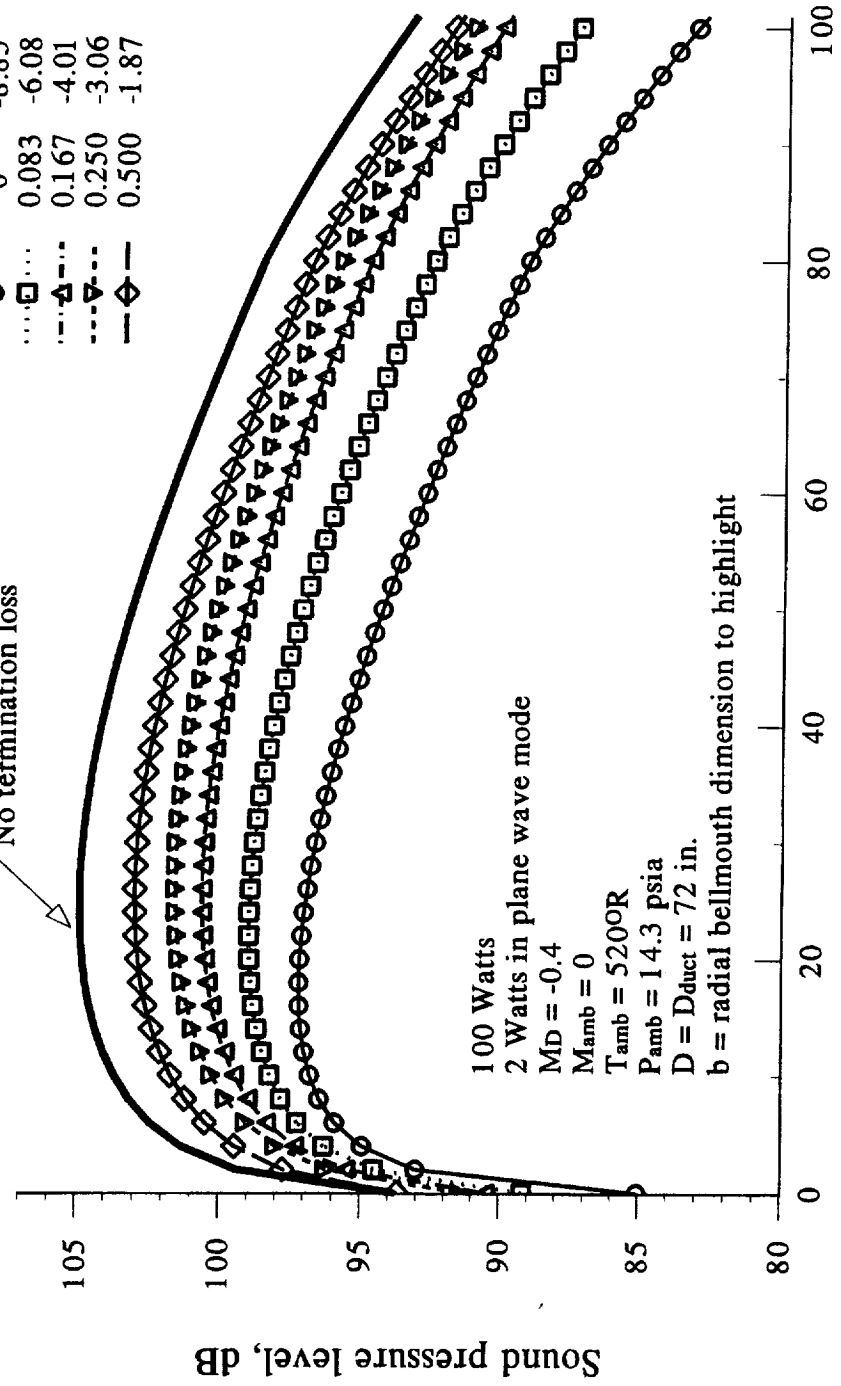

Figure 21. Fan inlet broadband noise radiation directivities, 100 ft. radius, effect of bellmouth size at $\eta = 0.5$

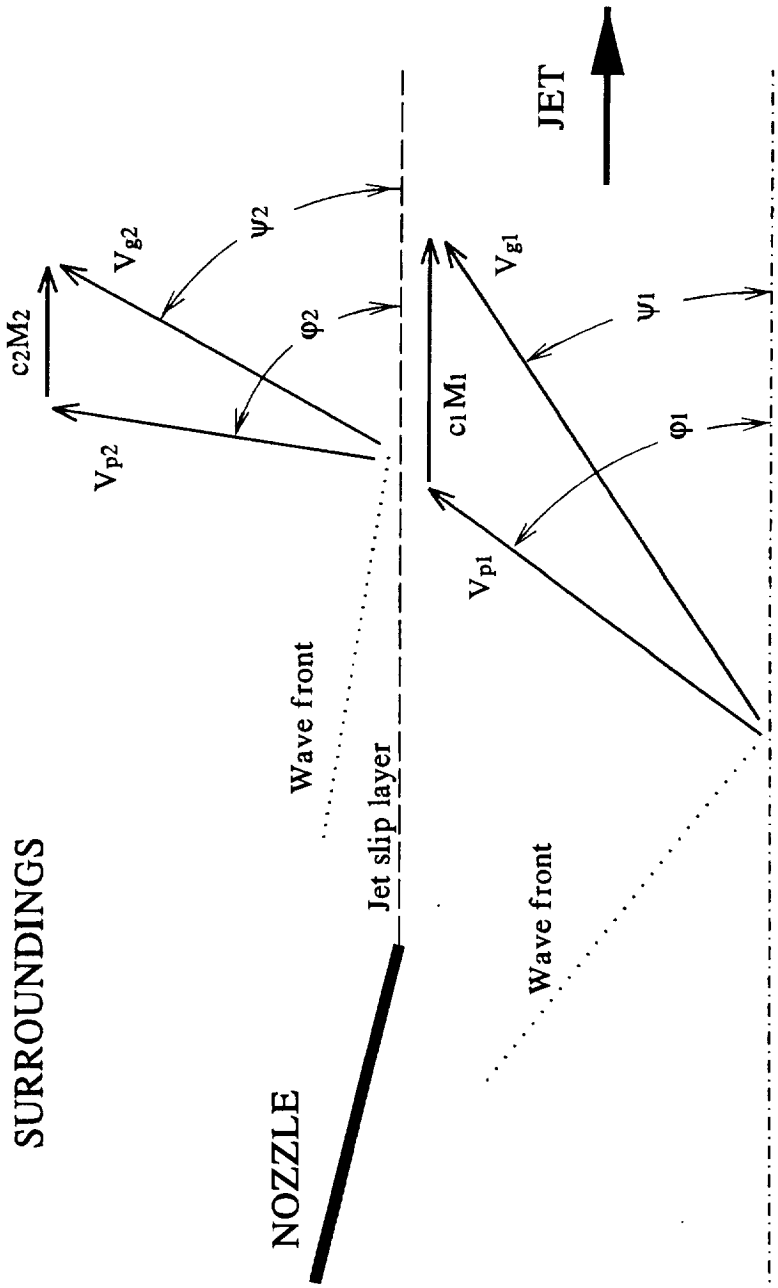

Figure 22. Schematic of refraction through the jet slip layer

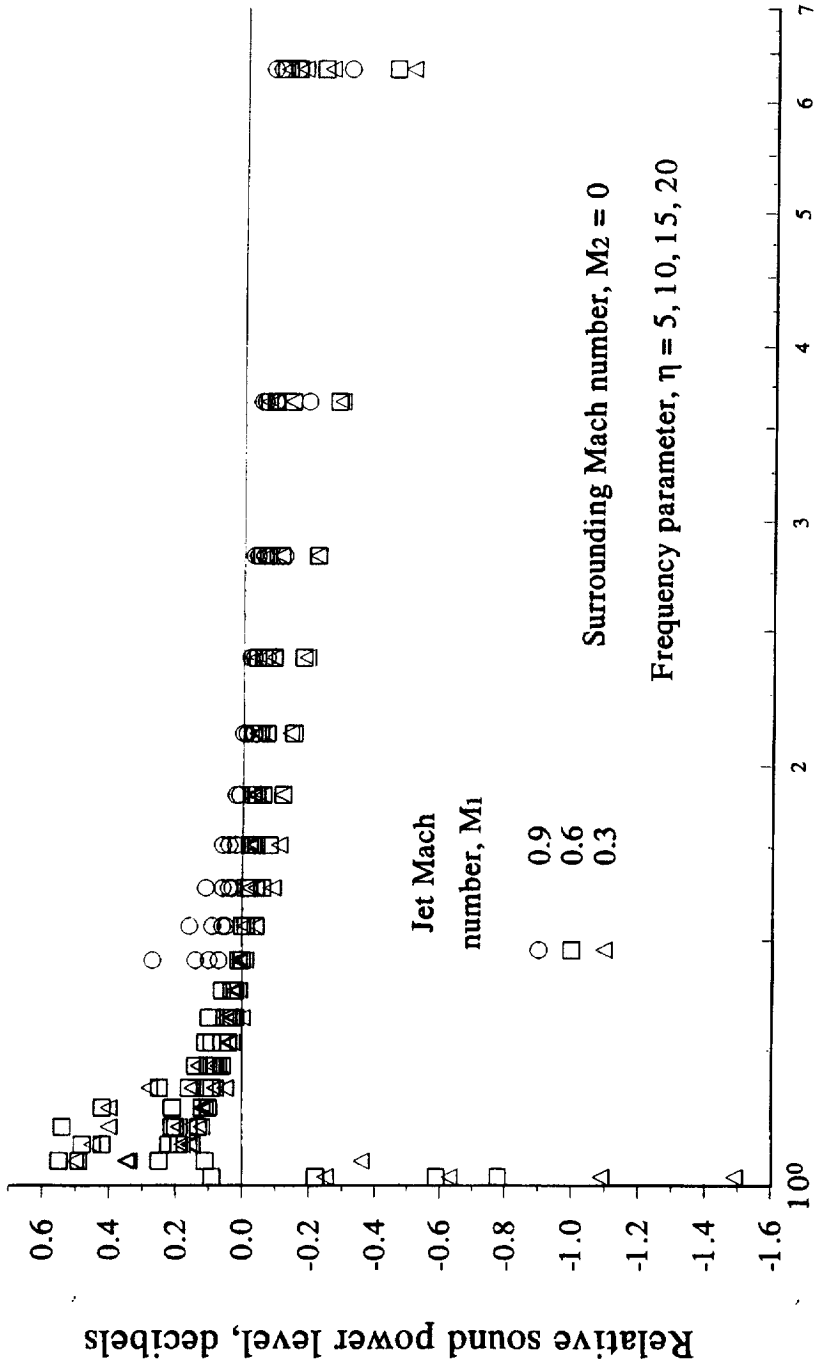

Figure 23. Integrated far-field acoustic power, aft radiation with refraction, integration aft axis to flange

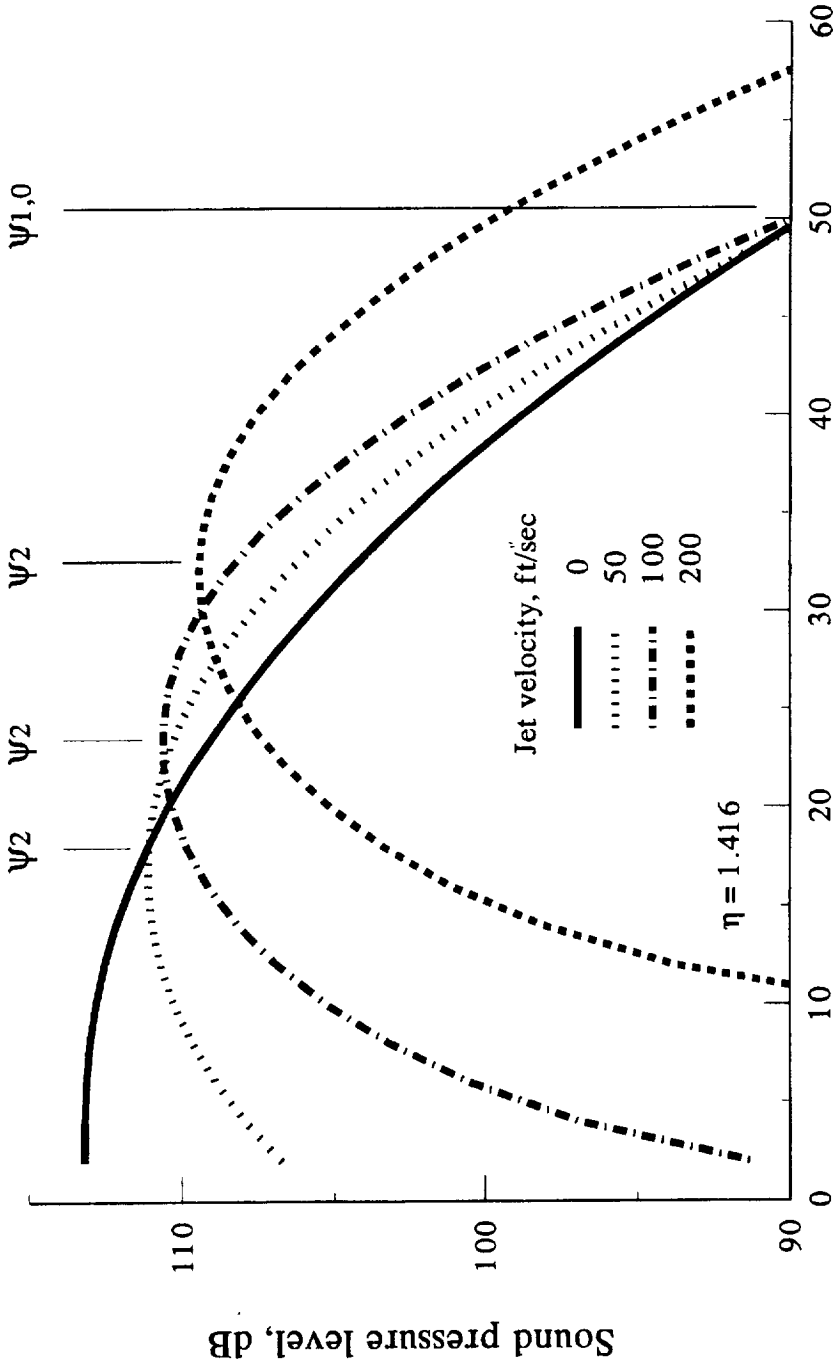

Figure 24. Schematic of sound refraction model, aft plane wave radiation

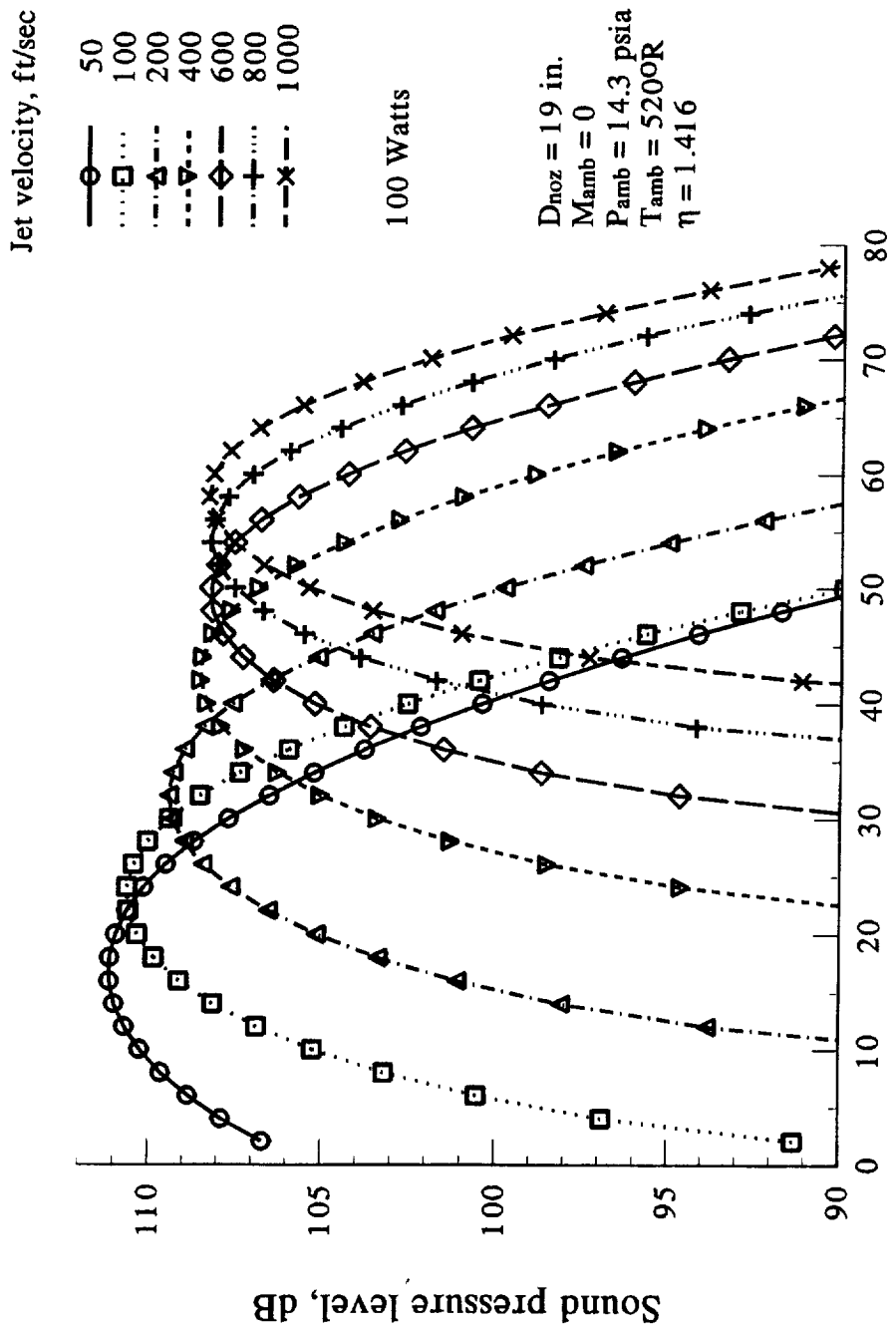

Figure 25. Plane wave radiation directivities, model behavior with increasing jet velocity, 1000 Hz, calculations made for 100 ft. radius

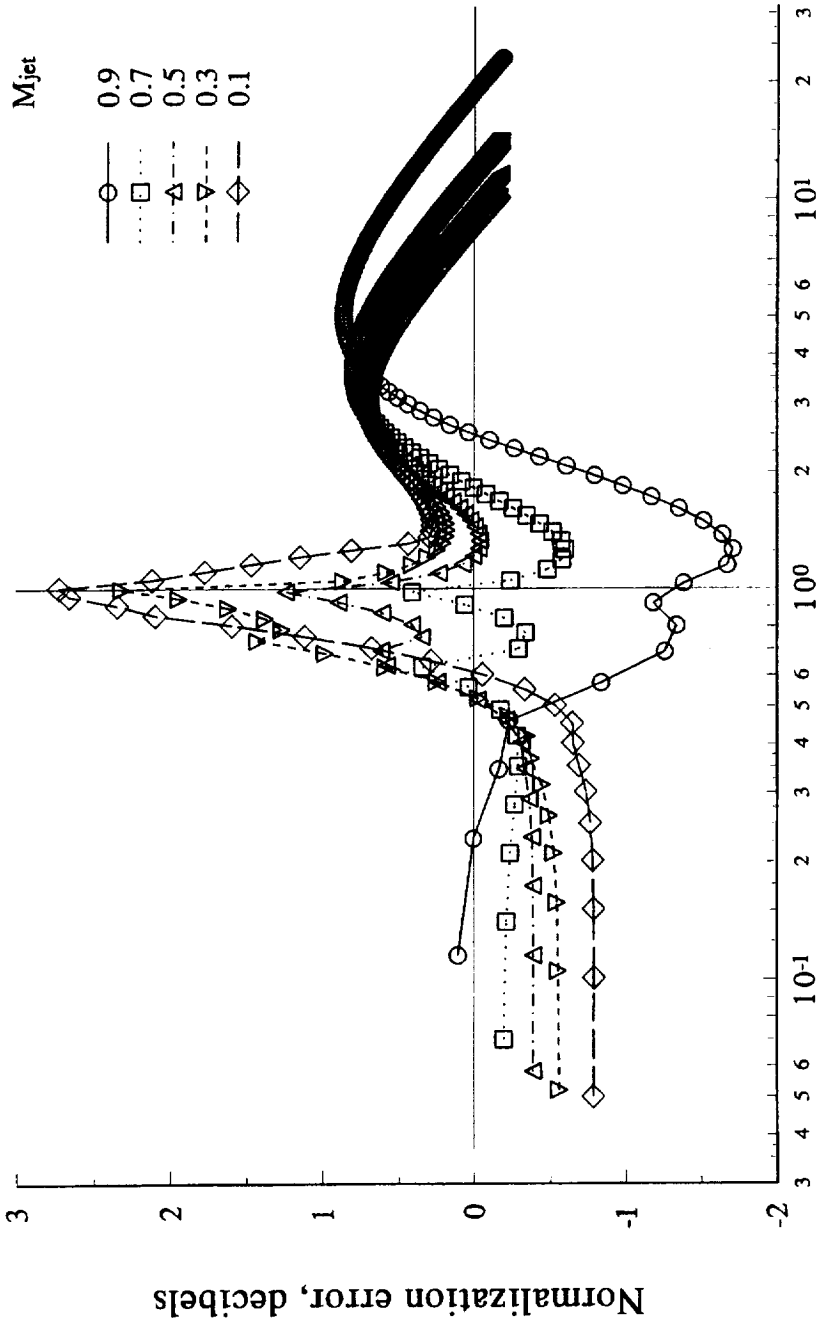

Figure 26. Normalization error for refracted plane wave radiation

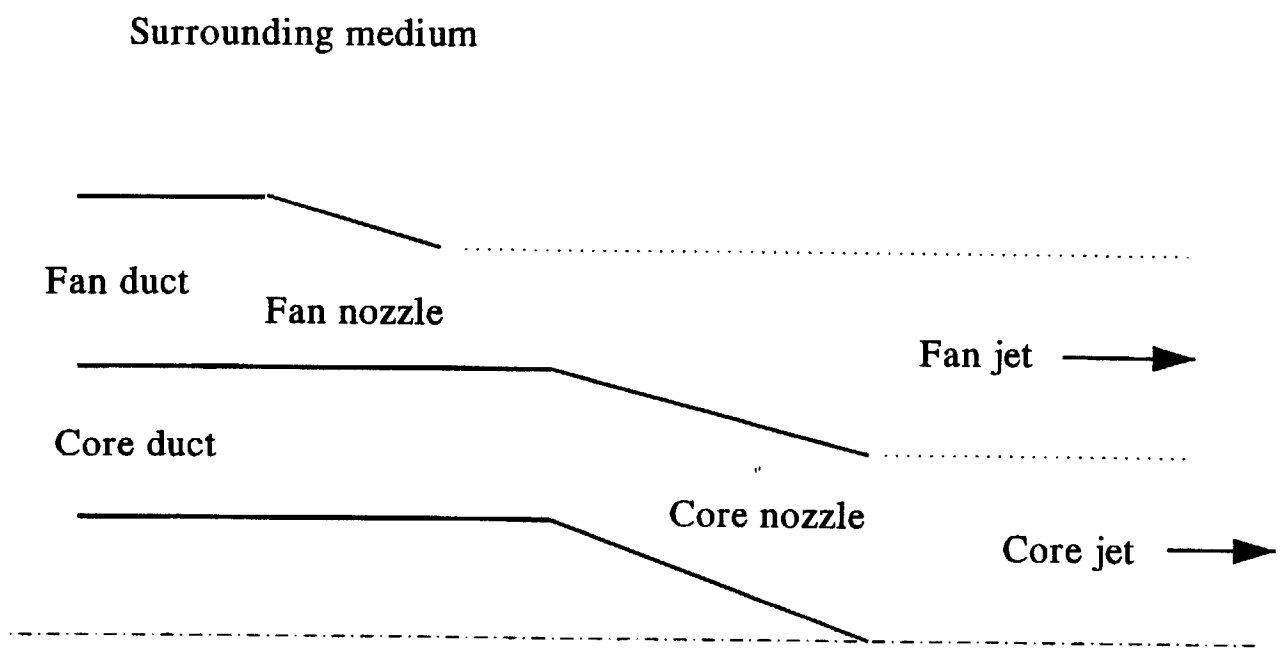

Figure 27. Schematic of aft fan and core geometry used for sample problems

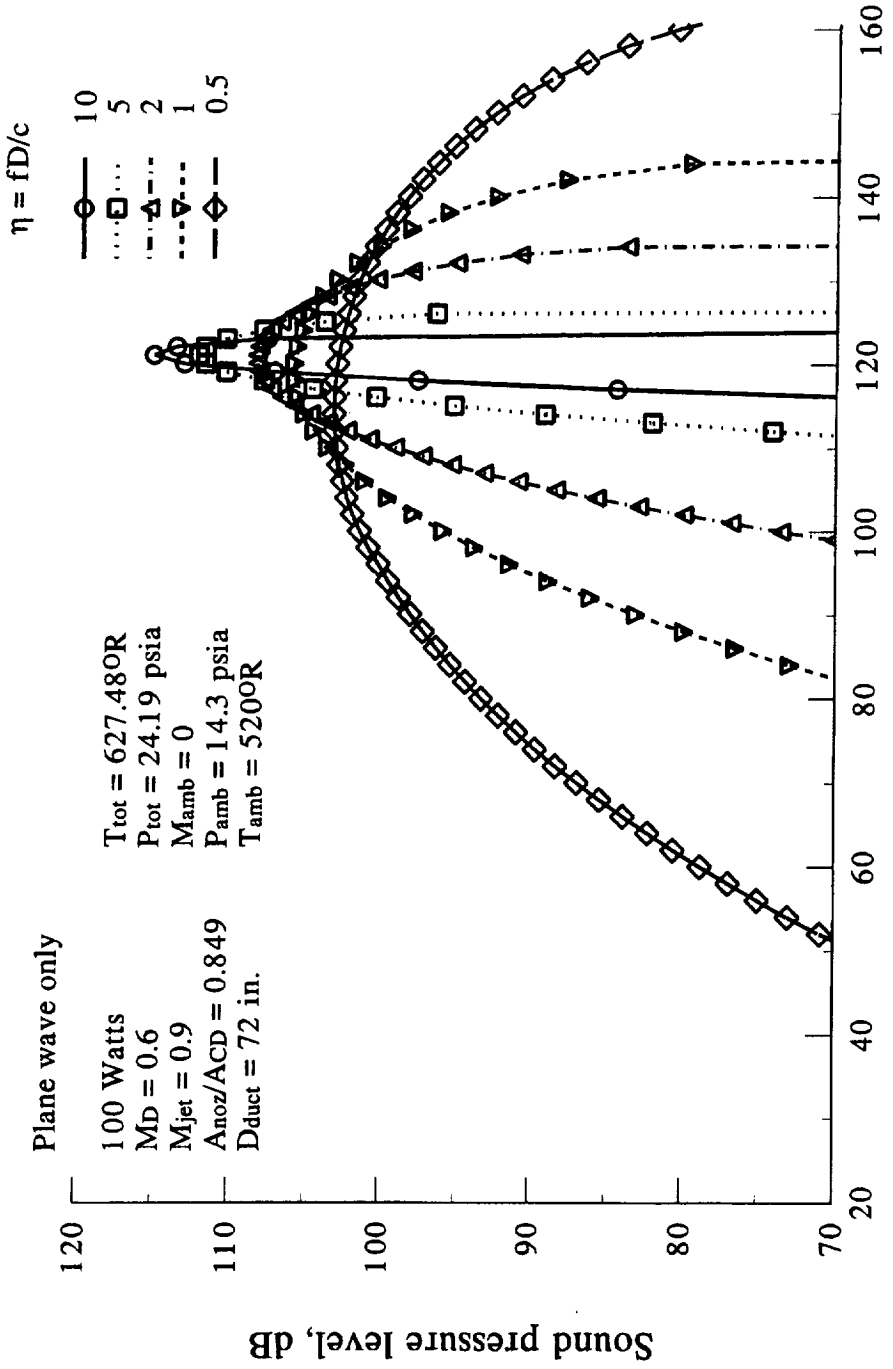

Figure 28. Fan aft plane wave noise radiation directivity, vary frequency
100 ft. sideline, all acoustic power in plane-wave mode

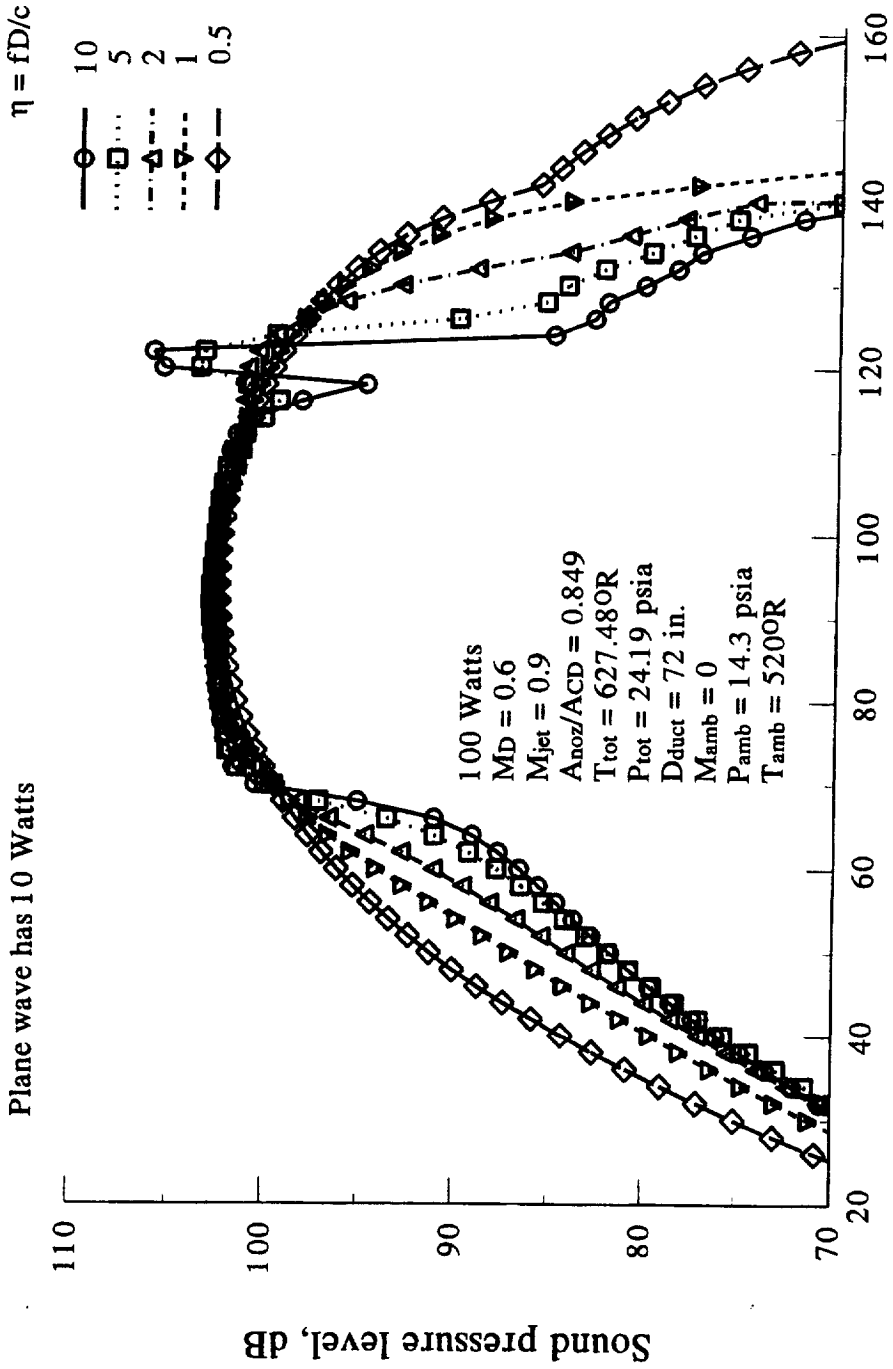

Figure 29. Fan aft broadband noise radiation directivities, vary frequency 100 ft. sideline, equal acoustic power per mode simulation

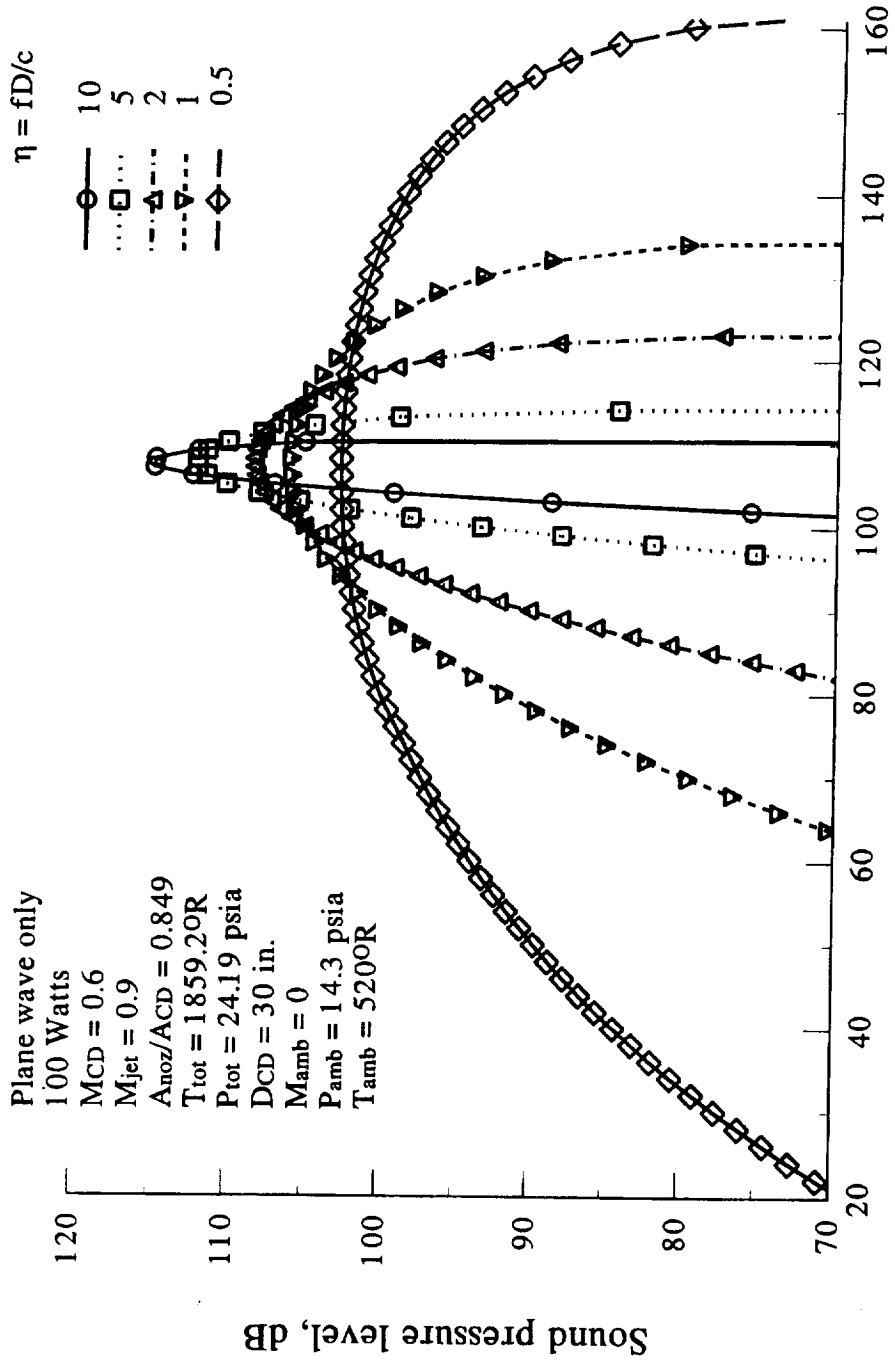

Figure 30. Core plane wave noise radiation directivities, vary frequency 100 ft. sideline, all acoustic power in plane-wave mode

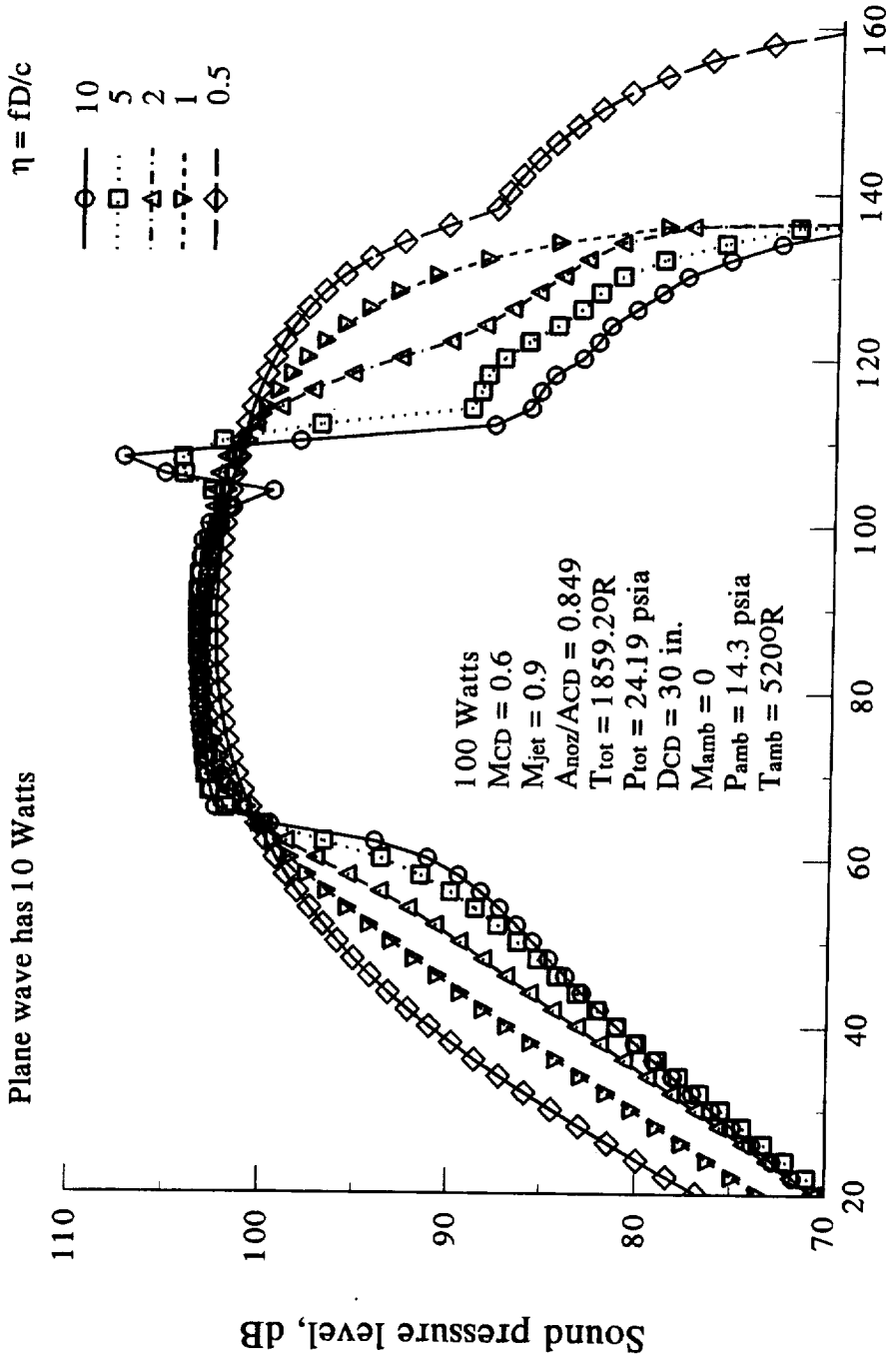

Figure 31. Core broadband noise radiation directivities, vary frequency
100 ft. sideline, equal acoustic power per mode simulation

Figure 32. Correction to convert wind tunnel sound pressure levels to equivalent static measurements, fan inlet noise

REPORT DOCUMENTATION PAGE

Form Approved
OMB No. 0704-0188

1. AGENCY USE ONLY (*Leave blank*)	2. REPORT DATE	3. REPORT TYPE AND DATES COVERED
	August 2000	Final Contractor Report

4. TITLE AND SUBTITLE

Aeroacoustic Prediction Codes

5. FUNDING NUMBERS

WU–522–81–11–00
NAS3–27720

6. AUTHOR(S)

P. Gliebe, R. Mani, H. Shin, B. Mitchell, G. Ashford, S. Salamah, and S. Connell

7. PERFORMING ORGANIZATION NAME(S) AND ADDRESS(ES)

GE Aircraft Engines
Advanced Engineering Programs Department
One Neumann Way
Cincinnati, Ohio 45215–6301

8. PERFORMING ORGANIZATION REPORT NUMBER

E–12363

9. SPONSORING/MONITORING AGENCY NAME(S) AND ADDRESS(ES)

National Aeronautics and Space Administration
John H. Glenn Research Center at Lewis Field
Cleveland, Ohio 44135–3191

10. SPONSORING/MONITORING AGENCY REPORT NUMBER

NASA CR—2000-210244
R99AEB169

11. SUPPLEMENTARY NOTES

P. Gliebe and H. Shin, GE Aircraft Engines, Advanced Engineering Programs Department, One Neumann Way, Cincinnati, Ohio 45215–6301; R. Mani, B. Mitchell, G. Ashford, S. Salamah, and S. Connell, GE-Corporate Research Development, P.O. Box 8, Schenectady, New York 12301. Project Manager, Dennis Huff, Structures and Acoustics Division, NASA Glenn Reseach Center, organization code 5940, (216) 433–3913.

12a. DISTRIBUTION/AVAILABILITY STATEMENT

Unclassified - Unlimited
Subject Categories: 71 and 07 Distribution: Nonstandard

This publication is available from the NASA Center for AeroSpace Information, (301) 621–0390.

12b. DISTRIBUTION CODE

13. ABSTRACT ***(Maximum 200 words)***

This report describes work performed on Contract NAS3–27720 AoI 13 as part of the NASA Advanced Subsonic Transport (AST) Noise Reduction Technology effort. Computer codes were developed to provide quantitative prediction, design, and analysis capability for several aircraft engine noise sources. The objective was to provide improved, physics-based tools for exploration of noise-reduction concepts and understanding of experimental results. Methods and codes focused on fan broadband and "buzz saw" noise and on low-emissions combustor noise and compliment work done by other contractors under the NASA AST program to develop methods and codes for fan harmonic tone noise and jet noise. The methods and codes developed and reported herein employ a wide range of approaches, from the strictly empirical to the completely computational, with some being semiempirical, analytical, and/or analytical/computational. Emphasis was on capturing the essential physics while still considering method or code utility as a practical design and analysis tool for everyday engineering use. Codes and prediction models were developed for: (1) an improved empirical correlation model for fan rotor exit flow mean and turbulence properties, for use in predicting broadband noise generated by rotor exit flow turbulence interaction with downstream stator vanes; (2) fan broadband noise models for rotor and stator/turbulence interaction sources including 3D effects, noncompact-source effects, directivity modeling, and extensions to the rotor supersonic tip-speed regime; (3) fan multiple-pure-tone in-duct sound pressure prediction methodology based on CFD analysis; and (4) low-emissions combustor prediction methodology and computer code based on CFD and actuator disk theory. In addition, the relative importance of dipole and quadrupole source mechanisms was studied using direct CFD source computation for a simple cascade/gust interaction problem, and an empirical combustor-noise correlation model was developed from engine acoustic test results. This work provided several insights on potential approaches to reducing aircraft engine noise. Code development is described in this report, and those insights are discussed.

14. SUBJECT TERMS

Turbofan engine noise; Aeroacoustics; Fan noise; Noise prediction; Combustion noise; Turbulence; Fan wakes; Subsonic jet noise

15. NUMBER OF PAGES

323

16. PRICE CODE

A14

17. SECURITY CLASSIFICATION OF REPORT	18. SECURITY CLASSIFICATION OF THIS PAGE	19. SECURITY CLASSIFICATION OF ABSTRACT	20. LIMITATION OF ABSTRACT
Unclassified	Unclassified	Unclassified	